THE UNIVERSITY OF HULL

THE PROGNOSTIC VALUE OF ADVANCED MR IN GLIOMAS

being a Thesis submitted for the Degree of

Doctor of Philosophy

in the University of Hull

by

Lawrence Kenning, BSc (Hons.), MSc

May 2014

Summary of Thesis submitted for PhD Degree

by

Lawrence Kenning

on

The Prognostic Value of Advanced MR in Gliomas

This work examines the prognostic value of advanced MR at selected time points during the early stages of treatment in glioma patients. In this thesis, serial imaging of glioma patients was conducted using diffusion tensor imaging (DTI), dynamic contrast enhanced (DCE) and dynamic susceptibility contrast (DSC) MRI. A methodology for the processing and registration of multiparametric MRI was developed in order to simultaneously sample whole tumour measurements of multiple MR parameters with the same volume of interest.

Differences between glioma grades were investigated using functional MR parameters and tested using Kruskal-Wallis tests. A 2-stage logistic regression model was developed to grade lesions from the preoperative MR, with the model retaining the apparent diffusion coefficient, radial diffusivity, anisotropic component of diffusion, vessel permeability and extravascular extracellular space parameters for glioma grading. A multi-echo single voxel spectroscopic sequence was independently investigated for the classification of gliomas into different grades.

From preoperative MR, progression-free survival was predicted using the multiparametric MR data. Individual parameters were investigated using Kaplan-Meier survival analysis, before Cox regression modelling was used for a multiparametric analysis. Radial diffusivity, spin–lattice relaxation rate and blood volume fraction calculated from the DTI and DCE MRI were retained in the final model.

MR parameter values were also investigated during the early stages of adjuvant treatment. Patients were scanned before and after chemoradiotherapy, with the change in MR parameters as well as the absolute values investigated for their prognostic information. Cox regression analysis was also performed for the adjuvant treatment imaging, with measures of the apparent diffusion coefficient, spin–lattice relaxation rate, vessel permeability and extravascular extracellular space, derived from the DTI and DCE datasets most predictive of progression-free survival.

In conclusion, this thesis demonstrates multiparametric MR of gliomas during the early stages of treatment contains useful prognostic information relating to grade and progression-free survival interval.

Acknowledgements

Firstly I would like to thank Yorkshire Cancer Research for the financial support I received during my studies, and the wider funding for the Centre for MR Investigations. I would also like to give a special thanks to all the patients who volunteered their time, and without whom this research would not have been possible.

I would like to express my gratitude to my two supervisors; Dr Martin Lowry for sharing his expertise on MR image analysis, IDL and spectroscopy, and Dr Martin Pickles for his guidance throughout this project, and expertise on medical statistics. I am most grateful and privileged they took the time to share their insights into MR imaging and spectroscopy with me. I would also like to thank Professor Lindsay Turnbull for making this project possible, and for her continued support throughout my studies.

I also thank Dr Martine Dujardin, Daniel Siddons and Julie Pounder for helping with study patients, and Dr Peter Gibbs for physics and I.T. support. Additionally I thank Dr Arfan Ahmed and Dr Victor Lazar, who were students at the Centre for MR Investigations for the useful discussions on a variety of MR topics. I would like to express my appreciation for the help and assistance given to me by all the other members of staff at the Centre for MR Investigations, and the Brain and CNS multidisciplinary team with whom I have had the pleasure of working.

Finally, I would also like thank my parents, Gary and Mary Kenning, my grandparents, Alex and Joan Kenning, and my girlfriend Emily Baillie for all of their support and encouragement throughout my studies.

Contents

1 A Background in Gliomas (Non-MR Literature)

1.1 Introduction

Gliomas are a type of intrinsic brain tumour, which present challenges for both imaging and therapeutics, ultimately resulting in poor outcomes for patients with the disease. With no routine screening tests available for brain tumours, patients normally present with advanced forms of the disease. Presentation can be seizures, headaches or sensory problems, but these symptoms are very non-specific and can be caused by a range of neurological conditions. Figure 1 shows the appearance of a high grade glioma. In this case, the lesion was unresectable due to the deep-seated location within the brain.

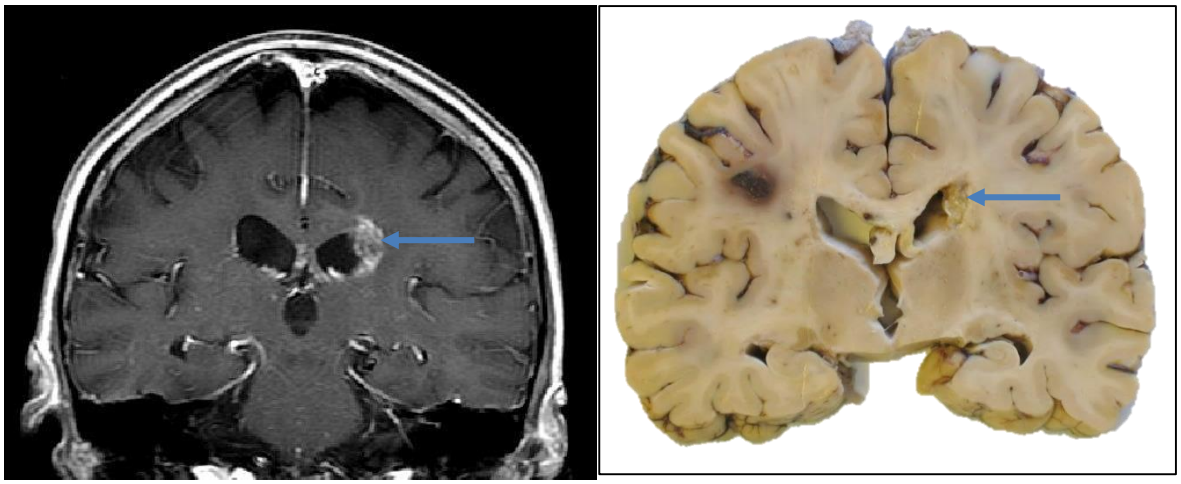

Figure 1 - Example images of a high grade glioma. Left shows the last available in vivo post-contrast T_1 weighted coronal spin echo slice through a section of the tumour. The post mortem specimen can be seen on the right with the patient having also sustained an area of haemorrhage between imaging and death. The patient underwent chemoradiotherapy and survived the disease for 539 days following initial biopsy.

1.2 Level of Incidence

In 2010, over 9000 new cases of CNS tumours were diagnosed in the United Kingdom (1). Unfortunately, it is not known what causes theses tumours to grow, however, as seen in Figure 2, the incidence of newly diagnosed CNS tumours increases with age.

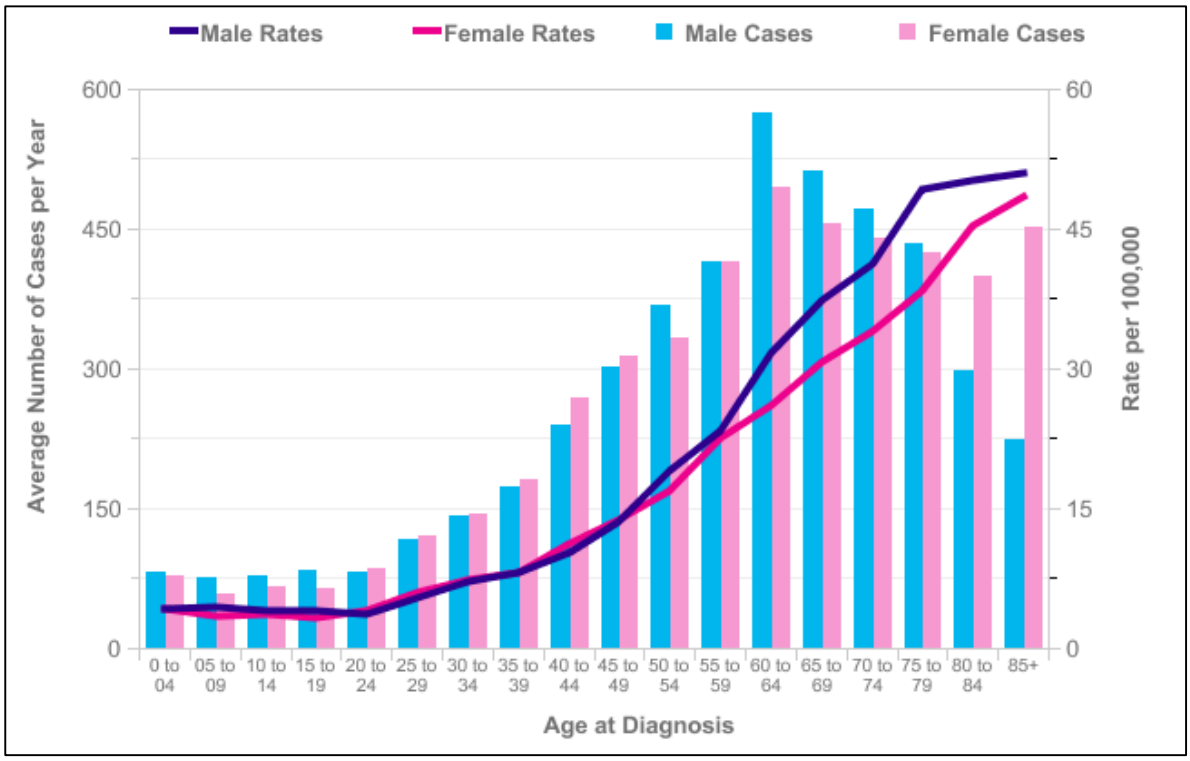

Figure 2- Reproduced from Cancer Research UK (1). This figure shows the average number of new central nervous system tumours per year per age group for men and women.

1.3 Prognosis

The prognosis for this cohort of cancer patients is extremely poor. In 2008, over 3500 people in the UK died from a brain or CNS related tumour (1). Furthermore, the number of deaths related to brain and CNS tumours has not reduced over the last 40 years. The 5 year survival rate appears to have only marginally increased since 1971 with women continuing to survive longer than men, though the fact remains that less than 20% of people live with a brain or CNS tumour more than 5 years (Figure 3).

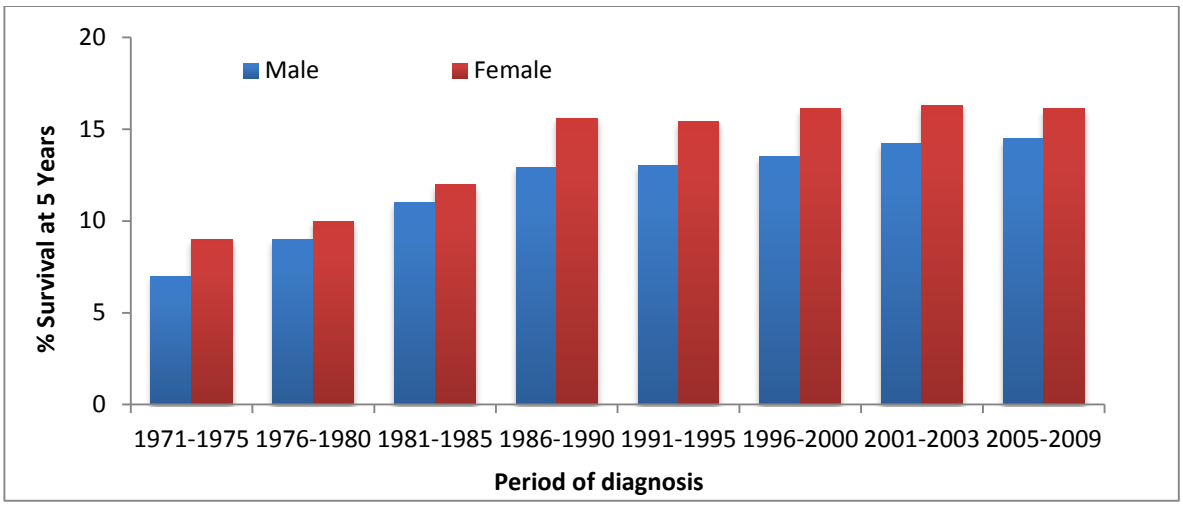

Figure 3 - Five-year age-standardised survival for brain cancer by sex for patients diagnosed in England and Wales, 1971-2009. The standardisation process adjusts the data for effects of age. Reproduced from Cancer Research UK (1).

The late presentation of this disease means that key structures in the brain are often infiltrated or destroyed by the tumour, reducing the likelihood of a complete resection and subsequent beneficial outcome (2, 3). Given that the incidence of brain tumours increases with age, other age related co-morbidities may also play a role in the poor prognosis associated with this disease due to the aggressive treatment regimens required to control the disease.

An important randomised phase III study in 2009 (4) comparing radiotherapy versus chemoradiotherapy in glioblastoma multiforme patients reported median survival times of 12.1 (11·2–13·0, 95% CI) and 14.6 (13·2–16·8, 95% CI) months for radiotherapy and chemoradiotherapy respectively. Two year survival was also increased from 10.9% (7·6–14·8%) to 27.2% (22·2–32·5%) when using temozolomide in conjunction with radiotherapy. For patients treated with chemoradiotherapy, the extent of resection correlated with the median survival time. Biopsy only yielded a median survival of only 9.4 (7·5–13·6, 95% CI) months compared to partial resection 13.5 (11·9–16·4, 95% CI) months and complete resection, 18.8 (16·4–22·9, 95% CI) months. A similar trend was reported for the radiotherapy cohort with shorter median survivals reported [7·8 (6·4–10·6, 95% CI), 11·7 (9·7–13·1, 95% CI), 14·2 (12·1–16·1, 95% CI) in months] for biopsy, partial

resection and complete resection respectively. Additional factors such as cell-type (5, 6), proliferation (7) and genetic mutations (8) affect the prognosis for the patient, and are discussed later in this chapter.

1.4 Glioma Cell Types

The glial cell from which a neoplasm originates, affects the growth characteristics, response to treatment and overall prognosis of the tumour. This section examines the two macroglia (groups of neuroglial cells) that are found to give rise to the most common gliomas.

1.4.1 Glial Cells

The role of glial cells (Figure 4) is to protect and support the neurons in the brain with the functions of these cells including supplying oxygen and nutrients, insulating neurons to prevent signal interference between them and the removal of dead neurons.

1.4.1.1 Astrocytes

The most abundant macroglia are astrocytes, which are well connected to the blood supply and form the basis of the blood brain barrier (BBB). Astrocytes can be further split into two subtypes, fibrous and protoplasmic. Fibrous astrocytes are predominantly found in white matter and have long thin dendritic branches. Conversely, protoplasmic astrocytes are shorter and thicker, and mainly existing in grey matter. Astrocytes can give rise to astrocytomas, which are the most common type of intrinsic brain tumour, often advancing to glioblastoma multiforme.

1.4.1.2 Oligodendrocytes

Oligodendrocytes are the other common type of macroglia. These cells participate in the formation of myelin sheaths which protect the neuronal cells. The myelin sheath insulates the nervous cells allowing small electrical signals to be more efficiently propagated along the neurons. Oligodendrocytes give rise to oligodendrogliomas which are a common differential for low grade astrocytic tumours.

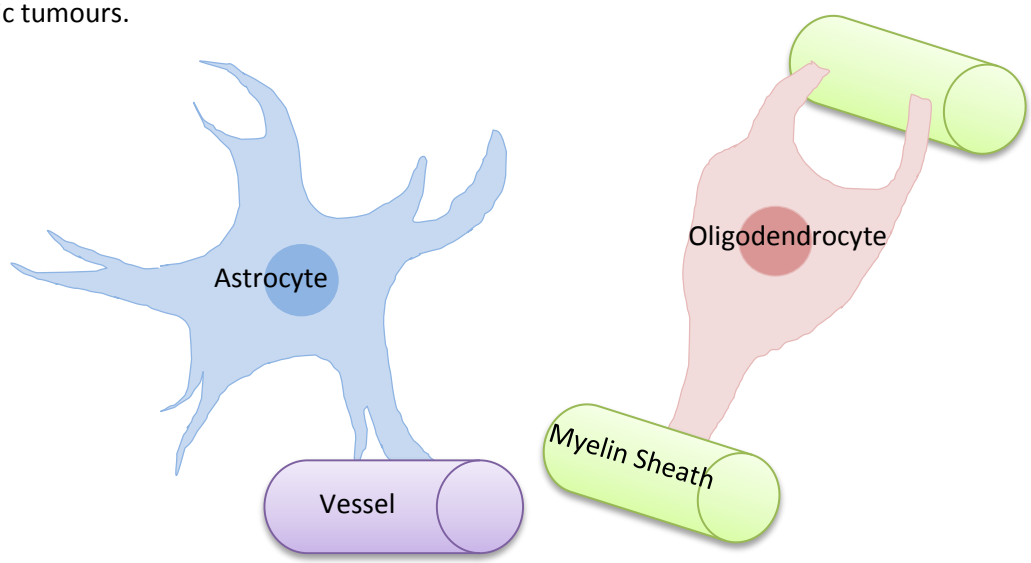

Figure 4 - Representative drawings of both an astrocyte and an oligodendrocyte. The astrocyctic cell connects to to blood vessels in order to transport oxygen and nutrients whilst the oligodendrocyte connects to myelin sheaths ensuring the neuron is well protected and can efficiently propagate a signal.

1.5 WHO Tumour Grading

Gliomas are graded by the World Health Organisation (WHO) on a scale of I-IV determined by how normal the cells look (6). The more abnormal the cells look, the higher the grade. In the brain, a WHO grade I tumour would be classed as the slowest growing type of cells, and considered the lowest risk; whereas a WHO grade III or IV, depending on the cell type, would be classed as an aggressive fast growing tumour. Tumour cells are assessed on the cell pleomorphism, mitotic activity, vascular proliferation and the amount of necrosis. The grade of tumour determines the level of treatment. Gliomas (Table 1) are often divided into two groups; low grade, which are grades I and II, and high grade which are grades III and IV. This is based on their histological appearance and behaviour. Distinguishing imaging features believed to separate a high grade lesion from a lower grade diagnosis include the presence of contrast-induced enhancement, heterogeneous appearance, large amounts of oedema and often a cystic component (Figure 5).

Table 1 - Summary table of recognised glioma subtypes and the respective WHO grades reproduced from (6).

Astrocytic Tumours	**I**	**II**	**III**	**IV**
Subependymal giant cell astrocytoma	**X**			
Pilocystic astrocytoma	**X**			
Pilomyxoid astrocytoma		**X**		
Diffuse astrocytoma		**X**		
Pleomorphic xanthoastrocytoma		**X**		
Anaplastic astrocytoma			**X**	
Glioblastoma				**X**
Giant cell glioblastoma				**X**
Gliosarcoma				**X**

Oligodendroglial Tumours	**I**	**II**	**III**	**IV**
Oligodendroglioma		**X**		
Anaplastic oligodendroglioma			**X**	

Oligoastrocytic Tumours	**I**	**II**	**III**	**IV**
Oligoastrocytoma		**X**		
Anaplastic oligoastrocytoma			**X**	

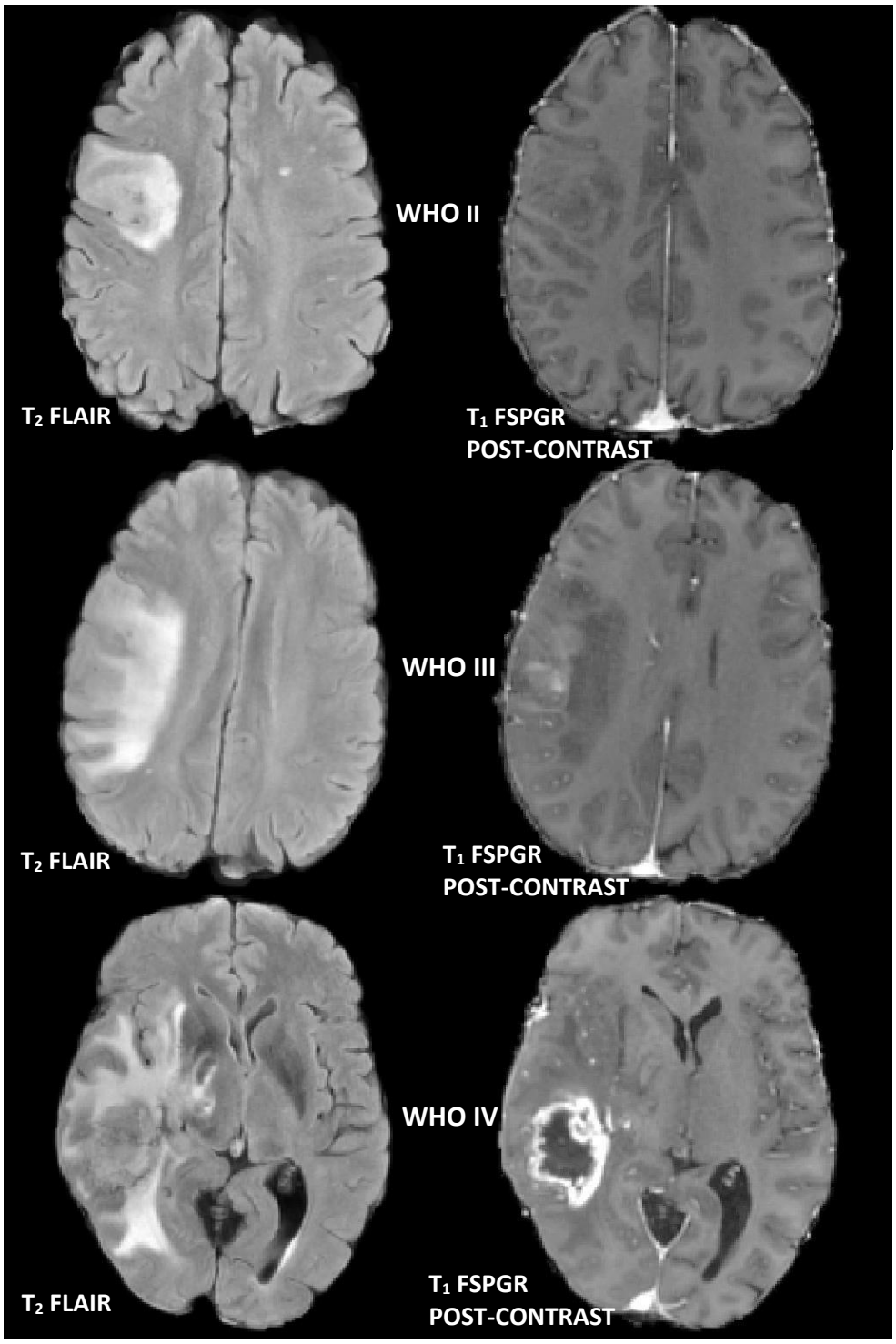

Figure 5 - Example grade II, III and IV gliomas from top to bottom respectively.T_2 weighted FLAIR imaging can be seen in the left column while post-contrast T_1 weighted FSPGR can be seen in the right. Note the increasing amounts of oedema with high grade lesions as well as the presence of enhancement, and the formation of a necrotic core in the grade IV lesion.

1.6 Histopathological Staining of Gliomas

The diagnosis of glioma is made at a cellular level by a neuropathologist, and is considered the gold standard against which other diagnostic modalities are measured. The limitation of this technique for diagnosis is that it requires a sufficient volume of malignant tissue within the sample, and assumes the tissue sample is representative of the whole tumour. This is not always the case in heterogeneous tumours such as glioblastoma multiforme.

1.6.1.1 Haematoxylin and eosin stain (H&E Staining)

H&E Staining is a general purpose staining used for the tissue diagnosis of lesions. From the staining, cell atypia, pleomorphism, vascular proliferation and the amount of necrosis can be commented on by a neuropathologist. A sample from a glioblastoma multiforme can be seen in Figure 6.

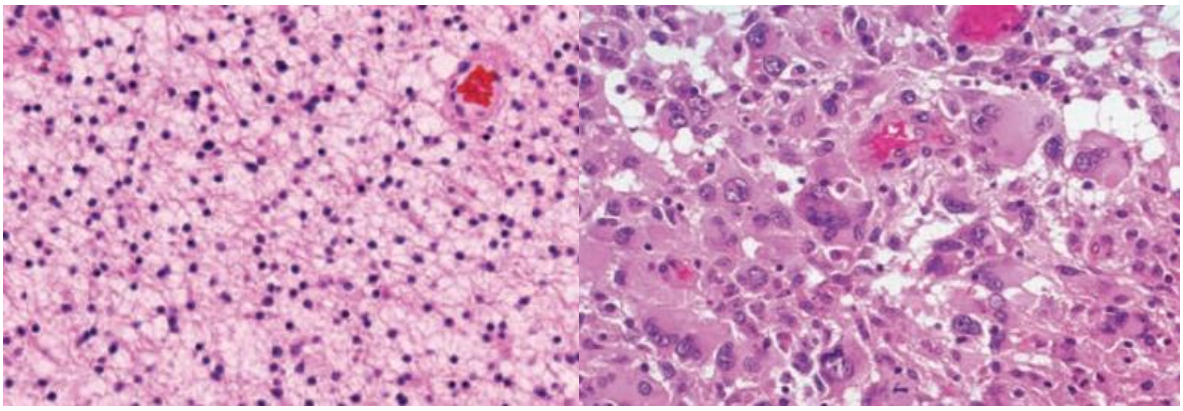

Figure 6 – Left - H&E staining from a diffuse astrocytoma with uniform appearance. Right - glioblastoma multiforme showing increased levels of anaplasia and irregular cell formation. Reproduced from the WHO classification of tumours in the CNS (6).

1.6.1.2 Antigen Ki-67/ MIB-1

Ki-67 and MIB-1 are markers for cell proliferation. Furthermore it is possible to observe Ki-67 and MIB-1 through all parts of the cell cycle except for the rest state. In low grade lesions small amounts of mitotic activity have been reported (Figure 7) while in high grade lesions the amount of mitotic actively is vastly increased (9). Following this, a study investigating the correlation between Ki-67

and disease related survival found that tumours with lower Ki-67 values had a higher median survival time (7).

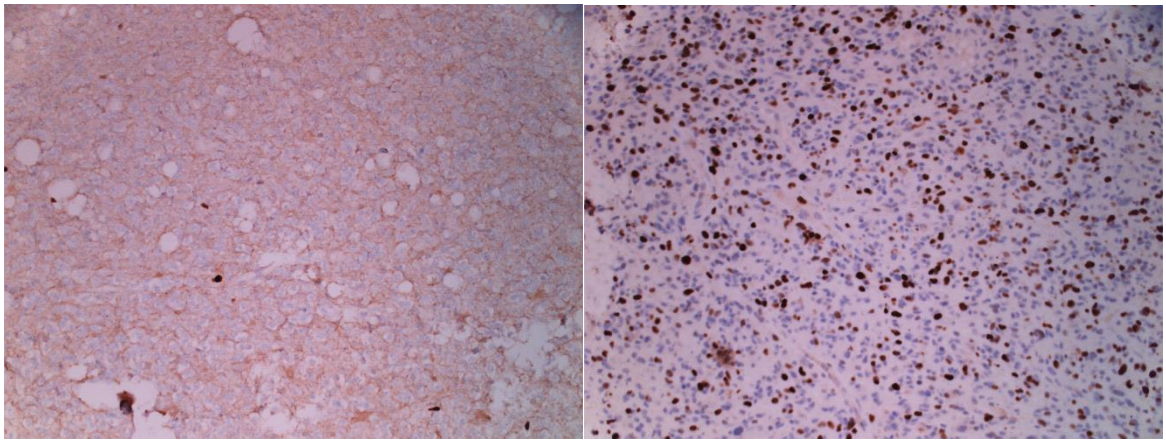

Figure 7 - Low mitotic activity (dark stained cells) in a low grade glioma (Left). High levels of mitotic activity on the MIB-1 staining in a high grade glioma (Right). Produced from this institution.

1.6.1.3 Glial fibrillary acidic protein *(GFAP)*

This protein is specific to astrocytes, and is produced as a reaction to disease or injury in the brain (Figure 8). It can be used to differentiate glioblastoma multiforme from metastases and lower grade lesions (10).

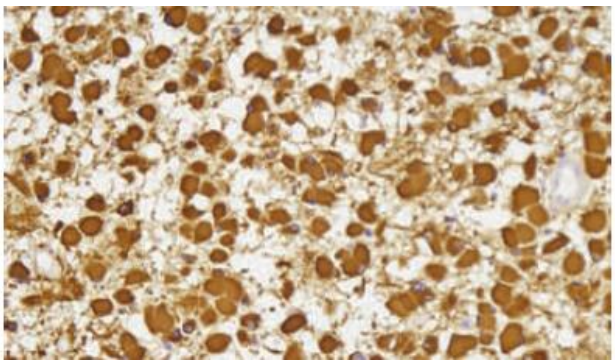

Figure 8 - The dark cells show the expression of GFAP. Reproduced from the WHO classification of tumours in the CNS (6).

1.7 Glioma Development and Growth

Each type of glioma as classified by the World Health Organisation, has a different set of genetic mutations which change with grade. The environment in which the tumour exists, and the genetic mutations present, controls the cell growth. The growth rate of a tumour can be simplified into two components: cell proliferation and cell loss. Factors that affect tumour growth include the amount of apoptosis and the cell cycle time.

Specific mutations are also more likely to occur in certain pathologies. Figure 10 shows the percentages of grade II pathologies with two known mutations (TP53 and loss of heterozygosity for 1p and/or 19q). Whilst there is overlap between groups, there are clear differences between astrocytomas and oligodendrogliomas at grade II. Different pathologies of the same grade can also result in different median survival times. In Figure 11, all the lesions in the study (5) were WHO grade II. However, the median survival times showed tumours with an oligodendroglial component to have a more favourable prognosis.

1.7.1.1 Hypoxia inducible factor (HIF-1α)

HIF-1α is a constitutively produced protein that acts as a potent activator of angiogenesis (11) which may explain the abnormal vasculature seen in tumours (Figure 9), which in turn can lead to a cycle of hypoxia and further HIF-1α up regulation. Activation of the HIF-1α pathway can also explain the extensive vascular hyperplasia seen in glioblastomas (11). Under normal conditions HIF-1α is a microenvironment regulator and controls the invading properties of the cell. A reduction in HIF-1α has been shown to reduce cell migration in gliomas.

1.7.1.2 Vascular Endothelial Growth Factor (VEGF)

VEGF is responsible for angiogenesis and ensures tissues in the body receive enough blood to survive. Its increased production in tumours leads to neo-vascularity which is essential for malignant

tumour growth. Angiogenesis caused by a neoplasm leads to pathological vessels with increased permeability. Studies have shown a correlation between tumour blood volume and malignancy (12).

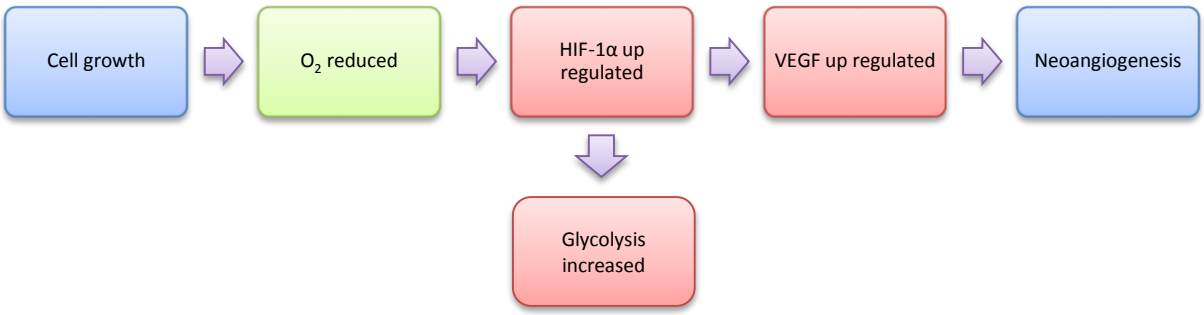

Figure 9 - Schematic showing how HIF-1α is up regulated and how this can lead to neoangiogenesis

1.7.1.3 Epidermal Growth Factor Receptor (EGFR)

EGFR is responsible for controlling cell proliferation. Once mutated, cell growth is no longer regulated allowing tumours to grow rapidly. This mutation is often is observed in the presence of the 10q deletion (13).

1.7.1.4 Tumour Suppressor Gene P53 (TP53)

TP53 is a tumour suppressor gene that prevents cells with damaged DNA (potentially cancerous cells) from proliferating. Mutated/deleted TP53 genes have been shown to be involved in initiation and development of astrocytomas.

1.7.1.5 Loss of heterozygosity (LOH)

The deletion of genes can be associated with differing types of CNS tumours. One of the most common and well described LOH cases is the 1p/19q deletion observed in oligodendrogliomas. Tumours with the 1p19q deletion have been found to be more chemo-sensitive and have an improved prognosis (5). LOH on chromosome 10q is a frequent mutation for both primary and secondary glioblastomas (14).

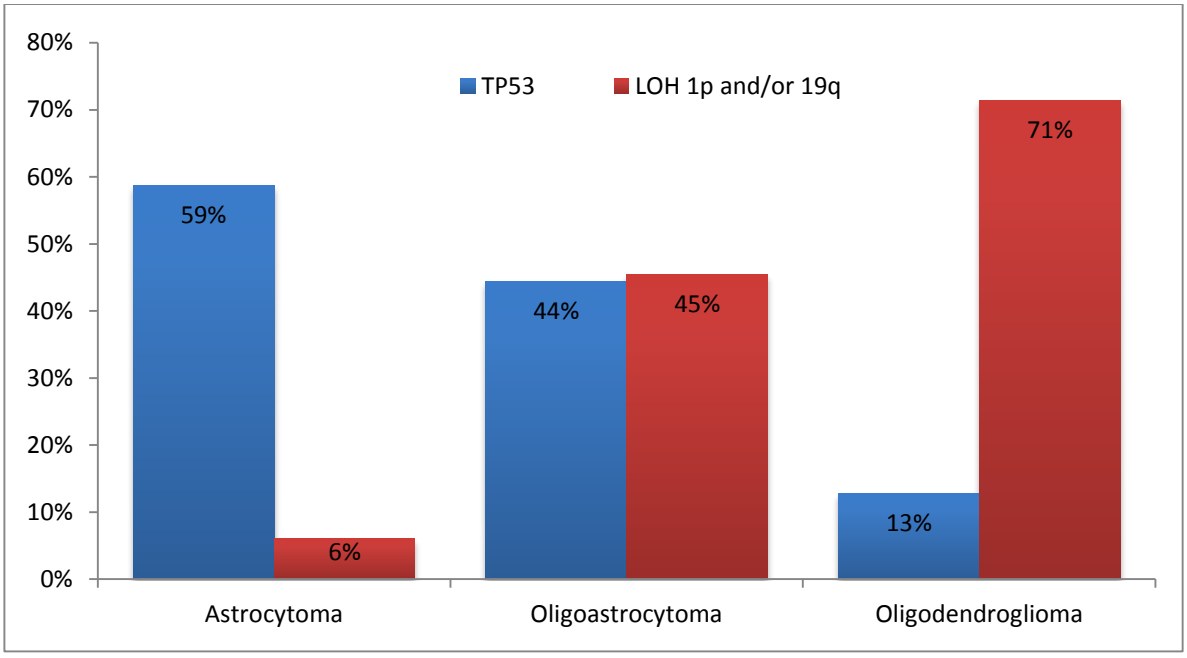

Figure 10 –An overview of genetic mutations measured from 122 WHO grade II gliomas. Whilst there is overlap between groups, it can be seen that mutated TP53 is more commonly seen in astrocytic tumours whilst a loss of heterozygosity (LOH) for 1p and/or 19q means the tumour is more likely to be an oligodendroglioma. Graph generated from data by Okamoto et al. (5)

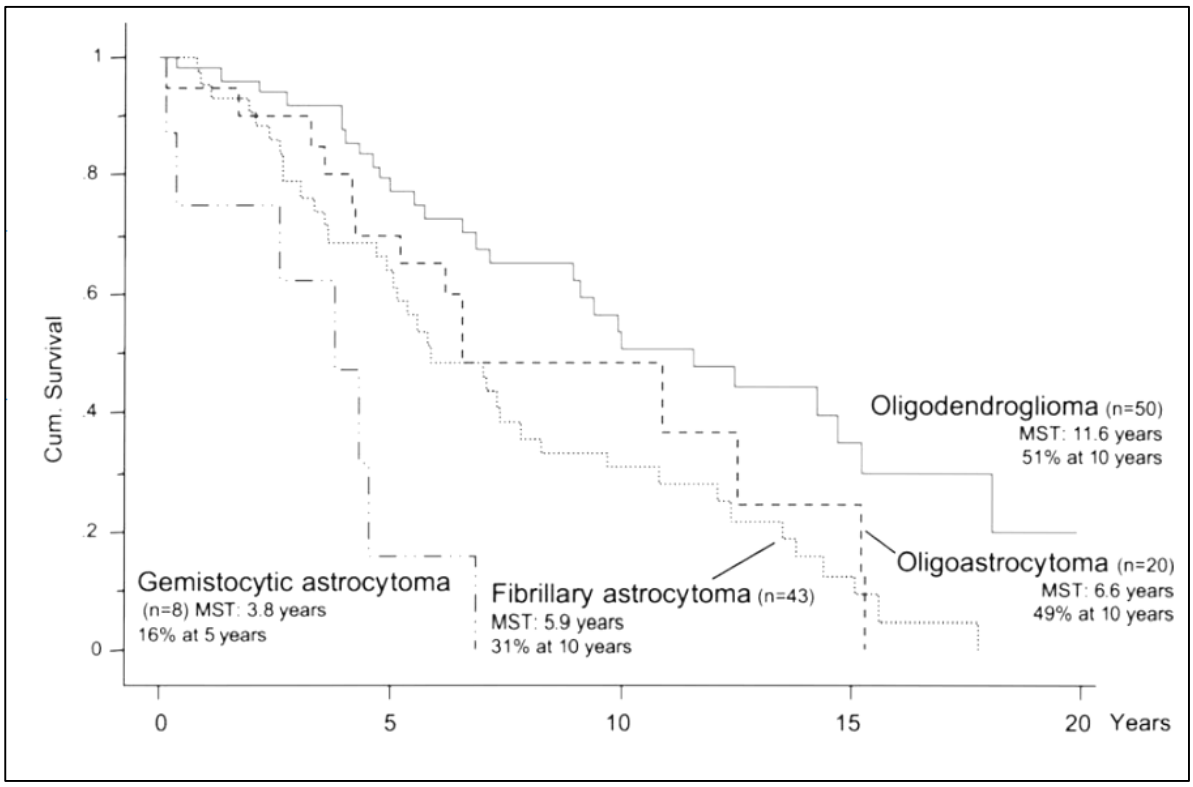

Figure 11 - Differences in median survival time can be seen between different pathologies of the same WHO grade. Patients with an oligodendroglial component had a higher median survival than those with just an astrocytic component. Reproduced from (5).

1.7.1.6 Isocitrate dehydrogenase (IDH)

The IDH mutation refers to three enzymes, IDH1, IDH2 and IDH3 respectively. The first two enzymes are particularly relevant to gliomas, with the finding that in low grade gliomas, 65-90% contain a mutation of one of the IDH enzymes (15) and up to 12% of glioblastomas carry a mutated IDH1 enzyme. The IDH1 mutation has also been found in secondary glioblastoma following low grade transformation (16, 17). Mutant IDH1 positive patients have been shown to have a favourable prognosis (8, 17, 18). It is thought that the loss of normal IDH1 and IDH2 activity may actually stabilise HIF-1α within the cell. IDH1 has been shown to play a unique role in the pathogenesis of gliomas. Both IDH1 and IDH2 are responsible for converting $NADP^+$ to NADPH which is linked to the suppression of apoptosis.

1.7.1.7 O^6-methylguanine DNA methyltransferase (MGMT)

MGMT is a gene located at chromosomal position 10q26 and is responsible for encoding a DNA repair enzyme that can negate the effects of alkylating chemotherapeutic agents such as temozolomide. If the MGMT gene is active it can repair damage to the DNA quickly so the tumour cells are able to continue reproducing. Malignant brain tumours may have the MGMT gene inactivated due to methylation of its promoter region. Current research (19) suggests methylated MGMT will lead to a better treatment response from chemotherapy as the tumour cells will have no way of repairing the DNA damage originally caused by the alkylating agent. In gliomas MGMT methylation can be viewed as a favourable prognostic marker to both radiotherapy and chemotherapy (8). Pseudoprogression has been observed more frequently in MGMT methylated tumours following chemoradiotherapy, but this patient group have a longer median survival (4, 20, 21).

1.8 Treatment Options

1.8.1 Surgery

When appropriate, surgery is offered to the patient depending on their performance score, co-morbidities, tumour appearance and position of tumour within the brain. The extent of surgery ranges from a stereotactic biopsy, used for tissue sampling, to a full resection which is optimal.

Stereotactic biopsy is preferable for gliomas situated in eloquent areas when a histological diagnosis is required for further treatment. This could be for a low grade glioma possibly undergoing transformation to a higher grade, or high grade glioma where resection carries a high risk of morbidity. Stereotactic biopsies rely on imaging techniques, primarily MRI, to guide the surgeon to the lesion. This is normally images from a post-contrast, high resolution T_1-weighted sequence.

A more aggressive surgical option is a partial resection in which surgery is done to reduce the mass effect of the tumour, helping to reduce the intracranial pressure for the patient as well as any midline shift. This type of surgery is often carried out to improve the patient's quality of life but is not a curative surgery. Tumours involved in key structures such as the ventricles or crossing the midline are examples of when a partial resection may be preferential. The percentage of resection is dependent on the likelihood of creating a new morbidity. An example of this could be the resection of a lesion located near the motor strip where a complete resection could cause permanent limb weakness.

A complete resection is possible for patients who are suitable and the tumour can easily be located for excision. A lesion close to the skull, may be seen as favourable indicator for a complete resection. Studies have also shown that glioma survival is directly linked to the extent of resection so patients who have complete resection have a more favourable prognosis (2, 3).

1.8.2 Radiotherapy

Radiotherapy is used for both palliative and curative treatments, and relies on ionising radiation to try and treat malignant neoplasms. It depends on calculating the correct dose of radiation for the size of the tumour and delivering it in an accurate manner whilst reducing the dose to the surrounding tissue. The aims of radiotherapy are to treat tumours while maintaining a sufficiently high quality of life for the patient and potentially prolonging their survival time.

This treatment is targeted at the DNA of rapidly dividing cancer cells, since this is when they are most susceptible to damage. Radiation damage to the DNA subsequently means those cells are unable to divide and eventually leads to cell death. Normally, x-rays are used as the source of ionising radiation.

Currently radiotherapy planning in this NHS trust is done using CT several weeks post-surgery, but the use of postoperative MR fusion with the CT is becoming more preferable given the superior soft tissue contrast provided by the MR. As with surgery, eloquent areas must be avoided to reduce the risk of a deficit in quality of life. These areas include the brain stem and optic nerves.

Depending on the grade of the tumour, up to 60 Greys of radiation may be given to a single lesion. This is often fractionated to allow the surrounding tissue to repair/recover from a reduced dose. Typically this is split into 30 fractions which equates to 5 days a week over a total of 6 weeks.

1.8.3 Chemotherapy

Chemotherapeutic agents actively target proliferating cells; however, there is a reduced effect against low-proliferating cells which is why only high grade tumours are currently treated with chemotherapy. The effectiveness of chemotherapeutic agents is also dependant on the cells position in the cell cycle meaning that phase specific agents need to be delivered at the correct interval.

Chemotherapy agents are often used in combination, in an attempt to kill cancerous cells throughout the entire cell cycle. Advantages of combination chemotherapy include actively treating cells through several stages of the cell cycle, reducing the risk of cell resistance to both agents and additive interactions with certain combinations of drugs. The effectiveness of chemotherapy is reduced with the increase of tumour size due to the likelihood of agent resistant cells, probability of metastatic spread and the distance the drug has to travel from the vasculature.

Temozolomide (Temodal®) is the first line chemotherapeutic agent to treat gliomas. It is taken orally meaning the patient does not have to travel to hospital to receive chemotherapy once radiotherapy is complete. An important feature of temozolomide is that it can radio-sensitise some gliomas increasing median survival times (4). Some tumours are more resistant to chemotherapy and can initiate DNA repair, however, temozolomide alkylates the DNA of the tumour, damaging it and initiating cell death. This alkylating effect also benefits radiotherapy which also targets the tumour DNA to disrupt the cell cycle.

Current practice requires a histological diagnosis of high grade glioma in order to prescribe chemotherapeutic agents. While the dose of radiotherapy may be limited per patient chemotherapy can be prescribed for indefinite amounts of time provided the patient remains sufficiently well.

1.8.4 Additional Therapeutic Approaches

With disease progression commonly occurring following standard treatment regimes, novel treatments are also considered in some NHS Trusts. Given these treatments are still unproven; the use of such therapeutics is limited by strict guidelines. Novel treatments also often have a very high financial cost associated with them, reflecting the extensive research and development costs needed to bring a new drug into the clinic. Adjuvant therapeutics also have added complications when interpreting imaging, with both pseudo-progression and pseudo-response being potential imaging complications of many treatments (22).

1.8.4.1 Carmustine Wafers (Gliadel®)

Newer approaches to drug delivery include dissolvable chemotherapy wafers which are inserted into the tumour cavity at the end of surgery (23). The guidelines for such treatments are restrictive though at present, with an intra-operative diagnosis of glioblastoma multiforme required and at least 90% of the tumour resected along with the ventricles remaining intact. The initial trial showed significantly better survival for patients with carmustine wafers over those with placebo wafers (24).

1.8.4.2 Bevacizumab (Avastin®)

Bevacizumab is a monoclonal antibody which attempts to block neoangiogenesis. It does this by binding to vascular endothelial growth factor A (VEGF) which is particularly prominent in tumours. VEGF is responsible for promoting cell migration and endothelial cell growth and is involved in inhibiting apoptosis. Whilst the presence of contrast enhancement can appear reduced due to the maturing of leaky vessels following the administration of bevacizumab (25), the underlying tumour can often progress and remain undetected using conventional imaging.

1.8.5 Typical Treatment Pathway for a High Grade Glioma

Treatment varies according to the grade, genetic status and location of the tumour. However, the current best standard (4) for a high grade glioma can be seen below (Figure 12):

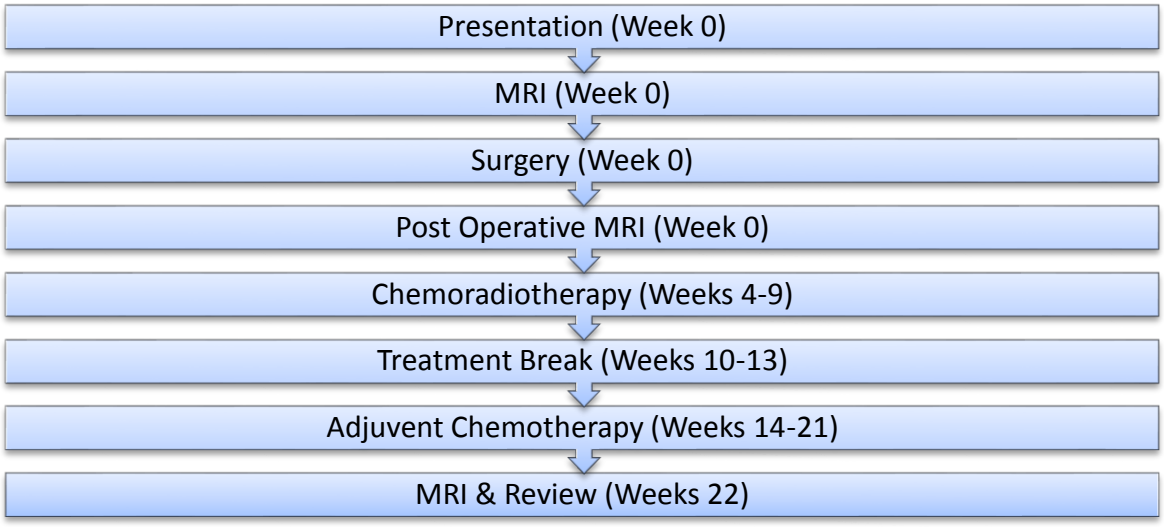

Figure 12 - Typical treatment pathway for a high grade glioma during the first 6 months from diagnosis.

1.9 Tumour Regrowth

One of the main problems associated with malignant brain tumours is that the boundaries of the lesion are difficult to detect/visualise both with MR imaging and during surgery. Since the brain is an eloquent organ, maximum safe resection margins as sometimes achieved with other organs are simply not possible giving rise to the hypothesis that gliomas often reoccur from the residual disease often not visible to surgeons. One way to visualise the problem is as an iceberg (26). Surgeons and radiologists may only see the top of iceberg (tumour) due to the increased cell density. However, reoccurrence only takes a single remaining tumour cell to fully regrow. Given gliomas potential to extend beyond the detectable margin as defined by morphological imaging (larger iceberg base under the water), the disease normally reoccurs. Hence, radiotherapy uses extended margins (2-3cm) to incorporate as much of the residual disease in the radiation field as possible.

1.10 Cell Death

There are different mechanisms for cell death which are thought to be important for determining a tumour's response to treatment. Unfortunately, so far morphological imaging techniques have been unable to differentiate these.

1.10.1.1 Necrosis - Premature cell death

Necrosis is where many cells simultaneously die due to one or more processes such as hypoxia, energy depletion and inflammatory response. It is by this mechanism that radiotherapy works.

1.10.1.2 Apoptosis - Programmed cell death

Apoptosis differs from necrosis as it is a programmed death of cells (27). Apoptosis is considered the primary cause of cell death in gliomas and is associated normally with a high proliferation rate. The apoptotic index can be found to increase with anaplasia. A lack of apoptosis may be linked to tumour development and growth.

1.10.1.3 Autophagy – Internal cell breakdown

The mechanism by which autophagy acts is not fully understood but it is recognised for its importance in maintaining the balance between cell growth and death. It is known to breakdown intracellular components to prioritise and distribute energy throughout the cell. Autophagy is seen to be increased when cells are placed under nutritional stress and non-vital components of the cell are absorbed and broken down by lysosomes (28). Using the same principles, autophagy is also used in the cell repair as it removes damaged organelles from the cell and redistributes the nutrients.

1.11 Tumour Biochemistry

1.11.1 Spectroscopically Visible Metabolites in Brain Pathologies

Due to the lower concentrations of the metabolites compared to water in vivo, magnetic resonance spectroscopy is generally regarded as having very low sensitivity. Only metabolites with concentrations of millimolar or above can be seen in a spectrum.

1.11.1.1 Choline (3.24ppm)

Choline is related to membrane synthesis and degradation and consists of three contributing molecules, free choline, phosphocholine (PC) and glycerophosphocholine (GPC), however, at 3.0T and below, it is not possible to resolve the different types of choline. Studies have suggested levels of choline become elevated when there is increased membrane turnover (29), for instance in tumour cases where cell growth is high, suggesting choline may be an indicator of cellularity. It has also been reported that an increase in phosphocholine (PC) compared to glycerophosphocholine (GPC) appears to be an indicator of malignant transformation when using phosphorous spectroscopy (30, 31). More recent work suggests that GPC was more common in the non-enhancing portion of astrocytic tumours regardless of grade (32).

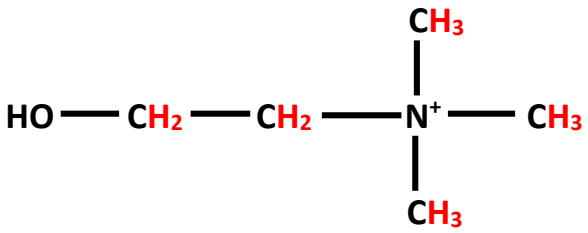

Figure 13 – Free choline molecule. The red hydrogen atoms denote the protons which are MR visible in a 1H spectrum. The methyl components (CH_3) generate a resonance at 3.24ppm while the methylene molecules (CH_2) generate peaks at 3.56ppm and 4.07ppm.

1.11.1.2 Creatine (3.06ppm)

The creatine (Cr) peaks are found at 3.06ppm and 3.91ppm which are a composite of creatine and phosphocreatine. Both metabolites are involved in cellular energy homeostasis, acting as a buffer for adenosine triphosphate (ATP). The second peak generated from creatine at 3.91ppm can be observed provided water suppression is effective and linewidths are sufficiently narrow. Malignant tumours with high metabolic activity deplete the energy stores leading to reduced creatine levels. It has been reported that creatine also appears reduced in cerebral ischemia (33).

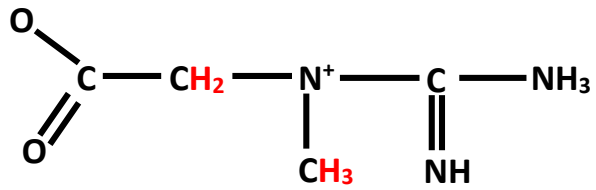

Figure 14 - Creatine molecule. The red hydrogen atoms denote the protons which are MR visible in a 1H spectrum. The methyl component (CH_3) generates a resonance at 3.06ppm while the methylene molecule (CH_2) produces a resonance at 3.93ppm.

1.11.1.3 N-acetylaspartate (2.02ppm)

N-acetylaspartate (NAA) is the largest resonance observed in spectra from normal appearing brain. Using immunocytochemical staining, it has been shown that NAA is mainly restricted to dendrites, axons and neurons and is traditionally employed as a neuronal marker. Consequently, the highest NAA concentrations can be found in white matter. NAA levels have also been found to consistently decrease in diseases affecting neuronal function loss such as brain tumours and multiple sclerosis (34). However, it is worth noting that changes in NAA concentrations are very non-specific and so changes in the levels of NAA alone are often non-diagnostic but once combined with other sequences can add to the diagnostic confidence.

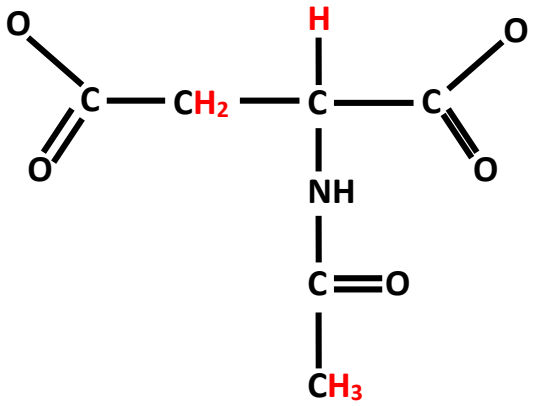

Figure 15 - N-acetylaspartate molecule. The red hydrogen atoms denote the protons which are MR visible in a 1H spectrum. The methyl component (CH_3) produces a resonance at 2.02ppm while the methylene moiety (aspartate group) (CH_2) generates a peak at 2.52ppm.

1.11.1.4 Lactate (1.33ppm)

Lactate (Lac) produces a doublet that resonates at 1.33ppm and in healthy brains is very hard to detect due to its low concentration. However, in some cases where oxygen is restricted (ischemia and hypoxia), the Krebs cycles cannot operate and instead of glucose being converted into CO_2, it is metabolised into lactate (33). In tumours, this is thought to be untrue with the Warburg effect (35) hypothesising that tumours increase glycolysis, producing lactate even in the presence of oxygen. Although the presence of lactate is non diagnostic, it can be an indicator of disease in the brain. At an echo time of 144ms it can be seen in the anti-phase position allowing distinction from lipid which shares the same chemical shift difference (Figure 17).

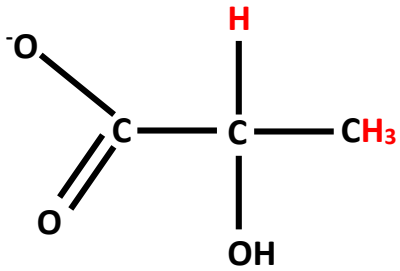

Figure 16 - Lactate molecule. The red hydrogen atoms denote the protons which are MR visible in a 1H spectrum. The methyl component (CH_3) produces a doublet at 1.33ppm while the lone proton generates a quadruplet at 4.12ppm.

The reason a doublet is produced rather than the single peak resonances of other metabolites found in the brain, is due to the weak interactions between the lone hydrogen and the methyl group and subsequently the two locations where the hydrogen appears on a spectrum. The lone hydrogen is affected by the other three hydrogen atoms which are part of the CH_3 group and subsequently is affected by the magnetic field produced by each of them. The number of peaks produced is equal to one more than the number of atoms seen. This means the single hydrogen atom produces a quartet (four peaks) which is observed at 4.12ppm with peak heights of 1:2:2:1. The reverse happens for the CH_3 group which interacts with the lone hydrogen and when combined with the plus one due to quantum reasons, it becomes viewed as two peaks (a doublet), this time at 1.33ppm. The two MR visible components of lactate are AX coupled, describing how influential they are on each other. The 1.33ppm peak is labelled A while the distant 4.12ppm peak is labelled X as a measure of the size of the coupling.

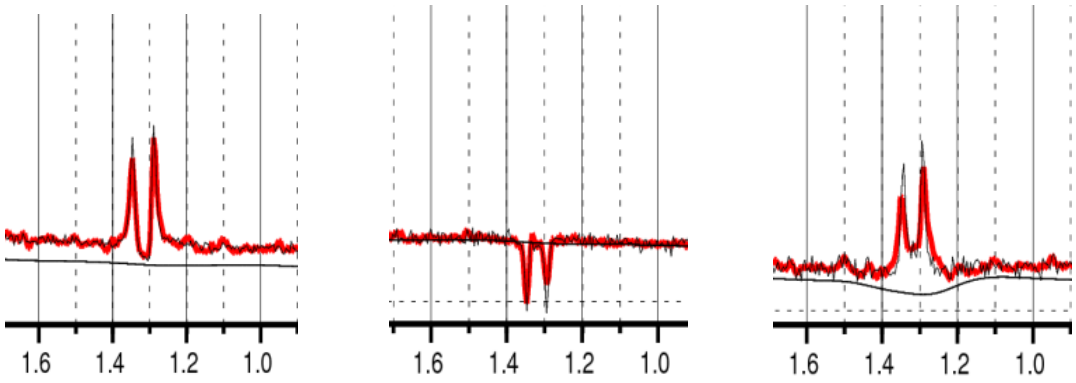

Figure 17 - Evolution of lactate signal with increasing echo time. Left - TE=35ms, Middle - TE=144ms, Right - TE=288ms

1.11.1.5 Lipid (5.3, 4.1, 2.0, 1.3 & 0.9ppm)

Lipid molecules are associated with an increase in membrane turnover, and only MR visible, if rapidly tumbling, hence the reason that they are not usually visible in normal brain tissue. Small concentrations of lipid may be visible at short echo times under normal concentrations due the short T_2 relaxation times of the molecule, however, at high enough concentrations, they become visible at longer echo times. The key peaks for *in vivo* spectroscopy are the 0.9 and 1.3ppm resonances, with the 1.3ppm peak area nominally proportional to the $(CH_2)_n$ chain length.

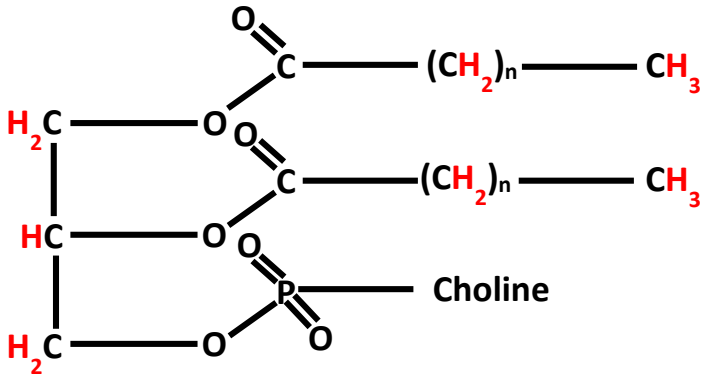

Figure 18 – Phosphatidylcholine molecule. The red hydrogen atoms denote the protons which are MR visible in a 1H spectrum. The methyl (CH_3) component produces a peak at 0.9ppm peak while the 1.3ppm peak arises from the methylene (CH_2) chains.

Lipid detected using proton spectroscopy has been shown to be the result of cell necrosis (36, 37) and importantly, the amount of lipid observed is proportional to the extent of necrosis (38) in the tissue. The presence of detectable lipid concentrations preoperatively has also been shown to correlate with higher grade tumour and poorer survival rates (39).

1.11.1.6 Myo-inositol (3.55ppm)

Myo-inositol (mI) can be easily seen in a spectrum if a short TE is used, and is associated with a range of different diseases, though it is thought to be a glial cell marker. Levels of mI are found to drop during stroke and rise during Alzheimer's disease. Research carried out shows a trend toward lower mI levels in anaplastic astrocytomas and glioblastoma multiforme compared with those of low-grade astrocytomas (40). The role of mI remains uncertain though it has been proposed that myo-inositol/sodium co-transporter activity is thought to help regulate cell osmosis.

1.11.1.7 Glutamate and glutamine (2.35 & 2.45ppm)

Glutamate (Glu) and glutamine (Gln) are the most abundant amino acids in the brain but due to their similar chemical shift, they are hard to distinguish. This is due to the strong AB coupling they share, and causes an overlap of the peaks at lower field strengths (<3.0T), and so are grouped together under the title of Glx.

1.11.1.8 Alanine (1.46ppm)

Like lactate, alanine forms a doublet, which can be seen at 1.46ppm. This metabolite can only be seen when present at elevated levels, which occurs as a result of increased glycolysis (41) for example in meningiomas.

1.11.1.9 2-Hydroxyglutarate (2.25ppm)

This metabolite is been found to be associated with the IDH1 mutation exclusively found in gliomas and more specifically LGG (42). Only recently has this metabolite become visible using specially optimised *in vivo* spectroscopic sequences. Due to the complex coupled system, sequence parameters must be optimised to phase the multiple peaks correctly (42).

2 Physics of MR

2.1 Principles

The principles behind magnetic resonance imaging (MRI) and magnetic resonance spectroscopy (MRS) are fundamentally the same, and are an evolution of those from nuclear magnetic resonance (NMR). The human body predominantly consists of water and fat which in turn, are mainly comprised of hydrogen. Each hydrogen atom consists of a single proton with an orbiting electron, with the nucleus then rotating around its own axis. The rotating motion of the charged proton creates a magnetic field also known as a magnetic moment. It is possible to describe this phenomenon using electromagnetic theory where:

$$\mu = Ai \qquad \text{Equation 1}$$

The magnetic moment is given the symbol μ, while *A* is the area of the orbiting proton and *i* is the current travelling in the loop induced by the proton. By substituting:

$$A = \pi r^2 \qquad \text{Equation 2}$$

and

$$i = \frac{qJ}{2\pi m r^2} \qquad \text{Equation 3}$$

into equation 1, where *q* is charge, m is mass and *J* is the angular momentum, it is possible to derive the relationship between the orbital angular momentum and the magnetic moment, using a new atom specific constant, the gyromagnetic ratio, equal to $\frac{e}{2m_p}$ for ^{1}H where $q=e$ (1.6×10^{-19} C) and $m=m_p$ (1.7×10^{-27} Kg)

$$\mu = \gamma J \qquad \text{Equation 4}$$

This uses J as the angular momentum and γ, the gyromagnetic ratio (42.58 $MHzT^{-1}$)

The magnitude of the total angular momentum can be defined as:

$$|J| = \hbar\sqrt{I(I+1)} \qquad \text{Equation 5}$$

where *I* is the spin quantum number (hydrogen = *½)* and ħ, the reduced Planck constant equalling 1.05×10^{-34} Js.

The energy of the magnetic moment when placed in a magnetic field can be described using:

$$U = -\mu_z B_0 \qquad \text{Equation 6}$$

where B_0 is the magnetic field strength and μ_z is the measureable component of the magnetic moment. By substituting in the resolvable component of J ($m_z\hbar$), the energy of the magnetic moment can be determined as:

$$U = -\gamma m_z \hbar B_0 \qquad \text{Equation 7}$$

Subsequently, it is possible to describe the amount of energy required to change energy states with an additional magnetic field using equation 8, where $\hbar\omega_0$ is the Bohr frequency condition:

$$\Delta U = \hbar\omega_0 = |-\gamma \Delta m_z \hbar B_0| \qquad \text{Equation 8}$$

with the transitions between energy levels as seen in Figure 19. The number of energy levels in which a spin can exist is calculated using the selection rule (2I+1). For hydrogen this is 2 levels, I=½ ($\Delta m_z = \pm 1$).

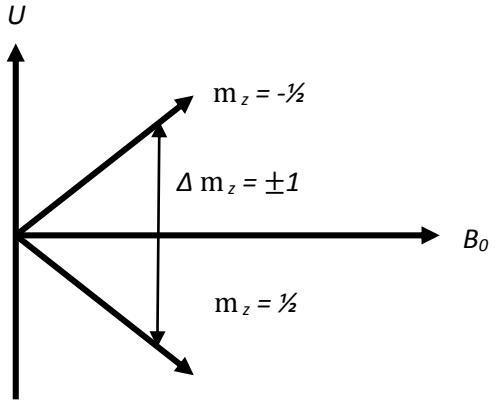

Figure 19 – Transition between energy states

The implications of equation 8 are that the an increase in field strength will increase the amount of energy required to change energy levels but the small difference in the spin energy will also increase as a function of field strength.

When under the influence of a uniform B_0 magnetic field, a torque effect is applied to the magnetic moment which causes it to try and align parallel to the magnetic field (Figure 20). Given the torque only affects the component of ω_0 perpendicular to both B_0 and μ, the net result is a rotation of μ in a cone-like shape around the B_0 axis. This phenomenon is known as Larmor precession with rotational frequency given by:

$$\omega_0 = \gamma B_0 \qquad \text{Equation 9}$$

where B_0 is the magnetic field strength, γ is the gyromagnetic ratio (2.7 x 10^8 rad s^{-1} T^{-1} for ^1H) and ω_0 the angular velocity, is approximately 42.58 MHz for a proton at 1T.

Due to Boltzmann's energy distribution ($N_1/N_2=e^{(-E1-E2)/KT)}$), the protons either align parallel (spin up) or anti-parallel (spin down) to the direction of the B_0 magnetic field (Figure 20). The amount of energy a proton has governs the direction a spin points. For any given proton, it will always attempt to be in the lowest energy state possible, which is the spin up position.

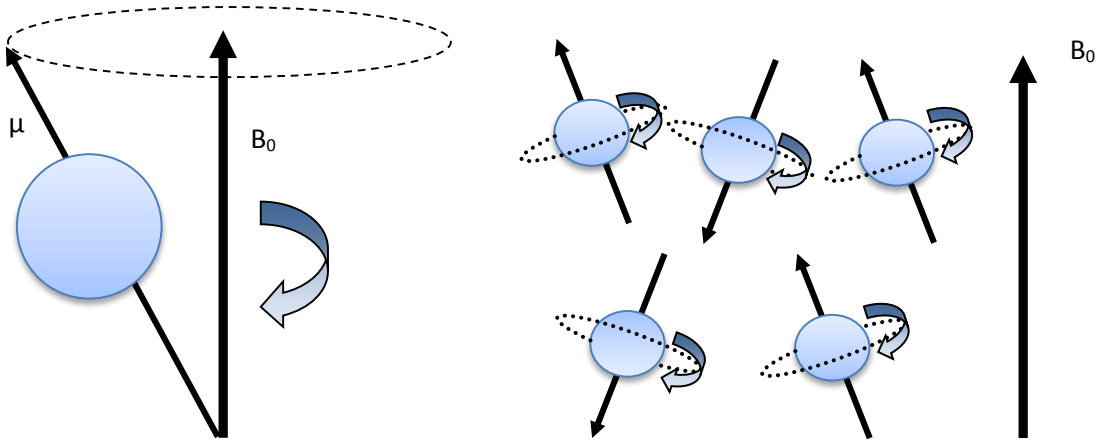

Figure 20 – Precession of the magnetic moment (left). The spin of protons when under the influence of a magnetic field (right)

The bulk magnetisation of a collection of spins, M_0 ($\sum \mu$) is the result of the combined individual magnetic moments from the sample (Figure 21).

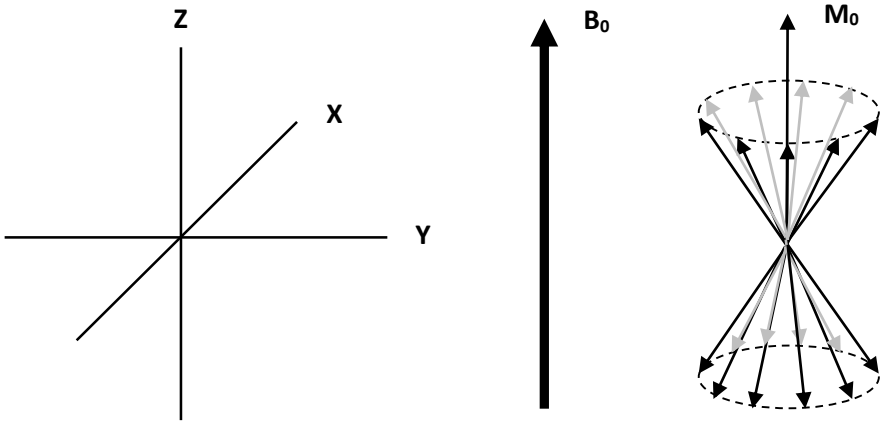

Figure 21 - The net magnetisation (M_0) of protons under a magnetic field (B_0)

2.1.1 Excitation

The bulk magnetisation can be rotated away from the B_0 direction by the application of an additional magnetic field called a B_1 field. By applying this B_1 field for a given time at the correct Larmor frequency (on the order of MHz, i.e. radiofrequency), the magnetisation can be rotated through any angle. For a simple RF pulse, the generator can be simply switched on and off, with the flip angle produced being expressed as:

$$\alpha = \gamma B_1 t_p \qquad \text{Equation 10}$$

where α is the flip angle, γ is the gyromagnetic ratio, $B_1$is the strength of the RF pulse and t_p is the RF pulse duration. The flip angle can be adjusted by either changing the pulse duration or the strength of the applied field (B_1).

To apply a B_1 field, a radiofrequency (RF) coil is positioned adjacent to the sample. An RF generator is then connected to the coil and electromagnetic pulses are produced, alternating the magnetic field. Depending on the energy of the pulse, it is possible to manipulate the spins further, so a 180^o pulse causes inversion of the equilibrium population difference meaning more spins exist at an

elevated energy state, while a 90° pulse causes spins to precess together which is known as being phase coherent.

2.1.2 Free Induction Decay

High energy state spins return to equilibrium by exchanging energy with the environment, a process known as relaxation. As Boltzmann's equilibrium distribution is restored by relaxation, the magnetisation is attenuated as transverse relaxation occurs (T_2) (see pg. 40). Since the spins behave as rotating magnets they will induce a current in a nearby coil, thus enabling the loss of magnetisation to be detected as signal. The plot of magnetisation vs. time is referred to as free induction decay (FID) and can be seen in Figure 22.

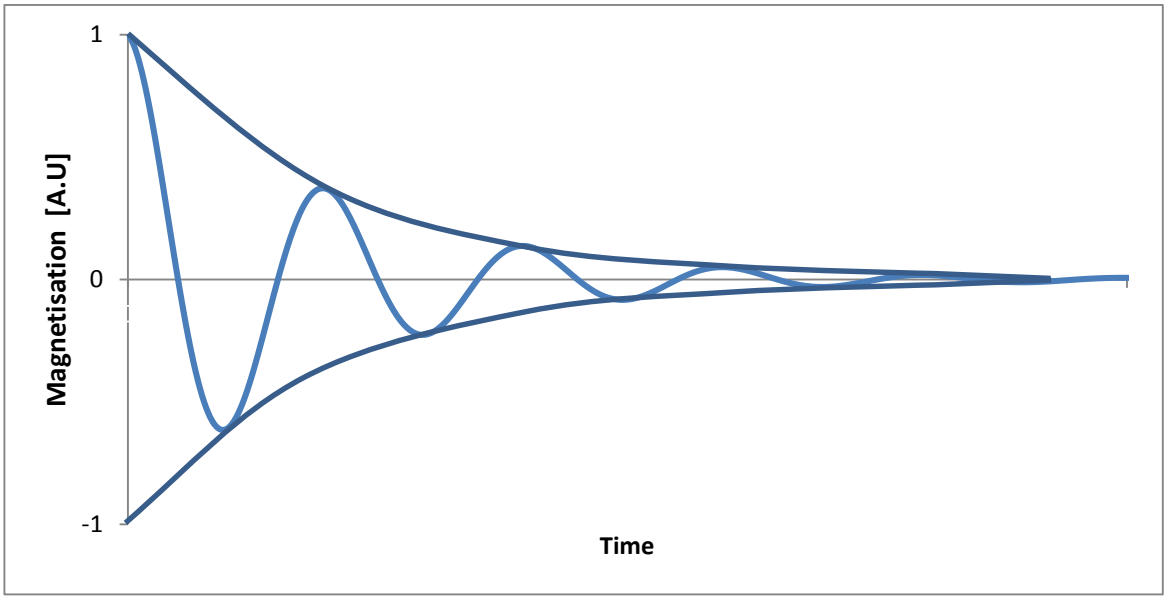

Figure 22 – Free induction decay curve (FID) for a single resonance. FIDs can be characterised by the damped sinusoidal shape.

A Fourier transform of this FID would result in a spectrum with a single peak. This is because currently there is no spatial information encoded into the signal which is why further steps are needed before an image can be generated.

2.2 Electron Shielding and Chemical Shift

An additional phenomenon to consider when performing spectroscopy is chemical shift which occurs due to the shielding of the nuclei from the B_0 static magnetic field via the surrounding electrons. A constant σ can describe the amount of shielding that occurs and varies with the position of the nucleus within a given molecule. This shielding constant can then be used to describe the magnetic field's effect on the nucleus in relation to the static field the molecule is subject to. The frequency (ω) of the chemical shift can be determined using the known field strength (B_{eff}) and the gyromagnetic ratio (γ) by:

$$\omega = \gamma B_{eff} \quad \text{Equation 11}$$

$$B_{eff} = B_0 (1 - \sigma) \quad \text{Equation 12}$$

By substituting equation 12 into 11, it is possible to account for the effects of electron shielding in chemical shift producing:

$$\omega_0 = \gamma(1 - \sigma)B_0 \quad \text{Equation 13}$$

It can also be seen in equation 13 that the absolute chemical shift difference (Hertz) is directly proportional to the field strength. The differences in chemical shifts subsequently allow molecular structure to be determined with the amplitude of the peaks being proportional to the number of hydrogen atoms present in the case of ^1H spectroscopy.

To remove the field dependency seen in equation 11, it is possible to work using relative chemical shifts termed ppm (parts per million), using the following equation where:

$$\delta = \frac{\omega_1 - \omega_{ref}}{\omega_{ref}} \times 10^6\ ppm \quad \text{Equation 14}$$

Since these are relative chemical shift (δ), they remain constant, despite the actual frequency changing with field strength, allowing the comparison of spectra acquired at different field strengths. The frequency difference between peaks becomes larger at higher field strengths which in turn is beneficial.

2.3 T_1 and T_2 Relaxation

T_1 and T_2 relaxation describe the mechanisms by which spins return back to a state of equilibrium following excitation from a RF pulse. T_1 relaxation, also referred to as spin-lattice relaxation, affects the longitudinal magnetisation and is named due to the interaction of individual spins with the rest of the volume (lattice). The T_2 relaxation (transverse magnetisation) also known as spin-spin relaxation happens in the xy plane. Spin-spin refers to the interaction between spins and the small local magnetic fields produced by each spin.

2.3.1 T_1 Relaxation (Spin-Lattice)

Spin-lattice relaxation is the recovery of the z component (longitudinal magnetisation) of the bulk magnetisation after excitation, and can be described using the appropriate equations developed by Bloch (43) for the z axis:

$$\frac{dM_Z}{dt} = -\gamma[\boldsymbol{M} * \boldsymbol{B}]_Z - \frac{(M_Z - M_0)}{T_1} \qquad \text{Equation 15}$$

By calculating the cross product of equation 15 after an RF pulse assuming that only the B_0 field is present:

$$\frac{dM_Z}{dt} = -\frac{(M_Z - M_0)}{T_1} \qquad \text{Equation 16}$$

It is possible to solve equation 16 for M_z:

$$M_Z(t) = M_Z(0)e^{-t/T_1} + M_0\left(1 - e^{-t/T_1}\right) \qquad \text{Equation 17}$$

however, after a 90° pulse, $M_Z(0)$ is equal to 0 and this can be rewritten as:

$$M_Z = M_0\left(1 - e^{-t/T_1}\right) \qquad \text{Equation 18}$$

The return of the magnetisation back to M_0 along the z axis after a 90° pulse is called T_1 relaxation with full magnetisation effectively being restored after approximately $5T_1$ (see Figure 23). The return back to M_0 can be accredited to the thermal motion of nearby molecules removing energy from the

excited dipoles. The tumbling rate of the surrounding molecules affects the rate at which relaxation occurs. In water, a relatively small molecule, energy is dispersed less quickly from the excited dipoles due to the spatial separation of water molecules and the fast molecular tumbling rate, resulting in a longer recovery time (longer T_1).

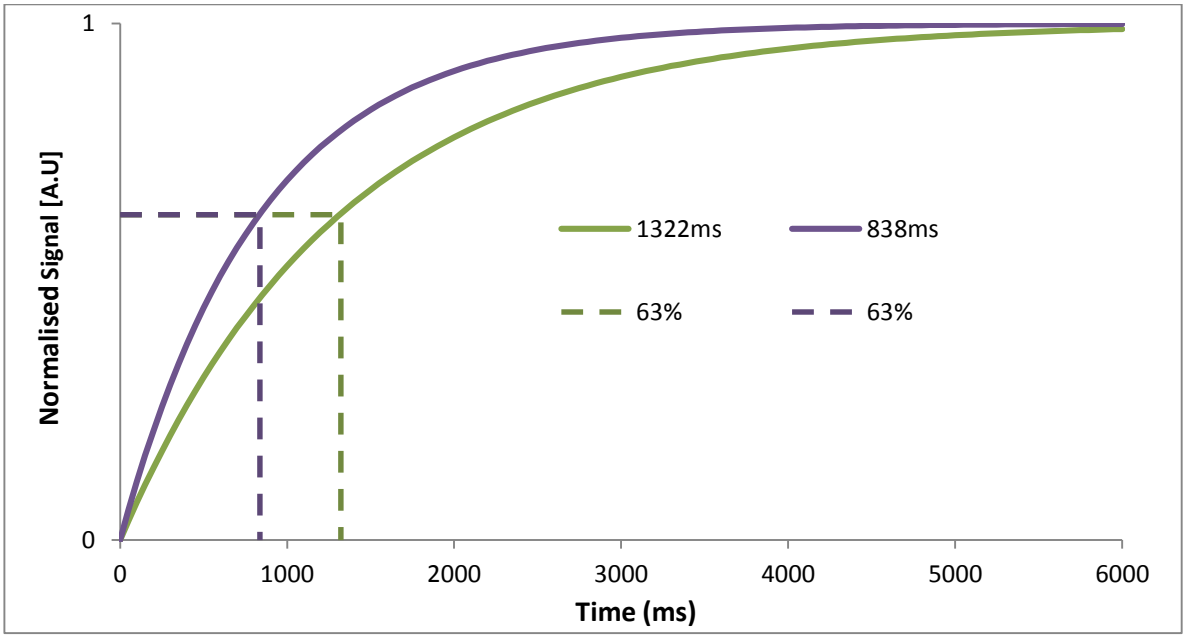

Figure 23 - T_1 Recovery of M_z. Values of 1322ms and 838ms were used to represent grey and white matter (44).

2.3.2 T_2 Relaxation (Spin-spin)

As T_1 relaxation occurs, the spins also rotate in the xy plane (M_{xy}). Simultaneously, T_2 relaxation is occurring at a quicker rate and represents the loss of phase coherence following a pulse. The decay of the transverse magnetisation follows the Bloch equation for the xy plane:

$$\frac{dM_{x,y}}{dt} = \omega_0 M_{y,x} - \frac{M_{x,y}}{T_2} \qquad \text{Equation 19}$$

once solved following the removal of the RF pulse, gives:

$$M_{x,y} = M_{x,y}(0)e^{-t/T_2} \qquad \text{Equation 20}$$

The decay in magnetisation will then look similar to Figure 24 and takes approximately five times the T_2 for the magnetisation to return to zero.

Interactions taking place between spins from different nuclei are due to the microscopic differences in the B_0 magnetic field which causes changes in the frequencies of the rotating nuclei as shown by:

$$\omega = (e/2m_e)B_0 = \gamma B_0 \qquad \text{Equation 21}$$

Where e = 1.6×10^{-19} C, m_e = 9.1×10^{-31} Kg, ω = angular velocity and B_0 = static magnetic field

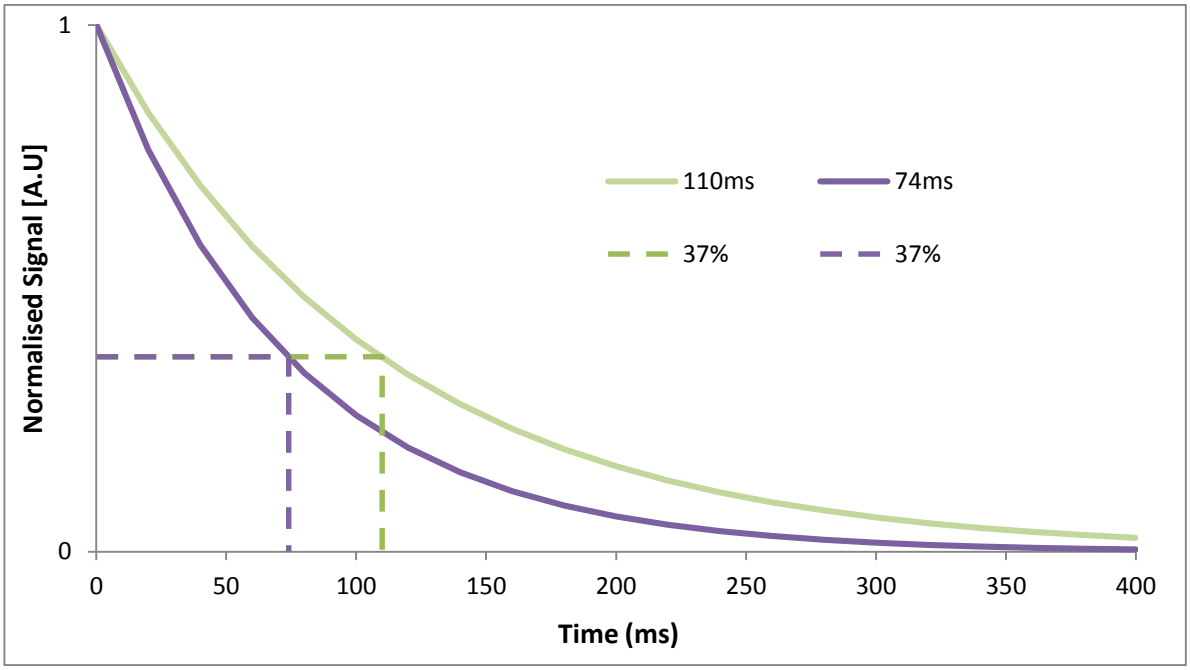

Figure 24 - T_2 relaxation in M_{xy} plane. Values of 110ms and 74ms which were used to represent grey and white matter (44).

This effect causes the spins to both speed up and slow down, leading to a loss of phase coherence over time. As a result, energy is transferred between spins of different frequencies, which is the cause of T_2 relaxation.

2.3.3 Basic Pulse Sequence

The simplest pulse sequence to cause excitation is the application of a single 90° pulse, which equalises the spin populations and causes groups of spins to initially precess together.

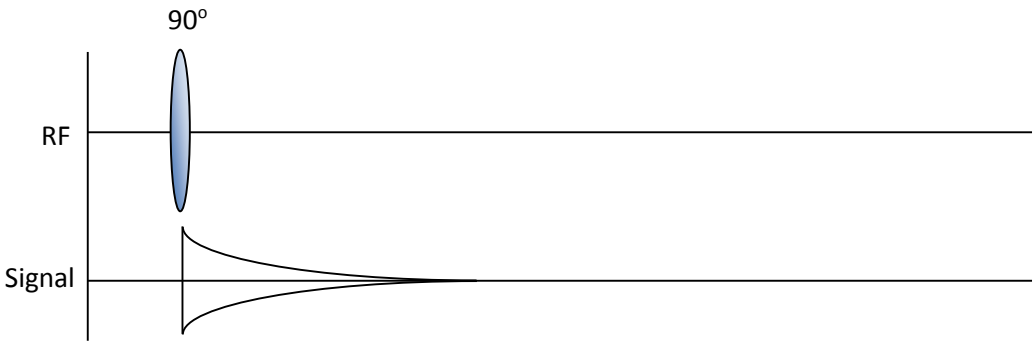

Figure 25 - Simple single pulse excitation sequence without relaxation

The 90° pulse is applied (Figure 25) at the Larmor frequency and tips the bulk magnetisation from the Z plane into the XY transverse plane (Figure 26). As the spins return back to equilibrium, RF is emitted which is measured as electromotive force (EMF) by a receiver.

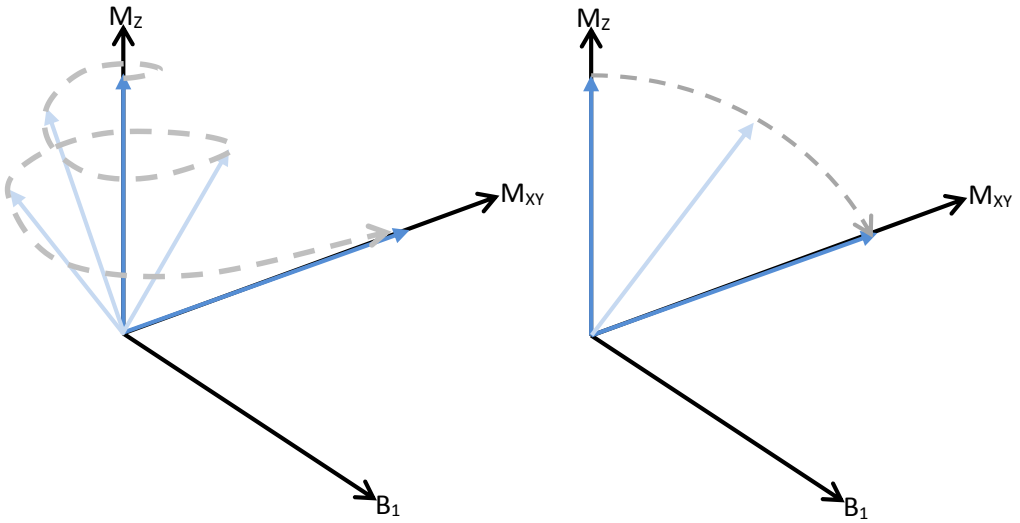

Figure 26 - Diagram showing how the application of a 90° pulse tips the spins into the M_{xy} plane. Right shows in the laboratory frame of reference where the viewer is stationary relative to the spin. Left shows the same pulse application viewed from the rotating frame of reference where the viewer is rotating at the same rate as the spin.

2.3.4 A Simple Pulse Sequence with Spatial Encoding

In MR, an echo rather a FID is normally recorded due to the time required to implement the spatial encoding pulses. Using selective excitation simultaneously with frequency and phase encodings, spatial information about the spins is able to be stored (Figure 27). Initially, a slice selection gradient is used to localise a slab of tissue to excite with the RF pulse. Crusher gradients can then be used to destroy any signal from outside of the desired volume. A phase encoding gradient can be used to further localise the signal for a particular location within the excited slab whilst a frequency encoding gradient is employed subsequently, recording the signal amplitude over time as the echoes evolve.

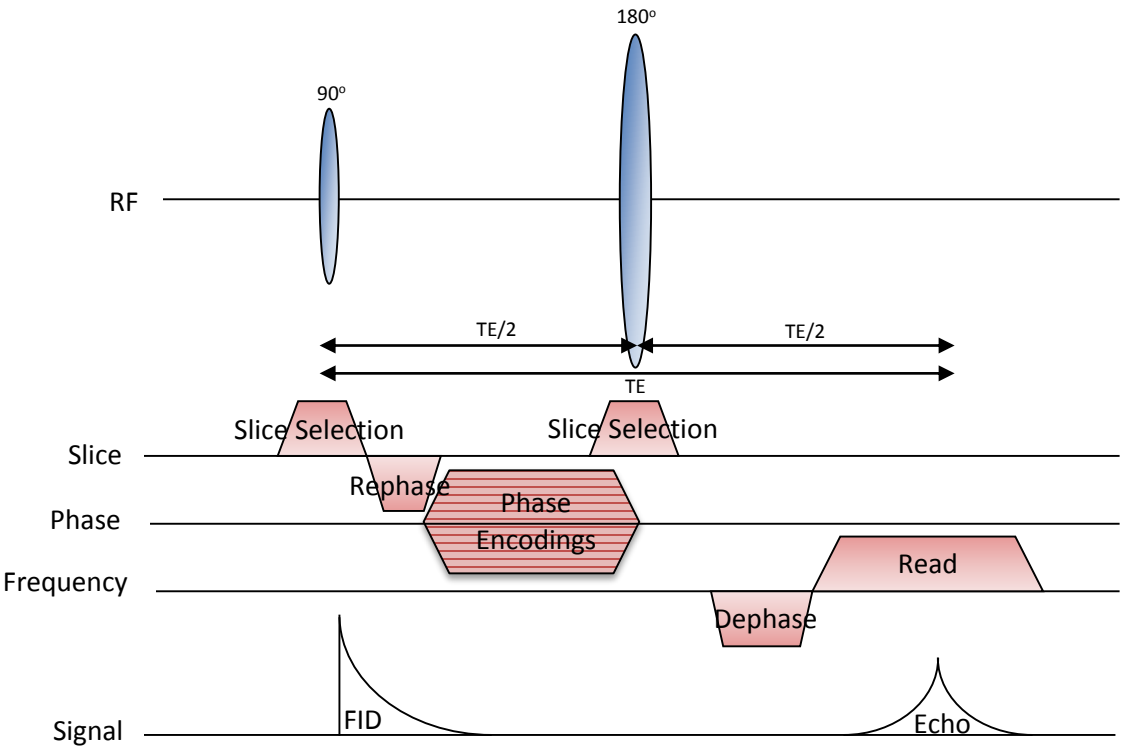

Figure 27 – Spin Echo based pulse sequence diagram demonstrating how the use of frequency and phase encodings in addition to slice selection gradients can enable 3D encoding of MR data.

2.3.5 Slice Selection

Selective excitation allows the capture of multiple images known as slices rather than a single image of the entire volume of interest. In order to produce selective excitation, a specifically designed RF excitation pulse is used at the same time as a gradient (small spatially varying linear magnetic field) and contains a narrow band of frequencies centred on the Larmor frequency.

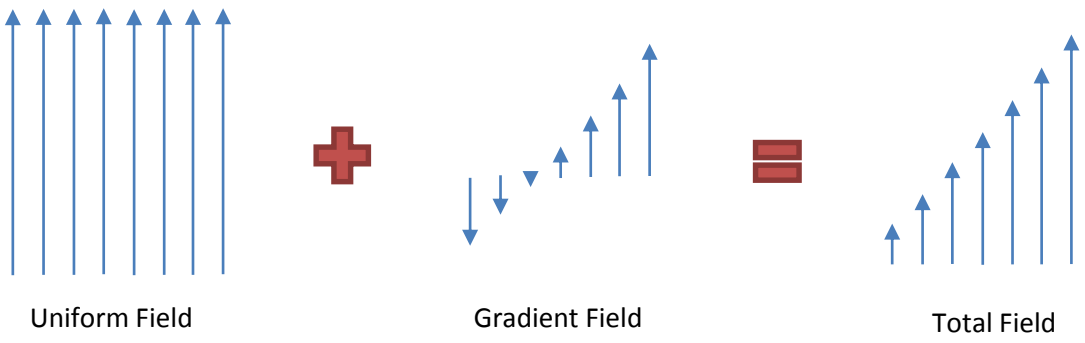

Figure 28 - The addition of a gradient field can be used to increase or decrease the precession rate of spins in a field. The change in precession is observed as higher or lower spin frequencies compared to the Larmor frequency and are subsequently used to spatially localise signals.

The presence of the gradient causes the position of the resonant frequency to be different at each location in the gradient direction. Where the effect of the gradient is 0 (the isocentre), the normal Larmor frequency applies. At points further away along the selection axis, a higher or lower frequency will be required to achieve resonance at a particular point on the gradient. Thus a B_1 frequency bandwidth can be chosen that excites only the protons in a small region of space with thickness defined by the strength of the gradient and the bandwidth of the pulse. If there is no resonance then there will be no MR signal produced. For example, if the slice-select gradient is applied along the Z direction then a slice can be selected in the transverse plane (Figure 29). Increasing the gradient strength with a constant bandwidth results in a reduced slice thickness.

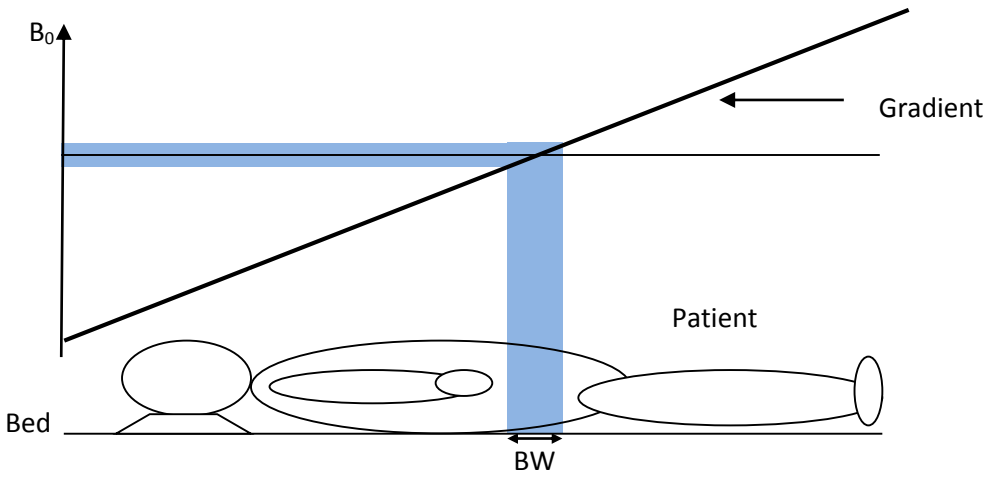

Figure 29 - Slice selection using a gradient to excite a slab of spins centred on the Larmor frequency.

2.3.6 Frequency Encoding

Whilst it is relatively simple to observe a resonance using NMR, the addition of spatial encoding is a defining feature of MR. In order to translate the signal into an image, a frequency encoding gradient is applied to one of the in-plane dimensions during the time for which a signal (the echo) is acquired. Frequency encoding acquires a series of measurements for the duration of a single gradient. Each line of k-space is filled when the frequency encoding gradient is applied during the readout phase, with the amplitude of each sampling point then represented as a grey level (Figure 30).

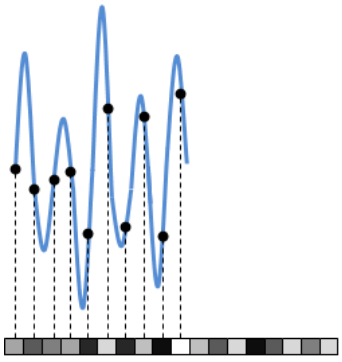

Figure 30 – The digitisation process during the readout phase in MR. Here the amplitude of the signal at fixed time intervals is measured and recorded as a grey level.

2.3.7 Phase Encoding

An MR sequence consists of multiple repetitions of the excitation process, and uses different phase encoding gradient strengths until all spatial frequencies have been interrogated. By using phase encoding, it is possible to alter the position at which frequency encoded data is assigned in an array. The application of a phase encoding gradient for a given time can cause the precession of the nuclei to be sped up or down depending upon their position along the y axis. This causes the spins to dephase in a progressively greater manner for the duration of the gradient with these relative differences between signals from differing locations. Thus spatial information can be associated with the different signals produced in an acquisition. The use of a frequency encoding gradient in conjunction with phase encoding in two orthogonal directions allows data from each echo to be a digitised sampling point with a unique location within an array.

2.3.8 K-Space and Image Reconstruction

K-space is an array of digitised raw MR echoes that exists before spatial and spectral Fourier transformations are applied, and consists of the values from different spatial frequencies. In conventional imaging, the k-space matrix is filled one line at a time (Figure 31) using the data sampled during the frequency encoding. Once k-space is complete, fast Fourier transforms (FFT) can be applied (Figure 32) converting the spatial frequency information into a spatial density distribution map of the spins, otherwise known as an image.

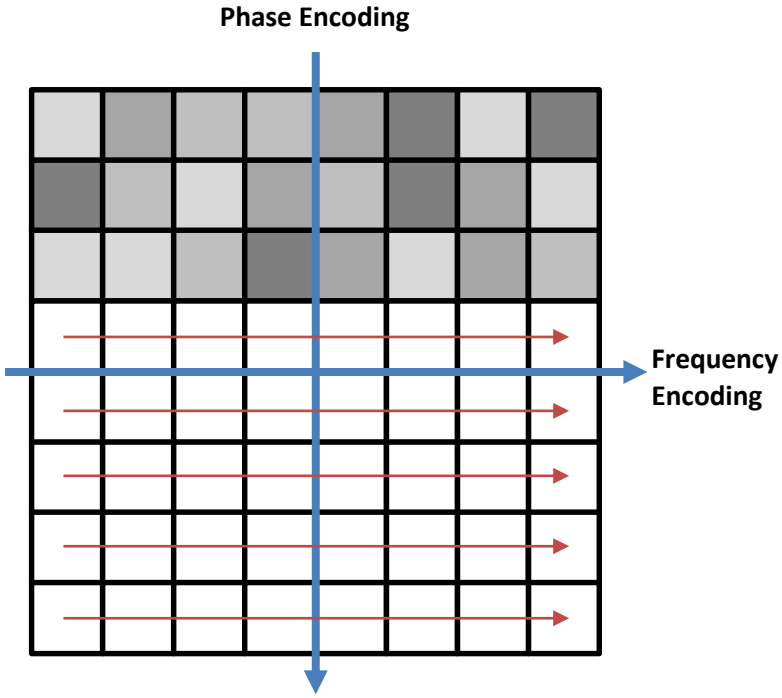

Figure 31 – Digitised lines of signal acquired during the frequency encoding are used to fill the array. By adjusting the phase encoding gradient, unique spatial properties are assigned to each pixel.

Due to the nature of Fourier transformations, there is no direct relationship between any given position in k-space and the final position in a reconstructed image. The k in k-space refers to wave number of the echo which is given by:

$$k = \gamma G t \qquad \text{Equation 22}$$

where G = gradient amplitude (T m^{-1}, γ = the gyromagnetic ratio (s^{-1} T^{-1}) and t = duration of gradient (s); k is therefore measured in m^{-1}.

A k-space matrix shares the same number of points as an image has pixels. Furthermore if there are 256 frequency encoding steps, this equates to 256 sampling points which is represented as 256 columns in k-space for temporary data storage. In a k-space matrix, the middle of k-space provides the signal and image contrast information (low spatial frequencies), while the periphery of k-space provides finer details such as edges, boundaries and the resolution of the image (Figure 32).

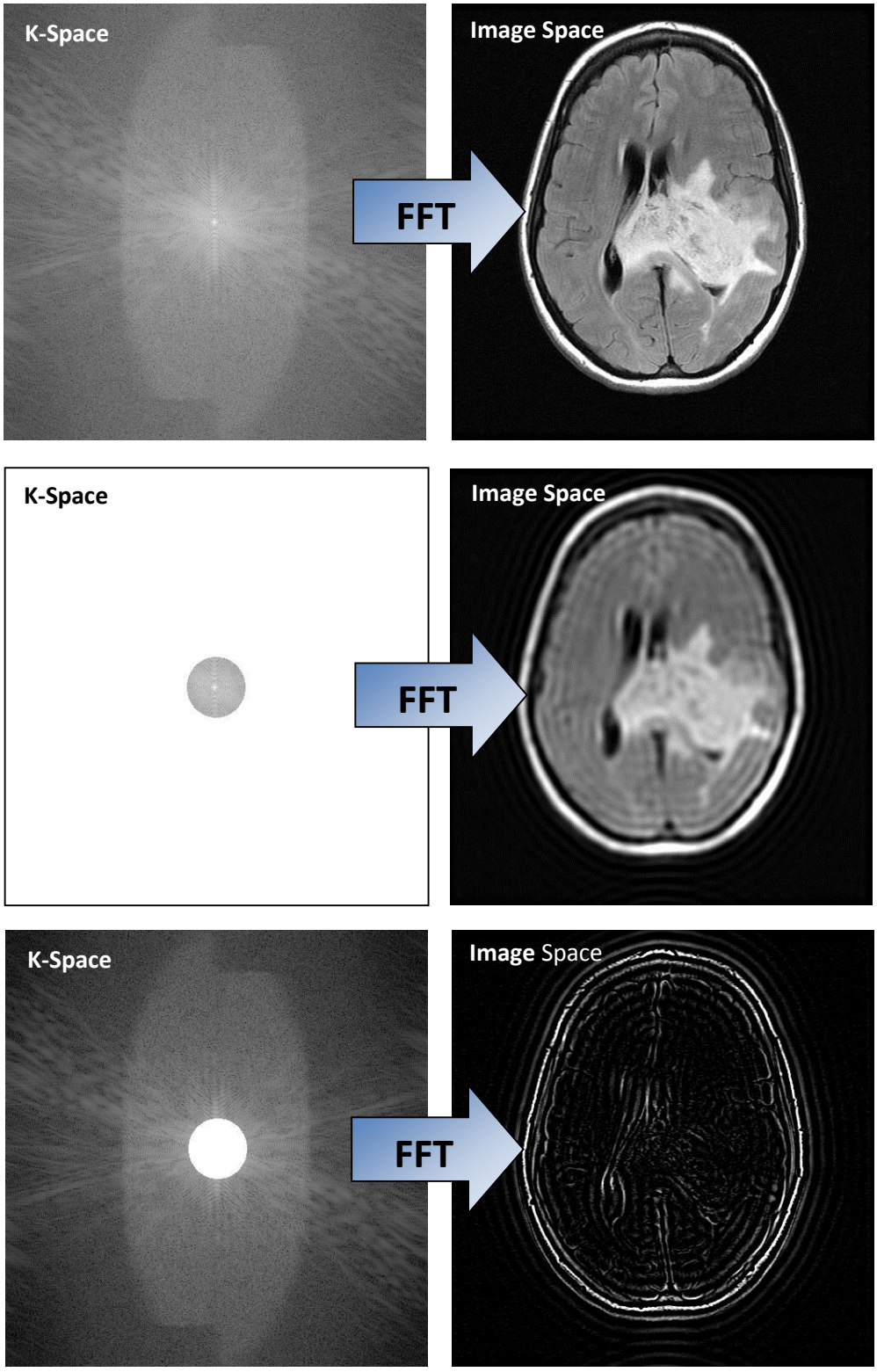

Figure 32 - Fourier transformation from k-Space to an image (top). In a k-space matrix, the middle of k-space is the image contrast information (middle), while the outside of k-space makes up the edges, boundaries and resolution of the image (bottom). These images were generated using imageJ by first performing a reverse FFT of the DICOM image, before subsampling the different regions of k-space and performing a forward FFT to understand their meaning.

2.4 Acquisition Optimisation

2.4.1 Automatic Prescan

At the start of each sequence whether for imaging or spectroscopy, the scanner runs a short automatic prescan, in which it tries to optimise characteristics of both the transmitter and the receiver. By placing an object in the scanner, the Larmor frequency can change, so a process called frequency tuning is needed to ensure water is exactly on resonance for each scan in order for gradients to have the desired effect.

Following frequency tuning, the correct amount of power is calculated, in order to produce the correct flip angle for a given sequence to work properly, which is called the transmitter gain (TG). This is done by adjusting the output on the RF power amplifier. Likewise the receiver gain (RG) is accordingly adjusted to optimise the signal.

2.4.2 Magnet Shimming

The quality of imaging and spectroscopy is heavily dependent on the homogeneity of the B_0 field. Shimming is a technique which tries to correct for inhomogeneities in the magnetic field by sampling the field in the X, Y and Z directions. There are two types of shim; static and dynamic. A static shim is a permanent correction to the magnetic field which is applied by engineers in order to make the magnetic field as homogeneous as possible by correcting field distortions when the magnet bore is empty. However when a person/phantom is placed in the field, it can alter it sufficiently to cause imaging problems so the magnet is also dynamically shimmed before every sequence, to improve the uniformity of the field. Electric coils built into the magnet housing are used to help improve field homogeneity in the X, Y and Z directions by producing linear magnetic field gradients which correct the main field into a more homogenous state as seen in Figure 33.

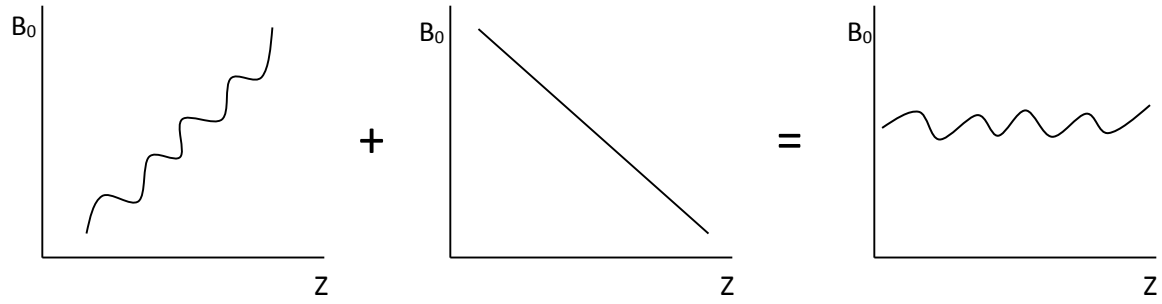

Figure 33 - This diagram shows how the addition of a magnetic field gradient (middle) onto an existing magnetic field (left) can help correct for inhomogeneities in the B_0 field (right).

2.4.3 Signal to Noise

Signal to noise ratio (SNR) is one measure of the image quality for an acquisition and is affected by a host of parameters. It represents the amount of signal available in relation to the underlying noise. Part of getting the highest SNR possible is optimising the trade-off between different acquisition conditions. Table 2 is a list of the user changeable parameters that can affect SNR. The SNR is also proportional to the strength of the B_0 field.

Table 2 – Parameters to improve SNR and the subsequent effects.

SNR Increase	**Disadvantage**
Increase voxel size (reduce encodings) Increase FOV	Decrease spatial resolution
Increase NEX ($\sqrt{NEX}$ *increase in SNR*)	Longer scan time
Decrease receiver bandwidth	Less noise sampled Limits number of slices for a given TR Limits minimum TE Longer sampling time Increased chemical shift displacement error
Increase slice thickness	Partial volume effects
Decrease TE	Reduces T_2 weighting/Increases T_1 weighting
Increase TR	Reduces T_1 weighting/Increases T_2 weighting
Flip angle: T_1 weighting T_2* weighting P.D weighting	 Flip=high, TR=short, TE=short Flip=low, TR=long, TE=long Flip=low, TR=long, TE=short

3 MR Imaging Techniques

This chapter examines some of the different magnetic resonance sequences available for neuro-oncological imaging on a 3.0T GE magnetic resonance (MR) scanner; however similar sequences are also available from other vendors.

MR has several distinct advantages over computer tomography (CT) which include superior soft tissue contrast used to diagnose pathology and increased sensitivity to subtle changes between scans. MR is a non-ionising modality which is well suited for serial observations unlike CT. MR also has several less favourable qualities compared to CT such as longer acquisition times and increased sensitivity to motion. MR imaging is also predominantly non-quantitative unlike CT which is now standardised. Despite these shortcomings, conventional MR has an important role in the management of gliomas, with MR imaging used by neurosurgeons for treatment planning and stereotactic procedures. MR imaging is also the modality of choice for monitoring glioma patients.

Determining the malignancy of a brain tumour can often be difficult especially given the sometimes unreliable nature of contrast uptake, thus, some of these additional techniques described have been developed to help determine a tumour's characteristics (45). A full review of MR for the diagnosis and monitoring of brain tumours can be found in Chapter 4 - Review of MR Studies, page 95.

3.1 Excitation Techniques

These excitation techniques expand upon the basic pulse sequence described on page 42 and are designed to exploit the different tissue properties of the body.

3.1.1 Spin Echo (SE)

SE sequences use two RF pulses to create an echo (Figure 34 & Figure 35). Following the application of a 90° RF pulse; the magnetisation is rotated into the *XY* direction known as the transverse plane. The bulk magnetisation begins to dephase causing a reduction in the strength of the magnetisation. By then applying a 180° RF pulse in the *Y* direction at TE/2, it is possible to rotate the plane in which the spins sit and subsequently they rephase, which causes the formation of an echo which produces the image signal. In general, SE sequences produce the highest quality images but require more time to achieve this.

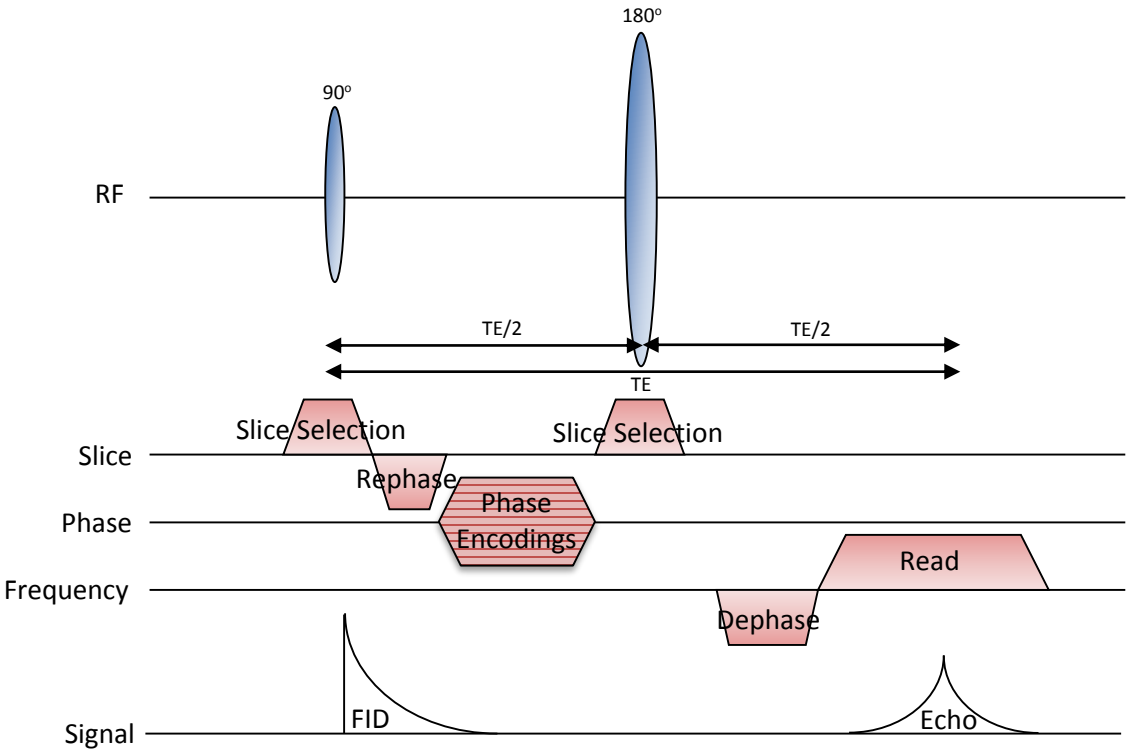

Figure 34 - Spin-Echo pulse sequence diagram

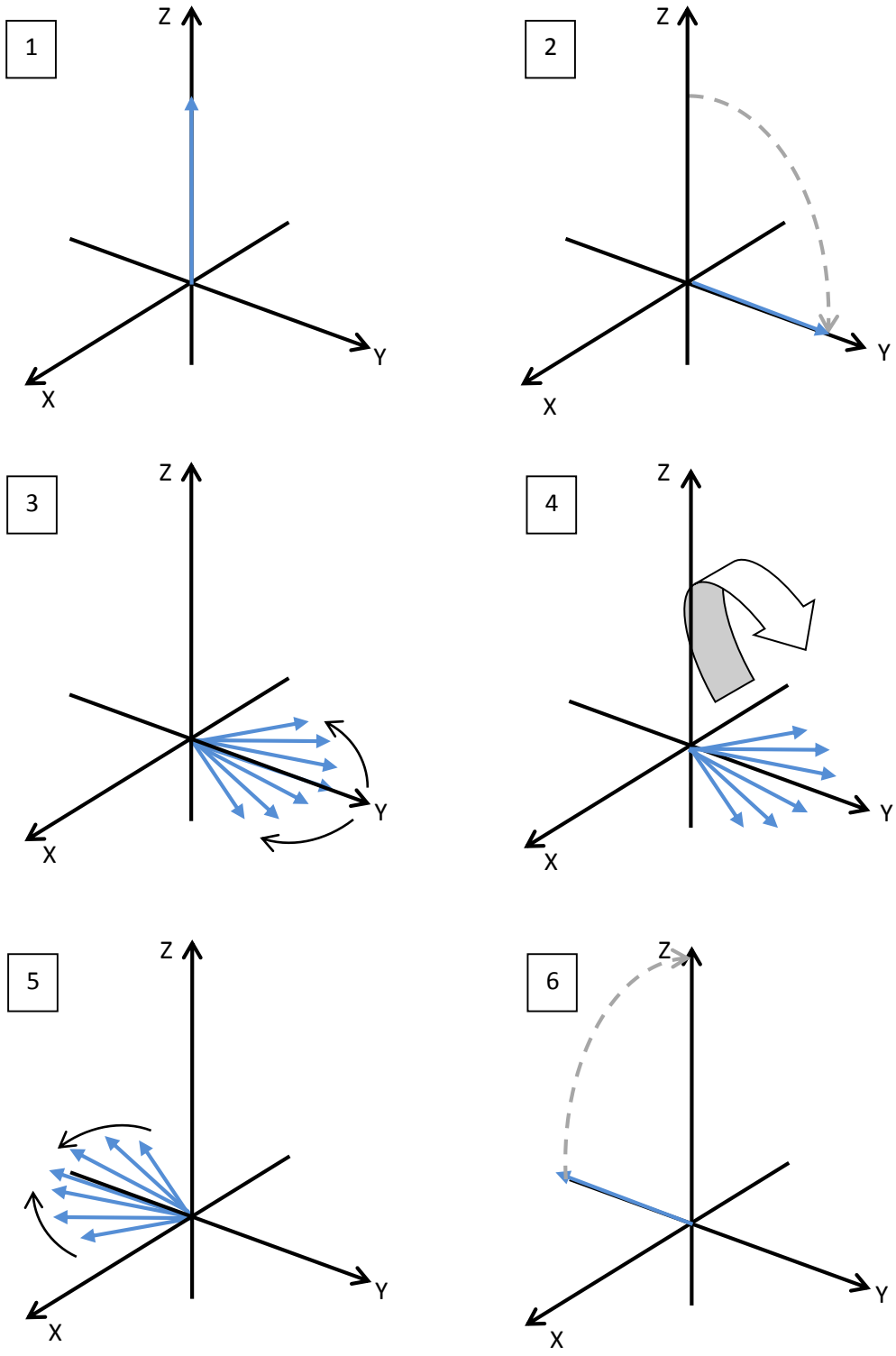

Figure 35 –Spin Echo diagram. Initially the bulk magnetisation lies in the Z direction (1), however, following the application of a 90° RF pulse; the magnetisation is rotated into the XY direction known as the transverse plane (2). Here the bulk magnetisation begins to dephase causing a reduction in the strength of the magnetisation (3). By then applying a 180° RF pulse in the X direction at TE/2, it is possible to rotate the plane in which the spins sit (4) and subsequently they rephase (5), which causes the formation of an echo (6).

3.1.2 Gradient Echo (GE/GRE)

Gradient echo sequences differ from spin echo sequences by replacing the 180° refocusing pulse with a reversed gradient (Figure 36 and Figure 37). The quality of the magnet also influences the measured signal, so when measuring T_2 relaxation with a gradient echo, the magnet inhomogeneity contributes to the final measured signal, known as T_2*. This can be expressed as:

$$\frac{1}{T_2^*} = \frac{1}{T_2} + \frac{\gamma \Delta B_0}{2} \qquad \text{Equation 23}$$

T_2* decays quicker than T_2 relaxation, and so the signal produced by GE imaging is lower than that of an equivalent SE sequence. As a result, it is not possible to produce T_2 weighted GE images of similar contrast to SE sequences, however T_2* weighted images are useful for looking for regions of susceptibility caused by blood products. The absence of the 180° refocusing pulse allows the TR of the sequence to be reduced; allowing the rapid acquisition of T_1 weighted images. The flip angle of the pulse sequence is also used to control the image contrast.

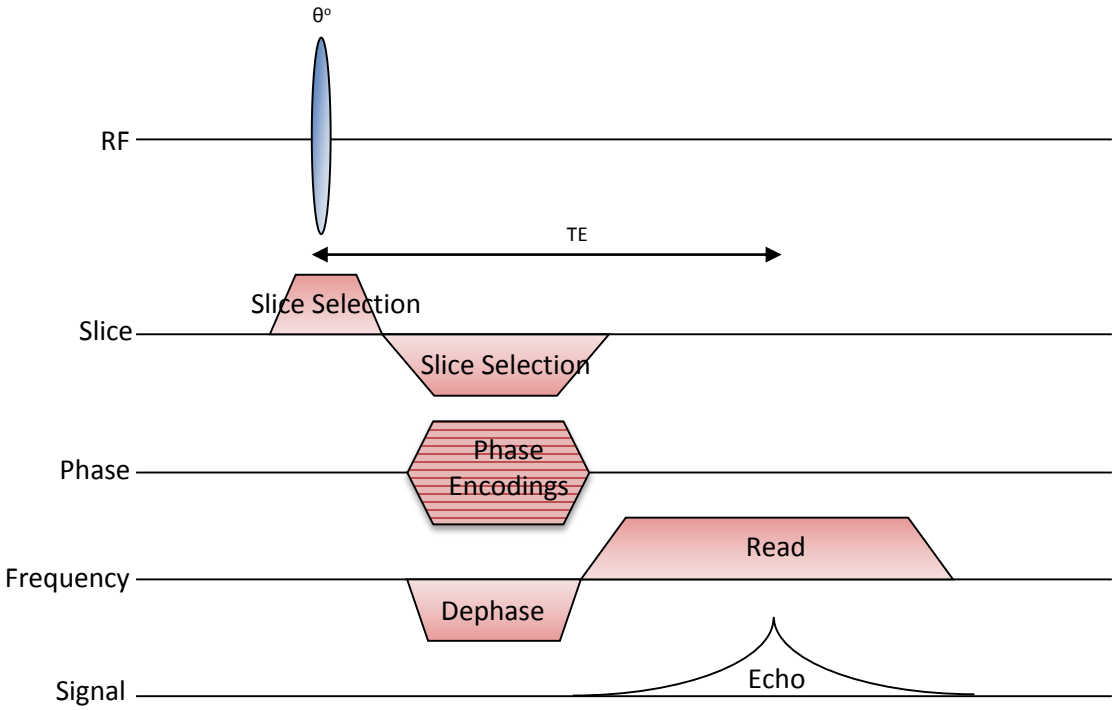

Figure 36 – Gradient Echo pulse sequence diagram

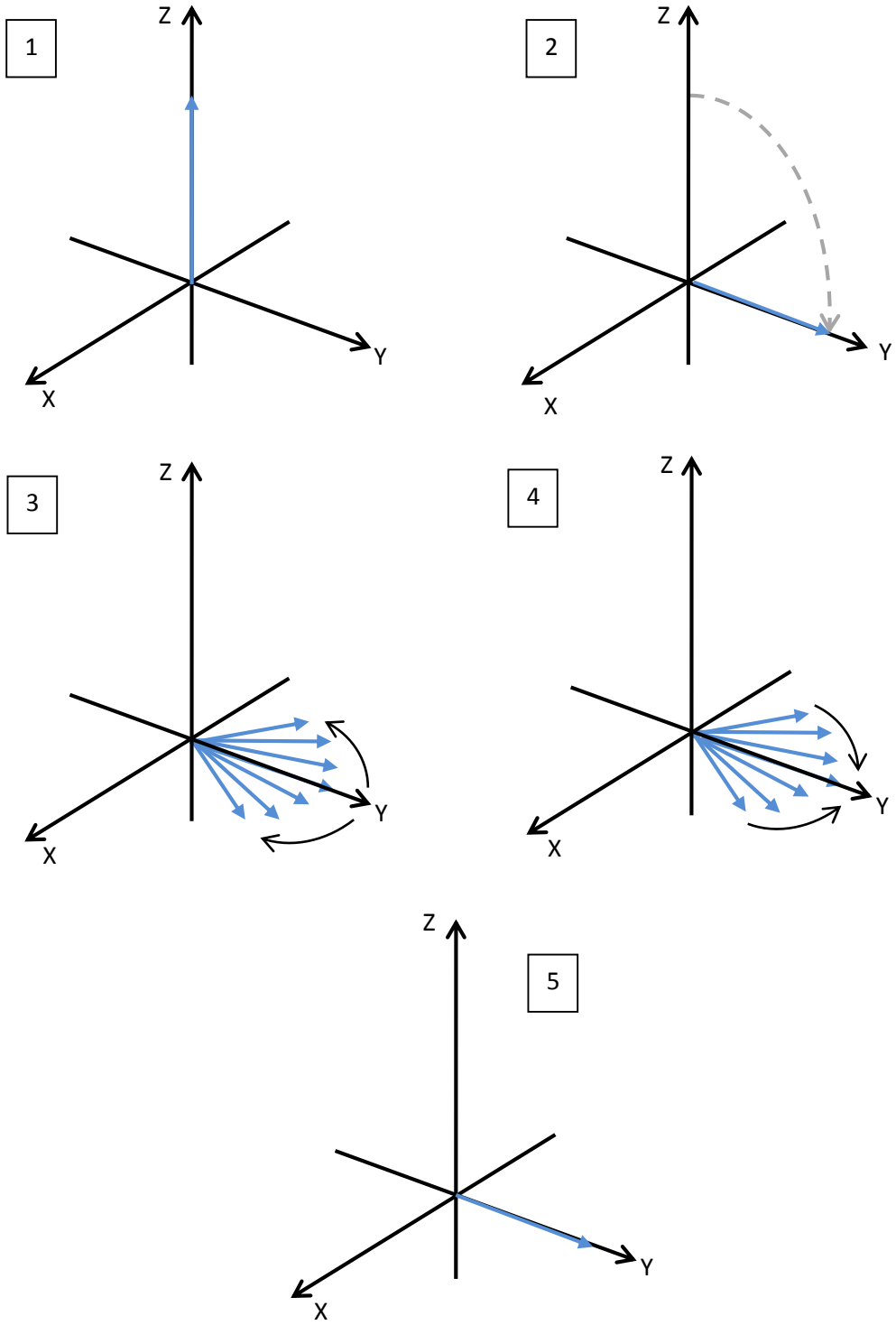

Figure 37 –Gradient Echo diagram. Initially the bulk magnetisation lies in the Z direction (1), however, following the application of a ϑ^{o} RF pulse; the magnetisation is rotated into the XY direction known as the transverse plane (2). Here the bulk magnetisation begins to dephase causing a reduction in the strength of the magnetisation (3). By reversing the gradient, it is possible to rephase the spins (4), which causes the formation of an echo (5) and produces a signal.

3.2 Image Contrast

The relaxation time for a given tissue, describes how long it takes for spins to return back to equilibrium following excitation from a RF pulse. T_1 and T_2 (spin-lattice and spin-spin respectively) relaxation times are dependent on the type of tissue involved. The T_2 relaxation time is always shorter than the T_1 relaxation time for a given tissue and in general, images will have contrast through a weighting in one of the following three ways: T_1, T_2 or proton density (PD). High proton densities give rise to higher signal intensities which subsequently appear as brighter pixels. In a T_1 weighted image, tissue with a long T_1 produces the lowest signal (Figure 38) and therefore would be the darkest pixels, whereas in a T_2 weighted image, tissue with the longest T_2 produce the brightest pixels (Figure 39).

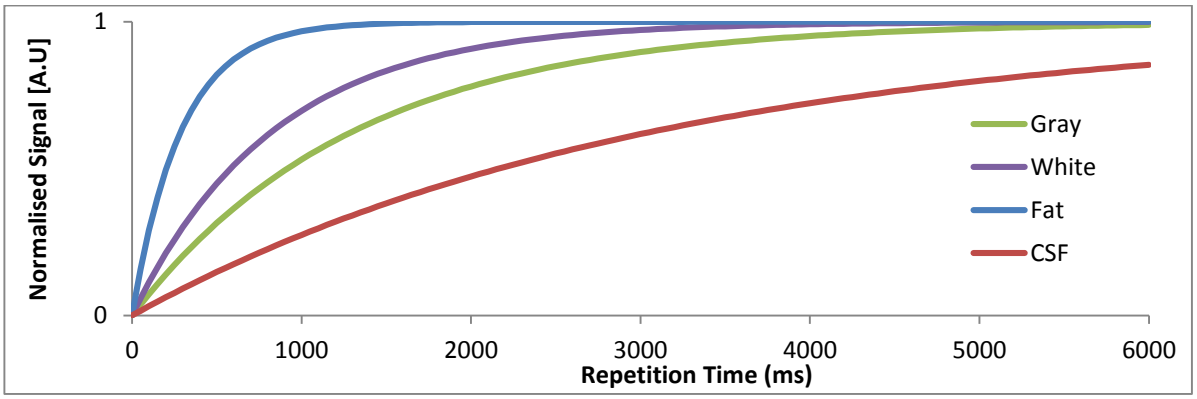

Figure 38 - Example T_1 relaxation recovery curves at 3.0T for grey and white matter, fat and CSF using a spin echo. The differences observed with a short TR are what give rise to the tissue contrast.

T_1 weighted sequences provide images with good tissue contrast in the brain. Fluids appear very dark in relation to the mid greys of water based tissue and bright fat based tissue (Figure 38). The use of T_1 weighted sequences is mainly to define the clear boundaries between different tissue types. T_2 weighted sequences produce images where fluid and fat appears very bright while brain tissues appear mid grey (Figure 40). Despite the lack of contrast when using PD weighted imaging, it still has some clinical applications such as distinguishing the articular cartilage from the cortical bone and menisci. For neuro-oncological imaging however, PD imaging is not routinely used.

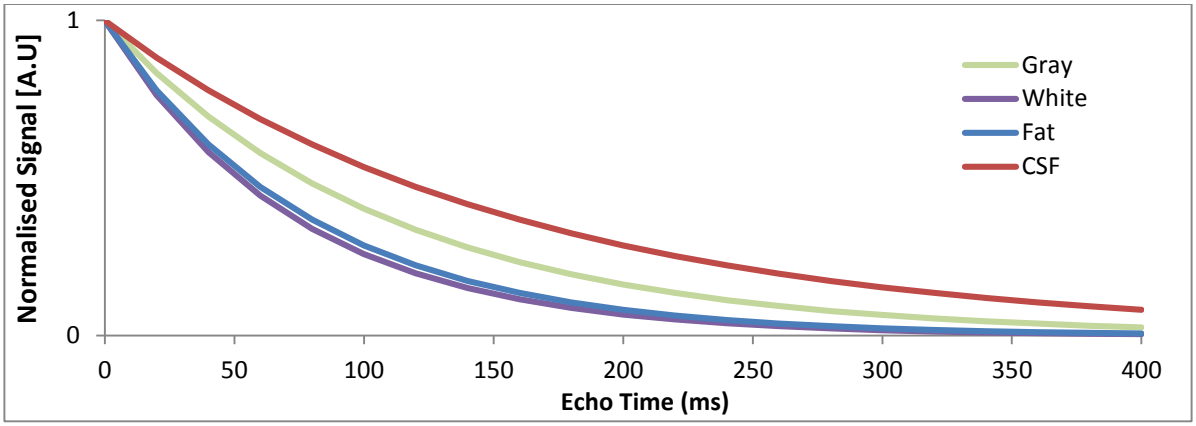

Figure 39 - Example T_2 relaxation curves at 3.0T for grey and white matter, fat and CSF using a spin echo.

Fluid Attenuated Inversion Recovery (FLAIR) is a T_2 weighted sequence with an inversion recovery pulse designed to null CSF at the correct inversion time (~2500ms). This sequence is ubiquitous in neuroimaging due to its ability to suppress signal from CSF while maintaining the other characteristics of a traditional T_2 weighted sequence. Separation of oedema from CSF is a good example of its use (Figure 40), but can also be used to visualise subtle abnormalities.

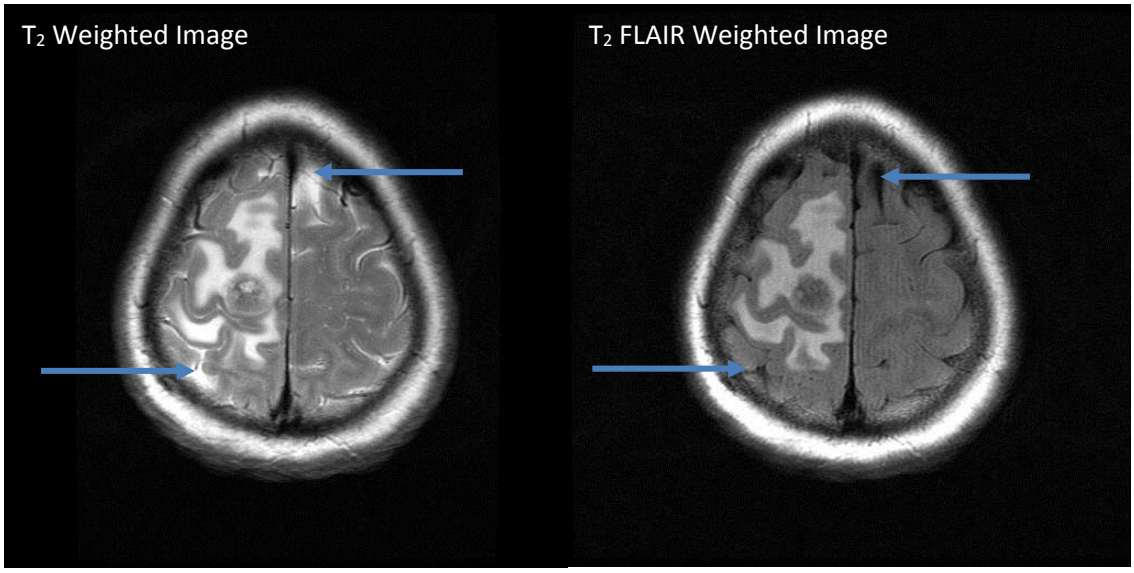

Figure 40 - T_2 weighted imaging (left) and T_2 weighted FLAIR imaging (right) of the same slice through a brain tumour. Note how the signal from the CSF has been nulled following the inversion recovery pulse with only oedema remaining hyperintense.

3.3 Contrast Enhanced MR

The tissue contrast observed from conventional T_1 or T_2 weighted images may not be sufficient to delineate the disease or identify regions of higher grade transformation. By using a contrast agent, it is possible to further enhance the imaging characteristics of tissue. Contrast agents are injected into the body and circulate through using the blood vessels, with the most vascular tissue, normally a tumour, leaking the contrast agent into the extracellular space (Figure 41) before the normal blood vessels disperse the agent evenly throughout the smaller vessels of the body.

In healthy brain tissue, gadolinium based compounds (contrast) cannot pass through the blood brain barrier (BBB) and so remain intravascular. With the presence of tumours or other pathology, the permeability of the BBB increases causing the contrast agent to leak out into the surrounding tissue (Figure 42). This in turn changes the T_1 and T_2 relaxation properties of the tissue.

Most gadolinium (Gd) paramagnetic contrast agents have five or seven unpaired electrons (46), each with their own magnetic moments and have the benefit of being able to affect both T_1 and T_2 relaxation times. This is made possible by the local paramagnetic susceptibility that occurs in the vessels/tissues where it accumulates. The T_1 shorting effect that is produced, leads to an increase in signal intensity seen on a T_1 weighted image meaning the most vascular tissue appears the brightest, with this often known as “enhancement”. Likewise, the T_2 shortening effect also leads to a loss of signal when viewed on a T_2 weighted image.

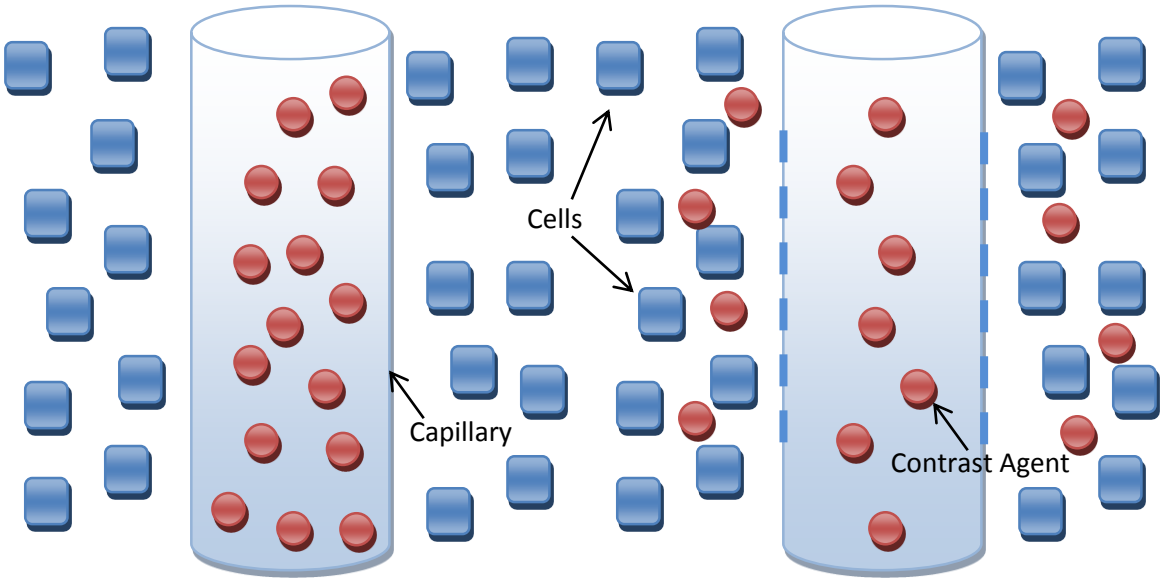

Figure 41 - Two capillaries with contrast agents in them. Left shows normal tissue and a non-leaky capillary. Right shows tumour with leaky capillaries. The contrast agent in this situation can now move into the extracellular spaces changing the relaxation properties of the tissue.

As well as effecting the T_2 relaxation for images, gadolinium can also have an effect on spectroscopic data, causing a broadening in spectral peaks. It is advised to perform spectroscopy before the injection of contrast agents during an examination. This does have a trade-off though, due to the exact location of the disease often being difficult to see without contrast.

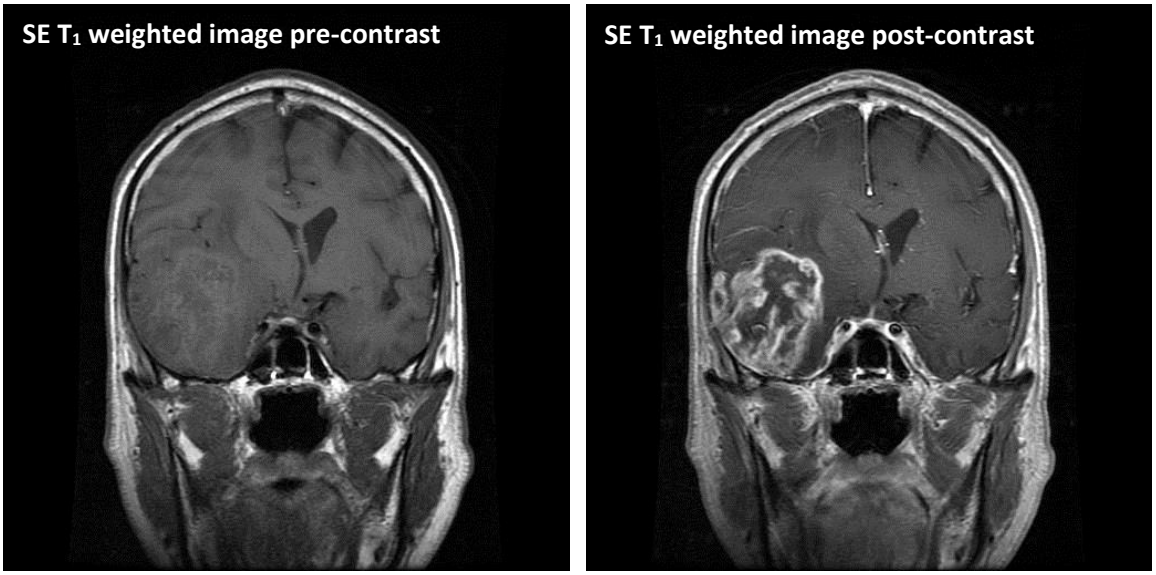

Figure 42 – Example coronal T_1 weighted spin echo images of a patient with a glioblastoma multiforme before (left) and after (right) the administration of a paramagnetic contrast agent. The tumour has more permeable vessels such that contrast agent accumulates in the extracellular space.

3.4 Diffusion Weighted Imaging (DWI)

Diffusion weighted imaging is a useful tool for neurological imaging and is generally acquired as part of a routine head examination. It can add additional information for the differential diagnosis of cases such as cerebral abscess versus glioblastoma multiforme (47) and is also extremely sensitive to ischemic changes for the detection of stroke (48). DWI can also provide useful information on treatment response in tumours (49).

3.4.1 Principles

Le Bihan (50) and Merboldt *et al* (51) both pioneered diffusion weighted imaging, with the first papers presented in 1985. Le Bihan determined that the net diffusion of water was likely to vary between different pathological tissues, and that by utilising magnetic gradient pulses, could sensitise the MR sequence to the diffusion of water (b-factor). Unfortunately, the sequences available in the 1980's were slow and highly sensitive to motion, however, when implemented using echo planar imaging in the 1990's, the images could be acquired much more rapidly. This subsequently led the development of diffusion tensor imaging (DTI)(52) and intravoxel incoherent motion (IVIM)(53).

Current day DWI still uses an echo planar sequence to measure the change in MR signal produced by the random molecular movement of water molecules (Figure 43), known as self-diffusion (53). From MR diffusion measurements, an insight into tissue structure and organisation can be gained. The advantage of echo planar imaging is the rapid acquisition time, which means movement artefacts are reduced and signal averaging can be applied. In order to produce a diffusion weighted image, a pulsed gradient spin echo (PGSE) method (Figure 44) consisting of a 90^{o}–180^{o} spin-echo pair of RF pulses with large and equal gradients placed on either side of the 180^{o} pulse is applied.

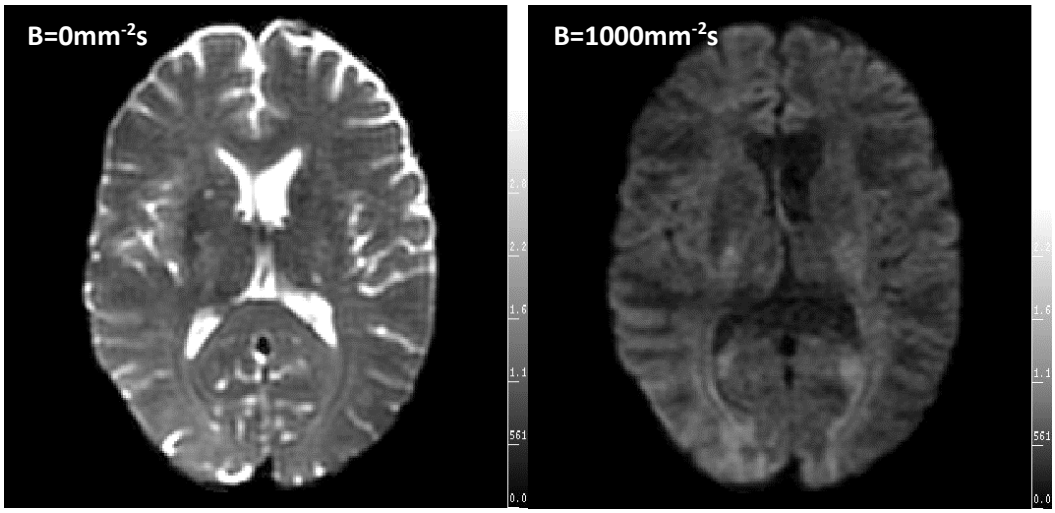

Figure 43 - EPI image with no diffusion weighting applied (b=0mm^{-2}s)(left) and an EPI image of the same slice with a diffusion weighting applied (b=1000mm^{-2}s)(right) both windowed identically. Note the global decrease in signal once a diffusion weighting is applied.

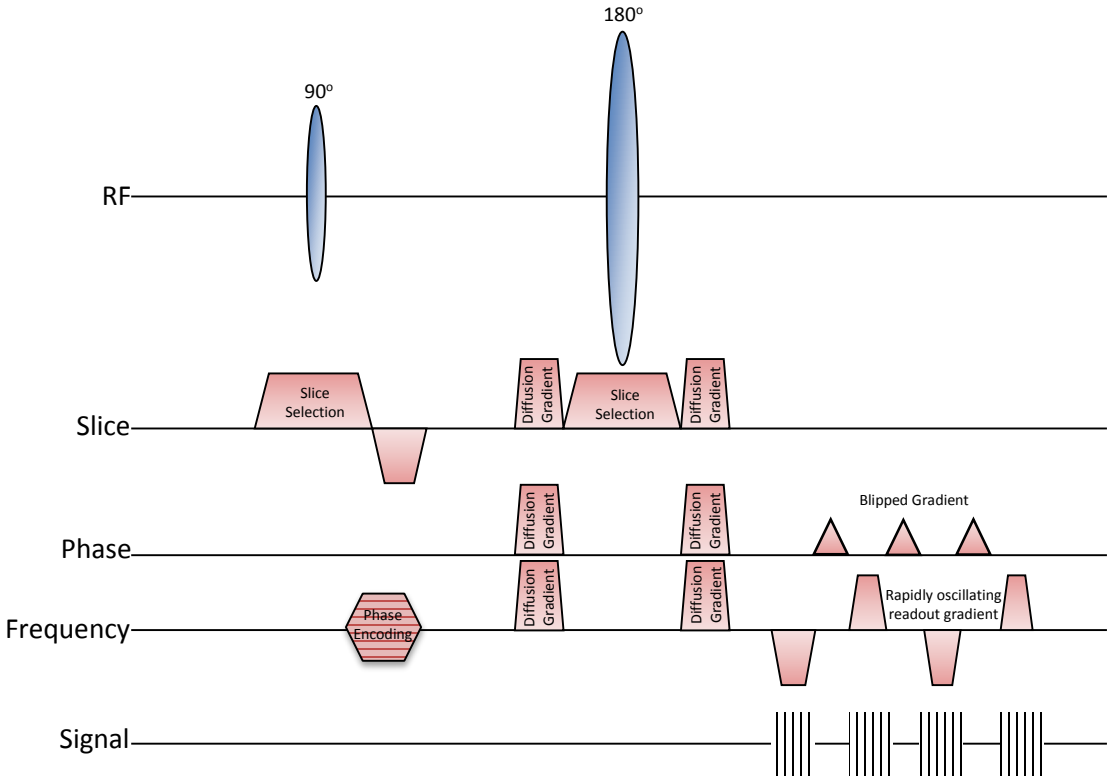

Figure 44 – Spin echo - echo planar pulse sequence diagram

Figure 45 demonstrates how the use of rapid gradient switching can be used to measure the signal loss due to self-diffusion.

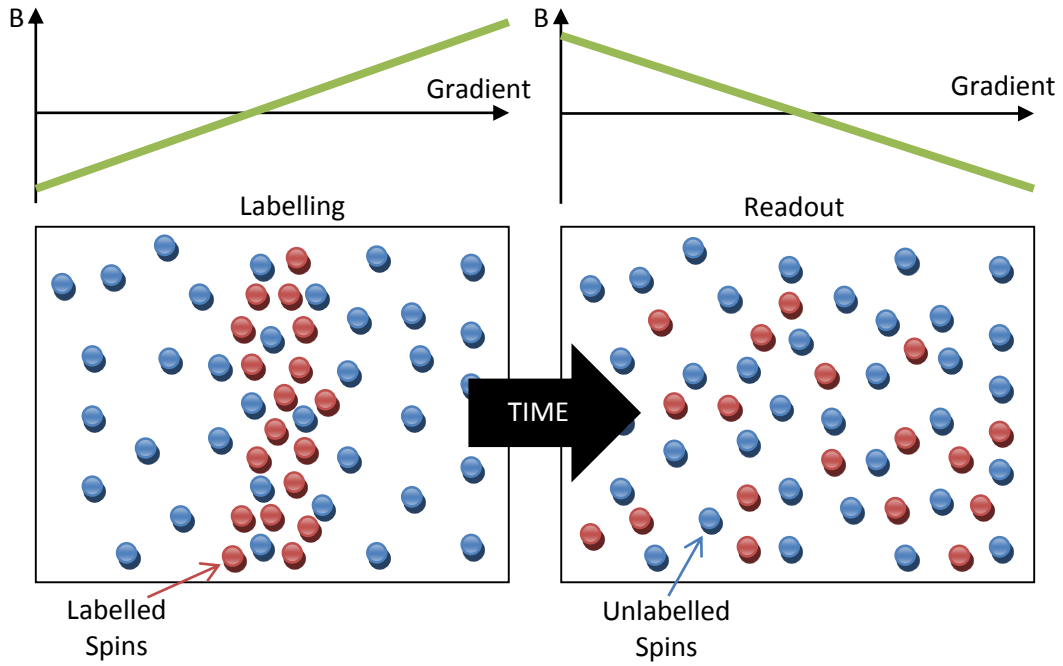

Figure 45 - Application of a diffusion gradient to a selected spatial region (left). This is called the labelling phase. Following self-diffusion during a set period of time, an inverse gradient is applied to the same region (right). When no diffusion is present, 100% of the signal is recovered because all of the spins rephrase correctly; however, if diffusion is present, the amount of signal rephased is reduced as the spatial location of the labelled spins alters, causing the signal to be incorrectly refocused, and subsequently reduced.

By controlling a series of parameters (strength of the gradient, pulse width and the centre to centre spacing) one can control the degree of weighting more commonly known as the *b*-value.

$$b = \gamma^2\delta^2G^2(\Delta - \frac{\delta}{3}) \qquad \text{Equation 24}$$

where γ = gyromagnetic ratio, δ = gradient duration, G = gradient amplitude, Δ = time between gradients.

In DWI more mobile molecules have lower signal intensities while the more static molecules provide a higher MR signal (Figure 46). The signal strength can be described by the equation.

$$log\left(\frac{S_b}{S_0}\right) = -bD \qquad \text{Equation 25}$$

Where in this case S_b is the signal strength using the *b*-value and S_0 is the signal strength at $b = 0$, *b* is the *b*-value and *D* is the self-diffusion coefficient otherwise known as the apparent diffusion coefficient (ADC) in MR. This model assumes that the diffusion measured is a mono-exponential model and that no perfusion effects are present.

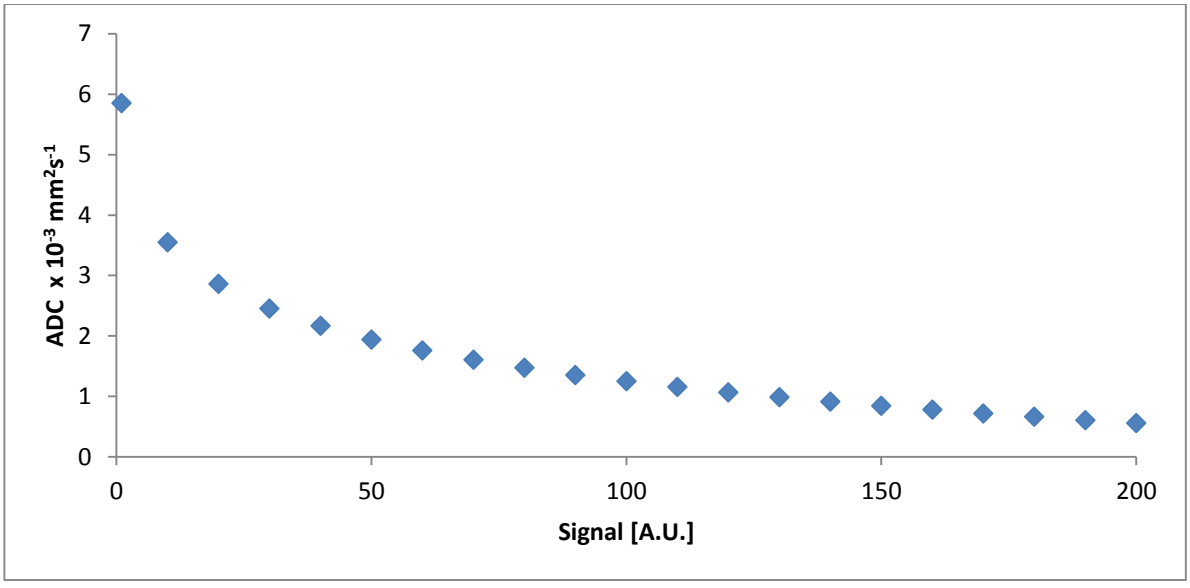

Figure 46 - Synthesised data showing that decreased signal results in higher apparent diffusion values. The b-value was set to 1000mm^{-2}s and S_0 was 350.

DWI works on the basis of all the molecules moving in a random motion with unique phase changes. This ideally results in a net loss of signal intensity for each voxel provided enough diffusion weighting is applied (Figure 46). Pure water is said to be isotropic, meaning that the movement of molecules is completely random and not biased in any direction. This in turn should mean that a gradient could be applied in any direction with no change in results. The diffusion behaviour in the human body is partially anisotropic however, meaning the diffusion paths are more favourable in certain directions (Figure 47)(Table 3).

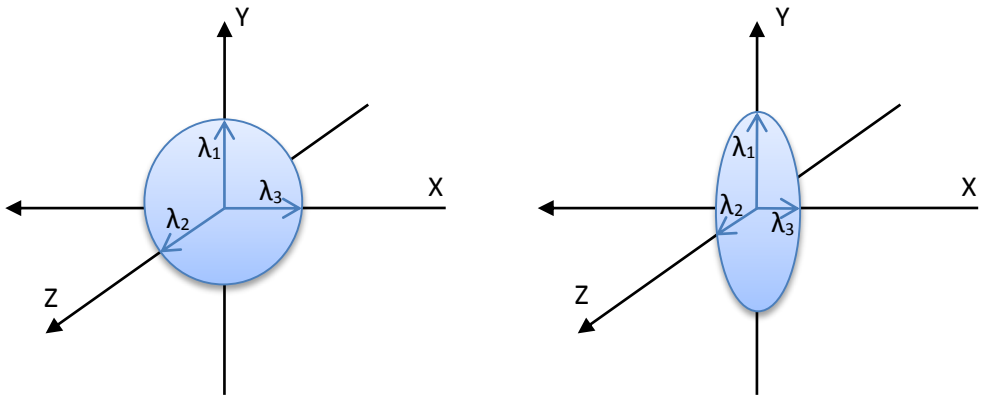

Figure 47 – Ellipsoids created from the 3 eigenvalues derived from the diffusion tensor, representing isotropic diffusion with no principal diffusion direction ($\lambda_1=\lambda_2=\lambda_3$) (left), and anisotropic diffusion ($\lambda_1>\lambda_2\geq\lambda_3$) (right).

Table 3 - Differences in diffusion direction cannot be seen using ADC values.

Isotropic Diffusion	**Anisotropic Diffusion**
$ADC_x = 1\ mm^2/sec$	$ADC_x = 0.8\ mm^2/sec$
$ADC_y = 1\ mm^2/sec$	$ADC_y = 1.4\ mm^2/sec$
$ADC_z = 1\ mm^2/sec$	$ADC_z = 0.8\ mm^2/sec$
Mean ADC = 1 mm^2/sec	**Mean ADC = 1 mm^2/sec**

3.4.2 Measurement of ADC

The apparent diffusion coefficient can be calculated from two or more images with differing *b*-values. Standard implementations of diffusion weighted sequences collect signal from three principal axes, X, Y, Z, before averaging the signal. The units of ADC are mm^2/s and represent the magnitude of the diffusion occurring. ADC values are also known to change according to the cellular conditions within a volume of excitation with the signal predominately arising from the extracellular component (Figure 48). Restricted diffusion happens where physical barriers like cell membranes occur. A higher ADC value implies more self-diffusion and therefore a lower cellularity. Without knowledge of the diffusion direction it is possible for the ADC to be the same in both isotropic and anisotropic situations.

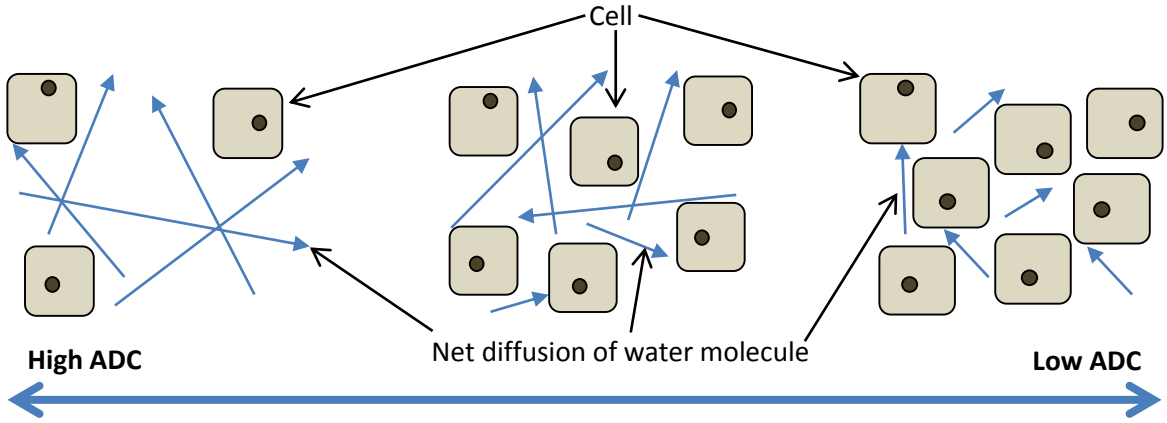

Figure 48 - Examples of mean diffusion in different tissues. Left - low cellularity in necrosis for example allows the water to move freely and uninterrupted, meaning the diffusion signal is very low once the readout gradient is applied and subsequently the apparent coefficient value is high. Middle – Diffusion in normal tissue results in some reduction of signal and a subsequent intermediate ADC value. Right - In solid tumour, there is increased cellularity so the the water molecules do not move very far and as a result, more signal is retained. Low ADC values are associated with this tissue type.

3.4.3 Diffusion Tensor Imaging (DTI)

Diffusion Tensor Imaging shares the same basic set of principles as DWI. It differs by using more sampling gradients to measure the rate of diffusion (minimum of 6 diffusion weighted directions) (54). The differing gradients subsequently allow the measurement of the tensor. The advantage of using this method to measure diffusion includes access to calculations for the fractional anisotropy (FA), a measure of diffusion directionality, as well as potentially improved accuracy of ADC measurements due to a higher number of diffusion measurements. Diffusion tractography is a tool to visualise the white fibre tracts in the brain, identified by their high FA values. By measuring diffusion in multiple directions, the additional benefit of increased SNR due to signal averaging is added. The main limitation of DTI is time, with the number of gradients used being the main determinant of acquisition time. In diffusion tensor imaging an ellipsoid is used to describe the direction of the diffusion. This relies on knowing the three major vectors and their angles.

3.4.3.1 Calculations of ADC and FA from DTI

As previously stated, once diffusion weighted images are acquired for six or more directions, it is possible to calculate the orientation in which diffusion is occurring for any given voxel. The more directions used, the higher the accuracy of the orientation is likely to be. From the diffusion tensor, 3 eigenvalues (λ_1, λ_2 and λ_3) are produced regardless of the number of gradient directions which are the principal diffusion components. The two most commonly calculated parameters from diffusion tensor imaging can be seen below.

Apparent Diffusion Coefficient (**ADC**) [x10^{-3}mm^2/sec]

$$ADC = \frac{\lambda_1+\lambda_2+\lambda_3}{3} \qquad \text{Equation 26}$$

Fractional Anisotropy (**FA**) [A.U.]

$$FA = \sqrt{\frac{3}{2}}\sqrt{\frac{(\lambda_1-ADC)^2+(\lambda_2-ADC)^2+(\lambda_3-ADC)^2}{{\lambda_1}^2+{\lambda_2}^2+{\lambda_3}^2}} \qquad \text{Equation 27}$$

3.4.4 Diffusion Artefacts

3.4.4.1 Chemical Shift Displacement

Chemical shift misregistration is an artefact that can occur in diffusion weighted imaging. By examining a phantom experiment of ethanol, it is possible to demonstrate how chemical shift occurs. Ethanol comprises of three different chemical groups (CH_2, CH_3 and OH), with each group resonating at a slightly different frequency due to changes in the B_0 field experienced as a result of electron shielding. These chemical shifts subsequently produce bands (Figure 49) of the three different chemicals peaks as they are excited in differing spatial locations.

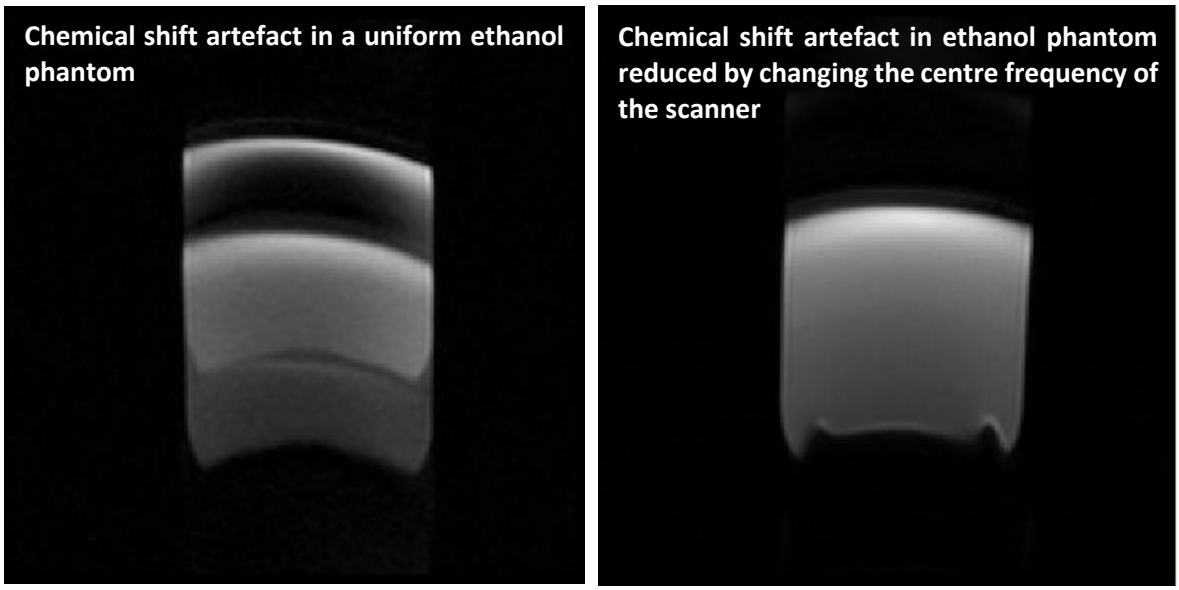

Figure 49 - Example of Chemical Shift in Ethanol at b = 200 mm^2s^{-1} (left). Example of Ethanol at b = 200 mm^2 s^{-1} with no chemical shift following a change in centre frequency (right)

Normally MR scanners are set to scan using a centre frequency relating the resonances present. However for ethanol, the spectrum produced is not symmetrical, which causes the banding. The solution being to manually change the RF to focus on the third peak, that of the CH_3. This peak has largest resonance related to having the highest number of hydrogen protons. With the chemical shift corrected for, the phantom now has a more uniform appearance.

3.4.4.2 Susceptibility Artefacts

Figure 50 shows an example of EPI susceptibility artefacts seen in the brain. The cause for such artefacts is due to the magnetic susceptibility interface between the bone and tissue. The interface causes the dephasing of spins and a subsequent frequency shift which causes the bright and dark regions adjacent to the interface. The level of distortion can worsen depending on the two substances and how large the difference in magnetic susceptibility is at the interface (e.g. water and air).

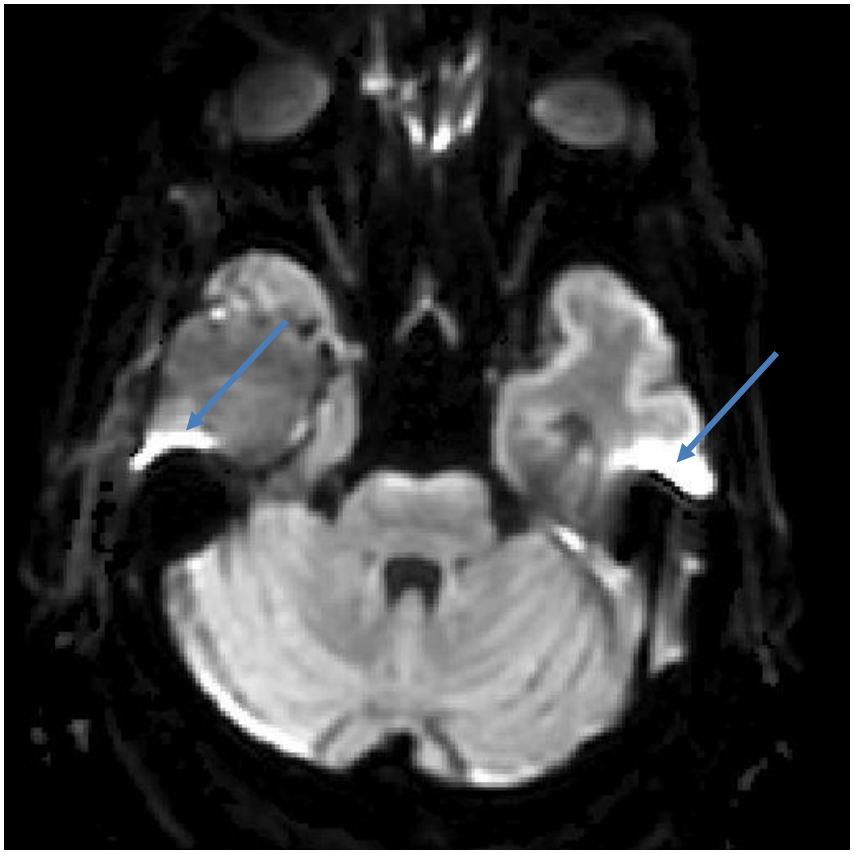

Figure 50 – Isotropic diffusion weighted image from a glioma patient. This image shows two areas with prominent susceptibility artefact generated from the interface between the petrous bone and the tissue of the temporal lobes.

Old blood products with large amounts of hemosiderin such as bleeds can also cause susceptibility artefacts which destroy characteristic information about the surrounding tissue. These areas often appear with low signal intensities for both the $b = 0 mm^2 s^{-1}$ and the higher b-value images.

3.4.4.3 Eddy Currents

Eddy currents are another type artefact that EPI is particularly sensitive to due to the rapid gradient switching. These currents can distort the image causing a combination of shear, scale and shift effects. The rapid gradient switching and strong diffusion gradients induce currents in the hardware which subsequently produce additional smaller magnetic fields. This causes a non-uniform magnetic field as the pulse sequence runs and subsequently the pulse shapes differ to the desired shape causing distortions. Figure 51 is an example of the geometric distortion caused by the eddy currents. This problem can make the registration of EPI to spin or gradient echo sequences problematic. Pre-emphasis and/or active shielding are used to reduce the effects of eddy currents.

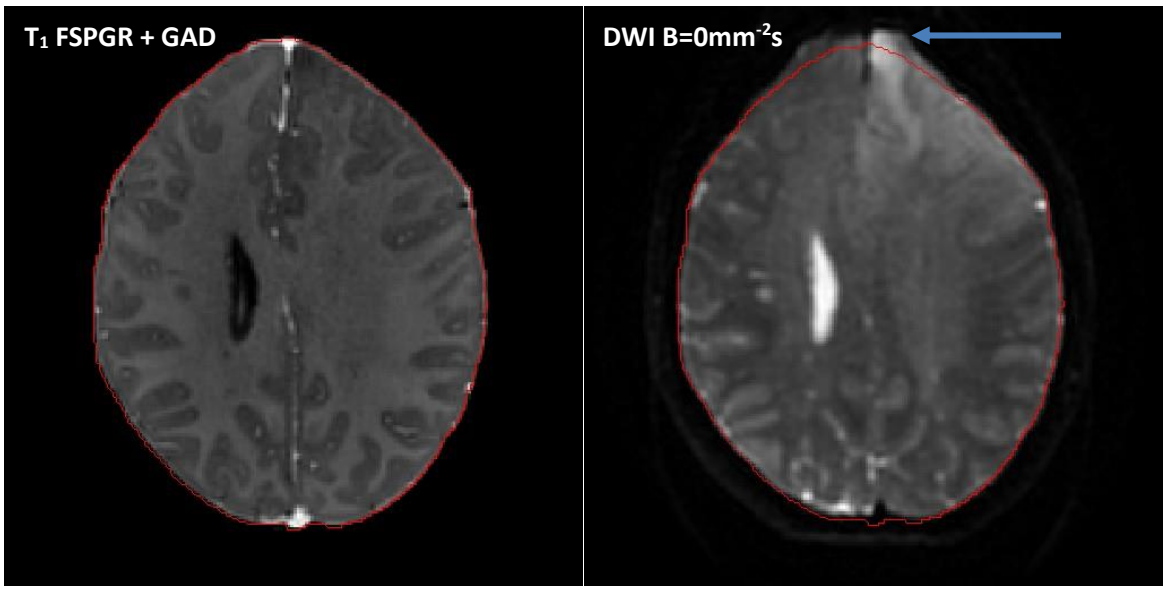

Figure 51 - Axial post-contrast T_1 weighted FSPGR from a glioma patient (Left). The red line denotes the edge of the brain as defined by this sequence. A T_2 weighted b=0 s/mm^2 (right) was overlaid with the same red edge mask. The anterior aspect of the diffusion imaging can be seen to be elongated as a result of eddy currents.

3.5 Dynamic Contrast Enhanced MRI (DCE)

Dynamic Contrast Enhanced MRI is a T_1 weighted perfusion technique that directly measures the effect of the contrast agent bolus passing through vessels of the tissue (Figure 52). A selected volume is imaged rapidly before and during the contrast agent injection allowing a time course to be built for each pixel (Figure 53). DCE can be quantified in two ways, firstly empirical techniques which exams the area of the curve at a set time or the steepness of the initial upslope and the downslope. Secondly, pharmacokinetic (PK) modelling, pioneered by the likes of Tofts, Kermode, Larsson and Brix (55-58), where the concentration of contrast is considered in order to estimate the exchange of the agent between tissue compartments. Using PK models it is possible to measure the capillary permeability (K^{trans}) and the extracellular volume (v_e). A rate constant (k_{ep}) is also used to describe the interaction between the extravascular, extracellular space (EES) and the blood plasma.

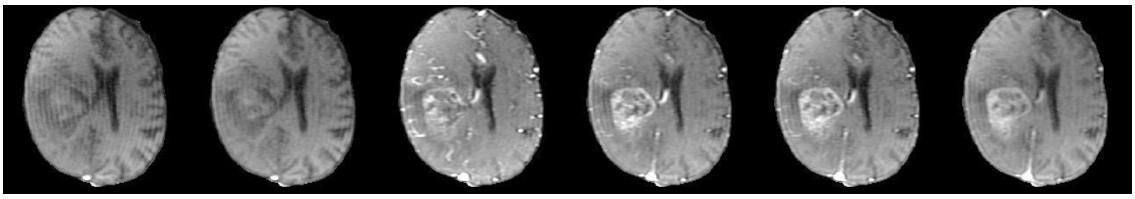

Figure 52 - Time course from a DCE acquisition in the head, with images from phases 1,5,9,13,17 and 51 with the window levels constant. The scan interval was 5 seconds per phase. Contrast agent was injected at the end of the 4th phase.

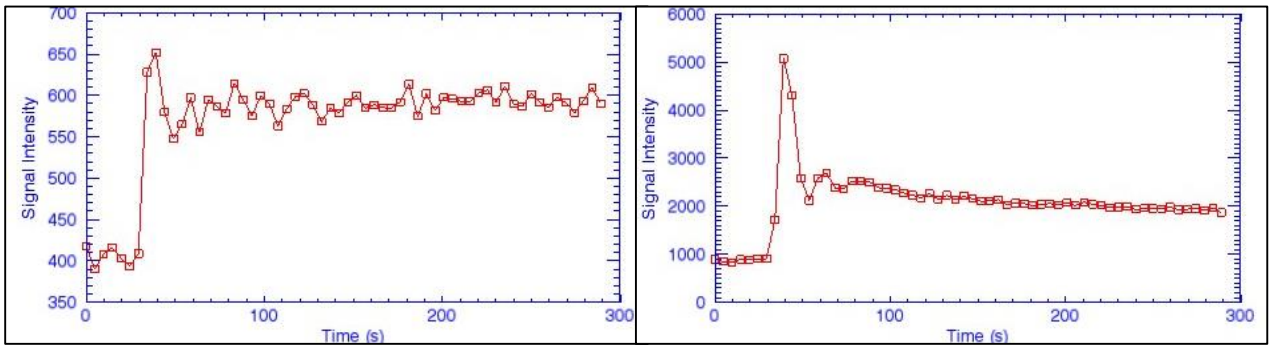

Figure 53 - Example time courses for two areas of enhancement in a brain. An enhancement curve from a high grade glioma can be seen on the left while an arterial input function (AIF) curve from the central sinus can be seen on the right.

The most common pharmacokinetic model used to describe the interaction between plasma and the ESS is the two-compartment model (56) (*Figure 54*). This simplistic model measures the K^{trans}

and k_{ep} to calculate the v_e. It is possible to add additional terms onto this model to measure the plasma volume (v_p) (59). However, calculation of v_p also requires identification of an arterial input function (AIF). In order to calculate a good AIF, a sequence with a high temporal resolution is required. Quantitative analysis of K^{trans} requires an estimation of a baseline T_1, and tissue constants for tissue density and haematocrit.

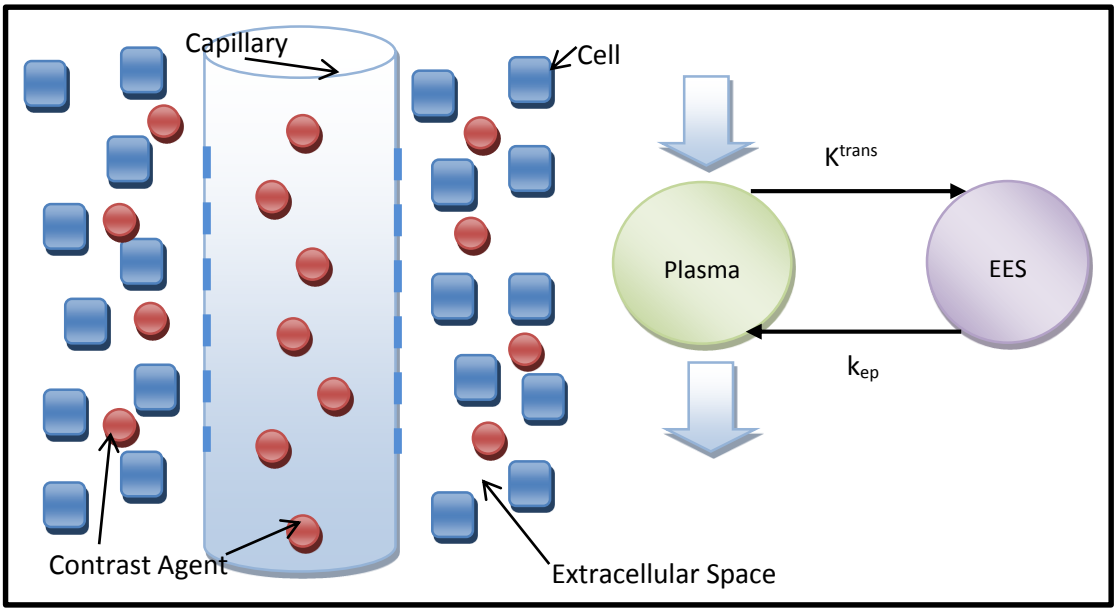

Figure 54 - Diagram of two-compartment model

For a DCE sequence to be successful the following criteria must be met:

- A high temporal resolution for AIF identification
- Heavily T_1 weighted (short TE and TR)
- Sufficient scan time to observe washout from slow leaking vessels

With DCE, the user must decide between spatial and temporal resolution. Temporal resolution is needed in order to correctly estimate an AIF while spatial resolution is needed to reduce partial volume effects.

3.5.1 DCE Artefacts

When examining dynamically acquired data it is important to examine the quality of the time course. Errors with the acquisition of the data, such as motion lead to non-sensical parameter maps once processed. Figure 55 shows two cases where the time courses acquired were not suitable for quantification due to acquisition problems.

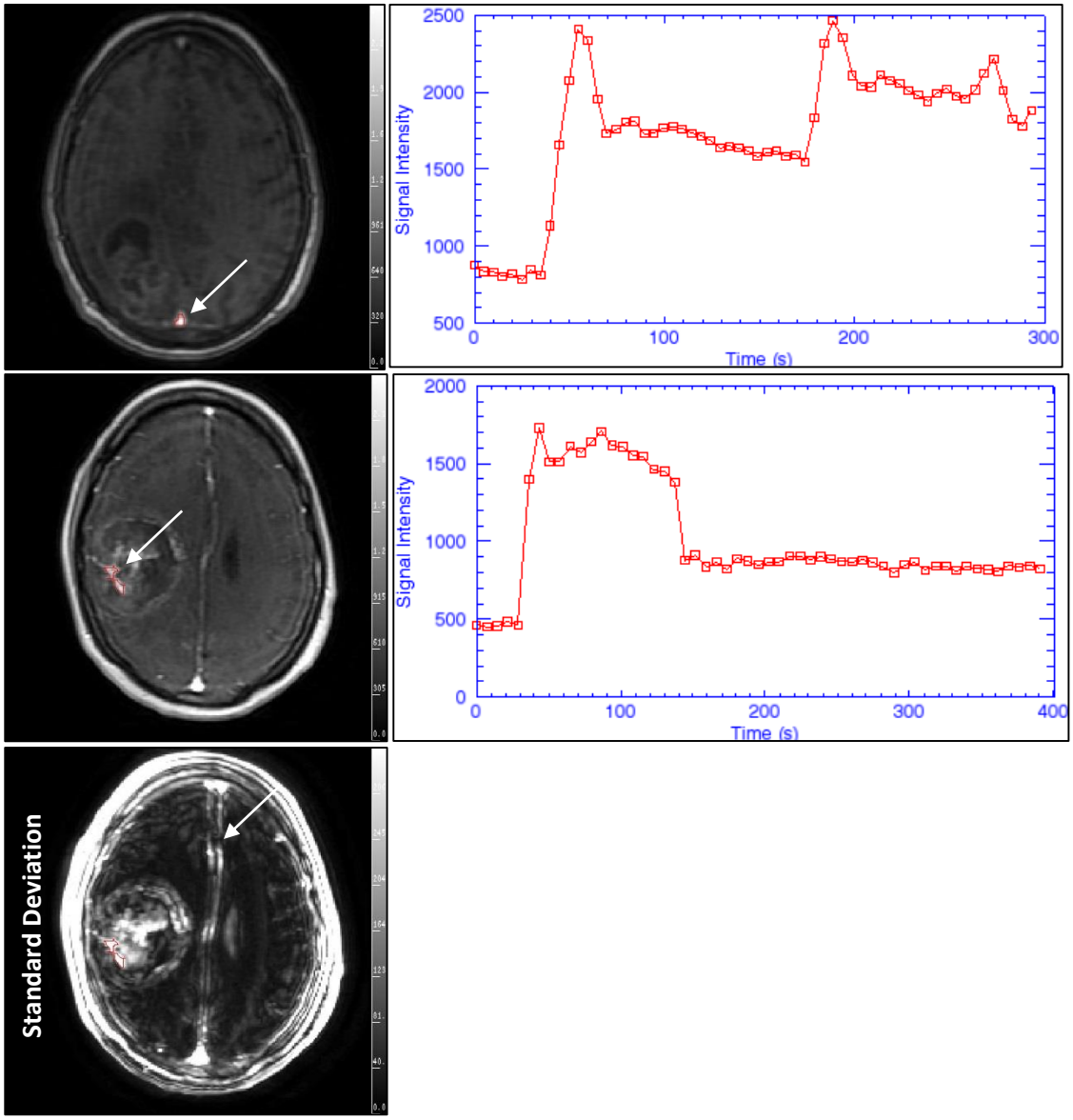

Figure 55 – (Top) The time course has two large increases in signal which was caused by a pump injector delivering the contrast agent in two parts due to a back pressure problem. The bottom time course was taken from a patient with obvious motion, with an unusual drop in signal seen at around 150 second. A standard deviation map of the time course also shows gross artefacts.

3.5.2 DCE to Visulise Gadolinium Enhancement in the Presence of Blood Products

Traditionally, pre- and post-contrast T_1 weighted images are acquired to assess whether tissue shows signal enhancement following the administration of gadolinium. However, this may require the patient to be removed from the scanner to administer the contrast agent and relies on the patient not moving. The compression of the pads within the head coil and the interval between the two sequences normally means that subtracted images can contain high levels of artefact. With DCE however, both pre- and post-contrast T_1 weighted images are acquired sequentially, which improves contrast visualisation (Figure 56) whilst minimising the effect of motion. This, combined with a high temporal resolution, allows images to be motion corrected post-acquisition to allow for any small movements in the scanner. The administration of the contrast agent with an injector pump also reduces the opportunity for patient motion.

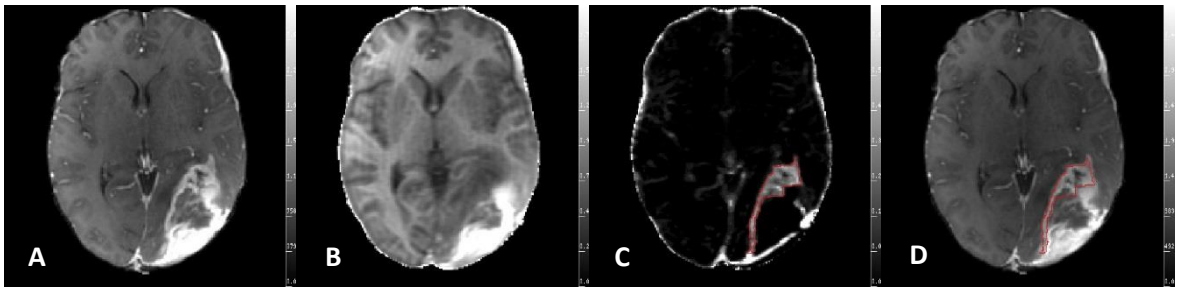

*Figure 56 –Postoperative imaging of a gliosarcoma with gadolinium (**A**). Demonstration of enhancement and blood products on the post-contrast T_1 weighted imaging. Pre-contrast imaging (**B**) shows blood in the acute stage which is bright on T_1 weighted imaging, however, the post contrast imaging (left) fails to delineate the enhancing tumour from the blood products. On the DCE v_e map scaled between 0 and 0.75 ml of space/ml of tissue (**C**) contrast enhancement is apparent with no sign of the blood product. A region of interest contoured from the DCE (**C**) around the enhancing portion of the tumour can be seen to fit around a select section of the T_1 post-contrast imaging (**D**).*

This enhanced visualisation of gadolinium uptake has the potential to improve radiotherapy planning in patients with blood products following an acute bleed. Likewise, tumours which present with a bleed could also be better visualised using this method.

3.6 Dynamic Susceptibility Contrast Imaging (DSC)

Dynamic susceptibility contrast, otherwise known as T_2* perfusion imaging, is a method for measuring the blood supply to tissue. First described in the 1980's by Villringer *et al* (60), DSC is able to measure the cerebral blood flow (CBF)[ml/minute/100 gram], cerebral blood volume (CBV) [ml/100 gram] and mean transit time (MTT)[seconds]. These are often used in relation to normal appearing contralateral tissue or a fixed area of tissue, and given the prefix 'r' when appropriate to represent these are relative values.

DSC is a T_2* weighted acquisition relying on the susceptibility effect caused by the bolus of contrast as it passes through blood vessels (Figure 57). In order to ensure contrast is administered at a fast rate to maintain a tight bolus, a pump injector is often used with the added benefit that contrast can be administered remotely from the scanner control room. Due to the high temporal nature of this type of acquisition, the spatial resolution is often reduced to allow a greater volume of coverage.

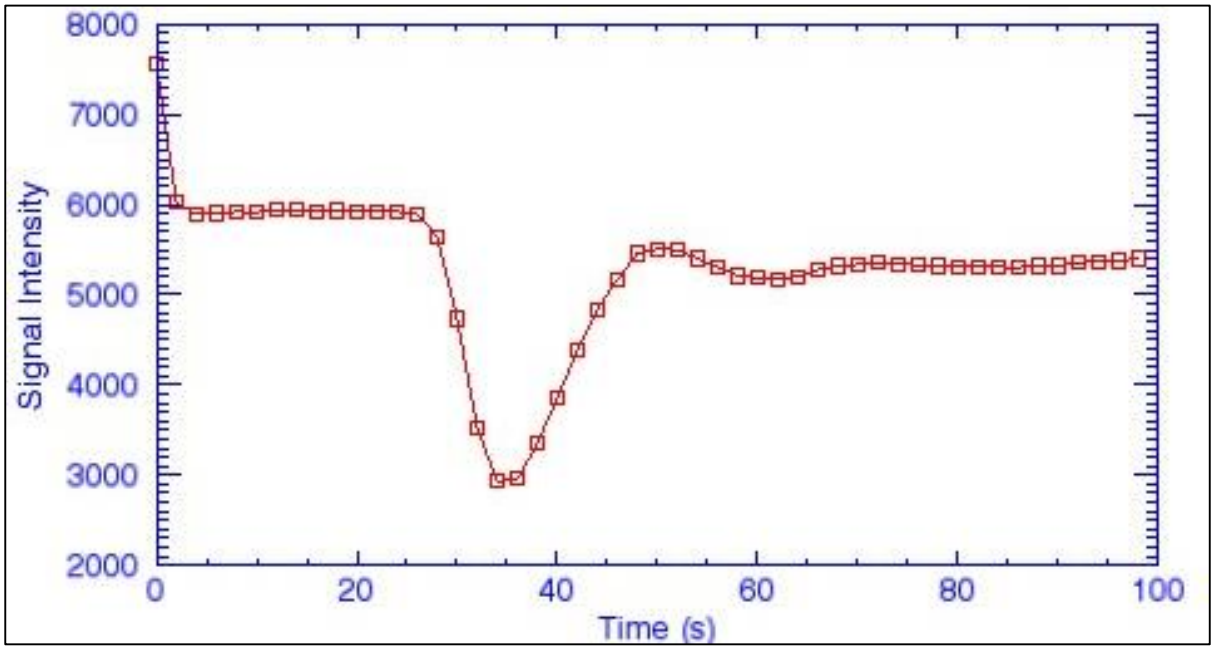

Figure 57 - Example DSC time course from a high grade glioma measured with a 2 second temporal resolution.

The simplest way to interrogate a DSC dataset is by an integration of the bolus once converted to a concentration curve (Figure 58).

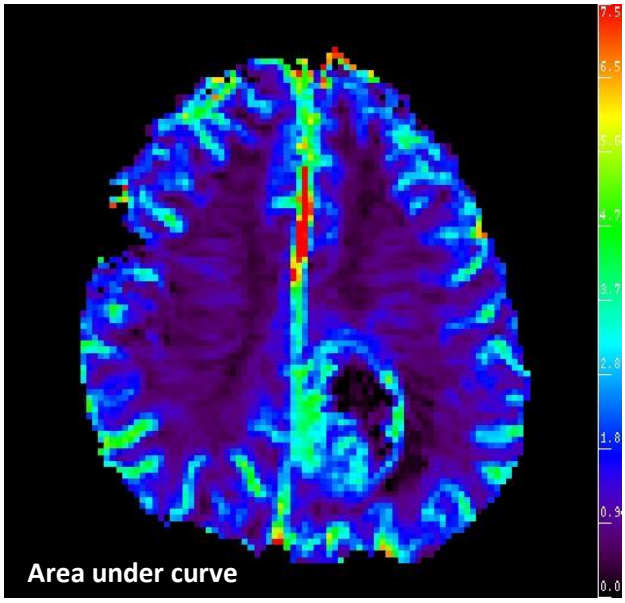

Figure 58 - Example DSC map showing the area under the curve (AUC) white matter normalised and scaled between 0 and 7.5 [A.U.].

However, a one compartment model can also be applied in order to describe the blood volume purely based upon the flow and mean transit time (MTT).

$$Volume = Flow\ x\ Mean\ Transit\ Time \qquad \text{Equation 28}$$

In magnetic resonance, the venous tracer concentration is not directly measured, instead the amount of contrast in the surrounding tissue being used as in indication.

The shape and size of the bolus can be used to roughly estimate characteristics about the blood vessels. Bolus height is comparable to CBF, bolus area representative of CBV and the time over which the bolus occurs being the MTT (Figure 59). Further analysis can be carried out using pharmacokinetic modelling in which the arterial input function (AIF) is measured from one of brains major arteries.

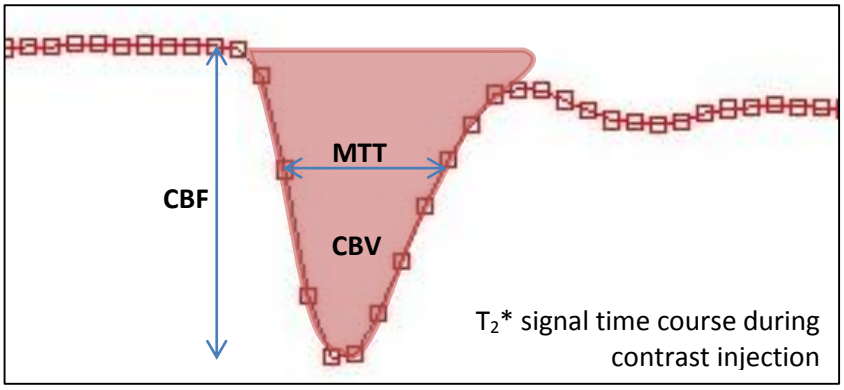

Figure 59 - Representation of cerebral blood volume (CBV), cerebral blood flow (CBF) and mean transit time (MTT) calculated from the first pass of a T_2 dynamic time course following an injection of gadolinium.*

There are many challenges associated with absolute DSC quantification, including the correct identification of the AIF, partial volume effects when measuring the AIF and having a good knowledge of tissue specific constants. Partial volume effects caused by different tissue types is also important to resolve if white matter is to be used for normalisation (61). The benefits of absolute quantification are strong however, with most papers in publication now using absolute quantification.

In DSC, it is possible for both T_1 and T_2* dominant leakage to occur once the BBB is disrupted depending on a multitude of factors including field strength, tumour type, sequence parameters and contrast dose (62). T_1 dominant situations cause underestimation of CBV while T_2* dominant leakage leads to an overestimation the CBV value (12) and subsequent calculations of the MTT (63). Pre-loading of the tissue prior to DSC injection can reduce the concentration gradient of the contrast agent, which subsequently reduces the amount of contrast leakage from the vessels (64). By accounting for leakage, greater statistical differences can be found when predicting tumour response (65).

Both spin echo (SE) and gradient echo (GE) echo planar imaging (EPI) sequences can be used for DSC, each with their own advantages. SE sequences have better spatial resolution for a set period of time and are sensitive to small changes, for instance in capillaries, as well as being less prone to

susceptibility effects. GRE on the other hand offers the opportunity to measure larger vessels which can occur in tumours. It is believed that vessel size supplying the tumour may give some prognostic indicator (66). The use of a hot-spot approach also has limitations in a similar way to absolute quantification. Primarily, finding the correct reference tissue can be difficult especially in cases such as butterfly gliomas or tumours with large amounts of mass effect.

An effective DSC protocol requires:

- Rapid bolus injection
- T_2* gradient echo or spin echo single shot echo planar sequence
- High number of sampling points during the bolus (high temporal resolution)

The signal intensities reported following a DSC acquisition can be converted to contrast agent concentration. Where C(t) is concentration, S(t) is signal intensity and S_0 is the baseline signal intensity.

$$C(t) \propto \Delta R2^*(t) \quad \text{Equation 29}$$

$$\Delta R2^*(t) \propto -ln\left(\frac{S(t)}{S_0}\right)/TE \quad \text{Equation 30}$$

The CBV can be defined as the area under the tissue concentration curve during the first pass (bolus). CBF arises from the height of the tissue concentration curve after any corrections. Finally the MTT can be calculated as a ratio of the CBV/CBF.

3.6.1 DSC Artefacts

As stated, DSC relies on a contrast bolus to cause a local susceptibility effect which decreases the signal of tissue according to the amount of contrast in the vessels. However, the bolus cannot be visualised when the signal is already low (in the noise floor). One reason for low signal is due to iron contained in hemosiderin which is a residual product of blood (Figure 60). This can cause a gross underestimation of the tumour blood volume (Figure 61).

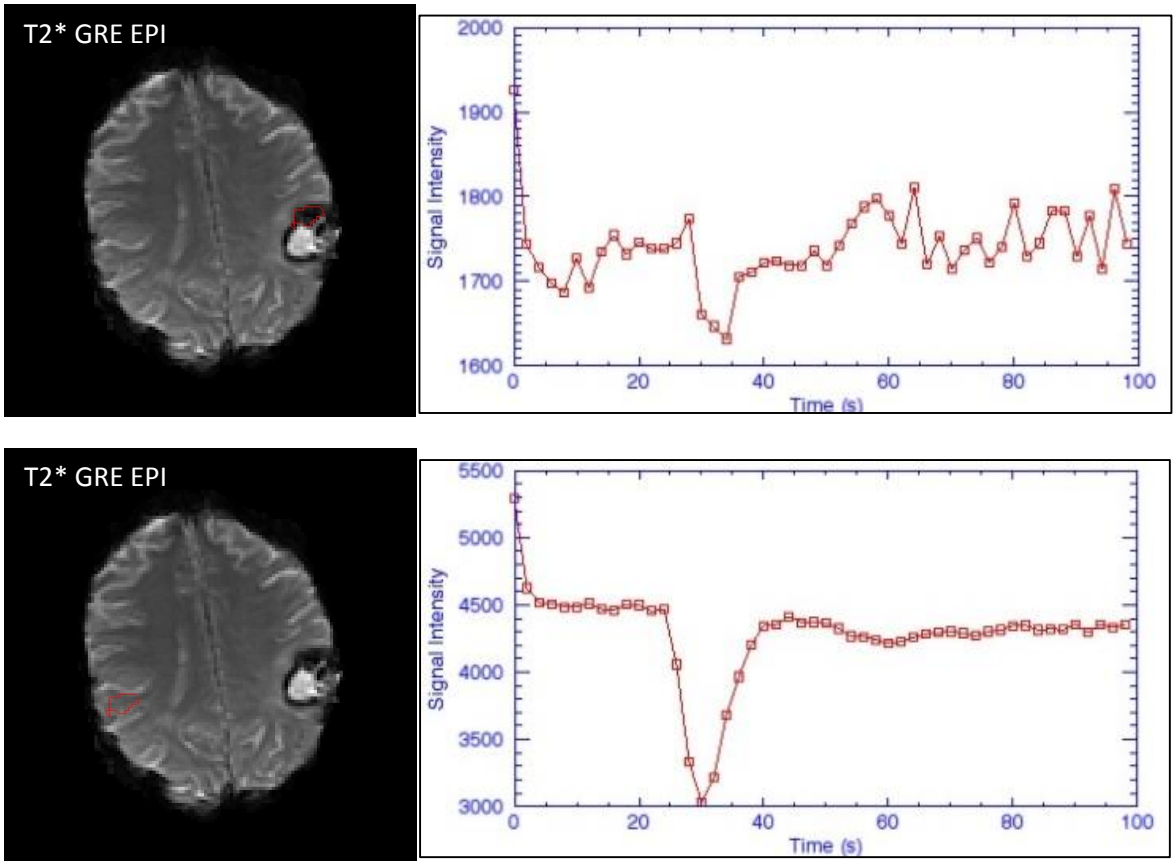

Figure 60 – (Top left) example DSC acquisition where large amounts of hemosiderin are present. A small ROI can be seen on the tumour cavity rim with low signal. The subsequent time course (top right) has very little signal change. The bolus is also poorly defined. (Bottom left) the same ROI was moved to the contralateral tissue. The time course (bottom right) shows a greater baseline signal as expected with a much larger bolus as the local susceptibility effect can be observed.

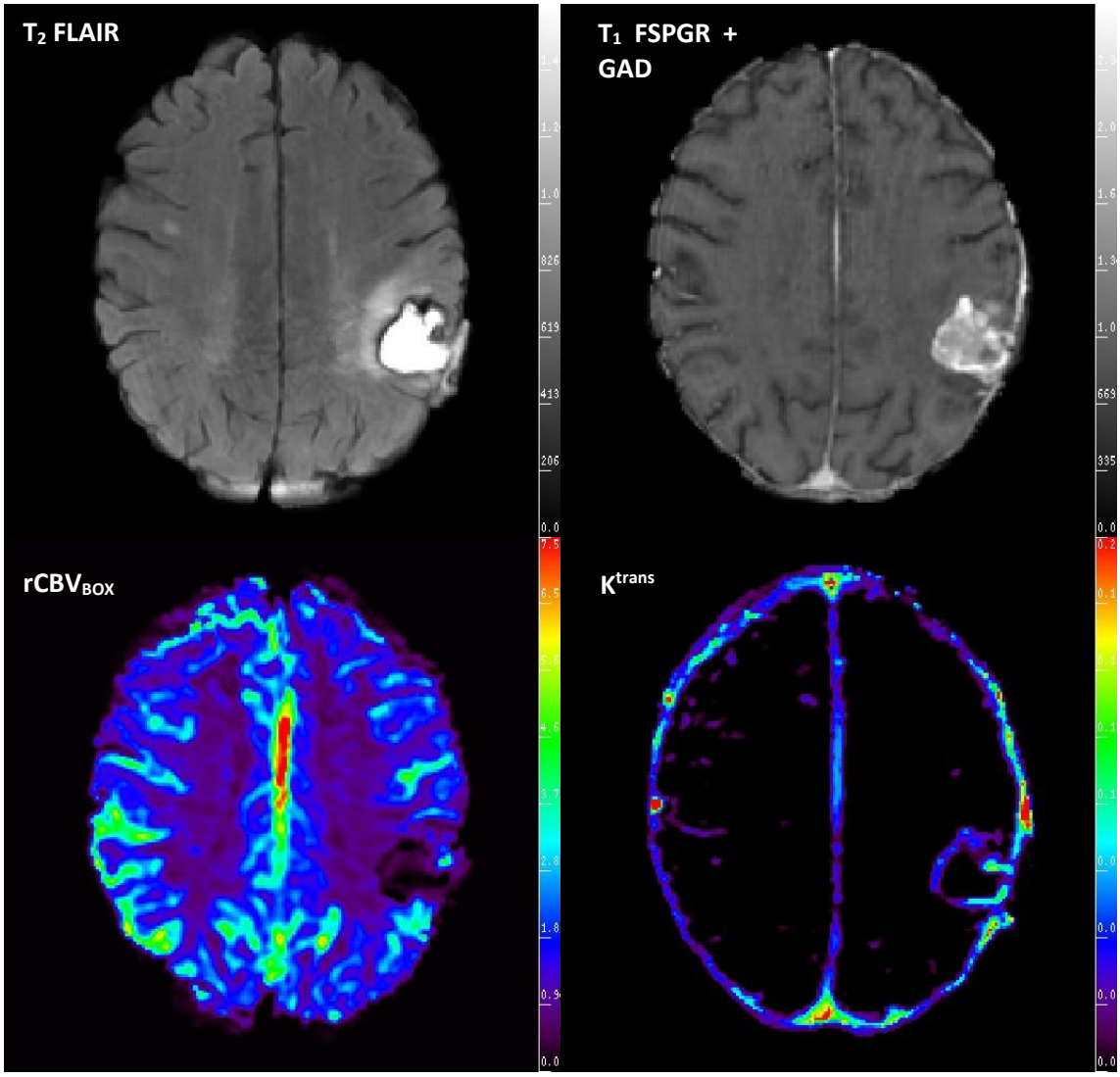

Figure 61 – Hemosiderin, blood product and tumour seen on morphological imaging (top left and top right). The rCBV map (bottom left) scaled between 0 and 7.5 shows no blood volume in the rim of the tumour cavity due to the hemosiderin destroying the local susceptibility effect caused by the contrast bolus. K^{trans} (0-0.2min^{-1}) the same location shows enhancement on the rim of the cavity to which the DSC was insensitive to.

Metal objects such as surgical clips also cause local susceptibility artefacts which destroy the bolus effect from the contrast agent. This limits the use of DSC for detecting residual tumour within the first week of surgery due to blood products and surgical clips. Since the sequence is susceptibility weighted, regions adjacent to a tissue-air interface are often lost. The underlying echo-planar sequence is also subject to the same eddy current problems as experienced with DWI.

3.7 Magnetic Resonance Spectroscopy (MRS)

Magnetic resonance spectroscopy is a technique for interrogating metabolic information for a given volume of tissue. In order to visualise the metabolites in a spectrum, the water must be sufficiently suppressed, since the high concentration at which it exists, produces a peak several magnitudes greater than that of the metabolites of interest. Each metabolite produces a unique spectral pattern of peaks which appear at a specified frequency along the chemical shift axis, a property which is used to help identify them.

3.7.1 Sequences

The two clinically available spectroscopy sequences are STEAM (90°-90°-90°) and PRESS (90°-180°-180°), each with their own advantages. PRESS (spin echo) is more commonly used since it has up to twice as much SNR compared to STEAM (stimulated echo). This can be explained by the second 90^{o} pulse that STEAM uses, which causes the direction of magnetisation to be split into two. Once refocused with the third 90^{o} pulse, only half of the original magnetisation is realigned and thus only half the signal remains. Unfortunately there is no classical explanation for the reason why STEAM only produces ½ the SNR and so quantum mechanics must be used instead. PRESS uses a similar technique, but the use of two 180^{o} pulses ensures realignment of all the spins.

Due to the three 90° pulses STEAM uses, it can produce sharper slice profiles than PRESS. The higher bandwidths available with 90° pulses also result in less chemical shift displacement error. Another clinical consideration is that STEAM is more susceptible to motion effects than PRESS (34) especially if the mixing time (TM) is long. Historically STEAM was used to reach shorter echo times that PRESS was not capable of achieving. In this thesis only PRESS was used, and so STEAM is not mentioned in more detail.

*3.7.1.1 **P**oint **RES**olved **S**pectroscopy (PRESS)*

PRESS is a Spin Echo sequence, designed by Paul Bottomley in 1987 (67) while working for General Electric. In PRESS, a 90° pulse is followed by two 180° pulses, so that the primary magnetisation can be refocused again by the third pulse. In practice at 3.0T, flip angles of 137 ° are used for the refocusing pulses due to the need for a larger excitation bandwidth, in an effort to minimise chemical shift artefacts, and SAR. Each pulse has a slice selective gradient on one of the three principal axes, so that only protons within the voxel at the intersection are subject to all three RF pulses. The signal intensity depends on the pulse spacing and relaxation times. Additional phase encoding gradients can be added to enable multivoxel acquisitions.

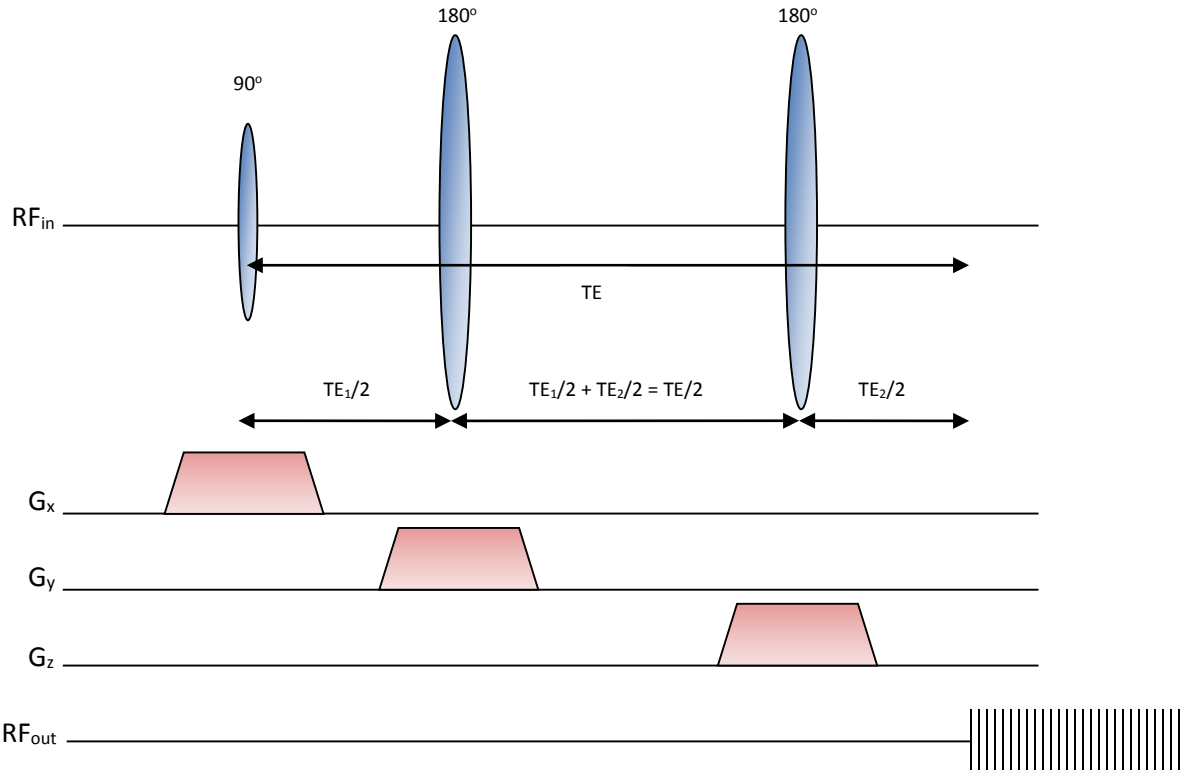

Figure 62 - PRESS pulse sequence

In Bottomley's original paper (67), he describes the advantages of using PRESS, saying it "yields sharply defined volumes localised in all three dimensions", though later going on to describe the limitations stating that the metabolites to be examined must possess a sufficiently long T_2 relaxation value in order for detection.

3.7.2 Single Voxel Spectroscopy (SVS)

The simplest way to acquire spectroscopic data is in the form of a single localised voxel (volumetric pixel) using three mutually orthogonal slice selective pulses to excite the volume of tissue where all slices intersect. To stop unwanted signal from outside of the voxel, crusher gradients are used with the addition of six saturation bands which encompass the prescription box. Additional saturation bands can also be used to stop signal interference caused by areas of susceptibility such the nasal cavity, or bone from the skull base. The effectiveness of crusher gradients and the quality of spatial localisation needs to be highly efficient when considering the size of the voxel in relation to overall volume of tissue in a brain. SVS has utility when investigating focal abnormalities (Figure 63) and, depending on the pathology in question, several echo times may also be used. SVS has the advantage of being able to produce high SNR data by spectroscopic standards compared to multivoxel techniques. Some of limitations though of the technique include the poor spatial coverage, and relies heavily on the user to optimally place the voxel. Partial volume effects are another issue with SVS given the typical voxel size is between 3-8ml at 3.0T. Due to the higher number of signal averages over the same time, single voxel spectroscopy produces higher SNR spectra for a given voxel, however is less efficient compared to multivoxel techniques.

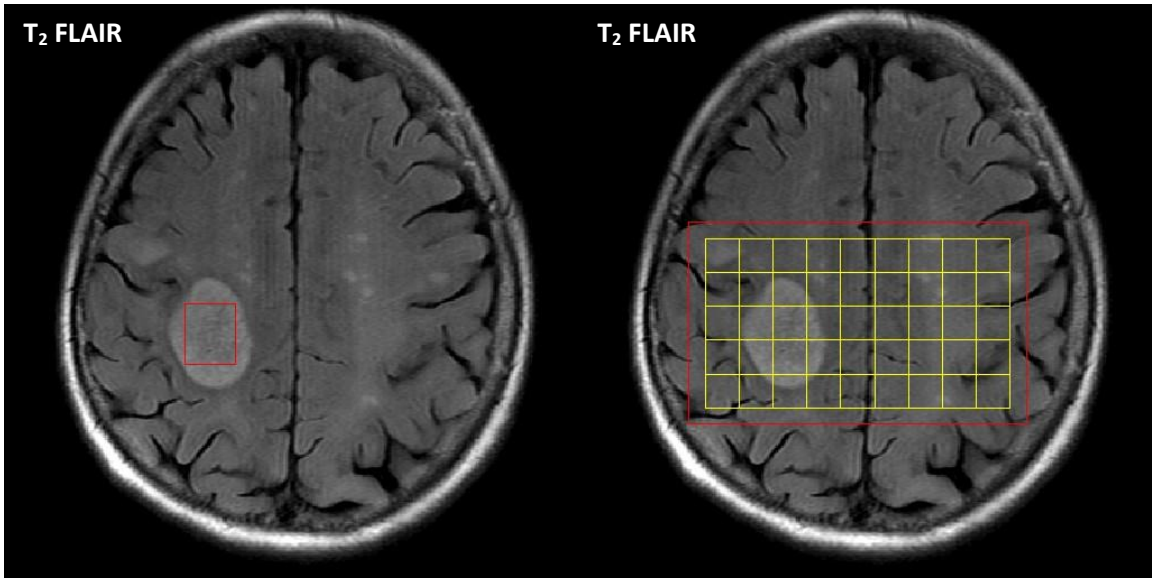

Figure 63 - Example prescriptions for single and multivoxel spectroscopy in a high grade glioma (left). Note how the voxel is entirely encompassed within the abnormality. This minimises the amount of normal tissue contaminating the spectrum. Prescription of 2D-multivoxel magnetic resonance spectroscopic imaging is also demonstrated (right).The red box shows the oversized prescription box implemented to improve the effective slice profile of the PRESS excitation box. The grid is positioned to avoid contamination from the skull while sampling the tumour and contralateral tissue. Additional saturation bands are not shown for the prescriptions but were used.

3.7.3 Magnetic Resonance Spectroscopic Imaging (MRSI)

Multivoxel spectroscopy has the advantage of being able to measure spectra from multiple locations simultaneously. This has several benefits, including contralateral tissue for comparison, and the ability to investigate heterogeneous pathologies. Typical volume of interest for 2D-MRSI are 60-100mm in any in-plane direction with a nominal voxel size of up to 1.5cm^3. Larger nominal voxel sizes yield higher SNR spectra but compromise the spatial resolution. The thickness of the box also plays a role in the SNR of the acquisition, with thicker boxes having a higher SNR, but are subject to partial volume effects when the box can extend beyond the region of interest.

Figure 63 shows a typical 2D-MRSI prescription with the abnormality encompassed by the PRESS volume of interest whilst also encompassing apparently normal contralateral tissue but avoiding subcutaneous lipid from the skull which could contaminate the useful spectra.

When the number of phase encodings is too low in a given direction, the point spread function of large resonances can become an issue and bleed into adjacent voxels causing artefactual peaks. To resolve the issue, a higher number of phase encodings should be used even if the resulting grid extends beyond the head. Whilst this could be classed as “dead time”; it does reduce the point spread function of large resonances. MRSI is subject to positional limitations given the cuboid shape is not ideal for fitting within the brain; because of this, it is possible to have spectra contaminated by lipid from the fat around the skull if due care is not taken.

3D-MRSI has the advantage of having superior coverage and potentially being more time efficient compared to multiple 2D-MRSI acquisitions, given the reduced number of prescriptions, shims and a prescans. However, the downfall of 3D-MRSI is the long acquisition time, required for phase encoding in all directions. A typical 3D-MRSI with 12x12x8 phase encodings, TR=1s and 1 NEX would take nearly 20 minutes using a conventional k-space encoding scheme. This risks the patient becoming restless during acquisition and potential ruining the entire acquisition. However, the continuous extended coverage has the potential to pick up disease beyond the abnormality on conventional imaging. If the number of phase encodings was to be reduced in one direction to speed up the acquisition, the effect of the point spread function would also be more prominent in that direction.

3.7.4 Echo Time

The echo time (TE) used to acquire a spectrum heavily influences the apparent concentrations (Figure 64 & Figure 65). This is due to the differing T_2 relaxation times of each metabolite. N-acetylaspartate, creatine and choline all have relatively long T_2 relaxation times (>200ms) meaning they are visible on spectra for a large range of echo times (short and long). In comparison, myo-inositol, glutamine, glutamate and lipids all have short T_2 relaxation times which results in the observed signal, decaying quickly as a function of relaxation time, subsequently meaning they are not visible at longer echo times. Short TE spectra potentially also have more visible metabolites due to increased SNR associated with shorter echo times. However, whilst lipid is a useful metabolite that is visible at shorter echo times, it can also affect the baseline of a spectrum, potentially altering metabolite quantification.

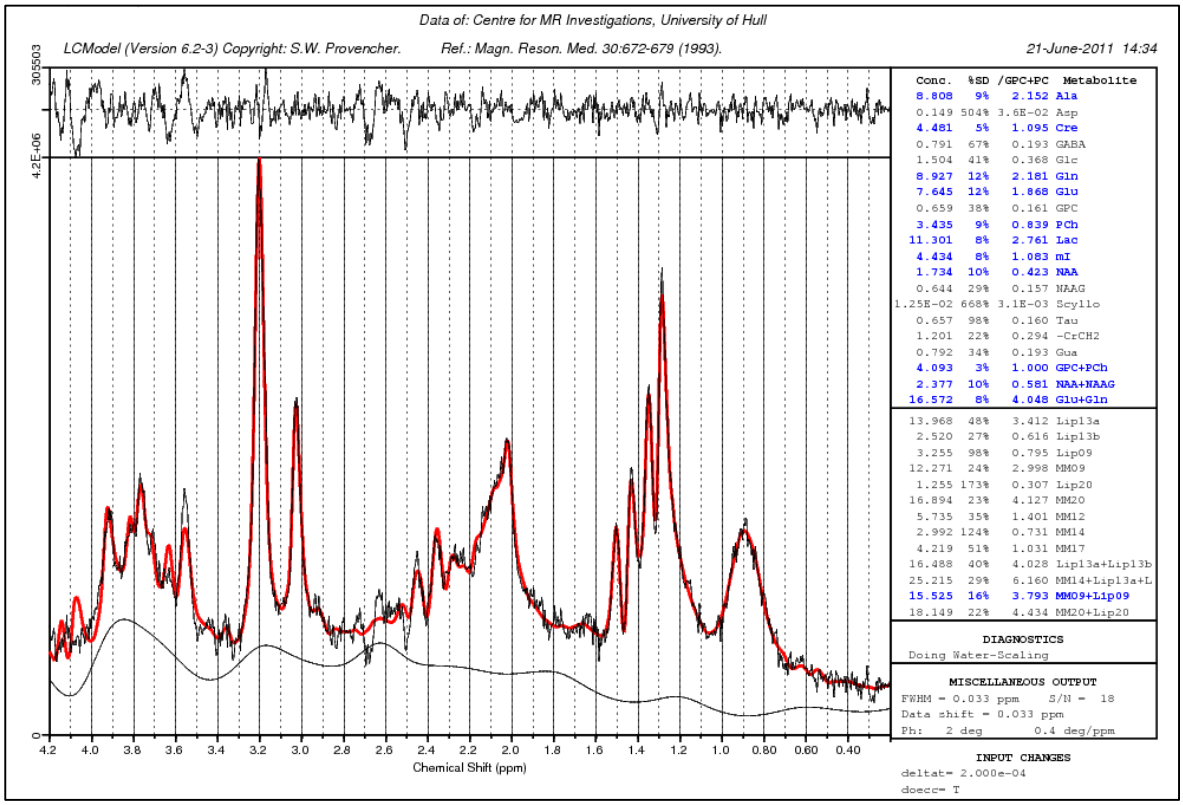

Figure 64 - Example 35ms PRESS single voxel acquired from a high grade glioma. Notable peaks at this echo time include myo-inositol (3.55pm), choline (3.24ppm), creatine (3.06), glutamine (2.45ppm), glutamate (2.35ppm), N-acetylaspartate (2.02ppm), alanine (1.46ppm), lactate (1.33ppm) and lipid (2.00, 1.30 & 0.90ppm)

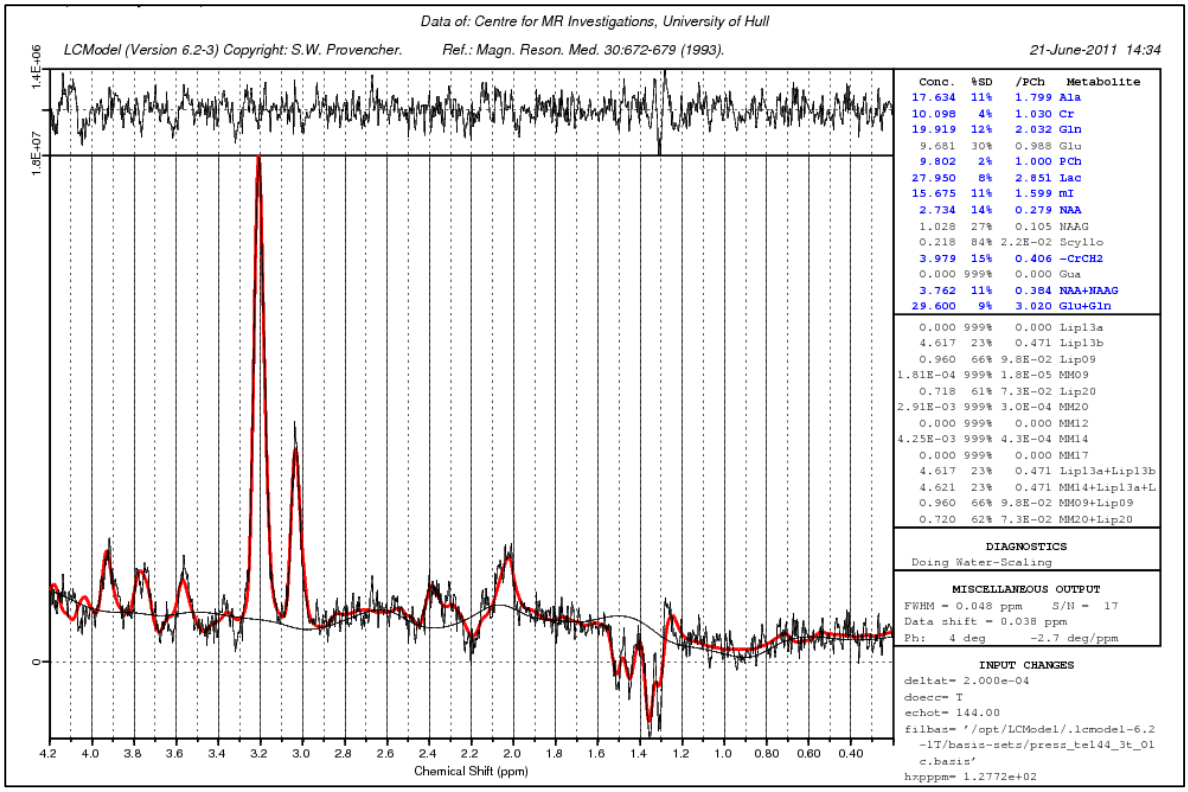

Figure 65 - Example 144ms PRESS single voxel spectrum acquired from the same patient as Figure 64 from tissue found to be a high grade glioma. Notable peaks at this echo time include choline (3.24ppm), creatine (3.06), N-acetylaspartate (2.02ppm), alanine (1.46ppm) and lactate (1.33ppm). Due to the AX_3 coupling of lactate and alanine the doublets produced appear in the anti-phase position at the 144ms echo time.

3.7.5 TE-Averaged PRESS (TEA-PRESS)

TEA-PRESS is a spectroscopic sequence capable of acquiring spectra at multiple echo times in a single acquisition (Figure 66). The advantage of this technique is that it is possible to accurately measure the T_2 relaxation times for a range of metabolites in a single sequence. Additionally, the use of multiple echo times means it is possible to simultaneously excite metabolites with both short and long echo times in the same acquisition cutting down on overall scan time rather than repeating the same spectroscopic examination using several echo times. The final advantage of TEA-PRESS, is that the evolution of coupled metabolites can be followed, and coupling effects observed (Figure 66).

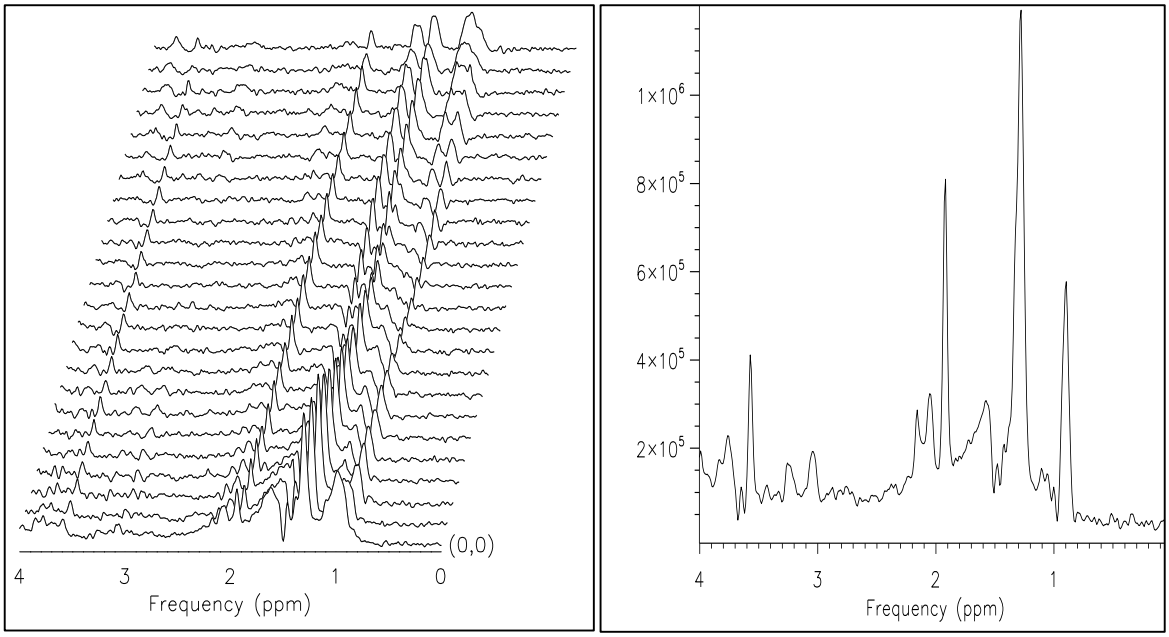

Figure 66 - Example TEA-PRESS spectra (right) from an abscess showing the 40-280ms frames. Note how the resonance at 1.3ppm decays quicker than the choline signal due to its short T_2 relaxation time. Combined spectra (right) of all echo times shows a short echo weighted spectra with improved baseline and cancellation effects due to the longer echo spectra. Note the doublet that evolves over the time course at 1.33ppm (lactate).

3.7.6 Lactate-Editing

Neuro-radiologists and oncologists are constantly looking for improved means to characterise brain tumours and assess response to treatment. The concentration of lactate in gliomas could potentially act as a prognostic biomarker for patients. The level of lactate in tumours is a marker of elevated glycolysis which in turn could be an indication that the tumour is becoming stressed by its environment, and is likely to initiate a proliferative response (11). Lipid and lactate are known to commonly coexist in gliomas, yet both resonate at around 1.3ppm. Unfortunately the large amounts of lipid often found in high grade gliomas obscure the smaller lactate signal causing cancellation effects in the lipid peak and total loss of quantification for lactate. However, at 144ms echo times, lactate presents as an inverted doublet due to J-coupling while lipid can be seen as an upright singlet, providing a mechanism to separate them using a simple editing scheme.

Star-Lack *et al*, first published the use of BASING pulses in 1997 (68) where they were implemented for water and lipid suppression. Since then, lactate editing using BASING pulses has been successfully demonstrated to work in tissue with a high lipid content (69). One of the first implementations dates to 2005 in which it was used as part of a 3D-MRSI sequence using the BASING pulses to undertake J-difference editing in brain tumours (70).

In our institution, a similar sequence has been developed where the frequency of the BASING pulses was alternated between 0Hz (on) and -198Hz (off) from water to minimise movement effects. Broadband pulses of 180° (71) replaced the 137° refocusing pulse used in the standard 3.0T PRESS sequence reducing the effects of chemical shift displacement and ensuring full excitation of both lactate regions given their differing spectral separation from the centre frequency. By summing or subtracting the BASING off and on data, it is possible to produce singlet only and coupled only spectra.

3.7.7 Spectroscopic Processing Techniques

Instead of an image, spectroscopy produces a number of echoes which require additional processing for interpretation. When the data is acquired using a phased array coil, the signal from each element requires combing appropriately using the correct weightings to maximise the SNR. This is achieved using a coil combine algorithm, where a weighted average of the signal is calculated enabling the signals from all elements to be combined into a single signal. The calculation is based on a weighting factor determined by the SNR produced by each element within the coil (72), and is mainly dependent on the distance of that element from the VOI. The combined signal can be converted to a spectrum following fast Fourier transformation. However, to optimise the visualisation of a spectrum, the following steps can be used to improve the appearance of spectra and are ordered according to how SAGE (GE Healthcare, USA) processes spectroscopic data.

3.7.7.1 Spectral Apodisation

This filter can be applied to the line shape of a signal by utilising a Gaussian or Lorentzian apodisation function to preferentially suppress noise at the tail of the signal, potentially making metabolite peaks more apparent, as the noise becomes smoothed and thus improves the apparent SNR. The trade off from the SNR increase is the broadening of the spectral peaks and a reduction of spectral resolution. Spectral apodisation can also reduce truncation artefacts by forcing the tail of the signal to zero at the end of the acquisition window.

3.7.7.2 Spatial Apodisation

Spatial apodisation is the application of a truncation filter in the spatial domain of the signal. Subsequently as a result, it is possible to reduce any voxel bleed effects that are particularly predominant in MRSI. This type of apodisation is applied by multiplying all the spatial dimensions of the data by a Fermi filter; however, the disadvantage of this is the reduction in the true spatial resolution. The Fermi filter decreases the point spread function in all dimensions from a voxel by reducing the residual excess signal to a circular distribution around the point.

3.7.7.3 Spectral Zero Filling and Spatial Zero Filling

A spectral zero fill increases the number data points in the signal by appending (N x data length) zeroes to the tail of the signal. This technique results in an increase in spectral resolution once Fourier transformed. A spatial zero fill can be done simultaneously and interpolates the data prior to FFT which is the optimal stage for any interpolation steps.

3.7.7.4 Fourier Transformation (FT)

A FT is a mathematical operator which is able to take both the real and imaginary components of the signal and convert them into a complex spectrum. By carrying out a FT on a signal it is able to convert the signal which is based in the time domain, into a spectrum that exists in the frequency domain. Spatial and spectral FFTs are applied sequentially in SAGE.

3.7.7.5 Phase Correction

Phase shifts occur in spectroscopy due to various hardware and sequence settings. After a FT the phase shifts cause signal to be arbitrarily distributed between the real and imaginary channels. Phase correction attempts to separate the absorption and dispersion modes as best as possible. Phase can be corrected by zero-order phase correction which is a constant, and by first order phase order correction which is a function of frequency.

3.7.7.6 Baseline Correction

This tool can be applied when looking to quantify peak areas. Due to noise, the baseline in a spectrum can sometimes be incorrect for the integration of peak areas. When comparing peak areas between subjects, having both spectra starting from zero signal intensity makes the areas directly comparable. Baseline correction is carried out using a cubic spline fit to account for effects of water and macromolecules which distort it.

3.7.8 Spectroscopy Processing Software

3.7.8.1 SAGE

Developed by General Electric, SAGE (Spectral Analysis by General Electric, GE Healthcare, USA) is a complete spectral processing package, able to process raw P-files (GE's file format) into spectra. Figure 67 shows a spectrum processed using GE's spectral processing program, SAGE. Quantification can be done through the calculation of peak amplitudes or areas. More advanced quantification can be achieved using Marquardt fitting where *a priori* information about peak positions and lineshape is generated and fitted against the data.

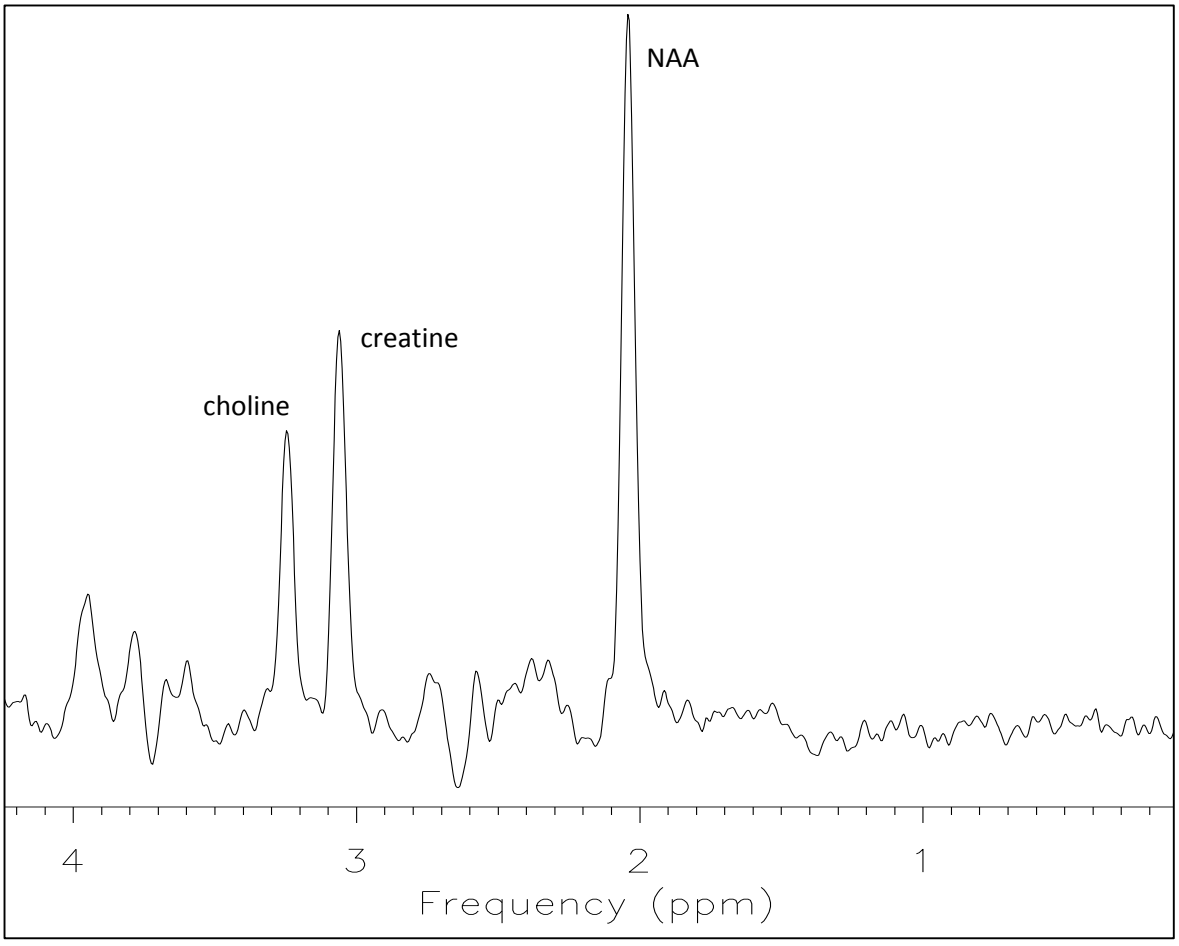

Figure 67 - Single voxel processed with SAGE using 2.5Hz spectral apodisation. Data was acquired on a 3.0T scanner using 144ms PRESS in normal appearing white matter.

3.7.8.3 Linear Combination Model (LCModel)

An advanced alternative to quantifying data using SAGE, is using specialist line fitting software such LCModel (73). Since 1993 when LCModel was released, it has been cited nearly two thousand times and is acknowledged as a standard for spectroscopy quantification. The software uses frequency domain rather than time domain fitting, however SAGE is still required to provide the necessary spatial Fourier transform for multivoxel data (74). Subsequently, LCModel uses a separately acquired basis set to fit the data with *a priori* data which is field strength, sequence and echo time specific. A basis set is a collection of model spectra acquired from a phantom of known concentrations under specific conditions. As well as line fitting, LCModel also has statistical descriptors built into it, describing the quality of the fit using Cramer-Rao lower bounds. As demonstrated in Figure 68 and Figure 69, LCModel individually fits each peak independently before combining the fits into a single profile (Figure 69).

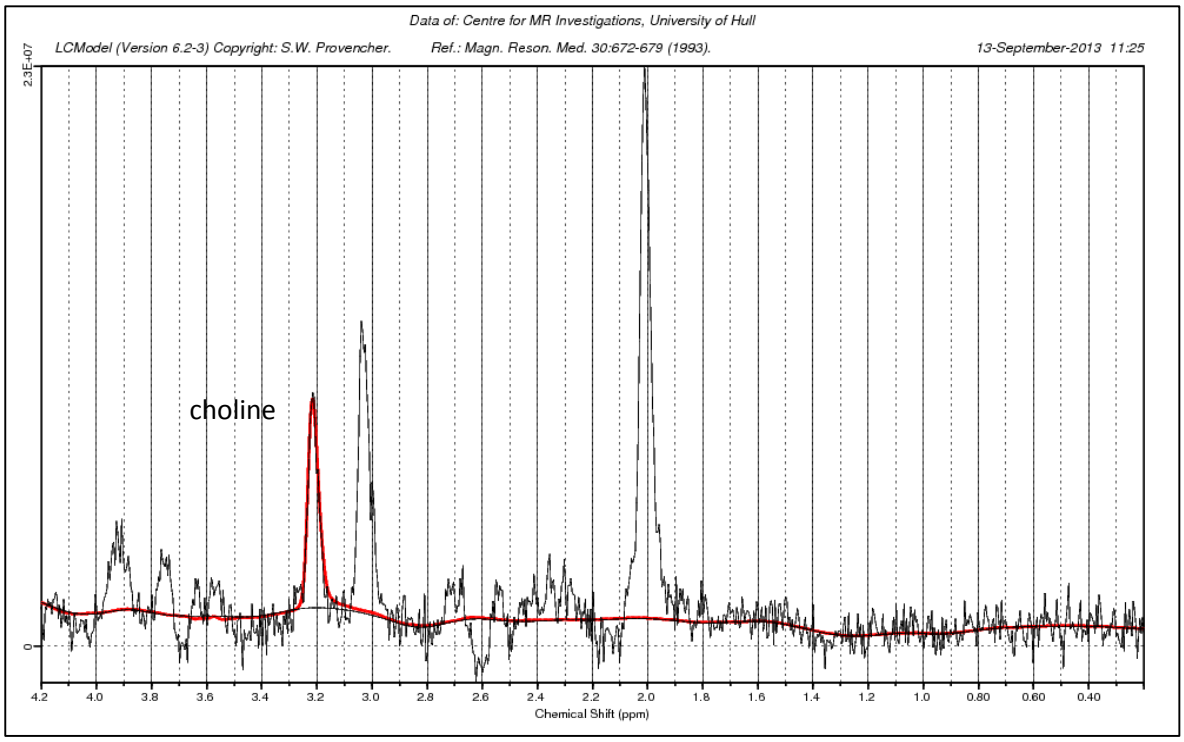

Figure 68 - Example fit for choline observed in a single voxel spectrum acquired using PRESS 144ms at 3.0T processed and processed with LCModel.

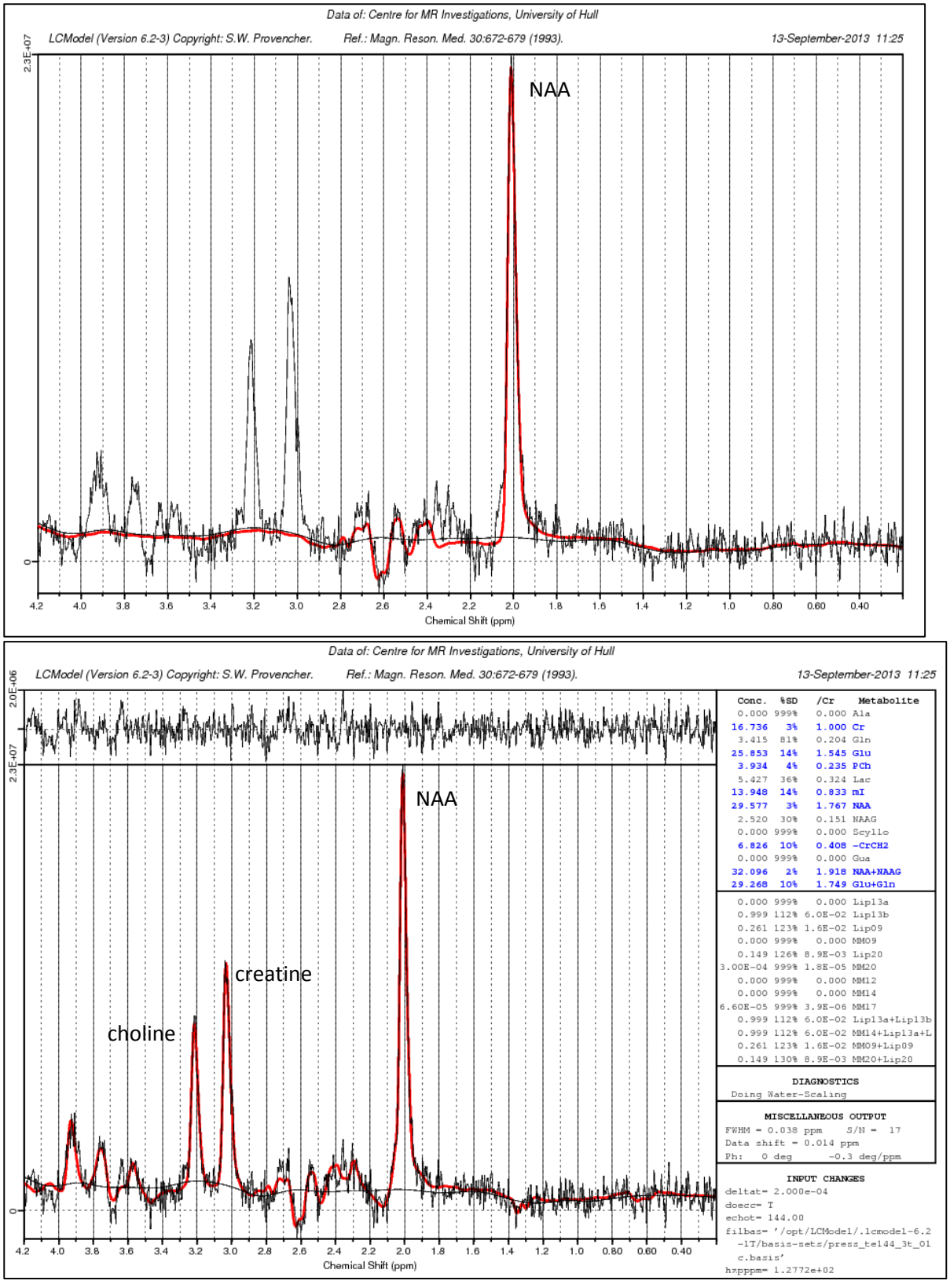

Figure 69 - Example fits for N-acetyl aspartate (top)).Note how LCModel also fits the smaller aspartyl peak of NAA at 2.6ppm. The combined lineshape for all metabolites can be seen in the bottom image.

3.7.9 Ready Brain

Ready Brain is a General Electric (GE) automatic slice positioning tool built into the scanner platform to allow repeatable slice orientation (75) (Figure 70). The concept of this technique is to use a line from the anterior commissure (AC) to the posterior commissure (PC) to decide slice orientation. There is literature supporting the standardisation of neuroimaging, where it is concluded that adoption of Talairach space (AC-PC line) to prescribe images would lead to more reproducible images that are easier to interpret (76). Ready Brain acquires a 3D volume of the head that is planned from a standard localizer sequence. This volume scan can be acquired in less than 15 seconds and is automatically processed by the scanner. Subsequent imaging is then linked to the processed Ready Brain sequence which provides the option of whether the image sequence is to be prescribed axially, sagitally, or coronally to the AC-PC line. A second example of Ready Brain, and its potential for low grade glioma monitoring can be seen in Appendix B (pg. 324).

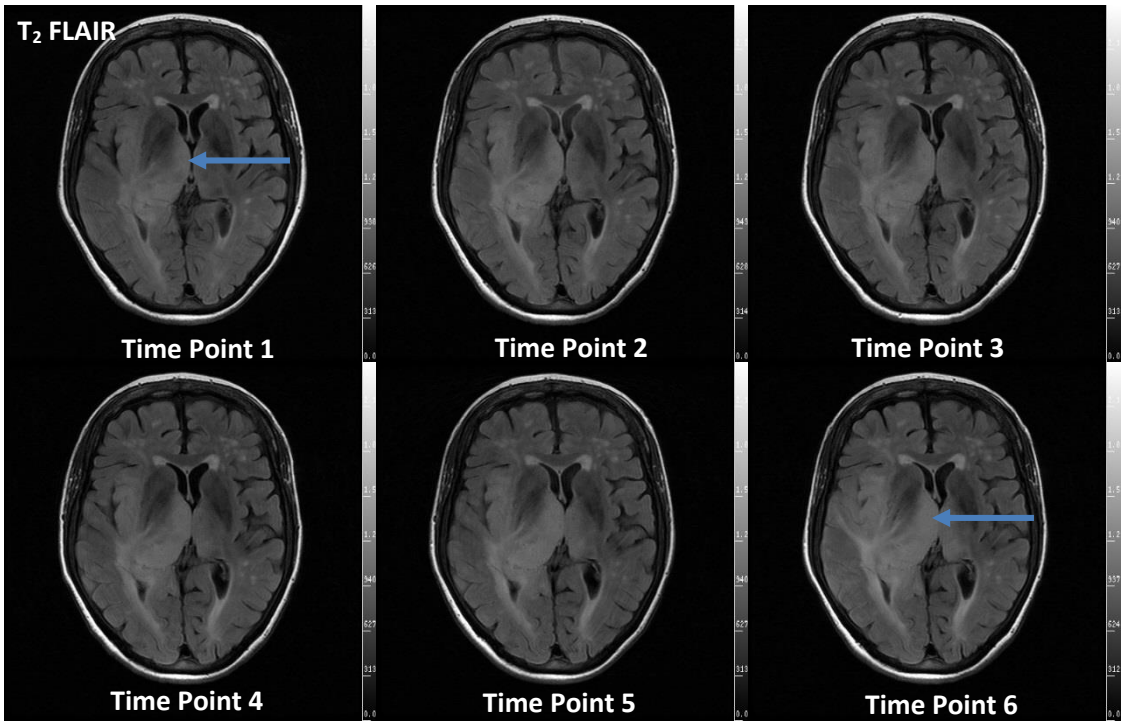

Figure 70 - Ready Brain prescribed FLAIR imaging from a low grade glioma patient scanned every 4 months starting from top left to bottom right. Note the subtle expansion of the T_2 abnormality.

4 Review of MR Studies

4.1 Relevant Methods, Novel Techniques and Limitations

This review is designed to highlight the use of advanced magnetic resonance techniques in the brain, and more specifically brain tumours, to demonstrate the range of sequences and processing methods in use, as well as the data sampling schemes currently used in this area of research. The main topics of advanced neuro-oncological MR covered are: differential diagnosis, outcome prediction and monitoring response to therapies. This chapter also includes literature on novel methods which relate to these fields. Within each of these main sections, the topics have been divided into their fundamental groups which are: morphological imaging, diffusion, perfusion, magnetic resonance spectroscopy and finally multiparametric studies that utilise two or more of the techniques.

4.2 Advanced MR Techniques for the Diagnosis of Gliomas

4.2.1 Diffusion Studies

In a large study of 275 patients with brain tumours, mean apparent diffusion coefficient (ADC) measurements were taken using a multi b-value diffusion scheme (77), with values ranging from 0 to 1000s/mm^2 in steps of 250s/mm^2. Using regions of interest (ROIs) drawn from post contrast T_1 imaging, ADC values were reported to be significantly different for a range of differential diagnoses, such as lymphoma versus glioblastoma. However, there was still significant overlap between the more difficult differentials such as glioblastoma multiforme versus metastatic carcinoma. Whilst this study clearly demonstrated the potential of diffusion weighted imaging (DWI) for differential diagnoses, the ROI approach used was user dependant and so the reproducibility of the sampling scheme used in this study could be questioned. The quality of the data should also be considered given potential volume averaging effects caused by using 7.5mm thick diffusion slices acquired at

1.5T. Given the *b*-value intervals, perfusion effects were not accounted for, which could lead to an incorrect calculation of the ADC.

In an alternative approach to tumour region of interest measurements, Tozer *et al* (78) applied histogram analysis to split low grade gliomas into subtypes. These subtypes were oligodendroglioma, oligoastrocytoma and astrocytoma (WHO II). Significant differences in the ADC values were observed between subtypes of low grade gliomas (LGG) (peak location of astrocytoma versus oligodendroglioma, P=0.027), suggesting histogram analysis may aid in tumour diagnosis in cases where a tissue sample is not available. This study benefited from whole tumour measurements. Expanding on this research, Khayal *et al* (79) implemented a red-green-blue (RGB) colour map scheme derived from the ADC histograms. In this paper, different components of the ADC maps were assigned a colour based on their diffusion characteristics and the mixed tissue types within a given voxel (Figure 71). Overall an effective technique for the subtyping of low grade gliomas purely based upon visual inspection was created. Whilst the work appeared to be particularly good for the grade 2 cases examined, this method may be potentially insensitive to high grade transformations, where areas of lesion become more cellular and consequently simulate normal appearing tissue as the ADC decreases with increasing cellularity.

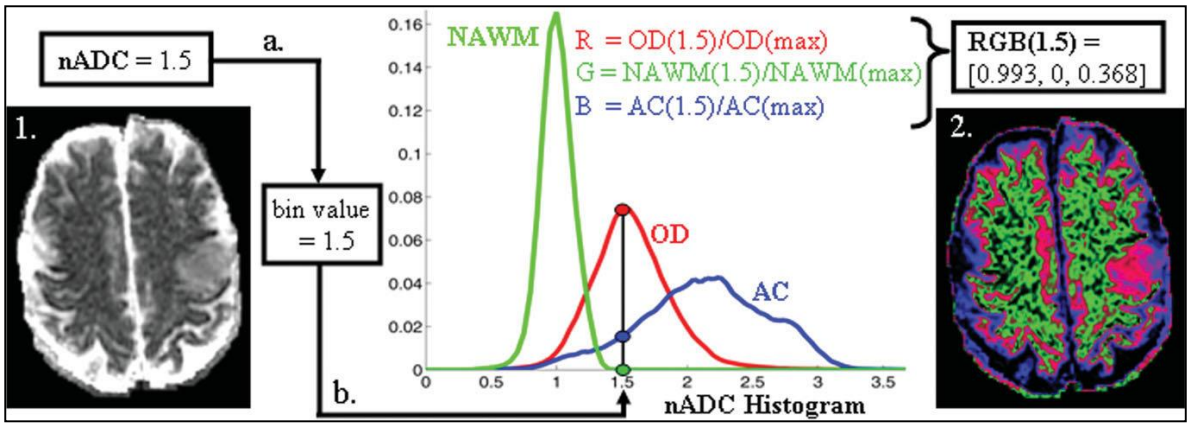

Figure 71 – This figure shows the mapping a normalised ADC map (1) to an RGB map (2). The colours are representative of probabilities of the voxel belonging to one of the three tissue groups. OD=oligodendroglioma, AC=astrocytoma, NAWM=normal appearing white matter. Reproduced from (79).

Histogram analysis may also yield significant differences between populations where mean measurements are not appropriate in heterogeneous tissue. A prime example is low grade versus high grade gliomas and the use of ADC values. Low grade lesions are normally characterised by high ADC values while high grade gliomas contain a mixture of very high and very low ADC measurements which can average out to be the same as those of low grade gliomas. By using histogram analysis (80), a sensitivity of 86% and a specificity of 89% was achieved in differentiating between high and low grade glioma groups. The advantage of a histogram based analysis for tumour measurements is that the whole abnormality is sampled rather than user based subsampling, meaning measurements should theoretically be more reproducible and potentially automatable.

Central nervous system lymphoma is sometimes indicated as a differential for glioblastoma multiforme due to its strong enhancement characteristics. Using high b-value diffusion (4000s/mm^2), lymphoma (minimum ADC = $0.390\pm0.081\times10^{-3}mm^2s^{-1}$) and glioblastoma (minimum ADC = ($0.617\pm0.098\times10^{-3}mm^2s^{-1}$) were differentiated (81) with 91% sensitivity and 92% specificity when using an ADC cut-off value of $0.5\times10^{-3}mm^2s^{-1}$. The differences in minimum ADC were greater with a b-value of 4000 than of 1000 s/mm^2, suggesting that a mono-exponential model for diffusion may not be suitable for this disease.

Whist diffusion weighted imaging appears unable to detect the difference between glioblastoma multiforme and metastasis, diffusion tensor imaging (DTI) does appear to. Rather than examining the ADC of the tumours, by looking at the fractional anisotropy (FA) in the lesion and the surrounding tissue it is possible to differentiate the two histologies with 92% sensitivity and 100% specificity. This can be explained by way that the two types of tumours grow, with metastasis displacing tissue as the lesion expands, whist glioblastoma multiforme infiltrates the surrounding brain (82). A continuation of the use DTI to differentiate between glioblastoma multiforme and

metastasis uses parameters such as p (isotropic component), q (anisotropic component) and fractional anisotropy (FA) to successfully split the two histologies (83).

Price *et al* (84), have published research identifying tumour infiltration using diffusion tensor imaging. By splitting the diffusion tensor into the isotropic (p) and anisotropic (q) components, disrupted white matter tracts can be successfully identified, with the ratio of p and q, otherwise known as the relative anisotropy (RA) being used to characterise tissue properties. In contrast, Goebell *et al* (85) investigated the differences in tumour architecture between grade II and III gliomas using DTI. When comparing 23 gliomas, no differences in fractional anisotropy ratios (FA of pathology / FA of contralateral tissue) were apparent between the central regions of the tumours. Significant differences were however seen in the tumour borders with grade III gliomas having a median FA ratio of 0.449±0.137 compared to grade II gliomas which had a median tumour border FA ratio of 0.733±0.307 (P=0.01).

Finally, Jenkinson *et al* (86) have investigated the potential link between cellularity and ADC in different oligodendroglial genotypes by sampling the tumour multiple times during biopsy; however, no relationship was found between cellularity and ADC in this study. Higher grade lesions were found have a more cellular appearance though. From a study with a larger cohort (87), it was possible to predict whether an oligodendroglial lesion was grade 3 with 83.3/81.0% specificity/sensitivity based on the dichotomisation of the ADC or the appearance of both enhancement and calcification. The suggested threshold for grade 3 lesions was ADC values below $0.925x10^{-3}$ mm^2s^{-1}.

4.2.2 Perfusion Studies

Emblem *et al* (88) have shown glioma grading to be possible using histogram analysis of blood volume heterogeneity derived from dynamic susceptibility contrast (DSC) blood volume maps. Fifty-three glioma patients were imaged at 1.5T and graded by 4 different neuroradiologists using ROI and hotspot methods. In this study histogram analysis demonstrated higher levels of agreement between radiologists than the hotspot technique. An Increase in diagnostic accuracy was also observed in this study when using the histogram method for grading. In a similar study (89) investigating whether histogram analysis versus region of interest (ROI) analysis should be used in the grading of gliomas with DSC imaging, it was found that the relative cerebral blood volume (rCBV) tumour histogram was just as effective as the maximum rCBV region when correlated with tumour grade. The paper did comment, that inexperienced operators could get comparable results using histogram techniques compared to experienced operators using ROI methods.

DSC perfusion can not only be used to determine tumour grade, but also predict chromosome deletion. Law *et al* (90) demonstrated that higher blood volume measurements (rCBV) in gliomas were associated with the deletion of the 1p chromosome segment (10.54±2.93 vs. 4.84±2.43, P=0.012)). Loss of hetrozygosity has been shown to improve responsiveness to chemotherapy and subsequently improved survival. It is worth noting the small cohort of 16 patients in this preliminary study.

When differentiating lymphoma from glioblastoma, CBV measurements derived from DSC have proved useful along with leakage corrected CBV and K_2 (63). However, because lymphoma had such a high leakage rate, CBV was underestimated in this lesion type and actually aided in differentiating from Glioblastoma. The use of leakage correction has been shown to improve the ability of DSC to differentiate to between glioma grades (12).

Perfusion weighted imaging has been shown to differentiate glioblastoma multiforme from single brain metastases. In a cohort of forty three patients, 27 proved to be glioblastomas while the remaining 16 were brain metastases. It was found that the average peak height (maximum point on a DSC concentration curve) was higher in the peritumoural region of glioblastomas compared to brain metastases. The mean signal recovery in the enhancing portion of the lesion was also significantly higher in glioblastoma multiforme compared to a single brain metastasis (91).

Blood volume can also be measured using T_1 weighted dynamic contrast-enhanced MRI (DCE). In a study (92) of 27 patients with gliomas that underwent DCE MRI, CBV and K^{trans} were calculated and found to correlate with histological grade and survival respectively. DCE can also be used to estimate tumour grade. Both CBV and K^{trans} were found to correlate with tumour grade in a study of 39 glioma patients (93). This study used a temporal resolution of 5 seconds and a 1.5T magnet. Regions of interest were taken from 3 slices of the enhancing portions of the tumours, suggesting suboptimal sampling of the DCE MRI.

With the development of techniques such as arterial spin labelling (ASL), perfusion does not have to be carried out using contrast agent. Perfusion imaging produced by ASL has been correlated with histopathologic vascular density. ASL is most commonly used to derive the cerebral blood flow (CBF) in absolute units. Furthermore, ASL has be used to distinguish between high and low grade gliomas based on the vascular densities (94). One limitation of the technique is that it cannot derive the cerebral blood volume and therefore cannot generate a mean transit time (MTT) either. ASL also has the benefit of being a repeatable perfusion sequence if motion or technical failures occur during an initial acquisition.

4.2.3 Spectroscopic Studies

Magnetic resonance spectroscopy is a tool that has been in the transition to clinical use for many years now, but is still considered a research tool because of the acquisition time, interpretation problems and the necessary skills needed to make full use of its capabilities. Garcia-Gomez *et al* (95) investigated spectroscopy as a clinical tool with the publication of their paper entitled: 'Multiproject-multicenter evaluation of automatic brain tumour classification by magnetic resonance spectroscopy'. As part of a 5 year study called eTUMOUR, scientists were able to report 90% accuracies using short echo single voxel spectroscopy for diagnosis in an automated fashion using the INTERPRET learning technique. The only problematic differential was the glioblastoma multiforme versus metastatic carcinoma, which appears to be a repeating theme throughout neuroradiology.

Automated assessment of spectroscopy is a topic that has been of keen interest for some time now. McKnight (96) proposed an automated technique for quantitative assessment of 3 dimensional magnetic resonance spectroscopic imaging (3D-MRSI) in glioma patients in 2001. This technique used an iterative z-score method to categorise voxels into normal or abnormal based on the amount of choline and N-acetyl aspartate (NAA) present. The limitation with this Z-score method is the tendency to overestimate abnormal voxels on healthy brains due to the iterative method behind it.

Spectroscopy is a non-invasive tool for tissue characterisation, which is why it has grown to be popular with researchers. Paediatric brain tumours are one cohort of patients who particularly benefit from the non-invasive nature of the technique. Short echo single voxel spectroscopy has been shown to be of use in a group of 60 paediatric tumours. From Panigrahy *et al* (97), it can be noted that in medulloblastomas, taurine can be found to be significantly higher than all other histologies. Creatine can be found in its lowest concentrations in pilocytic astrocytomas, while

guanidinoacetate was found to be reduced in low grade and anaplastic astrocytomas. Overall conclusions from the paper suggest that preoperative spectroscopy could improve non-invasive diagnoses.

Pilocytic astrocytomas are unusual compared to other astrocytic lesions, being the only WHO grade I tumour from this cell type that is known to take up contrast agents, a property not usually associated with other low grade brain tumours. Spectroscopically they have also been reported to be slightly different to other low grade gliomas. Hwang *et al* (98) used a short echo stimulated echo acquisition mode (STEAM) and a longer echo point resolved spectroscopy (PRESS) single voxel sequence in 8 paediatric pilocytic astrocytomas and found lactate present in all of them.

Proton magnetic resonance (MR) spectroscopy has also been used to differentiate between neoplastic and non-neoplastic brain lesions following stereotactic radiotherapy. Schlemmer *et al* (99) investigated this topic examining 66 lesions in 50 patients, with choline/creatine and choline/NAA ratios found to differ between the two types of lesion.

Metabolic profiling of brain tumours is thought to provide the ability to differentiate tumours with similar imaging characteristics. Grade III astrocytomas were reported as having consistently higher choline than grade II astrocytomas but the amount of choline in glioblastomas varied by a large amount (100). Higher levels of choline and creatine correlated with low amounts of lactate and lipid indicating metabolite levels are diluted by necrosis in high grade gliomas. Macromolecules, lipid and lactate are all thought to increase with tumour grade as hypoxic tissue turns necrotic. Interestingly metabolic profiling of brain metastases has also been able to differentiate the original primary *in vivo* at 3.0T. By using principal components analysis (PCA) it has been shown that lung and breast derived lesions are significantly different (101).

As previously mentioned, one of the most difficult discriminations in MR is between glioblastoma multiforme and single brain metastasis. Fan *et al* (102) used single voxel spectroscopy to do so in

their 2004 paper. The results show differences between the choline to creatine ratio in the peritumoural region which agrees with conceptual ideas based on glioblastoma multiforme invading the surrounding tissue, while metastases not doing so. The study also reports differences in the myo-inositol and glutamine/glutamate to creatine ratios in tumoural tissue.

The question of echo time (TE) selection is one for consideration, due to advantages and trade-offs for each echo time. Longer echo times (144-288ms) are more robust and less susceptible to lipid and large molecules which affect the baseline; however, shorter echo times (25-35ms) contain more spectroscopic information about metabolites with shorter T_2 relaxation times and improves the SNR of the acquisition. In a paper (103) comparing short and intermediate echo time sequences at 3T using single voxel spectroscopy, choline to creatine and choline to NAA ratios were significantly lower at the shorter echo times regardless of tumour grade. Short TE spectroscopy was found to be slightly more accurate than intermediate echo times, possibly due to the SNR increase associated with shorter echo times. The discussion refers to the poor lactate inversion at intermediate echo times at 3T being enough reason to consider the use of shorter echo times, however, if lipid is present then splitting the 1.3ppm resonance is still difficult.

Majos *et al* (104) have also done work comparing short and long echo times for the classification of proton MR spectroscopy (Figure 72). After observing 151 spectroscopic studies, nine metabolites were identified using short (30ms) and long (136ms) echo times. Using a leave one out method, short echo correctly identified 81% of tumours compared to long echo which correctly classified 78% of cases. Overall short echo spectroscopy was found to be better for tumour classification with the exception of meningioma which was easier to identify using long echo spectra which demonstrated alanine in the anti-phase doublet at 1.46ppm caused by J-coupling effects.

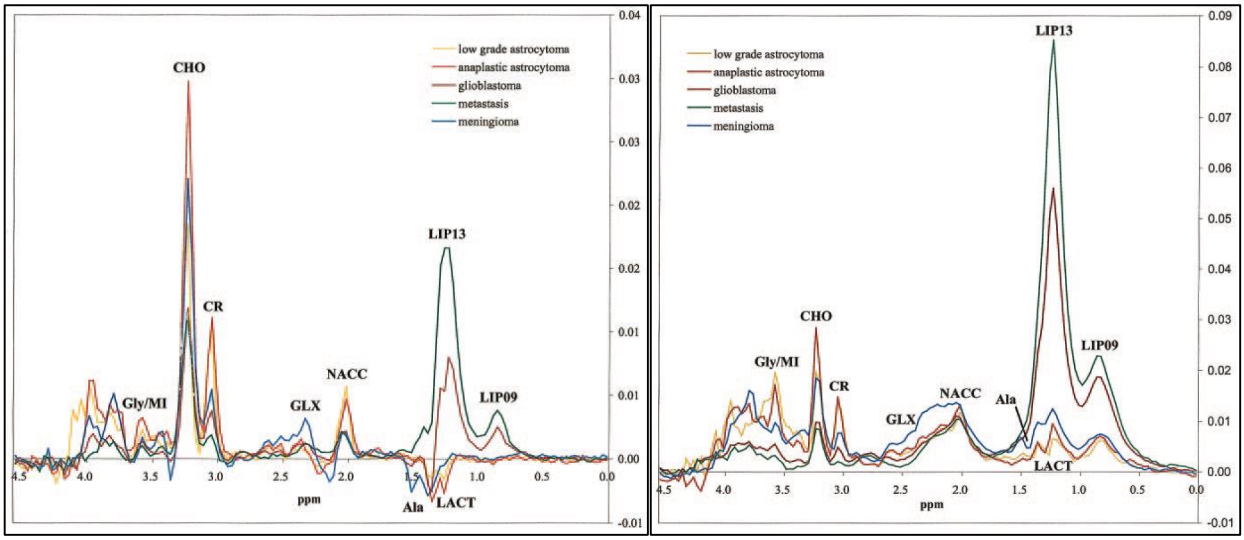

Figure 72 – Mean spectra at short TE (TE =30) of the five tumour types included in the study (right), Mean spectra at long TE (TE =136) of the five tumour types included in the study (left).Reproduced from (104).

Additional work with single voxel short echo time spectroscopy has been investigated, in an effort to improve the discriminatory power of spectroscopy in brain lesions. Weis *et al* (105) used short echo times to take advantage of the additional information available spectroscopically, from metabolites with short T_2 relaxation times such as lipids and macromolecules, it was found that the mean difference spectra between LCModel fits and the raw data were best for classification of grade II, III and IV gliomas. The mean spectra of the lipid and macromolecules (1.4 - 0.0 ppm) were also useful for the classification of tumour grade.

Spectroscopy can also be used to differentiate between brain tumour reoccurrence and radiation injury. 2D-MRSI was carried out on 29 patients with a new enhancing lesion post-treatment for a malignant neoplasm. Spectroscopy was successful in 97% of cases with choline to creatine and choline to NAA ratios being significantly higher in tumour reoccurrence than radiation induced changes (106). In a similar cohort of 25 brain tumour patients receiving treatment (107), choline to NAA and choline to creatine ratios were used to successfully differentiate between progression and radiation injury. The area under the receiver operator curve (ROC) was reported at 0.98. The

increased spatial resolution of the multivoxel acquisition appears to benefit the statistical significance of the spectroscopy due to the reduction in partial volume effects.

As with all techniques, spectroscopy needs to be correlated and validated with a gold standard which in this scenario is a tissue sample. Dowling *et al* (108) compared voxels acquired using 3D-MRSI retrospectively centred on the biopsy sites for 79 specimens. The study showed that tissues with similar imaging properties could have differing spectral characteristics which were accredited to a range of histologies including astrogliosis, necrosis and neoplasm. The test-retest reliability and reproducibility of short echo time spectroscopy has been examined using 3T (109). Twenty-one healthy subjects volunteered for short echo 2D-MRSI with NAA, creatine, choline and myo-inositol (mI) concentrations all found to be highly reproducible. The coefficients of variation were lower than those reported at 1.5T which is in keeping with the increased signal to noise ratio expected at 3T.

One of the advantages of multivoxel spectroscopy is its increased spatial coverage and resolution compared to single voxel spectroscopy. Sijen *et al* (110) took advantage of this to characterise human brain tumours and the surrounding oedema using proton 2D-MRSI. Different tissue types were assessed using two different repetition times (TR) to subsequently calculate the T_1 relaxation of metabolites. Two echo times were also used to calculate the T_2 relaxation times subsequently. In the study it was found that the T_2 relaxation times of choline and NAA in tumour were significantly reduced while in oedematous tissue the T_2 relaxation times of choline and creatine were also reduced. T_1 relaxation times of metabolites were found not to differ between normal appearing brain tissue, tumour or oedema. It is suggested that shorter echo times would be better due to the T_2 of choline measured in tumour and oedema shortening, and so be more sensitive to changes in concentration.

Further work on the T_2 relaxation times of brain tumours was performed by Opstad *et al* (111). This research concentrated on the relaxation times of the 1.3 and 0.9 ppm lipid peaks found in high grade gliomas and brain metastasis. The study revealed that brain metastases had a significantly longer T_2 relaxation time for the 1.3ppm lipid peak resulting in a higher 1.3/0.9 ppm lipid ratio.

One paper describes a differential for glioblastomas and brain metastases using the ratio of lipid peaks using short echo single voxels spectroscopy at 1.5T. The lipid peak area ratio (1.3 / 0.9 ppm peak areas) was able to provide 80% sensitivity and specificity. Further optimisation of the protocol could lead to better differentiation in this difficult to diagnose cohort (112)(*Figure 73*).

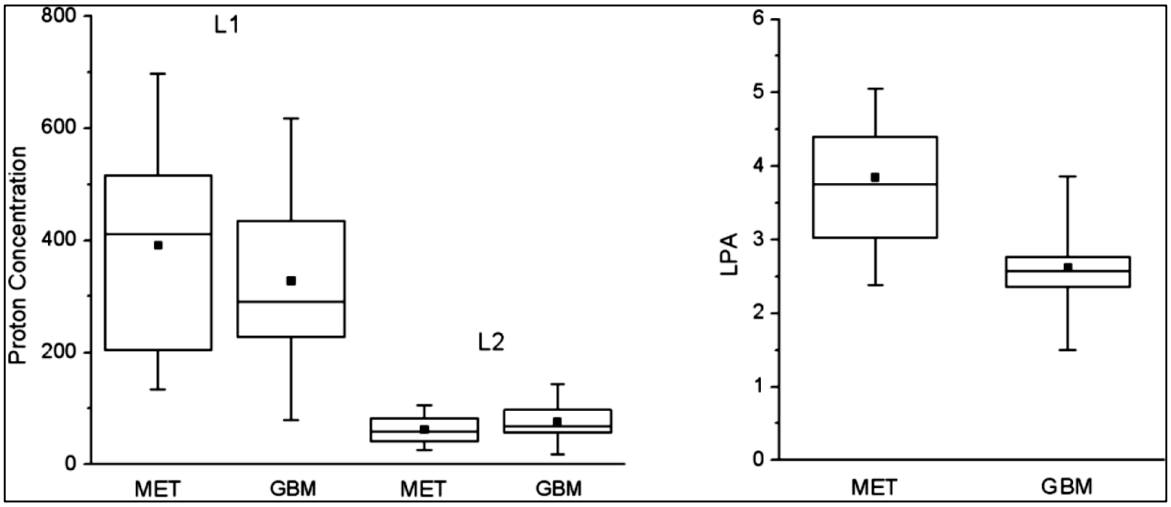

Figure 73 – Box plots of L1 (1.3 peak area), L2 (0.9 peak area), and lipid peak area (LPA) for tumour groups. The plots show the median values for each group (■) *with the box representing the 75th, 50th, and 25th percentile values from top to bottom, respectively. GBM, glioblastoma; MET, metastasis. Reproduced from (112).*

Limitations of *in vivo* spectroscopy include the comparatively low field strengths compared to small bore NMR machines and the total scan time patients can tolerate. Wright *et al* (113) used high-resolution magic angle spinning to perform more accurate metabolic quantification of brain tumour tissue samples. Using a 14.1T nuclear magnetic resonance (NMR) spectrometer it was possible to identify 29 MR visible metabolites from 65 different brain tumour samples. At this increased spectral resolution, the total choline seen at *in vivo* spectroscopy can be resolved into its different

subcomponents leading to increased differentiation between histologies. Interesting glioblastomas were found to contain significantly more creatine, glutamine and hypo-taurine than metastases.

Gliomatosis cerebri (WHO grade III) is another histological type benefiting from the use of MR spectroscopy for diagnosis. This type of tumour differs from other gliomas by infiltrating the brain but maintaining the brain's original structure. The diffuse nature of the disease makes defining tumour boundaries very difficult as is gaining prognostic information from conventional imaging techniques. Due to rarity of the disease, large cohorts are difficult to accumulate. One research group examined 7 gliomatosis patients pre-therapy to investigate survival prediction. It was found there was a significant inverse correlation between the choline to creatine ratio and overall survival. The NAA to creatine ratio was also found to be significantly reduced compared to normal volunteers (114).

Researchers have also been able to find significant differences in NAA and choline between grade 2 and 3 lesions using high spatial resolution spectroscopy with a nominal voxel size of $0.67x0.67x10mm^3$, suggesting that Cho/NAA has utility in tumour grading (115). Given the size of the voxels and 1.5T magnet used, it is important to consider the SNR when interpreting the paper.

Spectroscopy used in a serial manner can also be useful for the monitoring of lesions. Taillibert *et al* (116) present the case for serial MR spectroscopy in lymphoma patients, one of the differentials for glioma patients. In their paper they are able to conclude that the addition of MR spectroscopy increases the sensitivity when diagnosing lymphoma on MR.

4.2.4 Multiparametric Studies

In some situations, brain tumour patients are not able to receive contrast agents due to renal impairment, previous adverse reactions or inability to find venous access to the patient. Therefore contrast free imaging solutions are always of interest. Park *et al* (117) have conducted a clinical feasibility study using diffusion and susceptibility weighted imaging instead of contrast to diagnose brain tumours compared to traditional contrast MR exam methods with the addition of DSC. Seventy-three patients with intra-axial brain tumours were recruited and scanned at 3T. The study found non-contrast MR with the addition of DWI and susceptibility weighted imaging (SWI) to have a similar sensitivity and specificity to that of contrast MR. A combination of DWI, SWI and DSC in addition to conventional MR was found to have the most significant differential diagnoses (High- vs. low-grade gliomas, non-contrast protocol – P=0.0057, contrast protocol - P=0.0015, contrast + ADC + SWI protocol - P=0.0002) (Glial vs. non-glial tumours, non-contrast protocol – P=0.0295, contrast protocol - P=0.0252, contrast + ADC + SWI protocol - P=0.0012).

Combinations of diffusion, perfusion and spectroscopy have been used to improve the accuracy of brain tumour diagnoses. Law *et al* (118) looked retrospectively at 160 tumour patients who had undergone MR perfusion and spectroscopy. When differentiating between low and high grade gliomas, they found perfusion techniques in combination with MR spectroscopic ratios yielded a sensitivity of 93%, specificity of 60%, positive predictive value of 88% and negative predictive value of 79%, when using an rCBV cut-off of 1.75. Significant differences were seen in the relative cerebral blood volume, choline to creatine, choline to NAA and NAA to creatine measurements between low and high grade gliomas ($P<0.0001$, 0.0121, 0.001, and 0.0038). Di Costanzo *et al* (119) have also conducted a 3.0T multiparametric study to assess the grade and extent of brain tumours. Thirty-one tumour patients were recruited as part of the study and underwent diffusion, perfusion and spectroscopy prior to surgery. Using these techniques, three main categories of tissue were able to be identified. They were; tumour which had low apparent diffusion coefficient values, high relative

blood volume measurements and abnormal choline to NAA ratios. Oedema was found to have normal choline to NAA ratios with increased ADC values and decreased perfusion. Lastly mixed oedema and tumour tissue showed intermediate ADC and rCBV values and abnormal choline to NAA ratios. The authors of the paper felt that multiparametric MR could discriminate between vasogenic oedema, infiltrating tumour or normal tissue, and differentiate between low and high grade lesions. Whilst the results of the study were promising, the use of General Electric's Functool suite suggests the processing methods were suboptimal, with MRSI analysed from 'postage stamp' DICOM images. Additionally no attempts to correct leakage effects were made for the DSC.

As with all types of imaging, validation is important. Gupta *et al* (120) investigated the relationship between choline MR spectroscopy, apparent diffusion coefficient and histopathology. In this paper they hypothesised a relationship between the choline signal, cell density and ADC values. Following a study involving 18 brain tumour patients, 2 sides of this triangle were realised. Significant correlations were found between the choline signal and ADC values as well as the ADC and cell density. However the choline signal and cell density did not significantly correlate in this paper, probably due to the small number of patients. Gupta *et al* (121) have also previously published solely on the subject of an inverse correlation between choline magnetic resonance spectroscopy signal intensity and the apparent diffusion coefficient in glioma patients. This study used data from 20 glioma patients to demonstrate choline as a marker for cell density by correlating it with ADC measurements. Another group were keen to correlate the choline level measured using MR spectroscopy with the Ki-67 labelling index in gliomas. In a cohort of 26 glioma patients, surgical specimens were correlated with MR spectroscopic measurements. Significant correlations were found between the choline and Ki-67 measurements in homogeneous gliomas but not in heterogeneous lesions (29). This outcome was potentially related to tissue sampling and the averaging of choline concentrations which is less of a problem in homogenous tumours.

Calvar *et al* (122) have completed a similar study using spectroscopy, diffusion weighted imaging and Ki-67 labelling index for characterisation of brain tumours. In this study 47 patients were recruited and received short echo single time voxel spectroscopy and diffusion weighted imaging as part of a MR examination. A correlation between ADC values and Ki-67 labelling index was found to be significant and relative ADC values were found to show good discrimination between low and high grade gliomas.

Following this work, Khayal *et al* (123) continued to investigate the relationship between apparent diffusion coefficient values and the amount of choline. Thirty-seven low grade gliomas and 28 glioblastomas were scanned at 1.5T. No significant correlations were found in the low grade cohort either on a voxel by voxel basis or for the whole region. In the high grade group, there was a significant relationship when the whole region of interest was analysed. Bian *et al* (124) conducted a study involving the multiparametric characterisation of grade 2 glioma subtypes using MR spectroscopy, perfusion and diffusion weighted imaging. In their study, 56 newly diagnosed low grade gliomas were evaluated with advanced MR techniques. The 75^{th} percentile rCBV and median ADC were found to be significantly different between oligodendrogliomas and astrocytomas. Spectroscopically there were no significant differences found between groups.

Research has been conducted, combining diffusion weighted imaging with magnetic resonance spectroscopy to make the distinction between recurrent glioma and radiation injury. Fifty-five patients with a new contrast enhancing lesion in the vicinity of a previously resected and radiated lesion were included. In recurrent gliomas choline to creatine and choline to NAA ratios were significantly higher. Relative ADC measurements compared to contralateral tissue were also found to be higher in radiation injury than glioma (125). Fink *et al* (126) also compared glioma recurrence with post treatment effects using diffusion, perfusion and MR spectroscopy in a group of 40 patients, concluding multivoxel spectroscopy outperformed single voxel spectroscopy with the

maximum choline to NAA peak height and choline to creatine peak areas providing the highest area under the curve (AUC) values. A similar AUC was obtained by using the CBV ratio. The ADC ratio did not perform well in distinguishing between glioma and radiation injury. It is speculated that partial volume effects and voxel positioning were the main causes behind the single voxel spectroscopy's poor diagnostic power. Overall, perfusion and multivoxel spectroscopy should be used for differential cases of this type (*Figure 74*).

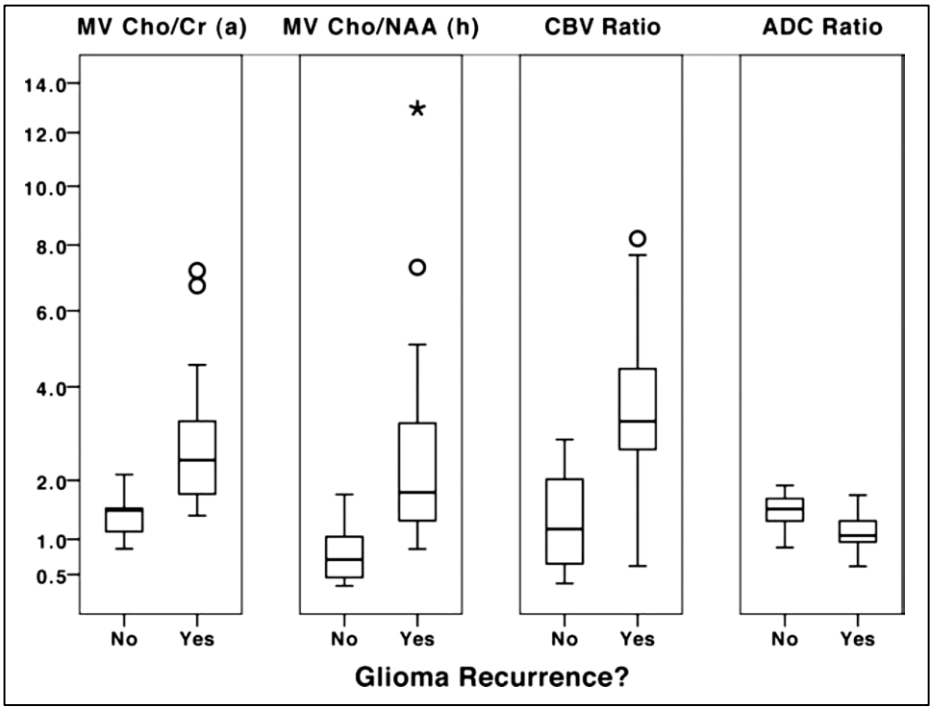

Figure 74 - Box plot displays for multivoxel (MV) Cho/Cr peak-area (a), multivoxel Cho/NAA peak-height (h), CBV ratio, and ADC ratio observed cases of glioma recurrence (Yes) and cases of post-treatment injury (No). Reproduced from (126).

Proton MRS and diffusion weighted imaging has been combined to discriminate between brain abscess and necrotic brain tumour. Fourteen patients underwent MR examinations at 1.5T including diffusion weighted imaging and single voxel spectroscopy. Additional peaks were found in most abscesses which included acetate, alanine and succinate. Lipid and lactate were found in most gliomas and abscesses ruling them out as discriminators. ADC differences were also seen on imaging with abscesses having much lower ADC values in the centre (47).

4.3 Prediction of Glioma Response and Progression

4.3.1 Morphological Studies

The extent of resection is believed to be a significant biomarker for survival. In a review paper assessing the extent of resection and its impact on patient outcome, Sanai *et al* (2) examined all major clinical publications from an 18 year period. After reviewing 28 papers on high grade resection, and 10 papers on low grade resection, the meta-analysis revealed more extensive resections are associated with longer life expectancy. In order to assess resection, early postoperative MR imaging in gliomas is often used to make the initial assessment. When predicting tumour growth, Ekinci's group (127) found 91% sensitivity and 100% specificity using early postoperative MR imaging (24 hours post-surgery) with a thick linear-nodular enhancement pattern present in 9 out of the 10 tumours which reoccurred.

The prognostic value in detecting recurrent glioblastoma multiforme (GBM) in surgical specimens taken from patients post radiotherapy in a cohort of 54 patients revealed that tissue samples could no longer aid in predicting outcome or dictating further patient management. Therefore advanced and robust imaging techniques needed to be developed to assist with patient management in those who have undergone radiotherapy (128).

Low grade gliomas are sometimes resected when pressure symptoms or mass effect are present. The advantages of resection also include a definitive tissue diagnosis as well as pressure relief for the patient. In a cohort of 42 low grade gliomas that underwent resection, it was found that lesions that extended to more than one lobe were the strongest predictors of malignant transformation, functional status and overall survival (3). Tumour progression also occurred in 67% of patients during an average follow up period of 31 months. The study also found that the extent of tumour volume pre or postoperatively had no significant effect on overall survival, suggesting that

preoperative tumour volume reflects the tumour's biological properties that remain unaltered following resection.

Tofts *et al* (129) showed quantitative analysis of whole-tumour gadolinium enhancement histogram predicted malignant transformation. In a small cohort of 21 patients, tumours were outlined using fluid attenuated inversion recovery (FLAIR) imaging. Pre- and post- contrast T_1 imaging were registered and subtracted following a double dose injection of gadolinium to produce a percentage enhancement (%E) map. Histograms for each tumour were generated with a threshold of %E greater than 10% used. Baseline enhancing volumes were higher in transformers and patients with less than 4ml of enhancing of tissue showed significantly higher 5 year survival.

The growth of 27 untreated low grade gliomas was followed in an attempt to predict transformation (130). Patients with higher tumour growth rates were found to transform sooner than slower growing lesions. The paper highlights the need for proper measurements of tumour volume in order to detect tumour transformation.

Monitoring response to radiotherapy in gliomas is an important clinical goal. One group investigated the predictive value of morphological imaging response criteria, one month after concurrent chemotherapy and radiotherapy in patients with glioblastoma (131). Tumour volumes were delineated on post contrast T_1 images before and after radiotherapy. Clinical progression was classified as when chemotherapy management was changed based on clinical and/or radiological progression. Thirteen of the twenty-five patients who completed the trial showed signs of early radiological progression, with 5 of those patients being pseudo-progressors after remaining radiologically stable for 6 months. Volumetric data was shown to be the most predictive measurement of overall survival when using ROC analysis. This study shows some of the difficulties in distinguishing glioma growth from pseudo progression.

4.3.2 Diffusion Studies

As well as ROI based DWI measurements, functional diffusion maps (fDMs) can be used to predict response to cytotoxic and anti-angiogenic treatments in high grade gliomas (132). fDMs were generated for areas of high T_2 signal on FLAIR imaging. In this paper (132), changes were observed in the fDMs before conventional imaging methods. The limitations of fDMs are related to quality of the registration that can be achieved prior to subtraction. Functional diffusion maps appear to be an early predictor for tumour progression, time to progression and overall survival in both cytotoxic and anti-angiogenic treatments making it a suitable tool for monitoring and predicting response to a new wave of cancer therapies.

One of the first functional diffusion maps papers comes from Moffat *et al* (133) who used it as a biomarker for early prediction of cancer treatment outcome. Using implanted 9L type brain tumours in rodents, they were able to prove the concept of functional diffusion maps as a marker for cell kill following chemotherapy. They found changes to correlate with drug dose and saw diffusion changes prior to T_2 imaging changes.

Subsequently, functional diffusion maps have become increasingly popular, as a surrogate imaging biomarker for early prediction of therapeutic response and survival (134). Forty-six glioma patients underwent diffusion imaging before and during therapy. In responders ADC values were found to increase in a larger portion of the tumour than in non-responders. Responders identified using fDMS also showed significantly longer survival. In a similar functional diffusion map study (135), 60 patients with high grade gliomas were assessed during treatment using diffusion weighted imaging at 1, 3 and 10 weeks. Tumours which showed the biggest increase in ADC on the fDMs had the longest survival (*Figure 75*).

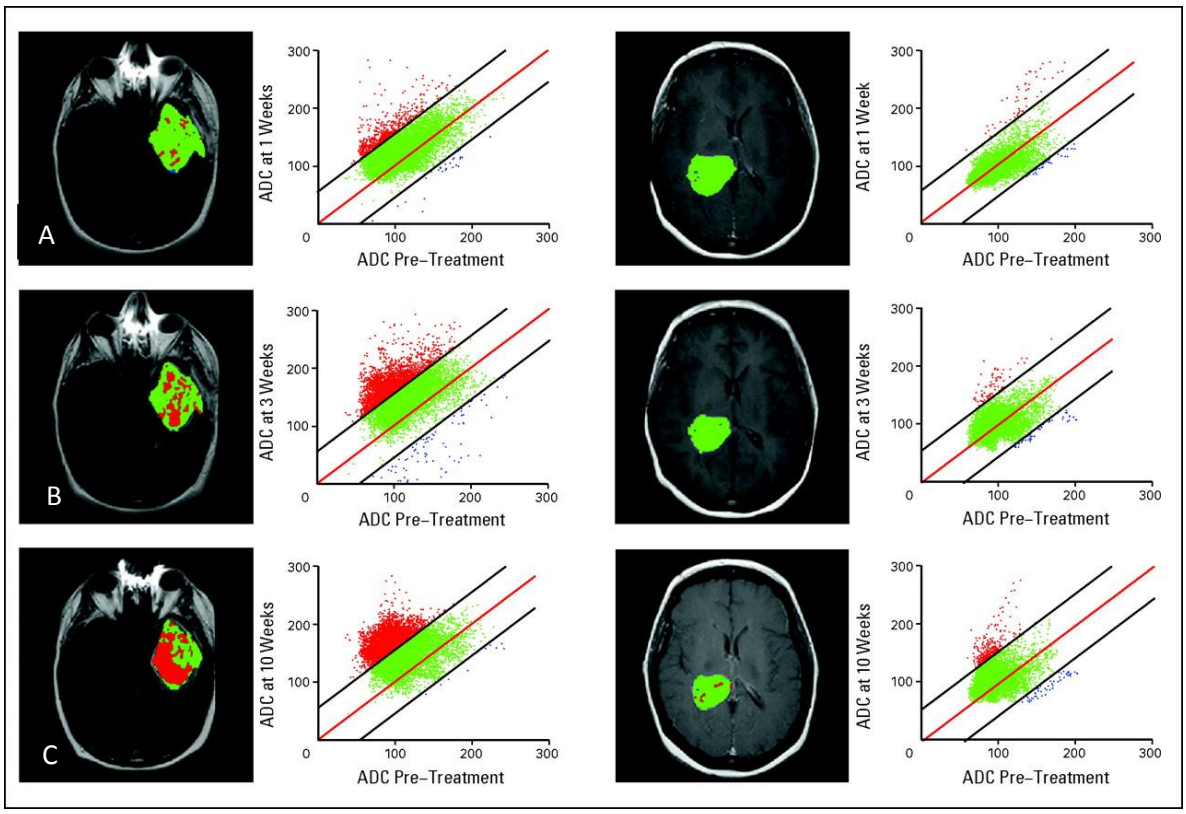

Figure 75 –Functional diffusion map analysis over time. Maps at (A) 1, (B) 3, and (C) 10 weeks for two patients treated with fractionated radiation therapy. The patient on the left was scored as responsive by fDM at 3 weeks but progressive disease by radiologic response at week 10 and had overall survival (OS) of more than 33 months. The patient on the right was scored as nonresponsive by fDM at 3 weeks but stable disease by Macdonald criteria and OS of 7 months. Red voxels indicate regions with a significant rise in apparent diffusion coefficient (ADC) at each time point compared with pre-treatment, green regions had unchanged ADC, and blue voxels indicate areas of significant decline in ADC. The scatter plots display data for the entire tumour volume and not just for the depicted slice at each time point, with the pre-treatment ADC on the x-axis and post-treatment ADC on the y-axis. The central red line represents unity, and the flanking blue lines represent the 95% CIs. Reproduced from (135).

Continuing with the concept of functional diffusion maps, *Ellingson et al* (136), have developed graded function diffusion maps to predict overall survival in recurrent glioblastoma treated with bevacizumab. In the study, it was found that restricting the fDM to between 0.25 - 0.4 $x10^{-9}$ m^2/ms increased the predictive power compared to traditional fDMs. This work also supports the mounting evidence that techniques like diffusion may be more suitable for monitoring advanced therapies compared to traditional morphological imaging techniques such as pre- and post- contrast imaging.

An extension of diffusion weighted imaging (DWI) is diffusion tensor imaging (DTI) in which diffusion gradients are applied in at least 6 directions in order to determine diffusion directionality. Price *et al* (137) took advantage of DTI to observe subtle disruption in the white matter tracts due to tumour infiltration. A cohort of 26 glioma patients was imaged 2 years after the initial treatment or at the time of reoccurrence. By splitting the tensor into the isotropic (p) and anisotropic (q) components, infiltration could be visualised. When the boundaries of p exceeded those of q infiltration was present but when the boundaries matched, the tumour was stable.

Other groups have expanded on the idea of functional diffusion maps to include diffusion tensor imaging. Paldino *et al* (138) used fDMs to look at survival following bevacizumab in recurrent glioblastoma. In a small cohort of 15 patients, serial DTI was undertaken at 1 and 3 days before treatment and 6 weeks into the treatment regime. Nine patients showed ADC changes within the FLAIR signal abnormality at the last time point. Four patients had increased ADC while 5 had decreased ADC values. It was found that patients who had ADC changes had a significantly shorter survival than patients who showed no ADC changes. The fractional anisotropic changes showed no significance in this study. Diffusion tensor imaging has also been seen to correlate well with clinical motor findings in patients with glioblastomas (139). Overall, fibre density and fractional anisotropy was lower in patients with motor deficits. ADC, FA and fibre density were all found to correlate with clinical score.

Yamasaki *et al* (140), investigated the prognostic value of ADC for glioma patients with postoperative chemoradiotherapy, looking at 33 patients over an 8 year period and measuring the ADC values before therapy. After exploring the mean, minimum and maximum values in the tumour, it was found the strongest statistical parameter was the extent of tumour resection followed by the minimum ADC, when correlated with overall survival. The minimum ADC was also the most powerful predictor in patients who did not receive surgery as part of their treatment. ADC measurements are

becoming increasingly more complex as scientists' understanding of the histology grows. One group (19) have published results demonstrating that bi-modal histograms predict tumour response in newly diagnosed glioblastoma treated with bevacizumab. By looking at the lower of the two mean ADC values gathered from the 2 compartment histogram model, researchers were able to stratify progression-free survival. It was also found that lower ADC values were associated with tumour MGMT promoter methylation which is thought to explain the more favourable outcome seen in tumours with the lower mean ADC in the left sided histogram (*Figure 76*).

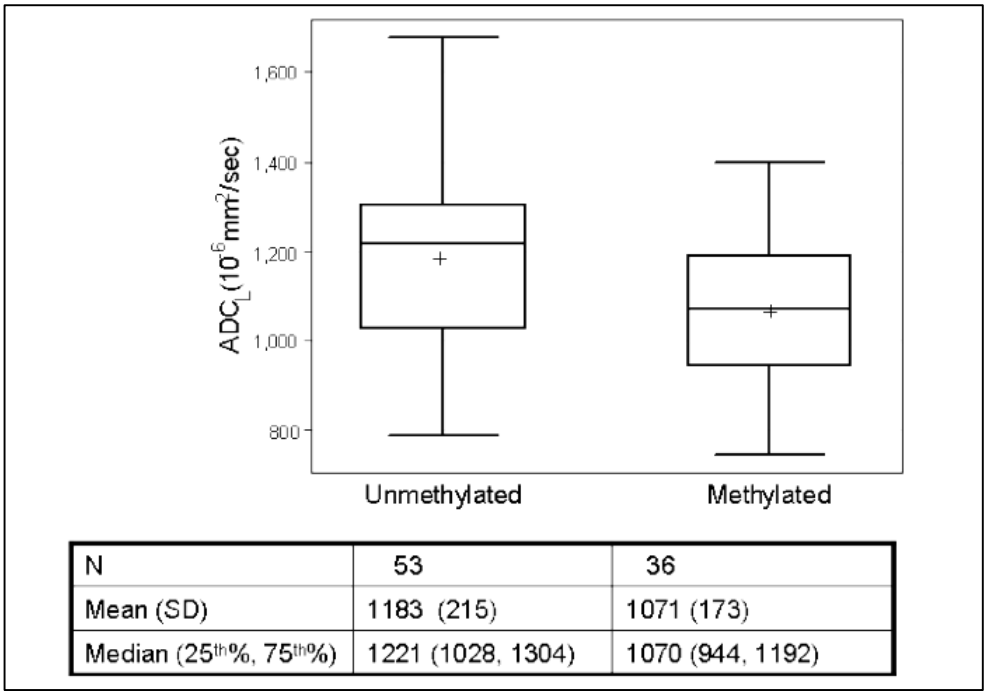

N	53	36
Mean (SD)	1183 (215)	1071 (173)
Median (25th%, 75th%)	1221 (1028, 1304)	1070 (944, 1192)

Figure 76 - A Box-and-whisker plot of ADC$_L$ values in MGMT promoter methylated and unmethylated tumours. Mean values are significantly different between the 2 groups (P =0.01). Reproduced from (19).

Previous work in a cohort of 46 patients receiving bevacizumab to treat recurrent glioblastoma also used ADC histograms to predict response. Using a bi-modal histogram analysis it was found that pre-treatment ADC values more accurately stratified 6 month progression than the change in enhancing tumour at the first follow up scan (141).

4.3.3 Perfusion Studies

Relative cerebral blood volume (rCBV) measured by DSC has been shown to be a predictor of patient clinical response in low grade gliomas. Thirty-five patients were recruited for the study, revealing that patients with a rCBV of less than 1.75 had a median progression time of 4620 days compared to patients who progressed median a mean time of 245 days (142).

Multi-institute studies can prove valuable when validating a new technique. In one particular study (143), DSC was used in a multi-centre study to predict patient outcome in a group of low grade glioma patients. Sixty-nine patients from 2 institutions were recruited for the study. There was a significant relationship between rCBV and time to progression. The threshold for survival also being a rCBV of 1.75 in this case. The other important aspect of this study is that rCBV appears to be consistent between centres.

Galbán (144) reports that parametric response maps (PRM) of rCBV were more significant than rCBV measurements in predicting overall survival based on scans 1 and 3 weeks into radiotherapy. The study population consisted of 44 HGGs, of which 36 were GBMs. Patients were imaged before and during treatment to produce the PRMs. However, it appears none of the patients underwent debulking meaning tissue remodelling was not as much of a problem. This treatment though could be considered suboptimal compared to patients who receive tumour resection.

In a small study of 13 patients, rCBV values were used to predict transformation from LGG to HGG up to 12 months in advance of traditional imaging techniques (145). It is worth noting that only 6 patients progressed during the study with lesions sampled using a minimum of six small ROIs.

4.3.4 Spectroscopic Studies

The prognostic value of choline and creatine was investigated in low grade gliomas with positive results. Forty-five glioma patients underwent MR spectroscopy of their tumours. Normalised creatine values were found to be predictive of progression and malignant transformation. While choline showed similar tendencies the overlap between the two groups was too large. Grade II gliomas with a tumour/normal tissue creatine ratio less than 1 were found to progress after a longer time interval (146).

Kuznetsov *et al* (147) published results in 2003 describing how proton magnetic resonance spectroscopy can predict the length of survival in patients with supratentorial gliomas. Using a leave one out logistic regression model featuring maximum choline and lipid values, number of voxels with low NAA and the number of voxels with increased lipid they were able to correlate survival with the model (r^2 = 0.81%). The MRSI data had an r value of 0.77 and median survival error was 1.7 months for the 54 patients who took part.

Magnetic resonance spectroscopy has also been shown to be predictive of proliferative activity in grade II diffuse low grade gliomas. Eighty-two patients underwent single voxel spectroscopy at 1.5T at short and long echo times before tissue sampling (148). Ki-67 is a marker for cell proliferation used in the World Health Organisation's (WHO) guide to grading brain tumours. Therefore validating spectroscopic finds against this marker is justified. Findings from the paper include tumours with a Ki-67 of less than 4% being free from lactate and lipid in the spectra. Tumours with lactate peaks but no lipid were found to have a Ki-67 between 4 and 8%. Lesions with a Ki-67 greater than 8% were found to have the highest choline to NAA ratio as well as containing peaks from lipid in the spectra.

4.3.5 Multiparametric Studies

Saraswathy *et al* (149) evaluated MR biomarkers to predict survival in glioblastoma patients prior to adjuvant therapy, in a population of 68 patients imaged at either 1.5T or 3.0T before and during fractionated radiotherapy and chemotherapy. MR spectroscopy was acquired along with diffusion and perfusion imaging, finding patients with larger lesions based on anatomic imaging, spectroscopy and blood volume measurements had a higher chance of poorer outcome. High levels of lipid and lactate found in the lesion also lead to a higher likelihood of poor survival. Thirty-five patients from this study also received lactate-edited spectroscopy in which the lipid and lactate signals are able to be separated; revealing lipid signal was more likely to arise from the enhancing tissue rather than the non-enhancing component of the lesion. Maximum lactate values from any part of the lesion were found to be a significant factor in survival.

Spectroscopy has been used to predict changes in perfusion in a group of low grade gliomas (150). Thirty-one patients were enrolled in the study with participants receiving dynamic susceptibility perfusion and single voxel proton spectroscopy. Significant correlations were found between the maximum relative cerebral blood volume and the following ratios: lactate to creatine, choline to NAA and lipid to creatine. Researchers were able to discriminate between tumours with a rCBV of 1.7 or more using the lactate to creatine ratio with a sensitivity of 75% and a specificity of 95%.

The relationship of preoperative imaging parameters has been investigated in relation to survival within a cohort of untreated glioblastoma patients (39). Fifty-six glioblastomas were scanned immediately before surgery receiving perfusion, diffusion and multivoxel spectroscopy as part of their MR exam. A median survival time of 517 days were reported. The tumour volume based on anatomical imaging was not a significant predictor of survival but the volume of necrosis and contrast enhancing tissue as a percentage of the overall T_2 abnormality was linked to poorer survival. The volume of tissue with an increased choline to NAA was also found to be linked to survival.

Tumours with a larger region of ADC values that were 1.5 times higher than normal white matter also had less favourable outcomes.

One group that reports different results to the growing trend of functional imaging being more useful than conventional imaging is Caseiras *et al* (151). In their study of low grade glioma transformation, they found six month tumour growth to be a stronger predictor of transformation than diffusion and perfusion weighted imaging along with the tumour volume at admission. Thirty-four patients were recruited for this study and were scanned every 6 months with a median follow up time of 2.4 years. The authors point out that volume measurement can easily be obtained from normal clinical MR exams now, and changes in volume are the strongest predictors of progression. This relies on clinicians delineating the lesion on all slices, which is time consuming, and that the volumetric sequence acquired shows the lesion which is not always the case with T_1 SPGR.

Hlaihel *et al* (152) have looked at the predictive power of conventional, perfusion and spectroscopy in anaplastic transformation of low grade oligodendrogliomas. This relatively small study cohort had 5 of the 21 patients recruited progress during follow up. A choline to creatine ratio of above 2.4 was associated with an 83% risk of transformation after an average delay of 15.4 months. The spectroscopy was found to be better than DSC and morphological imaging at detecting anaplastic transformation with a sensitivity of 80% and a specificity of 94%. The mean annual growth rate was 3.65mm in this cohort with tumours growing more than 3mm a year having a greater risk of transformation. Spectroscopy is thought to be able to predict anaplastic progression before perfusion changes with a predictive score of 83%.

4.4 Monitoring of Gliomas during Follow Up and Therapy

4.4.1 Morphological Studies

In a review of MRI in treatment of adult gliomas, the topic of tumour size measurement arises. Gliomas often have irregular shapes so cross sectional measurements usually have quite high errors associated with them. The presence of cystic areas also complicates the tumour measurement since these areas do not respond to treatment. The use of computer aided volumetric analysis may be more accurate in measuring early changes previously not seen using cross sectional methods. Tumour heterogeneity is another problem when assessing glioma response to therapy so techniques that may delineate tumour margins better such as MRSI and DWI (153) are of keen interest.

A comparison study of 1D vs. 2D vs. 3D techniques (154) for the measurement of recurrent gliomas has been carried out in 70 patients who received chemotherapy. The tumour response was assessed by the volumetric method, as well as bi- and uni-dimensional measurements. These results were then correlated with the survival data. The findings of the study showed that only 3D measurements accurately reflected changes in the tumour and that only a volumetric approach could significantly predict overall survival. Volumetric analysis of conventional MR has been used to assess the response to chemotherapy in glioblastoma patients with a limited degree of success (155). Fluid attenuated imaging and post contrast MR were used to try and predict progression-free survival and overall survival. It was found that the volume of hyperintense T_2 signal pre and post therapy has no predictive power. The initial post contrast imaging was predictive of progression-free survival but not overall survival. However, the ratio of the FLAIR to post contrast imaging was shown to be predictive of both the progression-free and overall survival.

Ensuring a tumour is fully covered by the radiotherapy field is being seen as increasingly important if the therapy is to be successful. In a brief paper, Shukla *et al* (156) looked for T_2 changes between pre-therapy MR and images taken at 5 weeks into radiotherapy. They found in 20% of patients that the tumour had grown during the time of therapy (3/15 patients). Therefore they suggest boost dosages based on mid-therapy imaging. It is also commented that postoperative contrast MR to assess the resection of enhancing tissue could lead to better treatment planning.

In treated glioblastoma patients, the question of tumour progression vs. radionecrosis occurs regularly. In a study (157) examining the difficulties separating the two pathologies, 50 patients receiving chemoradiotherapy were reviewed with 30% of the group showing some signs of clinical or radiological worsening. Seventy percent of reoperations for progression showed some form of tumour reoccurrence or progression leaving 3 patients without signs of tumour. The authors went on to conclude that with the introduction of chemoradiotherapy, early radionecrosis is possible given temozolomide is a known radiosensitiser, and pseudoprogression being a recognised consequence of chemoradiotherapy in glioblastoma multiforme. In a cohort of 104 patients, 26% showed signs of radiological progression using MR contrast imaging, and of this sub-cohort, 32% of patients actually had pseudoprogression rather than recurrent disease. This paper highlights the limitations in assessing the response to chemoradiotherapy using conventional MR methods and how this can lead to unwarranted changes in therapy for the cohort of pseudo progression patients (158).

Occasionally low grade gliomas are given radiotherapy. The question of how to monitor the response exists since these tumours do not normally enhance on T_1 weighted imaging. In a cohort of 21 low grade glioma patients who underwent radiotherapy as part of their treatment, response was measured by fitting an ellipsoidal model of the tumour to computer tomography (CT) and T_2 images. It was found that low grade gliomas are moderately radio-responsive but the method used

to measure tumour volume over-estimated the number of partial responders unless a volume reduction of greater than 50% was seen. The paper concludes that better ways of measuring the response in low grade gliomas is needed (159).

One method of tumour volume measurement includes automated tissue segmentation. Constantin *et al* (160), demonstrate one method for segmentation using a combination of FLAIR and T_1 pre and post contrast imaging. The abnormal region was defined by the hyperintense T_2 region of the FLAIR. The enhancing part of the tumour was delineated by the post contrast T_1. Necrosis was assigned to the hypointense region on the T_1 imaging and hyperintense on the FLAIR. This way CSF should be dark on both weightings. Better tumour segmentation should ultimately lead to better volumetric measurements and subsequently better sensitivity to small volumetric changes early into therapy.

4.4.2 Diffusion Studies

One of the first papers to use ADC histograms to demonstrate changes due to treatment was that by Ross *et al* (161). Their paper entitled "Evaluation of cancer therapy using diffusion magnetic resonance" highlights changes in mouse and human brain tumours following both radiotherapy and chemotherapy. It was one of the first papers to show diffusion weighted imaging could be successfully used as a biomarker to treatment response. One report attempting to validate the functional diffusion maps, appears to show that the ADC changes observed in fDMs are a true reflection of the cellular conditions in the tissue of interest (162).

If ADC maps are to be used regularly in assessing therapeutic response, then a histogram based classification using Gaussian mixture modelling may be better suited to assessing glioblastoma treatment response (163). By taking into account to two main types of tissue in a glioblastoma (solid and necrotic) the histogram fit is better and the two components may be used separately to measure response.

Price *et al* (164), highlight the potential for assessing white matter tract invasion using diffusion tensor imaging in their 2003 paper. In this paper they use the relative anisotropy index (RAI) to measure white matter organisation throughout the brain of tumour patients, finding the abnormality on RAI maps often exceeded changes seen on conventional T_2 weighted images as seen in Figure 77. It was also suggested that DTI could help with radiotherapy planning if used with due care.

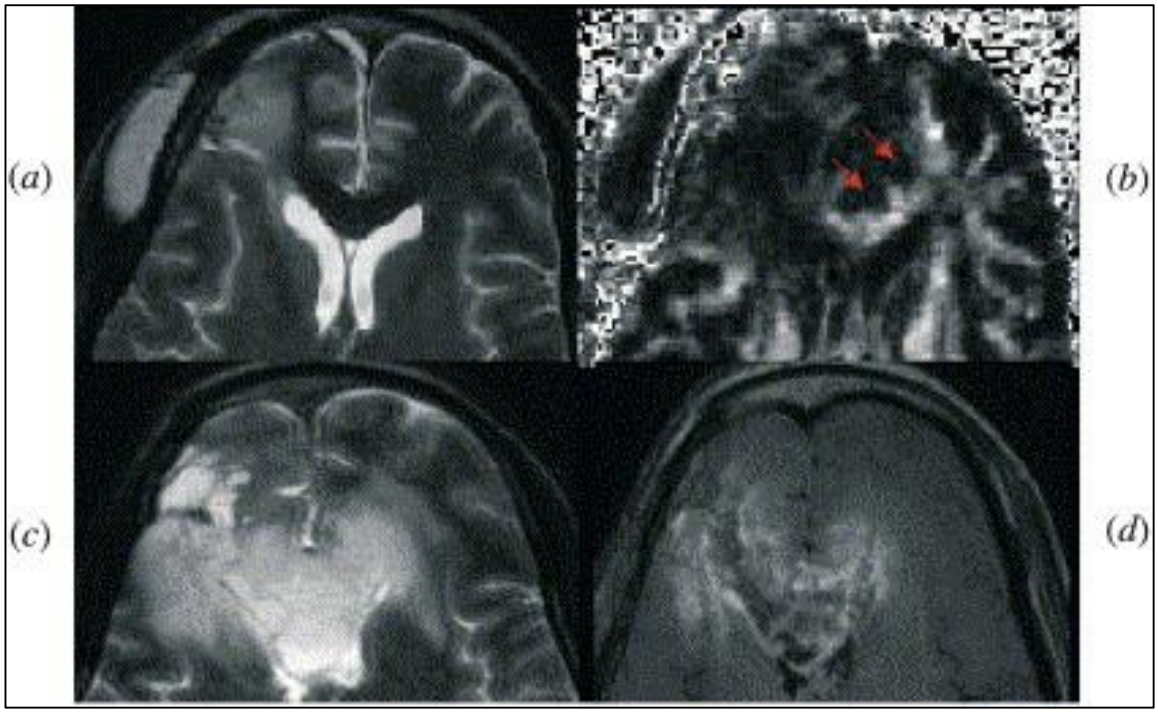

Figure 77 – *T_2-weighted (a) and RAI (b) images acquired in June 2000 of a 23 year-old man who had undergone a frontal lobectomy for a WHO grade IV glioma. There is no evidence of mass effect. There are focal defects in the genu of the corpus callosum (arrows). The RAI changes extend from the right frontal area of T_2-weighted abnormality, across the corpus callosum; to the normal left frontal lobe. Subsequent imaging in June 2002 demonstrated T2-weighted abnormalities (c) and gadolinium enhancement (d) across the corpus callosum. Reproduced from (164).*

Due to the heterogeneous nature of high grade gliomas effective measurement of the fractional anisotropy can be difficult. In a paper using diffusion tensor imaging to measure temporal changes in schwannomas, fractional anisotropy was able to show decreased values following stereotactic radiosurgery before other imaging sequences could see changes. This evidence helps support the hypothesis that fractional anisotropy could be a good way to measure solid tumour response following radiotherapy (165).

4.4.3 Spectroscopic Studies

While a lot of positive literature exists about spectroscopy for monitoring and prediction, occasional papers report contradicting results. One group conducted a study (166) in 14 low grade gliomas with multivoxel spectroscopy with the aim of predicting transformation. Compared to baseline spectroscopy, they classified progression as a 20% increase in the choline to NAA ratio or more. During the trial 7 patients showed signs of progression on imaging and 5 of those also showed spectroscopic progression. Four of the 5 patients with spectroscopic progression went on to have surgery with 3 cases being reported as high grade glioma while one case remained low grade. Of the 7 patients remaining stable, 4 showed spectroscopic progression but imaging features remained the same. This paper therefore concluded spectroscopy had no additional value for predicting transformation. Some of the pitfalls of this study include the very small cohort and the limited tissue samples available with only 4 patients sampled.

With the addition of carmustine wafers (Gliadel®) to the oncologists' choice of treatments, it is important to understand how to monitor the response to this new alternative treatment using MR. In a small study (167) of 3 patients the effect of the Gliadel wafers was measured in the peritumoural region with multivoxel spectroscopy which was seen as a decrease in the choline to NAA ratio and an increased NAA to creatine ratio. The study demonstrated the feasibility to use spectroscopy to monitor patients with implanted Gliadel wafers.

4.4.4 Multiparametric Studies

Alternative ways of monitoring brain tumours are always of interest. When looking at gene therapy induced apoptosis, diffusion and MR spectroscopy were used in rodent glioma models (168). In this study they found small changes in the levels of mobile lipid proceeded changes in ADC and indicated the initiation of tumour shrinkage. Correlations between some types of lipid and the apparent diffusion coefficient were found in this study as well. Serial imaging of Glioblastoma patients (169) before and after radiotherapy was carried out using perfusion and diffusion imaging in conjunction with conventional imaging techniques. Significant predictors were found for diffusion, perfusion and volume measurements.

Multivoxel spectroscopy was used in conjunction with diffusion tensor imaging to show regions of tumour infiltration. This 1.5T study (170) acquired the DTI with 12 directions and 50 2.8mm thick slices while the 2D-MRSI was spatially zero filled to produce a grid of 7.5mm^2 voxels. The authors found the two methods to be complimentary techniques with the diffusion tensor imaging providing a higher spatial resolution while the spectroscopy provided metabolic confirmation of proliferating cells.

4.5 Defining a Region of Interest

Defining a region of interest around a glioma is an unusually complicated problem. Gliomas are renowned for their poorly defined margins and oedematous regions. This section looks to the literature to help define the regions of interest for this thesis.

Yamasaki's 2005 paper measuring the ADC values of brain tumours (77) examines the use of manual ROI placements on the enhancing portion of the tumour, and hyperintense areas in non-enhancing lesions using a FLAIR sequence. Cystic areas were excluded using a criteria of hyperintense on T_2 weighted imaging and hypointense on FLAIR imaging. Necrosis was defined as the interior section of a lesion on T_1 gadolinium enhancing imaging. In this paper only the 'solid' portions of the tumour were compared.

Khayal examined the relationship between ADC and spectroscopy in 2008 (123), using a semi-automatic approach to define the different areas of the lesion. These were the contrast enhancing lesion (CEL), necrotic regions (NEC), T_2 hyperintenese region (T2 ALL) and the non-enhancing legion (NEL), which was defined as (T2 ALL – CEL – NEC). 3D-PRESS grids were then compared to these different regions by reducing the effecting resolution of the conventional imaging. This method for lesion segmentation was subsequently used in Sarawathy's 2009 paper (149) on the prediction of newly diagnosed glioblastoma survival. Gupta's paper in 2000 relating choline and ADC (120) is the first paper in which ADC maps were reduced in resolution down to the same in-plane resolution of the multivoxel spectroscopy for correlation. In this paper, only tissue which was subsequently resected was evaluated.

In 2009, Wang *et al* (83) investigated the role of alternative DTI parameters such as p, q, L and FA in the imaging of gliomas. Their method for ROIs was to highlight the gross tumour as well as the peritumoural oedema. Areas of necrosis and haemorrhage were excluded in this paper. Again a combination of T_2 weighted imaging and post contrast T_1 images were used to define regions. All

ROIs were registered to the b=0 sec/mm^2 diffusion slices and visually inspected. The gross tumour volume was expanded by 5 voxels then subtracted from the T_2 region to leave the peritumoral margin behind. Regions were also mirrored for normalisation in some situations. The method of Price *et al* in their paper (137), predicting glioma reoccurrence patterns relies on T_2-weighted and T_1-weighted pre- and post-gadolinium imaging to define regions of the tumour and follows a similar approach with the DTI by registering it to T_2–weighted anatomical imaging.

Di Costanzo's multiparametric paper (119) on tumour extent and malignancy, published in 2006, used a normalisation scheme for the spectroscopy in which the ROI around the tumour was normalised to a symmetrical contralateral ROI. The T_2* perfusion was processed with a similar normalisation scheme which was applied to contralateral tissue. ROIs consisted of the non-cystic, non-necrotic regions of the tumour as well as the tumour margins and areas of abnormal T_2 signal around the lesion.

In a study by Rees in 2008 (130) looking at low grade lesions and the risk of transformation, ROIs were defined by the extent of the T_2 hyperintense signal using a FLAIR protocol. The reason for the simplistic ROI approach relates to the fact that most low grade lesions do not enhance so separation of the solid tissue from the surrounding oedema is difficult especially in diffuse lesions.

Henson's review of the use of MRI in the treatment in adult gliomas (153) alludes to the difficulties in measuring tumour volume in clinical trials. The volume of disease is believed to be of particular significance when predicting malignant transformation, with tumour heterogeneity also providing a significant problem when measuring and defining tumour boundaries.

Finally, in Law's paper investigating T_2*-weighted perfusion from 2006 (142), two methods were applied for defining the ROI. For anatomical imaging a combination of T_2- and post-gadolinium T_1–weighted imaging was used to define tumour boundaries, whilst radiologists defined relative rCBV

using contralateral normal appearing white matter. Furthermore, ROIs in the lesion were chosen by the high CBV values.

4.6 Conclusions

Currently in oncological neuroimaging, there appears to no consensus as to the most appropriate method for sampling data, whether this is region or volume of interest based and which tissue types to include or exclude. While there are a host of advanced MR imaging techniques available (Table 4), most are yet to enter routine clinical practice guidelines with the exception of diffusion. Interpretation is just one of the barriers between research and clinical practice whilst the additional acquisition time of such sequences is still to be justified. Absolute quantification is the other issue, with cut-offs and thresholds not used routinely to influence patient management. Therefore in this thesis, a multiparametric approach for measuring treatment based changes is required with a view to providing thresholds for treatment response in this cohort of patients.

Key points from the literature to consider and potentially influence my work include:

- The use of histogram analysis as a less subjective method for tumour sampling
- Gaussian Mixture Modelling for statistics of multiple populations
- Leakage correction when measuring blood volume in gliomas
- Many of the MR sequences not being fully exploited when processed
- Most studies not investigating the most common and optimal treatment pathway, which is resection and chemoradiotherapy
- Functional diffusion maps have only been demonstrated in non-resected lesions
- Tissue separation appears to be important when sampling gliomas

Table 4 - A summary of the use of different MR techniques and the role they play oncological management in the brain.

MR Modality	Diagnosis	Prediction	Monitoring Response
Diffusion	DWI (77-79, 81, 86) DTI (82, 83, 85, 164)	DWI (49, 132-136, 140, 144, 162, 171-173) DTI (137)	DWI (138, 161)
Perfusion	DSC (12, 63, 88, 89, 91) DCE (92) ASL (94)	DSC (142-145)	DSC (65) DCE (174)
Spectroscopy	SVS (95, 97-100, 103-105, 112) 2D/3D-MRSI (96, 106-108, 110)	SVS (146, 148) 2D/3D-MRSI (147)	2D/3D-MRSI (166, 167)
Multiparametric	DWI+SWI+DSC (117) DSC+MRS (118) DWI+DSC+MRS (119, 124, 126) DWI+MRS (47, 122, 123, 125)	DWI+DSC+MRS (39, 149) DWI+DSC (151) DWI+MRS (150) DSC+MRS (152)	DWI+MRS (168, 170) DWI+DSC (169)

5 Study Overview

This study was a clinical investigation designed to follow patients with gliomas, a type of primary brain tumour, using imaging. Importantly, this project was designed only to observe changes in these tumours using MRI and MRS, with no additional intervention to individual patients. Ethics for the study entitled 'Survival prediction and treatment planning for brain tumours using advanced quantitative magnetic resonance imaging (MRI) and spectroscopy (MRS)' was approved in September 2010 by a local ethics committee (REC Ref: 10/H1307/27) and the regional NHS trust granted permission for research, with the study beginning to recruit patients in November 2010.

All study scans were carried out within the Hull-York Medical School's Centre for Magnetic Resonance Investigations (CMRI) at Hull Royal Infirmary, using a 3.0T MR750 Discovery system (GE Healthcare, Milwaukee, USA), software releases DV22.0/24.0 with an 8 channel phased array head coil. The study had two separate arms as is detailed in this chapter.

5.1 Declaration of Contributions

Lawrence Kenning: Attended multi-disciplinary team meetings. Patient Recruitment. Maintained patient database. Scanned majority of patients. Booked patients for repeat scans. Processed all data. Drew all volumes of interest. Created multiparametric registration scheme. Created white matter normalisation scheme. Processed all spectra.

Martin Lowry: Attended multi-disciplinary team meetings. Patient Recruitment. Coded DIVA (DTI, PK modelling, DSC models). Multi-flip and DCE motion correction scheme. Scanned any patients LK did not. Study Design. Chief Investigator

Martin Pickles: Protocol, logistics and statistical advice. Patient Consent. Principal Investigator

Lindsay Turnbull: Patient Consent. Cannulation. Screening

Martine Dujardin: Cannulation. Screening

Julie Pounder: Cannulation. Power injector setup and connection. Screening

Daniel Siddons: Power injector setup and connection. Screening

5.2 Inclusion Criteria

- Patients diagnosed with high grade intracranial tumours to be treated by surgery, chemotherapy and radiotherapy
- Patients diagnosed with low grade intracranial tumours and not to be treated by surgery
- Patients must be aged between 18 and 80 years
- Tumours should be of the glioma type, low or high grade, and not metastases or meningiomas

5.3 Exclusion Criteria

- Patients under 18 years of age will not be recruited into this study because of issues with informed consent from minors
- Patients with high grade tumours treated using Gliadel® will be excluded
- Standard MRI exclusion criteria relating to patient proximity with a 3 T magnetic field (e.g. cardiac pacemakers, neurological implants, metal fragments in the eyes) will be applied.
- Asthmatics and atopic patients or those with known allergic reactions to Gadolinium based MRI contrast agents will be excluded.

5.4 High Grade Arm

This arm of the study examined the preoperative MRI and MRS to identify prognostic information about the tumour and then compared pre- and post- chemoradiotherapy imaging to identify prognostic biomarkers relating to progression-free survival. The aim of the study, was to potentially help improve future individual patient management as well as providing improved means of non-invasive tumour grading.

5.4.1 Recruitment

Following presentation, whilst on a ward, patients were approached by a senior clinician about participating in the study, and told what participating involved. Following initial discussions, research members from the MRI centre went to explain further about the study and answer any arising questions. Consent was not taken until the patient arrived from the ward to the scanner preparation area sometime later, allowing as much time as possible for patient to make the decision to participate or not.

During the study, three main issues arose regarding consent:

5.4.1.1 Capacity

The first and most important issue regarding recruitment was the patient's capacity to consent. Often patients with brain tumours present very acutely with varying levels of dysphasia. Only patients with the capacity to consent were spoken to about the study. This decision was made by a senior clinician, with researchers having no involvement at this stage.

5.4.1.2 Travel

Due to the epilepsy often associated with having a brain tumour, patients are encouraged to surrender their driving licence. This meant that returning for follow up scans was a potential issue. The referral area for neuro-oncological treatment at this Trust (Figure 78), with which the research was done in collaboration, is quite large due to the sparse population density. Since the scans were for research purposes only, patients did not qualify for hospital transport meaning some patients could not commit to follow-up scans.

5.4.1.3 Time to Surgery & Scanner Availability

Due to the aggressive nature of high grade gliomas, patients were often scheduled for surgery in a matter of days. Allowing enough time for patients to make an informed decision was important if the study was to remain ethical. The other implication of having a short period of time was booking scanner time at such short notice. The scanner used in this study had clinical lists during the day so the solution was to scan patients in the evening slots on the day prior the surgery. This meant our recruitment was limited to the number of patients we could scan in an evening session which was approximately 2 hours.

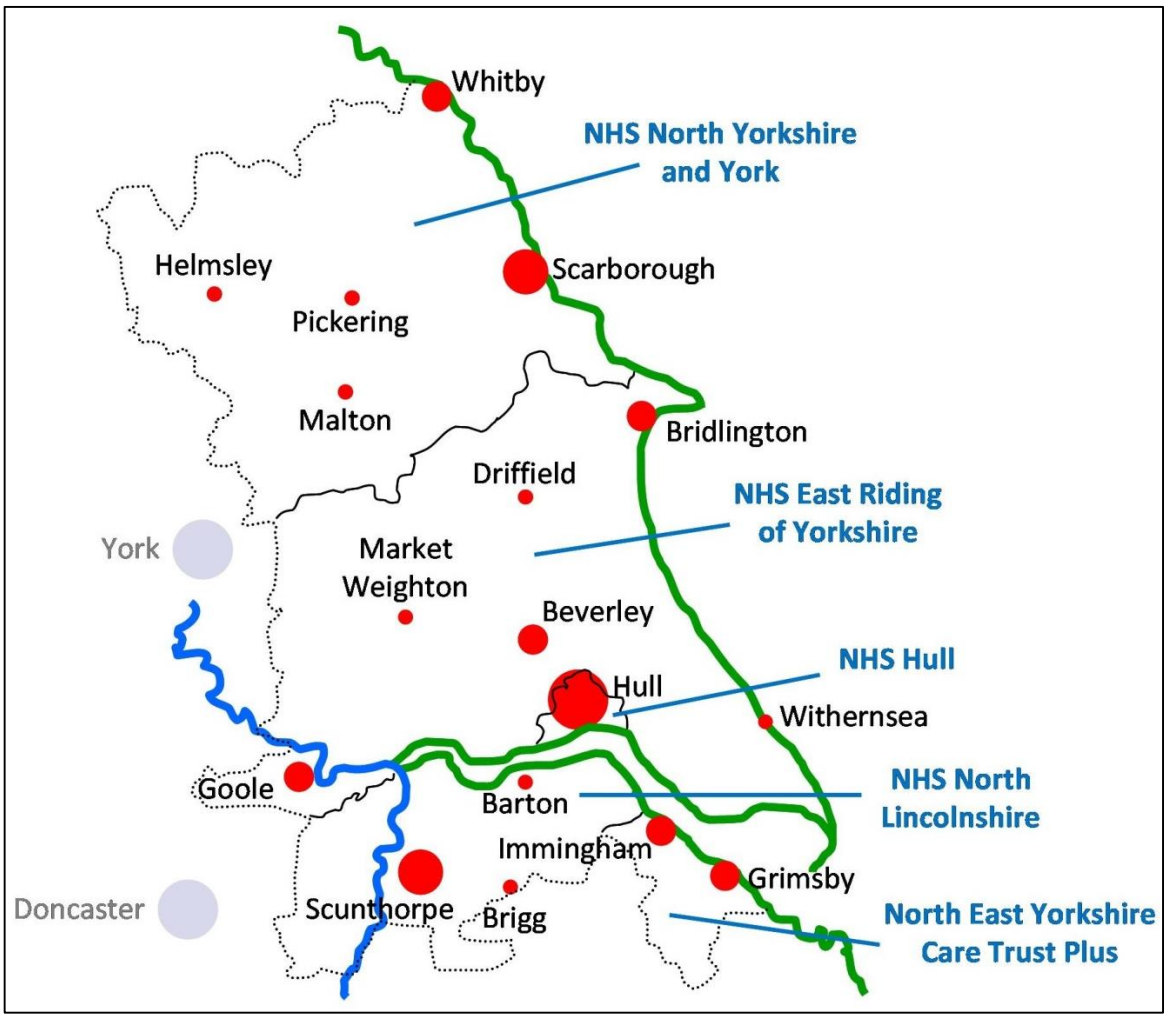

Figure 78 - Map of the referral area for neuro-oncology at Hull Royal Infirmary (175)

5.4.2 Scanning Interval

The high grade arm of the study involved having 3 scans for patients who were undergoing tissue sampling, either from biopsy or debulking, followed by chemoradiotherapy.

The 3 scans were:

1. Preoperative (Week 0). Patients were scanned as close to surgery as possible meaning the MR imaging should have been representative of the lesion.
2. Pre-chemoradiotherapy (Week 3). Patients were normally scanned during the week prior to receiving their first adjuvant treatment. This was to allow as much time as possible for post-surgical changes to settle down. Ideally patients would have been scanned within forty eight hours of surgery using the research protocol but this was not possible due to scanner time limitations and a lack of inpatient slots. In terms of clinical care and radiotherapy planning, patients received postoperative scans elsewhere in the hospital at 1.5T.
3. Post-chemoradiotherapy (Week 10). Patients were invited back during their treatment break for a final research scan so the pre- and post-chemoradiotherapy imaging could be compared.

5.5 Low Grade Arm

This side of the study was set up to identify and predict the transformation of radiologically diagnosed low grade gliomas to grades III or IV over time and whether advanced MR techniques could be identify transformation prior to conventional imaging methods.

5.5.1.1 Recruitment

Similar to the high grade gliomas, patients were approached by a senior clinician about participating in the study and told what was involved. These conversations often happened in outpatient clinics instead of wards. Again, consent was not taken until the patient arrived on the day for the initial scan, allowing as much time as possible for patient to make the decision.

Travelling was the main issue for low grade glioma patients who also had to surrender their driving licences.

5.5.1.2 Scanning Interval

Patients were scanned every 4 months for the duration of the study rather than every 6 months to a year following the trusts guidelines, with emphasis on spotting the transformation earlier when using a shorter time interval. Following progression, and when suitable, patients were then moved to the high grade arm of the study.

During the study, some patients elected for surgery while others required it due to mass effect and pressure symptoms. Once therapeutic treatment was given they were scanned according to the high grade glioma protocol otherwise they finished the study and were continued to be scanned by the NHS.

5.6 Imaging Protocol for Study Patients

Both low and high grade gliomas received the same imaging protocol as it was felt that the sequences in the study were suitable for both arms.

5.6.1 Scan Order

The order in which the protocol was run was particularly important, and was considered for some time, as to how to optimally accommodate all of the sequences. A complete running order can be seen in Table 5 (page 145).

The extended localiser sequence was to provide sagittal and coronal T_2 imaging to help plan the spectroscopic sequences later. These were the only sagittal images in the protocol. Ready Brain (75) was used for repeatable planning in which the same obliquity (AC-PC line) was used for each patient between scans (see Appendix B, pg. 324). This was done to minimise the amount of registration required, and preserve as much of the original data as possible.

The T_2 FLAIR was the first detailed sequence to be run as it was required to plan the spectroscopic sequences later. Following this, the DTI was acquired as it also needed to be pre-contrast, and provided time to prescribe to multivoxel spectroscopy onto the FLAIR imaging. The two spectroscopic sequences were acquired next to minimise the time between the FLAIR imaging being acquired for planning and prescription, and the spectroscopic pulse sequences being played out.

Coronal T_1 imaging was acquired at the request of neuro-radiologists and done close to the time when contrast was given. The multi-flip angle volumes were done immediately prior to the T_1 dynamics. This is because the multi-flip data was used to calculate the T_1 of the tissue which was required for the PK modelling of the T_1 DCE. By running a high resolution 3D T_1 FSPGR, the clinical requirements were met for surgery and it provided time for the amount of contrast to equalise between the brain tissue compartments. This meant the tissue was preloaded for the DSC, reducing

leakage effects. Finally post-contrast T_1 coronal images were collected so there was pre- and post-imaging acquired from the same location. A full breakdown imaging parameters can also be seen in Table 5 (page 145).

5.6.2 Prescription

Following the 3-plane localiser and ASSET calibration scans, FLAIR imaging was prescribed co-planar to the ACPC line as determined by the Ready Brain sequence. The DTI was then planned coplanar to the FLAIR. 2D-MRSI was prescribed onto FLAIR imaging (Figure 79) with the volume of interest positioned to cover the largest in-plane T_2 abnormality given the constraints of susceptibility and skull shape. Saturation bands were used to help optimise the acquisition by supressing skull based lipid and the propagation of susceptibility artefacts. Higher order shimming was also used for the multivoxel spectroscopic acquisitions. The single voxel TE-averaged PRESS was then prescribed to cover the most abnormal area of tissue based on FLAIR imaging. T_1 SE imaging was prescribed coronally, perpendicular to the ACPC line using Ready Brain.

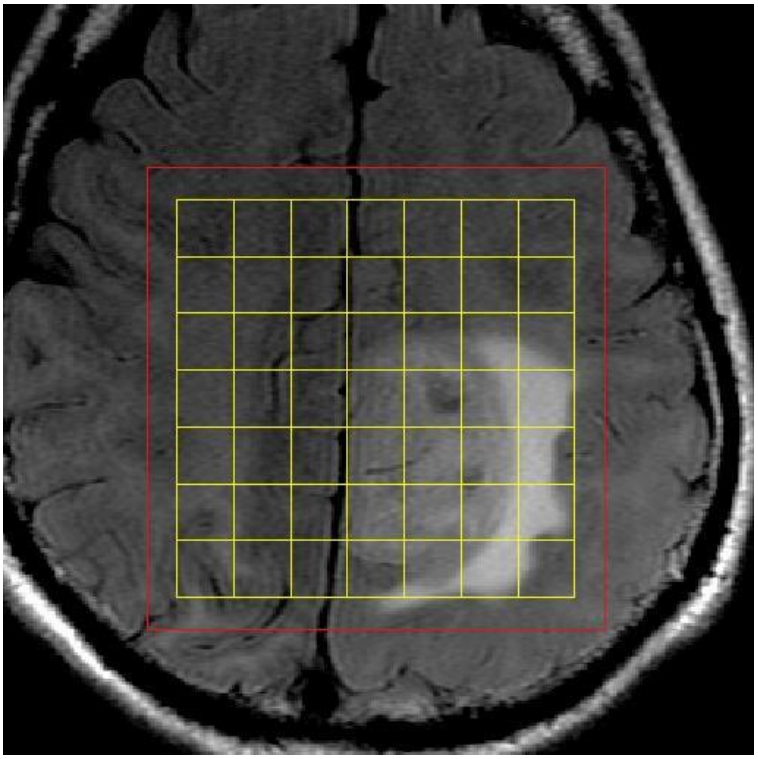

Figure 79 - Typical MRSI prescription with the yellow squares showing complete voxels while the red line denotes the edge of the VOI. This buffer zone extends the slice profile of the volume and ensures full excitation of the yellow voxels. The 2D-MRSI was prescribed onto the slice with the largest T_2 abnormality containing a solid tissue component and the MRSI grid was made as large as possible to cover contralateral tissue while avoiding subcutaneous lipid from the skull.

Multi-flip angle volumes were prescribed using the axial setting on Ready Brain for the 3° flip and subsequently copied for the other flip angles. Due to the temporal resolution versus spatial coverage trade-off, the T_1 dynamics were limited to 16 slices which were concentrated over as much of the T_2 abnormality as possible. The T_1 dynamic volume was also prescribed from the multi-flip angle prescription since it was required to have the same coverage. Patients received an injection (0.075ml/kg) of Dotarem® (Gadoteric acid 0.5mmol/ml) followed by 20ml of saline flush was delivered by pump-injector at 4ml/s following the 4^{th} phase of the T_1 dynamics.

The high resolution T_1 volume was next planned coplanar to the AC-PC line with sufficient coverage of the whole head to avoid wrap. The DSC planning was linked to the FLAIR prescription whilst ensuring the coverage was limited to a single acquisition. Again patients received an injection of Dotarem® (0.075ml/kg) followed by saline flush, this time after the 6^{th} phase of the acquisition. Finally post gadolinium coronal images were linked to the pre-contrast prescription.

5.6.3 Spectroscopic Parameters and Considerations

Three different spectroscopic sequences were acquired during this study. These were: single voxel TE-averaged PRESS, 2D multivoxel spectroscopy and 2D lactate-edited multivoxel spectroscopy. The 2D lactate-edited spectroscopy replaced the product 2D MRSI sequence during March 2012 as planned for in the ethics application.

5.6.3.1 TE-Averaged PRESS

Single voxel TE-averaged point resolved spectroscopy (TR=1200ms, 24 echoes, initial TE=40.18ms, TE step=9.984ms, 12 signal averages per echo time) was acquired from a voxel in the centre of lesions based upon FLAIR imaging, avoiding areas showing cystic cavities. The sequence scan time was 5.50 minutes, with voxel volumes ranging from 3.38-8.00ml depending on lesion size. No water reference frames were acquired as this would have considerably increased the acquisition time.

5.6.3.2 2D Multivoxel Spectroscopy (MRSI)

Two dimensional multivoxel point resolved spectroscopy (TR=1000ms, TE=144ms, 16x16x1 phase encodings, 16x16 field of view, 1 NEX) was acquired from a single slice covering the largest T_2 abnormality based upon FLAIR imaging whilst avoiding contamination from skull based lipid and susceptibility effects along with a half voxel buffer zone to improve slice profile. The sequence scan time was 4.20 minutes, with a slice thickness of 10mm for a nominal voxel volume of 1ml. No water reference frames were acquired with the MRSI, however up to two additional VSS saturation bands were used to help supress susceptibility and spurious signal.

5.6.3.3 2D Lactate-Edited Spectroscopy (MRSI)

Two dimensional lactate-edited point resolved spectroscopy (TR=1000ms, TE=144ms, 16x16x1 phase encodings, 16x16 field of view, 0.8 NEX) subsequently replaced the vendor's product 2D multivoxel sequence. Interleaved BASING pulses (68) were used to modulate the AX coupled lactate whilst minimising potential movement effects simultaneously. By alternating the frequency of the BASING pulses between 0Hz (on) and -198Hz (off) from water it is possible to control the modulation of AX coupled metabolites between the inphase and antiphase positions. Broadband pulses (71) replaced the 137° refocusing pulse used in the standard 3.0T PRESS sequence reducing the effects of chemical shift displacement and ensuring full excitation of both lactate regions given their differing spectral separation from the centre frequency. The advantages of broadband pulses include better excitation of the whole volume while removing the risk of unintentionally exciting skull based lipid. Consequently there is no requirement for voxel oversizing techniques such as OVERPRESS as used in some other spectral editing sequences. Data was still acquired from a single slice covering the largest T_2 abnormality based upon FLAIR imaging. The sequence scan time was 7.00 minutes due to the effective NEX equalling 1.6. In a similar manner to the previous MRSI sequence, the nominal voxel volume remained at 1ml.

5.6.3.4 High Order Shim

The purpose of a high order shim (HOS) is to minimise any inhomogeneity in the B_0 field for a specific area of acquisition. Normally an AutoShim would work in three planes, X,Y,Z and is referred to as a first order shim. While this is sufficient for some sequences at 3.0T, a second order or high order shim must be used for more sensitive sequences like spectroscopic and echo planar imaging, which are more susceptible to off-resonances effect which in turn can lead to blurring and signal loss from the magnet. The higher order shim contains the additional terms; XY, X^2-Y^2, ZX, ZY, Z^2, and Z^3 (176). By utilising a gradient echo sequence, HOS is able to measure and optimise the magnetic field over the correct VOI, this is done by recalculating the B_0 field for a given area and then attempting to correct the B_0 for the VOI selected (Figure 80).

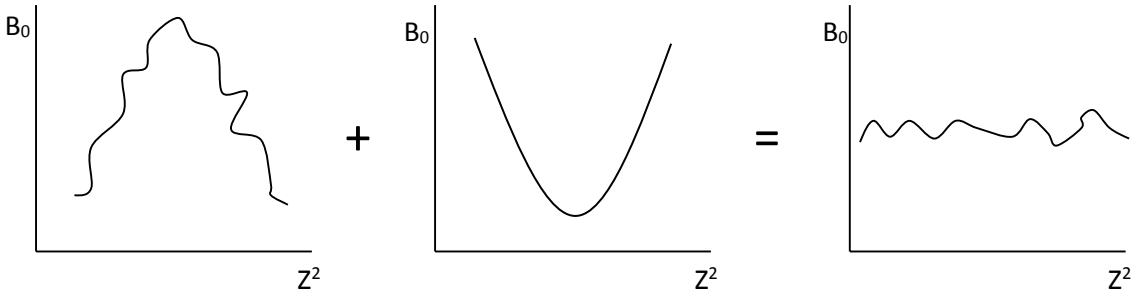

Figure 80 - Illustration of how higher order shimming is able to correct the field inhomogeneities using additional shimming terms

5.6.4 Imaging Protocol for Study Patients

Table 5 - Imaging parameters for a typical study examination. Contrast injections occurred during the T_1 weighted DCE and T_2 DSC sequences. The total scan time does not include prescan times or the time taken to set up the higher order shimming volume.*

SEQUENCE	2D/3D	TE (ms)	TR (ms)	FLIP ANGLE (°)	NEX	FOV (mm)	FREQUENCY	PHASE	THICKNESS (mm)	GAP (mm)	SLICES	TIME
3-Plane Localiser	2D	78.1	475	90	0.55	240x240	384	160	8	4	30	00:00:21
Asset Calibration Scan	2D	2.1	150	50	1	300x300	32	32	6	0	36	00:00:06
Ready Brain	3D	0.6	2.8	10	1	280x280	72	72	3	0	64	00:00:14
T_2 FLAIR	2D	192.2	9000	90	1	220x220	512	224	5	1	24	00:03:36
Diffusion Tensor Imaging	2D	87.4	6000	90	2	240x240	128	128	3	0	44	00:06:42
PRESS editing sequence	2D	144	1000	90	1.6	160x160	16	16	10	0	1x2	00:07:00
TE-Averaged PRESS	1D	40 - 278	1200	90	1	240x240	1	1	15-20	0	1	00:05:50
T_1 SE	2D	10	400	90	1	240x180	384	224	5	1	27	00:02:20
Multi-flip T_1W FSPGR	3D	1.6	5	3, 5, 10, 20, 40	2	240x190	192	96	4	0	5x16	00:01:41
T_1W FSPGR DCE	3D	1.6	5	20	1	240x190	192	96	4	0	16	00:05:05
T_1W FSPGR post contrast	3D	3.1	8.1	30	1	300x300	256	256	1.3	0	120	00:04:19
T_2* GRE-EPI DSC	2D	30	2000	60	1	220x220	128	128	7	0	21	00:01:40
T_1 SE post contrast	2D	10	400	90	1	240x180	384	224	5	1	27	00:02:20
												00:41:14

5.7 Limitations and Pitfalls

This section details some of problems and limitations that were seen during this study.

5.7.1 The Patient

Ultimately, patient welfare came above all other issues relating to this study. Therefore, standard treatment options were not always optimal to the patient and so they become ineligible for this study. It was the decision of a senior clinician, whether a patient was eligible for the study and if they were fit to give consent.

The severity of having a brain tumour and the acute nature of them often means patients are admitted to hospital following a seizure and proceed to surgery following a CT scan within a matter of hours. This made recruiting patients a difficult task due to time scales involved in treating a patient. This also made reserving a slot on the MR scanner difficult due to recruitment process associated with this cohort, and the high demand for MR imaging throughout most oncological cohorts.

Patients admitted with brain tumours often have serious symptoms due to the mass effect of a tumour which can lead to the loss of a range of functions including mobility, memory and speech. In order to image these patients, a compromise about imaging time and patient compliance has to be reached. Currently two of the biggest limitations of MR imaging are the acquisition time, and the rate at which imaging quality degrades due to patient motion, whether this is due to respiratory motion or the patient moving during the acquisition.

Overall this lead to a portion of patients being excluded because they could not comply with the study criteria.

5.7.2 Data Acquisition

The signal to noise ratio (SNR) fundamentally governs magnetic resonance imaging and spectroscopy. Users of magnetic resonance must therefore decide a trade-off between acquisition time, data quality, coverage and resolution. Some techniques such as spectroscopy are particularly dependant on SNR, due to the metabolites of interest producing signals approximately 10,000 times small than that of water. The field strength of a magnet is the main factor that governs the SNR of all sequences and in this study a 3.0T scanner was used. This was the highest field strength available in the region and also the upper limit for clinical imaging. Compared to 7.0T systems or higher, this could be seen as a limitation but these scanners are still heavily under development, with vendors still working to solve B_1 issues. 3.0T also has several advantages compared to higher field strengths such as the volume of literature in existence, reduced chemical shift artefact and less problems with SAR. Gradient performance also has the potential to limit the temporal resolution of dynamic data as well as the acquisition times of most echo-planar sequences, however compared to field strength, this is a minor limitation.

5.7.3 Computational Limits

Without having access to a computer cluster at the MRI centre, computation time was a limiting factor when considering registration/modelling pipelines for the post processing steps applied to the data. Therefore all post processing had to be achievable on a high end workstation (Intel i7 - 3.2GHz, 4 cores, 8 logical cores, 12GB RAM).

5.7.4 Screening Failures

Over the course of this study, several patients were recruited and subsequently excluded following screening failures. Two of the more likely differential diagnoses for glioblastoma multiforme are brain metastasis and cerebral abscess.

5.7.4.1 Cerebral Abscess

The first case (Figure 81) shows a typical presentation for a high grade tumour, with an enhancing walled lesion surrounded by oedema. Only following diffusion and/or spectroscopy (Figure 82) could the diagnosis of abscess be made from imaging, with the lesion containing a restricted centre which is representative of proteinaceous fluid caused by an infection and the presence of acetate at 1.92ppm in the spectrum. Subsequently the prognosis and treatment for the patient differs for that of a glioma patient.

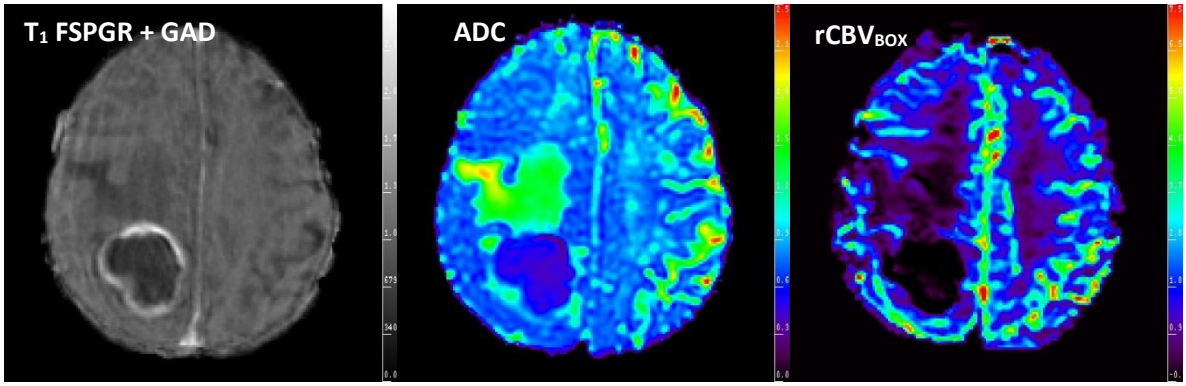

Figure 81 - Example of a cerebral abscess. On post-contrast imaging (left), the lesion was suggestive of an aggressive tumour, however the ADC map scaled 0 to 2.5x10^{-3}mm^{2}s^{-1} (centre) showed restricted diffusion in the centre of the lesion and no increased perfusion scaled 0-7.5 (right) as commonly seen in abscesses.

Given the case was a histologically proven abscess; it provides the opportunity to examine the effect of oedema on healthy brain tissue without the concern of tumour infiltration. In Figure 83, it can be clearly seen that the oedema causes a decrease in the fractional anisotropy giving an artificial impression that the fibres have been destroyed or infiltrated. This is because the oedema is appearing to influence the directionality of the diffusion caused by tissue swelling, providing more of an isotropic weighting to each voxel. By excluding the effect of isotropic diffusion and only

examining q (the anisotropic component of diffusion), it can be seen that the fibre tracts are in fact still present.

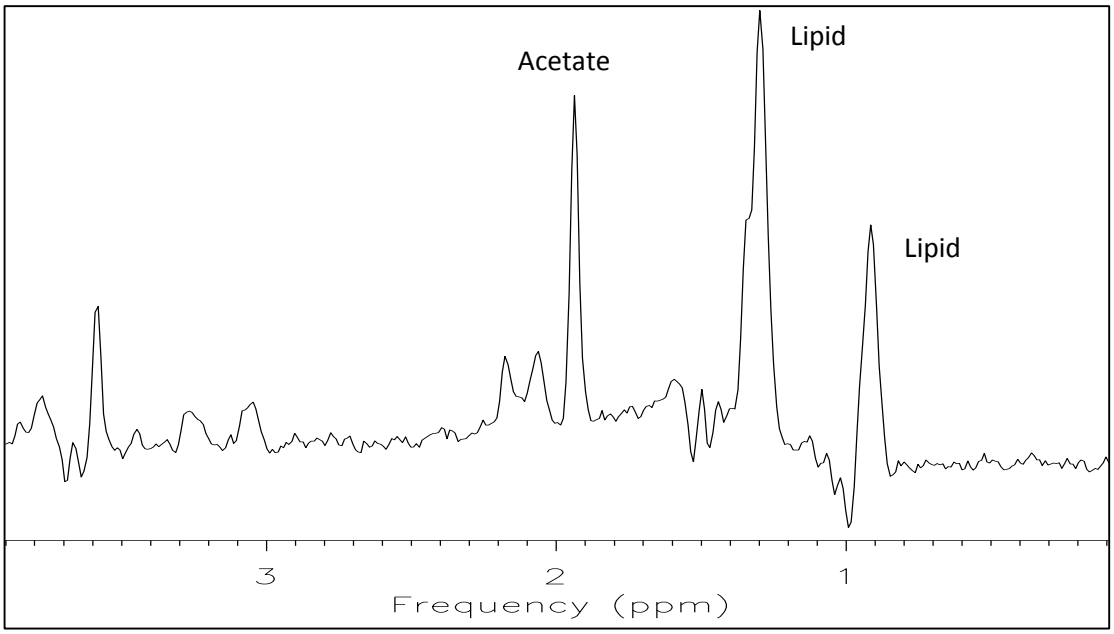

Figure 82 - TE-averaged PRESS spectrum from an abscess shows a range of metabolites not commonly seen in the brain such as acetate (1.92ppm) not to be confused with NAA (2.02ppm), and alanine (1.46ppm).

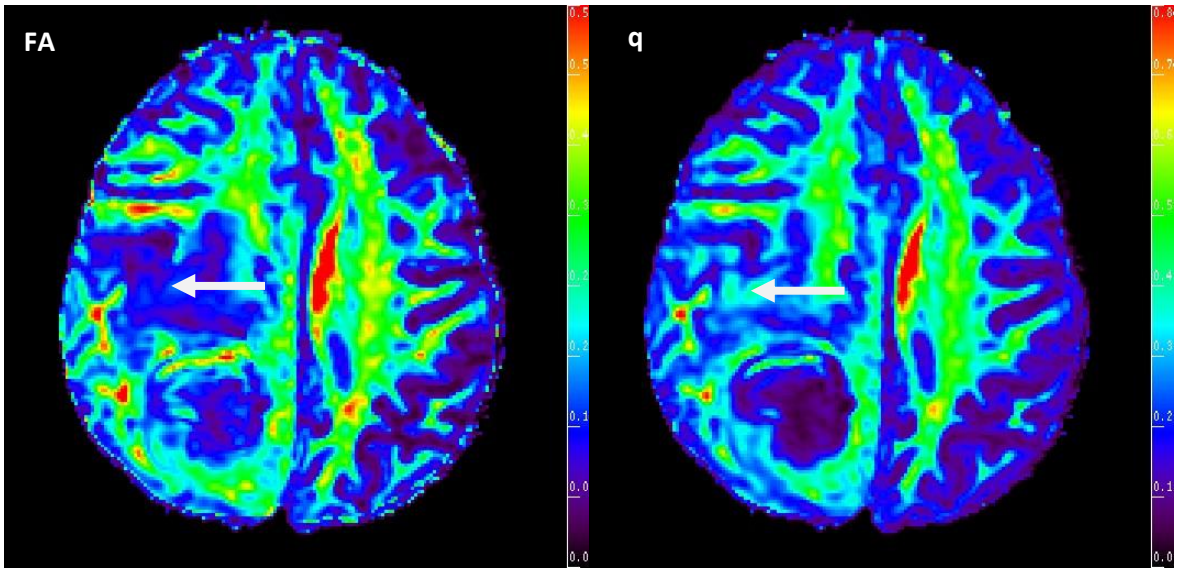

Figure 83 - Diffusion tensor imaging maps for FA 0-0.6 (left) and q 0-0.85 (right). It is worth noting than on the FA map, the white fibre tracts have a decreased fractional anisotropy where the oedema was present, however on the q map (anisotropic component of diffusion) the white fibre tracts appear largely intact and predominantly displaced. This example helps demonstrate that oedema has an effect on FA maps, even when there is no tumour, whilst on q maps oedema has a reduced effect.

5.7.4.2 Brain Metastasis

This is one of the most difficult differential diagnoses to consider when examining a potential glioblastoma multiforme. Over the course of this study, four patients with brain metastasis were included believing the lesion was a primary glial tumour following a normal staging CT scan. In all cases the tumour was a solitary lesion which made the differential even harder. An example brain metastasis can be seen in Figure 84.

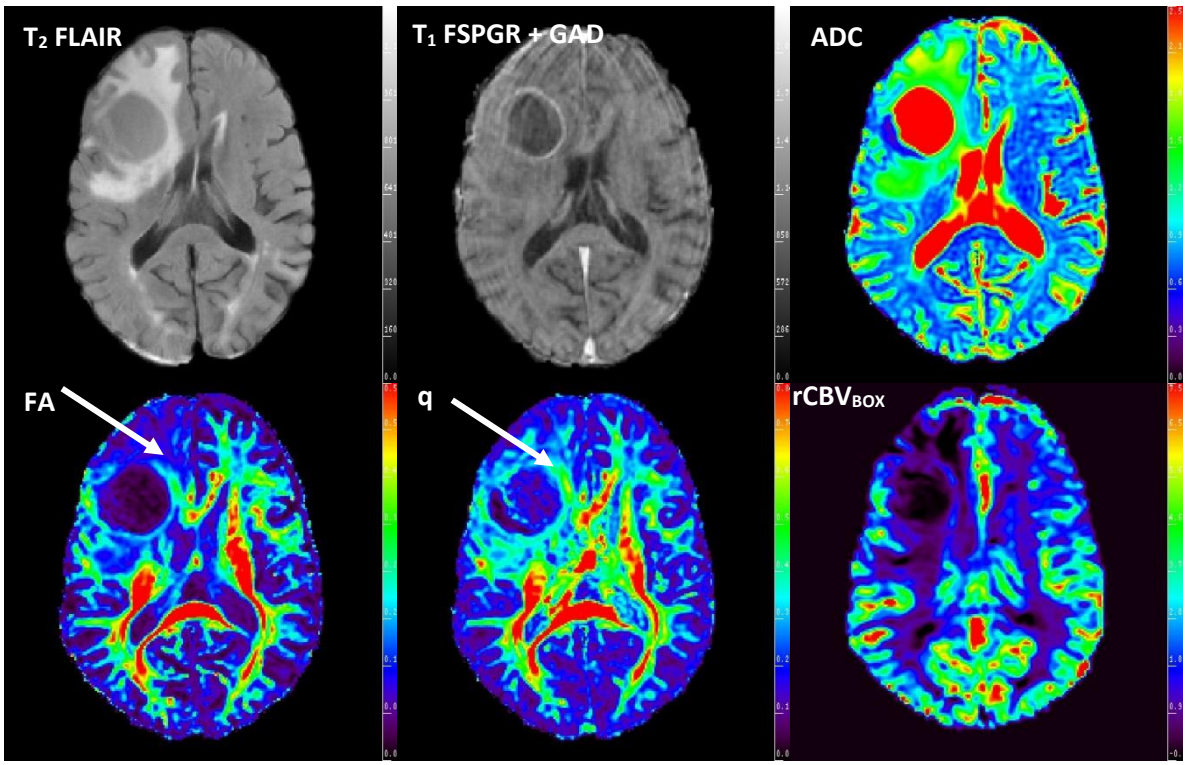

Figure 84 – From top right to bottom left, T_2 FLAIR, T_1 post-contrast, ADC 0-2.5x10^{-3}mm^{2}s^{-1}, FA 0-0.6, q 0-0.85 and Boxerman rCBV 0-7.5, of a representative slice from a lung metastasis patient. Note the enhancing rim lesion with necrotic core presenting in a similar manner to glioblastoma multiforme. The oedema gives the impression of possible tumour invasion based on the FA map which appears less likely on the q map suggesting oedema is lowering the FA not infiltrating tumour, which agrees with how metastases grow (expanding rather than invading). Metastases are also thought to have lower overall perfusion as seen on the DSC CBV map.

6 Image Processing, Sampling and Registration

MR studies of the brain are increasingly producing more images to examine. This, coupled with the increasing frequency of scans for patients on trials, and the aggressive nature of gliomas means assessing treatment response due to subtle differences and changing image obliquities can prove challenging. This chapter demonstrates a method for potentially observing subtle changes and sampling multiparametric data in glioma patients. This section describes the processing methods used in this thesis and explains the decisions made regarding different methods.

6.1 Image File Formats - Neuroimaging Informatics Technology Initiative & FSL

With the availability of increased computational power, retrospective motion correction was applied to all 'functional' datasets in the study. This decision was made in an attempt to optimise the data where possible given the additional processing time available outside of the clinical environment. The datasets suitable for this were the DTI, DCE and DSC 4D volumes. Functional MRI of the Brain Software Library (FSL)(177) was chosen as the tool for motion correction and registration given its well established reputation and citations in key papers from the literature review making use of its registration capabilities for similar tasks (136, 162).

FSL is a software package freely available to MR researchers and specialises in brain registration and segmentation. In order to present the data however, DICOM (Digital Imaging and Communications in Medicine) images needed to be first converted to the NIfTI (Neuroimaging Informatics Technology Initiative) format. Rather than each image having a combined data header file as is the case with DICOM, NIfTI generates one volume of data containing the entire image stack from the sequence and a single header file for the entire volume. From this section, all imaging data was stored and processed using the NIfTI format.

6.2 Diffusion Tensor Imaging

The diffusion tensor imaging (DTI) was one of the longer sequences (6 minutes 42 seconds) used in this study and so benefited from retrospective motion correction (Figure 85) & (Row 1 - Table 7, page 172). FSL contains a script called *Eddy Current Correct* which applies a linear registration (FLIRT)(178) with 12 degrees of freedom (dof). These additional degrees of freedom help to account for the geometric distortions that echo planar imaging generates. Importantly, *Eddy Current Correct* uses the *b*=0mm^2/sec image as the target for registration since it has the highest SNR. Due to the way in which diffusion imaging works; images with no diffusion weighting will always have the highest signal.

Following the *Eddy Current Correct* script, the diffusion data were pre-processed using FSL's brain extraction tool (BET). Skull removal from the volume was beneficial in two ways. Firstly, the number of pixels to process was reduced, speeding up the processing time; and secondly, the brain extraction would help with subsequent registration of the diffusion data to morphological imaging later in the processing.

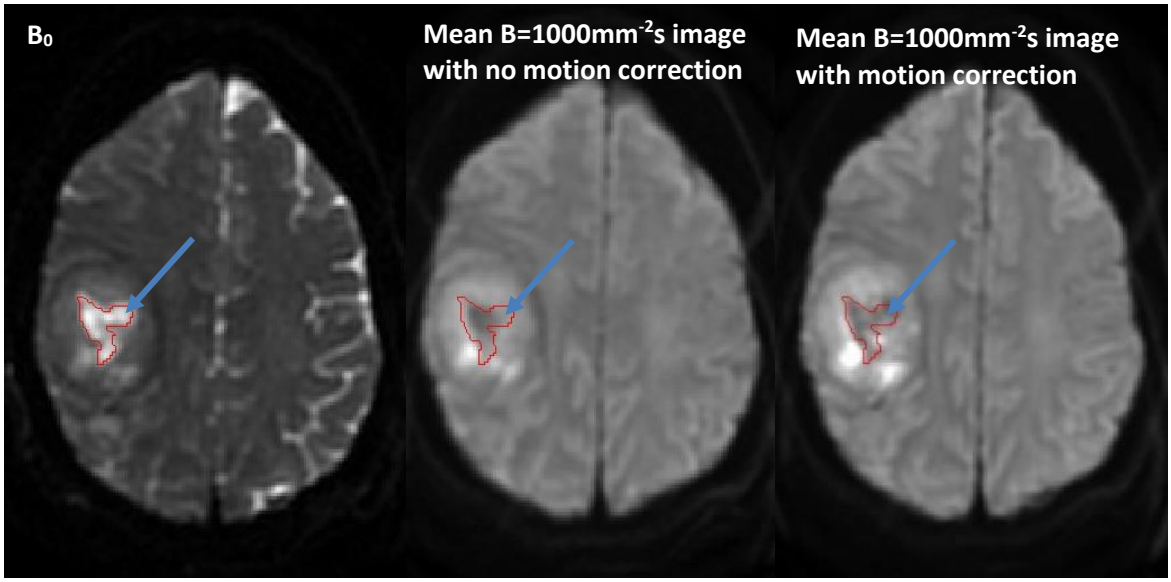

Figure 85 - (Left) Registration target (B_0 image). (Centre) Mean of the diffusion weighted images following patient motion. (Right) Mean of the registered diffusion weighted images. Note that the contrast in the frontal grey matter appear higher and the hyperintense regions in the lesion appear brighter as the signal has been correctly alligned. The blue arrow points to a region where the structure of the tumour appears to be closer to the B_0 image following registration.

The diffusion tensor was calculated from the *b*=0sec/mm^2 image and the 32 directionally different internally registered *b*=1000sec/mm^2 images using in-house software (*DIVA*, Lowry). The tensor of these producing 3 eigenvalues ($\lambda_1 > \lambda_2 > \lambda_3$) which were then used for multi-slice 2D calculations (179, 180) of:

Apparent Diffusion Coefficient (**ADC**) [x10^{-3}mm^2/sec]

$$ADC = \frac{\lambda_1+\lambda_2+\lambda_3}{3} \quad \text{Equation 31}$$

Fractional Anisotropy (**FA**) [A.U.]

$$FA = \sqrt{\frac{3}{2}}\sqrt{\frac{(\lambda_1-ADC)^2+(\lambda_2-ADC)^2+(\lambda_3-ADC)^2}{\lambda_1{}^2+\lambda_2{}^2+\lambda_3{}^2}} \quad \text{Equation 32}$$

Isotropic Component of Diffusion (**p**) [x10^{-3}mm^2/sec]

$$p = \frac{\lambda_1+\lambda_2+\lambda_3}{\sqrt{3}} \quad \text{Equation 33}$$

Anisotropic Component of Diffusion (**q**) [x10^{-3}mm^2/sec]

$$q = \sqrt{(\lambda_1-ADC)^2 + (\lambda_2-ADC)^2 + (\lambda_3-ADC)^2} \quad \text{Equation 34}$$

Relative Anisotropy (**RA**) [A.U.]

$$RA = \frac{q}{p} \quad \text{Equation 35}$$

Longitudinal Diffusion ($\boldsymbol{\lambda_L}$) [x10^{-3}mm^2/sec]

$$\lambda_L = \lambda_1 \quad \text{Equation 36}$$

Radial Diffusion ($\boldsymbol{\lambda_R}$) [x10^{-3}mm^2/sec]

$$\lambda_R = (\lambda_2+\lambda_3)/2 \quad \text{Equation 37}$$

These parameter maps were then combined into a single 4D volume which could be interogated using a NIfTI viewer.

Example DTI parameter calculated maps using the diffusion formulas previously described are displayed in Figure 86.

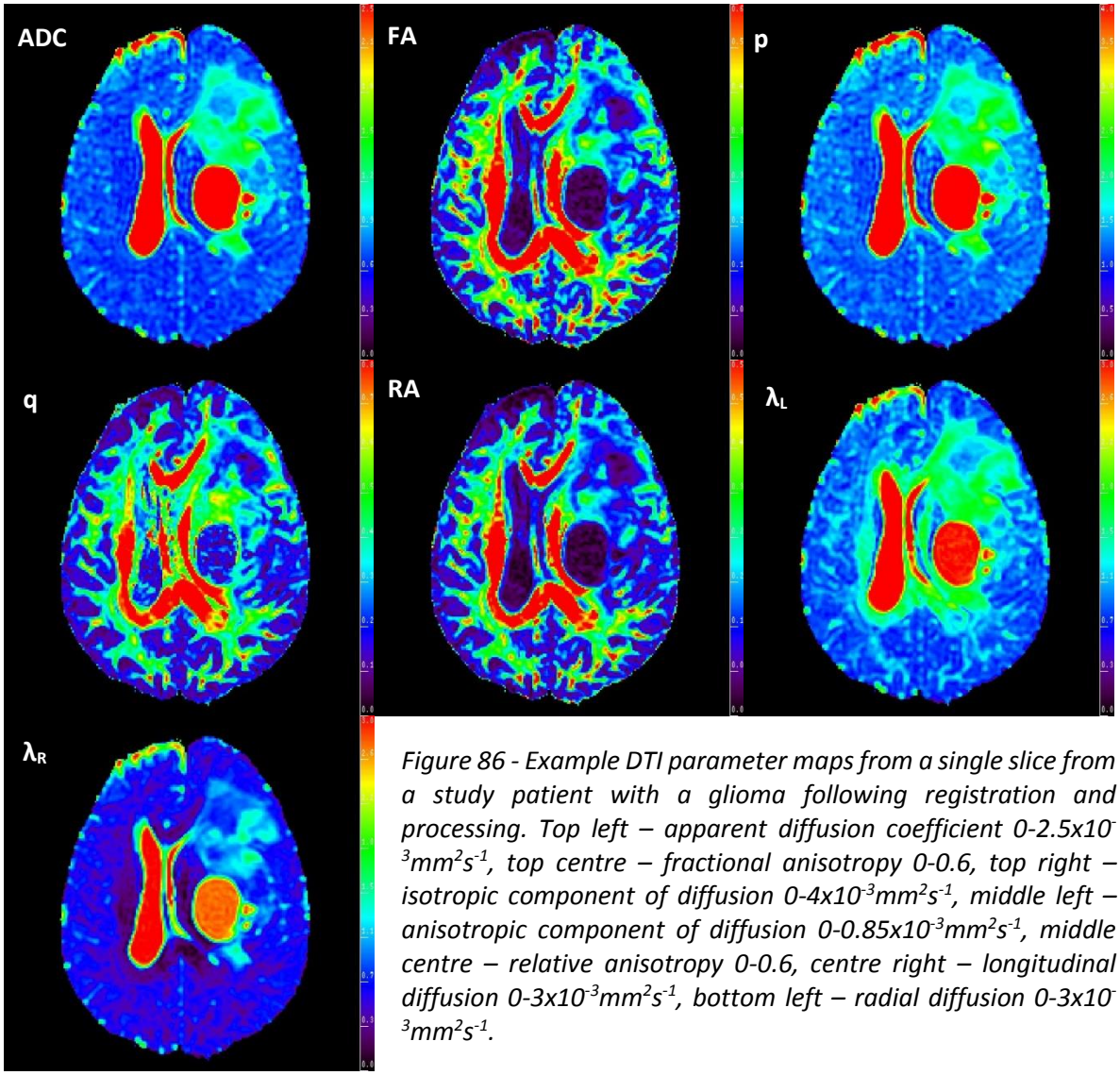

Figure 86 - Example DTI parameter maps from a single slice from a study patient with a glioma following registration and processing. Top left – apparent diffusion coefficient 0-2.5x10^{-3}mm^{2}s^{-1}, top centre – fractional anisotropy 0-0.6, top right – isotropic component of diffusion 0-4x10^{-3}mm^{2}s^{-1}, middle left – anisotropic component of diffusion 0-0.85x10^{-3}mm^{2}s^{-1}, middle centre – relative anisotropy 0-0.6, centre right – longitudinal diffusion 0-3x10^{-3}mm^{2}s^{-1}, bottom left – radial diffusion 0-3x10^{-3}mm^{2}s^{-1}.

6.3 Dynamic Contrast Enhancement Imaging

6.3.1 R_1 Mapping

In order to correctly estimate the amount of gadolinium in each voxel, R_1 mapping was completed, allowing for absolute quantification when using pharmacokinetic (PK) modelling of tissue compartments. Images were acquired with 5 different flip angles; 3°,5°,10°,20° and 40°. Retrospective motion correction was applied to the multi-flip angle data for optimal R_1 calculation; with the 10° flip angle volume chosen as the registration target given the high SNR and good tissue contrast required to aid the registration process. Rigid registration (FLIRT) using FSL was used with 6 degrees of freedom given the volumes were already spatially close together, and contained minimal geometric distortion.

The FSL brain extraction tool (BET) was applied to the 3° flip angle images based the well-defined margins between the brain and skull. A mask of the brain was created simultaneously, that was then applied to the remaining multi-flip angle volumes following spatial registration (Figure 87).

Using in-house software (*DIVA*, Lowry), maximum intensity projection (MIP), proton density (PD) R_1 and T_1 maps were generated as a 4D dataset (X, Y, Z, and parameter).

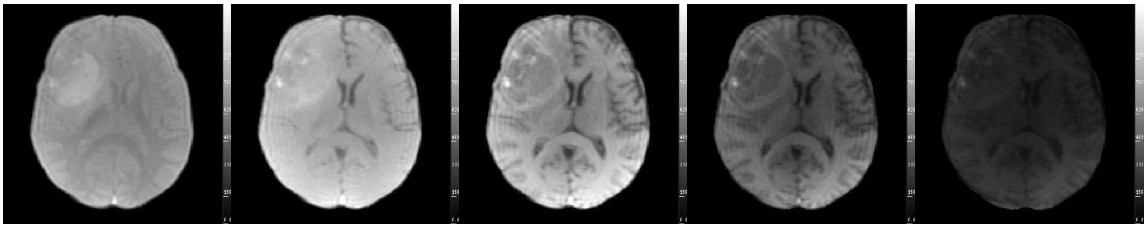

Figure 87- Example T_1 FSPGR slices through a glioma with varying flip angle all windowed to the same level (0-1250 A.U.). From left to right - 3, 5, 10, 20 and 40 degree flip angles.

The signal (S) measured from FSPGR images can be described by the expression

$$\frac{S}{S_0} = \frac{(1-exp^{-TR \cdot R_1})sin(\alpha)}{1-cos(\alpha)(exp^{-TR \cdot R_1})} \quad \text{Equation 38}$$

where S_0 is a constant; and α is the changing flip angle. The effect of flip angle (α) can be seen in Figure 88.

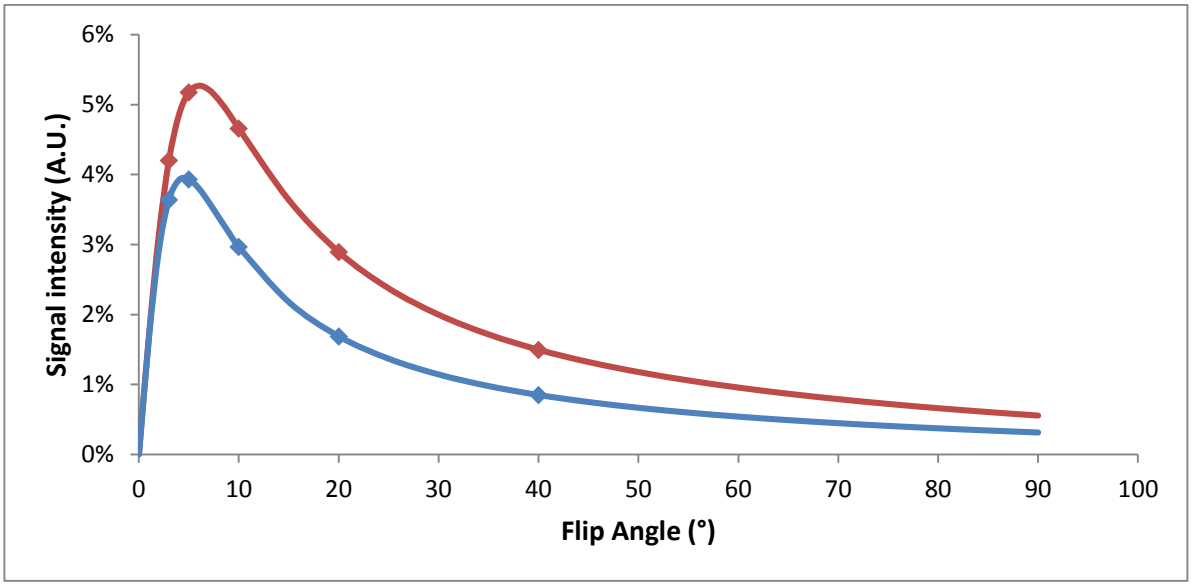

Figure 88 - Theoretical signal intensity curves for both white matter (T1=900ms) (red) and grey matter (T1=1600ms) (blue). For this simulation TR was set to 5 milliseconds, the same value as the data acquired in this study. The points along the two curves show where the flip angles chosen for this study fit.

T_1 maps were generated from the measured R_1 values from each curve produced from the multi-flip angle data using:

$$T_1 = \frac{1}{R_1} \quad \text{Equation 39}$$

Filtering of non-physiological T_1 values (<500ms or >4000ms) was applied to the R_1 maps then masked back onto the remaining volumes. This ensured that artefactual values were removed and not included for any further registration processes. Sample maps can be seen in Figure 89.

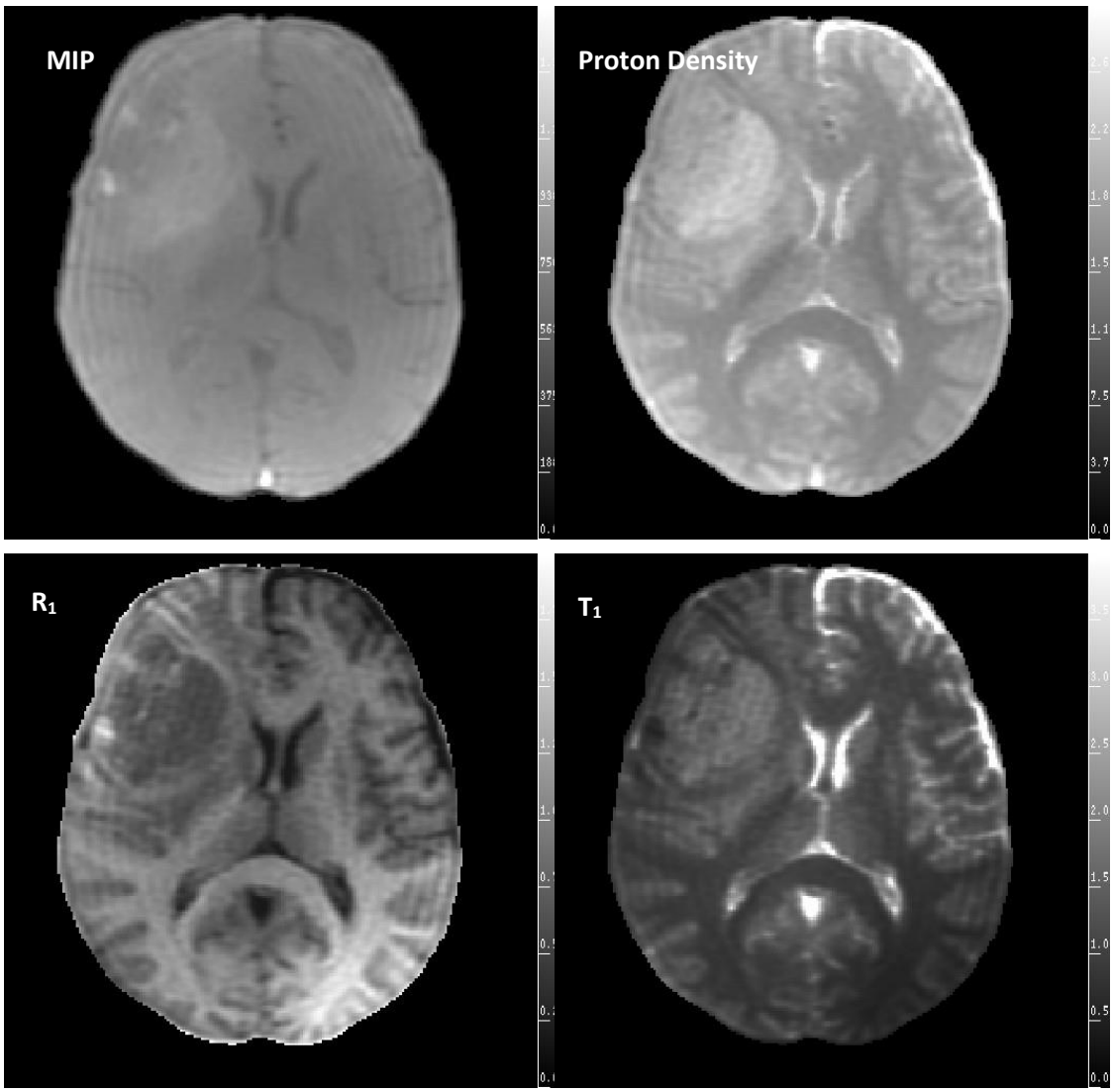

Figure 89 - Example maps from processed multi-flip imaging. From top left to bottom right: MIP, proton density, R_1 (0-2s^{-1}) and absolute T_1 value (0-4s).

6.3.2 Dynamic T_1 FSPGR

All phases of the T_1 dynamic were registered to the 10° multi-flip angle volume previously acquired (Figure 90). This subsequently allowed the same brain mask that was previously generated for the multi-flip angle data to be applied to the volume, removing the skull for all phases.

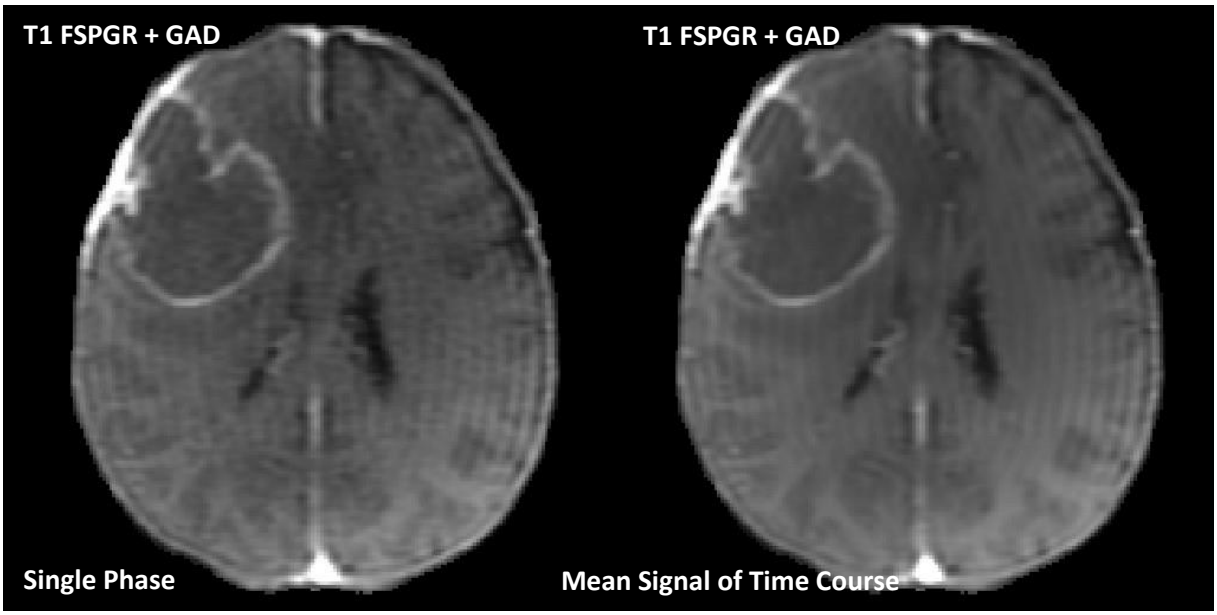

Figure 90 - Example slices through a glioma from T_1 weighted dynamic FSPGR data following contrast injection. Left shows an example post contrast phase while the right image shows the mean of the entire dynamic phase following registration. Visual inspection suggests there is no apparent motion over the time course following registration.

Pharmacokinetic (PK) modelling using a two compartment Tofts-Kety model (56) and a population AIF (181) was applied to the time course signal curves, of the T_1 dynamic contrast enhanced data. The difference in signal due to changing tissue T_1 values can be described by:

$$\Delta R_1(t) = R_1(t) - R_{1\,baseline} = r_1 \cdot C(t) \qquad \text{Equation 40}$$

Where $\mathbf{R_1}$ is the tissue relaxation rate $\left(\frac{1}{T_1}\right)$, $\mathbf{r_1}$ is the relaxivity of contrast agent and **C** is the concentration of the contrast agent in the tissue.

The following assumptions were made for the pharmacokinetic model (DIVA, Lowry):

- Relaxivity at 3.0T and 37°C of the contrast agent = 4.01($s^{-1}mM^{-1}$)
- Dose = 0.075(mMol/kg)
- Haematocrit = 0.42(ml cells/ml blood in capillaries)

The concentration of the contrast agent in the tissue C_t can be described using a Tofts-Kety model:

$$C_t = K^{trans} \cdot \left(AIF \otimes e^{-k_{ep} \cdot t}\right) + v_p \cdot AIF \qquad \text{Equation 41}$$

where $k_{ep} = \frac{K^{trans}}{\mathrm{v_e}}$ and $v_b = \frac{v_p}{1-\mathrm{haematocrit}}$.

DIVA uses a function called MPFIT (182) to fit the data with the model.

Whilst this processing scheme worked, the fitting of up to 100,000 voxels took just under 1 hour using a 2.8GHz i7 processor in IDL. To improve the processing time, principal components analysis of the signal-time course curves was performed to reduce the noise in the data, by only reconstructing the curves from the principal components that accounted for 98% of the variance. The noise reduced curves for each voxel were then clustered into a maximum of 160 groups using a k-means algorithm. Subsequently, PK modelling was then performed on the median curve of each clustered time course. This reduced the computation time for the dynamic volume whilst improving the SNR of each curve shape. Each slice of the volume was processed on a different CPU thread to speed up the overall process (up to 8 simultaneous slices / 4-5 seconds per slice).

The following maps were subsequently generated as part of the processed DCE volume using in-house software (DIVA, Lowry):

- Maximum Intensity Projection
- Clustered Proton Density
- Clustered R_1
- Bolus Arrival Time
- Leakage Rate (K^{trans}) (Figure 91)
- Extracellular Volume (v_e) (Figure 91)
- Blood Volume (v_b) (Figure 91)

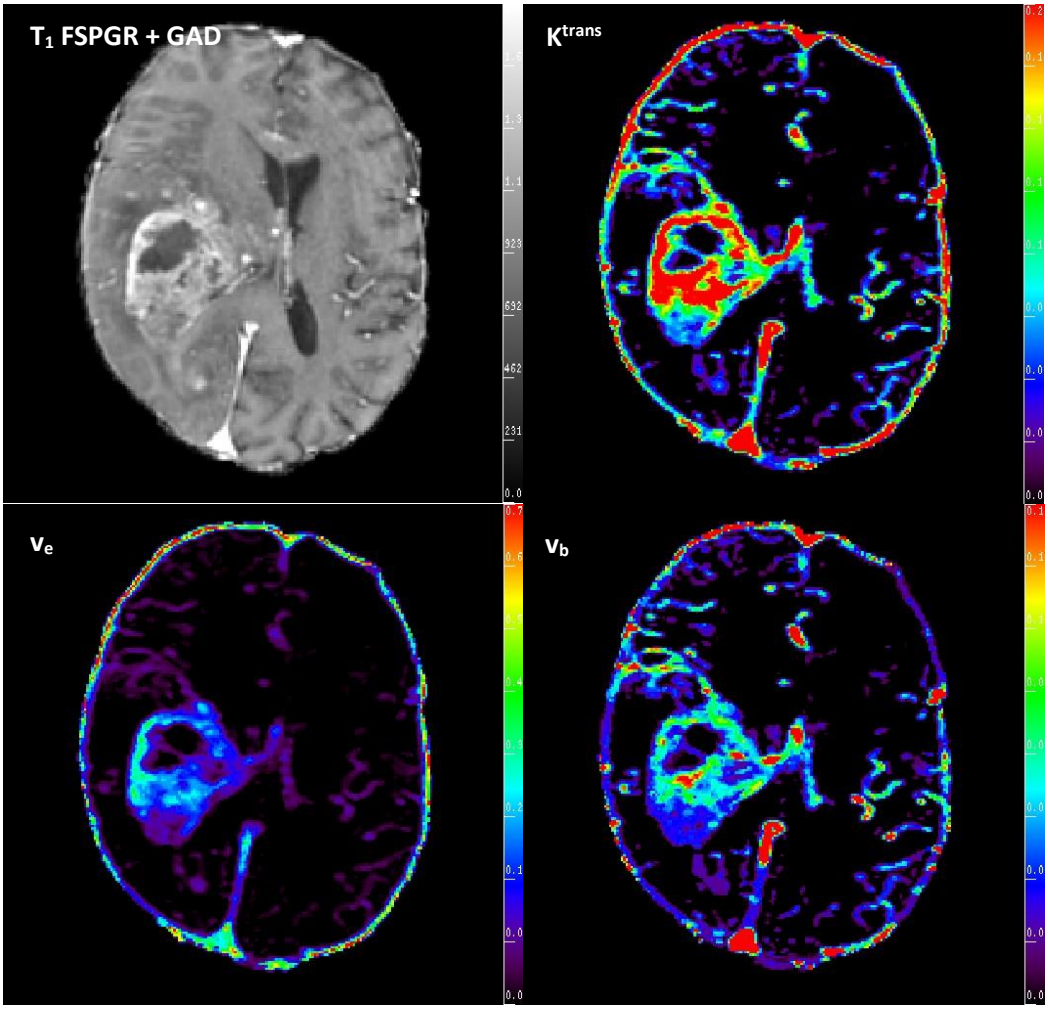

Figure 91 - Sample T_1 FSPGR post-contrast, K^{trans} (0-0.2min^{-1}), v_e (0-0.75) and v_b (0-0.15) maps in a glioma patient spatially registered together.

6.4 Dynamic Susceptibility Contrast Imaging

Given the DSC in this study was a GRE-EPI sequence; the data was initially treated in a similar manner to the diffusion tensor imaging. Datasets were retrospectively motion corrected (Figure 92) using FLIRT with 12 degrees of freedom by registering all the data to the 4th phase image where the image contrast was representative of the entire 4D volume, in preference to the first phase which had not reach saturation. Brain extraction (BET) used the first phase to remove the skull due to the higher SNR caused by the PD weighting.

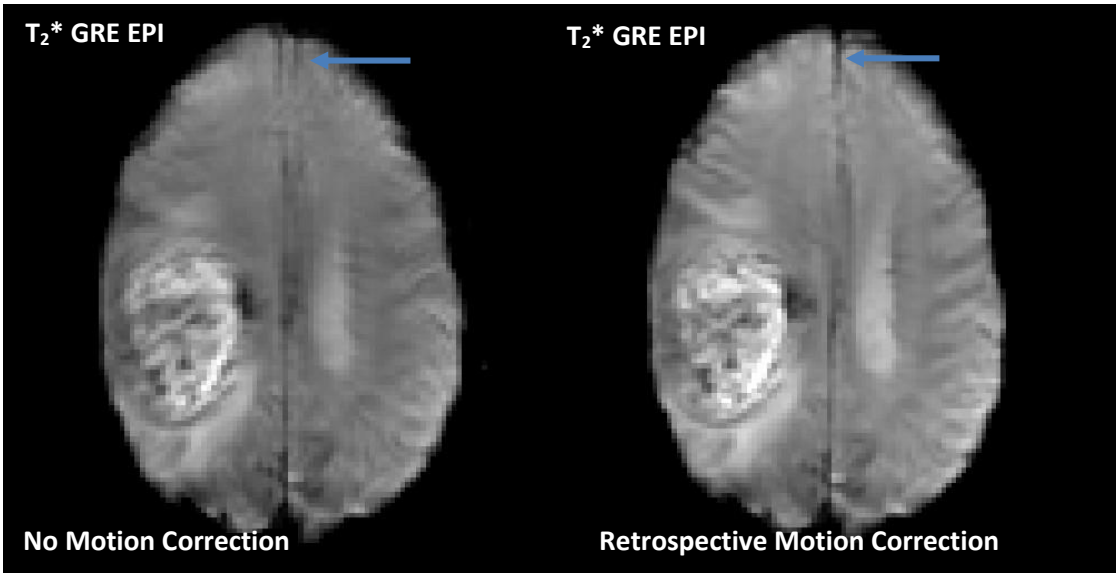

Figure 92 - Mean signal intensity for the time course for a single T_2 DSC slice in a glioma patient with moderate movement (left). Motion corrected mean signal intensity image (right). Note the reduction in tramline artefact along the midline.*

One approach to quantifying DSC is the use of a gamma variate fit of the concentration-time curve. The advantage of using a gamma variate function, is that recirculation effects of the tracer can be excluded from estimation of cerebral blood volume (183). An example gamma variate fit can be seen in Figure 93. It is important to note that this plot shows ΔR2* rather than signal. When the blood-brain barrier (BBB) becomes disrupted (i.e. in pathology) the contrast agent may accumulate in tissue causing the time course to not return to the baseline, and an incorrect estimation of blood volume. In this situation, the Boxerman model (12, 64) which attempts to correct for T_1 and T_2* dominant leakage can be used (Figure 94).

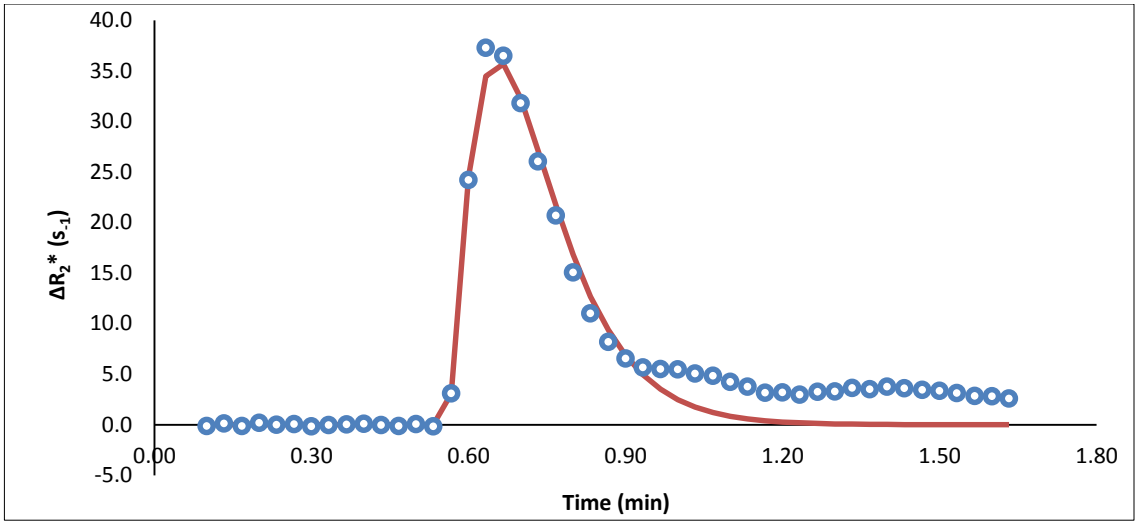

Figure 93 - ΔR_2 time course from DSC data. Raw data points can be seen in blue whilst a gamma variate fit of the data is shown in red. Note how the gamma variate returns to baseline prior to the data which displays signs of recirculation of the contrast agent.*

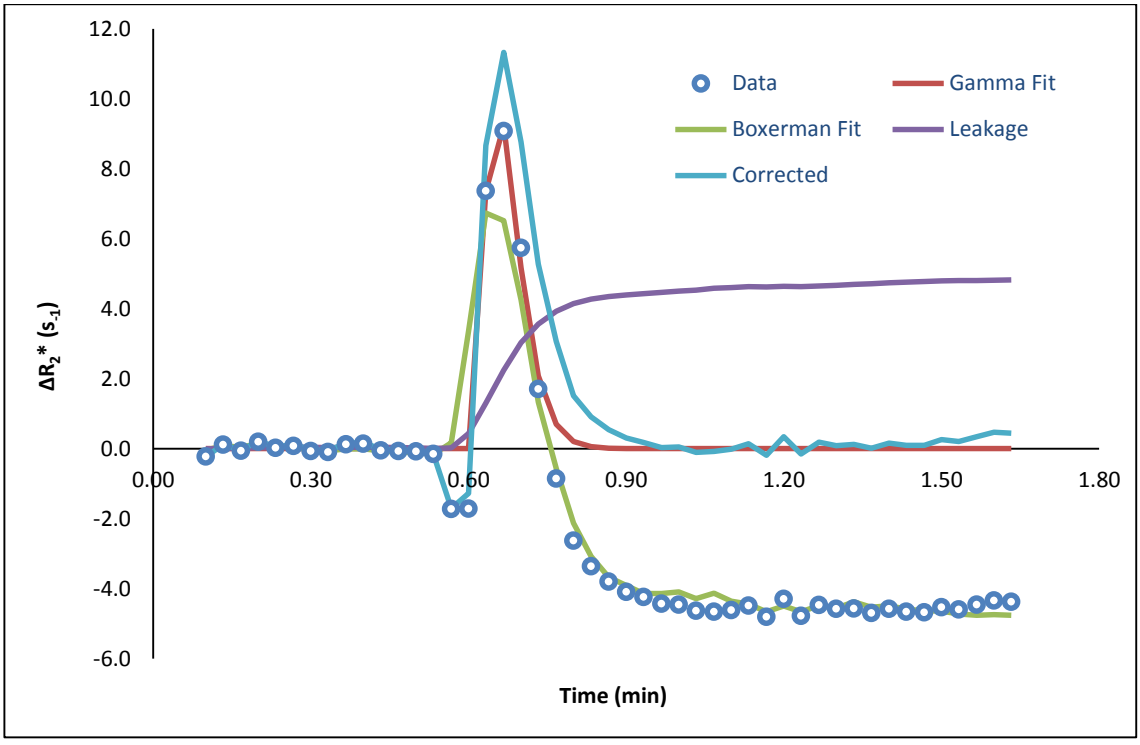

*Figure 94 - ΔR_2*time course from DSC data. Raw data which shows T_1 dominant leakage, can be seen in blue whilst a gamma variate fit of the data is shown in red. The Boxerman model is displayed in green whilst the leakage function (K_2) is shown in purple. The corrected data is displayed as aqua. Note how the corrected data now returns to baseline following the correction of leakage effects.*

The following maps were generated as part of the processed DSC volume using in-house software (DIVA, Lowry).

- Maximum Peak Concentration
- Area under the curve (AUC)
- Gamma variate fit cerebral blood volume (CBV_{GVF}) (183, 184)
- Gamma variate fit mean transit time (CBV_{MTT})
- Gamma variate fit cerebral blood flow (CBF_{GVF})
- Boxerman Model cerebral blood volume (CBV_{BOX}) (12)
- Boxerman value 1 (K_1)
- Boxerman value 2 (K_2)

Boxerman's expression for CBV (12), calculated from a dynamic signal intensity curve is as follows:

$$\Delta R2^*(t) = -\frac{1}{TE} ln \frac{S(t)}{S_0} \quad \text{Equation 42}$$

$$\Delta R2^* = K_1 \overline{\Delta R2^*}(t) - K_2 \int_0^t \overline{\Delta R2^*}(t')dt' \quad \text{Equation 43}$$

$$CBV = \int_0^t \Delta R2^*(t) \quad \text{Equation 44}$$

$$CBV_{corr} = CBV + K_2 \int_0^T dt'' \int_0^{t''} \overline{\Delta R2^*}(t')dt' \quad \text{Equation 45}$$

Where CBV is the uncorrected blood volume, $\overline{\Delta R2^*}$ is the whole brain average of signal change and K_2 is the leakage effect. K_1 is a scaled CBV map. Key images can be seen in Figure 95.

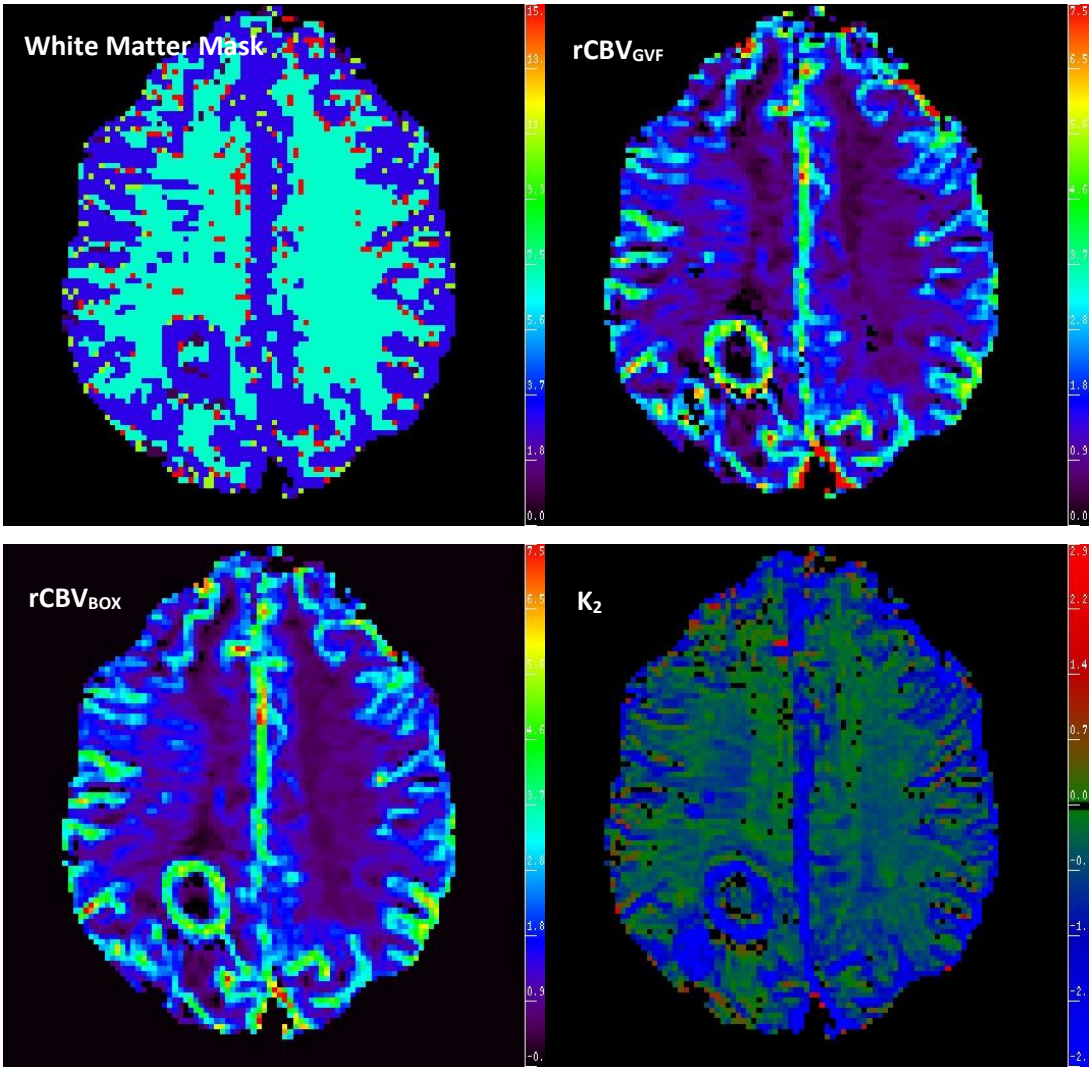

Figure 95 - Key Images from the DSC processing methods. Top left shows the white matter mask used for normalisation. Top right shows the rCBV map using a gamma variate fit (0-7.5). Bottom left shows the rCBV using the Boxerman model (0-7.5) which accounts for leakage. Bottom right shows the leakage map, with blue voxels being T_2 dominant leakage, red being T_1 dominant leakage and the green/black pixels containing voxels where the time course returned back to zero following the bolus injection. Where leakage is high, the gamma variate fit (top right) can fail as seen in the rim of the tumour resulting in a black pixel where no fit was achieved. The apparent leakage in normal appearing parenchyma is possibly a combination of recirculation effects, bolus dispersion and very small vessels.*

Given that absolute quantification of the T_2* dynamics was not possible due the absence of an AIF when using the Boxerman model (12), perfusion volumes were normalised to the global white matter. This was an automated process following the curve fitting routine. All pixels from the Boxerman fitted CBV maps were split into two populations using a Gaussian mixture model (GMM) (185). The assumption being made at this point is that grey matter has a higher cerebral blood volume than white matter. From this, the population with the lowest mean rCBV was then processed again using a GMM. This time, the aim being to separate white matter from partial volume grey/white matter. Mean parameter values from the largest three-dimensionally connected region of white matter was used to normalise the blood volume maps. The same mask for the white matter was then used to normalise all other CBV and CBF maps (Figure 96).

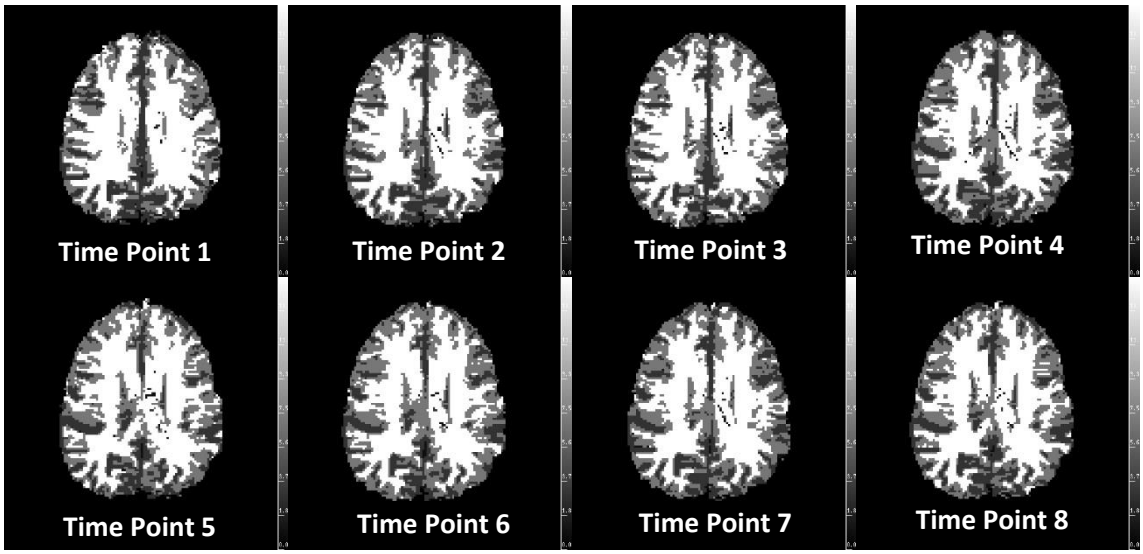

Figure 96 – Unregistered white matter normalisation maps as defined by two sequential Gaussian mixture models, for a single slice in one patient during 8 sequential scans. The white region shows the largest continuous 3D region of white matter to which cerebral blood volume measurements were normalised.

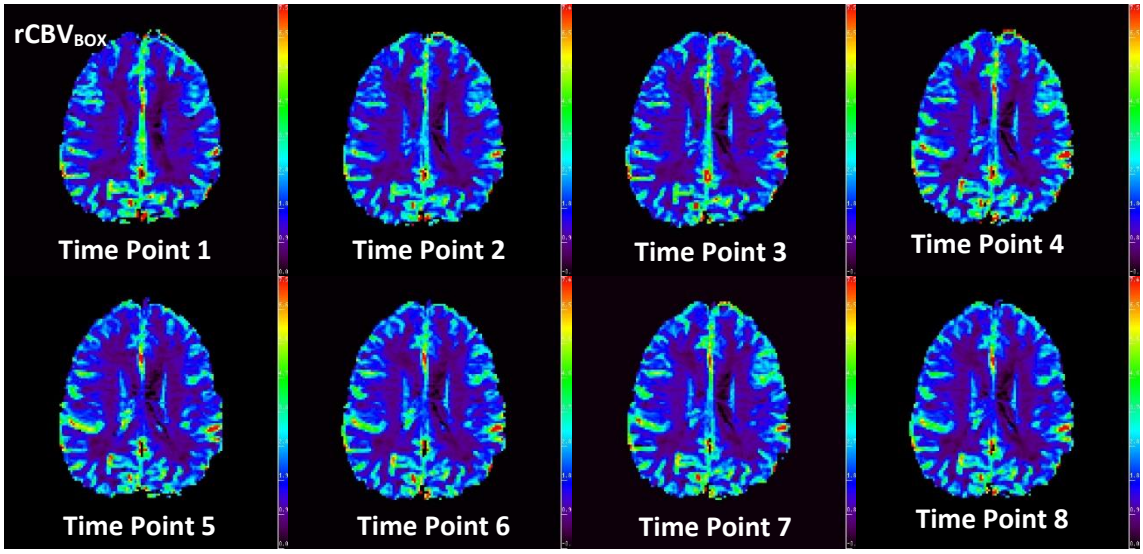

Figure 97 - Leakage corrected relative cerebral blood volume maps in a patient at 8 time points. All maps were windowed to the same level and were registered together via 3D FSPGR images acquired during the same exams. Window levels were identically scaled between 0 and 7.5 [A.U] following white matter normalisation.

As seen in Figure 97, there is strong visual agreement between the relative blood volumes observed in both grey and white matter structures. This method for normalisation is fully automated and can be included at the time of DSC processing. This method accounts for any potential dose changes and attempts to correct for biological variation when looking for subtle changes. The limitation of this method is that it is dependent on whole brain coverage in order to generate the white matter mask.

6.5 MR Spectroscopy

Analysis of the magnetic resonance spectroscopy (MRS) datasets was not included in this thesis, due to the single slice/voxel acquisition not complementing the whole tumour measurement approach used with other sequences. One exception to the exclusion of MR spectroscopy was in the section, Preoperative MR for Tumour Grading, in which single voxel TE-averaged PRESS was processed with LCModel (pg.221).

6.6 A Summary of Parameters

Table 6 has been included to show the parameter maps which have been included in the final 4D volume for further analysis. The T_2 weighted FLAIR was included as it was the only T_2 weighted morphological sequence and was required to draw the volume of interest (VOI) for the entire abnormality. Likewise the T_1 post contrast FSPGR, was included as a morphological sequence was needed in order to delineate the enhancing portion or the tumour.

From the processed diffusion data sets; ADC, FA, q, RA, λ_L and λ_R were chosen to be included in the final 4D volume. P was excluded as it is a $\sqrt{3}$ scaled version of the more commonly recognised ADC map, however it was required for the calculation of RA. The red, green and blue maps (λ_1, λ_2 and λ_3) as seen in Table 6 were produced in order to visualise the directionality of fibre tracts but were not useful for quantification.

The multi-flip angle data produced several maps however R_1 was the only quantifiable parameter map which was used in the quantification of the DCE. Given that PK modelling applied to the DCE only, K^{trans}, v_e and v_b were extracted for the final 4D volume. The remaining images were used for a visual quality assurance of the data.

Initial interrogation of the DSC data focused on the $rCBV_{GVF}$ produced using the gamma variate fit, and $rCBV_{BOX}$ and K_2 which were both produced using the Boxerman model (12). Parameters such as maximum peak concentration and area under curve were also excluded as they were potentially less quantitative. CBF and MTT maps were generated for any future work involving the DSC data.

Table 6 – The parameters produced by each type of raw data. Highlighted cells show the parameters which are to be included in the final 4D dataset for further interrogation.

	T_2 FLAIR	**T_1 FSPGR + Gad**	**DTI**	**Multi-flips**	**DCE**	**DSC**
1	S.I	S.I.	ADC	MIP	Max Enhancement	MASK
2			FA	P.D.	Clustered P.D	Max Peak Conc.
3			p	R_1	Clustered R_1	AUC
4			q	T_1	Bolus Arrival Time	$rCBV_{GVF}$
5			RA	Mask	K^{trans}	MTT_{GVF}
6			λ_L	Blank	v_e	$rCBF_{GVF}$
7			λ_R	Chi SQ.	v_b	$rCBV_{BOX}$
8			R		Cluster Number	K_1
9			G		Status	K_2
10			B		Mask	CHI SQ.
11					Chi SQ.	

6.7 Registration

With internal motion correction already discussed for each type of functional data, and brain extraction happening simultaneously, using the Functional MRI of the Brain Software Library (FSL) Brain Extraction Tool (BET) (186) (Row 2 - Table 7, page 172), parametric registration was the next step.

6.7.1 Parametric Registration

Following the individual parameter processing steps (Row 3 - Table 7), parametric volumes were created by registering the T_2 FLAIR, T_1 post-contrast, ADC, FA, q, RA, λ_L, λ_R, R_1, K^{trans}, v_e, v_b, $rCBV_{GVF}$, $rCBV_{BOX}$, and K_2 into a single 4D volume (X, Y, Z and parameter) (Figure 98). This was achieved by first applying a 6 dof rigid registration (FLIRT) of the T_1 post contrast images to the FA volume (Rows 4/5 - Table 7, page 172), thus producing a T_1 post-contrast volume of the same nominal voxel size as the diffusion acquisition (0.9375mm x 0.9375mm x 3mm). The DTI was chosen as the global voxel size as the slice thickness was close to the median slice thickness of all datasets while ensuring whole brain coverage unlike the DCE. The R_1 volume was registered to the T_1 post-contrast volume with 6 dof since they shared the same tissue contrast characteristics (Row 6 - Table 7, page 172). With the T_1 dynamic volume in the same space as the R_1 mapping volume, the same transformation matrix was applied to the K^{trans}, v_e and v_b volume (Row 7 - Table 7, page 172). The FA volume was then registered using 12 dof and FLIRT to the T_1 post-contrast volume given the similar appearance of white matter. The T_1 post-contrast volume was also the target for the FLAIR images which were thus resampled to the same resolution (Row 6 - Table 7, page 172).

The unregistered ADC volume was registered to the 1st phase of the T_2* dynamics with 12 dof. This was done because of the similar contrasts. Following this, the rCBV maps were registered back to the ADC using the inverse transformation matrix of ADC to 1st phase DSC registration. The FA to T_1

post-contrast volume matrix was then applied to produce rCBV volumes now in the same space as the registered diffusion.

With all volumes now in the same space as the T_1 post-contrast volume, *fslmerge* was used to combine parameter and anatomical imaging into a single combined volume (Row 8 - Table 7, page 172).

The advantages of this method include a degree of data reduction. By registering the different types of maps together, radiologists and researchers can cross examine areas of abnormality with ease using any NIfTI reader. Volumetric regions of interest drawn on a single type of anatomical imaging can also be used to sample all functional parameters simultaneously. Subtle changes are more likely to be identified on images that are co-planar, thus benefiting researchers and patients greatly. Subtraction of paired volumes can be used to create functional parameter maps to assess treatment response.

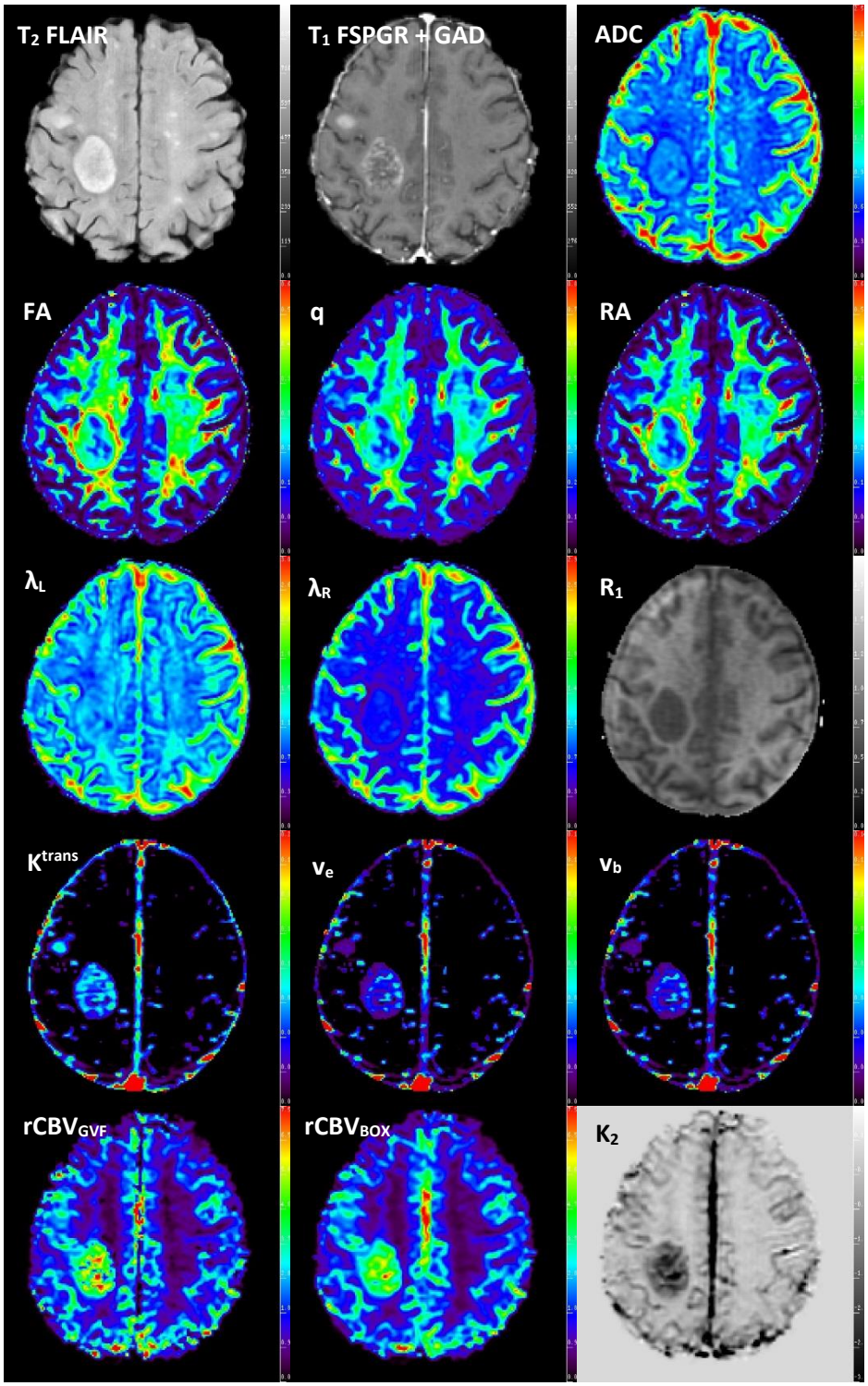

Figure 98 - Example slice from the 4D volume showing all 15 parameters spatially registered ready for temporal registration or sampling. From top left to bottom right: T_2 FLAIR, T_1 post contrast, ADC (0-2.5x10^{-3}mm^{2}s^{-1}), FA (0-0.6), q (0-0.85x10^{-3}mm^{2}s^{-1}), RA (0-0.6), λ_L (0-3x10^{-3}mm^{2}s^{-1}), λ_R (0-3x10^{-3}mm^{2}s^{-1}), R_1 (0-2s^{-1}), K^{trans}(0-0.2min^{-1}), v_e(0-0.75), v_b (0-0.15), $rCBV_{GVF}$(0-7.5), $rCBV_{BOX}$(0-7.5), and K_2(-3.3-0.7).

Table 7 - The steps taken in generating a combined 4D volume of parameters for a single scan. Row 1 shows what type of motion correction (ECC=eddy current correct, MC=motion correct) was applied to the data and the target image/phase (T=?). Row 2 shows which image the brain extraction (BET) was run on. Rows 1 and 2 were completed as a single task using a linux script. Row 3 shows the name of the desired maps and button in DIVA needed to generate them. This step was manually completed. Rows 4-7 were completed as a single linux script with wait points inserted to allow its completion (XFM=transform data to target space). Row 8 was another script which combined the volumes into a single 4D dataset.

	Multi-flips	**DCE**	**DSC**	**DTI**	**T_1 FSPGR + GAD**	**FLAIR**
1	MC (T=10^0) *dyn_correct*	MC (T=10^0)	ECC (T=4)	ECC (T=b0)		
2	BET (T=3^0)	Apply Multi-flip BET Mask	BET (T=1)	BET (T= b0)	BET	BET
3	Process - R1 *Calc. T1 Volume*	Process - PK *Process DCE +PCA*	Process -CBV *Process DSC*	Process - ADC/FA *Process DTI*		
4				Extract T=FA		
5					XFM (T=FA)	
6	XFM (T=T1 Vol.)			XFM (T=T1 Vol.)		XFM (T=T1 Vol.)
7		Apply XFM (T=T1 Vol.)	XFM (T=ADC)			
8	Merge Parameters					

6.7.2 Temporal Registration

Patients who completed three study scans had all subsequent 4D volumes registered together. Time point 2 (pre radiotherapy) was chosen as the registration target as it represented the middle set of imaging in the study and had the lowest amount of tissue remodelling between each set of adjacent scans. Each volume [time point 1 (preoperative) & 3 (post-therapeutic)] was registered to time point 2 using FLIRT with 6 degrees of freedom and a least squares cost function between the corresponding T_1 post-contrast volumes. The transformation matrix was then applied to the entire 4D parametric volume. An example dataset can be seen in Figure 99.

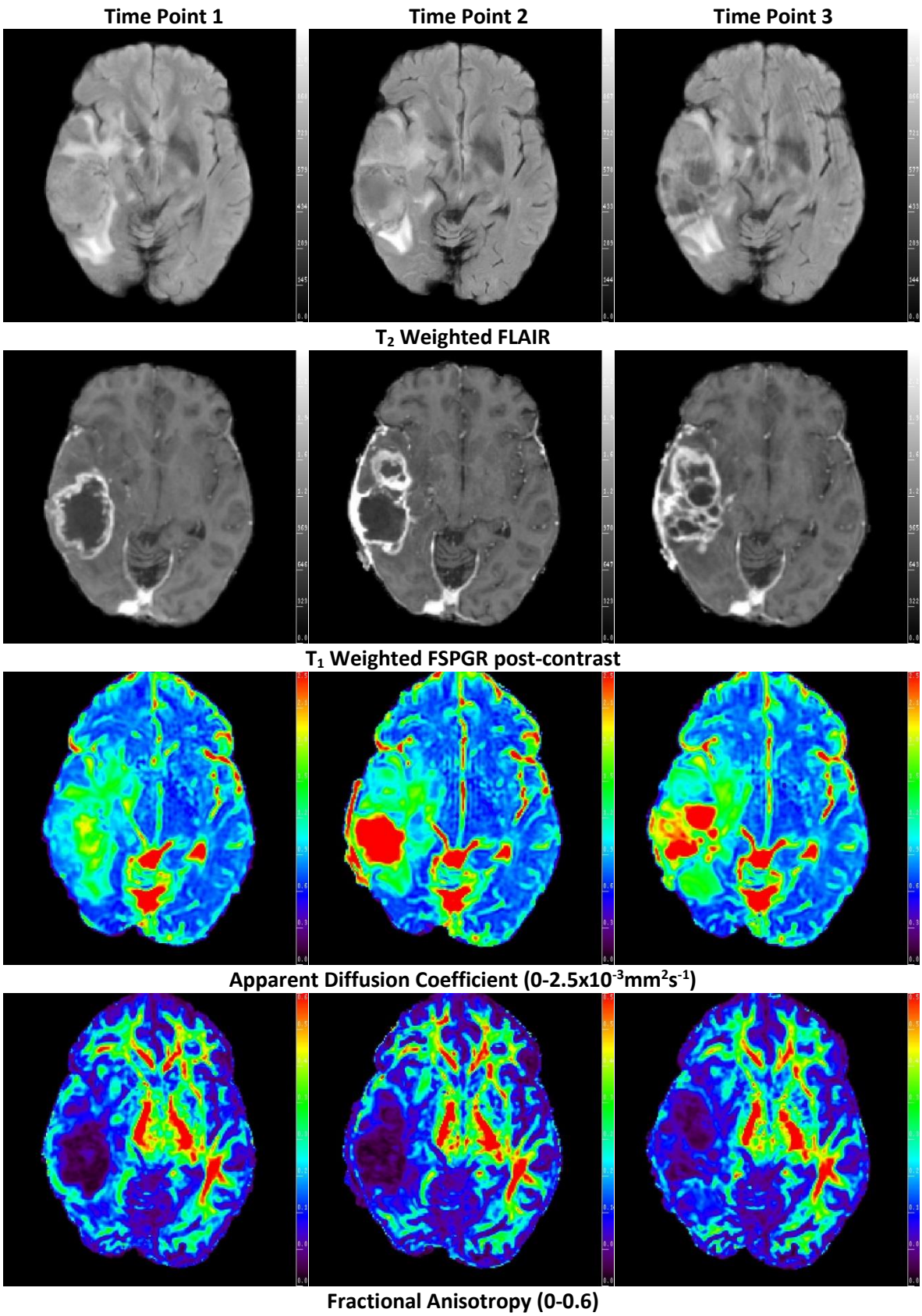
Time Point 1
Time Point 2
Time Point 3
T2 Weighted FLAIR
T1 Weighted FSPGR post-contrast
Apparent Diffusion Coefficient (0-2.5x10-3mm2s-1)
Fractional Anisotropy (0-0.6)

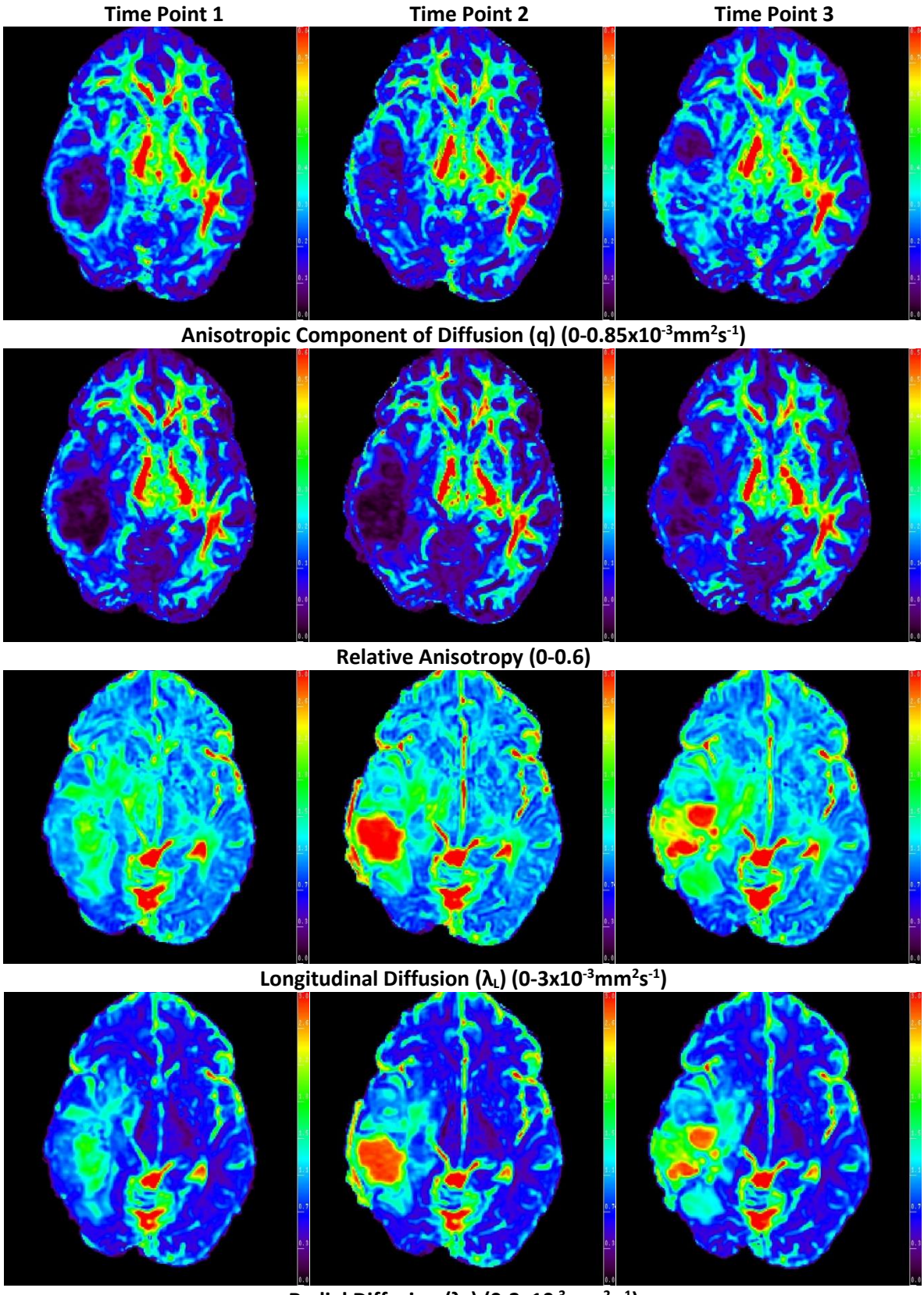
Time Point 1
Time Point 2
Time Point 3
Anisotropic Component of Diffusion (q) (0-0.85x10^{-3}mm^{2}s^{-1})
Relative Anisotropy (0-0.6)
Longitudinal Diffusion (λ_L) (0-3x10^{-3}mm^{2}s^{-1})
Radial Diffusion (λ_R) (0-3x10^{-3}mm^{2}s^{-1})

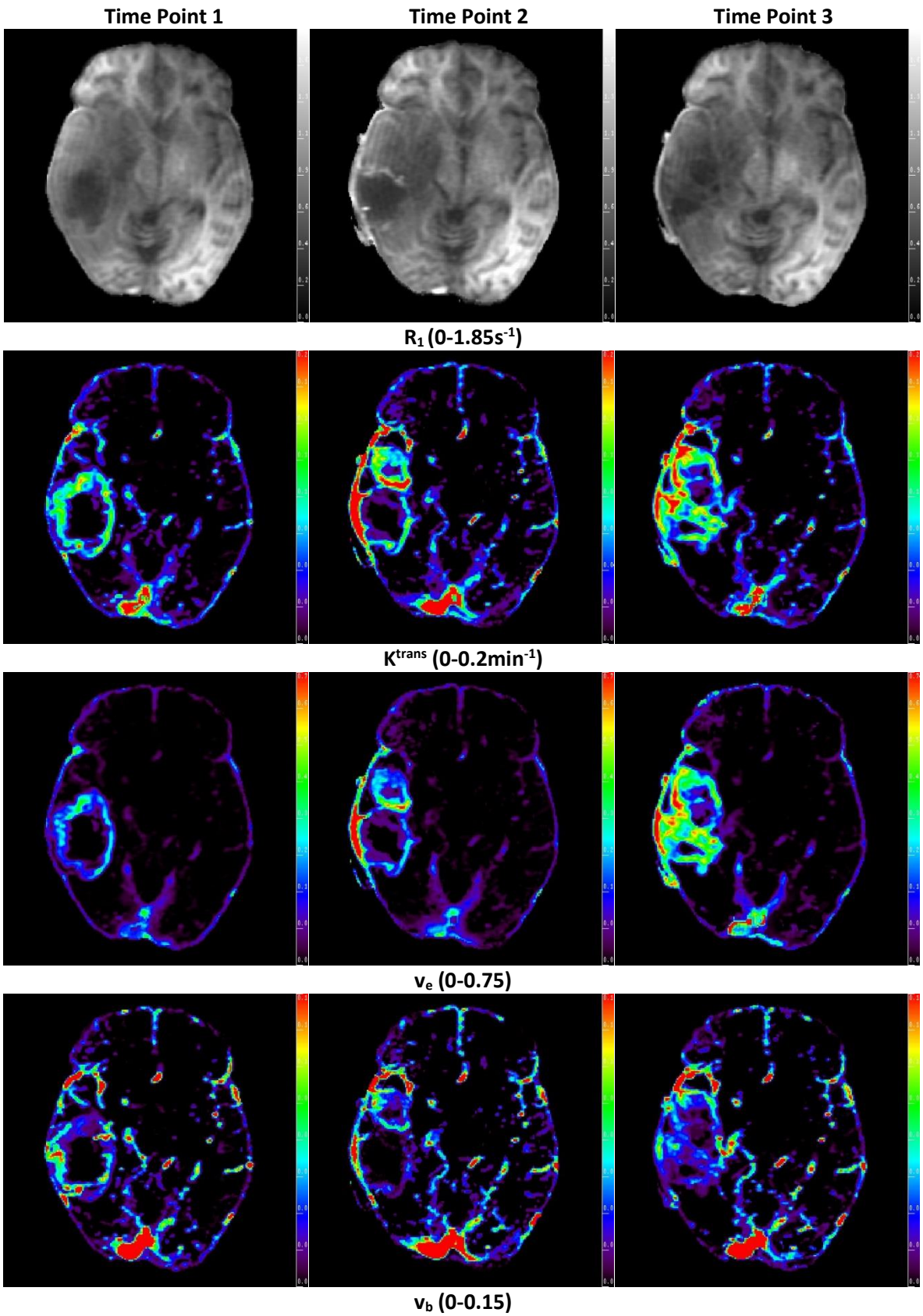
Time Point 1
Time Point 2
Time Point 3
R_1 (0-1.85s^{-1})
K^{trans} (0-0.2min^{-1})
v_e (0-0.75)
v_b (0-0.15)

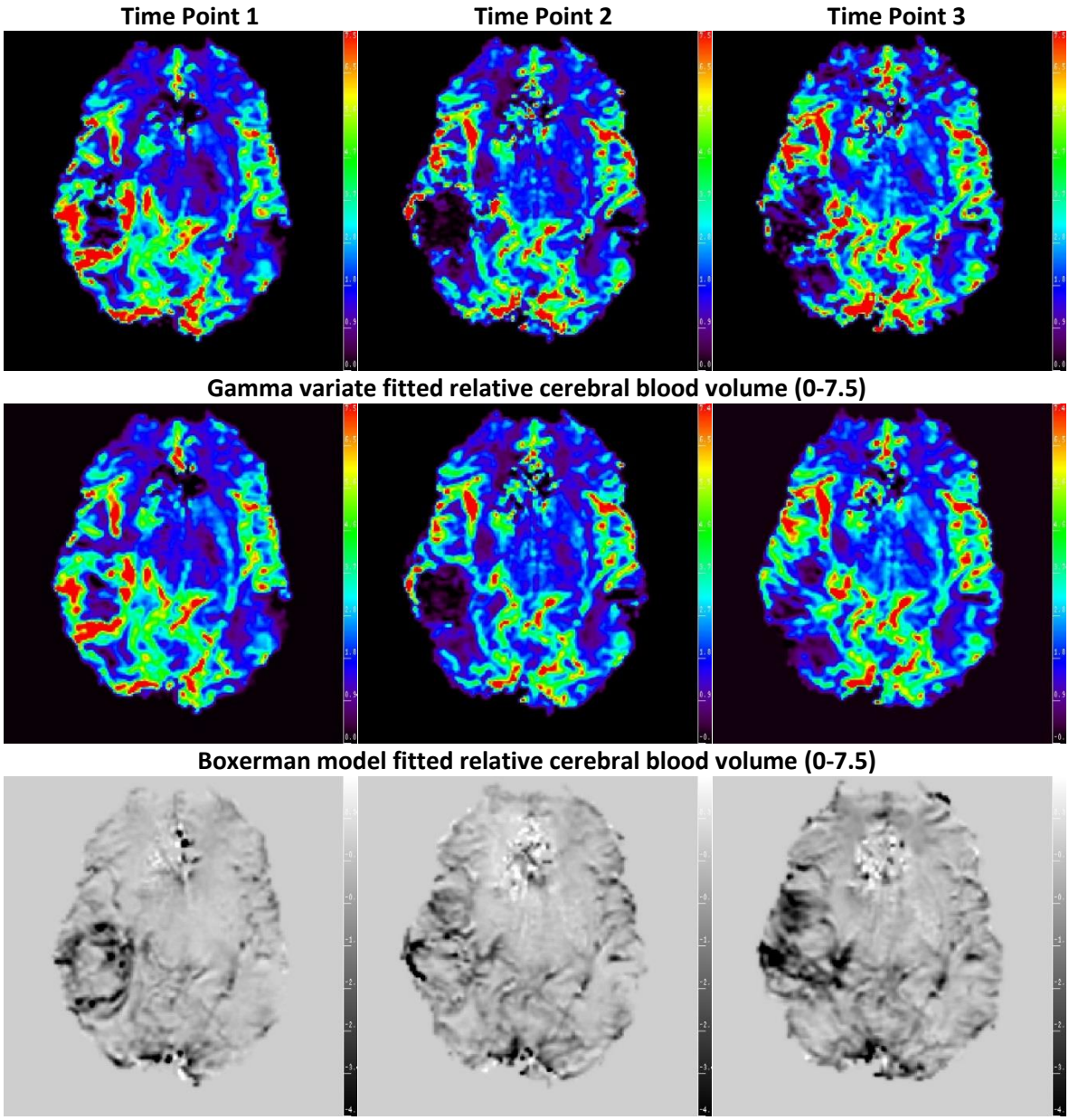

Figure 99 - Example of a complete registered data set with all parametric maps residing in the same space. This figure helps demonstrate not only the within scan registration but also the quality of the temporal registration. When examining the registration it is important to consider tissue remodelling and the effects of both steroids and radiotherapy. Time point 1 represents preoperative imaging. Time point 2 is prior to therapeutic treatment. Time point 3 is during the treatment break following chemoradiotherapy.

6.8 Data Sampling

With parametric maps existing in a single space for each patient, a single set of volumes of interest (VOI) could be drawn based upon morphological imaging to sample the functional data without biasing the selection.

6.8.1 Volumes of Interest

Following the protocoled registration and processing methods as detailed in this chapter, volumes of interest were contoured on all slices which contained evidence of disease on morphological imaging. This process was carried out using in-house software (DIVA, Lowry) using a combination of Otsu (187) and manual contouring tools. Up to 4 volumes of interest were drawn for each dataset (Figure 100). These were:

T_{2all} - which was defined from hyperintense regions as seen on T_2 weighted FLAIR imaging

T_{1all} – The hyperintense region as defined from the post-contrast 3D FSPGR

NEC - cystic and necrotic regions as defined from the T_{1all} hypointense regions from the post-contrast 3D FSPGR. These VOIs were drawn by inverting the image signal producing bright pixels more suited to Otsu techniques.

HMG – hyperintense regions as defined from the pre-contrast R_1 maps which were considered as haemorrhage

From these 4 volumes of interest (T_{2all}, T_{1all}, NEC and HMG), 3 final volumes of interest were generated for sampling the processed 4D volume of each patient (Figure 100).

TUM – This VOI was representative of the entire volume of disease and potentially included both solid and infiltrating tumour as well as oedema. It was defined as TUM = T_{2all} + T_{1all} – NEC – HMG.

NEL – This was the non-enhancing component of the lesion. It was calculated by subtracting the enhancing component from the total tumour VOI TUM as previously defined. NEL= TUM – T_{1all}

CEL – This VOI represented only the enhancing component of the lesion and was calculated using the following VOIs. CEL = T_{1all} – NEC – HMG

Each parameter was sampled with the 3 VOIs (TUM, CEL and NEL). Standard statistical descriptors were then calculated for each VOI, assuming a Gaussian distribution. These descriptors were: mean, standard deviation, skew, kurtosis, median, minimum and maximum.

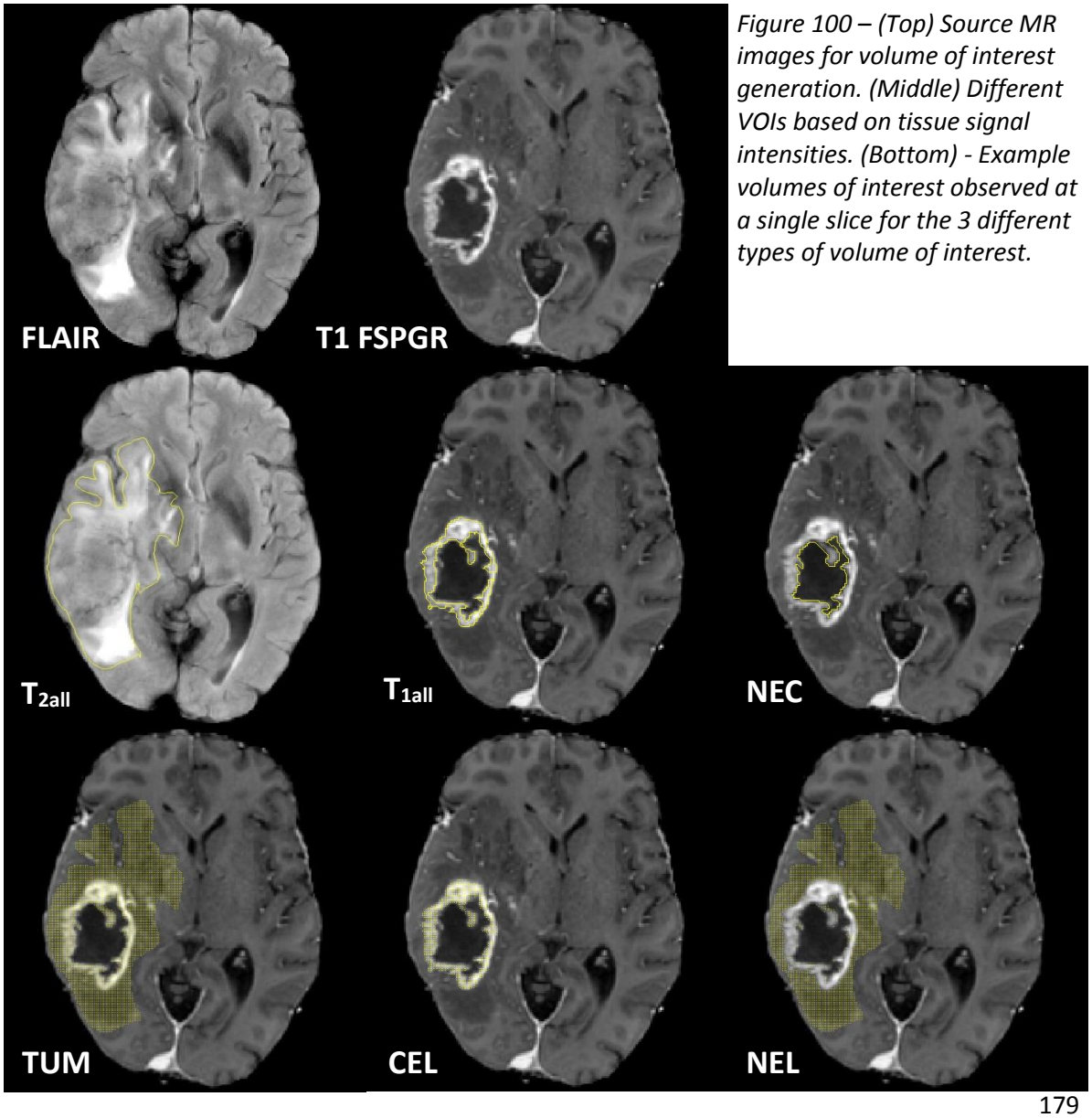

Figure 100 – (Top) Source MR images for volume of interest generation. (Middle) Different VOIs based on tissue signal intensities. (Bottom) - Example volumes of interest observed at a single slice for the 3 different types of volume of interest.

6.8.2 Gaussian Mixture Model

Given that many of lesions studied in this thesis were heterogeneous, it could be considered inappropriate to analyse parameters generated from them as a single population using statistics for a normal distribution. Therefore a Gaussian mixture model (GMM) (185) was also applied (DIVA, Lowry) for each VOI, splitting each sample into two populations. An example GMM fit can be seen in Figure 101. In this study the GMM was limited to two populations (0 and 1) to make sure all parameters were comparable between patients. Populations were also always ordered by the mean.

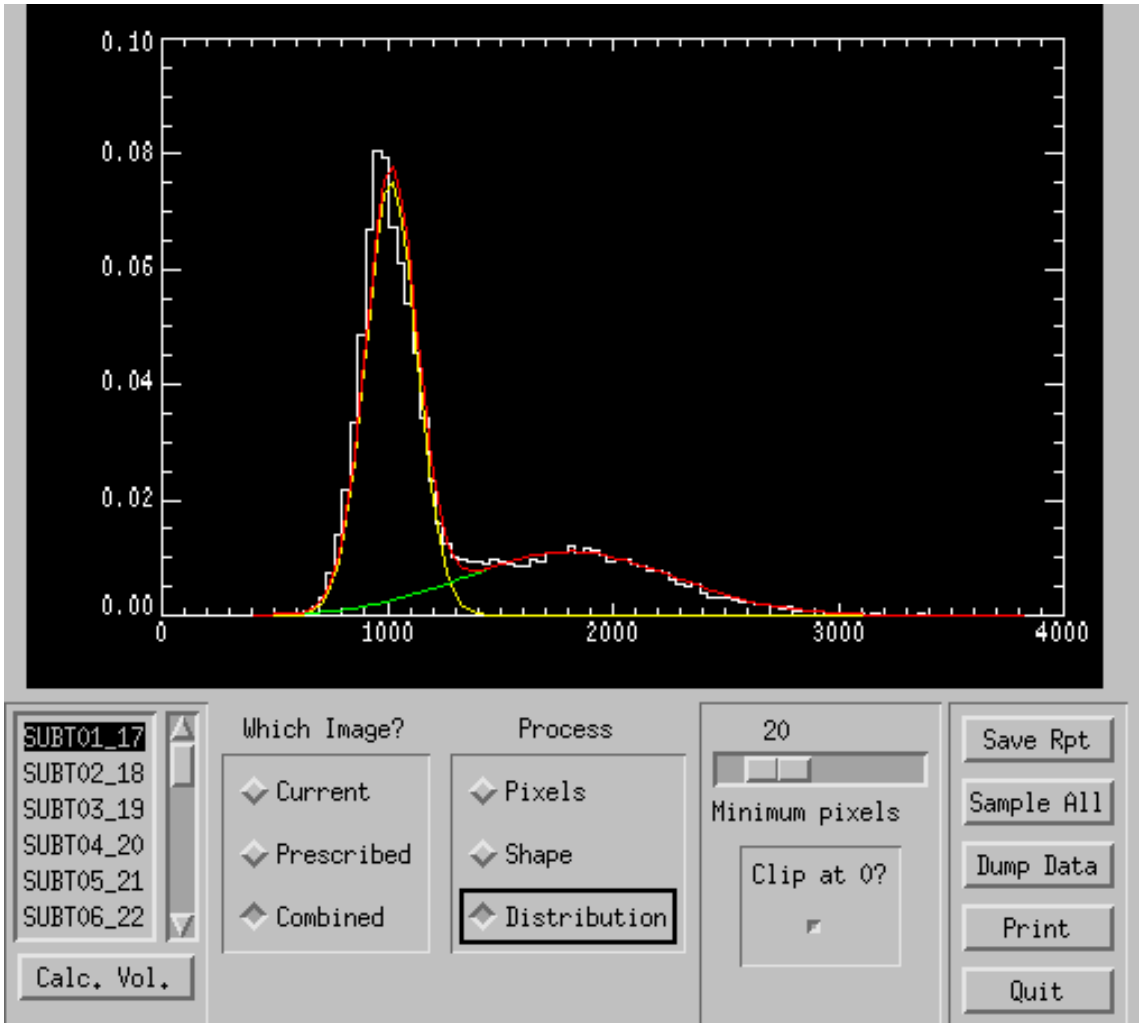

Figure 101 - Example Gaussian mixture model fit of a tumour histogram from a post-contrast FSPGR T_1 weighted volume. The white line is the raw data, while the yellow and green lines show the two populations decided by the model. The red line is the sum of the two populations and should be similar to the raw data.

Example scenarios where Gaussian mixture modelling may be appropriate within this study include:

- Non enhancing volume of interests (**NEL**)
  - separation of the low grade tumour/infiltrating component from oedema
- Enhancing volume of interests (**CEL**)
  - removal of small areas of necrosis or partial volume effects
  - separation of vessels from tumour
- Whole tumour volumes of interest (**TUM**)
  - redefining boundaries between enhancing and non-enhancing regions if registration was potentially poor
  - conventional imaging led to poor boundary definitions

The 3 VOIs were processed using a separate Gaussian mixture model (GMM) for every parameter (Figure 102). This was based on the hypothesis that using a GMM may be able to tease apart two populations within a given VOI, whether it was tumour versus oedema, or a higher grade component versus a lower grade region. Statistical descriptors were calculated for the two Gaussian probability distributions which were: standard deviation, skew, kurtosis and median. Given the perfect Gaussian distributions of the GMM, mean and median were synonymous in this situation.

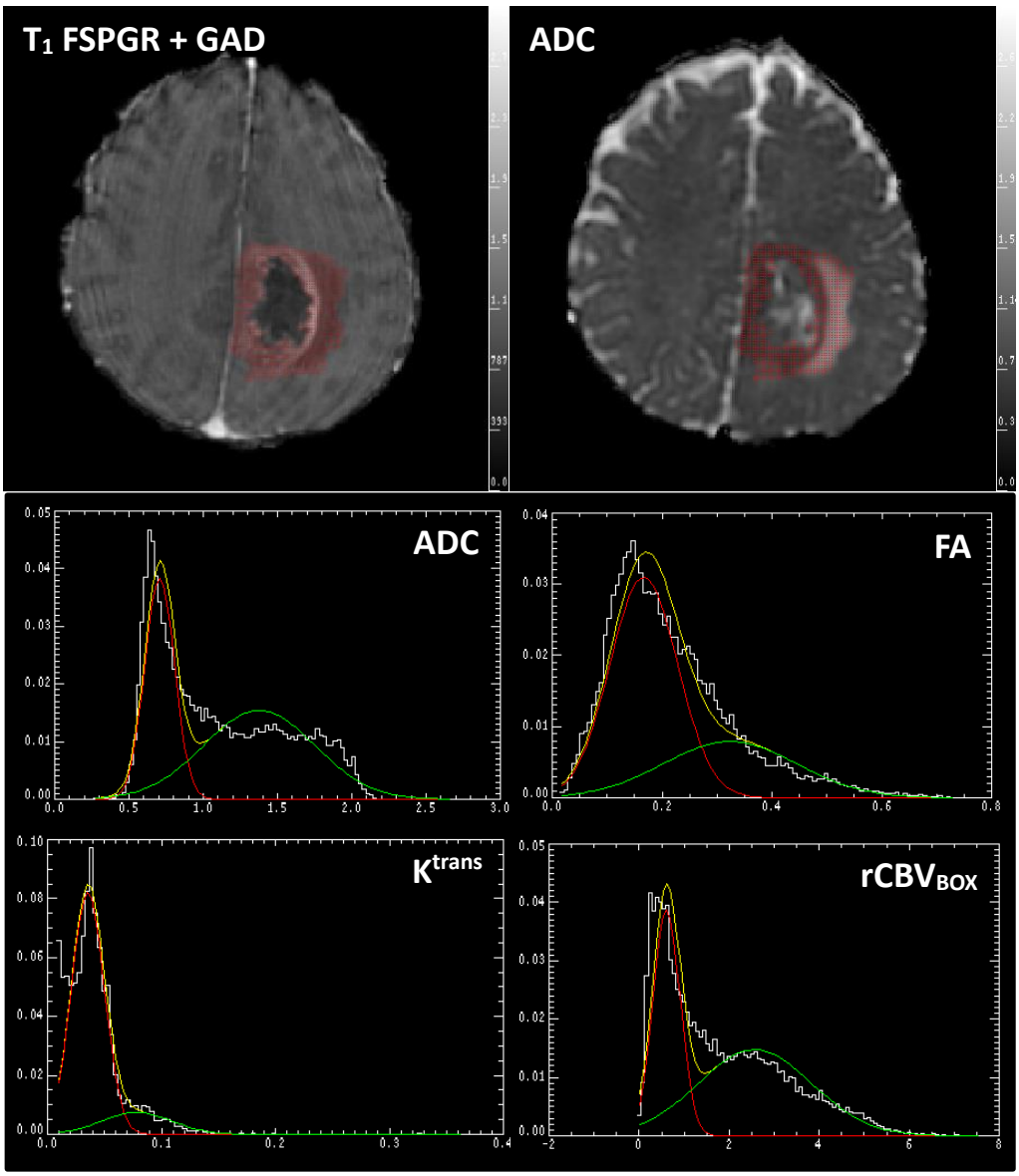

Figure 102 - Example GMM fits of 4 different parameter volumes from a GBM patient with the volume of interest shown on a single slice. In all cases it can be seen that the data (white) is of a non-Gaussian appearance and so at least 2 populations exist. Due to the unknown number of populations in each parameter and patient the GMM (yellow) was limited to 2 populations (red and green) to ensure the ability to directly compare different parameters with grade and response.

7 Preoperative MR for Tumour Grading

This chapter details findings from the preoperative MR scans of the study patients (Time Point 1). In this NHS trust, preoperative MR plays a vital role in the radiological diagnosis of brain neoplasms. Imaging is discussed at a multi-disciplinary team (MDT) meeting where key decisions are made regarding patient treatment. MR is further involved preoperatively, with imaging often used to guide surgeons before and during resection. Thus it is important to understand how imaging reflects the underlying pathology.

Patient inclusion criteria for this chapter:

- written consent obtained prior to 1st scan
- dataset for time point 1 (processed and registered as described in Chapter 6, pg. 151)
- histology available
- astrocytic or oligodendroglial cell type

Fifty eight patients with histologically proven glial tumours were identified; however, 3 datasets could not be processed due to excessive motion. This meant that 55 patients with a median age of 59 years (27-78) were selected for the final analysis in this chapter. A breakdown of patient age, gender and histology can be seen in Table 8. In most cases, dexamethasone (a steroid treatment) was prescribed to patients upon diagnosis to reduce brain swelling.

In this chapter, correlations between MR parameters are initially examined (7.1) before differences in MR parameters and glioma grade are explored (7.2). A model for grading gliomas is also presented (7.3). The single voxel TE-averaged PRESS is subsequently analysed separately due to the reduced coverage and an independent logistic regression model is developed (7.4). Finally case studies are presented to demonstrate the limitations of both MR and tissue sampling (7.5).

Table 8 - Patient demographic information

ID	Gender	Age	Histology	Grade
1	F	54	Gliosarcoma	4
2	M	60	Gliosarcoma	4
3	M	71	Glioblastoma Multiforme	4
4	F	33	Anaplastic Oligodendroglioma	3
5	M	74	Anaplastic Oligodendroglioma	3
6	F	68	Anaplastic Oligodendroglioma	3
7	M	71	Glioblastoma Multiforme	4
8	M	66	Glioblastoma Multiforme	4
9	M	45	Glioblastoma Multiforme	4
10	M	59	Glioblastoma Multiforme	4
11	M	38	Glioblastoma Multiforme	4
12	F	67	Glioblastoma Multiforme	4
13	F	48	Anaplastic Oligodendroglioma	3
14	F	69	Glioblastoma Multiforme	4
15	M	70	Glioblastoma Multiforme	4
16	F	63	Anaplastic Astrocytoma	3
17	F	67	Glioblastoma Multiforme	4
18	M	66	Glioblastoma Multiforme	4
19	M	42	Anaplastic Astrocytoma	3
20	M	66	Glioblastoma Multiforme	4
21	M	40	Diffuse Astrocytoma	2
22	M	29	Oligoastrocytoma	2
23	F	30	Anaplastic Astrocytoma	3
24	M	57	Glioblastoma Multiforme	4
25	M	72	Glioblastoma Multiforme	4
26	M	33	Diffuse Astrocytoma	2
27	F	70	Glioblastoma Multiforme	4
28	F	57	Anaplastic Oligodendroglioma	3
29	M	29	Anaplastic Astrocytoma	3
30	F	66	Glioblastoma Multiforme	4
31	F	55	Anaplastic Oligodendroglioma	3
32	F	39	Oligodendroglioma	2
33	M	49	Anaplastic Astrocytoma	3
34	M	63	Glioblastoma Multiforme	4
35	F	64	Glioblastoma Multiforme	4
36	M	56	Glioblastoma Multiforme	4
37	M	64	Glioblastoma Multiforme	4
38	M	52	Glioblastoma Multiforme	4
39	F	27	Glioblastoma Multiforme	4
40	F	65	Glioblastoma Multiforme	4
41	M	61	Glioblastoma Multiforme	4
42	F	63	Oligodendroglioma	2
43	M	70	Glioblastoma Multiforme	4
44	M	39	Oligodendroglioma	2
45	F	57	Glioblastoma Multiforme	4
46	M	40	Oligoastrocytoma	2
47	M	60	Glioblastoma Multiforme	4
48	F	31	Diffuse Astrocytoma	2
49	F	37	Diffuse Astrocytoma	2
50	M	50	Glioblastoma Multiforme	4
51	F	39	Oligodendroglioma	2
52	M	67	Glioblastoma Multiforme	4
53	F	78	Glioblastoma Multiforme	4
54	M	53	Glioblastoma Multiforme	4
55	F	61	Anaplastic Oligoastrocytoma	3

7.1 Correlations Between MR Parameters

7.1.1 Introduction

This initial section briefly examines the correlations between mean MR parameters sampled from glioma patients using a **TUM** VOI as detailed on pg. 178. Significant correlations between similar parameters (e.g. rCBV vs. v_b) may help demonstrate the robustness of the processing scheme. Likewise, replication of previously reported correlations may also help validate future findings from this study.

7.1.2 Methods

Multiparametric MR data was acquired from 55 patients with histologically confirmed gliomas. Following subsequent registration and image processing (Chapter 6), a 4D multiparametric volume (ADC, FA, q, RA, λ_L, λ_R, R_1, K^{trans}, v_e, v_b, $rCBV_{GVF}$, $rCBV_{BOX}$, and K_2) created from DTI, DCE and DSC data sets for each patient, was sampled using a **TUM** VOI contoured by the author.

7.1.3 Statistics

Mean parameter values were tested with a Pearson's correlation test in SPSS 20 (IBM, USA). Given the large number of pixels, median = 18157 (2617-63907), included in each VOI, measurements of mean values were considered suitable for describing the populations. Correlations with $P<0.05$ were treated as significant.

7.1.4 Results

Table 10 shows the R values and respective p-values of the correlations between differing MR parameters. Notable results include correlations between diffusivity parameters (ADC, λ_L and λ_R) and DSC derived parameters, and the DCE with DSC parameters. Within acquisition groups, all diffusivity, DCE and DSC parameters significantly correlated with each other. Fibre directionality parameters (FA, q and RA) did not all significantly correlate with diffusivity parameters (ADC, λ_L and

λ_R) despite being derived the same initial 3 eigenvalues. Given the normalisation process used to calculate fractional anisotropy and relative anisotropy (pg. 152), one might expect FA and RA to decrease in voxels where ADC is high.

Results are coloured coded according to the source of the data using the scheme in Table 9. This was implemented to improve the visualisation of trends with results.

Table 9 – Colour coding for different MR sequences and the parameters derived from them in this study.

DTI Diffusion			DTI Directionality			T_1 Maps	DCE MRI			DSC MRI		
ADC	λ_L	λ_R	FA	q	RA	R_1	K^{trans}	v_e	v_b	$rCBV_{GVF}$	$rCBV_{BOX}$	K_2

*Table 10 - Correlations between mean MR parameters sampled using a **TUM** VOI in 55 gliomas. Significant results are in **bold** whilst the strength of the correlation is visualised using a red-yellow-green colour chart where red are strong negative correlations and green are strong positive correlations.*

		λ_L	λ_R	FA	q	RA	R_1	K^{trans}	v_e	v_b	$rCBV_{GVF}$	$rCBV_{BOX}$	K_2
ADC	R	0.979	0.994	-0.593	0.112	-0.588	-0.288	-0.017	-0.002	0.058	-0.521	-0.466	0.353
	Sig.	**0.001**	**0.001**	**0.001**	0.415	**0.001**	**0.033**	0.902	0.989	0.674	**0.001**	**0.001**	**0.008**
λ_L	R		0.950	-0.423	0.311	-0.418	-0.218	0.033	0.049	0.085	-0.539	-0.486	0.323
	Sig.		**0.001**	**0.001**	**0.021**	**0.001**	0.111	0.812	0.720	0.539	**0.001**	**0.001**	**0.016**
λ_R	R			-0.673	0.005	-0.668	-0.321	-0.043	-0.029	0.043	-0.502	-0.447	0.362
	Sig.			**0.001**	0.974	**0.001**	**0.017**	0.755	0.834	0.756	**0.001**	**0.001**	**0.007**
FA	R				0.709	0.999	0.388	0.179	0.178	0.038	0.214	0.178	-0.357
	Sig.				**0.001**	**0.001**	**0.003**	0.191	0.193	0.782	0.117	0.194	**0.008**
q	R					0.708	0.273	0.254	0.262	0.134	-0.190	-0.187	-0.093
	Sig.					**0.001**	**0.043**	0.061	0.053	0.331	0.165	0.171	0.499
RA	R						0.380	0.173	0.174	0.032	0.212	0.176	-0.365
	Sig.						**0.004**	0.205	0.205	0.816	0.120	0.197	**0.006**
R_1	R							0.241	0.192	0.126	0.070	0.044	-0.198
	Sig.							0.076	0.160	0.360	0.612	0.752	0.147
K^{trans}	R								0.932	0.794	0.436	0.448	-0.458
	Sig.								**0.001**	**0.001**	**0.001**	**0.001**	**0.001**
v_e	R									0.783	0.391	0.395	-0.468
	Sig.									**0.001**	**0.003**	**0.003**	**0.001**
v_b	R										0.393	0.385	-0.489
	Sig.										**0.003**	**0.004**	**0.001**
$rCBV_{GVF}$	R											0.984	-0.567
	Sig.											**0.001**	**0.001**
$rCBV_{BOX}$	R												-0.578
	Sig.												**0.001**

*Table 11 - Correlations between mean MR parameters sampled using a **TUM** VOI in 55 gliomas.*

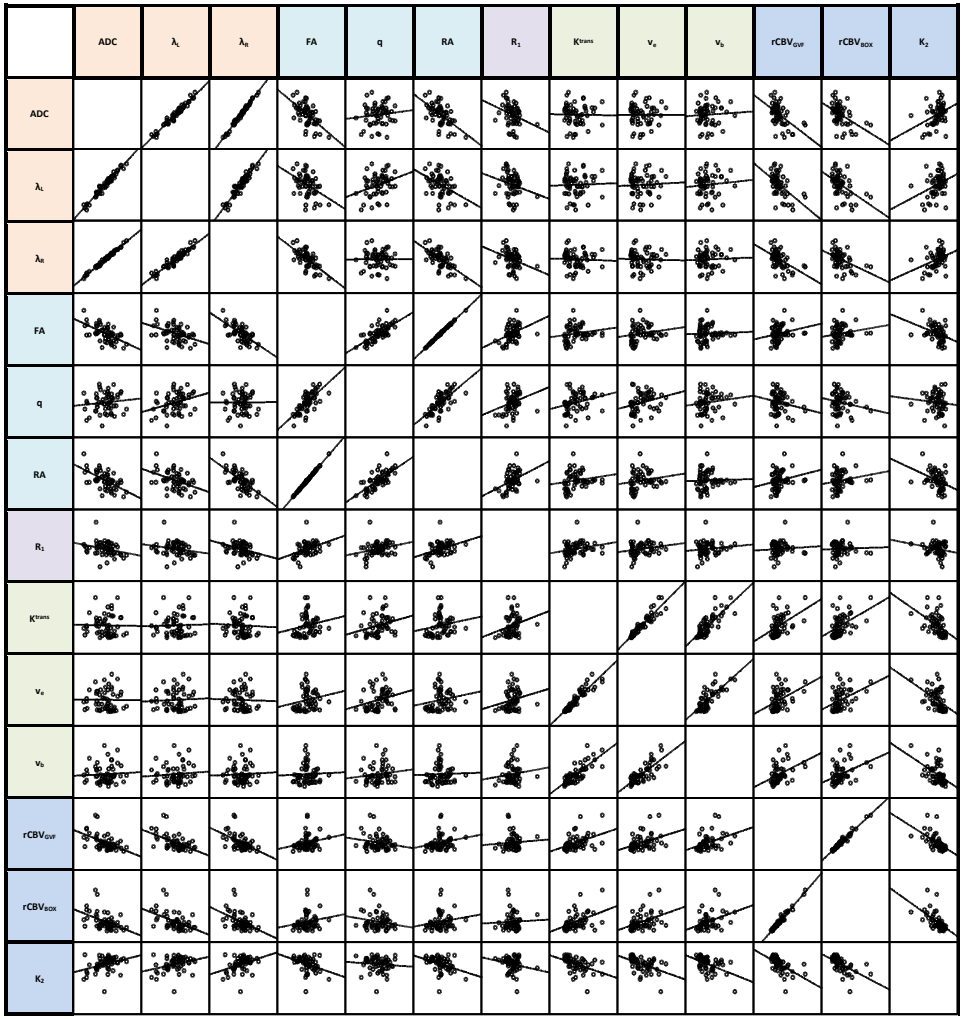

7.1.5 Discussion

The high number of significant correlations between MR parameters suggests that the processing and registration scheme implemented in this thesis is a systematic process for analysing gliomas. Catalaa *et al* (188) previously reported a significant negative correlation between rCBV and ADC values, which were observed in both the contrast enhancing (**CEL**) (R=-0.89, P=0.001), and non-enhancing regions (**NEL**) (R=-0.90, P=0.001) of grade IV gliomas. However, their correlations used data from only 9 patients compared to the 55 patients in Table 10. In this study, data from all grades was tested, and used a **TUM** VOI instead of **CEL** and **NEL**, meaning the volumes of interests used here were probably more heterogeneous than the VOIs used by Catalaa *et al*, explaining the lower R values observed in the results (R=-0.521, P=0.001).

Values of K_2 had significant correlations with K^{trans}, v_e, v_b, $rCBV_{GVF}$ and $rCBV_{BOX}$. With further investigation of K_2, it may be possible to determine the importance of this parameter, which also correlated with diffusivity measurements. Given K_2 is a correction factor for vessel leakage, K^{trans} is probably the most comparable parameter in terms of physiological meaning. Correlations between parameters derived from T_1 and T_2* dynamics have previously been described (66, 189, 190) in intra-axial tumours, and it is encouraging that the same trends are apparent using this methodology. The intra sequence correlations for the DCE parameters were similar to those reported by Mills *et al* (191) suggesting the model chosen was also robust for the estimations of PK parameters.

Other useful insights gained from the correlation table, include the absence of a relationship between ADC and q, which are derived from the same acquisition data (DTI), indicating the two parameters are independent, and thus both may contain usable diagnostic information, unlike FA and ADC which were strongly correlated.

Whilst a high number of parameters demonstrated significant correlations, it is important to recognise how much variation in one parameter can be explained by the other parameter. Only

variables derived from the same raw data came close to fully explaining all of the variance within any given parameter (e.g. ADC, λ_L and λ_R).

7.1.6 Conclusion

Although there appears to be considerable overlap between parameters, and subsequently the information contained, some encouragement can be gained by the replication of trends reported in other studies. The absence of correlations for some parameters such as q and R_1 is also noteworthy as the information contained is unrelated to that of other parameters and potentially useful in a multiparametric situation. Whilst it is not possible to ascertain which parameters from each sequence are optimal for the purposes of glioma grading or any subsequent survival prediction, the presence of similar trends from different sequences suggests the method for sampling data is systematic.

7.2 Associations of MR Parameters with Histology

7.2.1 Introduction

Multiple studies have demonstrated associations between MR parameter and grade (12, 45, 77, 92, 93, 100, 104, 108, 115, 118, 188, 192, 193), in some cases using several MR modalities. This study used 3 different types of functional MR (DTI, DCE and DSC), with volumes of interest (VOIs) used rather than the regions of interest (ROIs)/single slice analysis used to analyse some previous studies, to assess which parameters were best for glioma grading. Given gliomas are thought to become more heterogeneous with grade (194), descriptors such as standard deviation, skew and kurtosis may yield more significant relationships. Likewise, as data becomes potentially multimodal or shift in distribution (log normal), Gaussian mixture modelling (GMM) may be a more appropriate way to sample subpopulations within these lesions (141).

7.2.2 Methods

Initially patients were categorised according to the WHO grade (6) defined by the histology. Cell type was not considered for this section given the initial size of the cohort. Up to three different volumes of interest (**TUM**, **CEL** & **NEL** as detailed on pg. 178) were generated for each lesion using the 4D multiparametric volume (ADC, FA, q, RA, λ_L, λ_R, R_1, K^{trans}, v_e, v_b, $rCBV_{GVF}$, $rCBV_{BOX}$, and K_2), depending on whether it contained a contrast enhancing component as defined by the post-contrast imaging. Standard statistical descriptors (mean, standard deviation, skew, kurtosis, median, minimum and maximum) were generated for each type of VOI for every lesion. Gaussian mixture modelling was also applied generating a further two sets of statistical descriptors for each type of VOI where, VOI_0 is the Gaussian subpopulation with the lowest mean and VOI_1 is the population with the highest mean (**TUM**, $\mathbf{TUM_0}$ and $\mathbf{TUM_1}$)/(**CEL**, $\mathbf{CEL_0}$ and $\mathbf{CEL_1}$)/(**NEL**, $\mathbf{NEL_0}$ and $\mathbf{NEL_1}$). Non-parametric significance tests (Kruskal-Wallis) were used to examine the heterogeneity between different glioma grades, given the non-normal distribution of glioma grades ruling out the use of

correlations. If differences between glioma grades could be identified, then further analysis could be carried out to model the interactions between MR parameters and grade. Whilst this chapter is primarily for hypothesis generation, Bonferroni and non-corrected p-values ($P<0.05$) are both reported. Given the large number of statistical tests in this chapter, Bonferroni correction may be too strict a test given α is divided by the number of tests and potentially may remove truly significant results. Therefore, the false discovery rate (FDR) (195) for each type of VOI was also calculated using q-values generated from the p-values of the Kruskal-Wallis tests as a more conservative estimate of false positives.

7.2.3 Results

Results for the entire abnormality as defined by the **TUM** VOI (pg. 178) can be seen over the following pages (Table 34-Table 40). A breakdown of tumour grade revealed 10 grade II lesions, 12 grade III lesions and 33 grade IV lesions. ADC, FA, q, RA, λ_L, λ_R, R_1, K^{trans}, v_e, v_b, $rCBV_{GVF}$, $rCBV_{BOX}$, and K_2 were all tested for relationships with tumour grade. From 195 statistical tests, 103 significant p-values ($P<0.05$) were found. Subsequent q-value analysis revealed a false discovery rate (FDR) of 2.5%, resulting in 3/103 significant values likely to be false positives. Ten of 26 minimum and maximum parameter values were also associated with grade. A summary table of significant results using the **TUM** VOI can be seen in Table 12.

Results for the associations of the multiparametric data sampling using the contrast enhancing VOIs (**CEL**) with grade were summarised into a single table (Table 13). A breakdown of tumour grades revealed 4 grade II lesions, 6 grade III lesions and 33 grade IV lesions with an enhancing component on morphological imaging. Minimum and maximum values were not investigated with this VOI (**CEL**) as the values were reported using the **TUM** VOI. Of the 195 Kruskal-Wallis tests, 73 significant p-values ($P<0.05$) were reported. Subsequent q-value analysis revealed a FDR of 6.5%, indicating 5/73 significant values were likely to be false positives.

A summary of the **NEL** VOI defined results can be seen in Table 14. All tumours contained a non-enhancing portion and so shared the same cohort of patients as the **TUM** VOI. From 195 statistical tests, 80 significant p-values ($P<0.05$) were found. Subsequent q-value analysis revealed a FDR of 4.1%, resulting in 3/80 significant values likely to be false positives.

Associations between mean parameter values and glioma grade (Table 34)

Mean tumour measurements of λ_L showed no significant differences between tumour grade, whilst only $\mathbf{TUM_0}$ of ADC values displayed a significantly negative trend ($P=0.012$) (Figure 103). The radial diffusivity (λ_R) however, was significant for both $\mathbf{TUM_0}$ ($P=0.003$) and $\mathbf{TUM_1}$ ($P=0.042$) populations (Figure 103); despite the **TUM** VOI not showing a significant association with grade. The $\mathbf{TUM_0}$ λ_R measurements showed a significantly negative trend with glioma grade, however λ_R measured with $\mathbf{TUM_1}$ was found to be lower in grade III lesions than tumours of grade II and IV.

All diffusion parameters sensitive to directionality (FA, q, RA) were significantly related to grade ($P<0.05$), with directional diffusion found to increase with grade (Figure 104). Mean R_1 values using **TUM** and $\mathbf{TUM_0}$ were also related to tumour grade, displaying an increasing trend (Figure 105). All mean PK parameters derived by the DCE (K^{trans}, v_e, v_b) were significantly associated with grade ($P<0.001$), demonstrating an increasing trend with grade (Figure 106). From the DSC derived cerebral blood volume maps, **TUM** and $\mathbf{TUM_1}$ VOIs yielded significant positive trends when trying to associate $rCBV_{GVF}$ and $rCBV_{BOX}$ with grade (Figure 107). K_2 as defined by the Boxerman model sampled using **TUM** and $\mathbf{TUM_0}$ VOIs had a negative appearing trend with grade (Figure 108). After Bonferroni correction, all volumes of interest for K^{trans}, v_e and v_b were still found to be significant ($P<0.001$).

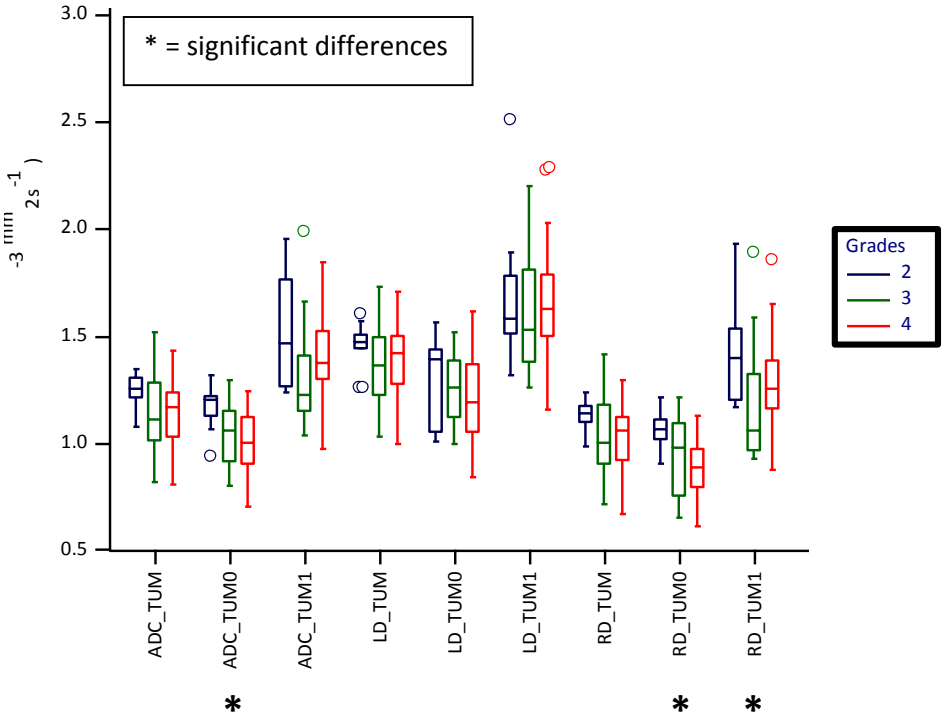

Figure 103 - Boxplot of mean parameter/VOI values clustered by grade using diffusivity based parameters. Clear circles show outliers (larger than the upper quartile plus 1.5 times the interquartile range) whilst solid circles show extreme outliers (larger than the upper quartile plus 3 times the interquartile range).

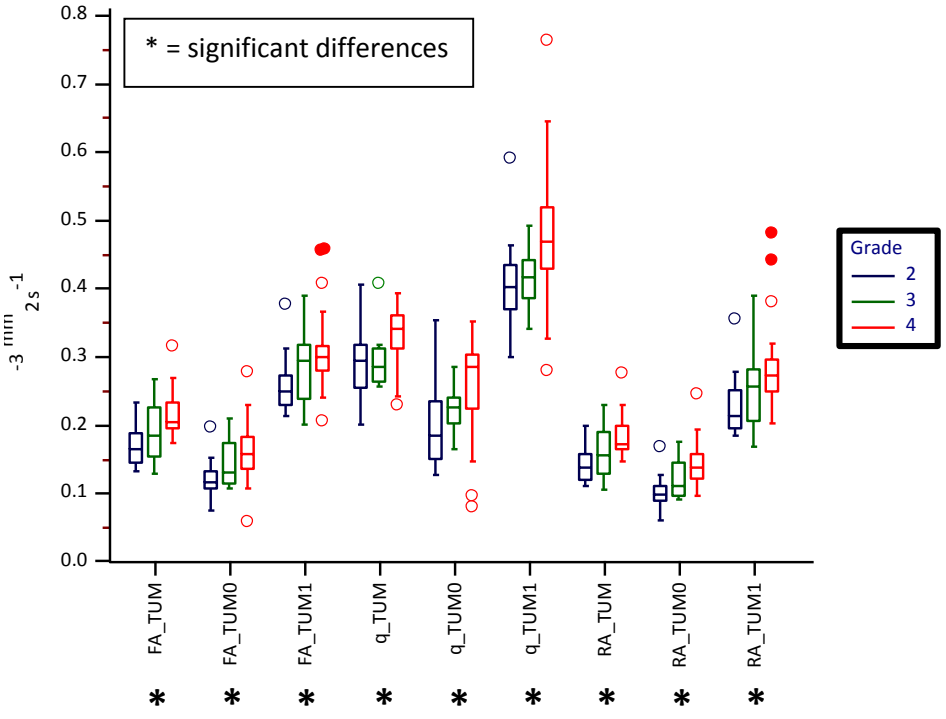

Figure 104 - Boxplot of mean parameter/VOI values clustered by grade using directional diffusivity based parameters. Clear circles show outliers whilst solid circles show extreme outliers.

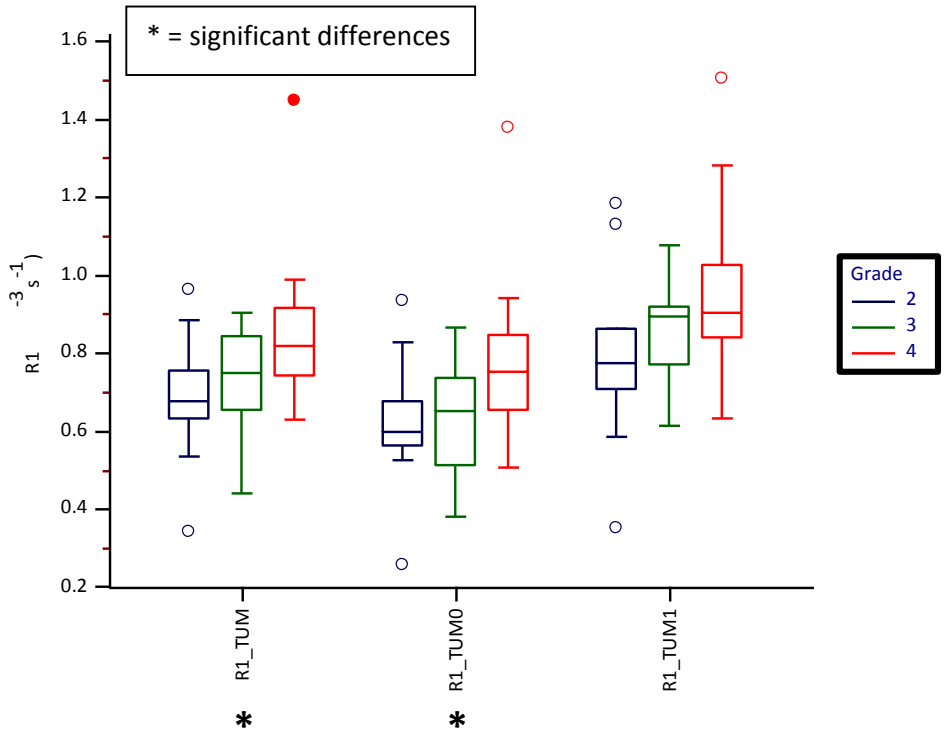

Figure 105 - Boxplot of mean parameter/VOI values clustered by grade using R_1 values. Clear circles show outliers whilst solid circles show extreme outliers.

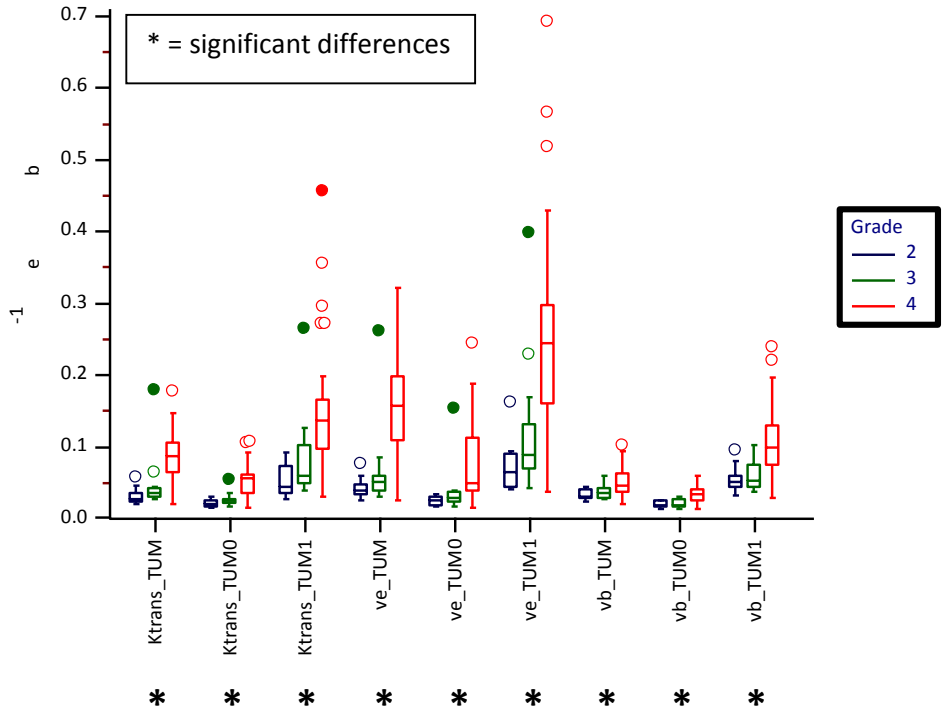

Figure 106 - Boxplot of mean parameter/VOI values clustered by grade using pharmacokinetic parameters. Clear circles show outliers whilst solid circles show extreme outliers.

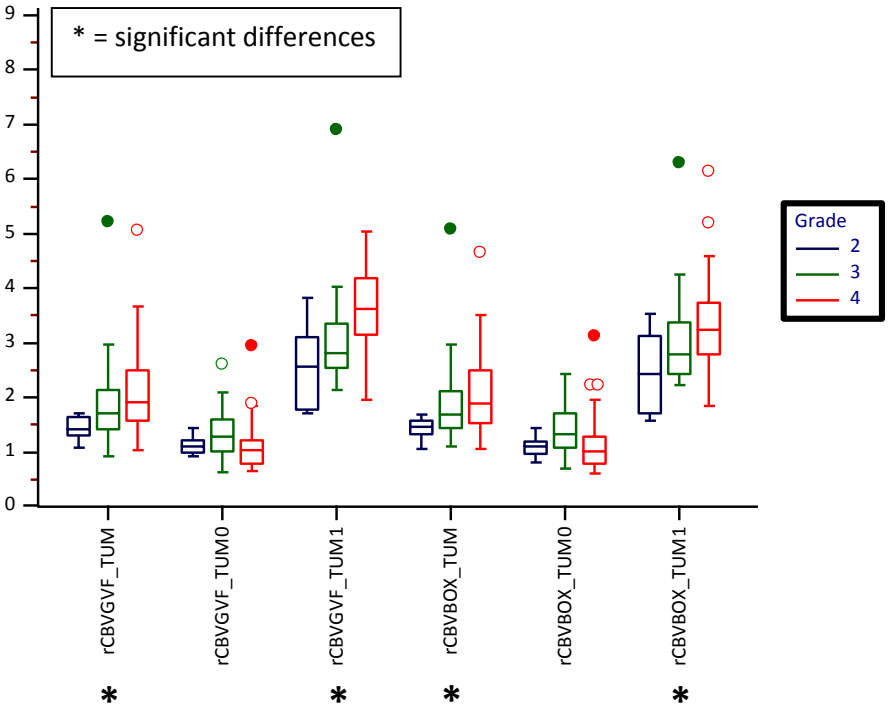

Figure 107 - Boxplot of mean parameter/VOI values clustered by grade using rCBV based parameters. Clear circles show outliers whilst solid circles show extreme outliers.

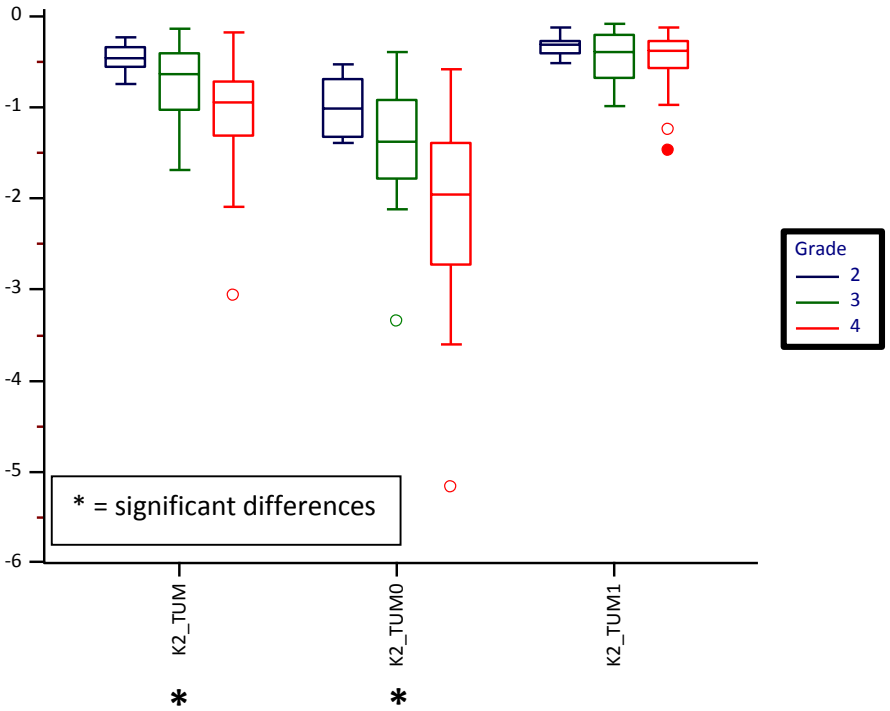

Figure 108 - Boxplot of mean parameter/VOI values clustered by grade using K_2 leakage. Clear circles show outliers whilst solid circles show extreme outliers.

Standard deviations of parameter values between glioma grades (Table 35)(Figure 109)

Standard deviations of ADC values for the **TUM** and **TUM_1** VOIs both showed a significant difference between tumour grades, with grade III tumours having a lower standard deviation than grade II and IV lesions. FA, q and RA all showed significant increasing trends between standard deviation and grade using **TUM_0**. Longitudinal and radial diffusivities also showed significant differences between standard deviation measurements and grade using the **TUM** VOI with grade III lesions once again reporting lower standard deviations than grade II and IV tumours. The standard deviation of radial diffusivity values was significantly different between grades for the **TUM_1** population which upon closer examination of the data appears to be caused by the difference in standard deviation of grade III tumours compared to grades II and IV. The standard deviation of R_1 values sampled using **TUM** and **TUM_1** VOIs also showed significant differences between glioma grade though no trend is apparent. K^{trans}, v_e, v_b, $rCBV_{GVF}$, $rCBV_{BOX}$ and K_2 all produced significantly increasing trends with grade for at least 1 of the VOI types. In some cases, such as K_2, the standard deviation increase appears to following the mean.

Skew of parameter values between glioma grades (Table 36)

The skew of the fractional anisotropy (FA) values for the **TUM** and **TUM_0** VOIs was significantly different between tumour grades with the biggest difference occurring between grade III and IV gliomas. Relative anisotropy (RA) values showed similar findings though these were not as significant. The skew of q measured using **TUM_0** was also significantly different between glioma grades. ADC, λ_L, λ_R were all non-significant as were $rCBV_{BOX}$ and K_2. Most PK parameters (K^{trans}, v_e, v_b) still show significant differences as observed with mean and standard deviation measurements; however, this was not to the same level of significance with no linear trend apparent. The TUM_1 $rCBV_{GVF}$ did show a significant increasing trend with skew values increasing with grade.

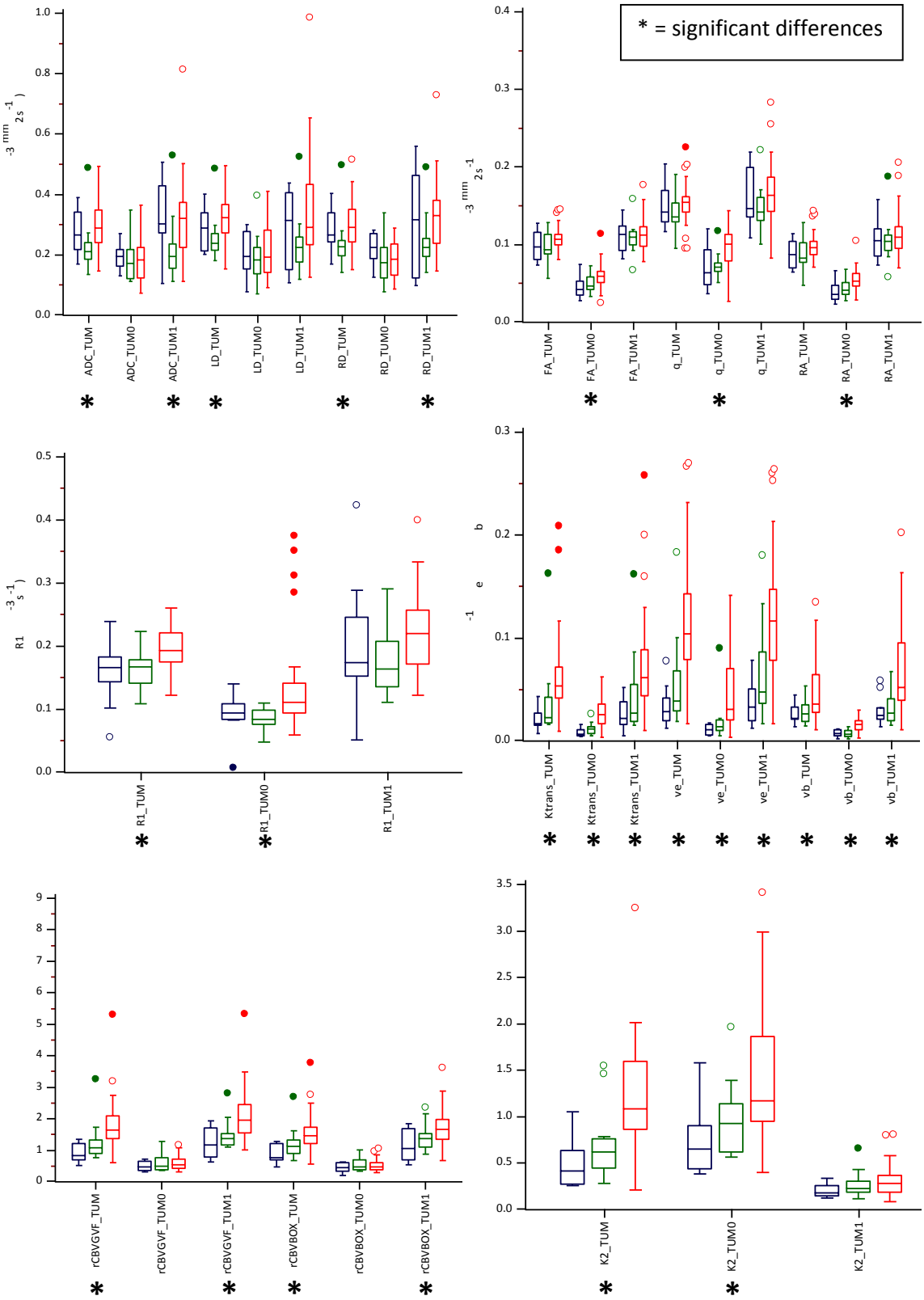

Figure 109 - Boxplot of standard deviations clustered by grade. Clear circles show outliers (larger than the upper quartile plus 1.5 times the interquartile range) whilst solid circles show extreme outliers (larger than the upper quartile plus 3 times the interquartile range).

Kurtosis of parameter values between glioma grades (Table 37)

Notable significant differences between the kurtosis of parameters sampled using a **TUM** VOI and tumour grade, included all FA populations, as well as **TUM** and $\mathbf{TUM_0}$ of v_e, $\mathbf{TUM_0}$ and $\mathbf{TUM_1}$ of v_b, and K_2 measured using $\mathbf{TUM_1}$.

Median parameter values between glioma grades (Table 38)

Median **TUM** measurements showed similar results to mean **TUM** measurements. The median number of pixels for a VOI was in the order of 18000, thus mean and median values had the potential to be similar. Given the GMM fits Gaussian curves to the data, mean and median were the same for $\mathbf{TUM_0}$ and $\mathbf{TUM_1}$. Small differences in the level of significance were observed for the median q and K_2 **TUM** VOIs.

Results for the minimum and maximum parameter values between glioma grades (Table 39 and Table 40)

These results are only taken from the **TUM** VOI as the GMM produces a probability distribution where it is impossible to determine the maximum value of the lowest distribution, likewise, the minimum value of the highest distribution. Maximum values of K^{trans}, v_e, v_b and $rCBV_{GVF}$ were all significantly associated with grade, however this is not a linear trend with the largest differences appearing between grade III and IV gliomas. Minimum ADC, λ_L, λ_R and K_2 were also found to be significantly related to grade, however the minimum diffusion measurements approach non-sensical values most likely caused by vessels, calcium or blood products. The minimum K_2 values (maximum T2* dominant leakage) were highly significant but were probably influenced by the large decrease in values between grade III and IV tumours.

7.2.3.1 CEL VOI (Table 13)

Mean parameter values between glioma grades (Table 41)

Mean parameter values for using a CEL VOI were largely non-significant with the exception of K^{trans}, v_e, v_b and K_2 which all reflect tumour vascularity and leakage. In most parameters there is a small increase between grade II and III tumours and a much larger increase for grade IV tumours. R_1 was also significantly associated with grade for some VOIs with values increasing with grade. **CEL**, **CEL_0** and **CEL_1** were all significant for K^{trans}, v_e, v_b and K_2, while R_1 was significantly associated with grade using **CEL** and **CEL_1**.

Standard deviations of parameter values between glioma grades (Table 42)

For all parameters, the standard deviation of at least one VOI (**CEL**, **CEL_0** or **CEL_1**) was significantly different ($P<0.05$) between tumour grade, with most parameters having two or three significant differences. The standard deviation of **R_1** values using **CEL** and **CEL_1** were the most significant results of all CEL based VOI measurements ($P<0.001$).

Skew of parameter values between glioma grades (Table 43)

All three VOIs (**CEL**, **CEL_0**, and **CEL_1**) for v_b significantly differed between tumour grade using the Kruskal-Wallis test, however the difference in median values was much larger between grade III and IV tumours than that of grade II and III. RA sampled using **CEL** and longitudinal diffusivity sampled using **CEL_1** also showed significant differences between grade, however these were nonlinear trends.

Kurtosis of parameter values between glioma grades (Table 44)

The kurtosis of the RA sampled using the **CEL** and **CEL_0** VOIs was significantly different between gliomas grades but no trend was noted. K^{trans} sampled using **CEL** was significant as was v_b sampled using **CEL** and **CEL_0**. The median v_b kurtosis was considerably high in grade IV lesions than those of

grades II and III. The use of the **CEL_1** VOI for $rCBV_{BOX}$ and K_2 also found significant differences between tumour grades, however no trend was present.

Median parameter values between glioma grades (Table 45)

The median values of parameters were found to be significant for the same VOIs as when examining the mean values of the contrast enhancing part of the lesions. In **CEL_0** and **CEL_1** VOIs, the p-values are the same as the mean data because of the Gaussian fitting process in the GMM.

7.2.3.2 NEL VOI (Table 14)

Mean parameter values between glioma grades (Table 46)

Twenty-three mean parameter measurements were significantly different between tumour grades for the non-enhancing portion of tumours. **NEL_0** was the only ADC population to significantly differ between grades, demonstrating a negative linear trend with grade. All VOIs measuring FA, q and RA showed significant differences between grades, with directional diffusion values increasing with grade, except q measured with **NEL** where a trend was not noted. **NEL** and **NEL_0** remained significant after Bonferroni correction. Radial diffusivity was significantly different between tumour grades when sampled with **NEL_0** and **NEL_1** VOIs. R_1 sampled using **NEL** and **NEL_0** showed a significant linearly increasing pattern with grade. All DCE derived parameters significantly differed between grades, with K^{trans} and v_e being more significant than v_b in identifying differences between grades. This measurement of significant differences in PK values between glioma grades from the apparently non-enhancing tissue may seem strange. However, the contrast enhanced MR sequence which the VOIs were contoured from was initiated 6 minutes after contrast agent delivery, allowing time for the rapid wash out of contrast agent. A combination of contrast dose (0.075ml/kg) and the flip angle (30°) of the T_1 FSPGR may explain the absence of enhancement, although interpolation effects from the registration and normal vessels within the oedema cannot be excluded. $rCBV_{GVF}$ and $rCBV_{BOX}$ did

not significantly differ between grades using **NEL**, **NEL_0** or **NEL_1**. K_2 of the DSC derived parameters sampled with **NEL_0** showed a significant negative pattern also.

Standard deviations of parameter values between glioma grades (Table 47)

K^{trans} and v_e demonstrated the greatest level of significance between grades when examining the standard deviation values within the non-enhancing portion of lesions. Other significant differences included ADC sampled using **NEL** and **NEL_1**, FA using **NEL_0**, q using **NEL_0**, RA using **NEL_0**, radial diffusivity using **NEL** and R_1 with **NEL_0**. **NEL_0** and **NEL_1** used to sample v_b both showed significant differences between the standard deviation of values and tumour grade, however the differences between grade IV tumours and lower grade lesions was quite large. $rCBV_{GVF}$ and K_2 sampled using **NEL** also significantly related with glioma grade.

Skew of parameter values between glioma grades (Table 48)

FA, q, RA, R_1, v_b and $rCBV_{GVF}$ all demonstrated significant differences between tumour grades. However, none of these relationships were significant following Bonferroni correction, with no linear patterns present in the data.

Kurtosis of parameter values between glioma grades (Table 49)

All VOIs used to sample FA values showed significant differences with grade, with **NEL** and **NEL_0** suggesting negative trends with grade. For RA only **NEL_1** was significant, and with q showing no significance at all. Other significant results were R_1 sampled with **NEL_1** and v_b sampled with **NEL** and **NEL_0,** however trends are not apparent.

Median parameter values between glioma grades (Table 50)

Median parameter values sampled using **NEL, NEL_0** or **NEL_1** all showed significant results for the same parameters as the mean values.

*Table 12 - Summary table of significant values, when using the **TUM** VOI to sample each parameter and correlated with grade using Kruskal-Wallis test for P<0.05 and Bonferroni corrected for P<0.00128 (0.05/39). Ten grade II lesions, 12 grade III lesions and 33 grade IV lesions contained a non-enhancing component on morphological imaging.*

Parameter	VOI	Mean Sig.	S.D. Sig.	Skew. Sig.	Kurt. Sig.	Med. Sig.
ADC	TUM	0.150	0.017	0.312	0.153	0.167
	TUM_0	0.012	0.610	0.515	0.153	0.012
	TUM_1	0.089	0.016	0.179	0.641	0.089
FA	TUM	0.003	0.199	0.001	0.009	0.002
	TUM_0	0.019	0.018	0.001	0.009	0.019
	TUM_1	0.046	0.893	0.401	0.010	0.046
q	TUM	0.002	0.237	0.059	0.426	0.001
	TUM_0	0.006	0.003	0.004	0.327	0.006
	TUM_1	0.012	0.154	0.052	0.572	0.012
RA	TUM	0.003	0.205	0.020	0.111	0.002
	TUM_0	0.002	0.001	0.015	0.097	0.002
	TUM_1	0.017	0.391	0.151	0.059	0.017
λ_L	TUM	0.350	0.020	0.492	0.098	0.389
	TUM_0	0.300	0.680	0.754	0.289	0.300
	TUM_1	0.606	0.064	0.061	0.352	0.606
λ_R	TUM	0.100	0.019	0.129	0.128	0.102
	TUM_0	0.003	0.171	0.136	0.103	0.003
	TUM_1	0.042	0.048	0.907	0.109	0.042
R_1	TUM	0.019	0.010	0.019	0.190	0.014
	TUM_0	0.012	0.012	0.015	0.425	0.012
	TUM_1	0.080	0.068	0.186	0.004	0.080
K^{trans}	TUM	0.001	0.001	0.136	0.534	0.001
	TUM_0	0.001	0.001	0.097	0.350	0.001
	TUM_1	0.001	0.001	0.669	0.872	0.001
v_e	TUM	0.001	0.001	0.001	0.001	0.001
	TUM_0	0.001	0.001	0.001	0.001	0.001
	TUM_1	0.001	0.001	0.516	0.550	0.001
v_b	TUM	0.002	0.005	0.008	0.003	0.001
	TUM_0	0.001	0.001	0.007	0.001	0.001
	TUM_1	0.001	0.001	0.041	0.198	0.001
$rCBV_{GVF}$	TUM	0.025	0.001	0.901	0.371	0.518
	TUM_0	0.126	0.525	0.857	0.318	0.126
	TUM_1	0.003	0.001	0.001	0.619	0.003
$rCBV_{BOX}$	TUM	0.024	0.001	0.555	0.274	0.319
	TUM_0	0.152	0.730	0.572	0.214	0.152
	TUM_1	0.013	0.021	0.133	0.817	0.013
K_2	TUM	0.001	0.001	0.096	0.084	0.035
	TUM_0	0.001	0.003	0.286	0.683	0.001
	TUM_1	0.500	0.075	0.058	0.032	0.500

*Table 13 – Summary table of significant values, when using the **CEL** VOI to sample each parameter and correlated with grade using Kruskal-Wallis test for P<0.05 and Bonferroni corrected for P<0.00128 (0.05/39). Four grade II lesions, 6 grade III lesions and 33 grade IV lesions contained an enhancing component on morphological imaging.*

Parameter	VOI	Mean Sig.	S.D. Sig.	Skew. Sig.	Kurt. Sig.	Med. Sig.
ADC	CEL	0.667	0.002	0.714	0.283	0.799
	CEL_0	0.985	0.018	0.869	0.332	0.985
	CEL_1	0.363	0.006	0.144	0.416	0.363
FA	CEL	0.467	0.020	0.090	0.080	0.613
	CEL_0	0.440	0.123	0.157	0.088	0.440
	CEL_1	0.263	0.010	0.416	0.784	0.263
q	CEL	0.508	0.035	0.660	0.332	0.610
	CEL_0	0.958	0.140	0.777	0.584	0.958
	CEL_1	0.644	0.018	0.968	0.616	0.644
RA	CEL	0.463	0.022	0.044	0.018	0.588
	CEL_0	0.440	0.097	0.065	0.030	0.440
	CEL_1	0.205	0.014	0.637	0.639	0.205
λ_L	CEL	0.726	0.003	0.840	0.254	0.915
	CEL_0	0.901	0.030	0.684	0.442	0.901
	CEL_1	0.452	0.002	0.015	0.204	0.452
λ_R	CEL	0.625	0.003	0.958	0.442	0.750
	CEL_0	0.836	0.017	0.951	0.588	0.836
	CEL_1	0.392	0.006	0.167	0.480	0.392
R_1	CEL	0.039	0.001	0.968	0.461	0.049
	CEL_0	0.071	0.002	0.835	0.420	0.071
	CEL_1	0.019	0.001	0.173	0.785	0.019
K^{trans}	CEL	0.008	0.006	0.138	0.035	0.009
	CEL_0	0.004	0.004	0.681	0.062	0.004
	CEL_1	0.004	0.009	0.226	0.133	0.004
v_e	CEL	0.005	0.002	0.184	0.387	0.005
	CEL_0	0.006	0.008	0.233	0.329	0.006
	CEL_1	0.002	0.001	0.573	0.323	0.002
v_b	CEL	0.028	0.037	0.006	0.002	0.035
	CEL_0	0.025	0.008	0.007	0.002	0.025
	CEL_1	0.017	0.014	0.024	0.612	0.017
$rCBV_{GVF}$	CEL	0.531	0.028	0.145	0.162	0.722
	CEL_0	0.402	0.131	0.236	0.174	0.402
	CEL_1	0.247	0.066	0.444	0.551	0.247
$rCBV_{BOX}$	CEL	0.214	0.034	0.286	0.479	0.273
	CEL_0	0.670	0.019	0.279	0.222	0.670
	CEL_1	0.174	0.071	0.937	0.019	0.174
K_2	CEL	0.019	0.025	0.058	0.050	0.013
	CEL_0	0.019	0.012	0.260	0.610	0.019
	CEL_1	0.034	0.015	0.057	0.046	0.034

*Table 14 – Summary table of significant values, when using the **NEL** VOI to sample each parameter and correlated with grade using Kruskal-Wallis test for P<0.05 and Bonferroni corrected for P<0.00128 (0.05/39). Ten grade II lesions, 12 grade III lesions and 33 grade IV lesions contained a non-enhancing component on morphological imaging.*

Parameter	VOI	Mean Sig.	S.D. Sig.	Skew. Sig.	Kurt. Sig.	Med. Sig.
ADC	NEL	0.250	0.029	0.502	0.195	0.385
	NEL_0	0.003	0.240	0.670	0.144	0.003
	NEL_1	0.078	0.038	0.212	0.860	0.078
FA	NEL	0.001	0.356	0.003	0.017	0.001
	NEL_0	0.001	0.023	0.004	0.016	0.001
	NEL_1	0.013	0.829	0.579	0.004	0.013
q	NEL	0.001	0.613	0.053	0.495	0.001
	NEL_0	0.001	0.004	0.004	0.353	0.001
	NEL_1	0.002	0.502	0.167	0.458	0.002
RA	NEL	0.001	0.311	0.033	0.095	0.001
	NEL_0	0.001	0.011	0.043	0.082	0.001
	NEL_1	0.009	0.514	0.244	0.048	0.009
λ_L	NEL	0.358	0.067	0.370	0.145	0.362
	NEL_0	0.579	0.431	0.862	0.345	0.579
	NEL_1	0.330	0.435	0.050	0.387	0.330
λ_R	NEL	0.117	0.023	0.347	0.198	0.161
	NEL_0	0.001	0.079	0.096	0.147	0.001
	NEL_1	0.026	0.158	0.909	0.211	0.026
R_1	NEL	0.007	0.060	0.021	0.139	0.006
	NEL_0	0.016	0.032	0.016	0.250	0.016
	NEL_1	0.072	0.189	0.614	0.006	0.072
K^{trans}	NEL	0.001	0.001	0.793	0.625	0.001
	NEL_0	0.002	0.004	0.801	0.714	0.002
	NEL_1	0.001	0.002	0.379	0.294	0.001
v_e	NEL	0.001	0.001	0.239	0.231	0.001
	NEL_0	0.005	0.005	0.223	0.181	0.005
	NEL_1	0.001	0.001	0.321	0.682	0.001
v_b	NEL	0.283	0.193	0.013	0.008	0.545
	NEL_0	0.050	0.036	0.014	0.004	0.050
	NEL_1	0.045	0.047	0.927	0.740	0.045
$rCBV_{GVF}$	NEL	0.326	0.016	0.405	0.822	0.265
	NEL_0	0.181	0.842	0.390	0.823	0.181
	NEL_1	0.226	0.078	0.004	0.484	0.226
$rCBV_{BOX}$	NEL	0.289	0.135	0.758	0.980	0.173
	NEL_0	0.091	0.616	0.629	0.981	0.091
	NEL_1	0.383	0.365	0.086	0.537	0.383
K_2	NEL	0.059	0.010	0.440	0.580	0.304
	NEL_0	0.044	0.171	0.172	0.301	0.044
	NEL_1	0.665	0.252	0.448	0.447	0.665

7.2.4 Discussion

Apparent Diffusion Coefficient

Using the **TUM** VOI sampling scheme, mean ADC values of tumours were not significantly different between glioma grades. However, the lower subpopulation of ADC values (**TUM_0**) was significantly related (P=0.012), with ADC values found to decrease with grade. This result agrees with previous publications (77, 196, 197), reporting increased cellularity and subsequently lower ADC values observed in higher grade lesions. A possible explanation for **TUM** and **TUM_1** VOI measurements not linked to grade, relates to the inclusion of oedema and lower grade components as defined by the T_{2all} VOI. The combination of GMMs and VOIs used in this study may have improved the measurement of ADC values in gliomas compared to ROI techniques which had previously been unable to distinguish tumour from oedema (198). Using a **NEL** VOI, the same statistical descriptors of ADC were found to be associated with lesion grade. Given that DTI is an EPI sequence, tissue mis-registration cannot be excluded, however, efforts were made to minimise the issue, such as thinner acquisition slices, and 12 degrees of freedom used to register the fractional anisotropy maps to the T_1 FSPGR volume.

The standard deviation of ADC values for the **TUM, TUM_1**, **CEL, CEL_0**, **CEL_1**, **NEL** and **NEL_1** VOIs were all significantly associated with grade, suggesting greater variation in the ADC values observed between grades, however, this trend is not apparent from immediate examination of the standard deviations values for each grade. Interestingly, when using the **CEL** VOIs (T_{1all} – NEC – HMG), standard deviation measurements were significantly different between tumour grades however, mean and median ADC values were not. Subpopulations of the **CEL** VOI did not improve the relationship between ADC values and tumour grade. Skew, kurtosis and maximum ADC value measurements using **TUM, CEL** or **NEL** VOIs failed to demonstrate any significant differences between grades. One reason for the smaller number of statistical descriptors that related to tumour grade when using a **CEL** VOI, could be explained if the enhancing portion of the lower grade lesions

actually represent higher grade transformation which was missed during tumour resection or tissue sampling, alternatively perfusion effects may distort the ADC values observed in higher grade lesions with enhancement. Minimum ADC values (most cellular voxels) did however distinguish between tumour grades (P=0.024) which agrees with previous studies reporting increasing amounts of cell proliferation in high grade gliomas (9) and decreasing minimum ADC values with tumour grade (197), however the minimum ADC values in this thesis appear to be physiologically too low (Grade II = 0.402, Grade III = 0.408, Grade IV =$0.099x10^{-9}mm^2s^{-1}$) . Blood vessels, calcification, blood products and noise could all cause a decrease in the observed minimum ADC value.

Longitudinal and Radial Diffusivity

Mean longitudinal λ_L and radial λ_R diffusivities were also examined, with the GMM subpopulation, **TUM_0** of the radial diffusivity significantly corresponded with grade. The rationale behind the radial diffusivity being related, is most likely due to the parameter being weighted towards the lowest ADC values which arise from eigenvalues 2 and 3 (λ_2 and λ_3) of the diffusion tensor. Given previous studies (77), which demonstrated the relationship between ADC and grade, it is maybe not surprising that the radial diffusivity is also significantly related to grade. The longitudinal diffusivity is weighted towards the fibre tract directionality (λ_1) and so the fact this parameter does not correlate with grade is perhaps not unexpected.

Radial diffusivity measured using **NEL_0** and **NEL_1** was significantly different between tumour grades, however, mean radial diffusivity using any variation of a **CEL** VOI did not significantly differentiate between grades. Min *et al* (199) examined ADC, FA, λ_L and λ_R values of oedema caused by a range of neoplasms, reporting the regression coefficient of λ_R vs. λ_L to be significantly higher in high grade gliomas than non-infiltrating lesions such as meningiomas and metastases. As discussed in the ADC results, the absence of relationship between **CEL** ADC values and grade could be related to tissue perfusion increasing the ADC values in high grade lesions, enhancement in apparent low grade

lesions actually representing higher grade transformation or a mismatch between the VOIs and the correct region on the DTI due to excessive geometric distortion. Mean values using **NEL_0** were also significantly associated with grade in a similar manner to **TUM_0**.

Standard deviations of radial diffusivity for **TUM** were significantly different between grades, possibly relating to tumour heterogeneity again. However, grade III tumours had lower standard deviations than grade II and IV tumours. This may be related to the volume ratio of tumour to oedema associated with the grade III tumours. Alternatively, this could relate to the pathology classification of tumours, given oligodendroglial tumours are only classified as grades II and III, whilst astrocytic tumours and reach grade IV. Grade IV tumours normally have macroscopic necrosis present, unlike grade III lesions, which subsequently increases the apparent diffusivity and thus the standard deviation. Skew and kurtosis of radial and longitudinal diffusivity values were not related to grade, and in a similar manner to ADC measurements, minimum values of longitudinal and radial diffusivities correlated significantly with grade, though values are more likely to represent artefact or blood products than tumour. Standard deviations of both longitudinal and radial diffusivities significantly differed between grades for **CEL**, **CEL_0** and **CEL_1**. Examination of the standard deviation values revealed an increasing trend with grade indicating higher levels of heterogeneity in more malignant lesions. One possible explanation could be that the diffusion imaging is more sensitive to regions of necrosis starting to form within the enhancing part of the tumour which is more likely in higher grade lesions. It is known that tumours can initiate cell death by autophagy to allow the peripheral regions to continue to grow and maintain sufficient blood supply.

Fractional Anisotropy, Anisotropic Component of Diffusion and Relative Anisotropy

Mean FA and RA values (fibre directionality) were both significantly related to lesion grade using the **TUM** VOI. Both of these parameters increased with grade with similar findings shown using **NEL**. Subpopulations of the **TUM** VOI also followed this trend (**TUM_0** and **TUM_1**) with GMM

subpopulations of q also following this pattern. This can be explained by the increased amounts of oedema associated with higher grade lesions causing more normal appearing white matter to be included in the T_{2all} VOI. It is possible that oedema does not decrease the measured values of fibre directionality as much as solid tumour, and so FA and RA, appear to increase with grade. Inoue *et al* (196) have previously reported increased FA and decreased ADC associated with increasing glioma grade. Catalaa *et al* (188) also observed the same findings in the non-enhancing region of gliomas when examining RA. When comparing non-enhancing gliomas, FA was previously found to be higher in high grade gliomas compared to lower grade gliomas when examining the T_2 abnormality in a similar manner to the **TUM** VOI (200). Mean **CEL** values of FA, q or RA did not correlate with grade in this study.

Standard deviation values of FA, q and RA were only significantly different for the lowest population (**TUM_0**), which also increased with grade. This may be due to increased heterogeneity caused by tumour infiltration. **CEL**, **CEL_1** and **NEL_1** VOIs produced significant results for all three diffusion directionality parameters. Skew gave rise to more significant results for **TUM** and **TUM_0** FA. The same pattern was observed with the relative anisotropy; however, only **TUM_0** of q showed significant differences between tumour grades. Despite the close relationship between all 3 parameters only significant differences between the kurtosis of FA measurements and the lesion grade were found. This significance was observed for all three populations (**TUM**, **TUM_0** and **TUM_1**). Minimum and maximum values of FA, q and RA were found to have no significance when examining the relationship between MR parameter and grade. Given these parameters are measured from tissue that could potentially contain oedematous tissue (very low anisotropy) and highly directional white matter (very high anisotropy); it is not unexpected that minimum or maximum values did not show significance differences between grades.

R_1 Measurements

Measurements of mean R_1 using **TUM** VOIs were found to relate to the tumour grade as did measurements of R_1 from **TUM_0**, with similar patterns seen for **CEL**, **CEL_1**, **NEL** and **NEL_0**. Historical data measuring glioma T_1 relaxation times at 1.5T (201) shows a similar trend once the reciprocal of the R_1 was calculated, however the values measured are quite different due to field strength, ROI size and measurement technique. The standard deviations of R_1 from **TUM** and **TUM_0** did not show a trend with grade, however mean **CEL** and **NEL** VOI values did significantly increase with grade suggesting R_1 measurements could be used for grading of new lesions. Skew was significant for the whole **TUM** and **TUM_0**, while the kurtosis of **TUM_1** was found to be significantly related to tumour grade.

Dynamic Contrast Enhanced Parameters

The most significant set of results relating MR findings to grade stems from the DCE datasets. K^{trans}, v_e and v_b were all significantly associated with grade ($P<0.001$) for all populations (**TUM**, **TUM_0** and **TUM_1**) (Figure 106), with standard deviations of each parameter also showing significant differences between grades. This may be related to the range of values; whereby large mean values are also more likely to have larger standard deviations. This has previously been described as measurement error proportional to the mean (202, 203). Previous studies also report significant correlations between K^{trans} and tumour grade (66, 92, 93, 204, 205). Whilst Jung *et al* (205) showed encouraging results, questions regarding the available SNR should be raised when the data was acquired at a temporal resolution of 2.25s and 3mm thick slices. Skew and kurtosis values of these parameters were mainly found to be significant as well, however no linear trend is visible. The DCE data suggests tumour vasculature increases with grade; however this increase is quite heterogeneous within the lesion and between grades. Maximum values of K^{trans}, v_e and v_b significantly differed between glioma grades ($P<0.001$). Statistical descriptors of PK parameters sampled with **CEL** were also significant

between with grades. Given contrast enhancement is associated with higher grade gliomas (194), it is maybe not surprising that DCE parameters sampled with **CEL** were associated with tumour grade. A possible reason for the higher p-values compared to **TUM** relates back the number of patients who have a glioma with contrast enhancement, which caused the lower grade groups to have N reduced. The potential of an imaging-histology mismatch would also cause an increase in the p-values for the **CEL** based statistical descriptors.

Relative Cerebral Blood Volume Measurements

Upon examination of the DSC derived blood volume, rCBV and $rCBV_{BOX}$; the mean values from the **TUM** and $\mathbf{TUM_1}$ VOIs significant increased with grade as expected (12, 88, 188, 192). However, given our DSC data was acquired after a contrast agent preload (¾ dose of gadolinium), the differences between rCBV and $rCBV_{BOX}$ are not as apparent in our data as with Boxerman's study (12). Alternative sampling schemes may also help to explain the differing values between this study, when compared to those of the literature. $\mathbf{TUM_0}$ of this parameter may actually represent apparently normal brain tissue which is why it does not correlate with glioma grade. Leakage defined by K_2 was also found to relate to grade, with more negative values (T_2* dominant leakage) observed in high grade lesions. Standard deviation measurements of these 3 parameters followed the same trend as the mean measurements. Skew and kurtosis were not related with the exception of the $\mathbf{TUM_1}$ K_2 kurtosis values. Maximum rCBV was significantly linked to grade, while minimum K_2 was also significantly related to grade. Friedman (192) reports a similar correlation for maximum normalised rCBV with GII, GIII, GIV = 7±5, 4±1, 12±7, r=0.557, P<0.0001, compared to the maximum rCBV of GII, GIII, GIV = 8.5, 11.7, 16.4, P=0.003 in this study. Cha (206) also reported a significant difference between glioma grades with their Kruskal-Wallis test for $rCBV_{max}$ (P=0.03). Differences arise however, in the choice of statistical test. This study used Kruskal-Wallis to test between groups which are non-uniformly distributed; whist Friedman used a Spearman rank correlation. The values Friedman reports are means rather than the median values used in this study, which are considered

more appropriate for reporting values for small non-Gaussian populations. The spearman rank correlation test used to test grade vs. maximum rCBV value may be inappropriate given the distribution of cases between the various grades, with 35/47 cases being grade IV. Interestingly, mean/median CBV measurements made using a **CEL** VOI did not significantly differ between glioma grades. A possible explanation could relate to the geometric distortion present in the DSC datasets. Given rim enhancement observed in gliomas is usually quite linear as a result of the necrotic centre in high grade gliomas, any mismatch between the VOI and the DSC data would result in incorrect sampling of the desired tissue. In conjunction with this, the DSC measures the local susceptibility effect in tissue adjacent to the vessels meaning CBV maps may not align correctly, even if a non-EPI sequence was used.

7.2.5 General Comments on the Methodology

From this section, it has been demonstrated that a volume of interest approach can be used for glioma grading without the necessity of identifying hotspots or small ROIs (198). This means that automated volumes of interest could be generated in the future for subsequent automatic tumour grading. The advantages of a VOI approach include a methodology that could be used in multi-centre trials whist not being as subjective as a hotpot ROI approach. In general, from examination of the summary tables, parameters generated from the diffusion tensor imaging showed more significant differences between grades using a **NEL** VOI. DCE and DSC derived parameters, however, performed better when using the **TUM** VOI. The use of a single VOI, either **TUM** or **NEL** to sample a 4D volume appears promising based on the number of significant results generated in this section. This could have large time saving benefits in future studies as well as being easy to implement in image analysis software. The single VOI approach is extremely useful for interrogating large datasets, which MR will continue to produce for the foreseeable future. It also has utility in sampling spatially lower resolution data such as CBF maps derived from arterial spin labelling.

The use of Gaussian mixture modelling (GMM) to identify subpopulations is worthy of further investigation. One example where a GMM improved the differentiation between MR parameter and tumour grade was the mean radial diffusivity values. Mean values measured using **TUM** did not significantly differ with grade. However, once the GMM was applied and subpopulations of the parameter generated, both $\mathbf{TUM_0}$ and $\mathbf{TUM_1}$ showed differences between tumour grades. The significant differences between MR parameters derived from EPI sequences and lesion grade also suggest the registration process employed in this study does not destroy differences in tissue parameters. Likewise, the motion correction scheme implemented in this study can also be used to examine gliomas.

Finally, it is worth noting that previous studies (80, 88, 118, 193, 207, 208) of glioma grading report differentiation of low and high grade gliomas (II vs. III & IV). This grouping mechanism may enable higher sensitivity and specificity values to be produced. In this thesis however, gliomas of differing grades as categorised by the World Health Organisation (6) were treated independently. This decision was made, based on the expected survival times associated with each grade of glioma as well as the potentially different treatment regimens associated with each pathology.

7.2.6 Conclusions

- The combination of processing and sampling methods for the DCE, DSC, and DTI as detailed in chapter 6 produced multiple significant differences between glioma grades.
- At least 1 statistical descriptor for each MR parameter found differences between grades.
- The **TUM** VOI yielded the highest number of significant results when relating MR parameters to tumour grades (103/195) and also had the lowest False Discovery Rate (2.5%).
- Mean, median and standard deviation produced the greatest number of significant results when using the **TUM** VOI.
- The use of Gaussian mixture modelling to exam sub-populations within tumours can improve glioma grading e.g. mean radial diffusivity.

Parameter Specific Comments

- **TUM_0** and **NEL_0** were the most useful VOIs to measure mean/median ADC values for glioma grading
    - Perfusion effects may artificially increase ADC values within **CEL**
    - **TUM_1** and **NEL_1** are more likely to represent oedema and low grade disease. Mean values did not correlate with grade
- Radial diffusivity appears to be a more significant parameter for glioma grading than ADC values
    - **NEL_0** is the optimal type of VOI to measure mean/median radial diffusivity values for glioma grading.
    - Radial diffusivity excludes λ_1 (which normally represents normal white matter tracts) from the diffusion calculation improving grading.
- Longitudinal diffusivity does not appear to be a useful parameter for glioma grading
- **TUM** and **NEL** are the best VOIs to assess tumour grade using FA, q and RA.

- p-values of q using **TUM** were more significant than those of FA and RA
- Using **NEL** and **NEL_0**, FA, q and RA all showed more significant differences between tumour grades ($P<0.001$)

- Mean R_1 using **TUM** VOIs were found to significantly differ between tumour grades
- Mean/median K^{trans}, v_e and v_b all significantly associated with grade ($P<0.05$) for all populations ((**TUM**, **TUM_0** and **TUM_1**)/(**CEL**, **CEL_0** and **CEL_1**)/(**NEL**, **NEL_0** and **NEL_1**)), with most populations $P<0.001$.
  - p-values were higher (less significant) in **CEL** VOIs than **TUM** and **NEL** VOIs for PK parameters.
  - v_e produced more significant results than K^{trans} and v_b.
- rCBV and $rCBV_{BOX}$ produced the highest number of significant differences when sampled using **TUM** and **TUM_1**.
  - Maximum $rCBV_{BOX}$ values distinguished between tumour grades whilst maximum $rCBV_{GVF}$ values did not.
- K_2 showed the most significant associations with tumour grade from the DSC derived parameters.

7.3 Logistic Regression of Multiparametric MR for Glioma Grading

7.3.1 Introduction

As previously demonstrated in this chapter, multiple preoperative MR parameters significantly differed between tumour grades. This is particularly important for non-resectable lesions, or tumours located in eloquent regions of the brain which can only be partially resected. This section uses logistic regression to combine parameters into a single model to enable multiparametric grading, which has previously been demonstrated in the prostate using T_2 weighted imaging in conjunction with DCE and DWI (209), and the brain using morphological imaging (210) and blood volume measurements (66).

7.3.2 Methods

Initially data was processed in the same manner as section 7.2.2, with the most significant results for each parameter providing input for a logistic regression model using a backward Wald methodology. A two-step decision tree was used to predict lesion classification. The first logistic regression model was to split grade IV lesions from lower grade tumours (II and III). Following this, a second logistic regression model was used to split grade II and III lesions. The most significant VOI for each parameter was retained when multiple VOIs showed significant associations with grade.

7.3.3 Results

Following non-parametric Kruskal-Wallis tests, 29/39 parameter means significantly differed between grades. Table 15 shows the list of parameters and the volume of interests (VOI), which served as input to the logistic regression model. These were the most significant VOIs for each parameter as defined by TUM. Using multiparametric MR, 82.8% of cases were correctly classified (Table 17) using the two-step logistic regression model decision tree. Key parameters for the first logistic regression model, which split grade IV lesions from grade II and III lesions (Table 16) were q, λ_R, K^{trans} and v_e, (Equation 46) whilst ADC allowed the distinction between grade II and III tumours.

Table 15 - Kruskal-Wallis tests comparing differences between tumour grades and MR parameters. The values in the parenthesis denote the number of patients in each group while the number outside is the tumour grade.

PARAM.	VOI	2 (10)	3 (12)	4 (33)	Sig. P=
		Median	Median	Median	
ADC	**TUM_0**	1.206	1.061	1.003	0.012
FA	**TUM**	0.165	0.186	0.206	0.003
q	**TUM**	0.295	0.285	0.341	0.002
RA	**TUM_0**	0.099	0.111	0.138	0.002
λ_R	**TUM_0**	1.067	0.982	0.891	0.003
R_1	**TUM_0**	0.600	0.654	0.753	0.012
K^{trans}	**TUM**	0.028	0.036	0.087	<0.001
v_e	**TUM**	0.039	0.051	0.158	<0.001
v_b	**TUM_0**	0.020	0.019	0.034	<0.001
$rCBV_{GVF}$	**TUM_1**	2.573	2.801	3.629	0.003
$rCBV_{BOX}$	**TUM_1**	2.432	2.795	3.244	0.013
K_2	**TUM_0**	-1.010	-1.379	-1.956	0.001

Table 16 - Logistic regression model 1, split grade IV lesions from lower grade tumours (left). Logistic regression model 2, split grade II lesions from grade III tumours (right).

Observed	Grade		Predicted		
			Grade		% Correct
			2+3	4	
		2+3	20	2	90.9
		4	2	31	93.9
Overall %					92.7

Observed	Grade		Predicted		
			Grade		% Correct
			2	3	
		2	7	3	70.0
		3	3	9	75.0
Overall %					72.7

Output for logistic regression analysis for grades 2+3 vs. 4 with 0.5 cut-off utilising a backward Wald methodology

$$-1.223 + (19.291 * \mathbf{q\_TUM}) + (-6.887 * \mathbf{\lambda_R\_TUM_0}) + (-163.500 * \mathbf{K^{trans}\_TUM}) + (124.824 * \mathbf{v_e\_TUM})$$

Equation 46

Output for logistic regression analysis for grades 2 vs. 3 with 0.5 cut-off utilising a backward Wald methodology

$$8.009 + (-7.034 * \mathbf{ADC\_TUM_0})$$

Equation 47

Table 17 – Combined tumour classification using 2-stage logistic regression model

Grade			Predicted Group Membership			Total
			2	3	4	
Original	Count	2	8	2	0	10
		3	5	6	1	12
		4	1	1	31	33
	%	2	80%	20%	0%	100%
		3	42%	50%	8%	100%
		4	3%	3%	94%	100%

82.8% of original grouped cases correctly classified.

7.3.4 Discussion

The multiparametric MR acquired in this study can be used to classify lesion grade. Parameters derived from DTI and DCE (ADC, q, λ_R, K^{trans} and v_e) appeared to be the most useful for this cohort of patients. DSC parameters may have been too similar to DCE parameters to be used in the final model as described in section 7.1 - Correlations Between MR Parameters, page 185. The initial p-values of DCE parameters were much smaller than those of the DSC and the logistic regression model may have reflected this. These findings are the reverse of Law *et al* (66) from 2004 which found rCBV to correlate with tumour grade better than K^{trans}. Differences between this study and the paper by Law *et al* include reclassification of tumour grades (GBM were WHO III at the time of print in 2004), increased field strengths (3.0T vs. 1.5T), calculation of K^{trans} from T_1 dynamic data rather than T_2* whilst rCBV was calculated from T_2* data in both studies and a shift to volumetric analysis compared to user defined ROIs. Law *et al* used a much higher temporal resolution (1 second compared to the 2 second temporal resolution employed in this study) for the DSC data and 5 second temporal resolution for the T_1 dynamic imaging, however they failed to correct for leakage effects by preloading the tissue with gadolinium. There is less literature about q and λ_R as historically DWI was used in favour of DTI due to lower field strengths and subsequently the longer acquisition time

required for DTI. Even in studies that utilised DTI, FA was often used due to the availability of parameter maps produced by scanner manufacturers.

Disappointingly, 42% of grade III lesions were classified as grade II using the logistic regression model developed by the data. This possibly reflects the ability of MR to detect small regions of transformation within a larger grade II tumour. The VOI approach chosen in favour of a hotspot methodology will contribute to some of this under-grading, with the grade II component being more prominent in the volume histograms. A further consideration for the poor differentiation of grade II and III lesions relates to considerable overlap in source data (Table 15) which saw closely paired data between grade II vs III or grade III vs IV values for 6/12 parameters. A greater number of grade II and III lesions may have improved the model for separating the two pathologies, however the number of patients in each group was a fair reflection of the split of glioma grades seen at this institution. As discussed, the spatial resolution of the MR data and the volumetric approach means this methodology is most likely not going to be sensitive to small regions of cellular change which would cause a tumour to receive a higher grade than the MR would suggest, due to partial volume effects and the statistical processes employed in this study. However, the advantage of this methodology is that it can be easily automated in the future for a potential computer aided diagnosis (CAD).

Higher values of q, the anisotropic component of diffusion, possibly relate to the greater volume of oedema associated with higher grade lesions. The ability to identify grade IV lesions using multiparametric MR appears to be excellent (94%). This work demonstrates that multiparametric MR could be used to grade lesions where tissue samples are unavailable. The same parameters could also be used to identify transforming lower grade lesions.

Interestingly, radial diffusivity and anisotropic component of diffusion were useful parameters for logistic regression modelling which are not available using conventional DWI. Therefore DTI should

be used instead of DWI for the grading of gliomas. This would also results in maps of the fibre tracts being available for surgeons to reduce surgical morbidities when operating in eloquent regions of the brain.

With key sequences identified for tumour grading, further efforts can be spent optimising the sequences further by correcting for geometric distortion and IVIM in the diffusion datasets as well as optimising the slice thickness and number of directions in the protocol. Methods for accelerating the DCE further whilst extending the spatial coverage should also be further investigated as techniques such as compressed sensing continue to develop.

7.3.5 Conclusions

To summarise, quantitative preoperative MR parameters can predict glioma grade with 83% accuracy. DTI, DSC and DCE were all shown to have added value for glioma grading when used individually, however for improved grading using logistic regression modelling; only DCE and DTI are required. Further efforts should be made to develop these sequences further. Grade IV lesions were identified with 94% accuracy which could be of use to clinicians when determining scan frequency and adjuvant treatment.

7.4 Single Voxel TEA-PRESS

7.4.1 Introduction

Short echo time spectroscopy (25-40ms) has been shown to have clinical utility for glioma grading given the increased sensitivity to metabolites with shorter T_2 relaxation times such as lipids and myo-inositol (37, 100, 105, 211) (Figure 110). However, acquisitions at shorter echo times are also more sensitive to eddy currents and macromolecules, often resulting in poor baselines. TE-averaged PRESS acquires spectra using a range of echo times, allowing the generation of a short echo time weighted spectrum with an improved baseline. This flatter baseline can be used for improved quantification to allow lesion grading.

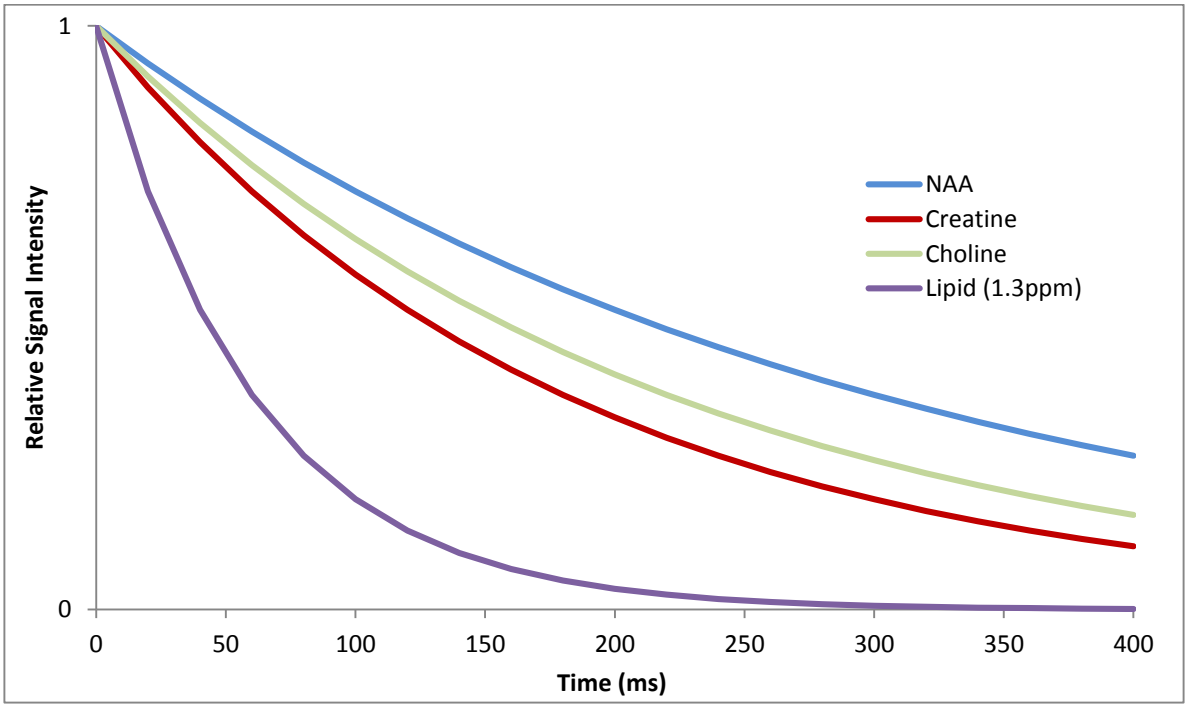

Figure 110 – 3.0T T_2 relaxation curves for NAA, creatine, choline and lipid. These show how increasing the echo time will attenuate the signal for all metabolites but at varying decay rates. The figure also demonstrates the necessity of short echo times to measure metabolites with a short T_2 relaxation time. The values used to generate the curves were taken from (212) (300,180,220ms for NAA, creatine and choline). Lipid T_2 was estimated to be in the order of 60ms based on the author's experience.

7.4.2 Methods

A total of 55 histologically proven gliomas had single voxel spectroscopy prescribed as part of a more extensive multiparametric study. All data were acquired prior to surgery using a 3.0T MR750 Discovery system (GE Healthcare, Waukesha, WI, USA) and an 8 channel phased array head coil. Whole brain, oblique axial, T_2 weighted FLAIR imaging. Echo time averaged point resolved spectroscopy (TE-averaged PRESS, TR=1200ms, 24 echoes, initial TE=40.18ms, TE step=9.984ms, 12 signal averages per echo time) was used to prescribe a voxel in the centre of lesions based upon FLAIR imaging attempting to avoid areas showing cystic cavities. Spectra were processed using Spectral Analysis by General Electric (SAGE), version 7 (GE Medical Systems, USA). Signal from each element was combined in the time domain using a signal weighting algorithm that scaled each element according to the average magnitude of the first 5 points of each echo. Averaged spectra of the 24 different echo times were presented to LCModel for quantification through the SAGE-LCModel interface (73, 74). Spectra were fitted with a TE=35ms basis set, 'tumor' (sic) control file and a calibration factor of 0.33. To make the data easier to manage, the output of each voxel (.tab file) was tabulated into a comma separated value (.csv) file.

Metabolites extracted for analysis were; myo inositol (mI), choline (Cho), creatine (Cre), glutamine and glutamate (Glx), N-acetylaspartate (NAA), lactate (Lac) and lipids (Lip1.3 & Lip0.9). Ratios are metabolites were also examined; Cho/NAA, Cho/Cre, Lip1.3/Cho, Lip1.3/0.9 and NAA/Cre. Non-parametric significance was determined using Kruskal-Wallis tests to examine any relationships between grade and MR parameter. The significant results were then the input for logistic regression models using a backward Wald methodology. A two-step decision tree was used to predict lesion classification. The aim of the first logistic regression model was to split grade IV lesions from lower grade tumours. Following this, a second logistic regression model was used to split grade II from III lesions. Spectroscopic and imaging parameters were subsequently combined and re-entered into a logistic regression model to see if a combination of imaging techniques improved glioma grading.

7.4.3 Results

In one case data was not acquired due to the excessively high line width reported during the auto prescan stage whilst attempting to acquire a spectrum from a temporal lobe gliosarcoma. Of the 54 datasets acquired, two spectra were of insufficient quality to quantify. One case was observed in a grade II oligodendroglioma which contained calcification and subsequently resulted in poor quality data with no observable metabolites. The other case was due to partial volume of a large cystic component associated with a GBM. This left 52 cases of sufficiently quality for analysis. Example spectra can be seen in Figure 111 and Figure 112. Interestingly, Figure 112 demonstrates the variability of the spectra produced by glioblastoma as lesions progress through various stages of necrosis caused by autophagy.

The results of the Kruskal-Wallis tests which examined the relationships of tumour grade with spectroscopic concentration and ratios can be seen in Table 18 with significant results ($P<0.05$) highlighted in red. Significant differences between glioma grade and metabolite concentrations were observed for myo-inositol, creatine, NAA, lactate and lipid (0.9 and 1.3ppm) concentrations. The ratios of lipid (1.3ppm) to choline, and lipid 1.3 to 0.9ppm concentrations were also significantly different between grades. NAA/Cre ratios were also determined to be significantly different between glioma grades. Kruskal-Wallis tests were also repeated for the data reclassified by cell type in Table 19 and Table 20. The small sample groups increased the p-values observed and skew the distributions of the data. The Kruskal-Wallis tests which examined the differences between tumour grade of astrocytic tumours with spectroscopic concentration and ratios can be seen in Table 19 with significant results ($P<0.05$) highlighted in red. The results are very similar to Table 18 given most tumours were of an astrocytic nature (40/52). Tumours which contain an oligodendrocytic component (oligodendroglioma, oligoastrocytoma, anaplastic oligodendroglioma and anaplastic oligoastrocytoma) were compared to spectroscopic parameters in Table 20, with only lactate and Glx significantly linked to grade.

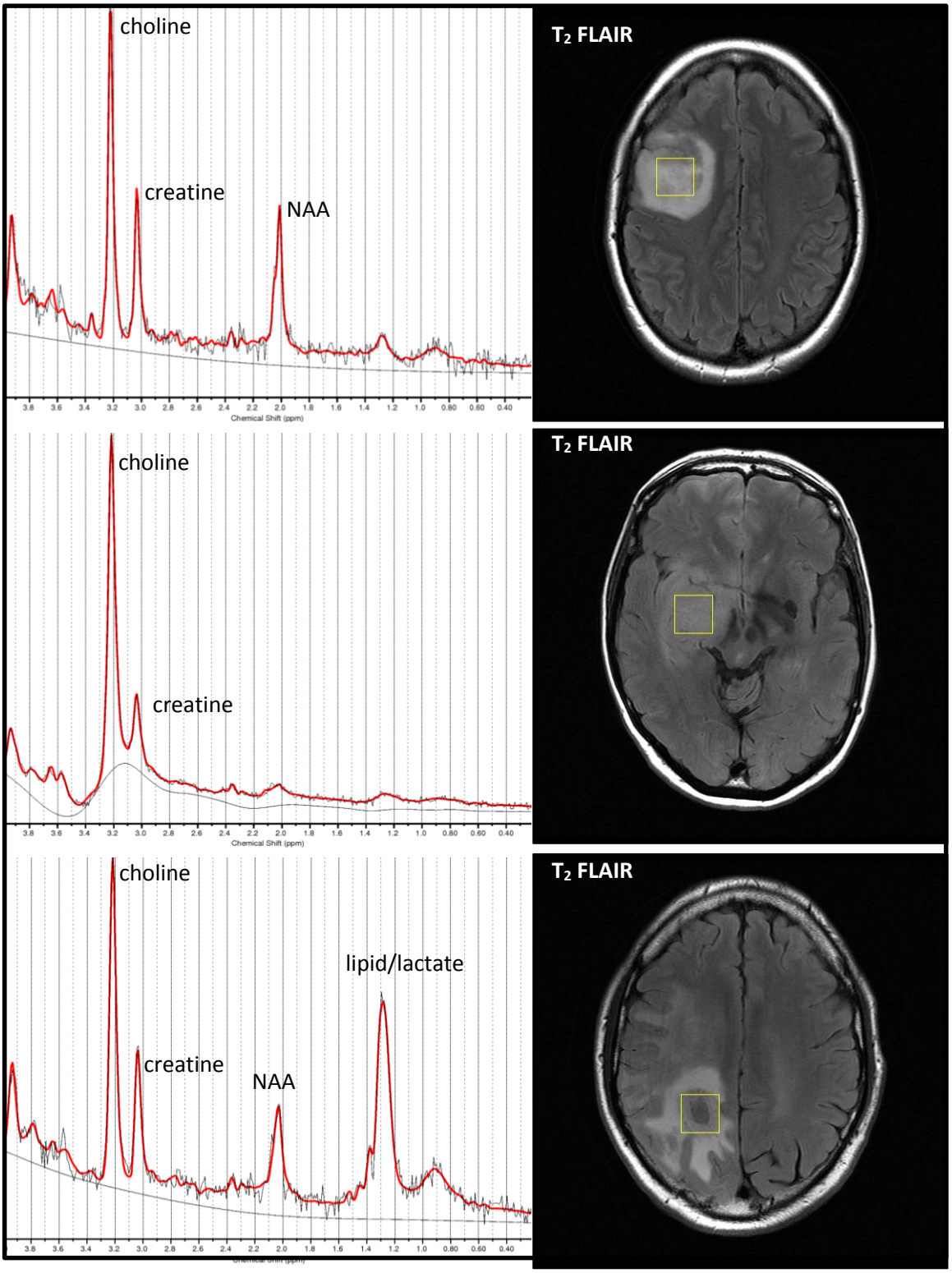

Figure 111 - Example LCModel fits of spectra and the respective voxel locations of grades II, III and IV gliomas (top, middle, bottom). The top case is a grade II oligodendroglioma, middle case is a grade III anaplastic oligodendroglioma whilst the bottom case is a glioblastoma (grade IV).

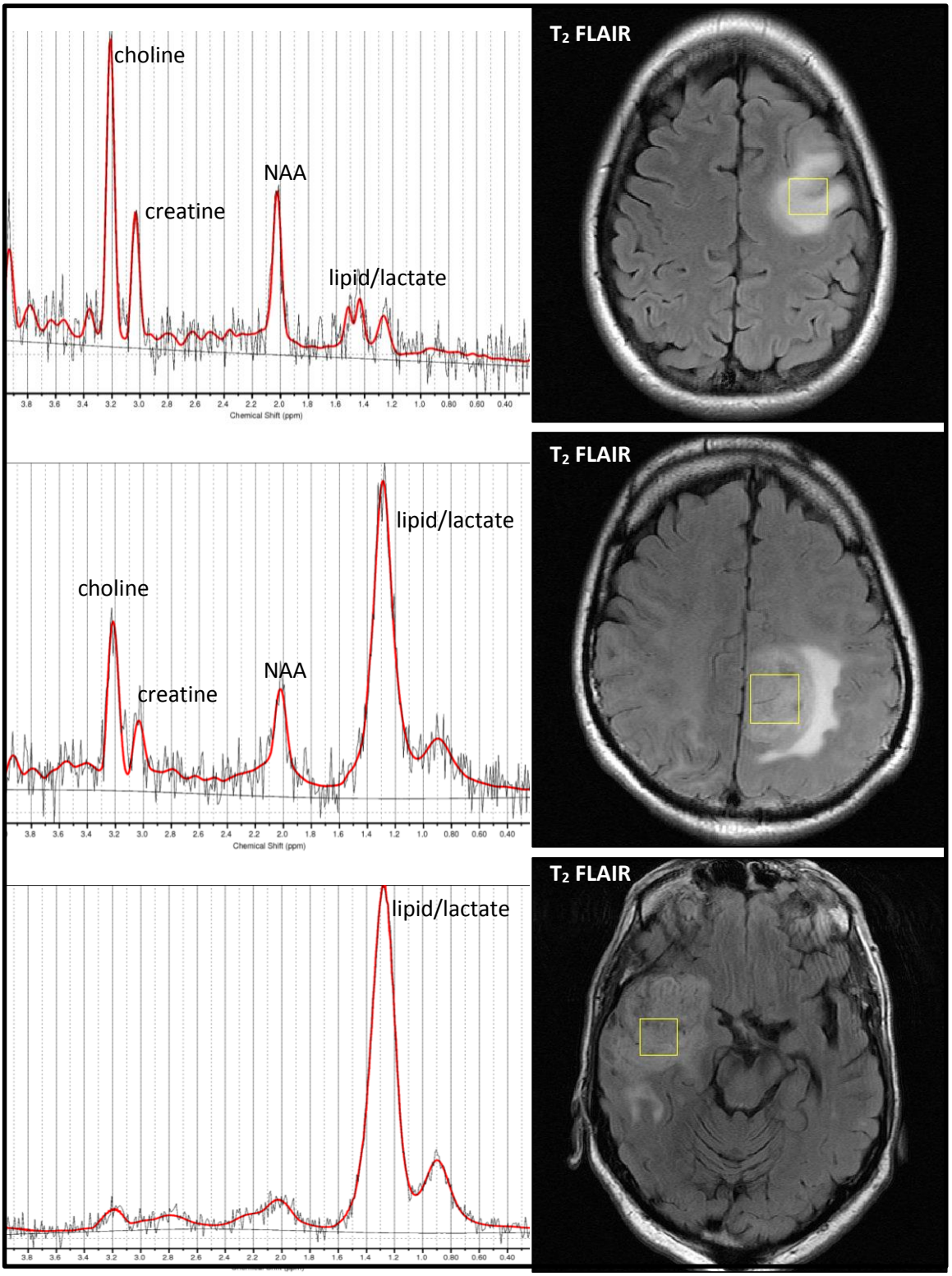

Figure 112 - Example LCModel fits of spectra and the respective voxel locations in 3 GBM patients. This figure demonstrates the variability of the spectra produced by glioblastoma as lesions progress through various stages of necrosis caused by autophagy.

Table 18 - Kruskal-Wallis test comparing metabolite concentrations with glioma grade. The values in parenthesis next to glioma grade denote the number of patients in each group.

MET.	WHO II (N=9)			WHO III (N=12)			WHO IV (N=31)			Sig.
	Min	Med	Max	Min	Med	Max	Min	Med	Max	
mI	0.157	2.074	3.041	0.381	2.057	8.968	0.000	0.102	4.579	0.001
Cho	4.048	5.166	7.610	1.998	5.689	23.754	0.561	3.672	9.855	0.132
Cre	5.313	6.874	12.540	3.179	9.223	15.984	0.000	3.748	16.625	0.022
Glx	0.000	3.856	10.269	2.147	5.045	12.511	0.000	4.355	14.594	0.330
NAA	2.185	4.727	10.268	0.997	5.921	10.708	0.000	1.694	9.841	0.002
Lac	0.000	0.312	2.268	0.000	0.000	2.266	0.000	5.226	73.208	0.001
Lip 1.3	4.638	5.827	11.983	1.191	6.820	152.926	4.888	63.497	221.481	0.001
Lip 0.9	2.583	3.498	7.121	1.030	3.255	14.546	1.509	10.526	26.322	0.001
Cho/NAA	0.420	1.182	3.221	0.285	0.897	23.825	0.000	1.401	3341.074	0.178
Cho/Cre	0.412	0.782	1.169	0.409	0.709	2.059	0.000	0.866	6.690	0.428
Lip1.3/Cho	0.648	1.128	2.708	0.486	1.167	34.931	0.847	15.232	311.843	0.001
Lip1.3/0.9	1.148	1.740	2.675	0.968	2.251	10.513	2.607	5.171	16.338	0.001
NAA/Cre	0.363	0.643	1.170	0.086	0.736	1.438	0.000	0.335	2.366	0.049

Table 19 – Relationships between metabolite concentrations and astrocytic tumours. The values in parenthesis next to glioma grade denote the number of patients in each group.

MET.	WHO II (N=4)			WHO III (N=5)			WHO IV (N=31)			Sig.
	Min	Med	Max	Min	Med	Max	Min	Med	Max	
mI	1.360	2.695	3.041	0.381	1.266	3.735	0.000	0.102	4.579	0.009
Cho	4.048	6.313	7.610	1.998	5.494	8.874	0.561	3.672	9.855	0.461
Cre	6.020	9.017	12.540	3.179	7.331	9.902	0.000	3.748	16.625	0.167
Glx	3.856	6.174	10.269	2.147	3.069	11.121	0.000	4.355	14.594	0.434
NAA	2.185	5.774	9.636	3.670	6.148	10.708	0.000	1.694	9.841	0.012
Lac	0.000	0.000	0.000	0.000	1.220	2.266	0.000	5.226	73.208	0.006
Lip 1.3	4.650	7.147	9.760	1.191	4.781	7.163	4.888	63.497	221.481	0.001
Lip 0.9	2.583	3.605	4.049	1.030	2.067	6.422	1.509	10.526	26.322	0.001
Cho/NAA	0.420	1.149	3.221	0.285	0.577	1.443	0.000	1.401	3341.074	0.107
Cho/Cre	0.412	0.644	1.169	0.409	0.749	0.896	0.000	0.866	6.690	0.404
Lip1.3/Cho	0.648	1.110	2.312	0.486	0.870	1.617	0.847	15.232	311.843	0.001
Lip1.3/0.9	1.148	2.270	2.675	0.968	1.527	4.642	2.607	5.171	16.338	0.001
NAA/Cre	0.363	0.560	0.981	0.621	1.154	1.438	0.000	0.335	2.366	0.037

Table 20 – Relationships between metabolite concentrations and oligo- and oligoastroglial cell type gliomas. The values in parenthesis next to glioma grade denote the number of patients in each group.

Metabolite	WHO II (N=5)			WHO III (N=7)			Sig.
	Min	Med	Max	Min	Med	Max	
mI	0.157	1.243	2.765	1.296	2.066	8.968	0.223
Cho	4.383	4.789	7.290	4.378	7.077	23.754	0.223
Cre	5.313	6.126	9.307	4.651	11.535	15.984	0.062
Glx	0.000	1.972	5.446	4.656	7.817	12.511	0.018
NAA	3.006	4.418	10.268	0.997	4.297	9.371	0.808
Lac	0.312	0.824	2.268	0.000	0.000	1.157	0.035
Lip 1.3	4.638	5.827	11.983	6.733	8.337	152.926	0.223
Lip 0.9	2.901	3.475	7.121	2.738	3.687	14.546	0.935
Cho/NAA	0.427	1.226	1.650	0.509	1.613	23.825	0.291
Cho/Cre	0.471	0.812	1.061	0.480	0.703	2.059	0.465
Lip1.3/Cho	1.054	1.128	2.708	0.488	1.178	34.931	0.935
Lip1.3/0.9	1.335	1.683	2.571	1.790	2.261	10.513	0.062
NAA/Cre	0.551	0.793	1.170	0.086	0.584	0.944	0.123

Logistic Regression of Glioma Grade

The significant metabolite concentrations and ratios from the Kruskal-Wallis tests as detailed by Table 18 were input into a backward Wald logistic regression model which attempted to split grades 2/3 and 4 gliomas. Subsequent splitting of grade II and III gliomas was not possible using the logistic regression as no parameters were kept by the model. Logistic regression of grades II and III vs. IV gliomas resulted in 81% of cases correctly classified (Table 21), however 7/13 parameters appear to have similar values between grade II and III lesions which reduces the correct classification ultimately. Following a joint logistic regression of spectroscopic and imaging parameters, all spectroscopic parameters were excluded from the model, producing the same results as section 7.3.

Grade 2+3 vs. 4 with 0.5 cut-off

$$-7.404 + (-0.162 * \text{Lip 1.3}) + (1.174 * \text{Lip 0.9}) + (1.553 * \text{Lip 1.3/0.9}) \quad \text{Equation 48}$$

Table 21 - Logistic Regression of TEA-PRESS parameters, and the ability to determine lesion grade.

Observed	Grade		Predicted		
			Grade		% Correct
			2+3	4	
		2+3	18	6	86
		4	4	24	77
Overall %					81

7.4.4 Discussion

Voxel Positioning

Spectroscopic data was acquired prior to contrast agent administration, given the potential of contrast agents to alter the apparent T_1 and T_2 relaxation times of metabolites in the brain. As a result, voxel positioning was determined by T_2 weighted FLAIR imaging, where the enhancing portion of a lesion is not usually apparent. Whilst efforts were made to sample the solid component of each lesion, regions of oedema and necrosis were included in some cases. Rotation of the spectroscopic voxel is not possible on a GE scanner at present (DV24.0), which also limits the quality of the prescription. Given the stated drawbacks of the voxel positioning, the under grading of lesions is perhaps not surprising. Seven out of 53 lesions were predicted to be a least 1 grade lower than the histology. In some cases this may have been due to voxel positioning errors, possibly missing the most malignant region the tumour, whilst on other occasions it may have been that the area of transformation was only apparent at a cellular level and the size of the voxel were simply too large to be sensitive to changes in small volumes of tissue.

Voxel Size

The acquisition of multiple echo times with sufficient SNR already requires a considerable amount to time (5-6 minutes). The implication of spatially encoding a second direction, is that the acquisition time increasing beyond clinical acceptable times, and hence the decision to remain with a single voxel approach. The drawback of the single voxel acquisition scheme is that the volume of tissue

required is greater than that of a multivoxel acquisition scheme, and so partial volume effects are present in this data.

Basis Set

Given the multiple echo times used in TEA-PRESS, a bespoke basis set would have been required for absolute quantification, however, the metabolite relaxation times in the brain metabolite phantom which belongs to the Centre for MR Investigations were quite different to those *in vivo*, rendering its use invalid. This resulted in a short echo time basis (35ms @ 3.0T) being chosen on the understanding that the values would not be comparable to those in the literature. However, for the purposes of this study, a systematic process for metabolite quantification was still possible. The quantification of J-coupled metabolites using this method should be viewed with caution due to averaging process employed in this methodology and cancellation effect on metabolites which demonstrate a signal evolution as a function of echo time (myo-inositol, lactate and Glx).

Relationships with tumour grade

The Kruskal-Wallis tests as shown in Table 18 highlighted significant relationships between glioma grade and myo-inositol, creatine, NAA, lactate and lipid (0.9 and 1.3ppm) concentrations. The ratios of lipid (1.3ppm) to choline, and lipid 1.3 to 0.9ppm concentrations were also significantly different between tumour grade as were NAA/Cre ratios. An increase in myo-inositol has previously been reported in low grade gliomas (213) which subsequently decreased with higher tumour grades (40). Likewise, increased lipid concentrations have been associated with high grade gliomas (37, 100, 214). However, Figure 112 demonstrates the lipid variability in glioblastomas and underlines the difficulty in using MRS to grade lesions. Howe *et al.* (100) reported increased choline concentrations between grade II and III gliomas with variable amounts of choline reported in grade IV lesions. Similar trends were found in this study, hence the high p-value and absence of relationship between the 3 different grades of glioma and choline concentration.

Oligodendrogliomas have previously been shown to have lower ADC values than astrocytomas (78, 79), suggesting they are a more cellular type of lesion compared to astrocytomas. Since choline is a marker of cell proliferation and density, oligodendrogliomas have the potential to have very high concentrations of choline (Figure 111) as a result of densely packed cells rather than increased cell proliferation. As a consequence, as seen in this study, choline may not differ with glioma grade, although in some multivoxel studies it was shown to correlate (188, 193). In some cases, choline was higher in grade II lesions than grade III lesions (Figure 114). The absence of a choline-grade relationship in this study also influenced ratios such as Cho/NAA and Cho/Cre, and their association with grade. Previous work suggests Cho/NAA can be used to identify lesion grade and extent (96, 118, 215), however this was not reflected in this study. One of the major limitations of assessing tumour grade using the total choline visible from proton MR, is the difficulty in distinguishing between phosphocholine (PC) and glycerophosphocholine (GPC). PC is known to relate to cell density and is normally the largest choline resonance in low grade gliomas, whilst GPC is representative of proliferation in tumours and increases in high grade gliomas (32). At 7.0T and below, resolving the 3 types of choline is impossible as the chemical shift separation which is proportional to the field strength is minimal between the 3 resonances (Figure 113).

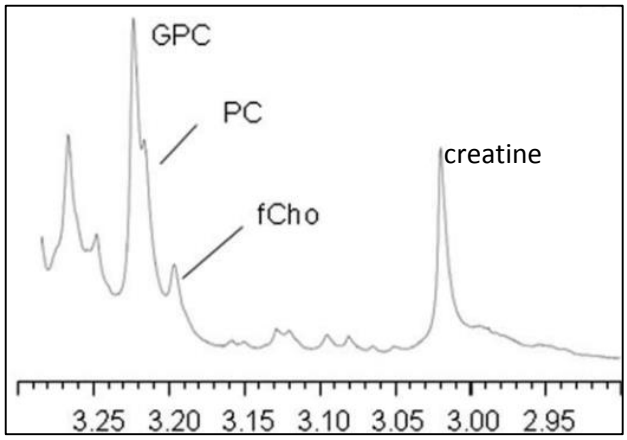

Figure 113 - Spectrum from a non-enhancing portion of an anaplastic astrocytoma acquired using a 500Hz (11.8T) scanner. The 3 choline resonances seen are glycerophosphocholine (GPC), phosphocholine (PC) and free choline which overlap even at high field strengths. Reproduced from (32).

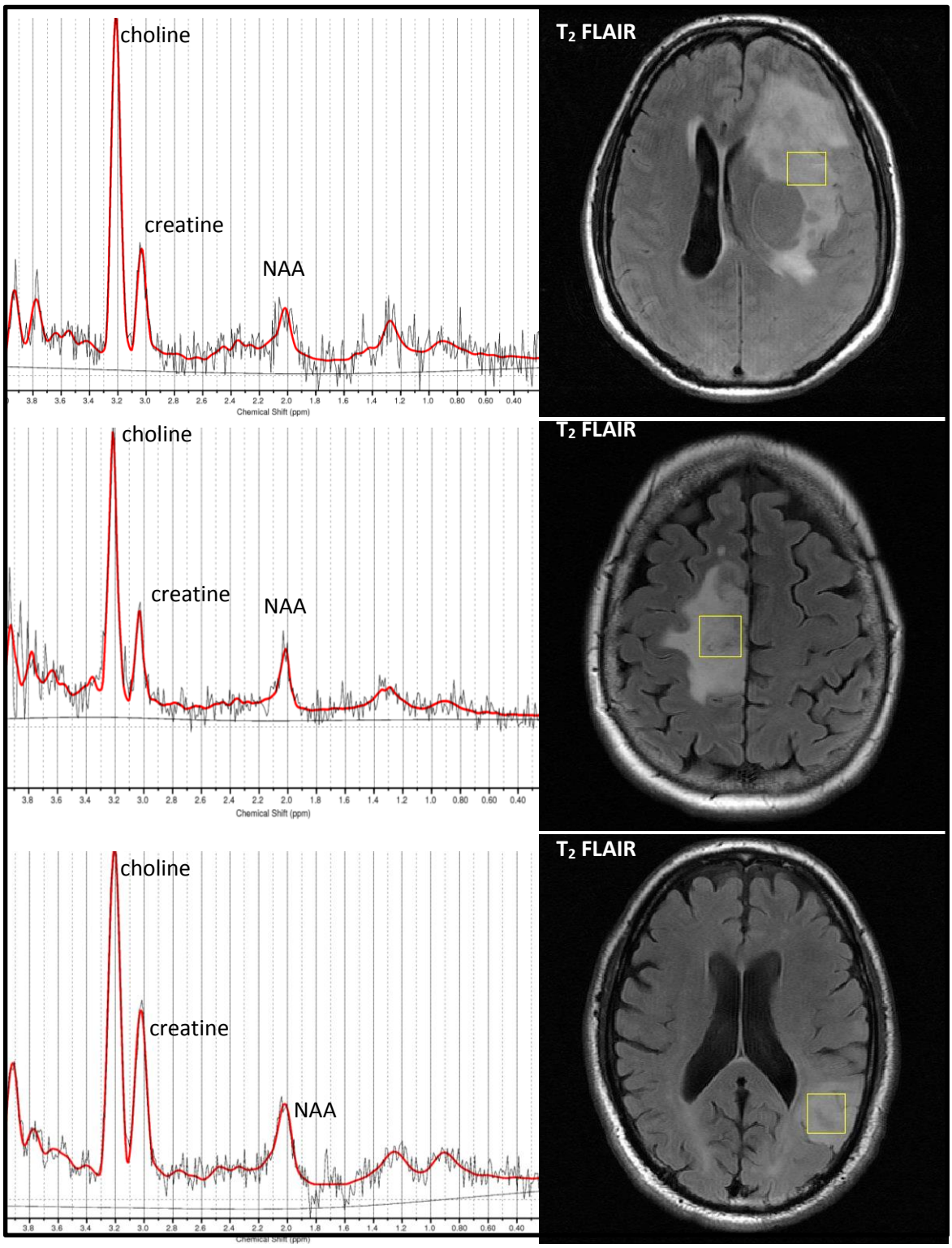

Figure 114 - Example spectra and the voxel prescription in two grade II gliomas (top & middle) and one grade III glioma (bottom). The top case is a diffuse astrocytoma, whilst the middle case was an oligodendroglioma. The bottom case was an anaplastic oligodendroglioma (grade III). Despite the difference in cell type and grade, all of the above spectra share a similar appearance.

Logistic Regression to determine glioma grade

Lipid resonances at 1.3 and 0.9ppm and the ratio of the 2 peaks were determined as the significant components used to identify grade 4 lesions. This suggests that both the concentration of lipid and the chain length of the lipid molecules which is reflected in the 1.3/0.9 ratio can be used for to identify grade 4 lesions. Opstad *et al* (112) have previously described a technique for differentiating glioblastomas and brain metastases from the ratio of lipid peaks using short echo single voxels spectroscopy at 1.5T.

Using the logistic regression model, 81% of cases were correctly classified. These findings relate to the amount of necrosis that MR is sensitive to, with one of the manifestations being an increase in the number of lipid droplets within tissues. In normal brain tissue, lipid is not measurable *in vivo* using MR due to the limited mobility of the molecules, however, following cell death the membranes of the cell breakdown, releasing mobile lipid droplets into the extracellular, extravascular space which are then detectable by ^{1}H MRS Figure 112. Lipid detected using proton spectroscopy has been shown to be the result of cell necrosis (36, 37) and importantly, the amount of lipid observed is proportional to the extent of necrosis (38) in the tissue. The presence of detectable lipid concentrations preoperatively has also been shown to correlate with higher grade tumour (39). However, the presence of lipid resonances in the spectrum of Figure 115 caused a complete overestimation of the lesion grade (predicted IV) which was histologically found to be grade II.

Due to the small grade II and III populations, in combination with the cell types contained with each grade, a logistic regression model was unable to identify grade II lesions from grade III lesions as seen in Figure 114. Further consideration is needed for the WHO grading of different cell types. Astrocytic tumours can be graded up to IV whilst oligodendrogliomas only reach grade III, therefore a necrotic anaplastic oligodendroglioma would still be graded as a III despite appearances of a grade IV.

The addition of single voxel spectroscopy does not improve the ability to grade gliomas when added to functional imaging parameters. The limited coverage, removal of heterogeneity and pre-contest voxel prescription all limit the quality of the spectroscopic data compared the volumes of interest contoured for the other parameters which encompassed the whole abnormality. In the future, multivoxel spectroscopy may perform more favourably as tumour heterogeneity is retained.

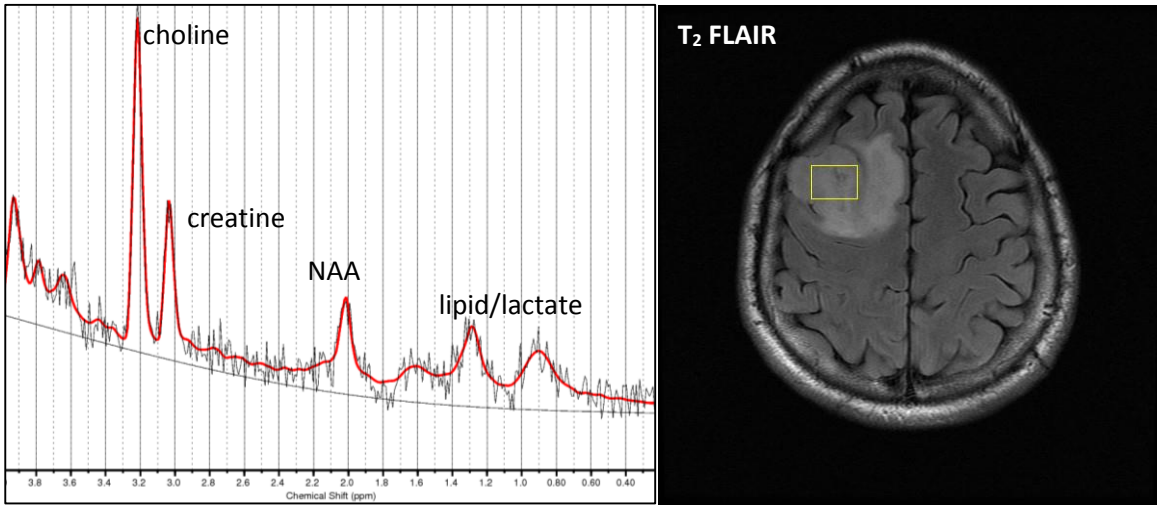

Figure 115 - Example case where logistic regression analysis failed to correctly identify lesion grade. Histology revealed the lesion to be a grade II oligoastrocytoma, however, the resonance at 1.3 and 0.9 ppm were identified as lipid causing the spectra caused it to be classified as a grade IV lesion using the model.

7.4.5 Conclusions

The quantification of the TEA-PRESS using an averaged spectrum and LCModel, produced mixed results, some of which was comparable to multiparameter MR data where grade IV lesions were mainly able to be correctly identified (81% accuracy). Grade II and III lesions were more difficult to distinguish most likely due to voxel placement, partial volume effects, and the considerable overlap in concentrations between grade II and III lesions (7/13 parameters had similar values). Improved spatial resolution is needed to correctly identify focal regions of anaplasia within these heterogeneous tumours in order to reflect the WHO grade they subsequently receive. 3D-MRSI is one solution to the issue of heterogeneity, however the technique has its own issues with planning and quantification.

7.5 Case Studies

This section details cases from the study where MR imaging and histology appeared to show levels of disagreement or resulted in suboptimal data acquisition. These cases have been chosen to show the pitfalls of both MR and histology, and the subsequent mismatch in grading that is possible.

In the first case presented (Figure *116*), the histology of the lesion was found to be a grade II diffuse astrocytoma. However, the patient only received a partial resection meaning the higher grade cells may not have been sent to neuropathologist for grading. From the preoperative imaging, a small region of enhancement was present in the deeper aspect of the tumour which also shows restricted diffusion and a small focus of increased $rCBV_{BOX}$. Sampling of this small region may have result in an increased grade. During the clinical scans at 6, 9 and 12 months, various small enhancing foci around the surgical cavity were observed.

The second case (Figure 117) shows a large diffuse bilateral abnormality initially thought to be gliomatosis cerebri. No visible contrast enhancement was observed on the preoperative scans, whilst ADC values were increased throughout the lesion and no obviously increased rCBV values in the lesion. Histology of lesion was found to be an anaplastic astrocytoma grade III due to the presence of mitotic figures and a focus of increased cellularity. The 3mm slice thickness of the DTI in combination with noise and resolution meant that MR would not have been sensitive to small focal regions of increased cellularity.

The final case (Figure 118) presented shows some of the problems of MR spectroscopy and voxel placement prior to the acquisition of contrast enhanced images. The proteinaceous necrotic fluid meant that the signal was not supressed on the FLAIR imaging, giving the impression of solid tissue. Following data acquisition and retrospective analysis, the PRESS box can clearly been seen to only include necrosis and no active tumour. Whilst this is fine if grading a known untreated glial lesion,

once treatment is given, radiation necrosis would prevent lesion grading using spectroscopy as no active tumour was present in the prescription box.

7.5.1.1 Case 1. Tissue sampling limitation

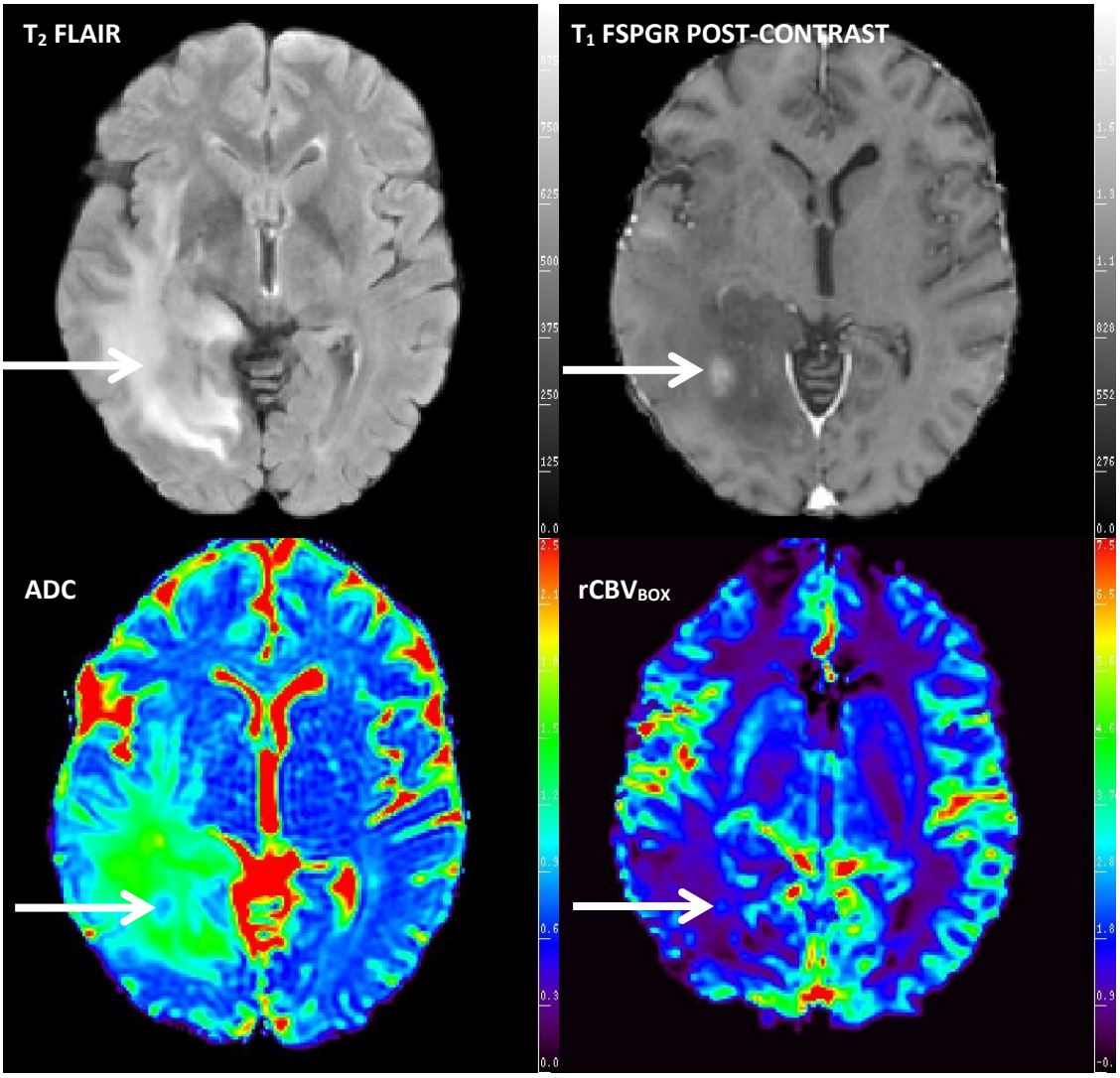

Figure 116 - *This example shows a study patient with a WHO grade II lesion, classified using tissue sampling from a partial resection (ADC=0-2.5x10^{-3}mm^{2}s^{-1} and rCBV$_{BOX}$=0-7.5). However, MR shows contrast enhancement in the deep aspect of the tumour coupled with decreased ADC and a small region of increased rCBV$_{BOX}$. All the MR imaging suggests transformation to a higher grade however, it is most likely that the enhancing tissue portion was never sent to the neuropathologist. During the clinical scans at 6, 9 and 12 months, various small enhancing foci around the surgical cavity have also been observed.*

7.5.1.2 Case 2. MR insensitive to high grade transformation

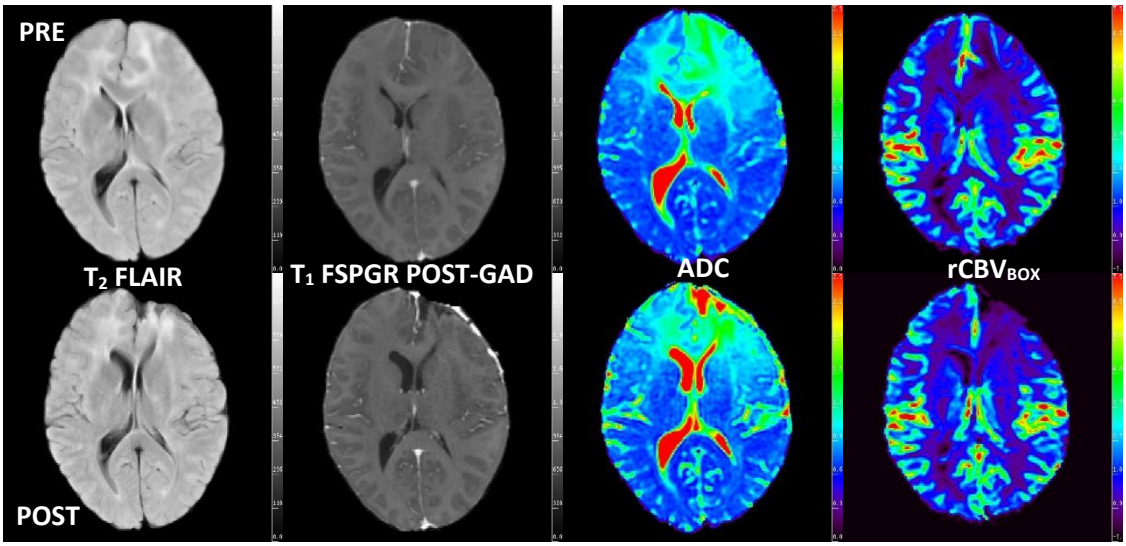

Figure 117 - *Example case of a grade III glioma which appeared to be lower grade based on MR, but was found to be high grade on histology resection (Scalings: ADC=0-2.5x10^{-3}mm^{2}s^{-1} and $rCBV_{BOX}$=0-7.5). The preoperative MR (top) shows an extensive hyperintense region on FLAIR imaging (left), absence of contrast enhancement throughout the entire abnormality (centre left), increased ADC values (centre right) and normal to low rCBV values (right). The 1 month post-surgical imaging (bottom) shows the extent of surgical resection, and indirectly the tissue sample which the pathologist received. Retrospective analysis of the imaging shows no high grade features in the section of tissue resection. A focus of higher cellularity with mitotic figures in a small region of the sample caused this lesion to be labelled as an anaplastic astrocytoma WHOIII. The 3mm slice thickness may have been the limiting issue for the MR.*

7.5.1.3 Case 3. Suboptimal Single Voxel Positioning

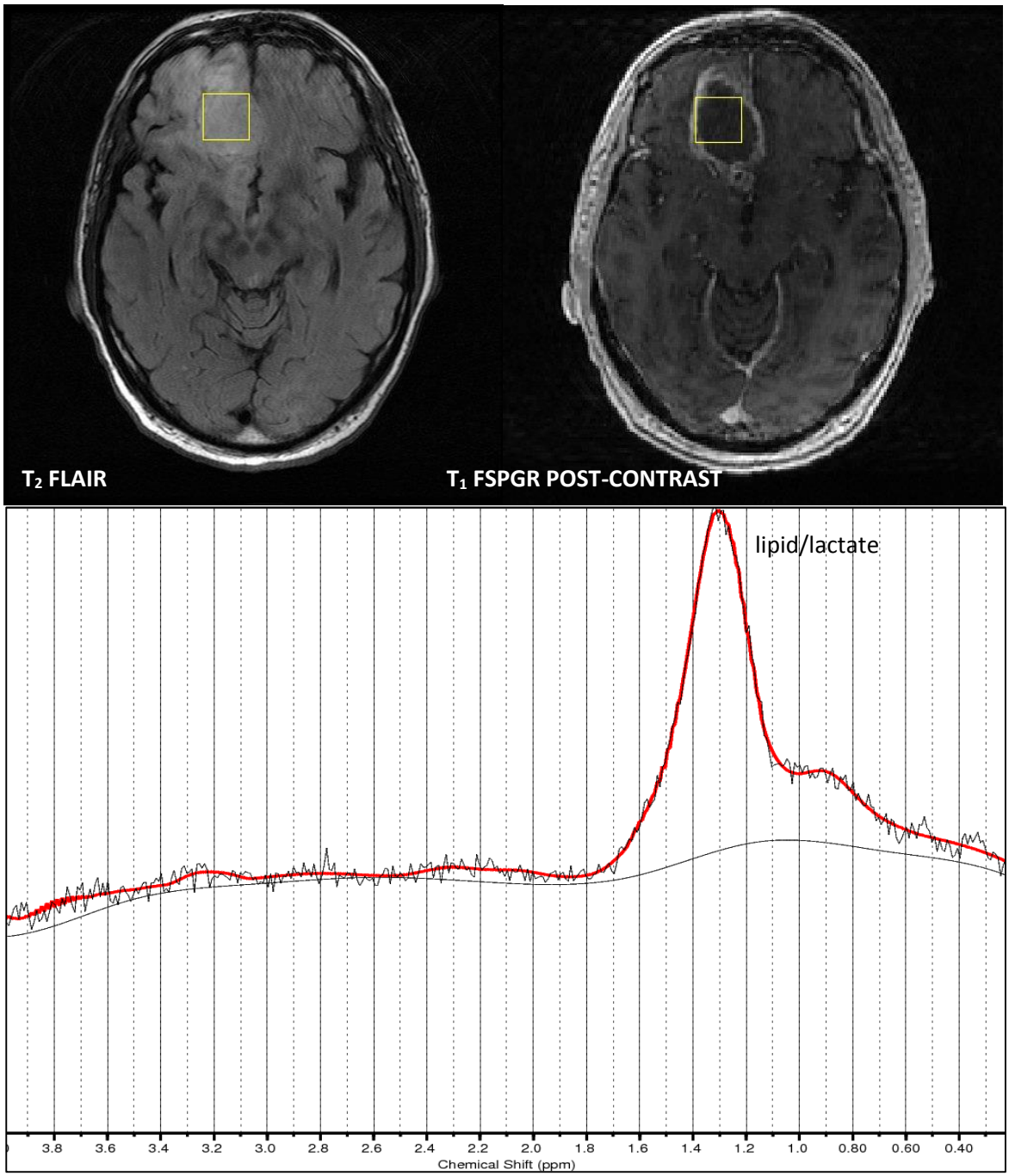

Figure 118 - This example shows a study patient with a WHO grade IV lesion. Single voxel TEA-PRESS was prescribed using only T_2 weighted FLAIR imaging (top left). Subsequent retrospective analysis revealed the prescription had been centred over the necrotic core of the lesion (top right) which contained no apparently active tumour as observed by the spectrum (bottom). The large resonance at 1.3ppm is representative of lipid droplets released as part of cell breakdown. Whilst the spectrum could still indicate a grade IV lesion, it would not be able to differentiate the lesion from a solitary brain metastasis.

7.6 Chapter Conclusion

The image processing scheme described in chapter 6 was successfully used to identify functional MR parameters that relate to glioma grade. Three different types of VOI were implemented with **TUM** and **NEL** VOIs producing a higher number of significant results. In gliomas, sampling multiparametric data from VOIs derived from the enhancing portion of lesion (**CEL**) does not appear to be an effective way of identifying lesion grade, partially because not all lesions enhance.

Individually, DTI, DCE and DSC all showed significant differences between tumours of different grade. Mean and median parameters produced the most significant differences between grades followed by standard deviation, then skew and kurtosis. Minimum and maximum values are also useful identifiers of lesion grade when the parameters are fully understood (e.g. low ADC and K_2 values relate to higher grades). When mean values sampled using a **TUM** VOI were input into a 2-stage logistic regression model, DTI and DCE parameters were found to produce the most predictive model for glioma grade. DSC parameters did not contain enough additional value for the logistic regression model. Further efforts should be made to optimised DTI and DCE in the brain.

Compared to histology, MRI and MRS have relatively poor spatial resolution despite advances in field strength and sampling schemes. Ultimately this means that MR is unable to identify the focal regions of cellular change which cause tumours to be classified as a higher grade than imaging suggests. Likewise, it is difficult to prove MR has identified small regions of transformation, given the difficulty in excising brain tumours. This means for the foreseeable future, there will continue to be a level of disagreement between imaging and pathology.

Given the promising results in this chapter to identify lesion grade using imaging, the same methodology should be able to be employed to predict progression-free survival in gliomas.

8 Prediction of Progression-Free Survival in Patients Diagnosed with Gliomas using MR Derived Parameters

8.1 Introduction

This chapter explores the ability of quantitative MR parameters derived from diffusion tensor imaging, dynamic contrast enhanced MRI and dynamic susceptibility contrast MRI to potentially predict progression-free survival at set time points prior to and during the early stages of adjuvant treatment in gliomas. If quantitative MR could identify patients likely to have a shorter progression interval, then surveillance imaging could be acquired more frequently, with the potential of a second surgical intervention closer to the time of reoccurrence. Alternatively, more aggressive treatments where a higher risk can be justified due to the potential benefit in patients likely to progress early.

Questions explored in this chapter are:

- Can preoperative MR parameters predict progression-free survival?
- Can MR parameters of residual disease prior to therapeutic treatment predict progression-free survival?
- Can changes observed in MR parameters as a result of treatment predict progression-free survival?
- Can MR parameters measured from the residual disease following treatment predict progression-free survival?

Finally, Cox regression models were generated for the different volumes of interests in both pre- and postoperative cohorts to identify the key MR parameters predictive of survival.

8.2 General Methodology

Multiparametric MR data was acquired from patients with histologically proven gliomas at three time points. As discussed on pg. 138, the 3 time points were:

1. Preoperative MR (Time Point 1 - Week 0).
2. Pre-chemoradiotherapy MR (Time Point 2 - Week 3).
3. Post-chemoradiotherapy MR (Time Point 3 - Week 10).

Volumes of interest (**TUM** and **CEL**) as detailed on pg. 178 were contoured for each lesion using the morphological imaging in the 4D multiparametric volume (FLAIR, T_1 FSPGR, ADC, FA, q, RA, λ_L, λ_R, R_1, K^{trans}, v_e, v_b, $rCBV_{GVF}$, $rCBV_{BOX}$, and K_2). The **TUM** VOI was selected based on the results of chapter 7, where **TUM** VOIs showed a greater number of significant differences between grades than **NEL** and **CEL** VOIs, whilst contrast enhancement is a key indicator used in the 'Response Assessment in Neuro-Oncology' criteria (RANO) (216) and therefore **CEL** VOIs were also investigated.

Mean and standard deviations were generated for each MR parameter of each lesion. This was based on the results of the previous chapter where mean/median values produced the greatest number of significant differences between differing grades of glioma, followed by standard deviation. Given the similarities between mean and median in large populations, mean was chosen as it compliments standard deviation measurements.

Gaussian mixture modelling was also applied; generating a further two sets of statistical descriptors for **TUM** (**TUM_0** and **TUM_1**) and **CEL** (**CEL_0** and **CEL_1**). Patients were dichotomised using the median of mean or standard deviations for each parameter and VOI population.

A critical event was classed either as tumour progression on conventional non-study MR imaging (increased volume of enhancement or oedema), a clear clinical deterioration as noted by a member of the care team or disease related death before 210 days. Censored data was defined as

radiologically stable MR imaging and/or clinical performance at 210 days from surgery or the closest follow up appointment. Kaplan-Meier survival analysis was calculated using IBM SPSS 20 for all dichotomised groups. Log rank tests were used to test for significant differences in survival interval noted between the dichotomised MR parameters.

Results are colour coded according to source of the data using the scheme in Table 22. This is implemented to improve the visualisation of trends within the results.

Table 22 – Colour coding for different MR sequences and the parameters derived from them in this study.

DTI Diffusion			DTI Directionality			T_1 Maps	DCE MRI			DSC MRI		
ADC	λ_L	λ_R	FA	q	RA	R_1	K^{trans}	v_e	v_b	$rCBV_{GVF}$	$rCBV_{BOX}$	K_2

8.3 Can Preoperative MR Parameters Predict Progression-Free Survival? (Time point 1)

This section examines whether quantitative preoperative MR can predict progression-free survival at 210 days from the initial study scan. With information about the likelihood of disease progression, patient's management could be changed to accommodate this new information.

8.3.1.1 Section Specific Methods

The same cohort of patients as investigated in chapter 7, (pg. 183) was used to examine whether preoperative MR parameters could be used to predict progression-free survival. Kaplan-Meier survival analysis was conducted twice; once for the entire cohort of 55 patients and once for the high grade lesions (45 patients). The second analysis was to rule out data biasing by including grade II lesions which are known to remain stable for a longer period of time. The enhancing portion (**CEL**) of the high grade tumours was also examined to see if MR parameters were predictive of progression-free survival. Cox regression survival analysis was implemented with the addition of grade, age and cell type, which are clinically relevant parameters, in order to determine the most useful parameters for clinicians to examine when identifying patients that might have disease progression shortly after treatment. To prevent the over-parameterisation of the Cox regression model, factor analysis was used to identify the principal components that explained the greatest amount of variance in the data. To approximately normalise the values between different MR parameters, in order to identify small changes, PK parameters were multiplied by 100, whilst all other MR parameters were multiplied by 10. Principal components analysis was calculated from the correlation matrix of MR parameters retaining components with eigenvalues greater than 1 (SPSS default). From the component matrix (i.e. the correlation between MR parameters and principal components) generated by SPSS, the two parameters which explained the most variance of each principal component were selected as the input for the Cox regression analysis. A backward Wald methodology was used to submit the factor analysis identified data to the Cox regression model.

The change in risk associated with a unit increase of imaging parameter was calculated as Hazard Ratio-1. The resulting sign determines the direction of risk change (i.e. 0.75-1 = -0.25 (-25%)), which means a unit increase in imaging parameter results in a 25% decreased risk.

8.3.1.2 Results

Entire Cohort Results

Using the mean **TUM** VOI for the 55 patients (grade II = 10, grade III = 12, grade IV = 33), 20 significant parameters were found to predict progression-free survival (Table 51). The false discovery rate was calculated to be 3.5% indicating 1 false positive result. Using the standard deviations of parameters instead found 21 significant results (Table 52) with a FDR of 1.2% which suggested 0 false positives in the data. Notable significant results include all mean FA, q, RA, K^{trans} and v_e **TUM** populations, and selected ADC, λ_R v_b and K_2 mean populations. Selected standard deviations of all parameters expect ADC, λ_L and λ_R were also significant predictors of progression-free survival. The volume of tumour abnormality was not a significant predictor of progression-free survival.

High Grade Results

When analysing only high grade gliomas (grades III and IV) (N=45), mean **TUM** VOIs showed 10 significant parameters capable of predicting progression-free survival at 210 days (Table 53). The results had a FDR of 11.4% indicating 1 false positive present in the results. Significant mean parameters were found for ADC, q, λ_R, K^{trans}, v_e and K_2, with 7 of the 9 significant MR results arising from GMM derived populations (volume was 10^{th} result). The standard deviations of parameters were equally predictive of progression-free survival in high grade gliomas from preoperative imaging (Table 54), with 11 significant results with a FDR of 5.4% and 1 false positive. Significant predictors of progression-free survival were q, RA, R_1, K^{trans}, v_e and $rCBV_{GVF}$. In the high grade cohort, the preoperative tumour volume was predictive of the progression-free survival interval.

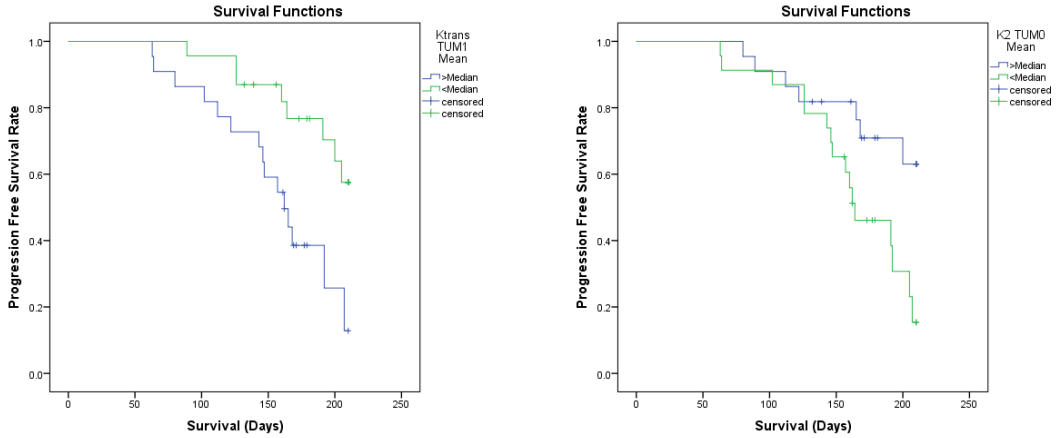

Figure 119 - Example Kaplan-Meier survival charts showing 2 examples of significant predictors of progression free survival in high grade gliomas using data sampled from the pre-operative MR scans. Mean values from K^{trans} TUM_1 (p=0.005)(left) and K_2 TUM_0 (p=0.016)(right) are shown above.

Of the 45 high grade lesions, contrast enhancement was present in 39 cases. Mean **CEL** values (Table 55) found 5 parameters to be significant predictors of progression-free survival with a false discovery rate of 27.6%. Populations of R_1, v_b and K_2 as well as the volume of enhancing tumour were significant predictors. For the standard deviations of **CEL** (Table 56), 5 parameters were also shown to be significant with a FDR of 16.4%, suggesting 1 parameter was a false positive. Of the 5 significant standard deviations that were predictive of progression-free survival, all were derived from GMM subpopulations.

Cox Regression Survival Analysis of High Grade Lesions

Factor analysis of the 21 significant predictors found using **TUM** to predict progression-free survival in high grade gliomas using preoperative imaging revealed 5 principal components (Table 23). The two variables that explained the most variance of each component were chosen as input for the Cox regression model using a backward W3ald methodology (Table 24). The mean radial diffusivity measured with $\mathbf{TUM_0}$ was found to be predictive of progression-free survival with every $0.1x10^{-3}$ mm^2s^{-1} increase in the mean $\mathbf{TUM_0}$ population of a tumour found to reduce the risk of a shorter progression-free survival interval by 34% (1-0.66). The volume of the tumour abnormality **TUM** was also found to be a predictor of progression-free survival with each 1ml increase in tumour abnormality before surgery being associated with a 1% increased risk in a shorter progression-free survival interval. The increased risk associated with a grade IV glioma compared to a grade III glioma was 179%.

The same methodology was repeated for the high grade **CEL** group which contained 39 patients, compared to 45 of the **TUM** cohort. Factor analysis of the 10 significant results found 3 principal components (Table 25). The top two parameters from each component were entered into the Cox regression analysis along with the clinical parameters (Table 26). A $0.1x10^{-3}s^{-1}$ increase in mean R_1 values was associated with 23% decreased risk of tumour progression at 210 days from surgery whilst a 1% increase in blood volume fraction was found to increase the risk of a shorter progression-free interval by 9%.

*Table 23 - Magnitude values of the correlations between the 21 parameters and each principal component. The input for the factor analysis were the significant predictors of progression-free survival identified using the Kaplan-Meier survival analysis of high grade glioma (N=45) parameters at time point 1 sampled using a **TUM** VOI. The cells highlighted in red show the parameters input into the Cox regression model.*

Parameter	Stat.	VOI	Component				
			1	2	3	4	5
ADC	Mean	TUM_0	0.20	0.73	0.48	0.12	0.29
q	Mean	TUM_1	0.20	0.66	0.46	0.09	0.36
λ_R	Mean	TUM_0	0.16	0.75	0.43	0.03	0.39
K^{trans}	Mean	TUM	0.92	0.02	0.20	0.05	0.04
K^{trans}	Mean	TUM_0	0.81	0.14	0.16	0.36	0.22
K^{trans}	Mean	TUM_1	0.92	0.10	0.07	0.00	0.10
ve	Mean	TUM	0.92	0.00	0.10	0.00	0.05
ve	Mean	TUM_1	0.91	0.14	0.08	0.08	0.13
K_2	Mean	TUM_0	0.36	0.55	0.11	0.51	0.36
Volume	Volume	TUM	0.38	0.03	0.48	0.33	0.06
q	S.D.	TUM	0.32	0.46	0.52	0.27	0.23
RA	S.D.	TUM_1	0.06	0.77	0.42	0.13	0.01
R_1	S.D.	TUM_0	0.38	0.30	0.41	0.54	0.08
K^{trans}	S.D.	TUM	0.88	0.14	0.08	0.20	0.20
K^{trans}	S.D.	TUM_0	0.84	0.11	0.08	0.31	0.18
K^{trans}	S.D.	TUM_1	0.87	0.13	0.01	0.06	0.16
v_e	S.D.	TUM	0.94	0.11	0.07	0.24	0.07
v_e	S.D.	TUM_0	0.72	0.00	0.23	0.32	0.08
v_e	S.D.	TUM_1	0.91	0.12	0.11	0.20	0.09
$rCBV_{GVF}$	S.D.	TUM_0	0.09	0.52	0.47	0.38	0.40
$rCBV_{GVF}$	S.D.	TUM_1	0.54	0.32	0.31	0.23	0.34

*Table 24 - Final model from a 210 day progression-free Cox regression survival analysis using the parameters identified using factor analysis of significant Kaplan-Meier results for 45 high grade gliomas sampled with **TUM** VOIs at time points 1.*

Time point	Parameter	Stat.	VOI	B	Sig.	Hazard Ratio	95.0% CI for Hazard Ratio	
							Lower	Upper
TP1	λ_R	Mean	TUM_0	-0.42	0.020	0.66	0.46	0.94
TP1	Volume	Volume	TUM	0.01	0.006	1.01	1.00	1.02
TP1	Grade	Grade	TUM	1.02	0.075	2.79	0.90	8.61

*Table 25 - Magnitude values of the correlations between the 10 parameters and each principal component. The input for the factor analysis were the significant predictors of progression-free survival identified using the Kaplan-Meier survival analysis of high grade glioma (N=39) parameters at time point 1 sampled using a **CEL** VOI. The cells highlighted in red show the parameters input into the Cox regression model.*

Parameter	Stat.	VOI	Component		
			1	2	3
R_1	Mean	CEL	0.20	0.94	0.19
R_1	Mean	CEL_0	0.14	0.94	0.14
v_b	Mean	CEL_1	0.92	0.06	0.17
K_2	Mean	CEL	0.55	0.24	0.50
Volume	Volume	CEL	0.69	0.34	0.19
RA	S.D.	CEL_1	0.41	0.26	0.34
K^{trans}	S.D.	CEL_1	0.78	0.04	0.40
v_e	S.D.	CEL_1	0.84	0.02	0.23
v_b	S.D.	CEL_1	0.89	0.05	0.34
K_2	S.D.	CEL_1	0.60	0.29	0.60

*Table 26 - Final model from a 210 day progression-free Cox regression survival analysis using the parameters identified using factor analysis of significant Kaplan-Meier results for 39 high grade gliomas sampled with **CEL** VOIs at time points 1.*

Time point	Parameter	Stat.	VOI	B	Sig.	Hazard Ratio	95.0% CI for Hazard Ratio	
							Lower	Upper
TP1	R_1	Mean	CEL_0	-0.32	0.035	0.73	0.54	0.98
TP1	v_b	S.D.	CEL_1	0.09	0.035	1.09	1.01	1.18

8.3.1.3 Discussion

Entire Cohort (N=55)

Functional parameters derived from preoperative MR appear to predict progression-free survival at 210 days from time point 1. From the mean measurements using the **TUM** VOI, all fibre directionality parameters (FA, q, RA) were found as significant predictors of progression-free survival, with tumour abnormalities that contained high levels of directionality found to progress more rapidly. This result is consistent with the observations in chapter 7, where increased directional diffusion was found in high grade lesions using mean **TUM** measurements (pg. 308). As suggested previously in this thesis, this observation is explainable by the increased amounts of oedema associated with higher grade lesions causing more apparently normal appearing white matter be included in the T_{2all} VOI, and subsequently the directional diffusivity appears increased in high grade lesions. This has also be observed by Inoue *et al* (196) and Liu *et al* (200), reporting increased FA and decreased ADC values with increasing glioma grade. Furthermore, the high directional diffusion present within the VOI suggests neurons are encompassed by the disease which is more likely to be infiltrating, rather than displacing normal brain making resection more difficult and reoccurrence more likely.

The lower GMM population (**TUM_0**) of the diffusion measurements was also found to be predictive of progression-free survival, with ADC and radial diffusivity both producing significant results. These results show that lower diffusivity values are associated with a shorter progression-free interval, suggesting the region of the tumour displaying low ADC and λ_R values is most likely to have high levels of cell proliferation. The use of T_1 and T_2* dynamic imaging to derive parameters such as K^{trans}, v_e and K_2 should be considered for preoperative MR assessment in these patients. From the data, it appears that tumours with high levels of vessel leakage progress more rapidly than less well perfused lesions and could be used as a surrogate for the extent of VEGF up regulation.

The use of Gaussian mixture modelling appears to improve the ability of MR to predict disease progression. For 8 out of 9 parameters, GMM subpopulations of parameters were better predictors of disease progression than whole tumour volumes of interest (**TUM**). This process is fully automated requiring no hot-spot techniques and accounts for the entire volume of abnormality. These results suggest the presence of non-Gaussian populations in these tumours and their parameter distributions, such that statistical descriptors such as mean and standard deviation should be used with caution for whole tumour measurements. Functional preoperative MR could be used to influence how radical surgical resection should be, as well as the scan interval and chemotherapeutic regimes for patients with high levels of vessel permeability.

High Grade Only Cohort (N=45)

Within the high grade population, **TUM_0** mean ADC and λ_R values were found to be significant predictors of progression-free survival. Mean q values measured with **TUM_1** were also a significant predictor from the DTI derived parameters. Lower diffusivity values were associated with a shorter progression-free interval, which can be related to increased cellularity (120) and elevated cell proliferation rates. Previous work (39) has shown the volume of tumour with a normalised ADC less than 1.5 to be predictive of survival in glioblastoma patients. All mean K^{trans} **TUM** populations significantly predicted progression-free survival, with **TUM** and **TUM_1** of v_e also being significant. In all cases, higher PK parameter values were associated with a shorter progression-free interval, with increasing values previously been shown to correlate with grade (93, 204). This may relate to an up-regulation of VEGF in the tumour, or reduced drug delivery through the new tumour vasculature. Mill *et al* (92) have previously reported a high K^{trans} as poor prognostic indicator in gliomas, despite only sampling 3 slices of tumour at 1.5T in each patient. The **TUM_0** population of K_2 in tumours was found to be a significant predictor of PFS with the parameter representing leakage, which is thought to be physiologically similar to K^{trans} which represents permeability. Figure 120 shows two glioblastoma tumours with similar appearances on post-contrast T_1 FSPGR imaging; however, the K_2

values throughout the tumours are quite different, with more T_2* dominant leakage in the tumour that progressed more rapidly. T_2* dominant leakage (% peak recovery) measured at 1.5T was found to be non-significant in predicting survival (39), however the author's felt the DSC acquisition could have been improved by using a phased array coil to increase the through plane coverage. The volume of tumour abnormality (**TUM**) was also predictive of tumour progression, with larger tumours at presentation more likely to progression 210 days later. This may be related to the difficulty in resecting larger lesions which are more likely to have invaded eloquent structures in the brain as well as potentially containing more spatially distinct mutations (217) which will respond to treatment differently.

The standard deviations of q sampled with **TUM** and RA sampled with $\mathbf{TUM_1}$ were predictive of progression-free survival, but all other DTI measurements were not. In both parameters, it would appear that a greater standard deviation is associated with a worse survival. This probably relates to the amount of white matter encompassed by the tumour abnormality, with infiltrative tumours progressing more rapidly than tumours that displace the brain. The standard deviation of all populations of K^{trans} and v_e proved to be significant predictors of progression-free survival at 210 days. The higher standard deviation suggests more heterogeneously enhancing tumours reoccur after a shorter period of time. The standard deviation of the non-leakage corrected $\mathbf{TUM_0}$ and $\mathbf{TUM_1}$ populations of $rCBV_{GVF}$ show increased blood volume heterogeneity in patients who progressed more rapidly following surgery, which is similar to the DCE results which showed increased heterogeneity was associated with poorer outcomes.

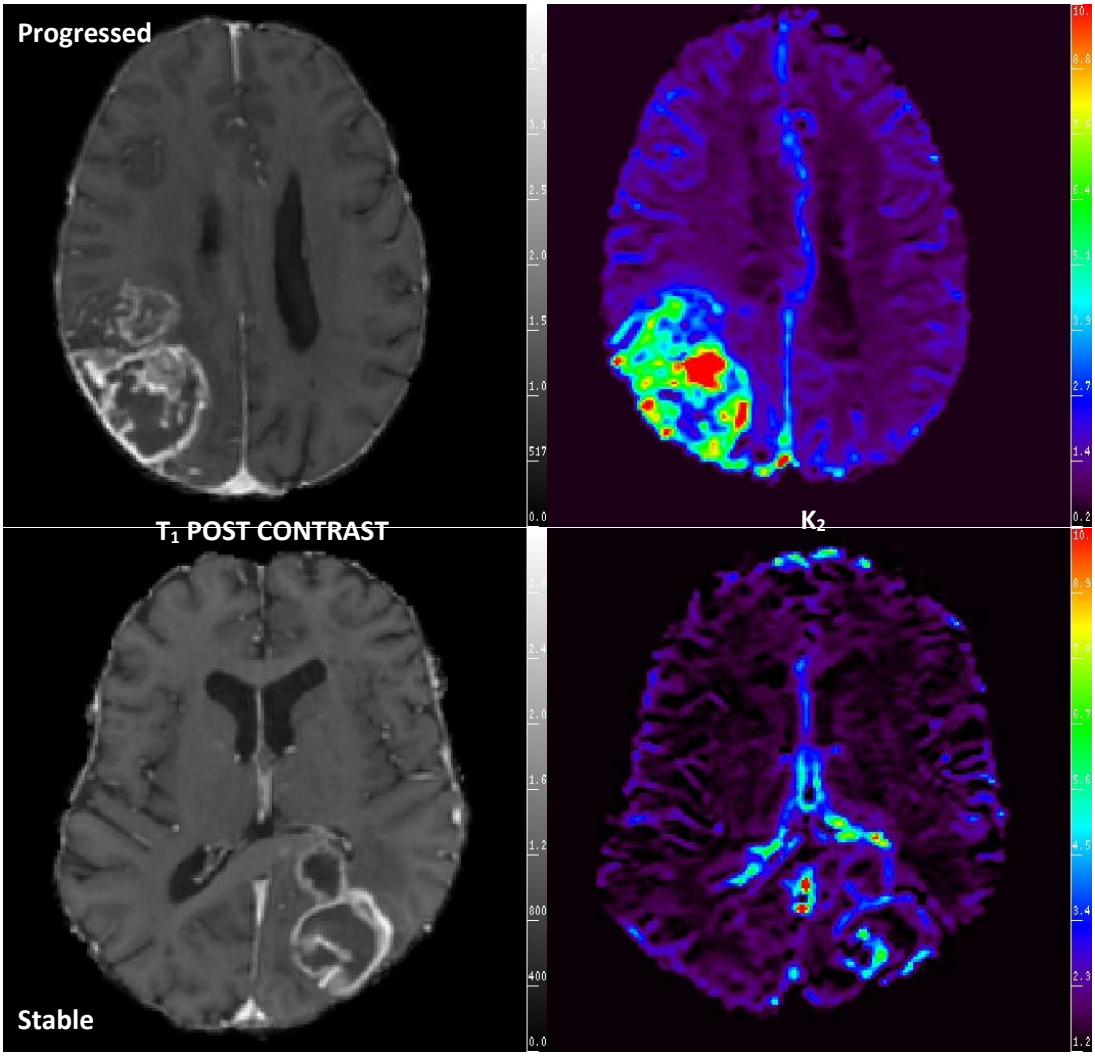

Figure 120 – Two patients with glioblastoma WHO IV tumours. Post-contrast T_1 FSPGR imaging is shown on the left, whilst K_2 maps (red pixels are more negative) are on the right to demonstrate the range of T_2 dominant leakage values observed. The top patient progressed before 210 days and had a TUM_0 K_2 value of -5.162 compared to bottom patient who remained stable at 210 days following surgery, with a TUM_0 K_2 value of -1.288.*

From the 39 high grade gliomas which demonstrated an enhancing component (**CEL**), no mean diffusion parameters from preoperative imaging were found to be significant predictors of progression-free survival. As discussed on page 206, factors such as geometric distortion have the potential to cause a VOI-data mismatch whilst perfusion effects may also lead to diffusion measurements using **CEL** being non-predictive. However, mean values for **CEL** and $\mathbf{CEL_0}$ of R_1, $\mathbf{CEL_1}$ of v_b and **CEL** of K_2 were all significant predictors of progression-free survival. Tumours which displayed a greater level of T_2* dominant leakage were more likely to have a shorter progression-

free interval, possibly indicating how advanced the disease is at presentation. The volume of enhancing tissue was also predictive, with tumours that contained more than 12.36ml of enhancing tissue more likely to have some type of progression before 210 days. Possible reasons include the amount of tumour that is surgically removable, and the number of mutations likely to have occurred in larger tumours.

From the standard deviations of diffusion tensor derived parameters sampled with **CEL**, only RA measured using the **CEL_1** VOI showed significant differences in progression-free survival. Standard deviations of K^{trans}, v_e, v_b and K_2 were all significant using **CEL_1**, suggesting a wider range of vascular tissues present in the tumours which progressed more rapidly. These MR parameters are possible surrogates for activity of VEGF present in the tumour. Given HIF1α activation is a precursor to VEGF up-regulation, increased vascularity could be used to predict tumours likely to infiltrate the surrounding tissue rapidly. HIF1α is normally used by the body to control the invading properties of cells and is also involved in cell migration.

Cox Regression

From 10 MR parameters, age, grade and cell type entered into the Cox regression model for high grade tumours measured using the **TUM** VOI sampling scheme, only 3 parameters were retained. These were radial diffusivity, volume and grade. The mean radial diffusivity measured with **TUM_0** was found to predictive of progression-free survival with every $0.1x10^{-3}$ mm^2s^{-1} increase in the mean of the **TUM_0** population of a tumour found to reduce the risk of a shorter progression-free survival interval by 34%. As previously discussed, lower diffusivity values can be related to increased cellularity (120) and an elevated cell proliferation index. Whilst O^6-methylguanine-DNA methyltransferase (MGMT) status was not available in this study, higher ADC values in glioblastomas have been associated with MGMT promoter methylation and a more favourable outcome (218, 219).

The volume of the tumour abnormality **TUM** was also found to be a predictor of progression-free survival (P=0.020) with each 1ml increase in tumour abnormality before surgery being associated with a 1% increased risk of a shorter progression-free survival interval. As discussed, this may be related to the difficulty in resecting larger lesions which are more likely to have invaded eloquent structures as well as potentially containing more spatially distinct mutations (217). Iliadis *et al* (220) examined preoperative glioblastoma tumour volumes and found the volume of T_2 abnormality to have a non-significant hazard ratio for overall survival and progression-free survival. Only performance score and the volume of enhancing tissue preoperatively were significant predictors of progression-free survival in the published study.

The difference between being diagnosed with a grade III and IV glioma was found to have 179% increased risk of a shorter progression-free survival interval. This agrees with literature (6), which associates shorter survival times with high grade lesions.

For the high grade **CEL** group, the top two components of each parameter were entered into the Cox regression analysis along with age, cell type and grade. Two significant parameters remained in the model, with a $0.1x10^{-3}s^{-1}$ increase in mean R_1 values associated with 23% decreased risk of tumour progression at 210 days from surgery and a 1% increase in blood volume fraction standard deviation found to increase the risk of a shorter progression-free interval by 9%. These results appear to suggest that useful information can be gained about the tissue conditions of the enhancing portion of the lesion. The longitudinal relaxation rate (R_1) appears to be lower in patients who progressed more rapidly. Likewise, the increase in v_b standard deviation most likely relates into higher v_b values within the certain regions of the enhancing portion of the tumour which subsequently causes an increase in the observed standard deviation.

Limitations

Whilst efforts were made to acquire the most representative data for the brain tumour cohort of this geographical region, there was some selection bias due to age and performance status at presentation. In this region, patients up to the age of 25 are referred to another medical centre which has additional expertise for the care of young adults with brain tumours, therefore no patients between 18 and 25 were recruited to the study.

Regarding performance status, if the patient was confused or dysphasic then consent to the trial was not possible despite treatment still potentially being offered on the grounds of best interest. This could cause a bias in the survival data given performance status is a known prognostic indicator (220).

It could be argued that the VOIs in this study are contoured by a physicist (the author) rather than a neuroradiologist, which could cause some small errors in the tumour boundaries. However, in most cases the boundaries of the T_1 and T_2 abnormalities were well defined which made contouring with the Otsu (187) tool relatively simple. The large number of pixels involved in each tumour's measurement will have removed some of the small differences between scientist and clinician drawn VOIs.

In terms of the MR data, the interpolation of some of the higher slice thickness sequences (DSC=7mm, FLAIR=5mm) and geometric distortion in the EPI images (DTI and DSC) are probably the main sources of measurement error. The interpolation of the T_2 FLAIR imaging will affect the T_{2all} VOI with over- and underestimations of the boundaries most likely, whilst the interpolation of the DSC data means linearly enhancing structures are less likely to correctly align, which will have had more effect on the **CEL** VOIs. As described on page 169, 12 DOF were used to register the DTI and DSC datasets to the T_1 FSPGR volume in an effort to align the data correctly whilst reducing image warping. Page 304 details fully how the data acquisition could be improved if another prospective

study was repeated. However, in terms of VOI generation switching the 2D T_2 FLAIR sequence for a 3D T_2 FLAIR volume would yield an immediate improvement, with only an additional 3 minutes of scan time.

8.3.1.4 Conclusions

Preoperative MR can predict progression-free survival at 210 days in high grade gliomas. When examining the cohort of 55 patients that included low and high grade tumours, 20 significant differences for mean MR parameters were evident between tumours that progressed or remained stable when sampled with the **TUM** VOI. A further 21 significant differences were evident using the standard deviations.

A more detailed analysis of only the high grade tumours using **TUM** by Cox regression revealed radial diffusivity, volume of tumour abnormality and grade to be the best indicators of progression-free survival at 210 days following Cox regression analysis. The use of Gaussian mixture modelling to identify the lower population of ADC values within the tumour appears to be a suitable alternative to arbitrary cut-offs as used by Crawford *et al* (39). Using the **CEL** VOI, measures of R_1 and v_b appear to better than grade or cell type at predicting which tumours are likely to progress after surgery.

Individually, DTI, DSC and DCE all showed significant predictors for progression-free survival using **CEL** or **TUM** with either mean or standard deviation as statistical descriptors. Longitudinal diffusivity was non-significant throughout this section. Less common parameters such as q and K_2 produced multiple significant predictions and are worth investigating further.

The use of advanced MR parameters, as identified in this section could be used to recognise patients who would benefit from more frequent scan regimes or for the inclusion of novel therapeutics where the likelihood of progression before 210 days after surgery was high.

8.4 Can Functional MR Parameters of Residual Disease Prior to Adjuvant Therapeutic Treatment Predict Survival Outcome? (Time point 2)

8.4.1.1 Introduction

This time point examines the MR parameters of residual tumour following surgery and whether it is possible to predict the time to progression in glioma patients. Scans at time point 2 were all immediately prior to chemoradiotherapy. Significant predictors of progression-free survival could influence treatment management in the future through increased scan intervals or alternative therapeutic options.

8.4.1.2 Section Specific Methods

Multiparametric MR data was acquired and processed in the same manner as section 8.2 for 33 patients with histologically proven gliomas. Patients were only included in this analysis if they completed scans at time point 2 and time point 3 so the data from time points could later be compared. Ten critical events were found to have occurred before 210 days after recruitment (approximately 180 days/6 months from time point 2). Of the cohort of 33 glioma patients, 28 gliomas had contrast enhancement present in both examinations, thus statistics relating to **CEL** had a reduced number of critical events (9) compared to **TUM**. All VOIs were contoured by the author, with care taken to exclude all regions of haemorrhage. Sample images of the registered data and VOIs can be seen in Figure 121. Note the hemosiderin present on the FLAIR imaging which may have had an effect on the DSC quantification.

Kaplan-Meier survival analysis was calculated for all dichotomised groups. The tumour volume within the VOI was also compared with outcome. Within tables, significant results are highlighted in red for the Kaplan-Meier survival analysis.

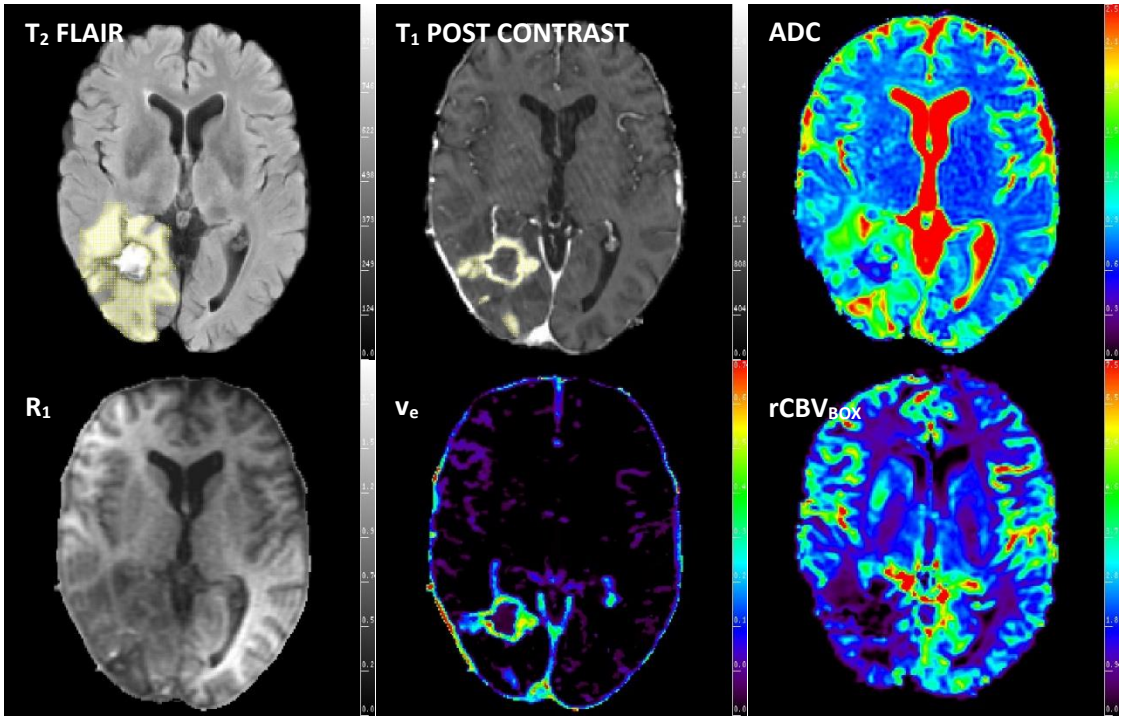

*Figure 121 - Sample postoperative, pre-chemoradiotherapy imaging at 3 weeks after surgery. FLAIR, T_1 FSPGR post-contrast, ADC (0-2.5x10^{-3}mm^{2}s^{-1}), R_1 (0-2s^{-1}), v_e (0-0.75) and $rCBV_{BOX}$ (0-7.5) images can from seen from top left to bottom right. Part of the **TUM** VOI can be seen on the FLAIR imaging whilst a section of the **CEL** VOI can be seen on the T_1 FSPGR post-contrast imaging. Note the exlusion of the post-surgical cavity from the analysis in the same manner as necrosis.*

8.4.1.3 Section Specific Results

Kaplan-Meier survival analysis (Table 57) was calculated for each parameter and VOI combination. Out of 40 dichotomised parameters, 8 were found to have a p-value less than 0.05. Following calculation of the FDR, 26% of cases were likely to be false discoveries which equated to 2 parameter-VOI combinations. Significant parameters ($p<0.05$) found using the Kaplan-Meier survival analysis were longitudinal (Figure 122) and radial diffusivity from the DTI and all PK parameters derived from the DCE. No DSC parameters significantly correlated with progression-free survival at this time point.

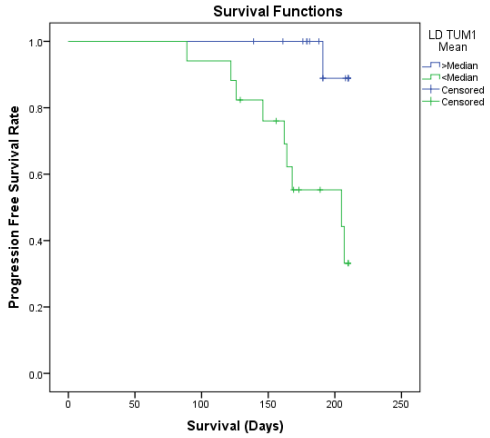

Figure 122 - Kaplan-Meier survival plot showing the prediction of progression free survival in high grade gliomas using the mean TUM_1 population of the longitudinal diffusivity (p=0.003) measured at time point 2.

Kaplan-Meier survival analysis of the standard deviation values measured using the **TUM** VOI for each parameter found 5 significant results (Table 58) with a FDR of 17.2% indicating 1 result in the table was likely to be a false discovery. Significant discoveries were found using the standard deviations of λ_L, K^{trans}, v_b and K_2 (Figure 123).

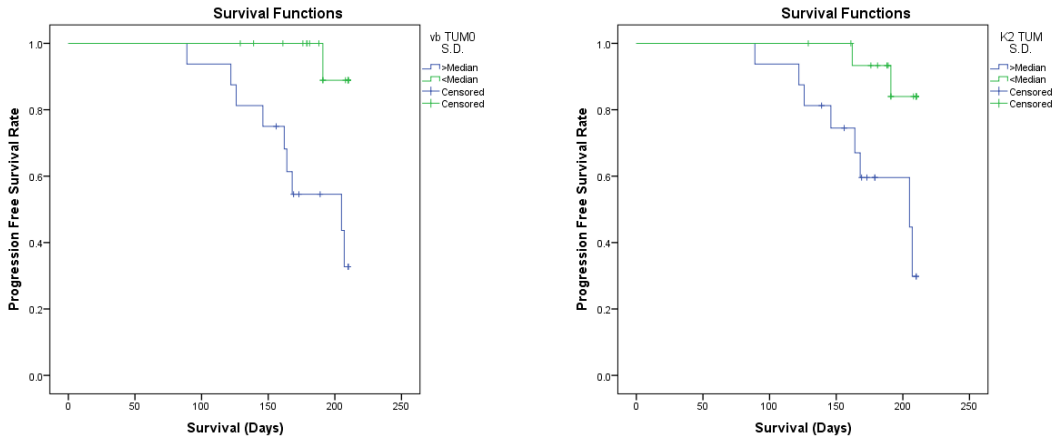

Figure 123 - Kaplan-Meier survival plots showing the prediction of progression free survival in high grade gliomas using the standard deviations of the v_b TUM_0 (p=0.003)(left) and K_2 TUM (p=0.009)(right) populations measured at time point 2.

Mean parameters values sampled using **CEL** (Table 59) were calculated for each parameter and VOI combination. Forty dichotomised parameters were input into the Kaplan-Meier survival analysis, with 5 parameters found to have a p-value less than 0.05. Following calculation of the FDR, 25.5% of cases were likely to be false discoveries which equated to 1 parameter-VOI combination. Significant parameters ($p<0.05$) found using the Kaplan-Meier survival analysis were q from the DTI and v_b calculated from the DCE. Once again, no DSC parameters significantly correlated with progression-free survival at time point 2.

Finally, the standard deviation values measured using the **CEL** VOI for each parameter revealed 4 significant results (Table 60) with a FDR of 29% indicating 1 result in the table was likely to be a false discovery. Significant results arose from DTI and DCE data only.

8.4.1.4 Section Specific Discussion

VOIs

Once the blood-brain barrier is disrupted, contrast enhancement around a surgical cavity is usually difficult to interpret, reducing the accuracy of the **CEL VOI**s. Only by scanning patients within 48 hours of surgery can contrast enhancement be considered as residual tumour. However, the availability of 3.0T in-patient slots ruled out scanning at this time interval. By using the **TUM** and **CEL** VOIs in combination with the Gaussian mixture modelling, the intention was that different tissue groups (e.g. tumour or oedema) could be distinguished independently without the need for user defined sub-VOIs.

DTI

Longitudinal diffusivity (λ_L) measured using **TUM_1** was found to be a significant predictor of progression-free survival prior to chemoradiotherapy. Patients with a λ_L higher than the median remained stable for significantly longer periods than patients with a lower λ_L. This parameter may have been sensitive to inflammation and oedema which has the potential to decrease following steroids. The higher diffusivity values may also indicate an absence of tumour infiltration and subsequently reduced progression. Radial diffusivity (λ_R) measured using **TUM_0** was also found to be a significant predictor for progression-free survival. Patients that had a lesion with high radial diffusivity faring better. This relates to some of the earlier findings in this study (pg. 185) which reported lower grade lesions to have higher ADC values than those of higher grade tumours, which means the cells are less dense or proliferating slower. Yamasaki's 2010 study (140) also reported diffusion derived parameters to be significant predictors of survival when using minimum ADC values. However, the mean ADC values in this study were found to be non-significant and were measured from the whole VOI rather than in Yamasaki's study which used multiple small ROIs. Given the result of surgery introducing artefact and the potential for solid tumour, infiltration, oedema, hemosiderin and inflammation, it is perhaps not surprising that mean ADC values could not predict

progression-free survival at this time point. In terms of measured values, median ADC values in this study were found to be comparable to those in a similar pre-chemoradiotherapy study (149) which reported median ADC values to be $1.09x10^{-3}mm^2s^{-1}$ for the whole T_2 abnormality compared to $1.14x10^{-3}mm^2s^{-1}$ in this thesis. Diffusion was not used to predict progression-free survival in the published study (149). In recurrent GBM, Ellingson *et al* (221) were able to demonstrate that the lower population of ADC values derived using a Gaussian mixture model was able to predict whether patients would responded to Bevacizumab. However, when predicting response to chemotherapy in recurrent GBM, ADC was non-significant in the published study.

When examining the distribution of parameter values within a given population of the tumour abnormality, the standard deviation of longitudinal diffusion within **TUM_0** was found to be a significant predictor of progression-free survival, with tumours with a smaller standard deviation progressing more rapidly. At this time point, all **TUM** parameters relating to diffusion directionality were non-significant in predicting progression-free survival. This may be related to the sampling method which used a single VOI rather than a detailed examination of the data trying to identify any potential regions of infiltration; a sign of tumour progression (137, 164).

Patients with a mean tumour value of q higher than the median, measured with a **CEL** VOI (**CEL** and **CEL_1**) demonstrated a significantly shorter time to progression. Given the scan interval one might speculate that q values may be able to differentiate between inflammatory enhancement and tumour enhancement, with inflammatory enhancement having lower q values caused by a higher degree of isotropic diffusion due to acute swelling. The cohort with the highest standard deviations of FA and q values, measured with **CEL_1** and **CEL** respectively from the enhancing portion of the lesion also had a significantly shorter progression-free interval. Increased standard deviations of FA and q suggest a greater level of heterogeneity within the contrast enhancing component of the

tumour, a possible indication the tumour is becoming more necrotic due to micro-environmental stresses.

DCE

At least one **TUM** VOI from each of the PK parameters significantly predicted progression-free survival. A high K^{trans}, v_e or v_b all suggested the patient would progress quicker than a patient with a tumour which displayed low PK parameter values. Previously high K^{trans} and v_b values have been associated with higher grade lesions (92). This has been observed in both this study (pg. 308) and the 2006 publication by Mills *et al* (92). The high K^{trans} in glioma patients could be considered a biomarker for an angiogenic switch (possibly suggesting HIF1α is up regulated), where neoangiogenesis is promoted and tumours continue to grow quicker, ultimately resulting in a shorter progression-free time. It would appear that despite increased vessel permeability, increased drug delivery is not possible, possibly due to increased flow, or abnormal vessel growth preventing drugs being able to diffuse through the tumorous tissue. The **TUM_0** and **TUM_1** fractional volume of extravascular extracellular space (v_e) were both significant predictors of progression-free survival in glioma patients, with a high v_e meaning patients are likely to progress quicker. Interestingly, the **TUM** VOI was not a significant predictor for v_e which suggests there may be two v_e populations existing at this time point. Mills *et al* (222) has previously proposed that ADC values would correlate with v_e values given both are measures of the extravascular extracellular space, however this was found to be non-significant in the publication. A similar situation is present in this study, with low diffusivity values (ADC and radial diffusivity) suggesting patients will progress quicker, while v_e is high in patients who progress more rapidly.

Increased standard deviation of K^{trans} (**TUM_0**) and v_b (**TUM_0** & **TUM_1**) produced significant predictions about a more rapid progression of the disease. The increased standard deviations of PK parameters suggests that tumours with a wider range of vessel conditions are present (different degrees of

leakage and blood volume), and potentially have more mutations or an up regulated HIF1α, thus they are less likely to respond to treatment.

Mean measurements of PK values using **CEL**, revealed v_b to be a significant predictor of progression-free survival using all populations of **CEL**. In **TUM**, v_b was also significant as previously described. A value higher than the dichotomised mean v_b in the residual enhancing tumour indicates a more rapid regrowth of the disease in glioma patients. The standard deviation of the **TUM$_0$** v_b also predicted a reduced progression-free survival interval, with increased variation being associated with a worse outcome.

DSC

The absence of significant results using mean **TUM** DSC derived parameters is perhaps not surprising given the recent surgery in patients; with hemosiderin and other blood breakdown products likely to destroy the MR signal at all points along the DSC time course. Therefore, rCBV estimations of the residual disease have the potential to be incorrect at the time of the scan, given the interval from surgery (3-4 weeks); and that post-surgical effects can persist for several months within the brain. Previously in this study, rCBV correlated with grade whilst K_2 appeared to predict progression-free survival from the preoperative MR. Whilst mean K_2 did not predict outcome from post-surgical imaging, the standard deviation of K_2 values did. No DSC parameters measured with a **CEL** VOI predicted progression-free survival.

Residual Tumour Volume

A previous study (149), imaging glioma patients before chemoradiotherapy, found the volume of the T_2 abnormality to be highly predictive of patient survival. However, in this study the volume of residual disease as measured using a **TUM** VOI was not able to significantly predict progression-free survival, despite the extent of resection being shown to be relate to survival (2). One explanation could be the inclusion of oedema/infiltration as defined on the T_2-weighted FLAIR in the residual volume calculation, however this was also included in the study by Saraswrathy *et al* (149). It is worth noting that the volume of residual disease was 2 times larger in this study 51±36ml vs. 24±15ml. An alternative explanation could be that as tumours become larger, more oncogenes become active. This means that at the point of resection, multiple tumour mutations have occurred and the tumour will continue to grow rapidly regardless of the residual disease. Likewise, with these mutations present, the tumour is most likely to have infiltrated some distance from the enhancing portion of the lesion and the tumour will reoccur equally quick regardless of the residual volume. The volume of enhancing tissue defined by **CEL** was also found to be non-predictive of outcome, possibly due to two types of enhancement (inflammatory and pathological) being present during the time point 2 scans, with median volume of enhancing tissue after surgery found to be 9.30ml.

In terms of clinical management, patients should receive the same chemoradiotherapy treatment regardless of residual tumour volume (**TUM** and **CEL**) given that volume seemingly makes no difference. Other functional parameters should be employed instead to determine candidates for further treatment or increased scan frequency.

Limitations

The biggest limitation of this section is the scan interval itself. As previously discussed, it was not feasible to scan patients within 48 hours of surgery. Subsequently some of the enhancement present is likely to be inflammatory with reactive changes also seen in the size of hyperintense T_2 abnormality. Figure 61 on pg. 79 demonstrates the effect of blood products on the DSC data and the inability to detect increased blood volume in any potential residual disease. The same effect is also present in the DTI data to a lesser degree.

Tumour regrowth is another issue which cannot be excluded from the volume calculations of the residual disease. In one study, 53% of tumours grew between surgery and radiotherapy (223) with tumour growth measured at between 0.3-18.3ml of new tissue in the four week interval until therapy.

8.4.1.5 Section Conclusions

The results from this cohort of patients, suggest that mean PK parameters derived from DCE MRI following surgery can predict progression-free survival. K^{trans}, v_e and v_b were all associated with quicker tumour progression, suggesting HIF1α is up regulated and poorer outcomes will be associated with these patients. The implementation of DCE prior to chemoradiotherapy could be beneficial in 2 ways. Firstly, contrast enhancement could be identified amongst blood products as seen in Figure 61 on pg. 79, to aid radiotherapy planning. Secondly, the PK parameters could also be used to identify patients who would benefit from more frequent scans given the likelihood of early tumour progression. At this time point it would appear that it is not worth conducting DSC examinations based on the blood products present and the more quantitative DCE approach.

8.5 Can Changes Observed in MR Parameters as a Result of Adjuvant Treatment Predict Progression-Free Survival? (Time point 3 – Time point 2)

8.5.1.1 Introduction

This section examines how changes in MR parameters measured from the residual tumour before and after chemoradiotherapy, could predict progression-free survival (PFS) in this cohort of glioma patients. Scans at time point 3 were acquired 2 weeks after the end of chemoradiotherapy whilst the time point 2 scans were acquired 1 week before chemoradiotherapy.

If patients with a shorter PFS interval could be identified then proactive action could be taken either in the form of increased scan frequency, allowing progression to be identified earlier or alternatively, a second line treatment could be prescribed instead, given the patient is likely to be non-response to first line therapies. Hopefully, by identifying longer-term treatment response earlier, patient care can be moved towards a more personalised approach.

8.5.1.2 Section Specific Methods

Multiparametric MR data was acquired from the same 33 patients with histologically proven gliomas as for time point 2. Patients were only included in this analysis if they completed scans at time point 2 and time point 3. Ten critical events were found to have occurred before 210 days after recruitment (approximately 180 days from time point 2). All VOIs (**TUM** and **CEL**) were contoured by the author as detailed on pg. 178. Mean and standard deviation values of each VOI were then subtracted (time point 3 – time point 2) in order to assess changes. Of the cohort of 33 glioma patients, only 28 gliomas had contrast enhancement present in both examinations, thus statistics relating to **CEL** had a reduced number of critical events (9) compared to **TUM**.

Kaplan-Meier survival analysis was calculated for all 40 dichotomised groups [(3 VOIs x 13 parameters) + volume] for each VOI. The volume of tumour in the VOI was also compared with

outcome. In each table, significant results for the Kaplan-Meier survival analysis are highlighted in red.

8.5.1.3 Section Specific Results

Kaplan-Meier survival analysis (Table 61 - Table 64) was calculated for the difference of each statistical descriptor, parameter and VOI combination. When examining the difference in mean parameter values measured using **TUM** following treatment (Table 61), 7 parameters were found to have a p-value less than 0.05. Following calculation of the false discovery rate (FDR), 11% of cases were likely to be false discoveries, equating to 1 parameter-VOI combination. Significant parameters ($p<0.05$) were all related to diffusivity measurements using the DTI and the change in volume. No DCE or DSC parameters significantly correlated with progression-free survival at this time point. The differences in standard deviation values measured using the **TUM** VOI for each parameter revealed 4 significant results (Table 62) however; the FDR was 53% suggesting half of all results in the table were false discoveries. All significant results were generated from the diffusion tensor imaging data.

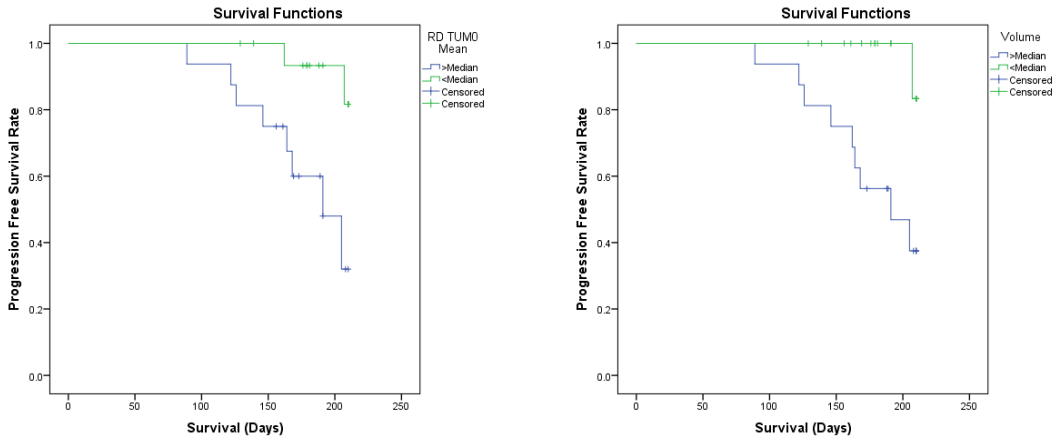

Figure 124 - Kaplan-Meier survival plots showing the prediction of progression free survival in high grade gliomas using the mean change in the radial diffusivity TUM_0 (p=0.007)(left) and change in TUM volume measured between time points 3 and 2 (p=0.004)(right).

The contrast enhancing portion of the lesion (**CEL**) was also assessed to see if changes in the residual enhancing portion of the tumour could predict progression-free survival (Table 63). In the same manner as the **TUM** measurements, the change in mean parameter values was initially assessed

with 3 significant results arising from the v_e and K_2 parameters. The FDR for the mean change in parameters using a **CEL** VOI was calculated to be 19.3% suggesting 1 parameter may be a false positive. The differences in standard deviation values measured using the **CEL** VOI for each parameter revealed 8 significant results (Table 64) with a FDR of 18% suggesting 1 or 2 results in the table were false discoveries. Significant results were generated from all three imaging types (DTI, DCE and DSC).

8.5.1.4 Section Specific Discussion

VOIs

As discussed in time point 2 (section 8.4.1.4), due to the scan interval in relation to that of surgery, VOIs were contoured with less certainty than time point 1, given the difficulty in distinguishing the surgical and inflammatory changes from any possible residual tumour. For this section, the values of independently contoured VOIs were compared rather than a pixel wise subtraction as carried out for functional diffusion maps (49, 162, 171, 172). The rationale behind this decision was due to the tissue remodelling which occurs following surgery and potential of mass effect causing subtraction artefacts. Previously most fDMs have been calculated in patients with recurrent disease where surgery had not recently occurred.

From the Kaplan-Meier survival analysis, a change in the volume of the tumour abnormality, defined as: **TUM** = $T_{2all} + T_{1all} - NEC - HMG$, was found to be a significant predictor of progression-free survival (P=0.004), with a decrease in volume more than 3012 pixels (7.94ml) found to be a predictor that the residual disease will remain stable for longer. The change in enhancing volume (**CEL**) was not found to be a significant predictor of progression-free survival however; this could be related to the possibility that some of the contoured enhancement represented inflammatory enhancement rather than residual disease.

DTI

Mean measurements of the change in diffusivity (ADC, λ_L and λ_R) over treatment were all significant predictors of progression-free survival when measured using both **TUM** and **TUM_0** VOIs. However, the direction of the change in diffusivity was opposite to the expected change. Previously, in solid tumours, ADC values have been shown to increase in tumours that respond to treatment (224) following reduced cell proliferation and increased cell death. In this study however, increasing ADC values of the whole abnormality (**TUM**) were found to be associated with a shorter progression-free survival interval. This observation may be due to the data sampling scheme used, whereby the whole abnormality was analysed rather than only the enhancing portion of the tumour. If the volume of oedema was to increase whilst the solid tumour remained the same, then the mean ADC of the lesion would increase. Thus, when using the methodology employed in this thesis to assess tumour response, changes in ADC values may be considered biomarkers for reactive changes in the surrounding brain due to tumour growth/infiltration rather than a direct measure of a solid tumour's response to therapy. Alternatively, the increase in ADC values could relate to tumour progression with firstly, increased amounts of micro-necrosis present throughout the active tumour (Figure 125) and secondly the potential of artificially elevated ADC values due to intravoxel incoherent motion (IVIM) (50, 225).

Changes in the standard deviation of ADC, FA, q and radial diffusivity values were all found to be significant predictors of progression-free survival. Increasing standard deviation values of diffusivity were associated with poorer outcomes, suggesting less 'normal' tissue exists within the VOI. The presence of necrosis increases ADC and λ_R values whilst solid, rapidly dividing tumour decreases values within local regions within the volume of interest. Overall this increases the overall standard deviation of the VOI.

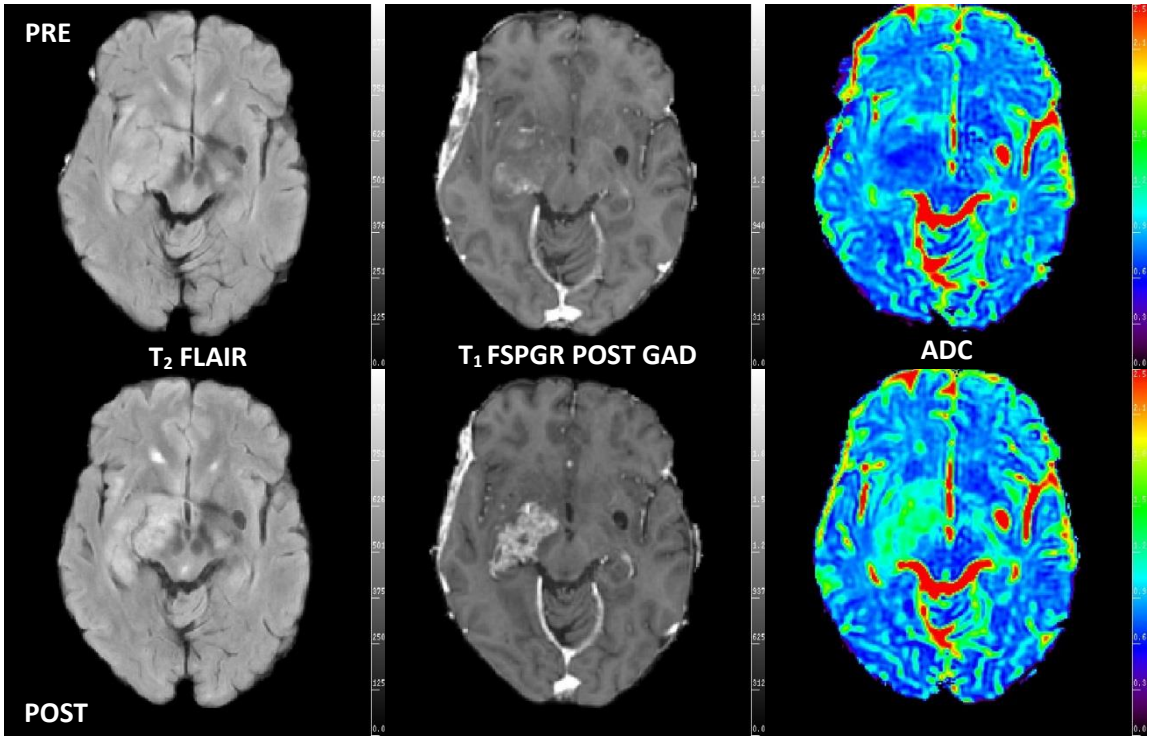

Figure 125 – Example images before and after chemoradiotherapy from a patient with an anaplastic oligoastrocytoma (ADC values scaled between 0-2.5x10^{-3}mm^{2}s^{-1}). Pre- and post-treatment images are not registered in this figure to show image quality, and the native ready brain prescription angle; however skull removal was performed. ADC values were observed to increase within the lesion following treatment (necrosis was excluded). The patient died 205 days after recruitment to the study. Importantly, the scan interval (2 weeks after therapy) was too short for treatment induced pseudo-progression.

From the enhancing portion of the tumour, a change in mean diffusion measurements was not predictive of progression-free survival for any DTI parameters in this study. However, decreasing standard deviation values of diffusivity within **CEL** were associated with poorer outcomes, suggesting that as the enhancing potion of the tumour becomes more homogeneous, progression occurs more rapidly. At a cellular level, this might suggest that the tumour can sustain itself without the need for autophagy and is displaying increased amounts of cell proliferation. This finding may also relate to cases where the chemoradiotherapy has not caused necrosis in the enhancing portion of the tumour, effectively where the treatment has failed.

DCE

Changes in mean PK parameters measured using **TUM** VOIs for each patient were not significant predictors of PFS. This pattern was also observed with changing standard deviation values of PK parameters using **TUM**. However, using a **CEL** VOI, changes in the mean and standard deviation values of v_e were highly significant predictors of PFS, with increasing mean and standard deviation values of v_e observed over the course of treatment, being associated with a shorter progression-free interval. Previously, v_e values have been shown to increase with glioma grade, as demonstrated in this study (pg. 195) and the literature (191, 204). Given increased grade is considered a poor prognostic indicator; an increasing v_e could also be considered as a poor prognostic biomarker (Figure 126). The increasing EES may be an indication that the tumour cells are under stress, with HIF1α and autophagy up regulated in order to sustain the tumour. Since high v_e values have previously been found in necrotising component of glioblastoma (226). An alternative explanation is that the increasing v_e values represent continued tumour progression regardless of treatment.

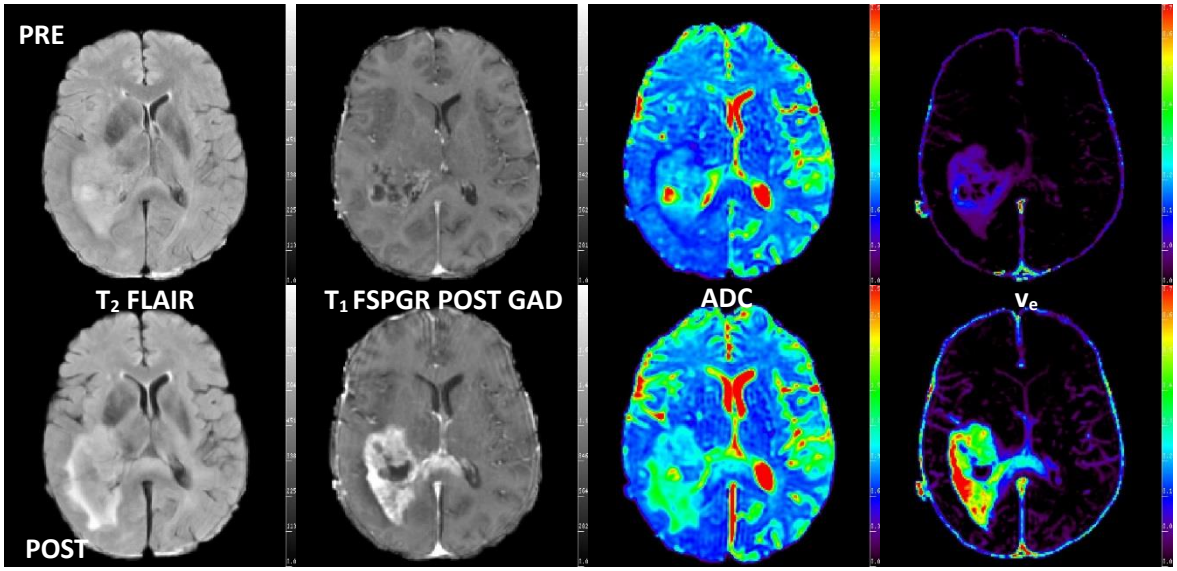

Figure 126 - Example of patient with a high grade glioma (ADC scaled 0-2.5x10^{-3}mm^{2}s^{-1}). Note the increase in enhancement and elevated v_e throughout the lesion following treatment (scaled 0-0.75). The patient died 126 days after recruitment into the study. Images are temporally registered to show how the tumour changed. It is also worth noting the amount of enhancement present using the DCE at time point 2 not seen on the FSPGR.

Changes in K^{trans} and v_b were not significant using any type of VOI and may relate to the early scan interval after treatment being too early to observe changes. Despite strong correlations existing between K^{trans} and v_e (pg. 187), it would appear changes in v_e can be observed prior to K^{trans} and v_b following treatment in gliomas. This could be due to v_e being a measure of the interstitial space which describes the cellular environment whilst K^{trans} and v_b are descriptors of tumour vasculature which may alter at a later time point. Alternatively, chemoradiotherapy may actually have little effect on the tumour vasculature and thus the PK parameters don't change with treatment, possibly explaining why gliomas normally reoccur.

DSC

Much like the DCE parameters in this section, changes in DSC derived parameters sampled using a **TUM** VOI were not significant predictors of progression-free survival. However, changes in the mean and standard deviation values of K_2 measured with **CEL** were significant predictors of progression-free survival. An increasingly more negative mean K_2 value within **CEL** was found to be a poor prognostic indicator. Patients with an increasing standard deviation of K_2 values within the enhancing portion of the tumour were also found to have a shorter progression-free survival interval. K_2 indicates T_1 or T_2*dominant leakage with a negative K_2 value being a T_2* dominant effect, i.e. sufficient EES (v_e) to allow trapping of the contrast agent.

Limitations

When comparing scans over the course of treatment, it is always difficult to measure parameters from the same volume of tissue at each time point. Therefore in this section, the same volume of interest methodology was employed at time point 2 and time point 3. Due to the evolution of the tumour cavity and tissue remodelling following surgery, some voxels of tissue may not have been included at both sections. If previously solid tumour had turned into obvious necrosis then it was excluded from analysis at the 3rd time point even though it could represent a treatment response.

Currently there is no imaging modality which can confidently differentiate treatment induced necrosis (apoptosis) from autophagy.

Radiotherapy can also induce T_2 changes in the brain, especially in white matter. This means the calculation of the **TUM** volume potentially could have been effected by tumour infiltration, oedema, solid tumour, radiation changes and steroid dose. Steroids can reduce the mass effect and swelling caused by tumours in the brain and subsequently the volume of T_2 change. Scanning within 2 weeks of the end of chemoradiotherapy should have minimised the amount of T_2 change caused by radiotherapy (227).

As discussed following the time point 2 data analysis, the scan interval could have had a profound effect, with inflammatory changes present even before treatment started as a result of surgery (Figure 127). This may explain why the change in volume of enhancing tumour was not a significant predictor of progression-free survival given the potentially false baseline caused by post-surgical enhancement. The evolution of blood products could also artificially change some tumour parameters as regions of susceptibility resolve.

The quality of the multiparametric volume registration could have an impact on the results, with VOIs defined using morphological imaging, meaning that incorrect registration would result in the sampling of undesired tissue such as necrosis, CSF or normal brain. Given this section examines differences in the mean values, robust registration was crucial. Examples of the registration quality (between sequences and time points) have been shown throughout this thesis to indicate the quality and confidence in the registration.

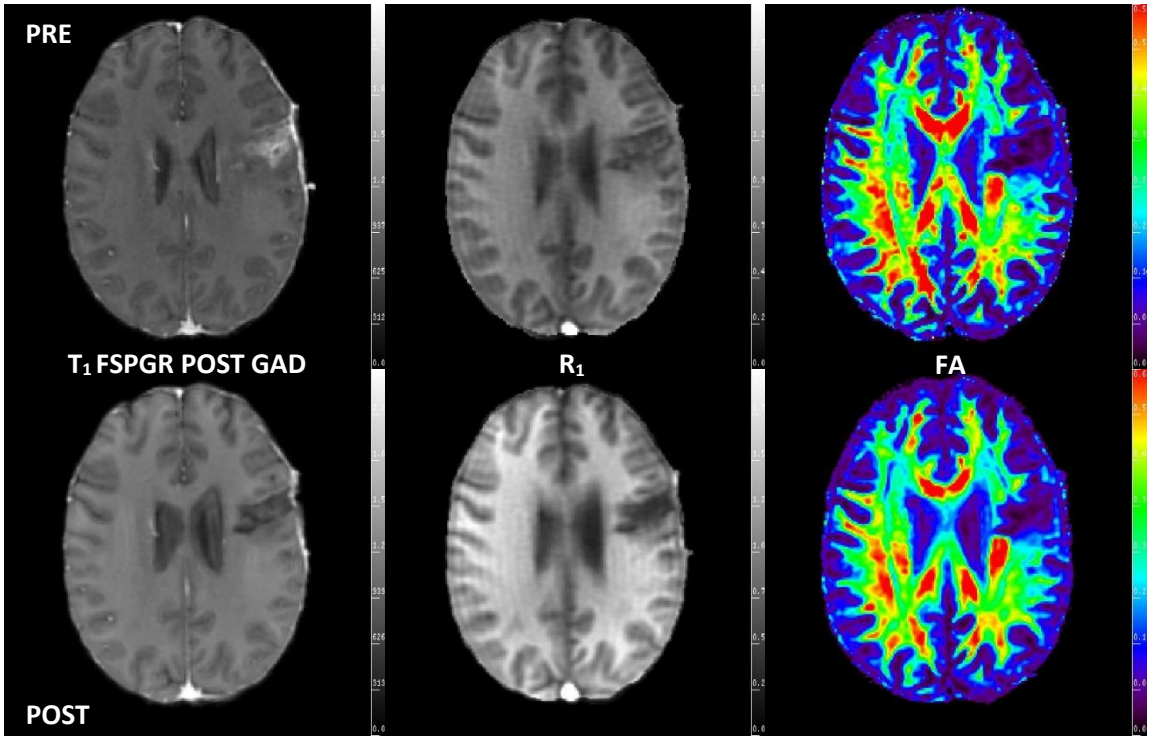

Figure 127 – Pre- and post-chemoradiotherapy images showing reduced enhancement. From left to right, contrast enhanced T_1-weighted FSPGR, R_1 (0-2s^{-1}) and fractional anisotropy (0-0.6) images. On the pre-chemoradiotherapy imaging contrast enhancement was present despite the lesion not enhancing prior to resection. The reduction in enhancement 2 weeks after the end of chemoradiotherapy most likely represents reduced inflammation around the surgical cavity rather than a reduction in enhancing tumour. Only by imaging patients within 48 hours of surgery can postoperative enhancement be ruled out. Note that the fractional anisotropy maps show no change.

Regarding the limitations of the diffusion parameters, perfusion and blood products followed by geometric distortion remain the main factors which could affect the measured values. Perfusion effects can cause artificially elevated ADC values due to intravoxel incoherent motion (IVIM) whilst hemosiderin has the potential to completely destroy the MR signal. Geometric distortion associated with echo-planar imaging can cause issues with the correct sampling of tissue, especially in frontal lesions where the distortion is greatest. Efforts to minimise this during the image processing scheme were employed, by utilising 12 degrees of freedom for registering the FA maps to the T_1-weighted volume. The two main limitations of the DCE data were coverage (Figure 128), which was limited to an 80mm thick slab through the lesion and SNR of data given the temporal resolution of 5 seconds. Unlike the other imaging sequences which included the whole brain, the DCE was restricted to encompass only the lesion and the immediate brain tissue.

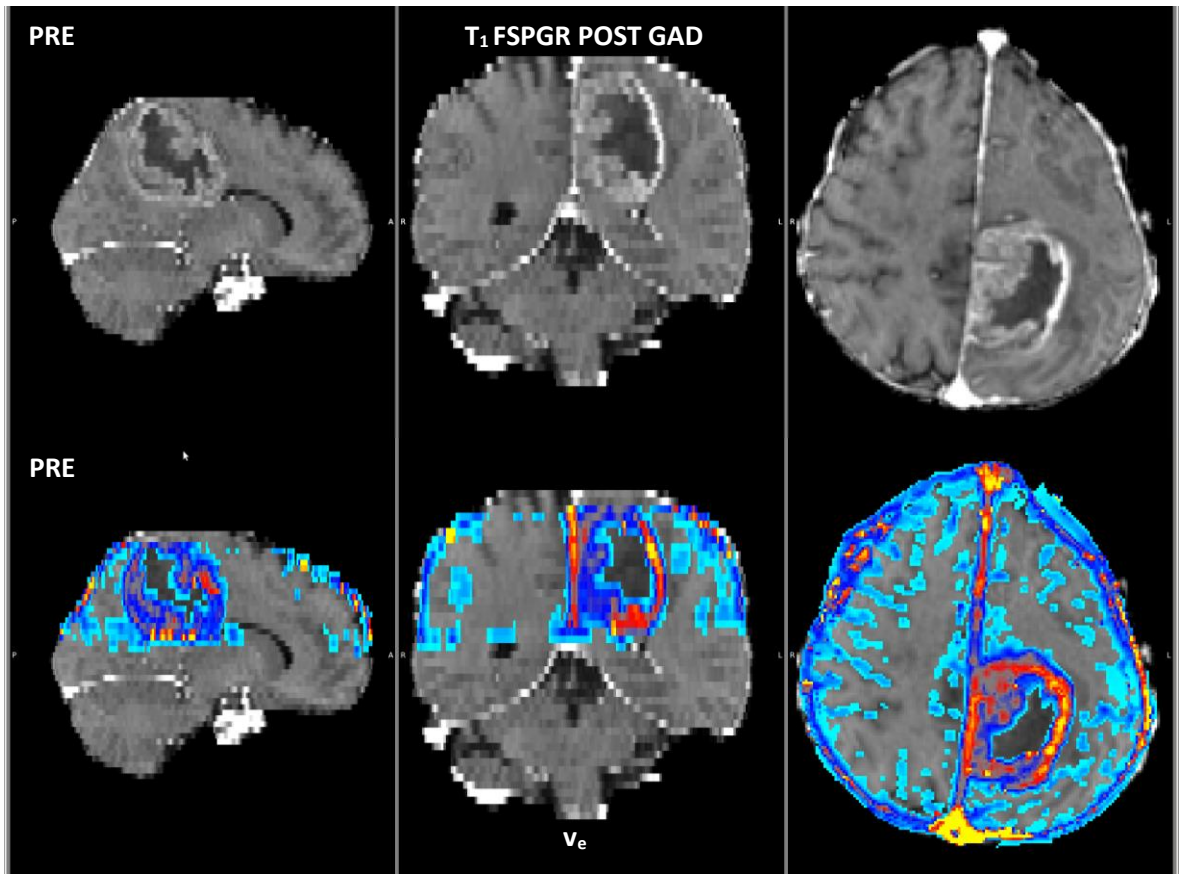

Figure 128 – Example of the limited through-plane coverage of the DCE visualised using FSL. The top row shows the T_1 FSPGR post-contrast imaging interpolated to 3mm thick slices in a glioblastoma patient. The bottom set of images shows a registered v_e volume interpolated from 4mm to 3mm slice thickness and overlaid on the T_1 FSPGR imaging.

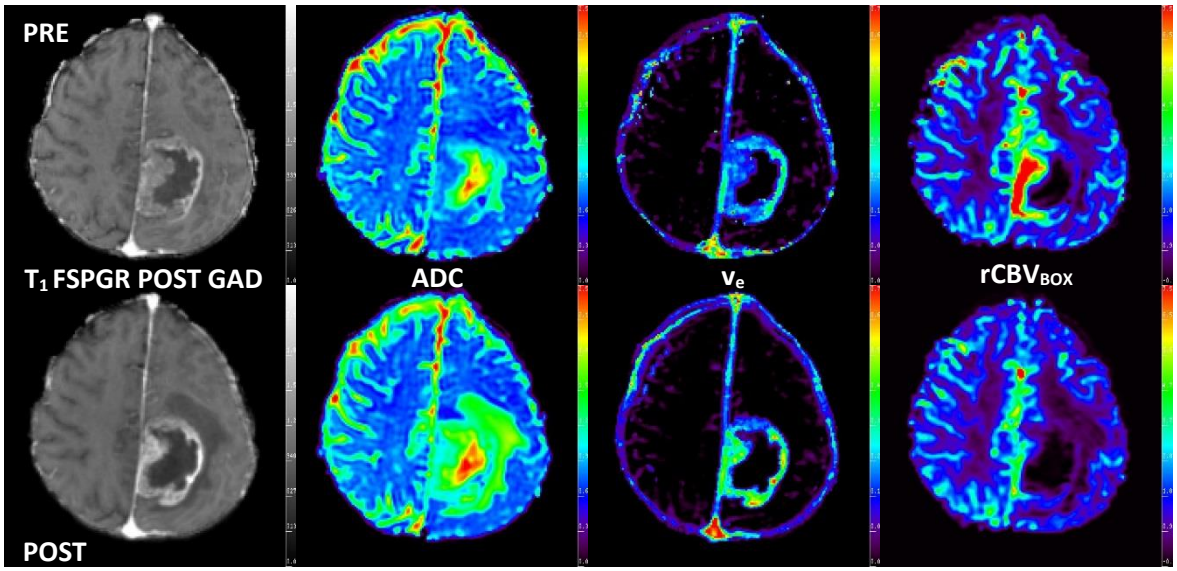

Figure 129 - Example of patient with a glioblastoma multiforme. Parameters are identically scaled between scans (ADC=0-2.5x10^{-3}mm^{2}s^{-1}, v_e=0-0.75, $rCBV_{BOX}$=0-7.5). Note the increase of v_e throughout the lesion following treatment whilst $rCBV_{BOX}$ decreases. The patient died 89 days after recruitment into the study. Images are temporally registered to show how the tumour changes.

The DSC was the least quantitative of the 3 imaging modalities used in this section and is reliant on the white matter masks produced to normalise the CBV values for comparison of values between scans and patients. As seen in Figure 129, the rCBV values appear similar in the normal appearing brain whilst appearing to change in the lesion.

8.5.1.5 Section Conclusions

The mean change of the apparent diffusion coefficient, longitudinal diffusivity and radial diffusivity measured using **TUM** and **TUM_0** populations were all significant predictors of progression-free survival with a mean increase being associated with a shorter progression-free interval. An increase in the standard deviation values of ADC, q and λ_R measured using **TUM_0** and a decrease in the FA measured with **TUM** were all significant predictors of a shorter progression-free survival. Changes in the mean whole tumour measurements of DCE and DSC parameters are not significant predictors in this cohort. However, when examining the enhancing portion (**CEL**) of the tumour at both time points, changes in mean v_e and K_2 measurements using **CEL** significantly predict progression-free survival. An increase in v_e or a decrease in K_2 over the course of treatment should be considered as a poor prognostic indicator in gliomas. The change in the volume of enhancing tumour (**CEL**) was not predictive of the progression-free survival interval. Changes in the standard deviations of ADC, λ_L, λ_R R_1 using **CEL** are however predictive, with all parameters becoming more homogenous in patients who progressed quicker. Standard deviation measurements of v_e and K_2 measured with **CEL** were also predictive of progression-free survival with increasing standard deviations found to have short progression-free intervals.

8.6 Can MR Parameters Measured from the Residual Disease Following Chemoradiotherapy Predict Progression-Free Survival? (Time point 3)

8.6.1.1 Introduction

This section examines the residual tumour after surgery and chemoradiotherapy, and whether MR parameters can predict the time to progression in this cohort of glioma patients. Scans at time point 3 were acquired 2 weeks after the end of chemoradiotherapy.

8.6.1.2 Section Specific Methods

Multiparametric MR data was acquired from the same 33 patients with histologically proven gliomas as for time point 2. Patients were only included in this analysis if they completed scans at time point 2 and time point 3 so the efficacy of different time points could later be compared. Ten critical events were found to have occurred before 210 days after recruitment (approximately 180 days from time point 2). All **TUM** VOIs were contoured by the author. Kaplan-Meier survival analysis was calculated for all dichotomised groups. In each table, significant results for the Kaplan-Meier survival analysis are highlighted in red.

8.6.1.3 Section Specific Results

Kaplan-Meier survival analysis (Table 65) was calculated for each parameter and VOI combination. Out of 40 dichotomised parameters, 8 were found to have a p-value less than 0.05. Following calculation of the FDR, 9.4% of cases were likely to be false discoveries which equated to 1 parameter-VOI combinations. Significant parameters ($p<0.05$) found using the Kaplan-Meier survival analysis were radial diffusivity from the DTI, K^{trans} and v_e PK parameters derived from the DCE and K_2 from the DSC parameters (Figure 130).

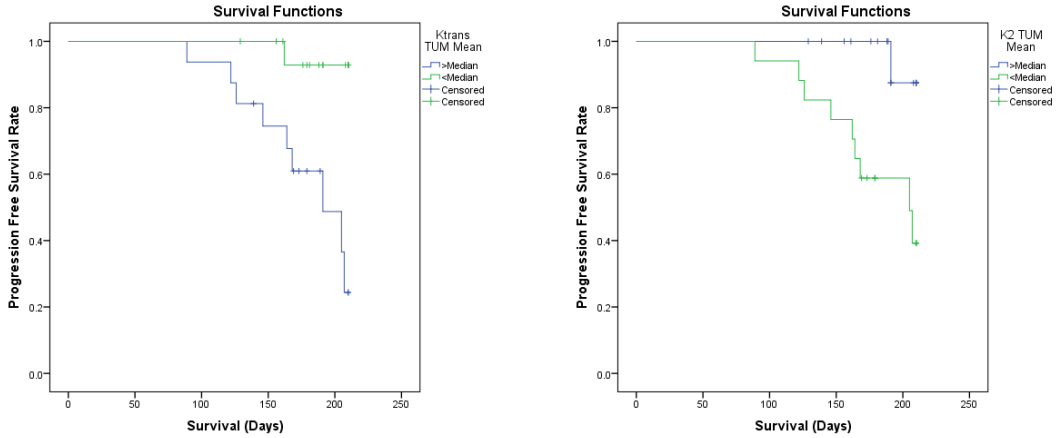

Figure 130 - Kaplan-Meier survival plots showing the prediction of progression free survival in high grade gliomas using the mean K^{trans} TUM (p=0.002)(left) and K_2 TUM (0.011) populations measured at time point 3 (right).

Standard deviations of MR parameters sampled with **TUM**, were found to have a FDR 10.4%, with 1 out of 6 significant results likely to be a false discovery. Significant progression-free survival predictions were found for K^{trans}, v_e, $rCBV_{BOX}$ and K_2. Mean values of **CEL**, showed 7 significant parameters with a FDR of 13.0%. Significant parameters were found for all populations of K^{trans} and v_e as well $rCBV_{BOX}$ sampled with **CEL**. Notably, v_e sampled using **CEL**, correctly identified the 9 patients who progressed before 210 days. These gliomas all had a mean **CEL** v_e greater than 0.215.

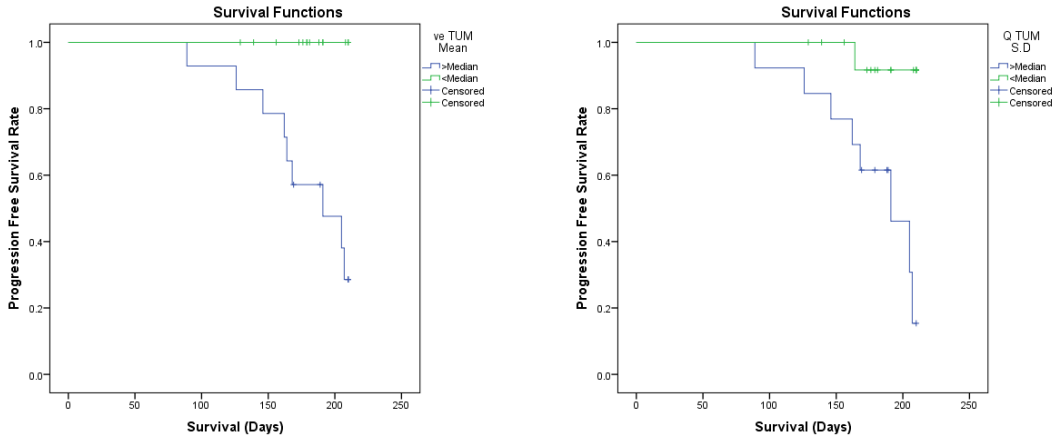

Figure 131 - Kaplan-Meier progression free survival plots for high grade gliomas using the mean v_e CEL (p=0.004)(left) and q CEL (0.004) standard deviation measured at time point 3 (right).

When examining the standard deviations of **CEL** sampled parameters, 5 significant results were found for q, K^{trans}, v_e and $rCBV_{BOX}$ populations. In this section, the FDR was only 2.9%, suggesting no false discoveries within the significant results.

8.6.1.4 Section Specific Discussion

DTI

At this time point, only longitudinal diffusion measured using **TUM** was found to be a significant predictor of progression-free survival using DTI, with higher mean longitudinal diffusivity values found to indicate a more rapid progression for patients. ADC measured with **TUM_0** suggested that lower diffusivity values were associated with poorer outcomes but the p-value did not reach significance. FA and q showed suggestive results with increased fibre directionality values observed within the **TUM** VOI being associated with worsened outcomes, which goes against *a priori* predictions (84, 137, 164). However, these did not reach significance. None of the standard deviation measurements of the **TUM** VOI were significant predictors of progression-free survival either. DTI parameters sampled using **CEL** were generally not predictive of progression-free survival with the exception of standard deviations of q within the **CEL** VOI which showed q to be highly predictive (P=0.004 and P=0.008 for **CEL** and **CEL_1** populations).

DCE

Mean values of K^{trans} and v_e measured using all populations of the **TUM** VOI were found to significantly predict progression-free survival. In all cases, high K^{trans} and v_e were associated with a shorter progression-free survival interval. These findings mirror the observations of PK parameters at time points 1 and 2. Interestingly, v_b was no longer a significant predictor of progression-free survival despite all populations being significant at time point 2. A possible loss of significance for v_b could relate to administration of chemoradiotherapy, and disruption of the tumour capillary network, changing the observable v_b. Standard deviations of K^{trans} and v_e for **TUM** were also found to be highly significant using the whole tumour abnormality VOI, where increased heterogeneity related to a shorter progression-free survival interval.

As expected, given the relationship between contrast enhancement and PK parameters, mean K^{trans} and v_e parameters were significant predictors of progression-free survival in both **TUM** and **CEL**, with higher values associated with a shorter progression-free interval. Mean v_e values sampled using **CEL** correctly identified all patients who progressed before 210 days. The standard deviations of K^{trans} and v_e for $\mathbf{CEL_0}$ were also found to be significant.

DSC

The mean K_2 value for **TUM** was found to be a significant predictor for progression-free survival. Given the parameter is associated with vessel leakage, much like K^{trans}, it is not surprising that a similar result is present. With much of the blood products dispersed at this time point, regions of local susceptibility would be expected to be reduced allowing more technically successful measurements of T_2* perfusion of the residual tumour. Standard deviations of $rCBV_{BOX}$ and K_2 were found to significantly predict progression-free survival. Mean and standard deviations of $rCBV_{BOX}$ proved to be significant when sampled with **CEL**. K_2 was no longer a significant predictor of progression-free survival when sampled with **CEL**, possibly due to the slice thickness the DSC was acquired with, or blood products which may have degraded the DSC data.

Residual Tumour Volume

In a similar manner to time point 2, the volume of residual disease as measured using a **TUM** or **CEL** VOI was not able to significantly predict progression-free survival. As previously proposed in this thesis, the initial tumour volume at time point 1 may result in a greater number of oncogenes, resulting in a poor prognosis regardless of the amount residual disease. Examination of the Kaplan-Meier results at this time point suggest residual volume has some influence on the time to progression, however it was found to be non-significant.

Limitations

The limitations of this section are comparable to the time point 2 limitations with tissue remodelling and surgical cavity evolution likely to still be present, with the possibility of inflammatory changes still causing some enhancement surrounding the surgical site. As previously discussed, radiotherapy can also induce T_2 changes in the brain, especially in white matter. This means the calculation of the **TUM** volume potentially could have been effected by tumour infiltration, oedema, solid tumour, radiation changes and steroid dose. However, scanning within 2 weeks of the end of radiotherapy should have minimised the amount of T_2 change caused by radiotherapy with is often a delayed effect.

Similar problems with imaging, processing and registration exist at this time point given the identical protocol to time points 1 and 2. However, hemosiderin induced susceptibility should be reduced at this time point as well as less acute blood products caused by the surgery.

8.6.1.5 Section Conclusions

Mean and standard deviations of K^{trans} and v_e sampled using **TUM** and **CEL** VOIs, were all significant predictors of progression-free survival for 210 days. Elevated PK parameters at 2 weeks post-chemoradiotherapy were predictive of progression-free survival. DTI in isolation has no prognostic value at this time point, whilst K_2 sampled with **TUM** and $rCBV_{BOX}$ sampled with **CEL** are still worth investigating. The blood volume fraction at this scan interval also has no prognostic value and K^{trans} and v_e are more useful predictors at this time point.

8.7 Cox Regression Survival Analysis

In order to reduce the number of significant results, to a few clinically useful parameters, Cox regression survival analysis was employed on the **TUM** and **CEL** cohorts of time points 2 and 3 as well as the change in parameter values between time points.

8.7.1.1 Methods

The significant results from the Kaplan-Meier survival analysis at time points 2, 3-2 and 3 (Sections 8.4.1.3, 8.5.1.3 and 8.6.1.3) were used to indicate which parameters served as the input for the Cox proportional hazard ratios test. Due to the high number of significant results and the potential of overlap between similar parameters and over parameterisation, the magnitude of the factor correlations from the factor analysis was used to identify which of the significant parameter/time point/GMM population/statistical descriptors contributed most to each of the principal components (see pg. 242). This was done separately for the **TUM** and **CEL** groups due to the differing numbers of patients. Cox regression survival analysis was calculated using the parameter with the greatest factor correlation of the parameter/time point/GMM population/statistical descriptors from each factor analysis component. All identified parameters were initially entered into the Cox regression model and subsequently removed using a backward Wald methodology. Clinical factors, which were age, grade and cell type, were simultaneously entered into the model at this point. In order to approximately normalise the values between different MR parameters, to identify small changes, PK parameters were multiplied by 100, whilst all other MR parameters were multiplied by 10.

8.7.1.2 Results

Factor analysis of the cohort sampled using the **TUM** VOI (N=33) revealed 8 principal components with eigenvalues greater than 1. (Table 27). The maximum absolute factor correlation values are identified in red and were selected as the input for Cox regression. The Cox model for **TUM**

parameters sampled during time points 2 and 3 (Table 29), shows a reduction in the number of significant MR parameters from 8 to 2, with a $0.1x10^{-3}mm^2s^{-1}$ increase in mean ADC values for **TUM** between scans found to be associated with a 101% (3-291%) increased risk of a shorter progression-free survival interval, whilst a $0.01min^{-1}$ increase in mean K^{trans} within the **TUM** VOI at time point 3 also found to have a 31% (9-57%) increased risk of a short progression-free survival interval.

The same process was repeated for the **CEL** VOIs (N=28) (Table 28). Table 30 shows a reduction in the number of significant parameters from 7 to 3. Both changes in R_1 and v_e standard deviations of **CEL** during treatment were significant predictors of progression-free survival. An increase in the standard deviation of R_1 values in **CEL** was found to reduce the risk of progression by 80% (37-93%) per $0.1s^{-1}$ increase, whilst an increase in the standard deviation of the **CEL** v_e increased the risk of progression before 210 days by 33% (5-68%) per 1% increase in extravascular extracellular space per volume of tissue. A $0.01min^{-1}$ increase in mean K^{trans} of the **CEL** VOI was also found to be associated with a 110% increased risk of a shorter progression-free survival. Patient age at presentation showed an 8% decreased risk per year, however, the confidence interval and p-value suggest it may have no effect. Cell type and tumour grade were not retained by the model.

*Table 27 - Magnitude values of the correlations between the 38 parameters and each principal component. The input for the factor analysis were the significant predictors of progression-free survival identified using the Kaplan-Meier survival analysis of time points 2 and 3 sampled using **TUM** VOIs.*

Parameter	Statistic	VOI	Time Point	Component							
				1	2	3	4	5	6	7	8
λ_L	Mean	TUM_1	TP2	0.01	0.09	0.03	0.33	0.04	0.04	0.00	0.02
λ_R	Mean	TUM_0	TP2	0.07	0.12	0.00	0.43	0.00	0.20	0.05	0.00
K^{trans}	Mean	TUM_0	TP2	0.55	0.06	0.20	0.02	0.03	0.05	0.01	0.02
v_e	Mean	TUM_0	TP2	0.46	0.07	0.05	0.04	0.00	0.18	0.06	0.00
v_e	Mean	TUM_1	TP2	0.15	0.01	0.12	0.07	0.35	0.01	0.05	0.14
v_b	Mean	TUM	TP2	0.59	0.20	0.12	0.02	0.00	0.00	0.00	0.01
v_b	Mean	TUM_0	TP2	0.60	0.06	0.00	0.09	0.01	0.08	0.03	0.01
v_b	Mean	TUM_1	TP2	0.58	0.18	0.14	0.02	0.02	0.00	0.00	0.02
λ_L	S.D.	TUM_0	TP2	0.05	0.03	0.01	0.55	0.03	0.01	0.10	0.01
K^{trans}	S.D.	TUM	TP2	0.55	0.06	0.20	0.02	0.03	0.05	0.01	0.02
v_b	S.D.	TUM_0	TP2	0.60	0.06	0.00	0.09	0.01	0.08	0.03	0.01
v_b	S.D.	TUM_1	TP2	0.58	0.18	0.14	0.02	0.02	0.00	0.00	0.02
K_2	S.D.	TUM	TP2	0.27	0.00	0.00	0.03	0.21	0.00	0.03	0.22
ADC	Mean	TUM	TP3-TP2	0.12	0.75	0.01	0.04	0.00	0.00	0.00	0.03
ADC	Mean	TUM_0	TP3-TP2	0.12	0.71	0.08	0.01	0.00	0.00	0.01	0.01
λ_L	Mean	TUM	TP3-TP2	0.11	0.73	0.02	0.07	0.00	0.00	0.00	0.01
λ_L	Mean	TUM_0	TP3-TP2	0.03	0.39	0.06	0.00	0.18	0.01	0.22	0.00
λ_R	Mean	TUM	TP3-TP2	0.12	0.71	0.00	0.02	0.00	0.01	0.00	0.05
λ_R	Mean	TUM_0	TP3-TP2	0.16	0.68	0.05	0.01	0.01	0.00	0.00	0.03
Volume	Volume	TUM	TP3-TP2	0.23	0.04	0.05	0.03	0.22	0.02	0.19	0.03
ADC	S.D.	TUM_0	TP3-TP2	0.47	0.00	0.13	0.12	0.09	0.01	0.00	0.02
FA	S.D.	TUM	TP3-TP2	0.09	0.23	0.14	0.03	0.01	0.00	0.00	0.08
q	S.D.	TUM_0	TP3-TP2	0.04	0.37	0.00	0.05	0.04	0.15	0.00	0.02
λ_R	S.D.	TUM_0	TP3-TP2	0.27	0.24	0.05	0.20	0.01	0.02	0.05	0.02
λ_L	Mean	TUM	TP3	0.03	0.18	0.18	0.10	0.10	0.19	0.05	0.02
K^{trans}	Mean	TUM	TP3	0.81	0.02	0.06	0.00	0.01	0.01	0.04	0.00
K^{trans}	Mean	TUM_0	TP3	0.72	0.00	0.12	0.00	0.03	0.06	0.01	0.01
K^{trans}	Mean	TUM_1	TP3	0.80	0.04	0.01	0.00	0.02	0.00	0.03	0.02
v_e	Mean	TUM	TP3	0.75	0.00	0.08	0.01	0.02	0.01	0.05	0.00
v_e	Mean	TUM_0	TP3	0.14	0.01	0.11	0.08	0.25	0.19	0.00	0.01
v_e	Mean	TUM_1	TP3	0.77	0.00	0.01	0.06	0.01	0.00	0.03	0.04
K_2	Mean	TUM	TP3	0.38	0.05	0.42	0.01	0.01	0.00	0.00	0.00
K^{trans}	S.D.	TUM	TP3	0.70	0.06	0.00	0.00	0.02	0.05	0.03	0.05
K^{trans}	S.D.	TUM_0	TP3	0.76	0.01	0.07	0.00	0.06	0.04	0.01	0.01
v_e	S.D.	TUM	TP3	0.73	0.01	0.00	0.03	0.00	0.05	0.05	0.03
$rCBV_{BOX}$	S.D.	TUM	TP3	0.43	0.05	0.03	0.00	0.10	0.01	0.13	0.06
K_2	S.D.	TUM	TP3	0.57	0.04	0.23	0.00	0.01	0.02	0.01	0.01
K_2	S.D.	TUM_0	TP3	0.47	0.02	0.14	0.00	0.01	0.05	0.08	0.00

*Table 28 – Magnitude values of the correlations between the 38 parameters and each principal component. The input for the factor analysis were the significant predictors of progression-free survival identified using the Kaplan-Meier survival analysis of time points 2 and 3 sampled using **CEL** VOIs.*

Parameter	Statistic	VOI	Time Point	Component						
				1	2	3	4	5	6	7
q	**Mean**	**CEL**	**TP2**	0.38	0.00	0.20	0.01	0.00	0.17	0.08
q	**Mean**	**CEL_1**	**TP2**	0.24	0.04	0.30	0.05	0.10	0.04	0.10
v_b	**Mean**	**CEL**	**TP2**	0.61	0.24	0.07	0.00	0.01	0.02	0.01
v_b	**Mean**	**CEL_0**	**TP2**	0.52	0.34	0.00	0.04	0.01	0.02	0.01
v_b	**Mean**	**CEL_1**	**TP2**	0.49	0.14	0.10	0.00	0.00	0.13	0.01
FA	**S.D.**	**CEL_1**	**TP2**	0.06	0.02	0.19	0.01	0.09	0.11	0.00
q	**S.D.**	**CEL**	**TP2**	0.35	0.00	0.26	0.15	0.00	0.03	0.01
λ_L	**S.D.**	**CEL_0**	**TP2**	0.01	0.22	0.15	0.12	0.04	0.01	0.26
v_b	**S.D.**	**CEL_0**	**TP2**	0.45	0.41	0.02	0.02	0.02	0.01	0.00
v_e	**Mean**	**CEL**	**TP3-TP2**	0.63	0.14	0.04	0.01	0.04	0.02	0.04
v_e	**Mean**	**CEL_0**	**TP3-TP2**	0.65	0.07	0.02	0.05	0.03	0.10	0.00
K_2	**Mean**	**CEL**	**TP3-TP2**	0.41	0.03	0.21	0.17	0.05	0.02	0.00
ADC	**S.D.**	**CEL**	**TP3-TP2**	0.12	0.62	0.06	0.00	0.15	0.05	0.00
λ_L	**S.D.**	**CEL**	**TP3-TP2**	0.07	0.58	0.05	0.00	0.23	0.04	0.00
λ_R	**S.D.**	**CEL**	**TP3-TP2**	0.15	0.63	0.04	0.00	0.12	0.04	0.00
R_1	**S.D.**	**CEL**	**TP3-TP2**	0.02	0.01	0.37	0.08	0.04	0.17	0.01
v_e	**S.D.**	**CEL**	**TP3-TP2**	0.28	0.16	0.00	0.02	0.00	0.03	0.28
v_e	**S.D.**	**CEL_0**	**TP3-TP2**	0.65	0.13	0.03	0.00	0.01	0.06	0.00
K_2	**S.D**	**CEL**	**TP3-TP2**	0.55	0.02	0.08	0.11	0.07	0.01	0.07
K_2	**S.D.**	**CEL_1**	**TP3-TP2**	0.11	0.07	0.22	0.25	0.03	0.04	0.08
K^{trans}	**Mean**	**CEL**	**TP3**	0.81	0.01	0.07	0.04	0.01	0.01	0.00
K^{trans}	**Mean**	**CEL_0**	**TP3**	0.89	0.00	0.02	0.00	0.01	0.01	0.00
K^{trans}	**Mean**	**CEL_1**	**TP3**	0.76	0.02	0.08	0.03	0.00	0.03	0.02
v_e	**Mean**	**CEL**	**TP3**	0.84	0.00	0.04	0.00	0.04	0.01	0.03
v_e	**Mean**	**CEL_0**	**TP3**	0.84	0.00	0.02	0.00	0.01	0.00	0.01
v_e	**Mean**	**CEL_1**	**TP3**	0.80	0.02	0.06	0.00	0.02	0.02	0.00
$rCBV_{BOX}$	**Mean**	**CEL**	**TP3**	0.31	0.21	0.07	0.01	0.31	0.01	0.00
q	**S.D.**	**CEL**	**TP3**	0.02	0.02	0.28	0.49	0.05	0.00	0.01
q	**S.D.**	**CEL_1**	**TP3**	0.04	0.05	0.22	0.38	0.01	0.02	0.05
K^{trans}	**S.D.**	**CEL_0**	**TP3**	0.84	0.00	0.08	0.04	0.00	0.00	0.01
v_e	**S.D.**	**CEL_0**	**TP3**	0.81	0.01	0.12	0.02	0.01	0.00	0.00
$rCBV_{BOX}$	**S.D.**	**CEL**	**TP3**	0.34	0.29	0.00	0.00	0.16	0.01	0.01

Table 29 - Final Model from a 210 day progression-free Cox regression survival analysis using the parameters with a p-value less than 0.05 as calculated during the Kaplan-Meier survival analysis of 33 patients sampled with TUM VOIs at time points 2 and 3.

Time Point	Parameter	Stat.	VOI	B	Sig.	Hazard Ratio	95.0% CI for Hazard Ratio	
							Lower	Upper
TP3-TP2	**ADC**	**Mean**	**TUM**	0.70	0.041	2.01	1.03	3.91
TP3	**K^{trans}**	**Mean**	**TUM**	0.27	0.003	1.31	1.09	1.57

Table 30 - Final Model from a 210 day progression-free Cox regression survival analysis using the parameters with a p-value less than 0.05 as calculated during the Kaplan-Meier survival analysis of 28 patients sampled with CEL VOIs at time points 2 and 3.

Time Point	Parameter	Stat.	VOI	B	Sig.	Hazard Ratio	95.0% CI for Hazard Ratio	
							Lower	Upper
TP3-TP2	**R_1**	**S.D.**	**CEL**	-1.59	0.006	0.20	0.07	0.63
TP3-TP2	**v_e**	**S.D.**	**CEL**	0.29	0.016	1.33	1.05	1.68
TP3	**K^{trans}**	**Mean**	**CEL_0**	0.74	0.007	2.10	1.22	3.62
Age	**Age**	**Age**	**Age**	-0.09	0.058	0.92	0.84	1.00

8.7.1.3 Discussion

From the Cox proportional hazard ratios test, the mean change in ADC values for the entire lesion was found to be predictive of the progression-free survival interval. The results suggest that an increase in the mean ADC values of **TUM_0** between time points 2 and 3 could be used as a prognostic indicator of a shorter progression-free survival interval. As commented on in section 8.5.1.4, these results go against previous studies (135, 144, 171, 172) that show increasing ADC values to be markers of solid tumour response. Possible explanations include an increase in perfusion (50, 225), subsequently increasing the observed ADC values or an increase in the volume of oedema for **TUM** which would result in higher ADC value observed in the VOI (Figure 132). Due to tissue remodelling, functional diffusion maps were not explored in this thesis, given most patients received some form of surgical resection. Higher values of K^{trans} measured at time point 3 were found to be predictive of a shorter progression-free survival interval. This is perhaps not surprising given high K^{trans}

correlates with the presence of contrast enhancement. This increased enhancement is subsequently reported as progression by the radiologist at the next clinical MR examination. An example of this can be seen in Figure 133. The elevated K^{trans} suggests tumour angiogenesis is present and unregulated allowing the tumour to grow rapidly and the disease to progress.

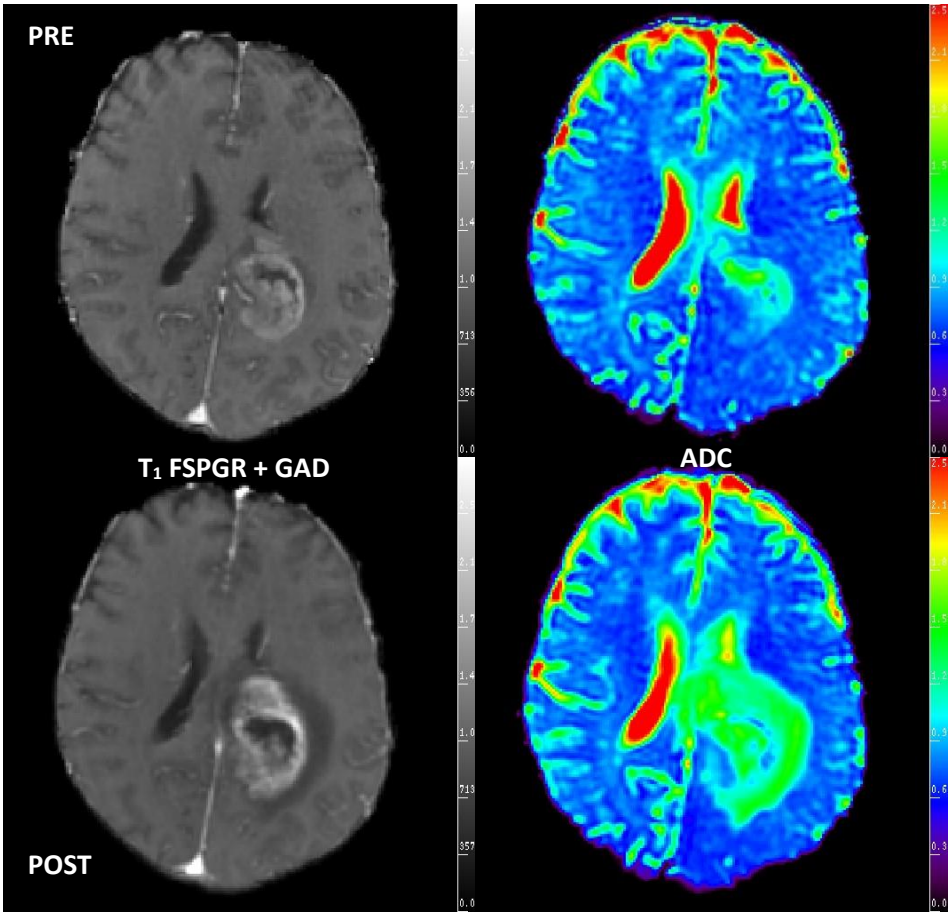

Figure 132 - Example T_1 FSPGR post-contrast and ADC images (0-2.5x$10^{-3}$$mm^2s^{-1}$) from a patient with a glioblastoma multiforme. Note the increased volume of oedema and increased of ADC values in the restricted region of the lesion following treatment. The patient died 89 days after recruitment into the study. Images are temporally registered to show how the tumour changes.

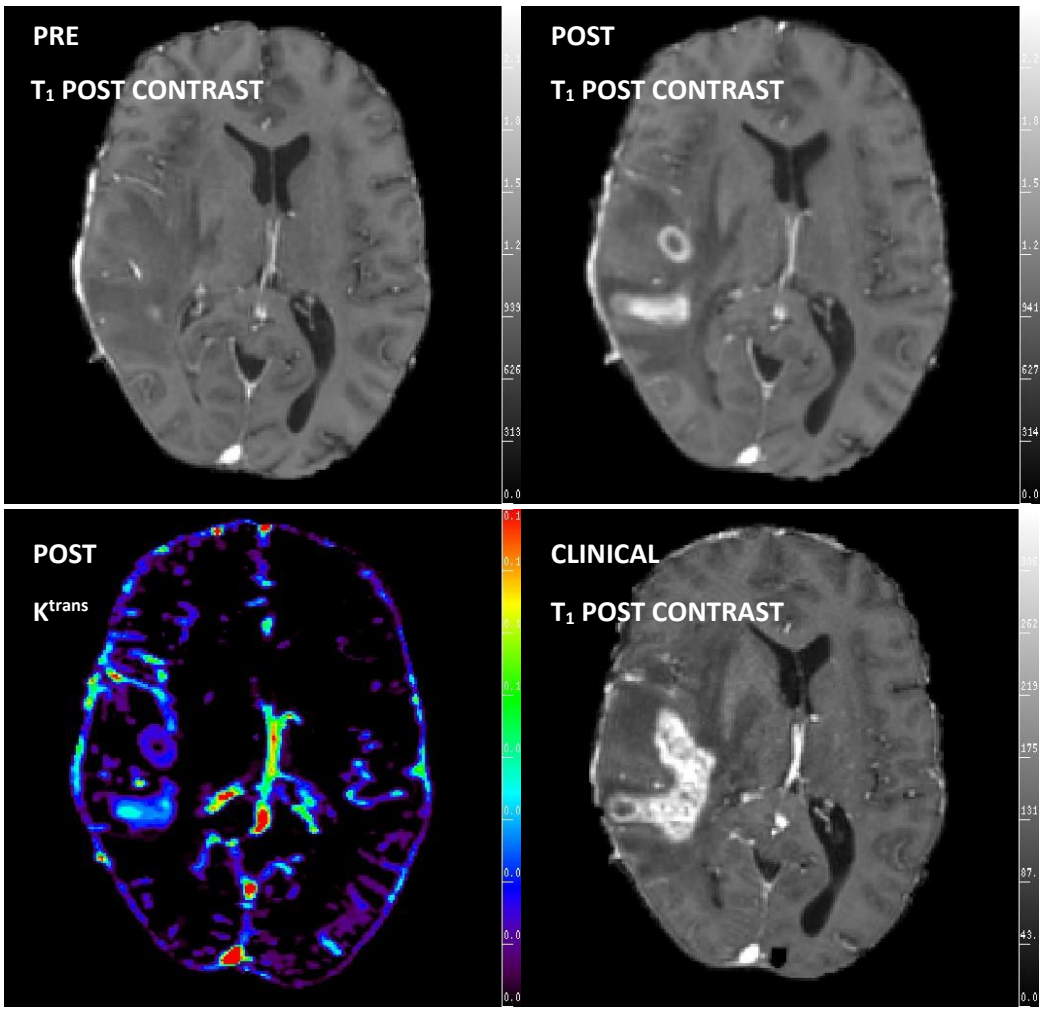

Figure 133 – Spatially registered images acquired at time points 2 and 3 (TP2, TP3), and the subsequent clinical MR acquired after the imaging study. A high K^{trans} (scaled 0-0.2min^{-1}) at time point 3 was followed by considerable tumour growth by the time the patient was clinically scanned 2 months later and reported as tumour progression by a neuroradiologist compared to the 48hrs postoperative imaging (not shown). Note the increased midline shift on the clinical scan compared to the study scans which also favours disease progression rather than pseudoprogression.

Changes to the standard deviations of R_1 and v_e values measured from the enhancing portion of tumours were shown to be predictive of progression-free survival. Standard deviations of v_e have been noted to differ between grades, as demonstrated in this study (pg. 195), with mean values of v_e also shown to increase in the literature (191, 204). Given the association between grade and v_e values, an increasing v_e could also be considered as a poor prognostic biomarker. High v_e values have previously been found in necrotising component of glioblastoma (226), thus increasing EES may be an indication that the tumour cells are under stress, with HIF1α and autophagy up regulated in order to maintain the tumour. Alternatively the increasing v_e values may represent continued tumour progression regardless of treatment (Figure 134).

Despite K^{trans}, v_e and v_b values all being significantly associated with a shorter progression-free survival interval at time point 2, none of the PK parameters featured in the final Cox regression model. This is partially a result of the factor analysis which only extracted the largest contributor for each component, and partially due to time point 3 parameters providing superior prognostic information. The problem with the Cox regression model is that there is no way to weight the time points within the model. Whilst knowing which tumours were likely to progress quicker at time point 3 is useful, knowing 2 months earlier at time point 2 is even more important.

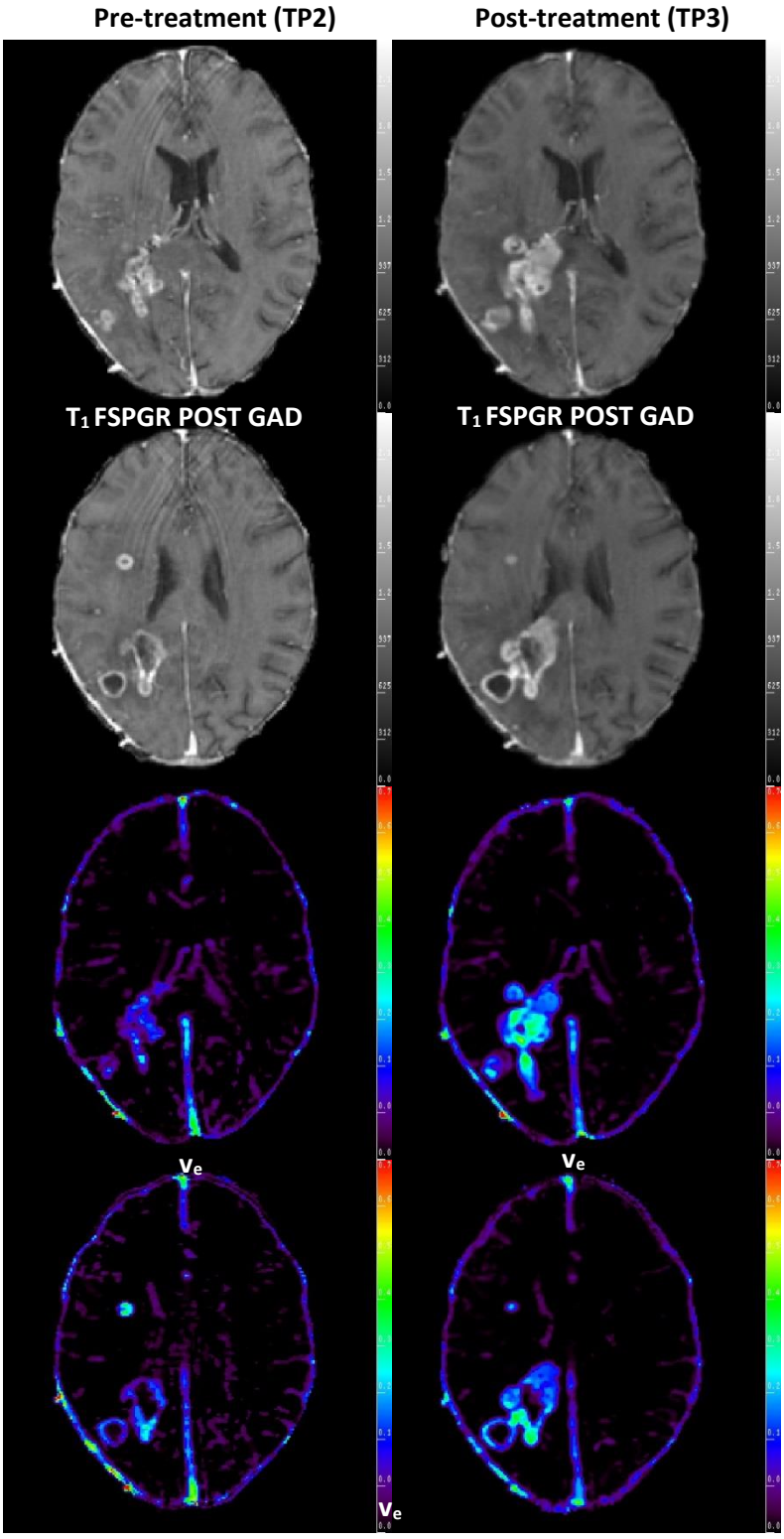

Figure 134 - Post-contrast T_1 weighted imaging of a glioblastoma at two different slice locations before and after chemoradiotherapy with v_e maps (scaled 0-0.75) of the same locations shown below. Note the increased range of v_e values shown by the tumour following therapy, which partially related to the increase of enhancing tissue within the tumour.

8.7.1.4 Conclusions

If using **TUM** VOIs, clinicians may want to examine the change in ADC values for the entire lesion before and after chemoradiotherapy as well as K^{trans} values at the end of chemoradiotherapy to identify patients likely to progress rapidly. However, if examining only the enhancing portion of the lesion (**CEL**) then clinicians may want to focus on the change in R_1 and v_e standard deviations during treatment, and K^{trans} values following treatment at time point 3 as a guide to which tumours are likely to have a shorter progression-free survival interval. Institutions may look to include DCE and DTI into clinical brain tumour protocols to potentially identify tumours likely to progress rapidly.

8.8 Conclusions

In this chapter, prediction of progression-free survival using quantitative MR was explored at time points 1, 2 and 3. The change in MR parameter values during treatment was also explored (time point 3 – time point 2).

Initially at time point 1, **TUM** and **CEL** VOIs were used to generate mean and standard deviations for each parameter of the preoperative 4D multiparametric MR datasets. From the cohort of 45 high grade gliomas, **TUM** VOI means showed 21 significant parameters capable of predicting progression-free survival at 210 days (Table 53 and Table 54), whilst mean and standard deviations of **CEL** sampled parameters (Table 55 and Table 56) found 10 significant predictors of progression-free survival.

DTI, DSC and DCE all showed significant results for identifying progression-free survival using either VOI (Table 31). Longitudinal diffusivity was non-significant at time point 1. Less commonly used parameters such as q and K_2 produced multiple significant predictions that are worth investigating further. The use of advanced MR parameters, as identified in this section could be used to recognise patients who would benefit from more frequent scan regimes or for the inclusion of novel therapeutics where the likelihood of progression after surgery before 210 days was high.

A Cox regression model was generated for each type of VOI at time point 1 to identify prognostic parameters for clinicians to use. From the **TUM** model, the key prognostic indicators were radial diffusivity, volume and grade. The mean radial diffusivity measured with $\mathbf{TUM_0}$ was found to be predictive of progression-free survival with every $0.1x10^{-3}$ mm^2s^{-1} increase in the mean for the $\mathbf{TUM_0}$ population of a tumour found to reduce the risk of a shorter progression-free survival interval by 34%. The volume of the tumour abnormality **TUM** was also found to be a predictor of progression-free survival (P=0.020) with each 1ml increase in tumour abnormality before surgery being associated with a 1% increased risk of a shorter progression-free survival interval, whilst the

difference between being diagnosed with a grade III and IV glioma was found to have 179% increased risk of a shorter progression-free survival interval.

From the high grade **CEL** VOIs, two significant parameters were identified; with a $0.1x10^{-3}s^{-1}$ increase in mean R_1 values associated with 23% decreased risk of tumour progression at 210 days from surgery whilst a 1% increase in blood volume fraction standard deviation was found to increase the risk of a shorter progression-free interval by 9%.

At time point 2, the results suggest that PK parameters derived from DCE MRI following surgery can predict progression-free survival (Table 32). Elevated values of K^{trans}, v_e and v_b were all associated with a short progression-free survival interval, suggesting the up regulation of HIF1α, with v_b producing the most significant results. The implementation of DCE prior to chemoradiotherapy has the potential to be beneficial in 2 ways. Firstly, contrast enhancement can be identified amongst blood products as seen in Figure 61 on pg. 79, to aid radiotherapy planning. Secondly, the PK parameters can also be used to identify patients that would benefit from more frequent scans given the likelihood of early tumour progression.

Between time points 2 and 3, the mean change of the ADC, longitudinal diffusivity and radial diffusivity measured using **TUM** and **TUM_0** populations were all significant predictors of progression-free survival with an increased mean being associated with a shorter progression-free interval. An increase in the standard deviation values of ADC, q and λ_R measured using **TUM_0** and a decrease in the FA measured with **TUM** were all significant predictors of a shorter progression-free survival. Changes in the **TUM** measurements of DCE and DSC parameters are not significant predictors in this cohort. However, using **CEL**, changes in mean v_e and K_2 measurements using **CEL** significantly predicted progression-free survival. The change in the volume of **CEL** was not predictive of the progression-free survival interval. Changes in the standard deviations of ADC, λ_L, λ_R R_1 using **CEL** are however predictive, with all parameters becoming more homogenous in patients who progressed

quicker. Standard deviation measurements of v_e and K_2 measured with **CEL** were also predictive of progression-free survival with increasing standard deviations found to have short progression-free intervals.

Following chemoradiotherapy at time point 3, mean and standard deviations of K^{trans} and v_e sampled using **TUM** and **CEL** VOIs were all significant predictors of progression-free survival for 210 days. Mean DTI parameters have little prognostic value at this time point, however, K_2 sampled with **TUM** and $rCBV_{BOX}$ sampled with **CEL** were significant. The blood volume fraction at this scan interval has no prognostic value with K^{trans} and v_e the more useful predictors at this time point.

Cox regression models for **TUM** and **CEL** VOIs were developed to reduce the number of significant results to a few clinically useful parameters. In the **TUM** model, the mean change in ADC values for the tumour between time points 2 and 3 was found to be a significant predictor of progression-free survival, with a $0.1x10^{-3}mm^2s^{-1}$ increase in mean ADC between scans found to be associated with a 101% increased risk of a shorter progression-free survival interval. A $0.01min^{-1}$ increase in mean K^{trans} within the **TUM** VOI at time point 3 found to be associated with a 31% risk of a shorter progression-free survival interval. **CEL** also identified K^{trans} from time point 3 being clinically useful at predicting progression-free survival (110% increased risk per $0.01min^{-1}$ increase in mean) as well as identifying changes in standard deviations of R_1 and v_e as prognostic biomarkers.

Table 31 - Visual summary of the Kaplan-Meier survival analysis test p-values generated for time point 1 using different MR parameters, statistical descriptors and sub-populations for 210 days progression-free survival from time point 1. Parameter colours are as follows: diffusivity = orange, directionality = aqua, tissue relaxation = purple, PK parameters = green and DSC derived parameters = blue. Red results were significant for P<0.05.

STAT	PARAM	VOI	TP1	
			TUM	CEL
MEAN	ADC	VOI	0.455	0.925
MEAN	ADC	VOI_0	0.041	0.324
MEAN	ADC	VOI_1	0.978	0.920
SD	ADC	VOI	0.083	0.211
SD	ADC	VOI_0	0.188	0.312
SD	ADC	VOI_1	0.052	0.794
MEAN	FA	VOI	0.651	0.884
MEAN	FA	VOI_0	0.117	0.125
MEAN	FA	VOI_1	0.147	0.161
SD	FA	VOI	0.207	0.932
SD	FA	VOI_0	0.690	0.230
SD	FA	VOI_1	0.260	0.731
MEAN	q	VOI	0.249	0.924
MEAN	q	VOI_0	0.058	0.832
MEAN	q	VOI_1	0.002	0.850
SD	q	VOI	0.014	0.434
SD	q	VOI_0	0.266	0.326
SD	q	VOI_1	0.148	0.242
MEAN	RA	VOI	0.301	0.938
MEAN	RA	VOI_0	0.129	0.161
MEAN	RA	VOI_1	0.420	0.161
SD	RA	VOI	0.147	0.484
SD	RA	VOI_0	0.316	0.230
SD	RA	VOI_1	0.003	0.040
MEAN	λ_L	VOI	0.177	0.970
MEAN	λ_L	VOI_0	0.376	0.643
MEAN	λ_L	VOI_1	0.220	0.769
SD	λ_L	VOI	0.112	0.591
SD	λ_L	VOI_0	0.750	0.926
SD	λ_L	VOI_1	0.501	0.714
MEAN	λ_R	VOI	0.455	0.925
MEAN	λ_R	VOI_0	0.041	0.313
MEAN	λ_R	VOI_1	0.867	0.383
SD	λ_R	VOI	0.164	0.211
SD	λ_R	VOI_0	0.085	0.144
SD	λ_R	VOI_1	0.081	0.794
MEAN	R_1	VOI	0.978	0.011
MEAN	R_1	VOI_0	0.684	0.001
MEAN	R_1	VOI_1	0.621	0.852
SD	R_1	VOI	0.950	0.369
SD	R_1	VOI_0	0.011	0.376
SD	R_1	VOI_1	0.950	0.458
MEAN	K^{trans}	VOI	0.040	0.277
MEAN	K^{trans}	VOI_0	0.012	0.381
MEAN	K^{trans}	VOI_1	0.005	0.355
SD	K^{trans}	VOI	0.010	0.138
SD	K^{trans}	VOI_0	0.002	0.204
SD	K^{trans}	VOI_1	0.000	0.003
MEAN	v_e	VOI	0.007	0.418
MEAN	v_e	VOI_0	0.062	0.138
MEAN	v_e	VOI_1	0.034	0.128
SD	v_e	VOI	0.002	0.384
SD	v_e	VOI_0	0.050	0.119
SD	v_e	VOI_1	0.013	0.033
MEAN	v_b	VOI	0.179	0.186
MEAN	v_b	VOI_0	0.082	0.230
MEAN	v_b	VOI_1	0.180	0.038
SD	v_b	VOI	0.187	0.474
SD	v_b	VOI_0	0.918	0.409
SD	v_b	VOI_1	0.066	0.003
MEAN	$rCBV_{GVF}$	VOI	0.602	0.930
MEAN	$rCBV_{GVF}$	VOI_0	0.748	0.889
MEAN	$rCBV_{GVF}$	VOI_1	0.354	0.660
SD	$rCBV_{GVF}$	VOI	0.331	0.148
SD	$rCBV_{GVF}$	VOI_0	0.035	0.525
SD	$rCBV_{GVF}$	VOI_1	0.022	0.059
MEAN	$rCBV_{BOX}$	VOI	0.689	0.959
MEAN	$rCBV_{BOX}$	VOI_0	0.629	0.791
MEAN	$rCBV_{BOX}$	VOI_1	0.200	0.803
SD	$rCBV_{BOX}$	VOI	0.073	0.255
SD	$rCBV_{BOX}$	VOI_0	0.363	0.260
SD	$rCBV_{BOX}$	VOI_1	0.075	0.141
MEAN	K_2	VOI	0.401	0.011
MEAN	K_2	VOI_0	0.016	0.244
MEAN	K_2	VOI_1	0.839	0.205
SD	K_2	VOI	0.114	0.521
SD	K_2	VOI_0	0.066	0.943
SD	K_2	VOI_1	0.339	0.016
VOL	VOL	VOI	0.031	0.014

Table 32 - Visual summary of the Kaplan-Meier survival analysis test p-values generated for time points 2 and 3 using different MR parameters, statistical descriptors and sub-populations for 210 days progression-free survival from time point 1. Parameter colours are as follows: diffusivity = orange, directionality = aqua, tissue relaxation = purple, PK parameters = green and DSC derived parameters = blue. Red results were significant for P<0.05.

STAT	PARAM	VOI	TP2		TP3-TP2		TP3	
			TUM	CEL	TUM	CEL	TUM	CEL
MEAN	ADC	VOI	0.506	0.744	0.030	0.369	0.103	0.850
MEAN	ADC	VOI_0	0.212	0.888	0.023	0.101	0.086	0.528
MEAN	ADC	VOI_1	0.060	0.639	0.068	0.228	0.648	0.341
SD	ADC	VOI	0.885	0.865	0.058	0.027	0.673	0.350
SD	ADC	VOI_0	0.147	0.193	0.325	0.638	0.066	0.452
SD	ADC	VOI_1	0.814	0.360	0.300	0.612	0.860	0.493
MEAN	FA	VOI	0.519	0.183	0.303	0.360	0.855	0.336
MEAN	FA	VOI_0	0.986	0.329	0.135	0.421	0.091	0.706
MEAN	FA	VOI_1	0.820	0.183	0.119	0.892	0.308	0.706
SD	FA	VOI	0.119	0.183	0.182	0.257	0.553	0.263
SD	FA	VOI_0	0.375	0.083	0.259	0.943	0.154	0.294
SD	FA	VOI_1	0.403	0.035	0.521	0.912	0.136	0.469
MEAN	q	VOI	0.488	0.024	0.118	0.566	0.169	0.053
MEAN	q	VOI_0	0.915	0.053	0.094	0.984	0.070	0.109
MEAN	q	VOI_1	0.566	0.012	0.095	0.124	0.122	0.864
SD	q	VOI	0.551	0.008	0.419	0.773	0.784	0.004
SD	q	VOI_0	0.183	0.053	0.510	0.614	0.169	0.110
SD	q	VOI_1	0.586	0.171	0.078	0.377	0.601	0.008
MEAN	RA	VOI	0.519	0.183	0.303	0.360	0.855	0.336
MEAN	RA	VOI_0	0.947	0.329	0.135	0.421	0.383	0.706
MEAN	RA	VOI_1	0.134	0.134	0.356	0.892	0.332	0.706
SD	RA	VOI	0.056	0.183	0.182	0.257	0.553	0.263
SD	RA	VOI_0	0.555	0.083	0.182	0.943	0.580	0.294
SD	RA	VOI_1	0.913	0.102	0.615	0.430	0.214	0.336
MEAN	λ_L	VOI	0.089	0.639	0.040	0.228	0.042	0.850
MEAN	λ_L	VOI_0	0.204	0.888	0.038	0.701	0.068	0.070
MEAN	λ_L	VOI_1	0.003	0.591	0.052	0.336	0.634	0.599
SD	λ_L	VOI	0.955	0.865	0.214	0.046	0.989	0.350
SD	λ_L	VOI_0	0.024	0.048	0.778	0.339	0.382	0.350
SD	λ_L	VOI_1	0.109	0.619	0.215	0.527	0.666	0.471
MEAN	λ_R	VOI	0.506	0.744	0.030	0.915	0.186	0.473
MEAN	λ_R	VOI_0	0.038	0.347	0.007	0.446	0.344	0.791
MEAN	λ_R	VOI_1	0.074	0.639	0.068	0.228	0.854	0.086
SD	λ_R	VOI	0.885	0.865	0.254	0.027	0.673	0.350
SD	λ_R	VOI_0	0.078	0.193	0.254	0.310	0.132	0.452
SD	λ_R	VOI_1	0.788	0.360	0.540	0.183	0.894	0.493
MEAN	R_1	VOI	0.595	0.602	0.064	0.459	0.158	0.218
MEAN	R_1	VOI_0	0.616	0.194	0.209	0.571	0.244	0.242
MEAN	R_1	VOI_1	0.144	0.744	0.325	0.318	0.608	0.363
SD	R_1	VOI	0.066	0.091	0.476	0.019	0.132	0.998
SD	R_1	VOI_0	0.365	0.965	0.090	0.724	0.120	0.198
SD	R_1	VOI_1	0.610	0.065	0.719	0.537	0.447	0.431
MEAN	K^{trans}	VOI	0.116	0.107	0.306	0.463	0.002	0.036
MEAN	K^{trans}	VOI_0	0.038	0.278	0.946	0.162	0.024	0.011
MEAN	K^{trans}	VOI_1	0.130	0.245	0.433	0.577	0.005	0.015
SD	K^{trans}	VOI	0.168	0.486	0.628	0.684	0.005	0.153
SD	K^{trans}	VOI_0	0.038	0.092	0.628	0.393	0.024	0.007
SD	K^{trans}	VOI_1	0.168	0.274	0.628	0.847	0.060	0.153
MEAN	v_e	VOI	0.146	0.889	0.071	0.002	0.002	0.004
MEAN	v_e	VOI_0	0.033	0.266	0.140	0.009	0.013	0.021
MEAN	v_e	VOI_1	0.047	0.791	0.856	0.096	0.006	0.015
SD	v_e	VOI	0.227	0.486	0.424	0.036	0.002	0.075
SD	v_e	VOI_0	0.163	0.586	0.938	0.015	0.076	0.015
SD	v_e	VOI_1	0.149	0.943	0.624	0.964	0.120	0.539
MEAN	v_b	VOI	0.028	0.023	0.909	0.967	0.276	0.224
MEAN	v_b	VOI_0	0.002	0.008	0.077	0.653	0.053	0.096
MEAN	v_b	VOI_1	0.028	0.008	0.218	0.503	0.053	0.096
SD	v_b	VOI	0.145	0.068	0.370	0.584	0.211	0.153
SD	v_b	VOI_0	0.003	0.008	0.370	0.317	0.053	0.096
SD	v_b	VOI_1	0.028	0.068	0.170	0.468	0.139	0.137
MEAN	$rCBV_{GVF}$	VOI	0.065	0.131	0.910	0.367	0.139	0.185
MEAN	$rCBV_{GVF}$	VOI_0	0.428	0.768	0.335	0.235	0.585	0.505
MEAN	$rCBV_{GVF}$	VOI_1	0.352	0.638	0.704	0.320	0.446	0.683
SD	$rCBV_{GVF}$	VOI	0.325	0.638	0.122	0.190	0.095	0.276
SD	$rCBV_{GVF}$	VOI_0	0.265	0.768	0.079	0.235	0.095	0.505
SD	$rCBV_{GVF}$	VOI_1	0.265	0.638	0.789	0.564	0.139	0.276
MEAN	$rCBV_{BOX}$	VOI	0.163	0.216	0.814	0.434	0.139	0.031
MEAN	$rCBV_{BOX}$	VOI_0	0.434	0.723	0.720	0.382	0.669	0.266
MEAN	$rCBV_{BOX}$	VOI_1	0.352	0.468	0.274	0.122	0.139	0.266
SD	$rCBV_{BOX}$	VOI	0.364	0.658	0.460	0.052	0.024	0.011
SD	$rCBV_{BOX}$	VOI_0	0.227	0.723	0.460	0.486	0.095	0.883
SD	$rCBV_{BOX}$	VOI_1	0.849	0.468	0.961	0.865	0.139	0.137
MEAN	K_2	VOI	0.452	0.216	0.156	0.026	0.011	0.060
MEAN	K_2	VOI_0	0.697	0.100	0.070	0.121	0.061	0.205
MEAN	K_2	VOI_1	0.906	0.637	0.056	0.121	0.604	0.319
SD	K_2	VOI	0.009	0.131	0.459	0.005	0.007	0.205
SD	K_2	VOI_0	0.201	0.100	0.873	0.191	0.017	0.124
SD	K_2	VOI_1	0.229	0.471	0.459	0.009	0.155	0.282
VOL	VOL	VOI	0.513	0.203	0.004	0.109	0.177	0.116

9 Conclusions and Future Works

9.1 Research Summary

In this thesis, a method for multiparametric image registration was implemented, with a view that the same acquisition and post-processing methodology could be used to identify lesion grade or predict progression-free survival in a cohort of glioma patients.

The image processing scheme described in chapter 6 was successfully used to identify functional MR parameters that relate to glioma grade. Individually, preoperative measurements using DTI, DCE and DSC all showed significant differences between grades. Mean and median parameters values produced the greatest number of significant differences between grades followed by standard deviations. When mean values sampled using a **TUM** VOI were the input to a 2-stage logistic regression model, DTI and DCE parameters were found to produce the most predictive model for glioma grade. DSC parameters did not contain enough additional value to be included in the resulting logistic regression model. The model correctly graded 94% of grade IV lesions, however found considerable overlap between grade II and III gliomas resulting in only 70% and 75% respectively being correctly identified. Compared to histology MR has poor spatial resolution despite advances in field strength. Consequently, spatial resolution may explain some of the disagreement observed between imaging and pathology, with averaging effects also playing a role. Single voxel spectroscopy performed less accurately at glioma grading than imaging methods due to limited coverage and partial volume effects. The implications of chapter 7 are that the grading of grade IV lesions in eloquent regions of the brain is possible. However, when trying to identify grade III lesions, MR is only moderately successful; and should only be used in conjunction with a targeted biopsy for grading.

From the preoperative MR, the volumes of **TUM** and **CEL** were predictive of progression-free survival using Kaplan-Meier analysis, however considerably more MR parameters were predictive of PFS when using **TUM** VOIs rather than **CEL** VOIs.

Cox regression analysis of the preoperative MR parameters in high grade gliomas found the mean radial diffusivity measured with $\mathbf{TUM_0}$ to be predictive of progression-free survival with every $0.1x10^{-3}$ mm^2s^{-1} increase in the mean of the $\mathbf{TUM_0}$ population of a tumour found to reduce the risk of a shorter progression-free survival interval by 34%. Grade and volume were also found to be significant predictors of PFS. From the **CEL** measurements, two significant parameters remained in the Cox regression model, with a $0.1x10^{-3}s^{-1}$ increase in mean R_1 values associated with 23% decreased risk of tumour progression at 210 days from surgery and a 1% increase in blood volume fraction standard deviation found to increase the risk of a shorter progression-free interval by 9%.

From pre-chemoradiotherapy scans, the results suggest that PK modelling parameters derived from DCE MRI following surgery can predict progression-free survival. The acquisition of DCE prior to chemoradiotherapy may be beneficial in 2 ways. Firstly, contrast enhancement can easily be identified amongst blood products to aid radiotherapy planning, and secondly, PK parameters can also be used to identify patients who would benefit from more frequent scans given the likelihood of early tumour progression.

Following chemoradiotherapy, the mean change of the apparent diffusion coefficient, longitudinal diffusivity and radial diffusivity measured using **TUM** and $\mathbf{TUM_0}$ populations were all significant predictors of progression-free survival. Changes in the mean whole tumour measurements of DCE and DSC parameters are not significant predictors in this cohort. When examining the **CEL** VOI of the tumour at both time points, changes in mean v_e and K_2 measurements significantly predict progression-free survival. An increase in v_e or a decrease in K_2 over the course of treatment should

be considered as a poor prognostic indicator in gliomas. The change in the volume of **CEL** was not predictive of the progression-free survival interval.

Mean and standard deviations of K^{trans} and v_e sampled using **TUM** and **CEL** VOIs at time point 3, were all also significant predictors of progression-free survival for 210 days. Elevated PK parameters at 2 weeks post-chemoradiotherapy were predictive of progression-free survival. DTI in isolation has no prognostic value at this time point.

Cox regression models of postoperative MR parameters for **TUM** and **CEL** VOIs were developed to reduce the number of significant results. In the **TUM** model, the mean change in ADC values for the tumour between time points 2 and 3 was found to be a significant predictor of progression-free survival as was the mean K^{trans} within **TUM** at time point 3. **CEL** identified K^{trans} from time point 3 being clinically useful at predicting progression-free survival as well as identifying changes in standard deviations of R_1 and v_e as prognostic biomarkers.

9.1.1 Recommendations

9.1.1.1 Glioma Grading

- From preoperative imaging, diffusion tensor imaging in conjunction with dynamic contrast enhanced MR could be used to help radiologically grade gliomas. The logistic regression of multiparametric MR found ADC, λ_R, q, K^{trans} and v_e could be used to grade gliomas

9.1.1.2 Prediction of Progression-Free Survival

- Preoperative MRI was also found to be predictive of progression-free survival with λ_R, R_1 and v_b calculated from the DTI and DCE found to contain prognostic information following Cox regression analysis
- From the post-surgical imaging, before and after chemoradiotherapy, measures of ADC, R_1, K^{trans} and v_e, derived from the DTI and DCE predicted progression-free survival

9.1.1.3 Sequence Choice for Neuro-imaging

- DCE and DTI datasets contain significant prognostic information about gliomas at all stages of treatment
- In the presence of DCE and DTI, DSC does not add additional information
- Multiparametric MR is better at glioma grading than single voxel MRS

9.1.1.4 VOIs and Gaussian Mixture Modelling

- Differences between tumour grades were observed using TUM, CEL and NEL, however TUM and CEL showed more significant differences
- Subpopulations of MR parameters sampled using Gaussian mixture modelling contained additional value

9.2 Future Work

A logical next step for the study described in this thesis would be the expansion of the high grade arm into a multi-centre trial. By including other sites, the number patients involved would greatly be improved and image phenotyping may be possible. It would also be interesting to compare the parameter values produced from different scanner vendors and establish universal MR values between vendors. The cohort followed in this study went through the optimal treatment pathway of surgery followed by chemoradiotherapy which is the same in all geographical regions of the UK and so recruitment would be relatively simple provided appropriate amounts of scanner time exist. In order to ensure consistency within the data, all image analysis would happen at a single site.

A first alternative use for the methodology described in this thesis, would be to follow patients undertaking second line chemotherapy treatments. With surgical changes less apparent, blood products would be less of an issue for EPI sequences, however given the serious nature of tumour reoccurrence or progression, patient capacity, and subsequently recruitment could be an issue.

Multiparametric MR is not restricted to the brain, hence a second use of the approach described in this thesis, could be to move to other relatively rigid organs such as the prostate. Diffusion weighted imaging and DCE are already common place in the prostate and thus the registration scheme could be adapted with relative ease.

A final use for the multiparametric registration approach to monitor treatment response, would be to examine a cohort of patients undertaking stereotactic radiosurgery (SRS). SRS is a relatively common treatment for brain metastases and meningiomas with a volume less than 20ml of enhancing tissue. If MR could predict which lesions would respond to SRS then patient management could be altered to reflect this new information, with surgery being an alternative treatment for some of the non-responsive lesions.

9.3 The Future of Neuro-oncological Imaging

This section briefly describes some of the new MR sequences which are starting to be available to radiologists and researchers.

Given MR's sensitivity to motion and how rapidly image quality degrades due to motion, methods for minimising this effect are very much of clinical interest. Vendors currently have 2 methods for dealing with various degrees of patient motion. The first is k-space oversampling scheme in which the centre of k-space is oversampled compared to the outside of k-space. This results in good image contrast information, whilst any motion which is likely to affect the spatial frequencies at the edge of k-space is less influential in the final image construction. The trade-off of this approach is that over-sampling schemes can take longer to acquire, and due to the reduced number of spatial frequencies, images can appear slightly blurred. In order to improve the image resolution in patients who move, sequences with prospective motion correction are starting to appear on scanners for selected sequences. By interleafing the standard acquisition sequence with a navigator echo sequence, the scanner can alter the acquisition plane to accommodate for motion. When motion is present, the scanner can subsequently replace lines of k-space with motion free data to improve the final image.

Phased array coil technology is another field which will directly benefit neuroimaging by decreasing the acquisition times of sequences through parallel imaging. With most imaging centres routinely using parallel imaging methods to speed up imaging time, it is now a question of how many receive elements scanners will support. Currently for neuroimaging, 8 channel head coils are common, however vendors are now starting to produce 32 head coils with some scanners supporting up to 64 and 128 receive channels.

One fast growing field which is becoming an attractive prospect to researchers and eventually clinicians is compressed sensing (228) (sparse sampling), in which k-space is pseudo randomly under-sampled in order to reduce scan times. The reduction in scan time can subsequently be utilised to improve either the spatial or temporal resolution of MR data, whilst also improving the SNR. Compressed sensing of MR sequences such as DCE (229, 230) and MRSI (231, 232) are currently hot topics for further investigation. The disadvantage of compressed sensing is that the reconstruction time required to regenerate a full sampled k-space is highly time consuming (in the order of hours). Moving the reconstruction of such sequences to GPU reconstruction engines may be one possible solution to reconstruct images in clinically viable times.

Another rapidly growing research area is that of multiband echo planar imaging (233). Rather than acquiring EPI data following a single excitation, multiple RF excitations are used to excite multiple slices simultaneously. Using a coil sensitivity map, the signal received from each channel can be used to reconstruct multiple slices through unaliasing the data. The implications are that EPI data can be further accelerated by factors of up to 16 given an appropriate number of receive elements in the coil.

With a huge number of neuroimaging techniques being developed for MR, it is impossible to describe all of them. However scan time reductions due to improved parallel imaging methods and reduced k-space sampling schemes will result in sequences which were previously research only due to long acquisitions (e.g. diffusion spectrum imaging), entering clinical practice due to clinically viable scan times.

9.3.1 If the study was to be repeated….

If a similar brain tumour study was to be repeated, then several changes could be made to improve the study. Whilst the diffusion tensor imaging was successfully employed and produced multiple significant results, uncontrollable factors such as perfusion effects and geometric distortion may have significantly altered some parts of the data. In the future, field mapping could be included in order to unwarp EPI distortion (234) and improve the subsequent registration. Secondly, intravoxel incoherent motion (50) should be considered to estimate any perfusion effects, potentially elevating ADC values in the enhancing portion of tumours. Currently, the diffusion tensor model assumes a mono-exponential decay of signal when a diffusion gradient is applied. However, there is sufficient evidence to suggest it is actually a bi-exponential decay. A diffusion acquisition scheme similar to diffusion kurtosis imaging (235) which utilises multiple b-values in at least 15 directions could be used to estimate both perfusion and diffusion fractions in tumours whilst maintaining information about fibre tract directionality and infiltration.

The DCE data also provided a host of significant results and excelled in tumour grading and prediction of progress free survival, however, coverage was the major limiting factor. In the future, compressed sensing (228-230) could be utilised to expand the DCE to whole brain coverage, or improve the temporal resolution of the data to produce better AIF estimations for pharmacokinetic analysis.

Slice thickness was the limiting factor of the DSC data. Whilst the SNR of the data was high, large partial volume effects would have been present in the data. The 7mm thick slices appeared subject to a greater level of geometric distortion of the front of the head and subsequently the data was potentially over interpolated during the registration process. In the future, AIF estimation may be necessary for DSC data; however the white matter mask scheme seemed a robust choice in processing. Developments in accelerating DSC such as CAIPIRINHA (multiband-EPI)(236) could lead

to improved blood volume estimations in the brain and a reduction of slice thickness due to high acceleration factors available with the technique.

Arterial spin labelling is a sequence that became available after the start of this study. The addition of another measure of blood volume (237) may have clinical utility and is suitable for patients who have renal impairment or poor venous access. The low spatial resolution of the images could be a limiting factor when registering the data, so morphological imaging of the same voxel size would probably be required if the CBV maps were to be incorporated into the multiparametric volume. The spin-echo read used for ASL would make the sequence suitable for imaging blood flow and volume in tissue containing regions of increased susceptibility.

MRSI is another sequence that benefits from compressed sensing (231, 232). With compressed sensing, acceleration factors of up to 10 are potentially useful, allowing the number of phase encodes to be increased to approximately 32x32 to allow whole brain coverage. The higher number of phase encodings reduces the point spread effect of lipid contamination, which would be present even with saturation bands covering the subcutaneous lipid in the skull. EPI-flyback (238) is another alternative method for accelerating MR spectroscopy to enable whole brain coverage. The flyback accelerates the MR spectroscopy by reducing the number of phase encoding directions by 1 and for further acceleration can be combined with compressed sensing (239).

In terms of registration, thinner slices of the same thickness for all sequences would help with the registration process. This would minimise the amount of interpolation required within a multiparametric volume. A move from 2D to 3D acquisitions would be possible for some of data series such as the FLAIR. Whilst 3D DWI (240, 241) is possible, no commercially available sequence exists for our scanner platform. Thinner datasets would also enable more accurate delineation of the tumour abnormality; however given the increase number of slices, automated VOI selection may be necessary. Automated VOIs would require uniform signal intensities throughout the brain

which is not currently possible on our scanner due to B_1 inhomogeneity shading artefacts; however, the installation of a multi-transit system would improve image uniformity. Furthermore, if more computational power was available, a constrained non-rigid registration could be implemented to correct for tissue remodelling and enable potentially more accurate functional diffusion maps, with the same technique being applied to the other functional parameters.

Finally, the question of the scan frequency and intervals arises. Ideally patients would be scanned more frequently to observe treatment induced changes earlier; however the practicality of this is questionable given the already restricted scanner availability and the transport issues that exist for glioma patients. If study patients were to be scanned within 48hrs of surgery, the problem of surgical clips would arise, potentially destroying all local EPI data whilst still having a reduced effect on the other datasets. An additional scan time point another 1-2 months after time point 3 would have been interesting to observe any delayed treatment effects.

A sample MR protocol incorporating many of the suggested improvements can be seen in Table 33. This protocol sacrifices reconstruction time for improved resolution and coverage.

Table 33 - Potential MR Protocol for a future glioma study, given all possible improvements. Total scan time is in the region of 50 minutes.

SEQUENCE	2D/3D	FOV (mm)	FREQ.	PHASE	THICKNESS /GAP (mm)	SLICES	TIME
3-Plane Localiser	2D	240x240	384	160	8/4	30	00:00:22
Ready Brain	3D	280x280	72	72	3/0	64	00:00:20
T_2 FLAIR CUBE	3D	240x240	256	256	1.5/0	140	00:06:00
T_1 IR-FSPGR	3D	240x240	256	256	1.5/0	140	00:03:30
DTI (16 dir, 4 b-values)	2D	240x240	128	128	3/0	44	00:06:45
CS PRESS editing sequence	3D	240x240	32	32	12/0	8	00:13:00
3D ASL	3D	240x240	128	128	3/0	44	00:07:00
CS Multi-flip T_1W FSPGR	3D	240x240	192	128	3/0	10x44	00:02:00
CS DCE	3D	240x240	192	128	3/0	44	00:05:50
T_1 IR-FSPGR post-contrast	3D	240x240	256	256	1.5/0	140	00:03:30
T_2* MULTIBAND DSC	2D	240x240	128	128	3/0	44	00:01:45

10 Appendices

10.1 Kruskal Wallis Tables

All the tables for section entitled ‘Associations of MR Parameters with Histology’ can be found over the following pages.

These cover **TUM**, **CEL** and **NEL** volumes of interest, and statistical metrics including mean, standard deviation, skew, kurtosis, median, maximum and minimum for time point 1.

*Table 34 - **Mean** values from the **TUM** VOI for each parameter, Kruskal-Wallis tested for P<0.05 and Bonferroni corrected for P<0.00128 (0.05/39) to examine differences between grades.*

Parameter	VOI	WHO II (N=10)			WHO III (N=12)			WHO IV (N=33)			Sig.
		Minimum	Median	Maximum	Minimum	Median	Maximum	Minimum	Median	Maximum	
ADC	TUM	1.078	1.257	1.350	0.823	1.116	1.523	0.808	1.169	1.432	0.150
	TUM_0	0.940	1.206	1.321	0.805	1.061	1.299	0.707	1.003	1.244	0.012
	TUM_1	1.240	1.468	1.955	1.038	1.226	1.988	0.976	1.376	1.849	0.089
FA	TUM	0.133	0.165	0.235	0.130	0.186	0.269	0.175	0.206	0.317	0.003
	TUM_0	0.075	0.117	0.197	0.108	0.131	0.210	0.059	0.158	0.280	0.019
	TUM_1	0.214	0.249	0.377	0.202	0.294	0.391	0.207	0.300	0.459	0.046
q	TUM	0.202	0.295	0.407	0.256	0.285	0.408	0.230	0.341	0.395	0.002
	TUM_0	0.127	0.185	0.354	0.165	0.227	0.287	0.081	0.287	0.352	0.006
	TUM_1	0.300	0.404	0.592	0.342	0.417	0.492	0.281	0.469	0.764	0.012
RA	TUM	0.111	0.138	0.200	0.107	0.157	0.230	0.148	0.173	0.277	0.003
	TUM_0	0.062	0.099	0.168	0.091	0.111	0.177	0.097	0.138	0.246	0.002
	TUM_1	0.186	0.215	0.356	0.169	0.257	0.391	0.204	0.273	0.483	0.017
λ_L	TUM	1.261	1.477	1.604	1.034	1.367	1.731	1.001	1.424	1.708	0.350
	TUM_0	1.009	1.397	1.564	0.999	1.261	1.523	0.842	1.196	1.621	0.300
	TUM_1	1.321	1.584	2.512	1.265	1.534	2.203	1.157	1.627	2.292	0.606
λ_R	TUM	0.986	1.144	1.239	0.718	1.005	1.419	0.671	1.065	1.295	0.100
	TUM_0	0.907	1.067	1.214	0.656	0.982	1.215	0.612	0.891	1.128	0.003
	TUM_1	1.173	1.398	1.932	0.930	1.063	1.894	0.876	1.256	1.860	0.042
R_1	TUM	0.345	0.677	0.964	0.441	0.750	0.904	0.632	0.820	1.449	0.019
	TUM_0	0.261	0.600	0.937	0.383	0.654	0.867	0.509	0.753	1.381	0.012
	TUM_1	0.355	0.775	1.185	0.616	0.896	1.078	0.633	0.904	1.506	0.080
K^{trans}	TUM	0.021	0.028	0.058	0.028	0.036	0.179	0.021	0.087	0.179	0.001
	TUM_0	0.016	0.020	0.031	0.017	0.026	0.054	0.016	0.057	0.108	0.001
	TUM_1	0.027	0.044	0.093	0.040	0.059	0.266	0.032	0.136	0.457	0.001
v_e	TUM	0.026	0.039	0.077	0.032	0.051	0.261	0.026	0.158	0.322	0.001
	TUM_0	0.017	0.026	0.034	0.018	0.029	0.154	0.016	0.050	0.245	0.001
	TUM_1	0.040	0.064	0.163	0.043	0.088	0.399	0.038	0.245	0.694	0.001
v_b	TUM	0.024	0.031	0.045	0.028	0.036	0.061	0.021	0.046	0.102	0.002
	TUM_0	0.014	0.020	0.026	0.014	0.019	0.031	0.014	0.034	0.060	0.001
	TUM_1	0.032	0.051	0.096	0.037	0.052	0.103	0.029	0.099	0.240	0.001
$rCBV_{GVF}$	TUM	1.075	1.409	1.720	0.916	1.702	5.218	1.043	1.919	5.064	0.025
	TUM_0	0.919	1.098	1.441	0.632	1.281	2.599	0.648	1.046	2.955	0.126
	TUM_1	1.708	2.573	3.833	2.129	2.801	6.897	1.957	3.629	8.179	0.003
$rCBV_{BOX}$	TUM	1.052	1.456	1.685	1.100	1.692	5.082	1.053	1.887	4.650	0.024
	TUM_0	0.805	1.104	1.450	0.704	1.325	2.420	0.611	1.009	3.137	0.152
	TUM_1	1.575	2.432	3.535	2.234	2.795	6.295	1.841	3.244	6.135	0.013
K_2	TUM	-0.747	-0.455	-0.235	-1.688	-0.637	-0.141	-3.060	-0.943	-0.169	0.001
	TUM_0	-1.394	-1.010	-0.523	-3.346	-1.379	-0.390	-5.162	-1.956	-0.579	0.001
	TUM_1	-0.512	-0.307	-0.123	-0.984	-0.393	-0.079	-1.474	-0.372	-0.120	0.500

*Table 35 – **Standard deviations** from the **TUM** VOI for each parameter, Kruskal-Wallis tested for P<0.05 and Bonferroni corrected for P<0.00128 (0.05/39) to examine differences between grades.*

Parameter	VOI	WHO II (N=10)			WHO III (N=12)			WHO IV (N=33)			Sig.
		Minimum	Median	Maximum	Minimum	Median	Maximum	Minimum	Median	Maximum	
ADC	TUM	0.169	0.265	0.389	0.136	0.210	0.487	0.146	0.288	0.492	0.017
	TUM_0	0.130	0.195	0.270	0.112	0.173	0.348	0.073	0.183	0.365	0.610
	TUM_1	0.104	0.302	0.507	0.112	0.195	0.529	0.112	0.321	0.815	0.016
FA	TUM	0.074	0.097	0.128	0.056	0.093	0.129	0.081	0.107	0.146	0.199
	TUM_0	0.028	0.043	0.075	0.034	0.047	0.073	0.025	0.059	0.114	0.018
	TUM_1	0.082	0.113	0.144	0.068	0.110	0.159	0.078	0.112	0.177	0.893
q	TUM	0.117	0.142	0.204	0.096	0.136	0.190	0.095	0.155	0.225	0.237
	TUM_0	0.037	0.064	0.121	0.051	0.071	0.118	0.027	0.101	0.144	0.003
	TUM_1	0.109	0.147	0.220	0.101	0.142	0.222	0.083	0.163	0.283	0.154
RA	TUM	0.065	0.087	0.114	0.048	0.083	0.129	0.071	0.097	0.144	0.205
	TUM_0	0.023	0.036	0.067	0.028	0.041	0.068	0.029	0.053	0.105	0.001
	TUM_1	0.074	0.105	0.158	0.059	0.105	0.188	0.070	0.110	0.206	0.391
λ_L	TUM	0.202	0.290	0.401	0.182	0.239	0.485	0.153	0.324	0.495	0.020
	TUM_0	0.078	0.195	0.300	0.070	0.183	0.396	0.092	0.193	0.411	0.680
	TUM_1	0.108	0.313	0.437	0.119	0.224	0.524	0.127	0.291	0.985	0.064
λ_R	TUM	0.169	0.266	0.403	0.141	0.226	0.497	0.152	0.291	0.516	0.019
	TUM_0	0.125	0.225	0.281	0.079	0.175	0.339	0.087	0.185	0.290	0.171
	TUM_1	0.100	0.316	0.560	0.142	0.225	0.491	0.146	0.331	0.729	0.048
R_1	TUM	0.056	0.166	0.239	0.110	0.167	0.224	0.123	0.193	0.261	0.010
	TUM_0	0.008	0.094	0.141	0.049	0.084	0.110	0.060	0.111	0.376	0.012
	TUM_1	0.051	0.174	0.424	0.112	0.164	0.291	0.122	0.220	0.401	0.068
K^{trans}	TUM	0.007	0.017	0.043	0.016	0.023	0.163	0.010	0.054	0.209	0.001
	TUM_0	0.004	0.007	0.017	0.005	0.012	0.026	0.004	0.025	0.062	0.001
	TUM_1	0.006	0.022	0.052	0.016	0.027	0.162	0.010	0.062	0.258	0.001
v_e	TUM	0.013	0.029	0.078	0.019	0.039	0.184	0.017	0.105	0.270	0.001
	TUM_0	0.005	0.011	0.018	0.005	0.014	0.090	0.004	0.031	0.142	0.001
	TUM_1	0.012	0.033	0.078	0.017	0.048	0.181	0.017	0.116	0.264	0.001
v_b	TUM	0.014	0.022	0.045	0.015	0.026	0.054	0.011	0.036	0.135	0.005
	TUM_0	0.003	0.007	0.011	0.003	0.006	0.014	0.003	0.016	0.030	0.001
	TUM_1	0.014	0.025	0.058	0.015	0.027	0.068	0.011	0.052	0.203	0.001
$rCBV_{GVF}$	TUM	0.510	0.832	1.361	0.774	1.088	3.269	0.613	1.633	5.299	0.001
	TUM_0	0.314	0.466	0.726	0.357	0.498	1.288	0.326	0.532	1.165	0.525
	TUM_1	0.620	1.181	1.936	1.092	1.373	2.804	1.024	1.961	5.322	0.001
$rCBV_{BOX}$	TUM	0.479	0.776	1.285	0.667	1.119	2.708	0.557	1.466	3.787	0.001
	TUM_0	0.198	0.448	0.633	0.344	0.471	1.007	0.300	0.482	1.060	0.730
	TUM_1	0.551	1.057	1.856	0.875	1.368	2.361	0.685	1.673	3.617	0.021
K_2	TUM	0.260	0.414	1.057	0.286	0.621	1.551	0.212	1.082	3.252	0.001
	TUM_0	0.387	0.651	1.578	0.564	0.928	1.968	0.398	1.174	3.411	0.003
	TUM_1	0.128	0.180	0.342	0.120	0.227	0.658	0.084	0.287	0.808	0.075

*Table 36 – **Skew** values from the **TUM** VOI for each parameter, Kruskal-Wallis tested for P<0.05 and Bonferroni corrected for P<0.00128 (0.05/39) to examine differences between grades.*

Parameter	VOI	WHO II (N=10)			WHO III (N=12)			WHO IV (N=33)			Sig.
		Minimum	Median	Maximum	Minimum	Median	Maximum	Minimum	Median	Maximum	
ADC	TUM	0.015	0.901	2.651	-0.682	0.281	2.457	-0.278	0.646	2.797	0.312
	TUM_0	0.199	1.654	2.833	0.328	1.356	2.774	0.243	1.632	3.161	0.515
	TUM_1	-1.142	-0.903	-0.258	-1.718	-1.176	0.243	-1.504	-0.930	0.209	0.179
FA	TUM	0.744	1.450	2.016	0.486	1.353	1.875	0.406	0.974	1.628	0.001
	TUM_0	1.689	2.150	2.603	1.363	2.087	2.499	1.268	1.830	2.298	0.001
	TUM_1	-1.047	-0.845	-0.499	-1.188	-0.917	-0.526	-1.191	-0.888	-0.244	0.401
q	TUM	0.531	0.989	1.772	0.454	1.015	1.797	0.300	0.843	1.900	0.059
	TUM_0	1.602	1.800	2.391	1.586	1.902	2.456	0.973	1.674	2.507	0.004
	TUM_1	-1.089	-0.838	-0.324	-1.163	-0.929	-0.597	-1.190	-1.024	-0.161	0.052
RA	TUM	0.910	1.963	2.426	0.720	1.596	2.403	0.621	1.287	2.359	0.020
	TUM_0	1.767	2.543	2.949	1.561	2.263	2.921	1.385	2.030	2.897	0.015
	TUM_1	-0.959	-0.805	-0.341	-1.158	-0.879	-0.419	-1.155	-0.886	-0.348	0.151
λ_L	TUM	-0.069	0.728	1.303	-0.975	0.318	1.200	-0.436	0.361	1.910	0.492
	TUM_0	0.109	1.563	2.008	0.294	1.236	1.583	0.111	1.414	2.371	0.754
	TUM_1	-1.240	-0.634	0.182	-1.887	-1.128	0.168	-1.591	-1.088	0.121	0.061
λ_R	TUM	-0.210	0.862	2.929	-0.521	0.207	2.540	-0.176	0.693	2.370	0.129
	TUM_0	0.094	1.600	3.118	0.214	1.128	2.845	0.401	1.621	2.717	0.136
	TUM_1	-1.146	-1.045	-0.582	-1.633	-0.820	-0.084	-1.467	-0.980	0.097	0.907
R_1	TUM	0.221	0.621	1.895	0.333	0.748	2.158	-0.393	0.381	2.042	0.019
	TUM_0	0.642	1.519	2.490	1.152	1.705	2.722	-0.219	1.332	2.646	0.015
	TUM_1	-1.199	-0.834	-0.258	-1.098	-0.877	-0.511	-1.279	-0.647	0.159	0.186
K^{trans}	TUM	0.669	1.824	3.120	0.783	1.867	4.650	0.401	1.369	7.535	0.136
	TUM_0	1.650	2.442	3.551	1.747	2.459	4.885	1.171	2.123	7.704	0.097
	TUM_1	-1.120	-0.716	-0.276	-1.057	-0.626	-0.039	-1.202	-0.757	1.316	0.669
v_e	TUM	0.847	1.521	2.669	0.482	1.867	4.381	-0.201	1.079	3.318	0.001
	TUM_0	1.792	2.244	3.143	1.532	2.493	4.609	0.864	1.821	3.731	0.001
	TUM_1	-1.064	-0.602	-0.022	-1.005	-0.589	-0.116	-1.261	-0.686	0.518	0.516
v_b	TUM	1.011	2.247	3.912	1.313	1.889	6.265	1.197	2.903	8.781	0.008
	TUM_0	1.910	2.755	4.168	2.061	2.424	6.331	1.943	3.337	8.512	0.007
	TUM_1	-0.870	-0.374	0.539	-1.002	-0.376	0.686	-1.095	-0.684	5.164	0.041
$rCBV_{GVF}$	TUM	0.914	2.002	2.821	0.172	2.238	2.886	0.286	1.927	5.559	0.901
	TUM_0	1.706	2.575	3.294	0.885	2.799	3.351	1.517	2.556	5.778	0.857
	TUM_1	-1.104	-0.881	-0.707	-0.931	-0.789	-0.568	-1.017	-0.616	-0.076	0.001
$rCBV_{BOX}$	TUM	0.855	1.578	3.005	0.433	1.968	3.175	0.158	1.668	5.347	0.555
	TUM_0	1.600	2.243	3.454	1.571	2.575	3.599	1.453	2.330	5.593	0.572
	TUM_1	-1.146	-0.850	-0.156	-1.092	-0.750	-0.346	-1.277	-0.675	0.071	0.133
K_2	TUM	-5.060	-3.071	-2.676	-7.387	-2.575	-0.899	-6.362	-2.352	-0.288	0.096
	TUM_0	-1.335	0.614	0.806	-2.776	0.600	0.973	-1.225	0.244	1.314	0.286
	TUM_1	-5.285	-3.510	-3.149	-7.578	-3.034	-1.726	-6.395	-2.822	-1.283	0.058

*Table 37 – **Kurtosis** values from the **TUM** VOI for each parameter, Kruskal-Wallis tested for P<0.05 and Bonferroni corrected for P<0.00128 (0.05/39) to examine differences between grades.*

Parameter	VOI	WHO II (N=10)			WHO III (N=12)			WHO IV (N=33)			Sig.
		Minimum	Median	Maximum	Minimum	Median	Maximum	Minimum	Median	Maximum	
ADC	TUM	0.131	2.079	19.745	-0.556	0.406	16.367	-0.980	1.162	13.800	0.153
	TUM_0	0.143	2.590	20.281	-1.075	0.722	17.062	-0.830	1.244	14.823	0.153
	TUM_1	-1.855	-0.194	1.010	-1.210	-0.415	1.480	-1.759	-0.488	2.195	0.641
FA	TUM	-0.108	3.096	6.430	-0.239	2.598	4.584	-0.323	1.230	4.493	0.009
	TUM_0	0.270	4.051	7.382	-0.074	3.498	5.691	-0.299	1.885	5.319	0.009
	TUM_1	-1.410	-1.224	-0.762	-1.540	-1.264	-0.759	-1.517	-1.044	-0.085	0.010
q	TUM	-0.627	1.534	5.356	0.061	1.047	5.806	-0.514	0.975	5.768	0.426
	TUM_0	-0.125	2.234	6.231	0.450	1.654	6.592	-0.321	1.502	6.347	0.327
	TUM_1	-1.382	-1.116	-0.230	-1.481	-1.094	-0.505	-1.583	-0.997	0.200	0.572
RA	TUM	0.368	5.979	9.888	0.363	3.605	9.025	-0.086	2.493	11.046	0.111
	TUM_0	0.638	6.829	10.733	0.540	4.519	10.043	0.406	3.270	11.551	0.097
	TUM_1	-1.429	-1.136	-0.580	-1.507	-1.335	-0.613	-1.655	-1.037	-0.277	0.059
λ_L	TUM	0.294	1.804	7.082	-0.523	0.301	5.298	-1.103	0.912	9.560	0.098
	TUM_0	-0.512	1.490	3.702	-1.307	0.183	5.746	-0.833	0.907	9.883	0.289
	TUM_1	-1.637	0.496	4.845	-1.671	-0.397	1.342	-1.679	-0.370	1.661	0.352
λ_R	TUM	0.384	1.692	21.994	-0.441	0.321	16.936	-0.918	1.020	11.375	0.128
	TUM_0	0.349	2.150	22.606	-0.971	0.504	17.648	-0.809	1.220	12.225	0.103
	TUM_1	-1.791	-0.384	0.959	-1.154	-0.024	2.827	-1.714	-0.628	1.864	0.109
R_1	TUM	-0.550	1.362	8.183	-0.395	0.269	6.426	-0.469	1.278	4.857	0.190
	TUM_0	-0.880	1.691	8.666	-0.054	0.745	7.544	-0.187	1.166	6.001	0.425
	TUM_1	-1.416	-0.402	1.144	-1.562	-0.999	-0.419	-1.469	-0.143	2.639	0.004
K^{trans}	TUM	0.058	4.288	16.298	0.278	5.170	39.715	-0.231	2.658	97.906	0.534
	TUM_0	0.846	4.743	16.722	0.644	5.840	37.762	0.259	3.245	96.922	0.350
	TUM_1	-1.685	-1.057	-0.547	-1.595	-1.022	2.547	-1.835	-0.883	15.988	0.872
v_e	TUM	0.613	2.781	11.715	-0.020	4.441	26.916	-0.952	1.156	23.049	0.001
	TUM_0	1.452	3.571	11.747	-0.277	4.723	26.282	-1.091	1.464	23.272	0.001
	TUM_1	-1.651	-0.920	0.688	-1.788	-0.900	0.640	-1.792	-0.998	2.042	0.550
v_b	TUM	0.890	6.990	23.641	1.281	4.749	61.653	1.556	11.946	112.299	0.003
	TUM_0	1.748	6.897	22.503	2.063	4.569	58.405	1.727	12.707	103.002	0.001
	TUM_1	-1.455	-0.285	3.659	-1.515	-0.766	7.771	-1.817	-1.088	61.148	0.198
$rCBV_{GVF}$	TUM	1.239	8.413	14.352	-0.771	8.103	16.343	-0.741	5.250	44.169	0.371
	TUM_0	1.716	9.358	14.888	-0.158	8.691	16.575	-0.391	6.018	44.100	0.318
	TUM_1	-1.541	-1.103	-0.670	-1.503	-1.013	0.004	-1.605	-1.018	1.212	0.619
$rCBV_{BOX}$	TUM	0.561	5.117	17.245	-0.664	6.479	19.727	-0.545	3.851	39.810	0.274
	TUM_0	1.282	5.815	17.668	-0.215	7.223	19.490	-0.334	4.651	40.213	0.214
	TUM_1	-1.410	-1.083	-0.404	-1.293	-1.027	1.011	-1.644	-1.040	0.882	0.817
K_2	TUM	9.723	18.232	53.095	0.569	13.046	147.928	-0.830	9.024	61.591	0.084
	TUM_0	-1.226	-0.265	16.330	-1.420	-0.760	58.231	-1.422	-0.264	11.574	0.683
	TUM_1	10.308	18.736	50.433	0.515	13.562	147.719	-0.515	8.191	58.065	0.032

*Table 38 – **Median** values from the **TUM** VOI for each parameter, Kruskal-Wallis tested for P<0.05 and Bonferroni corrected for P<0.00128 (0.05/39) to examine differences between grades.*

Parameter	VOI	WHO II (N=10)			WHO III (N=12)			WHO IV (N=33)			Sig.
		Minimum	Median	Maximum	Minimum	Median	Maximum	Minimum	Median	Maximum	
ADC	TUM	1.066	1.234	1.336	0.817	1.105	1.522	0.779	1.123	1.457	0.167
	TUM_0	0.940	1.206	1.321	0.805	1.061	1.299	0.707	1.003	1.244	0.012
	TUM_1	1.240	1.468	1.955	1.038	1.226	1.988	0.976	1.376	1.849	0.089
FA	TUM	0.104	0.146	0.214	0.120	0.161	0.258	0.150	0.189	0.310	0.002
	TUM_0	0.075	0.117	0.197	0.108	0.131	0.210	0.059	0.158	0.280	0.019
	TUM_1	0.214	0.249	0.377	0.202	0.294	0.391	0.207	0.300	0.459	0.046
q	TUM	0.160	0.259	0.385	0.226	0.257	0.405	0.217	0.322	0.367	0.001
	TUM_0	0.127	0.185	0.354	0.165	0.227	0.287	0.081	0.287	0.352	0.006
	TUM_1	0.300	0.404	0.592	0.342	0.417	0.492	0.281	0.469	0.764	0.012
RA	TUM	0.086	0.120	0.178	0.098	0.132	0.216	0.124	0.156	0.263	0.002
	TUM_0	0.062	0.099	0.168	0.091	0.111	0.177	0.097	0.138	0.246	0.002
	TUM_1	0.186	0.215	0.356	0.169	0.257	0.391	0.204	0.273	0.483	0.017
λ_L	TUM	1.205	1.465	1.574	1.021	1.352	1.723	0.975	1.376	1.756	0.389
	TUM_0	1.009	1.397	1.564	0.999	1.261	1.523	0.842	1.196	1.621	0.300
	TUM_1	1.321	1.584	2.512	1.265	1.534	2.203	1.157	1.627	2.292	0.606
λ_R	TUM	0.976	1.121	1.229	0.711	1.001	1.427	0.649	0.995	1.317	0.102
	TUM_0	0.907	1.067	1.214	0.656	0.982	1.215	0.612	0.891	1.128	0.003
	TUM_1	1.173	1.398	1.932	0.930	1.063	1.894	0.876	1.256	1.860	0.042
R_1	TUM	0.345	0.650	0.944	0.401	0.722	0.872	0.619	0.798	1.415	0.014
	TUM_0	0.261	0.600	0.937	0.383	0.654	0.867	0.509	0.753	1.381	0.012
	TUM_1	0.355	0.775	1.185	0.616	0.896	1.078	0.633	0.904	1.506	0.080
K^{trans}	TUM	0.018	0.024	0.046	0.022	0.029	0.123	0.018	0.066	0.125	0.001
	TUM_0	0.016	0.020	0.031	0.017	0.026	0.054	0.016	0.057	0.108	0.001
	TUM_1	0.027	0.044	0.093	0.040	0.059	0.266	0.032	0.136	0.457	0.001
v_e	TUM	0.022	0.034	0.045	0.025	0.040	0.224	0.020	0.128	0.295	0.001
	TUM_0	0.017	0.026	0.034	0.018	0.029	0.154	0.016	0.050	0.245	0.001
	TUM_1	0.040	0.064	0.163	0.043	0.088	0.399	0.038	0.245	0.694	0.001
v_b	TUM	0.018	0.024	0.034	0.019	0.027	0.038	0.017	0.036	0.067	0.001
	TUM_0	0.014	0.020	0.026	0.014	0.019	0.031	0.014	0.034	0.060	0.001
	TUM_1	0.032	0.051	0.096	0.037	0.052	0.103	0.029	0.099	0.240	0.001
$rCBV_{GVF}$	TUM	0.958	1.207	1.472	0.698	1.455	4.703	0.788	1.323	3.564	0.518
	TUM_0	0.919	1.098	1.441	0.632	1.281	2.599	0.648	1.046	2.955	0.126
	TUM_1	1.708	2.573	3.833	2.129	2.801	6.897	1.957	3.629	8.179	0.003
$rCBV_{BOX}$	TUM	0.967	1.254	1.477	0.812	1.477	4.784	0.786	1.345	3.728	0.319
	TUM_0	0.805	1.104	1.450	0.704	1.325	2.420	0.611	1.009	3.137	0.152
	TUM_1	1.575	2.432	3.535	2.234	2.795	6.295	1.841	3.244	6.135	0.013
K_2	TUM	-0.534	-0.336	-0.146	-1.477	-0.482	-0.091	-1.834	-0.629	-0.123	0.035
	TUM_0	-1.394	-1.010	-0.523	-3.346	-1.379	-0.390	-5.162	-1.956	-0.579	0.001
	TUM_1	-0.512	-0.307	-0.123	-0.984	-0.393	-0.079	-1.474	-0.372	-0.120	0.500

*Table 39 – **Minimum** values from the **TUM** VOI for each parameter, Kruskal-Wallis tested for P<0.05 and Bonferroni corrected for P<0.0038 (0.05/13) to examine differences between grades.*

Parameter	VOI	WHO II (N=10)	WHO III (N=12)	WHO IV (N=33)	Sig.
		Median	Median	Median	
ADC	TUM	0.402	0.408	0.099	0.024
FA	TUM	0.015	0.023	0.017	0.650
q	TUM	0.030	0.039	0.025	0.203
RA	TUM	0.012	0.019	0.015	0.466
λ_L	TUM	0.501	0.538	0.067	0.022
λ_R	TUM	0.121	0.276	0.063	0.029
R_1	TUM	0.090	0.356	0.059	0.163
K^{trans}	TUM	0.010	0.010	0.010	0.970
v_e	TUM	0.010	0.010	0.010	0.160
v_b	TUM	0.010	0.010	0.010	0.074
$rCBV_{GVF}$	TUM	0.011	0.011	0.010	0.170
$rCBV_{BOX}$	TUM	0.011	0.026	0.010	0.049
K_2	TUM	-6.350	-7.543	-13.520	0.002

*Table 40 – **Maximum** values from the **TUM** VOI for each parameter, Kruskal-Wallis tested for P<0.05 and Bonferroni corrected for P<0.0038 (0.05/13) to examine differences between grades.*

Parameter	VOI	WHO II (N=10)	WHO III (N=12)	WHO IV (N=33)	Sig.
		Median	Median	Median	
ADC	TUM	2.900	2.327	2.863	0.120
FA	TUM	0.744	0.685	0.785	0.247
q	TUM	1.112	1.008	1.147	0.356
RA	TUM	0.769	0.708	0.876	0.161
λ_L	TUM	3.330	2.543	3.221	0.057
λ_R	TUM	2.751	2.255	2.706	0.155
R_1	TUM	1.456	1.448	1.799	0.018
K^{trans}	TUM	0.136	0.198	0.475	0.001
v_e	TUM	0.240	0.312	0.724	0.001
v_b	TUM	0.176	0.200	0.425	0.001
$rCBV_{GVF}$	TUM	8.535	11.732	16.414	0.003
$rCBV_{BOX}$	TUM	7.946	11.010	13.509	0.106
K_2	TUM	0.841	0.952	1.098	0.765

*Table 41 – **Mean** values from the **CEL** VOI for each parameter, Kruskal-Wallis tested for P<0.05 and Bonferroni corrected for P< 0.00128 (0.05/39) to examine differences between grades.*

Param.	VOI	WHO II (N=4)			WHO III (N=6)			WHO IV (N=33)			Sig.
		Minimum	Median	Maximum	Minimum	Median	Maximum	Minimum	Median	Maximum	
ADC	CEL	0.805	1.115	1.167	0.747	0.968	1.324	0.782	1.105	1.540	0.667
	CEL_0	0.735	1.009	1.125	0.709	0.932	1.293	0.682	0.982	1.474	0.985
	CEL_1	0.905	1.193	1.428	0.950	1.200	1.462	0.820	1.264	1.953	0.363
FA	CEL	0.074	0.117	0.255	0.094	0.185	0.296	0.085	0.176	0.390	0.467
	CEL_0	0.053	0.076	0.194	0.037	0.131	0.263	0.056	0.121	0.318	0.440
	CEL_1	0.104	0.144	0.319	0.108	0.245	0.312	0.107	0.230	0.588	0.263
q	CEL	0.085	0.183	0.383	0.173	0.239	0.385	0.134	0.260	0.450	0.508
	CEL_0	0.065	0.165	0.306	0.073	0.166	0.313	0.083	0.166	0.408	0.958
	CEL_1	0.106	0.269	0.463	0.196	0.296	0.473	0.214	0.349	0.717	0.644
RA	CEL	0.060	0.097	0.216	0.077	0.155	0.251	0.070	0.148	0.350	0.463
	CEL_0	0.043	0.062	0.164	0.030	0.110	0.244	0.047	0.102	0.266	0.440
	CEL_1	0.086	0.119	0.273	0.089	0.206	0.281	0.087	0.197	0.504	0.205
λ_L	CEL	0.864	1.283	1.386	0.896	1.210	1.452	0.977	1.265	1.699	0.726
	CEL_0	0.799	1.170	1.235	0.823	1.174	1.430	0.782	1.167	1.379	0.901
	CEL_1	0.992	1.330	1.739	1.129	1.457	1.600	1.072	1.477	2.129	0.452
λ_R	CEL	0.775	0.997	1.125	0.673	0.874	1.260	0.626	1.016	1.460	0.625
	CEL_0	0.710	0.889	1.120	0.637	0.799	1.198	0.372	0.887	1.378	0.836
	CEL_1	0.880	1.111	1.333	0.903	1.095	1.364	0.691	1.186	1.880	0.392
R_1	CEL	0.612	0.624	0.657	0.365	0.729	0.941	0.552	0.786	1.459	0.039
	CEL_0	0.522	0.581	0.595	0.333	0.691	0.876	0.371	0.705	1.384	0.071
	CEL_1	0.639	0.682	0.702	0.435	0.777	1.078	0.591	0.893	1.517	0.019
K^{trans}	CEL	0.020	0.027	0.047	0.015	0.047	0.196	0.013	0.107	0.231	0.008
	CEL_0	0.014	0.022	0.033	0.013	0.029	0.129	0.012	0.076	0.136	0.004
	CEL_1	0.028	0.054	0.073	0.021	0.086	0.275	0.013	0.155	0.480	0.004
v_e	CEL	0.031	0.040	0.059	0.026	0.064	0.285	0.016	0.204	0.444	0.005
	CEL_0	0.015	0.023	0.034	0.021	0.048	0.261	0.013	0.154	0.303	0.006
	CEL_1	0.046	0.061	0.078	0.041	0.088	0.431	0.024	0.321	0.749	0.002
v_b	CEL	0.021	0.030	0.050	0.014	0.035	0.064	0.000	0.053	0.132	0.028
	CEL_0	0.015	0.021	0.037	0.013	0.025	0.042	0.000	0.039	0.075	0.025
	CEL_1	0.027	0.060	0.114	0.020	0.046	0.105	0.000	0.110	0.262	0.017
$rCBV_{GVF}$	CEL	2.106	2.538	2.735	1.252	2.698	6.273	0.837	3.156	8.074	0.531
	CEL_0	1.421	1.959	2.285	0.462	0.766	2.739	0.228	1.323	4.270	0.402
	CEL_1	2.587	3.327	5.418	1.889	3.291	7.684	1.285	4.478	11.735	0.247
$rCBV_{BOX}$	CEL	1.399	2.389	2.674	1.426	2.593	6.007	1.164	3.106	7.145	0.214
	CEL_0	1.068	1.947	2.042	0.819	2.187	2.597	0.082	2.217	4.800	0.670
	CEL_1	1.594	3.493	5.271	1.577	3.354	6.687	1.436	4.638	9.363	0.174
K_2	CEL	-1.072	-0.651	-0.341	-2.827	-2.426	-0.685	-6.036	-1.723	-0.104	0.019
	CEL_0	-1.532	-1.059	-0.381	-5.389	-3.289	-0.902	-9.904	-3.239	-0.134	0.019
	CEL_1	-0.479	-0.381	-0.278	-2.652	-1.684	-0.310	-4.579	-1.050	-0.072	0.034

*Table 42 – **Standard deviations** from the **CEL** VOI for each parameter, Kruskal-Wallis tested for P<0.05 and Bonferroni corrected for P< 0.00128 (0.05/39) to examine differences between grades.*

Param.	VOI	WHO II (N=4)			WHO III (N=6)			WHO IV (N=33)			Sig.
		Minimum	Median	Maximum	Minimum	Median	Maximum	Minimum	Median	Maximum	
ADC	CEL	0.108	0.133	0.310	0.088	0.152	0.195	0.086	0.248	0.576	0.002
	CEL_0	0.068	0.088	0.118	0.063	0.105	0.170	0.017	0.151	0.269	0.018
	CEL_1	0.100	0.135	0.357	0.034	0.186	0.237	0.045	0.329	0.687	0.006
FA	CEL	0.035	0.039	0.098	0.043	0.070	0.123	0.029	0.092	0.150	0.020
	CEL_0	0.011	0.014	0.056	0.008	0.035	0.078	0.014	0.044	0.081	0.123
	CEL_1	0.032	0.040	0.092	0.035	0.059	0.128	0.026	0.092	0.136	0.010
q	CEL	0.032	0.059	0.135	0.074	0.098	0.147	0.055	0.122	0.170	0.035
	CEL_0	0.013	0.041	0.077	0.014	0.047	0.072	0.029	0.059	0.105	0.140
	CEL_1	0.033	0.046	0.135	0.063	0.090	0.157	0.047	0.117	0.213	0.018
RA	CEL	0.029	0.033	0.089	0.036	0.061	0.112	0.024	0.083	0.163	0.022
	CEL_0	0.009	0.011	0.047	0.007	0.030	0.067	0.012	0.038	0.071	0.097
	CEL_1	0.027	0.034	0.089	0.030	0.053	0.124	0.022	0.085	0.175	0.014
λ_L	CEL	0.122	0.126	0.326	0.075	0.185	0.196	0.094	0.279	0.614	0.003
	CEL_0	0.057	0.078	0.138	0.062	0.116	0.177	0.059	0.156	0.594	0.030
	CEL_1	0.103	0.118	0.364	0.064	0.162	0.256	0.041	0.334	0.824	0.002
λ_R	CEL	0.113	0.139	0.317	0.107	0.144	0.226	0.090	0.258	0.563	0.003
	CEL_0	0.071	0.099	0.124	0.030	0.088	0.194	0.016	0.159	0.286	0.017
	CEL_1	0.103	0.148	0.372	0.075	0.177	0.234	0.051	0.345	0.633	0.006
R_1	CEL	0.053	0.084	0.143	0.056	0.063	0.128	0.044	0.164	0.310	0.001
	CEL_0	0.025	0.038	0.068	0.029	0.064	0.076	0.018	0.095	0.268	0.002
	CEL_1	0.043	0.084	0.189	0.044	0.059	0.123	0.051	0.170	0.358	0.001
K^{trans}	CEL	0.009	0.016	0.025	0.005	0.034	0.167	0.001	0.053	0.230	0.006
	CEL_0	0.002	0.007	0.012	0.002	0.011	0.050	0.000	0.032	0.059	0.004
	CEL_1	0.004	0.015	0.043	0.003	0.030	0.163	0.000	0.063	0.254	0.009
v_e	CEL	0.017	0.024	0.035	0.010	0.031	0.183	0.005	0.104	0.290	0.002
	CEL_0	0.003	0.008	0.013	0.003	0.022	0.106	0.002	0.063	0.125	0.008
	CEL_1	0.014	0.024	0.033	0.005	0.031	0.179	0.001	0.115	0.245	0.001
v_b	CEL	0.007	0.019	0.045	0.004	0.014	0.053	0.000	0.036	0.148	0.037
	CEL_0	0.003	0.007	0.015	0.001	0.006	0.016	0.000	0.017	0.042	0.008
	CEL_1	0.004	0.016	0.081	0.000	0.015	0.058	0.000	0.052	0.205	0.014
$rCBV_{GVF}$	CEL	0.496	1.308	1.670	0.667	1.517	3.355	0.204	2.252	5.536	0.028
	CEL_0	0.272	0.448	0.745	0.180	0.415	1.004	0.139	0.742	2.333	0.131
	CEL_1	0.574	1.360	2.304	0.510	1.222	2.654	0.139	2.191	5.250	0.066
$rCBV_{BOX}$	CEL	0.381	0.918	1.736	0.463	1.013	2.628	0.195	1.786	3.516	0.034
	CEL_0	0.186	0.409	0.706	0.144	0.615	1.004	0.050	0.993	1.678	0.019
	CEL_1	0.327	0.868	2.354	0.410	0.913	2.285	0.082	1.891	3.400	0.071
K_2	CEL	0.194	0.542	0.752	0.351	1.193	2.337	0.053	1.417	3.619	0.025
	CEL_0	0.223	0.678	0.701	0.307	1.317	2.507	0.050	1.874	4.440	0.012
	CEL_1	0.132	0.200	0.253	0.116	0.665	1.045	0.034	0.768	2.055	0.015

*Table 43 – **Skew** values from the **CEL** VOI for each parameter, Kruskal-Wallis tested for P<0.05 and Bonferroni corrected for P< 0.00128 (0.05/39) to examine differences between grades.*

Param.	VOI	WHO II (N=4)			WHO III (N=6)			WHO IV (N=33)			Sig.
		Minimum	Median	Maximum	Minimum	Median	Maximum	Minimum	Median	Maximum	
ADC	CEL	0.166	0.531	1.908	0.183	0.510	2.303	-0.211	0.886	2.706	0.714
	CEL_0	0.973	1.580	2.531	0.749	1.432	2.797	0.100	1.612	3.195	0.869
	CEL_1	-0.964	-0.862	-0.745	-1.269	-1.000	-0.741	-1.216	-0.760	0.422	0.144
FA	CEL	-0.029	0.760	1.900	-0.267	0.372	1.284	0.370	1.040	2.969	0.090
	CEL_0	1.341	1.750	2.532	1.008	1.528	2.082	1.492	1.877	3.407	0.157
	CEL_1	-0.980	-0.914	-0.804	-1.332	-0.929	-0.615	-1.199	-0.843	-0.218	0.416
q	CEL	0.316	0.997	1.583	0.225	0.673	1.303	0.140	0.763	2.041	0.660
	CEL_0	1.041	1.895	2.253	1.420	1.705	2.087	1.096	1.713	2.560	0.777
	CEL_1	-1.279	-0.894	-0.574	-1.293	-0.920	-0.612	-1.239	-0.990	0.027	0.968
RA	CEL	0.009	0.869	1.940	-0.120	0.414	1.547	0.484	1.269	3.420	0.044
	CEL_0	1.349	1.813	2.565	0.262	1.551	2.268	1.530	2.048	3.794	0.065
	CEL_1	-0.953	-0.850	-0.746	-1.308	-0.906	-0.370	-1.101	-0.838	0.193	0.637
λ_L	CEL	0.015	0.597	1.544	-0.198	0.598	1.558	-0.410	0.829	2.772	0.840
	CEL_0	1.378	1.623	2.267	0.548	1.352	2.228	0.272	1.595	3.229	0.684
	CEL_1	-1.097	-0.926	-0.774	-1.456	-1.160	-1.007	-1.307	-0.819	-0.124	0.015
λ_R	CEL	0.042	0.592	1.847	0.042	0.670	2.632	-0.120	0.693	2.538	0.958
	CEL_0	0.151	1.635	2.494	1.262	1.550	3.101	0.207	1.634	3.051	0.951
	CEL_1	-1.010	-0.913	-0.077	-1.287	-1.066	-0.062	-1.222	-0.822	0.113	0.167
R_1	CEL	0.011	0.398	1.647	-0.599	0.602	1.160	-1.086	0.502	1.529	0.968
	CEL_0	1.407	1.429	2.347	1.073	1.635	1.997	-0.323	1.562	2.257	0.835
	CEL_1	-1.004	-0.797	-0.357	-1.453	-1.101	-0.737	-1.398	-0.860	-0.010	0.173
K^{trans}	CEL	0.766	0.811	3.981	-0.887	0.757	2.289	0.000	1.168	7.830	0.138
	CEL_0	1.717	1.796	4.337	1.119	1.818	2.843	1.149	1.930	7.999	0.681
	CEL_1	-1.202	-1.075	-0.857	-1.661	-1.174	-0.245	-1.414	-0.976	-0.239	0.226
v_e	CEL	0.645	0.928	1.460	-0.477	0.396	1.295	-0.415	0.767	3.362	0.184
	CEL_0	1.671	1.820	2.192	0.304	1.520	2.079	1.137	1.675	3.769	0.233
	CEL_1	-1.125	-0.935	-0.125	-1.218	-1.031	-0.655	-1.274	-1.036	-0.326	0.573
v_b	CEL	0.043	1.026	4.532	0.574	0.907	1.894	0.000	2.559	5.462	0.006
	CEL_0	1.428	1.920	4.817	1.401	1.856	2.461	0.000	3.033	5.723	0.007
	CEL_1	-1.290	-1.146	-0.717	-1.195	-1.028	-0.407	-1.074	-0.718	1.544	0.024
$rCBV_{GVF}$	CEL	0.495	1.407	2.276	-0.218	0.097	1.700	-1.070	0.931	3.276	0.145
	CEL_0	1.346	2.160	2.825	1.286	1.418	2.388	1.148	1.807	3.695	0.236
	CEL_1	-0.987	-0.630	-0.259	-1.155	-0.957	-0.201	-1.683	-0.744	0.734	0.444
$rCBV_{BOX}$	CEL	0.348	1.076	2.336	-0.362	0.376	2.257	-0.596	0.880	3.113	0.286
	CEL_0	1.475	1.809	2.883	1.070	1.445	2.784	0.460	1.646	3.547	0.279
	CEL_1	-1.168	-0.943	-0.851	-1.319	-0.882	-0.221	-1.671	-0.948	0.119	0.937
K_2	CEL	-1.615	-1.120	-0.106	-2.157	-0.434	-0.026	-4.354	-1.283	0.252	0.058
	CEL_0	0.385	0.586	0.906	0.007	0.938	1.185	-0.113	0.917	1.457	0.260
	CEL_1	-2.100	-1.953	-0.830	-2.742	-1.439	-0.338	-4.671	-1.955	-1.016	0.057

*Table 44 – **Kurtosis** values from the **CEL** VOI for each parameter, Kruskal-Wallis tested for P<0.05 and Bonferroni corrected for P< 0.00128 (0.05/39) to examine differences between grades.*

Param.	VOI	WHO II (N=4)			WHO III (N=6)			WHO IV (N=33)			Sig.
		Minimum	Median	Maximum	Minimum	Median	Maximum	Minimum	Median	Maximum	
ADC	CEL	-0.248	0.377	3.660	-0.681	0.293	6.804	-0.855	1.395	12.033	0.283
	CEL_0	0.032	0.824	4.734	-0.087	0.692	8.087	-0.634	1.873	12.789	0.332
	CEL_1	-1.530	-0.765	-0.125	-1.756	-1.049	-0.089	-1.686	-0.833	5.389	0.416
FA	CEL	-0.624	0.076	4.662	-0.930	-0.004	1.370	-0.405	1.092	12.009	0.080
	CEL_0	-1.026	0.806	5.789	-0.667	-0.118	2.440	-0.476	1.365	12.671	0.088
	CEL_1	-1.524	-1.134	-0.501	-1.442	-0.962	0.464	-1.703	-0.929	0.018	0.784
q	CEL	-0.476	1.418	3.646	-0.740	-0.060	1.853	-0.583	0.656	5.648	0.332
	CEL_0	-0.103	1.925	4.668	-0.746	0.589	2.802	-0.856	1.171	6.725	0.584
	CEL_1	-1.404	-0.972	-0.702	-1.360	-1.014	-0.672	-1.811	-0.892	0.765	0.616
RA	CEL	-0.599	0.369	4.904	-0.908	-0.028	2.489	-0.307	2.418	16.759	0.018
	CEL_0	-0.995	1.121	6.026	-0.636	0.136	3.566	-0.306	2.615	17.062	0.030
	CEL_1	-1.522	-1.125	-0.520	-1.471	-0.989	0.272	-1.710	-0.877	2.004	0.639
λ_L	CEL	-0.601	0.361	2.391	-0.673	0.571	4.867	-0.985	1.546	13.125	0.254
	CEL_0	-0.850	0.903	3.500	-0.767	1.079	5.626	-1.320	1.718	14.088	0.442
	CEL_1	-1.493	-0.909	-0.334	-1.690	-0.993	-0.511	-1.834	-0.735	2.531	0.204
λ_R	CEL	-0.256	0.388	3.626	-0.727	0.567	8.738	-0.870	1.261	10.638	0.442
	CEL_0	0.172	0.782	4.761	-0.076	1.153	10.105	-0.879	1.602	11.397	0.588
	CEL_1	-1.558	-0.882	0.159	-1.805	-1.062	-0.119	-1.584	-0.840	3.223	0.480
R_1	CEL	-0.757	0.423	2.763	-0.287	0.361	0.866	-0.365	0.681	4.083	0.461
	CEL_0	-0.782	0.505	3.870	-0.860	0.605	1.978	-1.051	0.989	3.819	0.420
	CEL_1	-1.467	-0.459	0.017	-1.462	-0.852	0.936	-1.602	-0.481	4.309	0.785
K^{trans}	CEL	-1.063	-0.170	21.063	-1.018	-0.097	6.153	-2.750	2.543	100.336	0.035
	CEL_0	0.397	0.931	22.182	-1.547	0.700	7.170	-1.000	3.090	99.883	0.062
	CEL_1	-1.642	-1.527	-1.289	-1.535	-1.227	0.997	-1.791	-1.144	0.512	0.133
v_e	CEL	-0.767	0.316	2.126	-0.810	0.066	1.958	-1.428	0.530	25.770	0.387
	CEL_0	0.082	0.939	3.353	-0.870	0.323	2.935	-1.311	1.103	25.018	0.329
	CEL_1	-1.536	-1.419	-0.482	-1.445	-0.744	0.810	-1.718	-1.137	0.524	0.323
v_b	CEL	-1.348	0.026	26.402	-1.395	0.437	4.195	0.000	9.545	45.560	0.002
	CEL_0	-0.779	1.379	27.056	0.602	1.363	4.555	0.000	10.405	46.118	0.002
	CEL_1	-1.585	-1.436	-0.834	-1.568	-1.228	-0.808	-1.856	-1.246	11.583	0.612
$rCBV_{GVF}$	CEL	0.653	1.967	6.733	-1.288	-0.781	4.085	-0.784	1.305	13.324	0.162
	CEL_0	1.057	2.758	7.921	-1.223	-0.788	4.928	-1.609	1.839	14.343	0.174
	CEL_1	-1.654	-1.156	0.135	-1.578	-0.783	0.440	-1.732	-0.897	4.417	0.551
$rCBV_{BOX}$	CEL	-0.680	1.226	6.967	-0.766	0.013	9.734	-0.900	0.958	11.489	0.479
	CEL_0	-0.191	2.030	8.119	-0.857	0.093	10.601	-0.951	1.737	12.701	0.222
	CEL_1	-1.636	-1.472	-0.951	-1.292	-0.605	0.928	-1.675	-1.043	0.620	0.019
K_2	CEL	-0.028	1.324	5.988	-0.837	0.498	4.799	-0.859	2.875	27.848	0.050
	CEL_0	-1.395	-0.711	0.524	-1.720	-0.921	0.873	-1.730	-0.985	1.561	0.610
	CEL_1	0.665	1.613	6.733	-0.345	0.843	6.158	-0.773	3.301	28.402	0.046

*Table 45 – **Median** values from the **CEL** VOI for each parameter, Kruskal-Wallis tested for P<0.05 and Bonferroni corrected for P< 0.00128 (0.05/39) to examine differences between grades.*

Param.	VOI	WHO II (N=4)			WHO III (N=6)			WHO IV (N=33)			Sig.
		Minimum	Median	Maximum	Minimum	Median	Maximum	Minimum	Median	Maximum	
ADC	CEL	0.777	1.057	1.160	0.710	0.973	1.321	0.722	1.048	1.487	0.799
	CEL_0	0.735	1.009	1.125	0.709	0.932	1.293	0.682	0.982	1.474	0.985
	CEL_1	0.905	1.193	1.428	0.950	1.200	1.462	0.820	1.264	1.953	0.363
FA	CEL	0.064	0.113	0.236	0.099	0.160	0.298	0.064	0.163	0.348	0.613
	CEL_0	0.053	0.076	0.194	0.037	0.131	0.263	0.056	0.121	0.318	0.440
	CEL_1	0.104	0.144	0.319	0.108	0.245	0.312	0.107	0.230	0.588	0.263
q	CEL	0.077	0.174	0.364	0.177	0.216	0.374	0.109	0.244	0.421	0.610
	CEL_0	0.065	0.165	0.306	0.073	0.166	0.313	0.083	0.166	0.408	0.958
	CEL_1	0.106	0.269	0.463	0.196	0.296	0.473	0.214	0.349	0.717	0.644
RA	CEL	0.053	0.092	0.197	0.081	0.132	0.252	0.053	0.134	0.297	0.588
	CEL_0	0.043	0.062	0.164	0.030	0.110	0.244	0.047	0.102	0.266	0.440
	CEL_1	0.086	0.119	0.273	0.089	0.206	0.281	0.087	0.197	0.504	0.205
λ_L	CEL	0.833	1.266	1.314	0.851	1.205	1.453	0.918	1.232	1.702	0.915
	CEL_0	0.799	1.170	1.235	0.823	1.174	1.430	0.782	1.167	1.379	0.901
	CEL_1	0.992	1.330	1.739	1.129	1.457	1.600	1.072	1.477	2.129	0.452
λ_R	CEL	0.753	0.943	1.118	0.638	0.869	1.242	0.627	0.963	1.398	0.750
	CEL_0	0.710	0.889	1.120	0.637	0.799	1.198	0.372	0.887	1.378	0.836
	CEL_1	0.880	1.111	1.333	0.903	1.095	1.364	0.691	1.186	1.880	0.392
R_1	CEL	0.585	0.617	0.661	0.348	0.729	0.912	0.547	0.755	1.426	0.049
	CEL_0	0.522	0.581	0.595	0.333	0.691	0.876	0.371	0.705	1.384	0.071
	CEL_1	0.639	0.682	0.702	0.435	0.777	1.078	0.591	0.893	1.517	0.019
K^{trans}	CEL	0.016	0.023	0.040	0.015	0.037	0.164	0.013	0.095	0.158	0.009
	CEL_0	0.014	0.022	0.033	0.013	0.029	0.129	0.012	0.076	0.136	0.004
	CEL_1	0.028	0.054	0.073	0.021	0.086	0.275	0.013	0.155	0.480	0.004
v_e	CEL	0.026	0.033	0.054	0.024	0.059	0.293	0.016	0.184	0.413	0.005
	CEL_0	0.015	0.023	0.034	0.021	0.048	0.261	0.013	0.154	0.303	0.006
	CEL_1	0.046	0.061	0.078	0.041	0.088	0.431	0.024	0.321	0.749	0.002
v_b	CEL	0.017	0.025	0.044	0.013	0.029	0.049	0.000	0.044	0.100	0.035
	CEL_0	0.015	0.021	0.037	0.013	0.025	0.042	0.000	0.039	0.075	0.025
	CEL_1	0.027	0.060	0.114	0.020	0.046	0.105	0.000	0.110	0.262	0.017
$rCBV_{GVF}$	CEL	1.748	2.241	2.397	0.899	2.672	6.460	0.520	2.988	6.817	0.722
	CEL_0	1.421	1.959	2.285	0.462	0.766	2.739	0.228	1.323	4.270	0.402
	CEL_1	2.587	3.327	5.418	1.889	3.291	7.684	1.285	4.478	11.735	0.247
$rCBV_{BOX}$	CEL	1.359	2.165	2.222	1.435	2.483	6.078	0.992	2.927	6.403	0.273
	CEL_0	1.068	1.947	2.042	0.819	2.187	2.597	0.082	2.217	4.800	0.670
	CEL_1	1.594	3.493	5.271	1.577	3.354	6.687	1.436	4.638	9.363	0.174
K_2	CEL	-0.849	-0.534	-0.330	-3.017	-2.006	-0.674	-5.383	-1.413	-0.099	0.013
	CEL_0	-1.532	-1.059	-0.381	-5.389	-3.289	-0.902	-9.904	-3.239	-0.134	0.019
	CEL_1	-0.479	-0.381	-0.278	-2.652	-1.684	-0.310	-4.579	-1.050	-0.072	0.034

*Table 46 – **Mean** values from the **NEL** VOI for each parameter, Kruskal-Wallis tested for P<0.05 and Bonferroni corrected for P< 0.00128 (0.05/39) to examine differences between grades.*

Param.	VOI	WHO II (N=10)			WHO III (N=12)			WHO IV (N=33)			Sig.
		Minimum	Median	Maximum	Minimum	Median	Maximum	Minimum	Median	Maximum	
ADC	NEL	1.078	1.258	1.350	0.823	1.116	1.523	0.811	1.187	1.434	0.250
	NEL_0	0.945	1.211	1.321	0.805	1.063	1.299	0.750	0.993	1.279	0.003
	NEL_1	1.240	1.468	2.009	1.038	1.249	1.988	1.015	1.362	2.057	0.078
FA	NEL	0.134	0.166	0.233	0.130	0.188	0.269	0.179	0.216	0.290	0.001
	NEL_0	0.075	0.118	0.195	0.108	0.137	0.210	0.118	0.167	0.241	0.001
	NEL_1	0.214	0.249	0.384	0.202	0.293	0.391	0.245	0.308	0.442	0.013
q	NEL	0.204	0.297	0.409	0.256	0.291	0.408	0.239	0.366	0.474	0.001
	NEL_0	0.129	0.186	0.355	0.165	0.227	0.287	0.120	0.315	0.372	0.001
	NEL_1	0.300	0.404	0.597	0.342	0.419	0.496	0.291	0.490	0.672	0.002
RA	NEL	0.112	0.139	0.199	0.107	0.157	0.230	0.150	0.183	0.250	0.001
	NEL_0	0.062	0.099	0.166	0.091	0.116	0.177	0.099	0.145	0.209	0.001
	NEL_1	0.186	0.215	0.363	0.169	0.256	0.391	0.208	0.278	0.430	0.009
λ_L	NEL	1.261	1.479	1.624	1.034	1.366	1.731	0.997	1.464	1.710	0.358
	NEL_0	1.009	1.400	1.564	0.999	1.259	1.523	0.859	1.254	1.608	0.579
	NEL_1	1.321	1.584	2.587	1.265	1.534	2.203	1.164	1.644	2.683	0.330
λ_R	NEL	0.986	1.144	1.239	0.718	1.008	1.419	0.687	1.041	1.298	0.117
	NEL_0	0.913	1.078	1.214	0.649	0.989	1.215	0.628	0.853	1.179	0.001
	NEL_1	1.173	1.398	1.932	0.928	1.104	1.894	0.975	1.232	1.867	0.026
R_1	NEL	0.345	0.679	0.964	0.442	0.784	0.904	0.621	0.842	1.448	0.007
	NEL_0	0.261	0.601	0.937	0.384	0.680	0.867	0.257	0.745	1.378	0.016
	NEL_1	0.355	0.775	1.185	0.616	0.902	1.082	0.626	0.942	1.507	0.072
K^{trans}	NEL	0.021	0.028	0.058	0.028	0.036	0.069	0.021	0.053	0.087	0.001
	NEL_0	0.016	0.019	0.031	0.017	0.026	0.037	0.016	0.031	0.063	0.002
	NEL_1	0.027	0.044	0.093	0.040	0.059	0.130	0.032	0.093	0.156	0.001
v_e	NEL	0.026	0.038	0.079	0.032	0.049	0.116	0.027	0.077	0.187	0.001
	NEL_0	0.017	0.026	0.034	0.017	0.029	0.046	0.016	0.037	0.151	0.005
	NEL_1	0.040	0.065	0.164	0.043	0.089	0.186	0.038	0.131	0.263	0.001
v_b	NEL	0.024	0.031	0.045	0.023	0.036	0.046	0.021	0.036	0.068	0.283
	NEL_0	0.014	0.019	0.026	0.014	0.019	0.028	0.014	0.024	0.060	0.050
	NEL_1	0.032	0.051	0.096	0.037	0.053	0.099	0.029	0.068	0.169	0.045
$rCBV_{GVF}$	NEL	1.075	1.409	1.646	0.916	1.664	3.737	0.902	1.595	5.064	0.326
	NEL_0	0.919	1.092	1.423	0.632	1.260	2.705	0.649	0.996	2.402	0.181
	NEL_1	1.708	2.558	3.590	1.925	2.801	5.206	1.637	3.050	8.179	0.226
$rCBV_{BOX}$	NEL	1.052	1.456	1.667	1.100	1.692	3.778	0.823	1.490	4.650	0.289
	NEL_0	0.805	1.097	1.436	0.704	1.295	2.598	0.606	0.975	2.328	0.091
	NEL_1	1.575	2.418	3.214	1.811	2.774	5.658	1.371	2.643	6.135	0.383
K_2	NEL	-0.747	-0.453	-0.234	-1.565	-0.637	-0.141	-1.919	-0.760	-0.171	0.059
	NEL_0	-1.394	-1.015	-0.520	-3.256	-1.276	-0.390	-3.698	-1.427	-0.520	0.044
	NEL_1	-0.512	-0.306	-0.119	-0.952	-0.387	-0.079	-1.313	-0.388	-0.121	0.665

*Table 47 – **Standard deviations** from the **NEL** VOI for each parameter, Kruskal-Wallis tested for P<0.05 and Bonferroni corrected for P< 0.00128 (0.05/39) to examine differences between grades.*

Param.	VOI	WHO II (N=10)			WHO III (N=12)			WHO IV (N=33)			Sig.
		Minimum	Median	Maximum	Minimum	Median	Maximum	Minimum	Median	Maximum	
ADC	NEL	0.169	0.267	0.390	0.136	0.213	0.487	0.139	0.271	0.445	0.029
	NEL_0	0.130	0.195	0.272	0.109	0.143	0.348	0.053	0.168	0.353	0.240
	NEL_1	0.105	0.302	0.507	0.132	0.202	0.536	0.106	0.274	0.864	0.038
FA	NEL	0.074	0.098	0.128	0.056	0.093	0.130	0.077	0.105	0.156	0.356
	NEL_0	0.028	0.042	0.075	0.034	0.047	0.073	0.034	0.057	0.079	0.023
	NEL_1	0.082	0.113	0.148	0.068	0.109	0.159	0.075	0.111	0.165	0.829
q	NEL	0.117	0.142	0.205	0.096	0.136	0.191	0.088	0.148	0.230	0.613
	NEL_0	0.037	0.065	0.122	0.051	0.071	0.118	0.029	0.094	0.158	0.004
	NEL_1	0.109	0.147	0.220	0.101	0.141	0.223	0.050	0.158	0.239	0.502
RA	NEL	0.065	0.087	0.116	0.048	0.083	0.130	0.067	0.099	0.153	0.311
	NEL_0	0.023	0.036	0.067	0.028	0.041	0.068	0.028	0.052	0.087	0.011
	NEL_1	0.074	0.105	0.163	0.059	0.104	0.188	0.067	0.108	0.195	0.514
λ_L	NEL	0.202	0.290	0.401	0.182	0.250	0.485	0.150	0.295	0.476	0.067
	NEL_0	0.078	0.195	0.301	0.073	0.185	0.396	0.095	0.210	0.486	0.431
	NEL_1	0.109	0.312	0.434	0.119	0.224	0.531	0.115	0.268	0.657	0.435
λ_R	NEL	0.169	0.267	0.405	0.141	0.223	0.497	0.143	0.279	0.444	0.023
	NEL_0	0.125	0.226	0.281	0.076	0.163	0.339	0.085	0.183	0.342	0.079
	NEL_1	0.100	0.317	0.560	0.142	0.222	0.497	0.141	0.274	0.798	0.158
R_1	NEL	0.056	0.166	0.247	0.112	0.174	0.224	0.093	0.186	0.259	0.060
	NEL_0	0.008	0.094	0.141	0.049	0.085	0.149	0.039	0.108	0.433	0.032
	NEL_1	0.051	0.173	0.424	0.073	0.153	0.291	0.089	0.203	0.327	0.189
K^{trans}	NEL	0.007	0.017	0.044	0.017	0.023	0.058	0.010	0.043	0.070	0.001
	NEL_0	0.004	0.006	0.017	0.005	0.012	0.019	0.004	0.015	0.027	0.004
	NEL_1	0.006	0.022	0.052	0.016	0.027	0.086	0.010	0.048	0.108	0.002
v_e	NEL	0.013	0.026	0.079	0.018	0.039	0.099	0.017	0.066	0.149	0.001
	NEL_0	0.005	0.011	0.018	0.005	0.014	0.027	0.004	0.019	0.070	0.005
	NEL_1	0.012	0.034	0.078	0.017	0.048	0.134	0.017	0.071	0.201	0.001
v_b	NEL	0.014	0.022	0.045	0.014	0.025	0.054	0.011	0.028	0.078	0.193
	NEL_0	0.003	0.007	0.011	0.003	0.006	0.014	0.003	0.010	0.025	0.036
	NEL_1	0.014	0.025	0.058	0.015	0.026	0.068	0.011	0.034	0.148	0.047
$rCBV_{GVF}$	NEL	0.510	0.832	1.362	0.774	1.088	2.476	0.618	1.393	5.299	0.016
	NEL_0	0.314	0.463	0.684	0.357	0.490	1.275	0.304	0.492	0.993	0.842
	NEL_1	0.620	1.176	1.934	0.773	1.373	2.380	0.816	1.624	5.322	0.078
$rCBV_{BOX}$	NEL	0.479	0.776	1.248	0.667	1.119	2.242	0.562	1.093	3.787	0.135
	NEL_0	0.198	0.444	0.627	0.344	0.442	1.179	0.266	0.402	0.967	0.616
	NEL_1	0.551	1.052	1.719	0.670	1.367	2.251	0.604	1.312	3.617	0.365
K_2	NEL	0.260	0.417	1.057	0.286	0.586	1.527	0.214	0.757	2.002	0.010
	NEL_0	0.387	0.657	1.578	0.564	0.872	1.917	0.384	0.968	2.626	0.171
	NEL_1	0.128	0.180	0.342	0.120	0.225	0.639	0.084	0.272	0.730	0.252

*Table 48 – **Skew** values from the **NEL** VOI for each parameter, Kruskal-Wallis tested for P<0.05 and Bonferroni corrected for P< 0.00128 (0.05/39) to examine differences between grades.*

Param.	VOI	WHO II (N=10)			WHO III (N=12)			WHO IV (N=33)			Sig.
		Minimum	Median	Maximum	Minimum	Median	Maximum	Minimum	Median	Maximum	
ADC	NEL	0.015	0.902	2.651	-0.682	0.291	2.461	-0.300	0.392	2.942	0.502
	NEL_0	0.199	1.646	2.833	0.321	1.424	2.775	0.245	1.531	3.370	0.670
	NEL_1	-1.144	-0.903	-0.258	-1.718	-1.145	0.274	-1.515	-0.910	0.214	0.212
FA	NEL	0.744	1.475	2.016	0.486	1.353	1.874	0.283	1.007	1.699	0.003
	NEL_0	1.689	2.150	2.603	1.413	2.087	2.499	1.052	1.896	2.369	0.004
	NEL_1	-1.055	-0.845	-0.499	-1.186	-0.911	-0.526	-1.239	-0.883	-0.227	0.579
q	NEL	0.531	0.985	1.760	0.454	1.016	1.781	0.138	0.762	2.025	0.053
	NEL_0	1.602	1.800	2.383	1.586	1.902	2.444	0.517	1.606	2.513	0.004
	NEL_1	-1.090	-0.836	-0.324	-1.163	-0.917	-0.597	-1.216	-1.015	0.011	0.167
RA	NEL	0.910	1.965	2.426	0.720	1.596	2.385	0.390	1.321	2.665	0.033
	NEL_0	1.767	2.563	2.949	1.650	2.263	2.907	1.157	2.110	3.055	0.043
	NEL_1	-0.966	-0.805	-0.341	-1.150	-0.873	-0.419	-1.183	-0.894	-0.014	0.244
λ_L	NEL	-0.069	0.728	1.308	-0.975	0.318	1.363	-0.443	0.140	2.508	0.370
	NEL_0	0.109	1.563	2.016	0.524	1.377	1.739	0.179	1.306	2.917	0.862
	NEL_1	-1.239	-0.634	0.182	-1.887	-1.135	0.104	-1.597	-1.079	0.305	0.050
λ_R	NEL	-0.210	0.859	2.929	-0.521	0.189	2.527	-0.199	0.343	2.664	0.347
	NEL_0	0.094	1.598	3.118	0.229	1.128	2.826	0.234	1.491	3.051	0.096
	NEL_1	-1.156	-1.066	-0.575	-1.633	-0.926	0.073	-1.459	-0.971	0.157	0.909
R_1	NEL	0.221	0.607	1.895	0.311	0.650	2.147	-0.638	0.293	2.318	0.021
	NEL_0	0.642	1.533	2.490	1.212	1.691	2.713	-0.291	1.173	2.870	0.016
	NEL_1	-1.199	-0.828	-0.236	-1.292	-0.877	-0.511	-1.470	-0.750	-0.276	0.614
K^{trans}	NEL	0.669	1.810	3.116	0.778	1.867	4.650	0.401	1.888	7.395	0.793
	NEL_0	1.650	2.437	3.540	1.744	2.459	4.885	1.521	2.391	7.355	0.801
	NEL_1	-1.120	-0.705	0.096	-1.057	-0.742	-0.039	-1.207	-0.428	1.852	0.379
v_e	NEL	0.847	1.787	2.669	0.520	2.076	4.381	0.416	1.697	4.578	0.239
	NEL_0	1.792	2.403	3.143	1.540	2.664	4.609	1.345	2.311	4.771	0.223
	NEL_1	-1.064	-0.591	-0.022	-0.928	-0.637	-0.116	-1.222	-0.406	0.367	0.321
v_b	NEL	1.011	2.247	3.168	1.154	1.778	6.265	1.068	3.081	8.043	0.013
	NEL_0	1.910	2.755	3.443	2.000	2.387	6.331	1.851	3.406	8.101	0.014
	NEL_1	-0.870	-0.372	0.591	-0.999	-0.305	0.686	-1.116	-0.524	3.205	0.927
$rCBV_{GVF}$	NEL	0.914	2.025	2.821	0.192	2.236	2.886	0.336	2.277	4.059	0.405
	NEL_0	1.706	2.575	3.294	0.791	2.798	3.351	1.533	2.759	4.392	0.390
	NEL_1	-1.104	-0.881	-0.707	-0.878	-0.704	-0.277	-1.098	-0.667	0.494	0.004
$rCBV_{BOX}$	NEL	0.855	1.587	3.005	0.504	1.968	3.175	0.147	1.936	4.581	0.758
	NEL_0	1.600	2.250	3.454	1.627	2.575	3.599	1.447	2.548	4.699	0.629
	NEL_1	-1.146	-0.843	-0.156	-0.958	-0.683	-0.346	-1.177	-0.681	2.409	0.086
K_2	NEL	-5.066	-3.093	-2.708	-7.387	-2.575	-1.058	-4.704	-3.047	-0.512	0.440
	NEL_0	-1.367	0.616	0.806	-2.776	0.592	0.992	-1.641	0.304	1.259	0.172
	NEL_1	-5.286	-3.529	-3.177	-7.578	-3.034	-1.859	-5.008	-3.464	-1.447	0.448

*Table 49 – **Kurtosis** values from the **NEL** VOI for each parameter, Kruskal-Wallis tested for P<0.05 and Bonferroni corrected for P< 0.00128 (0.05/39) to examine differences between grades.*

Param.	VOI	WHO II (N=10)			WHO III (N=12)			WHO IV (N=33)			Sig.
		Minimum	Median	Maximum	Minimum	Median	Maximum	Minimum	Median	Maximum	
ADC	NEL	0.131	2.076	19.745	-0.582	0.424	16.469	-1.215	1.085	15.057	0.195
	NEL_0	0.143	2.581	20.281	-1.075	0.744	17.162	-1.002	0.510	15.938	0.144
	NEL_1	-1.855	-0.194	1.025	-1.360	-0.419	1.692	-1.768	-0.425	2.329	0.860
FA	NEL	-0.108	3.165	6.430	-0.239	2.598	4.555	-0.559	1.208	5.715	0.017
	NEL_0	0.270	4.134	7.382	-0.074	3.498	5.662	-0.533	1.974	6.509	0.016
	NEL_1	-1.410	-1.221	-0.762	-1.540	-1.282	-0.759	-1.505	-0.998	-0.372	0.004
q	NEL	-0.627	1.505	5.356	-0.030	1.045	5.806	-0.690	1.031	7.576	0.495
	NEL_0	-0.125	2.206	6.231	0.450	1.656	6.592	-0.637	1.421	8.475	0.353
	NEL_1	-1.382	-1.117	-0.230	-1.481	-1.034	-0.505	-1.759	-0.984	1.113	0.458
RA	NEL	0.368	5.969	9.888	0.363	3.605	8.841	-0.378	2.553	12.429	0.095
	NEL_0	0.638	6.786	10.733	0.540	4.519	9.855	-0.274	3.107	13.460	0.082
	NEL_1	-1.429	-1.132	-0.580	-1.505	-1.351	-0.613	-1.633	-1.018	0.467	0.048
λ_L	NEL	0.294	1.800	7.082	-0.563	0.301	5.350	-1.168	0.936	12.460	0.145
	NEL_0	-0.512	1.481	3.749	-1.307	0.201	5.787	-1.122	0.774	13.338	0.345
	NEL_1	-1.661	0.508	4.845	-1.736	-0.404	1.342	-1.785	-0.199	8.046	0.387
λ_R	NEL	0.384	1.690	21.994	-0.441	0.519	16.862	-1.207	1.008	12.868	0.198
	NEL_0	0.349	2.154	22.606	-0.971	0.534	17.566	-0.979	0.955	13.320	0.147
	NEL_1	-1.791	-0.384	0.746	-1.260	-0.024	3.079	-1.736	-0.494	1.477	0.211
R_1	NEL	-0.550	1.262	8.183	-0.846	0.126	6.359	-0.327	1.227	7.234	0.139
	NEL_0	-0.880	1.586	8.666	-0.320	0.427	7.475	-1.620	1.056	8.231	0.250
	NEL_1	-1.416	-0.402	1.130	-1.560	-0.999	-0.471	-1.476	0.107	3.964	0.006
K^{trans}	NEL	0.058	4.195	16.298	0.275	5.393	39.715	-0.445	6.247	83.618	0.625
	NEL_0	0.846	4.697	16.722	0.632	5.853	37.762	0.259	5.779	78.615	0.714
	NEL_1	-1.685	-0.937	1.362	-1.595	-0.988	1.760	-1.756	-0.321	19.158	0.294
v_e	NEL	0.613	4.433	11.715	0.066	6.921	26.916	-0.732	3.996	29.190	0.231
	NEL_0	1.452	4.437	11.747	-0.241	7.409	26.282	-0.417	3.607	28.259	0.181
	NEL_1	-1.643	-0.962	0.688	-1.622	-0.852	0.640	-1.735	-0.742	2.974	0.682
v_b	NEL	0.890	6.944	18.217	0.749	4.118	61.653	0.148	16.717	88.655	0.008
	NEL_0	1.748	6.897	15.793	1.833	4.429	58.405	1.220	15.027	86.760	0.004
	NEL_1	-1.455	-0.244	3.852	-1.585	-0.613	7.771	-1.514	-0.484	29.633	0.740
$rCBV_{GVF}$	NEL	1.239	8.252	14.352	0.095	8.070	16.343	-0.078	8.274	35.382	0.822
	NEL_0	1.716	9.194	14.888	0.235	8.651	16.575	-0.183	9.080	34.210	0.823
	NEL_1	-1.528	-1.103	-0.670	-1.503	-1.013	1.411	-1.489	-0.952	7.639	0.484
$rCBV_{BOX}$	NEL	0.561	5.166	17.245	-0.042	6.489	19.727	-0.293	5.240	43.128	0.980
	NEL_0	1.282	5.874	17.668	0.290	7.184	19.490	-0.206	6.002	37.838	0.981
	NEL_1	-1.317	-1.071	-0.404	-1.293	-0.988	1.011	-1.583	-0.906	24.325	0.537
K_2	NEL	9.929	18.232	52.880	1.165	13.046	147.928	-0.602	16.719	48.306	0.580
	NEL_0	-1.226	-0.286	16.509	-1.375	-0.769	58.231	-1.431	0.281	19.367	0.301
	NEL_1	10.533	18.736	50.143	1.729	13.562	147.719	0.203	15.184	48.355	0.447

*Table 50 – **Median** values from the **NEL** VOI for each parameter, Kruskal-Wallis tested for P<0.05 and Bonferroni corrected for P< 0.00128 (0.05/39) to examine differences between grades.*

Param.	VOI	WHO II (N=10)			WHO III (N=12)			WHO IV (N=33)			Sig.
		Minimum	Median	Maximum	Minimum	Median	Maximum	Minimum	Median	Maximum	
ADC	NEL	1.071	1.243	1.336	0.817	1.108	1.522	0.772	1.166	1.470	0.385
	NEL_0	0.945	1.211	1.321	0.805	1.063	1.299	0.750	0.993	1.279	0.003
	NEL_1	1.240	1.468	2.009	1.038	1.249	1.988	1.015	1.362	2.057	0.078
FA	NEL	0.105	0.146	0.211	0.120	0.166	0.258	0.158	0.200	0.287	0.001
	NEL_0	0.075	0.118	0.195	0.108	0.137	0.210	0.118	0.167	0.241	0.001
	NEL_1	0.214	0.249	0.384	0.202	0.293	0.391	0.245	0.308	0.442	0.013
q	NEL	0.161	0.259	0.388	0.225	0.259	0.405	0.230	0.342	0.450	0.001
	NEL_0	0.129	0.186	0.355	0.165	0.227	0.287	0.120	0.315	0.372	0.001
	NEL_1	0.300	0.404	0.597	0.342	0.419	0.496	0.291	0.490	0.672	0.002
RA	NEL	0.086	0.120	0.176	0.098	0.137	0.216	0.130	0.165	0.242	0.001
	NEL_0	0.062	0.099	0.166	0.091	0.116	0.177	0.099	0.145	0.209	0.001
	NEL_1	0.186	0.215	0.363	0.169	0.256	0.391	0.208	0.278	0.430	0.009
λ_L	NEL	1.211	1.465	1.583	1.021	1.350	1.723	0.971	1.475	1.764	0.362
	NEL_0	1.009	1.400	1.564	0.999	1.259	1.523	0.859	1.254	1.608	0.579
	NEL_1	1.321	1.584	2.587	1.265	1.534	2.203	1.164	1.644	2.683	0.330
λ_R	NEL	0.976	1.121	1.229	0.711	1.004	1.427	0.650	1.011	1.322	0.161
	NEL_0	0.913	1.078	1.214	0.649	0.989	1.215	0.628	0.853	1.179	0.001
	NEL_1	1.173	1.398	1.932	0.928	1.104	1.894	0.975	1.232	1.867	0.026
R_1	NEL	0.345	0.651	0.944	0.402	0.765	0.872	0.602	0.816	1.413	0.006
	NEL_0	0.261	0.601	0.937	0.384	0.680	0.867	0.257	0.745	1.378	0.016
	NEL_1	0.355	0.775	1.185	0.616	0.902	1.082	0.626	0.942	1.507	0.072
K^{trans}	NEL	0.018	0.024	0.047	0.022	0.029	0.049	0.019	0.041	0.082	0.001
	NEL_0	0.016	0.019	0.031	0.017	0.026	0.037	0.016	0.031	0.063	0.002
	NEL_1	0.027	0.044	0.093	0.040	0.059	0.130	0.032	0.093	0.156	0.001
v_e	NEL	0.022	0.034	0.045	0.025	0.039	0.082	0.021	0.057	0.178	0.001
	NEL_0	0.017	0.026	0.034	0.017	0.029	0.046	0.016	0.037	0.151	0.005
	NEL_1	0.040	0.065	0.164	0.043	0.089	0.186	0.038	0.131	0.263	0.001
v_b	NEL	0.018	0.024	0.034	0.019	0.027	0.035	0.017	0.027	0.064	0.545
	NEL_0	0.014	0.019	0.026	0.014	0.019	0.028	0.014	0.024	0.060	0.050
	NEL_1	0.032	0.051	0.096	0.037	0.053	0.099	0.029	0.068	0.169	0.045
$rCBV_{GVF}$	NEL	0.958	1.207	1.459	0.698	1.440	3.086	0.727	1.115	3.664	0.265
	NEL_0	0.919	1.092	1.423	0.632	1.260	2.705	0.649	0.996	2.402	0.181
	NEL_1	1.708	2.558	3.590	1.925	2.801	5.206	1.637	3.050	8.179	0.226
$rCBV_{BOX}$	NEL	0.967	1.253	1.467	0.812	1.456	3.339	0.688	1.151	3.728	0.173
	NEL_0	0.805	1.097	1.436	0.704	1.295	2.598	0.606	0.975	2.328	0.091
	NEL_1	1.575	2.418	3.214	1.811	2.774	5.658	1.371	2.643	6.135	0.383
K_2	NEL	-0.534	-0.335	-0.143	-1.122	-0.481	-0.091	-1.587	-0.498	-0.124	0.304
	NEL_0	-1.394	-1.015	-0.520	-3.256	-1.276	-0.390	-3.698	-1.427	-0.520	0.044
	NEL_1	-0.512	-0.306	-0.119	-0.952	-0.387	-0.079	-1.313	-0.388	-0.121	0.665

10.2 Kaplan-Meier survival analysis at Time Point 1

*Table 51 - Results of the 210 day progression-free survival using Kaplan-Meier survival analysis. **Mean** values from the **TUM** VOI for each parameter were dichotomised according to the median value. Logrank tests were used to test for significance at p<0.05.*

Param.	VOI	Median	N	Events	Estimate (Days)	95% Confidence Interval		Sig.
						Lower Bound	Upper Bound	
ADC	TUM	>= 1.197	27	8	189	175	203	0.072
		< 1.197	28	15	172	155	190	
	TUM_0	>= 1.066	27	7	193	179	206	0.006
		< 1.066	28	16	168	151	186	
	TUM_1	>= 1.376	27	9	184	169	199	0.184
		< 1.376	28	14	177	160	193	
FA	TUM	>= 0.199	27	15	173	156	189	0.050
		< 0.199	28	8	188	173	204	
	TUM_0	>= 0.148	27	17	167	151	183	0.003
		< 0.148	28	6	194	179	208	
	TUM_1	>= 0.292	27	17	165	149	182	0.002
		< 0.292	28	6	196	182	209	
q	TUM	>= 0.318	27	16	169	154	184	0.010
		< 0.318	28	7	192	176	208	
	TUM_0	>= 0.243	27	16	169	153	185	0.012
		< 0.243	28	7	192	178	207	
	TUM_1	>= 0.446	27	18	167	152	183	<0.001
		< 0.446	28	5	194	179	209	
RA	TUM	>= 0.169	27	16	170	154	187	0.014
		< 0.169	28	7	191	176	206	
	TUM_0	>= 0.128	27	16	169	153	186	0.018
		< 0.128	28	7	192	177	207	
	TUM_1	>= 0.266	27	16	166	149	184	0.013
		< 0.266	28	7	195	182	207	
λ_L	TUM	>= 1.425	27	8	189	175	203	0.072
		< 1.425	28	15	172	155	190	
	TUM_0	>= 1.269	27	10	188	175	202	0.255
		< 1.269	28	13	173	155	191	
	TUM_1	>= 1.622	27	14	173	155	190	0.163
		< 1.622	28	9	188	174	203	
λ_R	TUM	>= 1.068	27	8	189	175	203	0.072
		< 1.068	28	15	172	155	190	
	TUM_0	>= 0.929	27	7	194	182	207	0.002
		< 0.929	28	16	166	149	184	
	TUM_1	>= 1.256	27	9	185	170	201	0.145
		< 1.256	28	14	176	159	192	

R_1	TUM	>= 0.800	27	12	184	169	198	0.828
		< 0.800	28	11	177	160	195	
	TUM_0	>= 0.726	27	12	184	170	199	0.997
		< 0.726	28	11	177	159	194	
	TUM_1	>= 0.894	27	12	184	171	198	0.811
		< 0.894	28	11	177	158	195	
K^{trans}	TUM	>= 0.063	27	15	171	154	187	0.024
		< 0.063	28	8	190	175	205	
	TUM_0	>= 0.035	27	18	155	137	173	<0.001
		< 0.035	28	5	204	199	210	
	TUM_1	>= 0.100	27	18	156	139	173	<0.001
		< 0.100	28	5	202	193	211	
V_e	TUM	>= 0.104	27	16	165	147	183	0.004
		< 0.104	28	7	195	183	207	
	TUM_0	>= 0.039	27	16	165	147	182	0.002
		< 0.039	28	7	195	182	208	
	TUM_1	>= 0.163	27	18	158	141	176	<0.001
		< 0.163	28	5	202	193	211	
V_b	TUM	>= 0.042	27	13	176	159	193	0.219
		< 0.042	28	10	185	169	200	
	TUM_0	>= 0.027	27	14	169	151	187	0.069
		< 0.027	28	9	192	178	205	
	TUM_1	>= 0.080	27	15	169	152	186	0.023
		< 0.080	28	8	191	177	206	
$rCBV_{GVF}$	TUM	>= 1.677	27	12	177	160	194	0.585
		< 1.677	28	11	184	169	199	
	TUM_0	>= 1.097	27	11	183	166	200	0.705
		< 1.097	28	12	178	162	194	
	TUM_1	>= 3.237	27	13	177	161	193	0.265
		< 3.237	28	10	184	168	200	
$rCBV_{BOX}$	TUM	>= 1.685	27	13	175	158	192	0.277
		< 1.685	28	10	186	171	201	
	TUM_0	>= 1.092	27	10	184	168	199	0.677
		< 1.092	28	13	177	160	194	
	TUM_1	>= 3.072	27	13	178	162	194	0.334
		< 3.072	28	10	183	167	199	
K_2	TUM	>= -0.735	27	7	193	181	206	0.008
		< -0.735	28	16	168	150	185	
	TUM_0	>= -1.447	27	5	196	183	209	0.001
		< -1.447	28	18	166	149	183	
	TUM_1	>= -0.346	27	10	180	162	197	0.745
		< -0.346	28	13	181	166	196	
Volume	TUM	>= 47.87ml	27	14	172	154	190	0.185
		< 47.87ml	28	9	188	175	202	

*Table 52 - Results of the 210 day progression-free survival using Kaplan-Meier survival analysis. **Standard deviation** values from the **TUM** VOI for each parameter were dichotomised according to the median value. Logrank tests were used to test for significance at $p<0.05$.*

Param.	VOI	Median	N	Events	Estimate (Days)	95% Confidence Interval		Sig.
						Lower Bound	Upper Bound	
ADC	TUM	>= 0.268	27	15	173	158	189	0.079
		< 0.268	28	8	188	172	204	
	TUM_0	>= 0.183	27	10	192	182	202	0.178
		< 0.183	28	13	169	150	189	
	TUM_1	>= 0.287	27	14	172	154	190	0.160
		< 0.287	28	9	189	175	202	
FA	TUM	>= 0.104	27	15	169	151	187	0.031
		< 0.104	28	8	191	179	204	
	TUM_0	>= 0.055	27	15	171	155	187	0.054
		< 0.055	28	8	190	175	205	
	TUM_1	>= 0.112	27	13	172	154	191	0.275
		< 0.112	28	10	188	175	201	
q	TUM	>= 0.148	27	16	168	152	185	0.004
		< 0.148	28	7	191	177	206	
	TUM_0	>= 0.091	27	15	172	156	188	0.069
		< 0.091	28	8	189	173	205	
	TUM_1	>= 0.160	27	15	170	152	188	0.021
		< 0.160	28	8	190	176	204	
RA	TUM	>= 0.094	27	15	169	151	188	0.036
		< 0.094	28	8	191	178	204	
	TUM_0	>= 0.049	27	16	169	153	185	0.013
		< 0.049	28	7	192	177	207	
	TUM_1	>= 0.108	27	16	164	145	183	0.006
		< 0.108	28	7	197	186	207	
λ_L	TUM	>= 0.298	27	14	174	158	190	0.100
		< 0.298	28	9	186	170	202	
	TUM_0	>= 0.192	27	12	185	171	199	0.874
		< 0.192	28	11	176	159	194	
	TUM_1	>= 0.275	27	13	180	165	194	0.473
		< 0.275	28	10	181	164	199	
λ_R	TUM	>= 0.269	27	14	172	154	189	0.161
		< 0.269	28	9	189	175	203	
	TUM_0	>= 0.198	27	9	193	182	203	0.087
		< 0.198	28	14	169	150	188	
	TUM_1	>= 0.311	27	14	176	159	193	0.269
		< 0.311	28	9	185	170	201	

R_1	TUM	>= 0.181	27	13	182	168	195	0.526
		< 0.181	28	10	180	161	198	
	TUM_0	>= 0.100	27	16	168	150	186	0.013
		< 0.100	28	7	192	180	205	
	TUM_1	>= 0.201	27	12	179	163	195	0.915
		< 0.201	28	11	183	167	199	
K^{trans}	TUM	>= 0.042	27	16	167	150	184	0.003
		< 0.042	28	7	193	180	207	
	TUM_0	>= 0.017	27	18	157	140	175	<0.001
		< 0.017	28	5	202	193	211	
	TUM_1	>= 0.047	27	17	162	144	180	0.003
		< 0.047	28	6	199	188	209	
v_e	TUM	>= 0.080	27	16	167	149	184	0.005
		< 0.080	28	7	194	182	207	
	TUM_0	>= 0.021	27	16	165	147	182	0.003
		< 0.021	28	7	196	183	208	
	TUM_1	>= 0.079	27	18	159	141	177	<0.001
		< 0.079	28	5	202	193	210	
v_b	TUM	>= 0.032	27	13	174	156	192	0.224
		< 0.032	28	10	187	173	200	
	TUM_0	>= 0.011	27	13	175	158	191	0.268
		< 0.011	28	10	186	171	202	
	TUM_1	>= 0.042	27	15	169	152	186	0.029
		< 0.042	28	8	192	178	206	
$rCBV_{GVF}$	TUM	>= 1.387	27	16	165	147	183	0.002
		< 1.387	28	7	195	183	208	
	TUM_0	>= 0.524	27	15	171	155	188	0.043
		< 0.524	28	8	189	174	204	
	TUM_1	>= 1.679	27	16	168	151	185	0.004
		< 1.679	28	7	192	178	206	
$rCBV_{BOX}$	TUM	>= 1.273	27	16	166	148	183	0.006
		< 1.273	28	7	195	183	207	
	TUM_0	>= 0.482	27	13	177	160	194	0.349
		< 0.482	28	10	183	168	199	
	TUM_1	>= 1.516	27	16	169	152	186	0.012
		< 1.516	28	7	192	178	206	
K_2	TUM	>= 0.877	27	18	164	147	182	<0.001
		< 0.877	28	5	197	185	209	
	TUM_0	>= 1.053	27	17	171	155	187	0.006
		< 1.053	28	6	191	176	206	
	TUM_1	>= 0.238	27	15	178	163	193	0.156
		< 0.238	28	8	184	167	201	

*Table 53 - Results of the 210 day progression-free survival using Kaplan-Meier survival analysis of **high grade** lesions (N=45). **Mean** values from the **TUM** VOI for each parameter were dichotomised according to the median value. Logrank tests were used to test for significance at p<0.05.*

Param.	VOI	Median	N	Events	Estimate (Days)	95% Confidence Interval		Sig.
						Lower Bound	Upper Bound	
ADC	TUM	>= 1.164	22	10	177	160	195	0.455
		< 1.164	23	13	170	151	190	
	TUM_0	>= 1.025	22	9	186	170	202	0.041
		< 1.025	23	14	161	142	181	
	TUM_1	>= 1.343	22	11	170	151	189	0.978
		< 1.343	23	12	177	159	195	
FA	TUM	>= 0.205	22	13	177	161	192	0.651
		< 0.205	23	10	172	151	193	
	TUM_0	>= 0.156	22	14	165	146	184	0.117
		< 0.156	23	9	183	165	200	
	TUM_1	>= 0.300	22	14	166	148	185	0.147
		< 0.300	23	9	181	163	200	
q	TUM	>= 0.333	22	13	168	151	185	0.249
		< 0.333	23	10	180	160	199	
	TUM_0	>= 0.264	22	14	163	145	180	0.058
		< 0.264	23	9	184	166	203	
	TUM_1	>= 0.457	22	16	159	142	176	0.002
		< 0.457	23	7	189	171	207	
RA	TUM	>= 0.173	22	14	170	152	188	0.301
		< 0.173	23	9	178	159	197	
	TUM_0	>= 0.134	22	14	166	147	184	0.129
		< 0.134	23	9	182	163	200	
	TUM_1	>= 0.270	22	13	171	154	188	0.420
		< 0.270	23	10	177	157	197	
λ_L	TUM	>= 1.380	22	9	180	162	197	0.177
		< 1.380	23	14	168	148	187	
	TUM_0	>= 1.253	21	10	182	166	199	0.376
		< 1.253	24	13	167	147	186	
	TUM_1	>= 1.622	22	14	165	146	185	0.220
		< 1.622	23	9	182	165	200	
λ_R	TUM	>= 1.065	22	10	177	160	195	0.455
		< 1.065	23	13	170	151	190	
	TUM_0	>= 0.894	22	9	186	170	202	0.041
		< 0.894	23	14	161	142	181	
	TUM_1	>= 1.240	22	11	171	153	190	0.867
		< 1.240	23	12	176	158	194	

R_1	TUM	>= 0.819	22	12	178	161	195	0.978
		< 0.819	23	11	170	150	190	
	TUM_0	>= 0.736	22	11	179	162	196	0.684
		< 0.736	23	12	169	149	189	
	TUM_1	>= 0.901	22	11	183	169	198	0.621
		< 0.901	23	12	165	144	186	
K^{trans}	TUM	>= 0.069	22	14	164	145	182	0.040
		< 0.069	23	9	183	165	201	
	TUM_0	>= 0.040	22	14	157	136	177	0.012
		< 0.040	23	9	189	175	203	
	TUM_1	>= 0.122	22	15	156	136	176	0.005
		< 0.122	23	8	190	176	204	
v_e	TUM	>= 0.128	22	15	158	138	177	0.007
		< 0.128	23	8	189	173	204	
	TUM_0	>= 0.044	22	13	159	139	179	0.062
		< 0.044	23	10	188	172	203	
	TUM_1	>= 0.189	22	14	163	145	182	0.034
		< 0.189	23	9	183	165	201	
v_b	TUM	>= 0.043	22	13	168	149	187	0.179
		< 0.043	23	10	179	161	197	
	TUM_0	>= 0.029	22	13	163	143	183	0.082
		< 0.029	23	10	184	168	201	
	TUM_1	>= 0.089	22	13	166	147	185	0.180
		< 0.089	23	10	181	163	199	
$rCBV_{GVF}$	TUM	>= 1.818	22	10	178	160	197	0.602
		< 1.818	23	13	170	151	189	
	TUM_0	>= 1.079	22	11	176	157	196	0.748
		< 1.079	23	12	171	153	189	
	TUM_1	>= 3.362	22	12	173	156	191	0.354
		< 3.362	23	11	175	155	194	
$rCBV_{BOX}$	TUM	>= 1.856	22	10	177	158	196	0.689
		< 1.856	23	13	172	153	190	
	TUM_0	>= 1.083	22	10	178	160	196	0.629
		< 1.083	23	13	170	151	189	
	TUM_1	>= 3.101	22	13	169	151	188	0.200
		< 3.101	23	10	177	159	196	
K_2	TUM	>= -0.895	22	10	174	154	194	0.401
		< -0.895	23	13	173	156	190	
	TUM_0	>= -1.698	22	7	185	167	202	0.016
		< -1.698	23	16	164	146	182	
	TUM_1	>= -0.372	22	10	172	152	193	0.839
		< -0.372	23	13	175	158	192	
Volume	TUM	>= 46.69ml	22	15	160	140	180	0.031
		< 46.69ml	23	8	187	172	202	

*Table 54 - Results of the 210 day progression-free survival using Kaplan-Meier survival analysis of **high grade** lesions (N=45). **Standard deviations** of the **TUM** VOI for each parameter were dichotomised according to the median value. Logrank tests were used to test for significance at p<0.05.*

Param.	VOI	Median	N	Events	Estimate (Days)	95% Confidence Interval		Sig.
						Lower Bound	Upper Bound	
ADC	TUM	>= 0.268	22	15	166	148	183	0.083
		< 0.268	23	8	183	164	202	
	TUM_0	>= 0.177	22	10	188	176	199	0.188
		< 0.177	23	13	160	139	182	
	TUM_1	>= 0.285	22	15	160	140	180	0.052
		< 0.285	23	8	187	172	202	
FA	TUM	>= 0.105	21	13	165	144	187	0.207
		< 0.105	24	10	181	166	197	
	TUM_0	>= 0.057	22	12	171	153	190	0.690
		< 0.057	23	11	176	157	195	
	TUM_1	>= 0.112	22	13	164	144	185	0.260
		< 0.112	23	10	183	167	198	
q	TUM	>= 0.149	22	15	162	144	181	0.014
		< 0.149	23	8	184	167	201	
	TUM_0	>= 0.095	22	13	167	150	185	0.266
		< 0.095	23	10	180	161	199	
	TUM_1	>= 0.161	22	13	168	150	186	0.148
		< 0.161	23	10	179	160	198	
RA	TUM	>= 0.095	22	14	165	145	186	0.147
		< 0.095	23	9	182	166	198	
	TUM_0	>= 0.051	22	13	169	151	187	0.316
		< 0.051	23	10	178	159	197	
	TUM_1	>= 0.109	22	16	154	134	175	0.003
		< 0.109	23	7	193	181	206	
λ_L	TUM	>= 0.300	22	14	166	149	184	0.112
		< 0.300	23	9	181	162	200	
	TUM_0	>= 0.192	22	12	180	163	196	0.750
		< 0.192	23	11	168	148	189	
	TUM_1	>= 0.273	22	13	173	156	190	0.501
		< 0.273	23	10	175	155	195	
λ_R	TUM	>= 0.269	22	14	164	143	184	0.164
		< 0.269	23	9	184	168	200	
	TUM_0	>= 0.182	22	10	189	178	200	0.085
		< 0.182	23	13	159	138	181	
	TUM_1	>= 0.301	22	15	163	143	183	0.081
		< 0.301	23	8	185	169	201	

R_1	TUM	>= 0.185	22	12	180	166	194	0.950
		< 0.185	23	11	168	147	190	
	TUM_0	>= 0.100	22	16	159	139	179	0.011
		< 0.100	23	7	188	173	203	
	TUM_1	>= 0.212	22	12	172	153	190	0.950
		< 0.212	23	11	177	158	195	
K^{trans}	TUM	>= 0.049	22	15	160	142	179	0.010
		< 0.049	23	8	187	170	204	
	TUM_0	>= 0.020	22	15	152	132	173	0.002
		< 0.020	23	8	193	181	205	
	TUM_1	>= 0.058	22	17	151	132	170	0.000
		< 0.058	23	6	196	184	209	
v_e	TUM	>= 0.093	22	16	157	138	176	0.002
		< 0.093	23	7	191	176	206	
	TUM_0	>= 0.025	22	13	159	139	179	0.050
		< 0.025	23	10	187	172	203	
	TUM_1	>= 0.096	22	15	157	136	178	0.013
		< 0.096	23	8	191	177	204	
v_b	TUM	>= 0.034	22	13	166	145	187	0.187
		< 0.034	23	10	181	166	197	
	TUM_0	>= 0.013	22	11	176	159	192	0.918
		< 0.013	23	12	172	152	193	
	TUM_1	>= 0.046	22	14	162	143	182	0.066
		< 0.046	23	9	185	168	202	
$rCBV_{GVF}$	TUM	>= 1.588	22	12	169	149	189	0.331
		< 1.588	23	11	179	162	196	
	TUM_0	>= 0.524	22	15	163	144	182	0.035
		< 0.524	23	8	184	166	201	
	TUM_1	>= 1.748	22	14	163	144	182	0.022
		< 1.748	23	9	183	165	200	
$rCBV_{BOX}$	TUM	>= 1.387	22	14	163	143	182	0.073
		< 1.387	23	9	184	167	201	
	TUM_0	>= 0.482	22	13	170	151	189	0.363
		< 0.482	23	10	177	159	195	
	TUM_1	>= 1.603	22	14	164	145	184	0.075
		< 1.603	23	9	182	165	200	
K_2	TUM	>= 0.994	22	14	170	153	187	0.114
		< 0.994	23	9	178	158	198	
	TUM_0	>= 1.154	22	15	169	152	186	0.066
		< 1.154	23	8	179	159	199	
	TUM_1	>= 0.250	22	14	175	159	191	0.339
		< 0.250	23	9	174	153	194	

*Table 55 - Results of the 210 day progression-free survival using Kaplan-Meier survival analysis of **high grade lesions** (N=39). **Mean** values from the **CEL** VOI for each parameter were dichotomised according to the median value. Logrank tests were used to test for significance at p<0.05.*

Param.	VOI	Median	N	Events	Estimate (Days)	95% Confidence Interval		Sig.
						Lower Bound	Upper Bound	
ADC	CEL	>= 1.083	19	11	169	150	188	0.925
		< 1.083	20	11	169	147	190	
	CEL_0	>= 0.982	19	10	174	153	195	0.324
		< 0.982	20	12	164	144	183	
	CEL_1	>= 1.264	19	11	165	144	187	0.920
		< 1.264	20	11	172	152	192	
FA	CEL	>= 0.176	19	11	168	147	189	0.884
		< 0.176	20	11	169	149	189	
	CEL_0	>= 0.121	19	13	159	139	179	0.125
		< 0.121	20	9	177	157	197	
	CEL_1	>= 0.240	19	13	160	139	180	0.161
		< 0.240	20	9	177	157	197	
q	CEL	>= 0.259	19	11	165	144	186	0.924
		< 0.259	20	11	171	151	191	
	CEL_0	>= 0.166	19	11	169	150	189	0.832
		< 0.166	20	11	168	146	190	
	CEL_1	>= 0.332	19	11	167	146	188	0.850
		< 0.332	20	11	170	150	191	
RA	CEL	>= 0.148	19	11	168	147	189	0.938
		< 0.148	20	11	168	148	189	
	CEL_0	>= 0.103	19	13	160	139	180	0.161
		< 0.103	20	9	177	157	197	
	CEL_1	>= 0.203	19	13	160	139	180	0.161
		< 0.203	20	9	177	157	197	
λ_L	CEL	>= 1.260	19	11	168	148	187	0.970
		< 1.260	20	11	169	148	191	
	CEL_0	>= 1.167	19	11	171	149	192	0.643
		< 1.167	20	11	167	147	187	
	CEL_1	>= 1.477	19	11	163	141	185	0.769
		< 1.477	20	11	174	155	193	
λ_R	CEL	>= 1.000	19	11	169	150	188	0.925
		< 1.000	20	11	169	147	190	
	CEL_0	>= 0.880	19	10	174	154	195	0.313
		< 0.880	20	12	163	142	183	
	CEL_1	>= 1.180	19	12	161	140	182	0.383
		< 1.180	20	10	176	156	195	

R_1	CEL	>= 0.786	19	8	188	175	202	0.011
		< 0.786	20	14	148	126	170	
	CEL_0	>= 0.705	19	7	193	183	204	0.001
		< 0.705	20	15	144	123	166	
	CEL_1	>= 0.879	19	11	176	161	192	0.852
		< 0.879	20	11	161	137	184	
K^{trans}	CEL	>= 0.107	18	12	166	147	185	0.277
		< 0.107	21	10	171	150	193	
	CEL_0	>= 0.075	19	12	169	151	187	0.381
		< 0.075	20	10	169	147	192	
	CEL_1	>= 0.153	19	12	167	149	186	0.355
		< 0.153	20	10	170	148	192	
v_e	CEL	>= 0.197	19	12	168	150	186	0.418
		< 0.197	20	10	169	146	191	
	CEL_0	>= 0.151	19	12	158	136	180	0.138
		< 0.151	20	10	178	161	196	
	CEL_1	>= 0.310	19	13	162	143	181	0.128
		< 0.310	20	9	174	153	196	
v_b	CEL	>= 0.051	19	12	161	140	182	0.186
		< 0.051	20	10	175	155	195	
	CEL_0	>= 0.037	19	12	166	149	184	0.230
		< 0.037	20	10	170	148	193	
	CEL_1	>= 0.097	19	13	156	136	177	0.038
		< 0.097	20	9	178	158	198	
$rCBV_{GVF}$	CEL	>= 3.047	19	10	170	148	191	0.930
		< 3.047	20	12	168	149	187	
	CEL_0	>= 1.043	19	11	168	146	190	0.889
		< 1.043	20	11	168	149	187	
	CEL_1	>= 4.370	19	11	166	145	187	0.660
		< 4.370	20	11	170	150	190	
$rCBV_{BOX}$	CEL	>= 3.027	19	10	169	148	191	0.959
		< 3.027	20	12	169	149	188	
	CEL_0	>= 2.217	19	11	169	147	190	0.791
		< 2.217	20	11	169	149	188	
	CEL_1	>= 4.424	19	11	167	146	188	0.803
		< 4.424	20	11	169	149	189	
K_2	CEL	>= -1.760	19	7	185	168	202	0.011
		< -1.760	20	15	153	132	174	
	CEL_0	>= -3.239	19	8	171	149	194	0.244
		< -3.239	20	14	166	148	184	
	CEL_1	>= -1.106	19	9	175	154	195	0.205
		< -1.106	20	13	162	142	183	
Volume	CEL	>= 12.36ml	19	14	149	126	171	0.014
		< 12.36ml	20	8	187	172	201	

*Table 56 - Results of the 210 day progression-free survival using Kaplan-Meier survival analysis of **high grade lesions** (N=39). **Standard deviations** of the **CEL** VOI for each parameter were dichotomised according to the median value. Logrank tests were used to test for significance at p<0.05.*

Param.	VOI	Median	N	Events	Estimate (Days)	95% Confidence Interval		Sig.
						Lower Bound	Upper Bound	
ADC	CEL	>= 0.236	19	13	159	139	180	0.211
		< 0.236	20	9	178	158	198	
	CEL_0	>= 0.144	19	13	159	136	182	0.312
		< 0.144	20	9	178	160	195	
	CEL_1	>= 0.301	19	12	169	151	188	0.794
		< 0.301	20	10	168	146	190	
FA	CEL	>= 0.090	19	11	167	146	188	0.932
		< 0.090	20	11	170	150	190	
	CEL_0	>= 0.043	19	12	159	139	180	0.230
		< 0.043	20	10	177	158	197	
	CEL_1	>= 0.091	19	12	166	145	187	0.731
		< 0.091	20	10	170	150	191	
q	CEL	>= 0.120	19	12	161	140	182	0.434
		< 0.120	20	10	176	156	195	
	CEL_0	>= 0.056	19	12	163	143	184	0.326
		< 0.056	20	10	174	153	195	
	CEL_1	>= 0.113	19	13	160	139	181	0.242
		< 0.113	20	9	177	158	197	
RA	CEL	>= 0.079	19	12	162	141	183	0.484
		< 0.079	20	10	175	155	195	
	CEL_0	>= 0.037	19	12	159	139	180	0.230
		< 0.037	20	10	177	158	197	
	CEL_1	>= 0.083	19	14	156	136	176	0.040
		< 0.083	20	8	180	160	199	
λ_L	CEL	>= 0.248	19	12	164	143	186	0.591
		< 0.248	20	10	172	153	192	
	CEL_0	>= 0.156	19	12	164	141	187	0.926
		< 0.156	20	10	173	155	191	
	CEL_1	>= 0.311	19	12	169	150	187	0.714
		< 0.311	20	10	168	146	190	
λ_R	CEL	>= 0.241	19	13	159	139	180	0.211
		< 0.241	20	9	178	158	198	
	CEL_0	>= 0.155	19	14	158	137	180	0.144
		< 0.155	20	8	180	161	198	
	CEL_1	>= 0.309	19	12	169	151	188	0.794
		< 0.309	20	10	168	146	190	

R_1	CEL	>= 0.149	19	10	176	158	195	0.369
		< 0.149	20	12	161	139	182	
	CEL_0	>= 0.090	19	12	162	142	182	0.376
		< 0.090	20	10	175	154	196	
	CEL_1	>= 0.157	19	9	175	157	193	0.458
		< 0.157	20	13	162	139	184	
K^{trans}	CEL	>= 0.052	19	13	164	146	183	0.138
		< 0.052	20	9	172	150	195	
	CEL_0	>= 0.031	19	13	166	148	184	0.204
		< 0.031	20	9	172	150	194	
	CEL_1	>= 0.058	19	15	152	132	171	0.003
		< 0.058	20	7	185	166	204	
v_e	CEL	>= 0.098	19	12	164	143	185	0.384
		< 0.098	20	10	173	153	192	
	CEL_0	>= 0.061	19	13	160	140	180	0.119
		< 0.061	20	9	177	157	196	
	CEL_1	>= 0.102	19	14	154	133	176	0.033
		< 0.102	20	8	183	165	200	
v_b	CEL	>= 0.034	19	11	164	143	186	0.474
		< 0.034	20	11	171	152	191	
	CEL_0	>= 0.016	18	11	168	150	187	0.409
		< 0.016	21	11	169	148	191	
	CEL_1	>= 0.047	19	15	151	131	170	0.003
		< 0.047	20	7	185	167	204	
$rCBV_{GVF}$	CEL	>= 2.163	19	12	160	140	181	0.148
		< 2.163	20	10	174	154	194	
	CEL_0	>= 0.682	19	12	167	147	188	0.525
		< 0.682	20	10	170	149	190	
	CEL_1	>= 2.105	19	13	157	137	178	0.059
		< 2.105	20	9	178	158	197	
$rCBV_{BOX}$	CEL	>= 1.701	19	12	163	142	183	0.255
		< 1.701	20	10	173	153	194	
	CEL_0	>= 0.947	19	12	165	147	184	0.260
		< 0.947	20	10	172	150	194	
	CEL_1	>= 1.873	19	13	161	140	182	0.141
		< 1.873	20	9	175	156	195	
K_2	CEL	>= 1.417	19	13	171	153	189	0.521
		< 1.417	20	9	167	144	189	
	CEL_0	>= 1.553	19	12	178	163	193	0.943
		< 1.553	20	10	160	136	184	
	CEL_1	>= 0.742	19	14	155	136	174	0.016
		< 0.742	20	8	180	160	200	

10.3 Kaplan-Meier survival analysis at Time Point 2

*Table 57 - Results of the 210 day progression-free Kaplan-Meier survival analysis. **Mean** values from the **TUM** VOI at time point 2 for each parameter were dichotomised according to their median. Log rank tests were used to test for significance at p<0.05.*

Param.	VOI	Median	N	Events	Estimate (Days)	95% Confidence Interval		Sig.
						Lower Bound	Upper Bound	
ADC	TUM	>= 1.139	16	4	195	182	209	0.506
		< 1.139	17	6	190	173	207	
	TUM_0	>= 0.987	16	3	199	188	210	0.212
		< 0.987	17	7	187	169	205	
	TUM_1	>= 1.461	16	3	205	199	211	0.060
		< 1.461	17	7	181	162	200	
FA	TUM	>= 0.180	16	6	190	172	207	0.519
		< 0.180	17	4	195	182	208	
	TUM_0	>= 0.126	16	5	198	186	209	0.986
		< 0.126	17	5	188	170	206	
	TUM_1	>= 0.265	16	5	197	185	210	0.820
		< 0.265	17	5	188	170	206	
q	TUM	>= 0.273	16	4	198	186	210	0.488
		< 0.273	17	6	188	170	206	
	TUM_0	>= 0.183	16	5	194	181	207	0.915
		< 0.183	17	5	192	175	209	
	TUM_1	>= 0.395	16	6	194	181	207	0.566
		< 0.395	17	4	192	175	209	
RA	TUM	>= 0.151	16	6	190	172	207	0.519
		< 0.151	17	4	195	182	208	
	TUM_0	>= 0.107	16	5	200	191	209	0.947
		< 0.107	17	5	187	168	205	
	TUM_1	>= 0.242	16	7	187	169	204	0.134
		< 0.242	17	3	199	186	211	
λ_L	TUM	>= 1.360	16	3	201	191	211	0.089
		< 1.360	17	7	185	167	203	
	TUM_0	>= 1.247	16	3	199	189	210	0.204
		< 1.247	17	7	187	169	205	
	TUM_1	>= 1.656	16	1	208	204	212	0.003
		< 1.656	17	9	178	160	197	
λ_R	TUM	>= 1.032	16	4	195	182	209	0.506
		< 1.032	17	6	190	173	207	
	TUM_0	>= 0.898	16	2	202	192	212	0.038
		< 0.898	17	8	184	166	201	
	TUM_1	>= 1.411	16	3	205	198	211	0.074
		< 1.411	17	7	181	163	200	

R_1	TUM	>= 0.811	16	5	191	176	206	0.595
		< 0.811	17	5	193	177	209	
	TUM_0	>= 0.731	16	5	192	177	207	0.616
		< 0.731	17	5	193	177	209	
	TUM_1	>= 0.929	16	7	190	177	204	0.144
		< 0.929	17	3	195	179	211	
K^{trans}	TUM	>= 0.062	16	7	186	168	204	0.116
		< 0.062	17	3	200	189	211	
	TUM_0	>= 0.041	16	8	184	166	202	0.038
		< 0.041	17	2	201	190	213	
	TUM_1	>= 0.124	16	7	191	177	204	0.130
		< 0.124	17	3	195	178	211	
v_e	TUM	>= 0.116	16	7	184	166	202	0.146
		< 0.116	17	3	201	190	212	
	TUM_0	>= 0.059	16	8	182	163	201	0.033
		< 0.059	17	2	203	195	212	
	TUM_1	>= 0.262	16	8	184	166	202	0.047
		< 0.262	17	2	202	191	213	
v_b	TUM	>= 0.036	16	8	185	170	201	0.028
		< 0.036	17	2	201	187	215	
	TUM_0	>= 0.023	15	9	176	157	196	0.002
		< 0.023	18	1	208	204	212	
	TUM_1	>= 0.062	16	8	185	170	201	0.028
		< 0.062	17	2	201	187	215	
$rCBV_{GVF}$	TUM	>= 1.690	16	7	181	162	200	0.065
		< 1.690	17	3	204	197	211	
	TUM_0	>= 1.029	16	6	189	174	205	0.428
		< 1.029	17	4	196	181	212	
	TUM_1	>= 3.002	16	6	185	166	204	0.352
		< 3.002	17	4	200	190	210	
$rCBV_{BOX}$	TUM	>= 1.539	16	7	182	162	201	0.163
		< 1.539	17	3	204	196	211	
	TUM_0	>= 0.989	16	6	185	166	204	0.434
		< 0.989	17	4	200	190	210	
	TUM_1	>= 2.725	16	6	185	166	204	0.352
		< 2.725	17	4	200	190	210	
K_2	TUM	>= -0.656	16	4	198	189	208	0.452
		< -0.656	17	6	188	169	206	
	TUM_0	>= -1.333	16	5	199	190	208	0.697
		< -1.333	17	5	188	169	206	
	TUM_1	>= -0.354	16	5	198	188	208	0.906
		< -0.354	17	5	188	169	207	
Volume	TUM	>= 45.89ml	16	6	187	169	205	0.513
		< 45.89ml	17	4	199	187	210	

*Table 58 - Results of the 210 day progression-free Kaplan-Meier survival analysis. The **standard deviation** values from the TUM VOI for each parameter were dichotomised according to their median difference. Log rank tests were used to test for significance at $p<0.05$.*

Param.	VOI	Median	N	Events	Estimate (Days)	95% Confidence Interval		Sig.
						Lower Bound	Upper Bound	
ADC	TUM	>= 0.339	16	5	195	181	208	0.885
		< 0.339	17	5	191	174	208	
	TUM_0	>= 0.203	16	3	204	198	211	0.147
		< 0.203	17	7	182	163	201	
	TUM_1	>= 0.432	16	5	194	180	207	0.814
		< 0.432	17	5	192	176	209	
FA	TUM	>= 0.103	16	7	184	165	203	0.119
		< 0.103	17	3	201	192	211	
	TUM_0	>= 0.047	15	4	203	195	211	0.375
		< 0.047	18	6	184	166	202	
	TUM_1	>= 0.106	16	6	188	169	207	0.403
		< 0.106	17	4	198	187	208	
q	TUM	>= 0.146	16	4	198	182	213	0.551
		< 0.146	17	6	188	173	203	
	TUM_0	>= 0.072	16	7	191	178	205	0.183
		< 0.072	17	3	194	177	211	
	TUM_1	>= 0.154	16	4	197	181	213	0.586
		< 0.154	17	6	189	175	204	
RA	TUM	>= 0.093	15	7	182	162	202	0.056
		< 0.093	18	3	202	193	211	
	TUM_0	>= 0.041	16	6	192	176	208	0.555
		< 0.041	17	4	194	179	208	
	TUM_1	>= 0.103	16	5	194	178	210	0.913
		< 0.103	17	5	191	176	206	
λ_L	TUM	>= 0.363	16	5	194	181	208	0.955
		< 0.363	17	5	191	175	208	
	TUM_0	>= 0.214	16	2	205	199	212	0.024
		< 0.214	17	8	181	163	200	
	TUM_1	>= 0.462	16	2	202	192	212	0.109
		< 0.462	17	8	185	167	203	
λ_R	TUM	>= 0.352	16	5	195	181	208	0.885
		< 0.352	17	5	191	174	208	
	TUM_0	>= 0.205	16	3	205	198	211	0.078
		< 0.205	17	7	182	163	200	
	TUM_1	>= 0.406	16	5	193	179	207	0.788
		< 0.406	17	5	192	176	209	

R_1	TUM	>= 0.213	16	8	185	167	202	0.066
		< 0.213	17	2	202	191	213	
	TUM_0	>= 0.121	16	6	191	177	205	0.365
		< 0.121	17	4	194	178	211	
	TUM_1	>= 0.241	16	6	196	186	207	0.610
		< 0.241	17	4	190	171	208	
K^{trans}	TUM	>= 0.046	16	7	191	178	205	0.168
		< 0.046	17	3	195	178	211	
	TUM_0	>= 0.021	16	8	184	166	202	0.038
		< 0.021	17	2	201	190	213	
	TUM_1	>= 0.057	16	7	191	178	205	0.168
		< 0.057	17	3	195	178	211	
v_e	TUM	>= 0.106	16	7	192	178	205	0.227
		< 0.106	17	3	195	178	211	
	TUM_0	>= 0.038	16	7	187	169	205	0.163
		< 0.038	17	3	198	186	210	
	TUM_1	>= 0.138	16	7	188	170	205	0.149
		< 0.138	17	3	197	184	210	
v_b	TUM	>= 0.026	16	7	190	176	204	0.145
		< 0.026	17	3	196	180	212	
	TUM_0	>= 0.009	16	9	178	159	196	0.003
		< 0.009	17	1	208	204	212	
	TUM_1	>= 0.030	16	8	185	170	201	0.028
		< 0.030	17	2	201	187	215	
$rCBV_{GVF}$	TUM	>= 1.348	16	6	184	165	204	0.325
		< 1.348	17	4	201	192	210	
	TUM_0	>= 0.564	16	6	185	166	204	0.265
		< 0.564	17	4	201	191	210	
	TUM_1	>= 1.435	16	6	185	166	204	0.265
		< 1.435	17	4	200	190	210	
$rCBV_{BOX}$	TUM	>= 1.099	16	6	186	168	205	0.364
		< 1.099	17	4	199	188	211	
	TUM_0	>= 0.489	16	7	183	164	202	0.227
		< 0.489	17	3	203	194	211	
	TUM_1	>= 1.287	16	5	190	173	208	0.849
		< 1.287	17	5	195	182	208	
K_2	TUM	>= 0.689	16	8	180	160	199	0.009
		< 0.689	17	2	205	198	212	
	TUM_0	>= 0.831	16	6	183	164	203	0.201
		< 0.831	17	4	202	193	210	
	TUM_1	>= 0.269	16	6	186	166	205	0.229
		< 0.269	17	4	200	191	209	

*Table 59 - Results of the 210 day progression-free Kaplan-Meier survival analysis. **Mean** values from the **CEL** VOI at time point 2 for each parameter were dichotomised according to their median. Log rank tests were used to test for significance at p<0.05.*

Param.	VOI	Median	N	Events	Estimate (Days)	95% Confidence Interval		Sig.
						Lower Bound	Upper Bound	
ADC	CEL	>= 1.083	14	4	195	183	208	0.744
		< 1.083	14	5	190	170	210	
	CEL_0	>= 0.935	14	4	192	177	207	0.888
		< 0.935	14	5	194	177	211	
	CEL_1	>= 1.328	14	5	190	175	205	0.639
		< 1.328	14	4	196	179	213	
FA	CEL	>= 0.147	14	6	187	168	206	0.183
		< 0.147	14	3	198	185	210	
	CEL_0	>= 0.093	14	5	190	175	205	0.329
		< 0.093	14	4	194	177	212	
	CEL_1	>= 0.225	14	6	187	168	206	0.183
		< 0.225	14	3	198	185	210	
q	CEL	>= 0.199	14	7	185	170	199	0.024
		< 0.199	14	2	201	185	217	
	CEL_0	>= 0.137	14	7	186	171	200	0.053
		< 0.137	14	2	201	185	217	
	CEL_1	>= 0.285	14	7	180	160	199	0.012
		< 0.285	14	2	207	204	211	
RA	CEL	>= 0.124	14	6	187	168	206	0.183
		< 0.124	14	3	198	185	210	
	CEL_0	>= 0.079	14	5	190	175	205	0.329
		< 0.079	14	4	194	177	212	
	CEL_1	>= 0.201	14	6	185	165	205	0.134
		< 0.201	14	3	200	191	210	
λ_L	CEL	>= 1.300	14	5	190	175	205	0.639
		< 1.300	14	4	196	179	213	
	CEL_0	>= 1.111	14	4	192	177	207	0.888
		< 1.111	14	5	194	177	211	
	CEL_1	>= 1.503	14	4	195	181	208	0.591
		< 1.503	14	5	191	172	209	
λ_R	CEL	>= 0.992	14	4	195	183	208	0.744
		< 0.992	14	5	190	170	210	
	CEL_0	>= 0.832	14	3	198	186	210	0.347
		< 0.832	14	6	188	169	207	
	CEL_1	>= 1.273	14	5	190	175	205	0.639
		< 1.273	14	4	196	179	213	

R_1	CEL	>= 0.791	14	4	200	188	211	0.602
		< 0.791	14	5	186	166	205	
	CEL_0	>= 0.710	14	3	201	189	212	0.194
		< 0.710	14	6	185	166	204	
	CEL_1	>= 0.999	14	5	197	186	208	0.744
		< 0.999	14	4	189	169	208	
K^{trans}	CEL	>= 0.081	14	7	185	167	204	0.107
		< 0.081	14	2	201	189	213	
	CEL_0	>= 0.055	14	6	186	168	205	0.278
		< 0.055	14	3	201	189	213	
	CEL_1	>= 0.139	14	6	191	179	203	0.245
		< 0.139	14	3	195	176	214	
v_e	CEL	>= 0.192	14	5	189	171	208	0.889
		< 0.192	14	4	196	183	209	
	CEL_0	>= 0.115	14	6	181	161	201	0.266
		< 0.115	14	3	206	201	210	
	CEL_1	>= 0.325	14	5	195	183	206	0.791
		< 0.325	14	4	191	171	210	
v_b	CEL	>= 0.031	14	7	179	159	199	0.023
		< 0.031	14	2	207	203	211	
	CEL_0	>= 0.022	14	8	179	159	199	0.008
		< 0.022	14	1	207	202	212	
	CEL_1	>= 0.060	14	8	179	159	199	0.008
		< 0.060	14	1	207	202	212	
$rCBV_{GVF}$	CEL	>= 1.746	14	6	183	163	203	0.131
		< 1.746	14	3	203	195	211	
	CEL_0	>= 0.403	14	4	189	169	208	0.768
		< 0.403	14	5	197	185	209	
	CEL_1	>= 2.582	14	5	188	168	207	0.638
		< 2.582	14	4	198	186	210	
$rCBV_{BOX}$	CEL	>= 1.654	14	6	183	163	203	0.216
		< 1.654	14	3	203	195	211	
	CEL_0	>= 0.762	14	4	189	169	208	0.723
		< 0.762	14	5	197	185	208	
	CEL_1	>= 2.793	14	5	187	168	207	0.468
		< 2.793	14	4	198	186	210	
K_2	CEL	>= -0.904	14	3	203	195	211	0.216
		< -0.904	14	6	183	163	203	
	CEL_0	>= -1.496	14	3	204	196	211	0.100
		< -1.496	14	6	182	162	202	
	CEL_1	>= -0.540	14	4	202	194	210	0.637
		< -0.540	14	5	184	164	204	
Volume	CEL	>= 9.30ml	14	6	182	162	203	0.203
		< 9.30ml	14	3	203	195	211	

*Table 60 - Results of the 210 day progression-free Kaplan-Meier survival analysis. The **standard deviations** from the **CEL** VOI for each parameter were dichotomised according to the median difference. Log rank tests were used to test for significance at p<0.05.*

Param.	VOI	Median	N	Events	Estimate (Days)	95% Confidence Interval		Sig.
						Lower Bound	Upper Bound	
ADC	CEL	>= 0.359	14	4	194	181	207	0.865
		< 0.359	14	5	191	171	210	
	CEL_0	>= 0.159	14	3	200	191	210	0.193
		< 0.159	14	6	185	165	205	
	CEL_1	>= 0.388	14	4	197	185	208	0.360
		< 0.388	14	5	189	170	208	
FA	CEL	>= 0.086	14	6	187	168	206	0.183
		< 0.086	14	3	198	185	210	
	CEL_0	>= 0.035	14	6	182	162	202	0.083
		< 0.035	14	3	202	193	211	
	CEL_1	>= 0.093	14	7	182	163	202	0.035
		< 0.093	14	2	203	193	212	
q	CEL	>= 0.100	14	8	181	163	200	0.008
		< 0.100	14	1	205	195	215	
	CEL_0	>= 0.047	14	7	186	171	200	0.053
		< 0.047	14	2	201	185	217	
	CEL_1	>= 0.104	14	6	185	166	205	0.171
		< 0.104	14	3	200	190	210	
RA	CEL	>= 0.077	14	6	187	168	206	0.183
		< 0.077	14	3	198	185	210	
	CEL_0	>= 0.032	14	6	182	162	202	0.083
		< 0.032	14	3	202	193	211	
	CEL_1	>= 0.088	14	6	184	164	204	0.102
		< 0.088	14	3	201	192	210	
λ_L	CEL	>= 0.372	14	4	194	181	207	0.865
		< 0.372	14	5	191	171	210	
	CEL_0	>= 0.191	14	2	203	195	212	0.048
		< 0.191	14	7	182	161	202	
	CEL_1	>= 0.394	14	5	197	186	208	0.619
		< 0.394	14	4	189	169	209	
λ_R	CEL	>= 0.367	14	4	194	181	207	0.865
		< 0.367	14	5	191	171	210	
	CEL_0	>= 0.174	14	3	200	191	210	0.193
		< 0.174	14	6	185	165	205	
	CEL_1	>= 0.390	14	4	197	185	208	0.360
		< 0.390	14	5	189	170	208	

R_1	CEL	>= 0.185	14	7	189	174	203	0.091
		< 0.185	14	2	197	180	215	
	CEL_0	>= 0.103	14	5	195	183	207	0.965
		< 0.103	14	4	190	171	210	
	CEL_1	>= 0.211	14	7	183	163	203	0.065
		< 0.211	14	2	203	193	212	
K^{trans}	CEL	>= 0.046	14	6	195	184	206	0.486
		< 0.046	14	3	191	172	211	
	CEL_0	>= 0.023	14	7	184	166	202	0.092
		< 0.023	14	2	203	192	215	
	CEL_1	>= 0.057	14	7	193	181	205	0.274
		< 0.057	14	2	195	176	214	
v_e	CEL	>= 0.130	14	6	195	184	206	0.486
		< 0.130	14	3	191	172	211	
	CEL_0	>= 0.060	14	6	193	181	205	0.586
		< 0.060	14	3	194	175	213	
	CEL_1	>= 0.139	14	5	199	190	208	0.943
		< 0.139	14	4	186	165	207	
v_b	CEL	>= 0.023	14	7	188	173	203	0.068
		< 0.023	14	2	199	182	215	
	CEL_0	>= 0.008	14	8	179	159	199	0.008
		< 0.008	14	1	207	202	212	
	CEL_1	>= 0.028	14	7	188	173	203	0.068
		< 0.028	14	2	199	182	215	
$rCBV_{GVF}$	CEL	>= 1.602	14	5	188	168	207	0.638
		< 1.602	14	4	198	186	210	
	CEL_0	>= 0.309	14	4	189	169	208	0.768
		< 0.309	14	5	197	185	209	
	CEL_1	>= 1.509	14	5	188	168	207	0.638
		< 1.509	14	4	198	186	210	
$rCBV_{BOX}$	CEL	>= 1.250	14	5	189	171	207	0.658
		< 1.250	14	4	197	184	210	
	CEL_0	>= 0.485	14	4	189	169	208	0.723
		< 0.485	14	5	197	185	208	
	CEL_1	>= 1.302	14	5	187	168	207	0.468
		< 1.302	14	4	198	186	210	
K_2	CEL	>= 0.895	14	6	183	163	203	0.131
		< 0.895	14	3	203	195	211	
	CEL_0	>= 1.024	14	6	182	162	202	0.100
		< 1.024	14	3	204	196	211	
	CEL_1	>= 0.379	14	5	184	164	204	0.471
		< 0.379	14	4	203	195	210	

10.4 Kaplan-Meier survival analysis using differences between Time Points 3 and 2

*Table 61 - Results of the 210 day progression-free Kaplan-Meier survival analysis. The **difference in mean values** from the **TUM** VOI for each parameter was dichotomised according to the median difference. Logrank tests were used to test for significance at $p<0.05$.*

Param.	VOI	Median Difference	N	Events	Estimate (Days)	95% Confidence Interval (Days)		Sig.
						Lower Bound	Upper Bound	
ADC	TUM	>= 0.027	16	8	182	163	201	0.030
		< 0.027	17	2	203	194	212	
	TUM_0	>= 0.050	16	8	181	162	201	0.023
		< 0.050	17	2	204	196	212	
	TUM_1	>= 0.078	16	7	183	166	201	0.068
		< 0.078	17	3	200	188	212	
FA	TUM	>= 0.014	16	6	186	168	205	0.303
		< 0.014	17	4	199	187	210	
	TUM_0	>= 0.017	16	7	163	163	202	0.135
		< 0.017	17	3	195	195	211	
	TUM_1	>= 0.016	16	7	182	163	202	0.119
		< 0.016	17	3	203	194	211	
q	TUM	>= 0.026	16	7	186	168	204	0.118
		< 0.026	17	3	199	188	211	
	TUM_0	>= 0.037	16	7	185	166	204	0.094
		< 0.037	17	3	201	191	210	
	TUM_1	>= 0.060	16	7	183	164	202	0.095
		< 0.060	17	3	202	193	212	
RA	TUM	>= 0.012	16	6	186	168	205	0.303
		< 0.012	17	4	199	187	210	
	TUM_0	>= 0.013	16	7	182	163	202	0.135
		< 0.013	17	3	203	195	211	
	TUM_1	>= 0.021	16	6	183	164	202	0.356
		< 0.021	17	4	202	194	211	
λ_L	TUM	>= 0.081	16	8	183	164	202	0.040
		< 0.081	17	2	203	193	212	
	TUM_0	>= 0.068	16	8	182	163	201	0.038
		< 0.068	17	2	203	194	212	
	TUM_1	>= 0.047	16	7	182	164	200	0.052
		< 0.047	17	3	201	189	212	
λ_R	TUM	>= 0.001	16	8	182	163	201	0.030
		< 0.001	17	2	203	194	212	
	TUM_0	>= 0.044	16	8	178	159	197	0.007
		< 0.044	17	2	206	200	212	
	TUM_1	>= 0.055	16	7	183	166	201	0.068
		< 0.055	17	3	200	188	212	

R_1	TUM	>= -0.088	16	2	201	190	213	0.064
		< -0.088	17	8	185	168	202	
	TUM_0	>= -0.042	16	3	195	178	212	0.209
		< -0.042	17	7	190	176	204	
	TUM_1	>= -0.059	16	3	198	185	210	0.325
		< -0.059	17	7	188	171	206	
K^{trans}	TUM	>= -0.006	16	7	192	179	205	0.306
		< -0.006	17	3	194	177	211	
	TUM_0	>= -0.005	16	5	193	179	207	0.946
		< -0.005	17	5	192	175	208	
	TUM_1	>= -0.016	16	4	197	185	210	0.433
		< -0.016	17	6	188	171	205	
v_e	TUM	>= -0.001	16	8	185	167	203	0.071
		< -0.001	17	2	201	190	213	
	TUM_0	>= -0.014	16	3	203	194	211	0.140
		< -0.014	17	7	184	165	202	
	TUM_1	>= -0.026	16	5	197	185	210	0.856
		< -0.026	17	5	189	171	206	
v_b	TUM	>= -0.001	15	5	198	186	210	0.909
		< -0.001	18	5	188	171	205	
	TUM_0	>= -0.001	16	3	203	195	212	0.077
		< -0.001	17	7	182	164	201	
	TUM_1	>= 0.000	16	4	200	188	211	0.218
		< 0.000	17	6	186	168	204	
$rCBV_{GVF}$	TUM	>= -0.054	16	6	199	190	208	0.910
		< -0.054	17	4	188	169	207	
	TUM_0	>= -0.025	16	4	202	192	211	0.335
		< -0.025	17	6	184	166	202	
	TUM_1	>= -0.039	16	6	198	189	207	0.704
		< -0.039	17	4	189	170	207	
$rCBV_{BOX}$	TUM	>= -0.018	16	6	199	190	207	0.814
		< -0.018	17	4	188	169	207	
	TUM_0	>= -0.077	16	6	197	187	207	0.720
		< -0.077	17	4	189	171	208	
	TUM_1	>= -0.036	16	7	192	179	205	0.274
		< -0.036	17	3	194	177	211	
K_2	TUM	>= 0.012	16	2	197	180	214	0.156
		< 0.012	17	8	191	178	204	
	TUM_0	>= -0.047	16	2	197	180	214	0.070
		< -0.047	17	8	189	176	202	
	TUM_1	>= -0.003	16	2	197	180	214	0.056
		< -0.003	17	8	189	176	202	
Volume	TUM	>= -7.94ml	16	9	177	158	196	0.004
		< -7.94ml	17	1	210	209	210	

*Table 62 - Results of the 210 day progression-free Kaplan-Meier survival analysis. The **difference in standard deviation** values from the **TUM** VOI for each parameter were dichotomised according to the median difference. Logrank tests were used to test for significance at $p<0.05$.*

Param.	VOI	Median Difference	N	Events	Estimate (Days)	95% Confidence Interval		Sig.
						Lower Bound	Upper Bound	
ADC	TUM	>= -0.008	16	5	190	172	207	0.985
		< -0.008	17	5	195	182	208	
	TUM_0	>= -0.006	16	7	180	161	199	0.036
		< -0.006	17	3	205	198	211	
	TUM_1	>= -0.020	16	4	195	180	210	0.760
		< -0.020	17	6	191	176	207	
FA	TUM	>= 0.004	16	2	204	195	212	0.043
		< 0.004	17	8	183	164	201	
	TUM_0	>= 0.004	16	6	183	164	202	0.451
		< 0.004	17	4	202	194	211	
	TUM_1	>= 0.009	16	4	190	171	209	0.569
		< 0.009	17	6	195	183	207	
q	TUM	>= 0.000	16	5	187	168	205	0.834
		< 0.000	17	5	199	188	210	
	TUM_0	>= 0.006	16	8	180	161	199	0.030
		< 0.006	17	2	206	200	212	
	TUM_1	>= 0.006	16	7	182	162	201	0.189
		< 0.006	17	3	203	196	211	
RA	TUM	>= 0.004	16	4	194	180	208	0.803
		< 0.004	17	6	191	175	208	
	TUM_0	>= 0.003	16	5	186	166	205	0.867
		< 0.003	17	5	199	190	209	
	TUM_1	>= 0.011	16	4	190	171	209	0.516
		< 0.011	17	6	194	182	206	
λ_L	TUM	>= -0.010	16	6	185	165	204	0.388
		< -0.010	17	4	200	191	210	
	TUM_0	>= -0.006	16	7	183	164	203	0.092
		< -0.006	17	3	202	194	210	
	TUM_1	>= -0.030	16	4	195	181	210	0.568
		< -0.030	17	6	190	174	206	
λ_R	TUM	>= -0.012	16	5	190	172	207	0.985
		< -0.012	17	5	195	182	208	
	TUM_0	>= -0.008	16	8	176	157	195	0.002
		< -0.008	17	2	208	205	211	
	TUM_1	>= -0.016	16	3	200	189	212	0.221
		< -0.016	17	7	186	169	203	

R_1	TUM	>= -0.002	16	3	194	176	211	0.323
		< -0.002	17	7	192	179	205	
	TUM_0	>= -0.005	16	4	193	176	211	0.524
		< -0.005	17	6	192	179	205	
	TUM_1	>= -0.048	16	4	190	172	208	0.567
		< -0.048	17	6	195	183	207	
K^{trans}	TUM	>= -0.006	16	6	186	168	205	0.565
		< -0.006	17	4	198	187	210	
	TUM_0	>= -0.004	16	5	193	179	207	0.946
		< -0.004	17	5	192	175	208	
	TUM_1	>= -0.003	15	4	198	185	210	0.323
		< -0.003	18	6	188	171	205	
v_e	TUM	>= 0.001	16	7	186	168	204	0.226
		< 0.001	17	3	199	187	211	
	TUM_0	>= -0.011	16	4	197	185	210	0.570
		< -0.011	17	6	189	171	206	
	TUM_1	>= 0.005	16	6	187	168	205	0.607
		< 0.005	17	4	198	186	210	
v_b	TUM	>= 0.000	16	4	199	188	211	0.285
		< 0.000	17	6	186	169	204	
	TUM_0	>= -0.001	16	4	199	186	211	0.262
		< -0.001	17	6	186	169	204	
	TUM_1	>= -0.002	16	4	200	188	211	0.227
		< -0.002	17	6	186	169	204	
$rCBV_{GVF}$	TUM	>= -0.080	16	6	199	190	208	0.947
		< -0.080	17	4	188	169	207	
	TUM_0	>= -0.016	16	6	197	187	207	0.685
		< -0.016	17	4	189	171	208	
	TUM_1	>= -0.061	16	8	189	176	203	0.061
		< -0.061	17	2	198	182	214	
$rCBV_{BOX}$	TUM	>= 0.006	16	8	188	174	203	0.058
		< 0.006	17	2	199	183	214	
	TUM_0	>= -0.039	16	6	197	187	207	0.720
		< -0.039	17	4	189	171	208	
	TUM_1	>= -0.005	16	8	187	172	202	0.071
		< -0.005	17	2	200	185	214	
K_2	TUM	>= 0.005	16	8	190	177	203	0.084
		< 0.005	17	2	198	181	214	
	TUM_0	>= 0.064	16	7	187	174	201	0.094
		< 0.064	17	3	197	181	214	
	TUM_1	>= 0.002	16	8	189	176	203	0.058
		< 0.002	17	2	198	181	214	

*Table 63 - Results of the 210 day progression-free Kaplan-Meier survival analysis. The **difference in mean** values from the **CEL** VOI for each parameter was dichotomised according to the median difference. Logrank tests were used to test for significance at $p<0.05$.*

Param.	VOI	Median Difference	N	Events	Estimate (Days)	95% Confidence Interval		Sig.
						Lower Bound	Upper Bound	
ADC	CEL	>= 0.045	14	3	196	179	214	0.369
		< 0.045	14	6	190	175	204	
	CEL_0	>= 0.094	14	6	182	162	202	0.101
		< 0.094	14	3	203	195	211	
	CEL_1	>= 0.083	14	3	197	180	214	0.228
		< 0.083	14	6	189	174	204	
FA	CEL	>= 0.005	14	4	199	189	210	0.360
		< 0.005	14	5	186	166	206	
	CEL_0	>= 0.017	14	6	190	176	205	0.421
		< 0.017	14	3	196	179	213	
	CEL_1	>= 0.011	14	5	193	179	207	0.892
		< 0.011	14	4	192	174	210	
q	CEL	>= 0.042	13	4	202	194	211	0.566
		< 0.042	15	5	185	166	205	
	CEL_0	>= 0.030	14	5	194	180	208	0.984
		< 0.030	14	4	192	173	210	
	CEL_1	>= 0.034	14	3	203	195	211	0.124
		< 0.034	14	6	182	162	203	
RA	CEL	>= 0.006	14	4	199	189	210	0.360
		< 0.006	14	5	186	166	206	
	CEL_0	>= 0.014	14	6	190	176	205	0.421
		< 0.014	14	3	196	179	213	
	CEL_1	>= 0.009	14	5	193	179	207	0.892
		< 0.009	14	4	192	174	210	
λ_L	CEL	>= 0.068	14	3	196	179	214	0.228
		< 0.068	14	6	190	175	204	
	CEL_0	>= 0.094	14	5	190	171	208	0.701
		< 0.094	14	4	196	183	210	
	CEL_1	>= 0.005	14	3	197	180	214	0.336
		< 0.005	14	6	189	174	204	
λ_R	CEL	>= 0.045	14	4	190	171	210	0.915
		< 0.045	14	5	195	184	207	
	CEL_0	>= 0.070	14	5	185	164	205	0.446
		< 0.070	14	4	200	191	209	
	CEL_1	>= 0.032	14	3	197	180	214	0.228
		< 0.032	14	6	189	174	204	

R_1	CEL	>= -0.129	14	3	196	181	210	0.459
		< -0.129	14	6	189	171	207	
	CEL_0	>= -0.127	14	4	196	182	210	0.571
		< -0.127	14	5	188	170	207	
	CEL_1	>= -0.130	14	3	197	184	211	0.318
		< -0.130	14	6	188	170	207	
K^{trans}	CEL	>= 0.005	14	6	190	174	205	0.463
		< 0.005	14	3	196	179	213	
	CEL_0	>= -0.005	14	7	188	172	203	0.162
		< -0.005	14	2	198	181	215	
	CEL_1	>= -0.004	14	6	193	179	207	0.577
		< -0.004	14	3	192	174	211	
v_e	CEL	>= 0.037	14	9	*	*	*	0.002
		< 0.037	14	0	*	*	*	
	CEL_0	>= 0.018	14	8	177	158	197	0.009
		< 0.018	14	1	209	208	211	
	CEL_1	>= 0.021	14	7	184	164	203	0.096
		< 0.021	14	2	202	192	212	
v_b	CEL	>= -0.002	14	5	197	184	210	0.967
		< -0.002	14	4	189	170	208	
	CEL_0	>= -0.003	14	5	194	182	206	0.653
		< -0.003	14	4	191	172	211	
	CEL_1	>= -0.005	14	6	194	180	207	0.503
		< -0.005	14	3	193	174	211	
$rCBV_{GVF}$	CEL	>= -0.330	14	6	195	185	206	0.367
		< -0.330	14	3	190	170	211	
	CEL_0	>= -0.054	14	6	193	181	205	0.235
		< -0.025	14	3	192	172	211	
	CEL_1	>= -0.383	14	6	194	182	206	0.320
		< -0.383	14	3	192	172	211	
$rCBV_{BOX}$	CEL	>= -0.212	14	6	196	186	206	0.434
		< -0.212	14	3	190	169	211	
	CEL_0	>= -0.087	14	6	194	183	206	0.382
		< -0.087	14	3	193	173	212	
	CEL_1	>= -0.186	14	7	192	180	204	0.122
		< -0.186	14	2	195	176	214	
K_2	CEL	>= 0.037	14	1	201	185	218	0.026
		< 0.037	14	8	186	171	201	
	CEL_0	>= -0.272	14	2	198	181	215	0.121
		< -0.272	14	7	188	172	203	
	CEL_1	>= 0.032	14	2	198	181	215	0.121
		< 0.032	14	7	188	172	203	
Volume	CEL	>= -3.29ml	14	7	187	172	202	0.109
		< -3.29ml	14	2	201	184	217	

*Confidence interval could not determined due to the correct prediction of PFS

*Table 64 - Results of the 210 day progression-free Kaplan-Meier survival analysis. The **difference in standard deviation** values from the **CEL** VOI for each parameter were dichotomised according to the median difference. Logrank tests were used to test for significance at $p<0.05$.*

Param.	VOI	Median Difference	N	Events	Estimate (Days)	95% Confidence Interval		Sig.
						Lower Bound	Upper Bound	
ADC	CEL	>= -0.006	14	2	204	196	212	0.027
		< -0.006	14	7	181	161	201	
	CEL_0	>= 0.025	14	5	192	174	210	0.638
		< 0.025	14	4	193	179	208	
	CEL_1	>= -0.008	14	4	192	173	211	0.612
		< -0.008	14	5	193	180	206	
FA	CEL	>= 0.004	14	4	199	189	210	0.257
		< 0.004	14	5	185	166	205	
	CEL_0	>= 0.004	14	5	193	179	208	0.943
		< 0.004	14	4	192	173	210	
	CEL_1	>= -0.002	14	5	194	179	208	0.912
		< -0.002	14	4	191	173	210	
q	CEL	>= 0.012	14	5	195	184	207	0.773
		< 0.012	14	4	191	171	210	
	CEL_0	>= 0.012	14	5	194	180	208	0.614
		< 0.012	14	4	190	172	208	
	CEL_1	>= 0.003	14	4	199	189	210	0.377
		< 0.003	14	5	186	166	206	
RA	CEL	>= 0.002	14	4	199	189	210	0.257
		< 0.002	14	5	185	166	205	
	CEL_0	>= 0.005	14	5	193	179	208	0.943
		< 0.005	14	4	192	173	210	
	CEL_1	>= -0.002	14	4	196	182	210	0.430
		< -0.002	14	5	188	169	206	
λ_L	CEL	>= -0.017	14	3	204	197	211	0.046
		< -0.017	14	6	180	160	201	
	CEL_0	>= 0.017	14	6	190	172	208	0.339
		< 0.017	14	3	196	182	210	
	CEL_1	>= 0.010	14	3	198	186	211	0.527
		< 0.010	14	6	187	168	205	
λ_R	CEL	>= 0.003	14	2	204	196	212	0.027
		< 0.003	14	7	181	161	201	
	CEL_0	>= 0.018	14	3	201	190	211	0.310
		< 0.018	14	6	184	165	204	
	CEL_1	>= -0.017	14	3	200	188	212	0.183
		< -0.017	14	6	184	165	203	

R_1	CEL	>= -0.028	14	1	206	199	213	0.019
		< -0.028	14	8	181	161	200	
	CEL_0	>= -0.017	14	4	194	175	213	0.724
		< -0.017	14	5	191	177	204	
	CEL_1	>= -0.001	14	4	197	185	209	0.537
		< -0.001	14	5	187	168	207	
K^{trans}	CEL	>= -0.001	14	5	188	168	207	0.684
		< -0.001	14	4	198	187	209	
	CEL_0	>= -0.002	14	6	188	173	204	0.393
		< -0.002	14	3	197	181	214	
	CEL_1	>= -0.008	13	5	192	177	207	0.847
		< -0.008	15	4	193	176	210	
v_e	CEL	>= 0.006	14	7	179	159	199	0.036
		< 0.006	14	2	206	202	211	
	CEL_0	>= 0.008	14	8	179	159	199	0.015
		< 0.008	14	1	207	201	212	
	CEL_1	>= -0.004	14	5	186	166	207	0.964
		< -0.004	14	4	197	187	207	
v_b	CEL	>= -0.001	14	6	194	181	207	0.584
		< -0.001	14	3	192	173	211	
	CEL_0	>= -0.002	14	6	189	174	204	0.317
		< -0.002	14	3	197	180	214	
	CEL_1	>= -0.005	14	6	194	180	207	0.468
		< -0.005	14	3	193	174	211	
$rCBV_{GVF}$	CEL	>= -0.134	14	7	193	181	204	0.190
		< -0.134	14	2	195	176	214	
	CEL_0	>= -0.035	14	6	193	181	205	0.235
		< -0.035	14	3	192	172	211	
	CEL_1	>= -0.227	14	6	196	184	207	0.564
		< -0.227	14	3	191	172	211	
$rCBV_{BOX}$	CEL	>= -0.218	14	7	185	170	200	0.052
		< -0.218	14	2	200	184	217	
	CEL_0	>= -0.055	14	6	195	183	206	0.486
		< -0.055	14	3	193	173	212	
	CEL_1	>= -0.198	14	5	195	183	207	0.865
		< -0.198	14	4	191	171	210	
K_2	CEL	>= 0.082	14	8	177	158	196	0.005
		< 0.082	14	1	209	208	210	
	CEL_0	>= 0.121	14	7	189	175	204	0.191
		< 0.121	14	2	197	180	215	
	CEL_1	>= -0.042	14	8	179	159	198	0.009
		< -0.042	14	1	207	201	212	

10.5 Kaplan-Meier survival analysis using Time Points 3

*Table 65 - Results of the 210 day progression-free Kaplan-Meier survival analysis. **Mean** values from the **TUM** VOI for each parameter were dichotomised according to the median value. Logrank tests were used to test for significance at p<0.05.*

Param.	VOI	Median	N	Events	Estimate (Days)	95% Confidence Interval (Days)		Sig.
						Lower Bound	Upper Bound	
ADC	TUM	>= 1.171	16	6	181	163	200	0.103
		< 1.171	17	4	201	191	212	
	TUM_0	>= 1.076	16	7	184	166	202	0.086
		< 1.076	17	3	201	191	212	
	TUM_1	>= 1.487	16	4	200	191	209	0.648
		< 1.487	17	6	185	167	204	
FA	TUM	>= 0.205	16	5	193	176	210	0.855
		< 0.205	17	5	192	178	206	
	TUM_0	>= 0.147	16	7	182	163	201	0.091
		< 0.147	17	3	203	195	212	
	TUM_1	>= 0.288	16	6	185	166	204	0.308
		< 0.288	17	4	200	190	210	
q	TUM	>= 0.317	16	7	185	166	204	0.169
		< 0.317	17	3	200	190	210	
	TUM_0	>= 0.254	16	8	183	165	202	0.070
		< 0.254	17	2	202	193	212	
	TUM_1	>= 0.455	16	7	185	166	203	0.122
		< 0.455	17	3	200	190	211	
RA	TUM	>= 0.174	16	5	193	176	210	0.855
		< 0.174	17	5	192	178	206	
	TUM_0	>= 0.127	16	6	185	166	204	0.383
		< 0.127	17	4	200	190	210	
	TUM_1	>= 0.258	16	6	186	167	205	0.332
		< 0.258	17	4	199	188	210	
λ_L	TUM	>= 1.403	16	7	182	164	200	0.042
		< 1.403	17	3	202	191	212	
	TUM_0	>= 1.304	16	7	181	162	201	0.068
		< 1.304	17	3	204	196	211	
	TUM_1	>= 1.769	16	4	196	180	211	0.634
		< 1.769	17	6	190	175	205	
λ_R	TUM	>= 1.058	16	6	183	164	201	0.186
		< 1.058	17	4	201	191	212	
	TUM_0	>= 0.948	16	6	189	173	205	0.344
		< 0.948	17	4	196	182	210	
	TUM_1	>= 1.486	16	5	199	190	208	0.854
		< 1.486	17	5	186	167	205	

R_1	TUM	>= 0.767	16	3	202	192	212	0.158
		< 0.767	17	7	184	166	202	
	TUM_0	>= 0.698	16	3	186	191	212	0.244
		< 0.698	17	7	199	167	203	
	TUM_1	>= 0.912	16	4	201	190	211	0.608
		< 0.912	17	6	185	167	203	
K^{trans}	TUM	>= 0.050	16	9	178	159	197	0.002
		< 0.050	17	1	207	200	213	
	TUM_0	>= 0.028	16	8	179	160	198	0.024
		< 0.028	17	2	207	204	211	
	TUM_1	>= 0.090	16	9	177	158	197	0.005
		< 0.090	17	1	208	203	212	
v_e	TUM	>= 0.116	16	9	178	159	197	0.002
		< 0.116	17	1	207	200	213	
	TUM_0	>= 0.041	16	8	178	159	197	0.013
		< 0.041	17	2	206	200	213	
	TUM_1	>= 0.223	16	9	179	160	198	0.006
		< 0.223	17	1	207	200	213	
v_b	TUM	>= 0.029	16	7	189	174	204	0.276
		< 0.029	17	3	197	182	212	
	TUM_0	>= 0.018	16	8	186	170	201	0.053
		< 0.018	17	2	201	187	215	
	TUM_1	>= 0.054	16	8	186	170	201	0.053
		< 0.054	17	2	201	187	215	
$rCBV_{GVF}$	TUM	>= 1.464	16	7	186	171	202	0.139
		< 1.464	17	3	200	187	214	
	TUM_0	>= 0.884	16	6	190	175	205	0.585
		< 0.884	17	4	196	180	211	
	TUM_1	>= 2.639	16	6	190	175	205	0.446
		< 2.639	17	4	196	181	212	
$rCBV_{BOX}$	TUM	>= 1.461	16	7	186	171	202	0.139
		< 1.461	17	3	200	187	214	
	TUM_0	>= 0.901	16	6	190	175	205	0.669
		< 0.901	17	4	196	180	211	
	TUM_1	>= 2.510	16	7	186	171	202	0.139
		< 2.510	17	3	200	187	214	
K_2	TUM	>= -0.715	16	1	208	203	212	0.011
		< -0.715	17	9	180	162	198	
	TUM_0	>= -1.590	16	2	202	191	213	0.061
		< -1.590	17	8	185	168	202	
	TUM_1	>= -0.387	16	4	196	183	209	0.604
		< -0.387	17	6	190	172	207	
Volume	TUM	>= 9941	16	7	186	168	204	0.177
		< 9941	17	3	199	188	211	

Table 66 - Results of the 210 day progression-free Kaplan-Meier survival analysis. ***Standard deviations*** *from the* ***TUM*** *VOI of each parameter were dichotomised according to the median value. Logrank tests were used to test for significance at* $p<0.05$

Param.	VOI	Median	N	Events	Estimate (Days)	95% Confidence Interval		Sig.
						Lower Bound	Upper Bound	
ADC	TUM	>= 0.338	16	4	195	181	208	0.673
		< 0.338	17	6	191	174	207	
	TUM_0	>= 0.193	16	7	184	166	201	0.066
		< 0.193	17	3	201	190	212	
	TUM_1	>= 0.439	16	5	197	184	209	0.860
		< 0.439	17	5	189	172	206	
FA	TUM	>= 0.108	16	6	191	173	208	0.553
		< 0.108	17	4	194	181	208	
	TUM_0	>= 0.053	16	7	183	164	202	0.154
		< 0.053	17	3	203	194	212	
	TUM_1	>= 0.116	16	7	185	167	204	0.136
		< 0.116	17	3	199	188	210	
q	TUM	>= 0.143	16	5	192	175	210	0.784
		< 0.143	17	5	193	180	206	
	TUM_0	>= 0.091	16	7	185	166	204	0.169
		< 0.091	17	3	200	190	210	
	TUM_1	>= 0.163	16	6	188	169	207	0.601
		< 0.163	17	4	196	185	208	
RA	TUM	>= 0.098	16	6	191	173	208	0.553
		< 0.098	17	4	194	181	208	
	TUM_0	>= 0.046	16	6	187	168	205	0.580
		< 0.046	17	4	198	187	209	
	TUM_1	>= 0.115	16	7	186	168	205	0.214
		< 0.115	17	3	198	187	210	
λ_L	TUM	>= 0.355	16	5	194	181	208	0.989
		< 0.355	17	5	190	173	207	
	TUM_0	>= 0.229	16	6	187	169	205	0.382
		< 0.229	17	4	198	186	210	
	TUM_1	>= 0.429	16	4	197	184	210	0.666
		< 0.429	17	6	189	172	206	
λ_R	TUM	>= 0.340	16	4	195	181	208	0.673
		< 0.340	17	6	191	174	207	
	TUM_0	>= 0.198	16	7	189	173	205	0.132
		< 0.198	17	3	196	182	211	
	TUM_1	>= 0.430	16	5	198	187	209	0.894
		< 0.430	17	5	188	170	206	

R_1	TUM	>= 0.196	16	7	185	167	204	0.132
		< 0.196	17	3	199	188	211	
	TUM_0	>= 0.125	16	3	198	182	214	0.120
		< 0.125	17	7	187	173	202	
	TUM_1	>= 0.209	16	6	187	169	205	0.447
		< 0.209	17	4	199	187	211	
K^{trans}	TUM	>= 0.041	16	9	183	168	198	0.005
		< 0.041	17	1	203	189	216	
	TUM_0	>= 0.013	16	8	179	160	198	0.024
		< 0.013	17	2	207	204	211	
	TUM_1	>= 0.049	16	8	185	169	201	0.060
		< 0.049	17	2	200	186	214	
v_e	TUM	>= 0.122	16	9	178	159	197	0.002
		< 0.122	17	1	207	200	213	
	TUM_0	>= 0.024	16	7	185	170	201	0.076
		< 0.024	17	3	199	185	214	
	TUM_1	>= 0.139	16	7	183	164	203	0.120
		< 0.139	17	3	202	193	210	
v_b	TUM	>= 0.023	16	7	189	173	204	0.211
		< 0.023	17	3	197	182	212	
	TUM_0	>= 0.006	16	8	186	170	201	0.053
		< 0.006	17	2	201	187	215	
	TUM_1	>= 0.030	16	7	186	171	202	0.139
		< 0.030	17	3	200	187	214	
$rCBV_{GVF}$	TUM	>= 1.063	16	7	186	170	201	0.095
		< 1.063	17	3	201	187	214	
	TUM_0	>= 0.504	16	7	186	170	201	0.095
		< 0.504	17	3	201	187	214	
	TUM_1	>= 1.320	16	7	186	171	202	0.139
		< 1.320	17	3	200	187	214	
$rCBV_{BOX}$	TUM	>= 1.004	16	8	184	169	199	0.024
		< 1.004	17	2	202	189	216	
	TUM_0	>= 0.497	16	7	186	170	201	0.095
		< 0.497	17	3	201	187	214	
	TUM_1	>= 1.293	16	7	186	171	202	0.139
		< 1.293	17	3	200	187	214	
K_2	TUM	>= 0.834	16	9	182	164	199	0.007
		< 0.834	17	1	205	195	215	
	TUM_0	>= 1.110	16	8	181	163	199	0.017
		< 1.110	17	2	204	195	214	
	TUM_1	>= 0.272	16	7	184	164	203	0.155
		< 0.272	17	3	201	192	210	

Table 67 - Results of the 210 day progression-free Kaplan-Meier survival analysis. ***Mean*** *values from the* ***CEL*** *VOI for each parameter were dichotomised according to the median value. Logrank tests were used to test for significance at* $p<0.05$.

Param.	VOI	Median	N	Events	Estimate (Days)	95% Confidence Interval		Sig.
						Lower Bound	Upper Bound	
ADC	CEL	>= 1.255	14	4	196	183	209	0.850
		< 1.255	14	5	189	170	208	
	CEL_0	>= 1.075	14	5	187	168	206	0.528
		< 1.075	14	4	197	184	210	
	CEL_1	>= 1.431	14	3	201	191	211	0.341
		< 1.431	14	6	185	165	204	
FA	CEL	>= 0.147	14	6	192	178	206	0.336
		< 0.147	14	3	193	175	211	
	CEL_0	>= 0.113	14	5	192	178	207	0.706
		< 0.113	14	4	192	174	210	
	CEL_1	>= 0.234	14	5	192	178	207	0.706
		< 0.234	14	4	192	174	210	
q	CEL	>= 0.244	14	7	186	171	200	0.053
		< 0.244	14	2	201	185	217	
	CEL_0	>= 0.191	14	7	187	172	202	0.109
		< 0.191	14	2	201	184	217	
	CEL_1	>= 0.337	14	5	193	179	207	0.864
		< 0.337	14	4	193	175	211	
RA	CEL	>= 0.124	14	6	192	178	206	0.336
		< 0.124	14	3	193	175	211	
	CEL_0	>= 0.099	14	5	192	178	207	0.706
		< 0.099	14	4	192	174	210	
	CEL_1	>= 0.208	14	5	192	178	207	0.706
		< 0.208	14	4	192	174	210	
λ_L	CEL	>= 1.396	14	4	196	183	209	0.850
		< 1.396	14	5	189	170	208	
	CEL_0	>= 1.276	14	7	181	161	201	0.070
		< 1.276	14	2	205	198	213	
	CEL_1	>= 1.600	14	4	196	182	210	0.599
		< 1.600	14	5	189	171	208	
λ_R	CEL	>= 1.162	14	3	197	183	210	0.473
		< 1.162	14	6	189	170	208	
	CEL_0	>= 0.994	14	5	188	169	207	0.791
		< 0.994	14	4	196	183	210	
	CEL_1	>= 1.420	14	2	202	192	212	0.086
		< 1.420	14	7	184	164	203	

*Confidence interval could not determined due to the correct prediction of PFS

R_1	CEL	>= 0.727	14	3	201	190	212	0.218
		< 0.727	14	6	185	165	204	
	CEL_0	>= 0.603	14	3	202	191	212	0.242
		< 0.603	14	6	184	164	204	
	CEL_1	>= 0.824	14	4	201	190	211	0.363
		< 0.824	14	5	185	165	204	
K^{trans}	CEL	>= 0.080	14	8	187	172	201	0.036
		< 0.080	14	1	201	185	218	
	CEL_0	>= 0.047	14	8	180	160	199	0.011
		< 0.047	14	1	207	202	212	
	CEL_1	>= 0.116	14	8	179	159	199	0.015
		< 0.116	14	1	207	201	212	
v_e	CEL	>= 0.215	14	9	*	*	*	0.004
		< 0.215	14	0	*	*	*	
	CEL_0	>= 0.119	14	8	180	161	200	0.021
		< 0.119	14	1	207	201	212	
	CEL_1	>= 0.355	14	8	179	159	199	0.015
		< 0.355	14	1	207	201	212	
v_b	CEL	>= 0.032	14	7	189	174	204	0.224
		< 0.032	14	2	197	180	214	
	CEL_0	>= 0.017	14	7	188	174	203	0.096
		< 0.017	14	2	198	182	215	
	CEL_1	>= 0.054	14	7	188	174	203	0.096
		< 0.054	14	2	198	182	215	
$rCBV_{GVF}$	CEL	>= 1.330	14	6	189	174	203	0.185
		< 1.330	14	3	199	182	215	
	CEL_0	>= 0.376	14	5	190	172	207	0.505
		< 0.376	14	4	196	182	211	
	CEL_1	>= 2.427	14	4	199	188	209	0.683
		< 2.427	14	5	187	167	208	
$rCBV_{BOX}$	CEL	>= 1.343	14	7	180	161	200	0.031
		< 1.343	14	2	207	203	211	
	CEL_0	>= 0.735	14	6	185	165	204	0.266
		< 0.735	14	3	202	191	212	
	CEL_1	>= 2.424	14	6	185	165	204	0.266
		< 2.424	14	3	202	191	212	
K_2	CEL	>= -1.177	14	2	207	202	211	0.060
		< -1.177	14	7	180	161	200	
	CEL_0	>= -2.169	14	3	203	195	211	0.205
		< -2.169	14	6	183	163	203	
	CEL_1	>= -0.535	14	3	202	194	211	0.319
		< -0.535	14	6	183	163	203	
Volume	CEL	>= 1254	14	7	183	164	203	0.116
		< 1254	14	2	203	194	212	

Table 68 - Results of the 210 day progression-free Kaplan-Meier survival analysis. ***Standard deviations*** *from the* ***CEL*** *VOI of each parameter were dichotomised according to the median value. Logrank tests were used to test for significance at* $p<0.05$.

Param.	VOI	Median	N	Events	Estimate (Days)	95% Confidence Interval		Sig.
						Lower Bound	Upper Bound	
ADC	CEL	>= 0.386	14	3	198	187	210	0.350
		< 0.386	14	6	187	167	206	
	CEL_0	>= 0.180	14	3	197	184	210	0.452
		< 0.180	14	6	188	168	207	
	CEL_1	>= 0.406	14	4	198	188	209	0.493
		< 0.406	14	5	187	167	207	
FA	CEL	>= 0.086	14	4	203	196	210	0.263
		< 0.086	14	5	181	160	202	
	CEL_0	>= 0.038	14	6	190	175	204	0.294
		< 0.038	14	3	196	179	214	
	CEL_1	>= 0.099	14	6	192	178	207	0.469
		< 0.099	14	3	193	175	211	
q	CEL	>= 0.112	13	8	178	158	198	0.004
		< 0.112	15	1	206	199	213	
	CEL_0	>= 0.058	14	7	189	175	204	0.110
		< 0.058	14	2	197	179	215	
	CEL_1	>= 0.110	14	8	181	161	200	0.008
		< 0.110	14	1	206	198	214	
RA	CEL	>= 0.078	14	4	203	196	210	0.263
		< 0.078	14	5	181	160	202	
	CEL_0	>= 0.035	14	6	190	175	204	0.294
		< 0.035	14	3	196	179	214	
	CEL_1	>= 0.095	14	6	192	178	206	0.336
		< 0.095	14	3	193	175	211	
λ_L	CEL	>= 0.410	14	3	198	187	210	0.350
		< 0.410	14	6	187	167	206	
	CEL_0	>= 0.194	14	3	198	187	210	0.350
		< 0.194	14	6	187	167	206	
	CEL_1	>= 0.409	14	4	198	185	210	0.471
		< 0.409	14	5	188	169	207	
λ_R	CEL	>= 0.392	14	3	198	187	210	0.350
		< 0.392	14	6	187	167	206	
	CEL_0	>= 0.194	14	3	197	184	210	0.452
		< 0.194	14	6	188	168	207	
	CEL_1	>= 0.392	14	4	198	188	209	0.493
		< 0.392	14	5	187	167	207	

R_1	CEL	>= 0.166	14	5	197	185	209	0.998
		< 0.166	14	4	188	168	208	
	CEL_0	>= 0.082	14	4	201	191	211	0.198
		< 0.082	14	5	182	163	201	
	CEL_1	>= 0.182	14	6	191	177	206	0.431
		< 0.182	14	3	194	176	212	
K^{trans}	CEL	>= 0.045	14	7	189	174	203	0.153
		< 0.045	14	2	198	181	215	
	CEL_0	>= 0.021	14	8	179	159	198	0.007
		< 0.021	14	1	207	202	212	
	CEL_1	>= 0.047	14	7	189	174	203	0.153
		< 0.047	14	2	198	181	215	
v_e	CEL	>= 0.130	14	7	181	161	200	0.075
		< 0.130	14	2	206	201	211	
	CEL_0	>= 0.063	14	8	179	159	199	0.015
		< 0.063	14	1	207	201	212	
	CEL_1	>= 0.125	14	6	190	172	208	0.539
		< 0.125	14	3	195	180	210	
v_b	CEL	>= 0.023	14	7	189	174	203	0.153
		< 0.023	14	2	198	181	215	
	CEL_0	>= 0.005	14	7	188	174	203	0.096
		< 0.005	14	2	198	182	215	
	CEL_1	>= 0.026	14	7	189	174	203	0.137
		< 0.026	14	2	198	182	215	
$rCBV_{GVF}$	CEL	>= 1.353	14	6	191	177	206	0.276
		< 1.353	14	3	195	178	212	
	CEL_0	>= 0.297	14	5	190	172	207	0.505
		< 0.297	14	4	196	182	211	
	CEL_1	>= 1.357	14	6	191	177	206	0.276
		< 1.357	14	3	195	178	212	
$rCBV_{BOX}$	CEL	>= 1.108	14	8	180	160	199	0.011
		< 1.108	14	1	207	202	212	
	CEL_0	>= 0.416	14	5	193	179	207	0.883
		< 0.416	14	4	193	174	211	
	CEL_1	>= 1.154	14	7	189	174	203	0.137
		< 1.154	14	2	198	182	215	
K_2	CEL	>= 1.205	14	6	183	163	203	0.205
		< 1.205	14	3	203	195	211	
	CEL_0	>= 1.315	14	6	182	162	203	0.124
		< 1.315	14	3	203	195	211	
	CEL_1	>= 0.442	14	6	184	164	204	0.282
		< 0.442	14	3	202	193	211	

10.6 Low Grade Glioma Monitoring

This section briefly demonstrates benefits of automated planning to measure low grade glioma growth and potential transformation. Unfortunately clinical practice changed shortly after the study started, which saw most suspected low grade gliomas proceed to surgery rather than wait for signs of radiological progression. Previously 6 month glioma growth has been shown to be a useful clinical indicator of glioma transformation (151). Thick image slices in conjunction with differences in prescription angulation can lead to measurement error, potentially resulting in small changes being missed or underestimated.

In this glioma study Ready Brain (75), an automated planning tool was utilised for repeatable oblique planning of the FLAIR imaging. To demonstrate the benefits of repeatable planning, and the potential of improved sensitivity to small changes, the T_2 abnormality observed using FLAIR imaging of a suspected low grade glioma imaged 7 times as part of the glioma study was contoured using an Otsu algorithm (187) and converted into volume.

Given the patient was not on steroids, any change in size was likely to be pathological rather than pharmacological. The same slice from the 7 different scans can be seen in (Figure 135) with the day 0 imaging subtracted from the most recent imaging to show differences. No retrospective registration was used in this section. The volume of T_2 abnormality was then plotted against the number of days from the first study scan (Figure 138).

From examination of the serial imaging, it appears automated slice positioning tools such as Ready Brain can successfully be used to monitor slow growing lesions such as low grade gliomas and meningiomas. The subtracted imaging shows good agreement between the two imaging sets despite being acquired 2 years apart. The plot of T_2 abnormality volume versus time, shows an increasing linear trend which is to be expected in a low grade glioma.

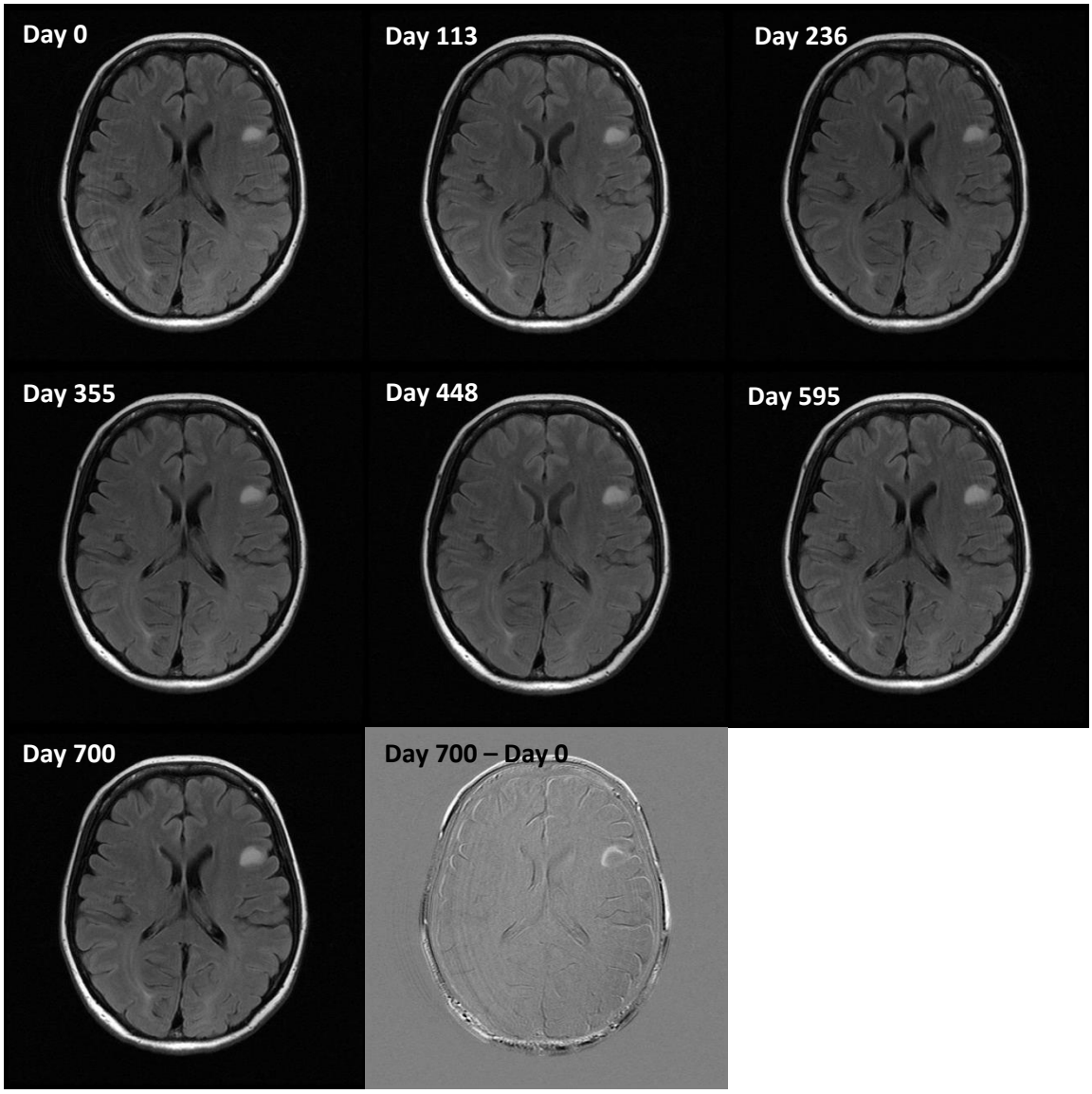

Figure 135 - Suspected low grade glioma imaged 7 times as part of the glioma study. Figure shows one slice of the FLAIR dataset planned using Ready Brain at 4 month intervals. Between any two subsequent scans, changes in the size of the abnormality could be missed, however serial volumetric measurement confirmed the lesions is growing slowly, especially when comparing the first and last scans where the difference in size is greatest.

The contoured VOIs depicted in Figure 136 show a more detailed view of the change in size of the T_2 abnormality over time, with the medial and anterior aspects of the lesions appearing to grow more rapidly than the lateral and posterior edges which abut grey matter rather than white matter. The distances between 3 anatomical landmarks were measured in the RL and AP directions (Figure 137). No differences in distance were observed between scans.

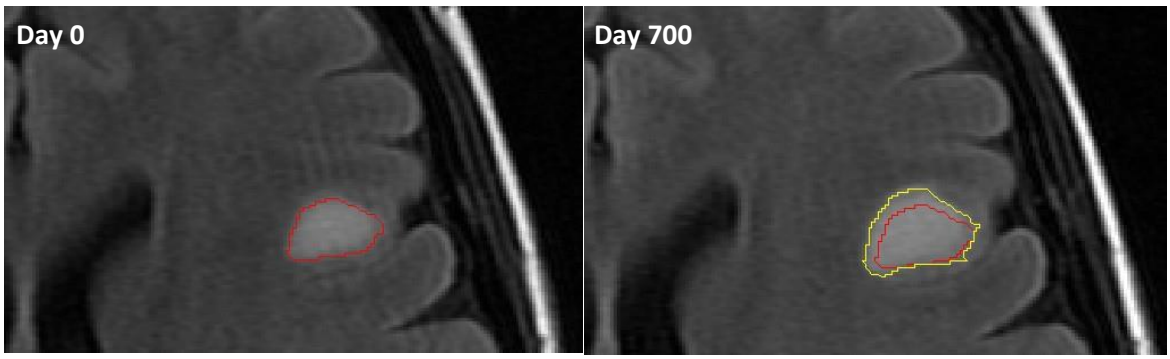

Figure 136 - T_2 abnormality contoured on the day of study recruitment (left), and a scan 700 days later (right) showing the original VOI (red) and the contoured T_2 abnormality at 700 days (yellow)

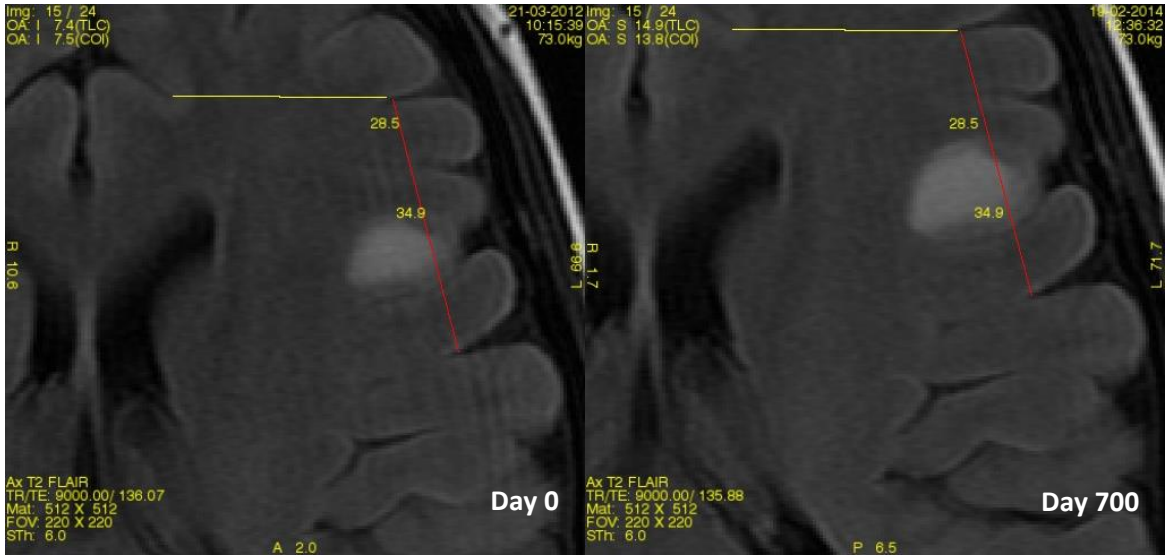

Figure 137 - The distances between 3 anatomical landmarks was measured in the RL (28.5mm) and AP (34.9mm) directions. No differences in distance were observed between scans over 700 days.

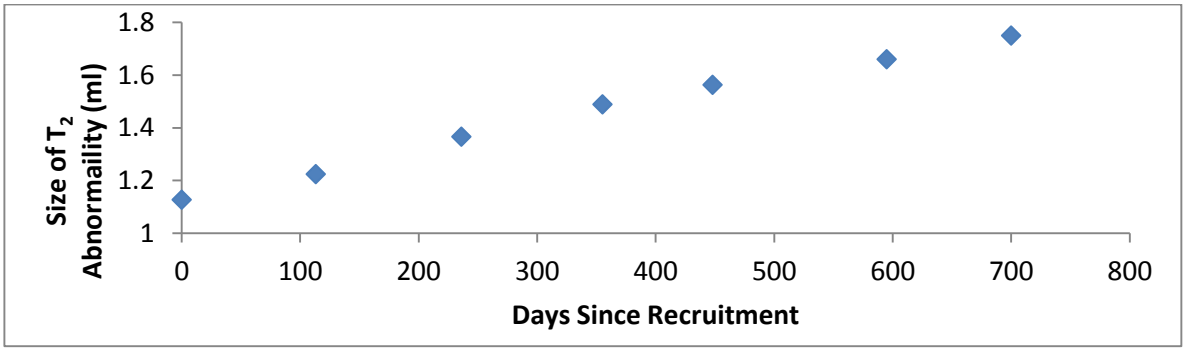

Figure 138 - Plot showing the size of T_2 abnormality measured from FLAIR imaging for a single patient with a suspected low grade glioma versus the number of days since study recruitment.

11 Abbreviations used in this Thesis

1H – Proton

2-HG - 2-Hydroxygluterate

AC – Anterior Commisure

ADC – Apparent Diffusion Coefficient

ASL – Arterial Spin Labelling

ASSET - Array Spatial Sensitivity Encoding Technique

b – b Factor

BAT – Bolus Arrival Time

BET – Brain Extraction Tool

CBF – Cerebral Blood Flow

CBV – Cerebral Blood Volume

CEL – Contrast Enhancing component of the lesion

CHESS – Chemical Shift Selective Suppression Pulses

CHO / PCH/ GCP – Choline

COV – Coefficient of Variation

CR / CRE / PCR – Creatine

DCE - Dynamic Contrast Enhancement

DOF – Degrees of Freedom

DSC - Dynamic Susceptibility Contrast

DTI – Diffusion Tensor Imaging

DWI – Diffusion Weighted Imaging

ECC – Eddy Current Correct

EES – Extravascular Extracellular Space

EPI – Echo Planar Imaging

FA – Fractional Anisotropy

FDR – False Discovery Rate

FFT – Fast Fourier Transform

FID – Free Induction Decay

FLAIR – Fluid Attenuated Inversion Recovery

FSE – Fast Spin Echo

FSPGR – Fast Spoiled Gradient Recalled Echo

GE/GRE - Gradient Echo

GBM – Glioblastoma Multiforme

GMM – Gaussian Mixture Model

HGG – High Grade Glioma

HOS – High Order Shim

IVIM – Intravoxel Incoherent Motion

K_2 – Leakage Rate

K^{trans} – Volume Transfer Coefficient

LCModel – Linear Combination Model

LGG – Low Grade Glioma

MDT – Multi-Disciplinary Team

mI – Myo-inositol

MR – Magnetic Resonance

MRS – Magnetic Resonance Spectroscopy

MRSI – Magnetic Resonance Spectroscopic Imaging

NAA - N-Acetylaspartate

NEC – Necrotic Region

NEL – Non-enhancing component of the lesion

NEX – Number of Experiments

PC – Posterior Commisure

PD - Proton Density

PFS – Progression-Free Survival

PK – Pharmacokinetic

PPM – Parts Per Million

PRESS – Point Resolved Spectroscopy

q – Anisotropic Component of Diffusion

R_1 - Spin-lattice relaxation rate

R_2 - Spin-spin relaxation rate

RA – Relative Anisotropy

rCBV – Relative Cerebral Blood Volume

RF – Radio frequency Pulse

ROI – Region of Interest

SAGE – Spectral Analysis by General Electric

SE - Spin Echo

SNR – Signal to Noise Ratio

STEAM – Stimulated Echo Acquisition Mode

SVS – Single Voxel Spectroscopy

SWAN – T_2 Star Weighted Angiography

T_1 - Spin – lattice relaxation time

T_2 - Spin – spin relaxation time

TE – Echo Time

TM – Mixing Time

TR – Relaxation Time

TUM – Tumour Abnormality

v_b – Blood Volume Fraction

v_e – Interstitial Volume Fraction (Extravascular Extracellular Space)

VOI – Volume of Interest

WHO – World Health Organisation

λ_L – Longitudinal Diffusivity

λ_R – Radial Diffusivity

12 Accepted Abstracts from this Thesis

I. Measurement of cell death in vivo using magnetic resonance with TE-averaged PRESS and DTI. Lawrence Kenning, Martin Lowry, and Lindsay W. Turnbull. ESMRM 2011 #362

II. Measurement of cell death in vivo using magnetic resonance with TE-averaged PRESS and DTI. Lawrence Kenning, Martin Lowry, and Lindsay W. Turnbull. NCRI 2011. #A13. *NCRI Student Prize*

III. Multivoxel lactate editing in glioma patients at 3.0T. Lawrence Kenning, Martin Lowry, Ralph Noeske, and Lindsay W. Turnbull. Proceedings of the International Society for Magnetic Resonance in Medicine. 2013. #0962

IV. A novel scheme for producing multiparametric volumes**.** Lawrence Kenning, Martin Lowry, and Lindsay W. Turnbull. Proceedings of the International Society for Magnetic Resonance in Medicine. 2013. #0975

V. Prediction of progression-free survival in high grade gliomas using preoperative MR. Lawrence Kenning, Martin Lowry, Martin Pickles, Christopher Rowland-Hill, Shailendra Achawal, Chittoor Rajaraman and Lindsay W. Turnbull. Proceedings of the International Society for Magnetic Resonance in Medicine. 2014. #1844

VI. Logistic regression of multiparametric MR for glioma grading. Lawrence Kenning, Martin Lowry, Martin Pickles, Christopher Rowland-Hill, Shailendra Achawal, Chittoor Rajaraman and Lindsay W. Turnbull. Proceedings of the International Society for Magnetic Resonance in Medicine. 2014. #1847

VII. The anisotropic component of diffusion improves visualisation of fibre tracts in the presence of oedema. Lawrence Kenning, Martin Lowry, and Lindsay W. Turnbull. Proceedings of the International Society for Magnetic Resonance in Medicine. 2014. #2686 *Diffusion Study Group Student Abstract Prize*

13 References

1. *Cancer Research UK, Brain, other CNS and intracranial tumours incidence statistics*. [07/05/2013]; Available from: http://www.cancerresearchuk.org/cancer-info/cancerstats/types/brain.
2. Sanai, N , Berger, MS. Glioma extent of resection and its impact on patient outcome. Neurosurgery 2008:62:753-64; discussion 264-6.
3. Mariani, L, Siegenthaler, P, Guzman, R*, et al.* The impact of tumour volume and surgery on the outcome of adults with supratentorial WHO grade II astrocytomas and oligoastrocytomas. Acta Neurochirurgica 2004:146:441-448.
4. Stupp, R, Hegi, ME, Mason, WP*, et al.* Effects of radiotherapy with concomitant and adjuvant temozolomide versus radiotherapy alone on survival in glioblastoma in a randomised phase III study: 5-year analysis of the EORTC-NCIC trial. Lancet Oncology 2009:10:459-466.
5. Okamoto, Y, Di Patre, PL, Burkhard, C*, et al.* Population-based study on incidence, survival rates, and genetic alterations of low-grade diffuse astrocytomas and oligodendrogliomas. Acta Neuropathologica 2004:108:49-56.
6. Louis, DN, Ohgaki, H, Wiestler, OD*, et al.* The 2007 WHO classification of tumours of the central nervous system. Acta Neuropathologica 2007:114:97-109.
7. Fisher, BJ, Naumova, E, Leighton, CC*, et al.* Ki-67: A prognostic factor for low-grade glioma? International Journal of Radiation Oncology Biology Physics 2002:52:996-1001.
8. Leu, S, von Felten, S, Frank, S*, et al.* IDH/MGMT-driven molecular classification of low-grade glioma is a strong predictor for long-term survival. Neuro-Oncology 2013:15:469-79.
9. Arshad, H, Ahmad, Z , Hasan, SH. Gliomas: Correlation of Histologic Grade, Ki67 and p53 Expression with Patient Survival. Asian Pacific Journal of Cancer Prevention 2010:11:1637-1640.

10. Jung, CS, Foerch, C, Schanzer, A*, et al.* Serum GFAP is a diagnostic marker for glioblastoma multiforme. Brain 2007:130:3336-3341.

11. Kaur, B, Khwaja, FW, Severson, EA, Matheny, SL, Brat, DJ , Van Meir, EG. Hypoxia and the hypoxia-inducible-factor pathway in glioma growth and angiogenesis. Neuro-Oncology 2005:7:134-153.

12. Boxerman, JL, Schmainda, KM , Weisskoff, RM. Relative cerebral blood volume maps corrected for contrast agent extravasation significantly correlate with glioma tumor grade, whereas uncorrected maps do not. American Journal of Neuroradiology 2006:27:859-867.

13. Ohgaki, H , Kleihues, P. Genetic pathways to primary and secondary glioblastoma. American Journal of Pathology 2007:170:1445-1453.

14. Sherman, JH, Prevedello, DM, Shah, L*, et al.* MR imaging characteristics of oligodendroglial tumors with assessment of 1p/19q deletion status. Acta Neurochirurgica 2010:152:1827-1834.

15. Sun, H, Yin, L, Li, S*, et al.* Prognostic significance of IDH mutation in adult low-grade gliomas: a meta-analysis. Journal of Neuro-Oncology 2013:1-8.

16. Juratli, TA, Kirsch, M, Robel, K*, et al.* IDH mutations as an early and consistent marker in low-grade astrocytomas WHO grade II and their consecutive secondary high-grade gliomas. Journal of Neuro-Oncology 2012:108:403-410.

17. Qi, ST, Yu, L, Gui, S*, et al.* IDH mutations predict longer survival and response to temozolomide in secondary glioblastoma. Cancer Science 2012:103:269-273.

18. Yan, H, Parsons, DW, Jin, GL*, et al.* IDH1 and IDH2 Mutations in Gliomas. New England Journal of Medicine 2009:360:765-773.

19. Pope, WB, Lai, A, Mehta, R*, et al.* Apparent Diffusion Coefficient Histogram Analysis Stratifies Progression-Free Survival in Newly Diagnosed Bevacizumab-Treated Glioblastoma. American Journal of Neuroradiology 2011:32:882-889.

20. Fabi, A, Russillo, M, Metro, G, Vidiri, A, Di Giovanni, S , Cognetti, F. Pseudoprogression and MGMT Status in Glioblastoma Patients: Implications in Clinical Practice. Anticancer Research 2009:29:2607-2610.

21. Brandes, AA, Franceschi, E, Tosoni, A*, et al.* MGMT promoter methylation status can predict the incidence and outcome of pseudoprogression after concomitant radiochemotherapy in newly diagnosed glioblastoma patients. Journal of Clinical Oncology 2008:26:2192-2197.

22. da Cruz, LCH, Rodriguez, I, Domingues, RC, Gasparetto, EL , Sorensen, AG. Pseudoprogression and Pseudoresponse: Imaging Challenges in the Assessment of Posttreatment Glioma. American Journal of Neuroradiology 2011:32:1978-1985.

23. Lin, SH , Kleinberg, LR. Carmustine wafers: localized delivery of chemotherapeutic agents in CNS malignancies. Expert Review of Anticancer Therapy 2008:8:343-359.

24. Brem, H, Piantadosi, S, Burger, PC*, et al.* Placebo-Controlled Trial of Safety and Efficacy of Intraoperative Controlled Delivery by Biodegradable Polymers of Chemotherapy for Recurrent Gliomas. Lancet 1995:345:1008-1012.

25. Thompson, EM, Frenkel, EP , Neuwelt, EA. The paradoxical effect of bevacizumab in the therapy of malignant gliomas. Neurology 2011:76:87-93.

26. Wang, C, Peacock, D, Rockne, R*, et al.* Prognostic Significance of Growth Kinetics in Newly Diagnosed Glioblastoma: Insights from a Novel Bio-Mathematical Model. Neuro-Oncology 2008:10:868-868.

27. Maiuri, MC, Zalckvar, E, Kimchi, A , Kroemer, G. Self-eating and self-killing: crosstalk between autophagy and apoptosis. Nature Reviews Molecular Cell Biology 2007:8:741-752.

28. Rosenfeldt, MT , Ryan, KM. The multiple roles of autophagy in cancer. Carcinogenesis 2011:32:955-963.

29. Shimizu, H, Kumabe, T, Shirane, R , Yoshimoto, T. Correlation between Choline Level Measured by Proton MR Spectroscopy and Ki-67 Labeling Index in Gliomas. American Journal of Neuroradiology 2000:21:659-665.

30. Podo, F. Tumour phospholipid metabolism. NMR in Biomedicine 1999:12:413-39.

31. Aboagye, EO , Bhujwalla, ZM. Malignant transformation alters membrane choline phospholipid metabolism of human mammary epithelial cells. Cancer Research 1999:59:80-4.

32. McKnight, TR, Smith, KJ, Chu, PW*, et al.* Choline Metabolism, Proliferation, and Angiogenesis in Nonenhancing Grades 2 and 3 Astrocytoma. Journal of Magnetic Resonance Imaging 2011:33:808-816.

33. Petroff, OAC, Graham, GD, Blamire, AM*, et al.* Spectroscopic Imaging of Stroke in Humans - Histopathology Correlates of Spectral Changes. Neurology 1992:42:1349-1354.

34. Barker, PB , Lin, DDM. In vivo proton MR spectroscopy of the human brain. Progress in Nuclear Magnetic Resonance Spectroscopy 2006:49:99-128.

35. Vander Heiden, MG, Cantley, LC , Thompson, CB. Understanding the Warburg Effect: The Metabolic Requirements of Cell Proliferation. Science 2009:324:1029-1033.

36. Zoula, S, Herigault, G, Ziegler, A, Farion, G, Decorps, M , Remy, C. Correlation between the occurrence of H-1-MRS lipid signal, necrosis and lipid droplets during C6 rat glioma development. NMR in Biomedicine 2003:16:199-212.

37. Murphy, PS, Rowland, JI, Viviers, L, Brada, M, Leach, MO , Dzik-Jurasz, ASK. Could assessment of glioma methylene lipid resonance by in vivo H-1-MRS be of clinical value? British Journal of Radiology 2003:76:459-463.

38. Cheng, LL, Anthony, DC, Comite, AR, Black, PM, Tzika, AA , Gonzalez, RG. Quantification of microheterogeneity in glioblastoma multiforme with ex vivo high-resolution magic-angle

spinning (HRMAS) proton magnetic resonance spectroscopy. Neuro-Oncology 2000:2:87-95.

39. Crawford, FW, Khayal, IS, McGue, C*, et al.* Relationship of pre-surgery metabolic and physiological MR imaging parameters to survival for patients with untreated GBM. Journal of Neuro-Oncology 2009:91:337-51.

40. Castillo, M, Smith, JK , Kwock, L. Correlation of myo-inositol levels and grading of cerebral astrocytomas. American Journal of Neuroradiology 2000:21:1645-1649.

41. Griffin, JL , Kauppinen, RA. A metabolomics perspective of human brain tumours. Federation of European Biochemical Societies Journal 2007:274:1132-1139.

42. Choi, C, Ganji, SK, DeBerardinis, RJ*, et al.* 2-hydroxyglutarate detection by magnetic resonance spectroscopy in subjects with IDH-mutated gliomas. Nature Medicine 2012:18:624-629.

43. Bloch, F. Nuclear Induction. Physical Review 1946:70:460-473.

44. Wansapura, JP, Holland, SK, Dunn, RS , Ball, WS. NMR relaxation times in the human brain at 3.0 tesla. Journal of Magnetic Resonance Imaging 1999:9:531-538.

45. Lev, MH, Ozsunar, Y, Henson, JW*, et al.* Glial tumor grading and outcome prediction using dynamic spin-echo MR susceptibility mapping compared with conventional contrast-enhanced MR: Confounding effect of elevated rCBV of oligodendroglimoas. American Journal of Neuroradiology 2004:25:214-221.

46. Hao, DP, Ai, T, Goerner, F, Hu, XM, Runge, VM , Tweedle, M. MRI contrast agents: Basic chemistry and safety. Journal of Magnetic Resonance Imaging 2012:36:1060-1071.

47. Lai, PH, Ho, JT, Chen, WL*, et al.* Brain Abscess and Necrotic Brain Tumor: Discrimination with Proton MR Spectroscopy and Diffusion-Weighted Imaging. American Journal of Neuroradiology 2002:23:1369-1377.

48. Chien, D, Kwong, KK, Gress, DR, Buonanno, FS, Buxton, RB , Rosen, BR. Mr Diffusion Imaging of Cerebral Infarction in Humans. American Journal of Neuroradiology 1992:13:1097-1102.

49. Ross, BD, Moffat, BA, Chenevert, TL*, et al.* Quantification of early brain tumor therapeutic response using functional diffusion maps. Neuro-Oncology 2005:7:394-394.

50. Le Bihan, D, *Imagerie de diffusion in-vivo par résonance magnétique nucléaire*, in *C R Acad Sci (Paris)*1985. 1109-1112.

51. Merboldt, KD, Hanicke, W , Frahm, J. Self-Diffusion Nmr Imaging Using Stimulated Echoes. Journal of Magnetic Resonance 1985:64:479-486.

52. Basser, PJ, Mattiello, J , Lebihan, D. Mr Diffusion Tensor Spectroscopy and Imaging. Biophysical Journal 1994:66:259-267.

53. Turner, R, Lebihan, D, Maier, J, Vavrek, R, Hedges, LK , Pekar, J. Echo-Planar Imaging of Intravoxel Incoherent Motion. Radiology 1990:177:407-414.

54. Moseley, ME, Cohen, Y, Kucharczyk, J*, et al.* Diffusion-Weighted Mr Imaging of Anisotropic Water Diffusion in Cat Central-Nervous-System. Radiology 1990:176:439-445.

55. Tofts, PS , Kermode, AG. Measurement of the Blood-Brain-Barrier Permeability and Leakage Space Using Dynamic Mr Imaging .1. Fundamental-Concepts. Magnetic Resonance in Medicine 1991:17:357-367.

56. Tofts, PS. Modeling tracer kinetics in dynamic Gd-DTPA MR imaging. Journal of Magnetic Resonance Imaging 1997:7:91-101.

57. Brix, G, Semmler, W, Port, R, Schad, LR, Layer, G , Lorenz, WJ. Pharmacokinetic Parameters in Cns Gd-Dtpa Enhanced Mr Imaging. Journal of Computer Assisted Tomography 1991:15:621-628.

58. Larsson, HBW, Stubgaard, M, Frederiksen, JL, Jensen, M, Henriksen, O , Paulson, OB. Quantitation of Blood-Brain-Barrier Defect by Magnetic-Resonance-Imaging and

Gadolinium-Dtpa in Patients with Multiple-Sclerosis and Brain-Tumors. Magnetic Resonance in Medicine 1990:16:117-131.

59. Tofts, PS, Brix, G, Buckley, DL*, et al.* Estimating kinetic parameters from dynamic contrast-enhanced T(1)-weighted MRI of a diffusable tracer: Standardized quantities and symbols. Journal of Magnetic Resonance Imaging 1999:10:223-232.

60. Villringer, A, Rosen, BR, Belliveau, JW*, et al.* Dynamic Imaging with Lanthanide Chelates in Normal Brain - Contrast Due to Magnetic-Susceptibility Effects. Magnetic Resonance in Medicine 1988:6:164-174.

61. Lee, MC, Cha, S, Chang, SM , Nelson, SJ. Partial-volume model for determining white matter and gray matter cerebral blood volume for analysis of gliomas. Journal of Magnetic Resonance Imaging 2006:23:257-266.

62. Knutsson, L, Stahlberg, F , Wirestam, R. Absolute quantification of perfusion using dynamic susceptibility contrast MRI: pitfalls and possibilities. Magnetic Resonance Materials in Physics Biology and Medicine 2010:23:1-21.

63. Toh, CH, Wei, K-C, Chang, C-N, Ng, S-H , Wong, H-F. Differentiation of Primary Central Nervous System Lymphomas and Glioblastomas: Comparisons of Diagnostic Performance of Dynamic Susceptibility Contrast-Enhanced Perfusion MR Imaging without and with Contrast-Leakage Correction. American Journal of Neuroradiology 2013.

64. Boxerman, JL, Prah, DE, Paulson, ES, Machan, JT, Bedekar, D , Schmainda, KM. The Role of Preload and Leakage Correction in Gadolinium-Based Cerebral Blood Volume Estimation Determined by Comparison with MION as a Criterion Standard. American Journal of Neuroradiology 2012:33:1081-1087.

65. Sawlani, RN, Raizer, J, Horowitz, SW*, et al.* Glioblastoma: A Method for Predicting Response to Antiangiogenic Chemotherapy by Using MR Perfusion Imaging-Pilot Study. Radiology 2010:255:622-628.

66. Law, M, Yang, S, Babb, JS*, et al.* Comparison of cerebral blood volume and vascular permeability from dynamic susceptibility contrast-enhanced perfusion MR imaging with glioma grade. American Journal of Neuroradiology 2004:25:746-755.

67. Bottomley, PA. Spatial localization in NMR spectroscopy in vivo. Annals of the New York Academy of Sciences 1987:508:333-48.

68. Star-Lack, J, Nelson, SJ, Kurhanewicz, J, Huang, LR , Vigneron, DB. Improved water and lipid suppression for 3D PRESS CSI using RF band selective inversion with gradient dephasing (BASING). Magnetic Resonance in Medicine 1997:38:311-321.

69. Smith, MA, Koutcher, JA , Zakian, KL. J-Difference Lactate Editing at 3.0 Tesla in the Presence of Strong Lipids. Journal of Magnetic Resonance Imaging 2008:28:1492-1498.

70. Li, XJ, Vigneron, DB, Cha, SM*, et al.* Relationship of MR-derived lactate, mobile lipids, and relative blood volume for gliomas in vivo. American Journal of Neuroradiology 2005:26:760-769.

71. Janich, MA, Schulte, RF, Schwaiger, M , Glaser, SJ. Robust slice-selective broadband refocusing pulses. Journal of Magnetic Resonance 2011:213:126-135.

72. Prock, T, Collins, DJ, Dzik-Jurasz, AS , Leach, MO. An algorithm for the optimum combination of data from arbitrary magnetic resonance phased array probes. Physics in Medicine and Biology 2002:47:N39-46.

73. Provencher, SW. Estimation of metabolite concentrations from localized in vivo proton NMR spectra. Magnetic Resonance in Medicine 1993:30:672-9.

74. McLean, MA, Woermann, FG, Barker, GJ , Duncan, JS. Quantitative analysis of short echo time (1)H-MRSI of cerebral gray and white matter. Magnetic Resonance in Medicine 2000:44:401-11.

75. Tao, X, Gupta, S. N. *Automatic Scan Plane Planning Method for Brain MRI* in *Proc. Intl. Soc. Mag. Reson. Med. 17*. 2009.

76. Weiss, KL, Pan, H, Storrs, J*, et al.* Clinical brain MR imaging prescriptions in Talairach space: Technologist- and computer-driven methods. American Journal of Neuroradiology 2003:24:922-929.

77. Yamasaki, F, Kurisu, K, Satoh, K*, et al.* Apparent Diffusion Coefficient of Human Brain Tumors at MR Imaging. Radiology 2005:235:985-991.

78. Tozer, DJ, Jäger, HR, Danchaivijitr, N*, et al.* Apparent diffusion coefficient histograms may predict low-grade glioma subtype. NMR in Biomedicine 2007:20:49-57.

79. Khayal, IS , Nelson, SJ. Characterization of low-grade gliomas using RGB color maps derived from ADC histograms. Journal of Magnetic Resonance Imaging 2009:30:209-213.

80. Jakab, A, Molnár, P, Emri, M , Berényi, E. Glioma grade assessment by using histogram analysis of diffusion tensor imaging-derived maps. Neuroradiology 2011:53:483-491.

81. Doskaliyev, A, Yamasaki, F, Ohtaki, M*, et al.* Lymphomas and glioblastomas: Differences in the apparent diffusion coefficient evaluated with high b-value diffusion-weighted magnetic resonance imaging at 3.0T. European Journal of Radiology 2012:81:339-344.

82. Wang, S, Kim, S, Chawla, S*, et al.* Differentiation between glioblastomas and solitary brain metastases using diffusion tensor imaging. NeuroImage 2009:44:653-660.

83. Wang, W, Steward, CE , Desmond, PM. Diffusion Tensor Imaging in Glioblastoma Multiforme and Brain Metastases: The Role of p, q, L, and Fractional Anisotropy. American Journal of Neuroradiology 2009:30:203-208.

84. Price, SJ, Peña, A, Burnet, NG*, et al.* Tissue signature characterisation of diffusion tensor abnormalities in cerebral gliomas. European Radiology 2004:14:1909-1917.

85. Goebell, E, Paustenbach, S, Vaeterlein, O*, et al.* Low-Grade and Anaplastic Gliomas: Differences in Architecture Evaluated with Diffusion-Tensor MR Imaging. Radiology 2006:239:217-222.

86. Jenkinson, MD, du Plessis, DG, Smith, TS, Brodbelt, AR, Joyce, KA , Walker, C. Cellularity and apparent diffusion coefficient in oligodendroglial tumours characterized by genotype. Journal of Neuro-Oncology 2010:96:385-392.

87. Khalid, L, Carone, M, Dumrongpisutikul, N*, et al.* Imaging Characteristics of Oligodendrogliomas That Predict Grade. American Journal of Neuroradiology 2012:33:852-857.

88. Emblem, KE, Nedregaard, B, Nome, T*, et al.* Glioma Grading by Using Histogram Analysis of Blood Volume Heterogeneity from MR-derived Cerebral Blood Volume Maps. Radiology 2008:247:808-817.

89. Law, M, Young, R, Babb, J, Pollack, E , Johnson, G. Histogram Analysis versus Region of Interest Analysis of Dynamic Susceptibility Contrast Perfusion MR Imaging Data in the Grading of Cerebral Gliomas. American Journal of Neuroradiology 2007:28:761-766.

90. Law, M, Brodsky, JE, Babb, J*, et al.* High cerebral blood volume in human gliomas predicts deletion of chromosome 1p: Preliminary results of molecular studies in gliomas with elevated perfusion. Journal of Magnetic Resonance Imaging 2007:25:1113-1119.

91. Cha, S, Lupo, JM, Chen, M-H*, et al.* Differentiation of Glioblastoma Multiforme and Single Brain Metastasis by Peak Height and Percentage of Signal Intensity Recovery Derived from Dynamic Susceptibility-Weighted Contrast-Enhanced Perfusion MR Imaging. American Journal of Neuroradiology 2007:28:1078-1084.

92. Mills, SJ, Patankar, TA, Haroon, HA, Balériaux, D, Swindell, R , Jackson, A. Do Cerebral Blood Volume and Contrast Transfer Coefficient Predict Prognosis in Human Glioma? American Journal of Neuroradiology 2006:27:853-858.

93. Patankar, TF, Haroon, HA, Mills, SJ*, et al.* Is volume transfer coefficient (K-trans) related to histologic grade in human gliomas? American Journal of Neuroradiology 2005:26:2455-2465.

94. Noguchi, T, Yoshiura, T, Hiwatashi, A*, et al.* Perfusion Imaging of Brain Tumors Using Arterial Spin-Labeling: Correlation with Histopathologic Vascular Density. American Journal of Neuroradiology 2008:29:688-693.

95. García-Gómez, J, Luts, J, Julià-Sapé, M*, et al.* Multiproject–multicenter evaluation of automatic brain tumor classification by magnetic resonance spectroscopy. Magnetic Resonance Materials in Physics, Biology and Medicine 2009:22:5-18.

96. McKnight, TR, Noworolski, SM, Vigneron, DB , Nelson Dr rer Nat, SJ. An automated technique for the quantitative assessment of 3D-MRSI data from patients with glioma. Journal of Magnetic Resonance Imaging 2001:13:167-177.

97. Panigrahy, A, Krieger, MD, Gonzalez-Gomez, I*, et al.* Quantitative Short Echo Time 1H-MR Spectroscopy of Untreated Pediatric Brain Tumors: Preoperative Diagnosis and Characterization. American Journal of Neuroradiology 2006:27:560-572.

98. Hwang, JH, Egnaczyk, GF, Ballard, E, Dunn, RS, Holland, SK , Ball, WS. Proton MR spectroscopic characteristics of pediatric pilocytic astrocytomas. American Journal of Neuroradiology 1998:19:535-40.

99. Schlemmer, HP, Bachert, P, Herfarth, KK, Zuna, I, Debus, J , van Kaick, G. Proton MR Spectroscopic Evaluation of Suspicious Brain Lesions After Stereotactic Radiotherapy. American Journal of Neuroradiology 2001:22:1316-1324.

100. Howe, FA, Barton, SJ, Cudlip, SA*, et al.* Metabolic profiles of human brain tumors using quantitative in vivo 1H magnetic resonance spectroscopy. Magnetic Resonance in Medicine 2003:49:223-232.

101. Sjobakk, TE, Johansen, R, Bathen, TF*, et al.* Metabolic profiling of human brain metastases using in vivo proton MR spectroscopy at 3T. BMC Cancer 2007:7.

102. Fan, G, Sun, B, Wu, Z, Guo, Q , Guo, Y. In vivo single-voxel proton MR spectroscopy in the differentiation of high-grade gliomas and solitary metastases. Clinical Radiology 2004:59:77-85.

103. Kim, J-h, Chang, K-H, Na, DG*, et al.* 3T 1H-MR Spectroscopy in Grading of Cerebral Gliomas: Comparison of Short and Intermediate Echo Time Sequences. American Journal of Neuroradiology 2006:27:1412-1418.

104. Majós, C, Julià-Sapé, M, Alonso, J*, et al.* Brain Tumor Classification by Proton MR Spectroscopy: Comparison of Diagnostic Accuracy at Short and Long TE. American Journal of Neuroradiology 2004:25:1696-1704.

105. Weis, J, Ring, P, Olofsson, T, Ortiz-Nieto, F , Wikström, J. Short echo time MR spectroscopy of brain tumors: Grading of cerebral gliomas by correlation analysis of normalized spectral amplitudes. Journal of Magnetic Resonance Imaging 2010:31:39-45.

106. Weybright, P, Sundgren, PC, Maly, P*, et al.* Differentiation Between Brain Tumor Recurrence and Radiation Injury Using MR Spectroscopy. American Journal of Roentgenology 2005:185:1471-1476.

107. Elmogy, SA, Mousa, AE, Elashry, MS , Megahed, AM. MR spectroscopy in post-treatment follow up of brain tumors. The Egyptian Journal of Radiology and Nuclear Medicine 2011:42:413-424.

108. Dowling, C, Bollen, AW, Noworolski, SM*, et al.* Preoperative Proton MR Spectroscopic Imaging of Brain Tumors: Correlation with Histopathologic Analysis of Resection Specimens. American Journal of Neuroradiology 2001:22:604-612.

109. Gasparovic, C, Bedrick, EJ, Mayer, AR*, et al.* Test-retest reliability and reproducibility of short-echo-time spectroscopic imaging of human brain at 3T. Magnetic Resonance in Medicine 2011:66:324-332.

110. Sijens, P , Oudkerk, M. 1H chemical shift imaging characterization of human brain tumor and edema. European Radiology 2002:12:2056-2061.

111. Opstad, KS, Griffiths, JR, Bell, BA , Howe, FA. Apparent T2 relaxation times of lipid and macromolecules: A study of high-grade tumor spectra. Journal of Magnetic Resonance Imaging 2008:27:178-184.

112. Opstad, KS, Murphy, MM, Wilkins, PR, Bell, BA, Griffiths, JR , Howe, FA. Differentiation of metastases from high-grade gliomas using short echo time 1H spectroscopy. Journal of Magnetic Resonance Imaging 2004:20:187-192.

113. Wright, AJ, Fellows, GA, Griffiths, JR, Wilson, M, Bell, BA , Howe, FA. Ex-vivo HRMAS of adult brain tumours: metabolite quantification and assignment of tumour biomarkers. Molecular Cancer 2010:9.

114. Guzmán-de-Villoria, JA, Sánchez-González, J, Muñoz, L*, et al.* 1H MR Spectroscopy in the Assessment of Gliomatosis Cerebri. American Journal of Roentgenology 2007:188:710-714.

115. Stadlbauer, A, Gruber, S, Nimsky, C*, et al.* Preoperative grading of gliomas by using metabolite quantification with high-spatial-resolution proton MR spectroscopic imaging. Radiology 2006:238:958-969.

116. Taillibert, S, Guillevin, R, Menuel, C*, et al.* Brain lymphoma: usefulness of the magnetic resonance spectroscopy. Journal of Neuro-Oncology 2008:86:225-229.

117. Park, SM, Kim, HS, Jahng, G-H, Ryu, C-W , Kim, SY. Combination of high-resolution susceptibility-weighted imaging and the apparent diffusion coefficient: added value to brain tumour imaging and clinical feasibility of non-contrast MRI at 3 T. British Journal of Radiology 2010:83:466-475.

118. Law, M, Yang, S, Wang, H*, et al.* Glioma Grading: Sensitivity, Specificity, and Predictive Values of Perfusion MR Imaging and Proton MR Spectroscopic Imaging Compared with Conventional MR Imaging. American Journal of Neuroradiology 2003:24:1989-1998.

119. Di Costanzo, A, Scarabino, T, Trojsi, F*, et al.* Multiparametric 3T MR approach to the assessment of cerebral gliomas: tumor extent and malignancy. Neuroradiology 2006:48:622-631.

120. Gupta, RK, Cloughesy, TF, Sinha, U*, et al.* Relationships Between Choline Magnetic Resonance Spectroscopy, Apparent Diffusion Coefficient and Quantitative Histopathology in Human Glioma. Journal of Neuro-Oncology 2000:50:215-226.

121. Gupta, RK, Sinha, U, Cloughesy, TF , Alger, JR. Inverse correlation between choline magnetic resonance spectroscopy signal intensity and the apparent diffusion coefficient in human glioma. Magnetic Resonance in Medicine 1999:41:2-7.

122. Calvar, JA, Meli, FJ, Romero, C*, et al.* Characterization of brain tumors by MRS, DWI and Ki-67 labeling index. Journal of Neuro-Oncology 2005:72:273-280.

123. Khayal, IS, Crawford, FW, Saraswathy, S*, et al.* Relationship between choline and apparent diffusion coefficient in patients with gliomas. Journal of Magnetic Resonance Imaging 2008:27:718-725.

124. Bian, W, Khayal, IS, Lupo, JM*, et al.* Multiparametric characterization of grade 2 glioma subtypes using magnetic resonance spectroscopic, perfusion, and diffusion imaging. Translational Oncology 2009:2:271-80.

125. Zeng, Q-S, Li, C-F, Liu, H, Zhen, J-H , Feng, D-C. Distinction Between Recurrent Glioma and Radiation Injury Using Magnetic Resonance Spectroscopy in Combination With Diffusion-Weighted Imaging. International Journal of Radiation Oncology*Biology*Physics 2007:68:151-158.

126. Fink, JR, Carr, RB, Matsusue, E*, et al.* Comparison of 3 Tesla proton MR spectroscopy, MR perfusion and MR diffusion for distinguishing glioma recurrence from posttreatment effects. Journal of Magnetic Resonance Imaging 2012:35:56-63.

127. Ekinci, G, Akpınar, İN, Baltacıoğlu, F*, et al.* Early-postoperative magnetic resonance imaging in glial tumors: prediction of tumor regrowth and recurrence. European Journal of Radiology 2003:45:99-107.

128. Tihan, T, Barletta, J, Parney, I, Lamborn, K, Sneed, PK , Chang, S. Prognostic value of detecting recurrent glioblastoma multiforme in surgical specimens from patients after radiotherapy: should pathology evaluation alter treatment decisions? Human Pathology 2006:37:272-282.

129. Tofts, PS, Benton, CE, Weil, RS*, et al.* Quantitative analysis of whole-tumor Gd enhancement histograms predicts malignant transformation in low-grade gliomas. Journal of Magnetic Resonance Imaging 2007:25:208-214.

130. Rees, J, Watt, H, Jäger, HR*, et al.* Volumes and growth rates of untreated adult low-grade gliomas indicate risk of early malignant transformation. European Journal of Radiology 2009:72:54-64.

131. Gladwish, A, Koh, ES, Hoisak, J*, et al.* Evaluation of early imaging response criteria in glioblastoma multiforme. Radiation Oncology 2011:6:121.

132. Ellingson, B, Malkin, M, Rand, S*, et al.* Volumetric analysis of functional diffusion maps is a predictive imaging biomarker for cytotoxic and anti-angiogenic treatments in malignant gliomas. Journal of Neuro-Oncology 2011:102:95-103.

133. Moffat, BA, Chenevert, TL, Meyer, CR*, et al.* The functional diffusion map: an imaging biomarker for the early prediction of cancer treatment outcome. Neoplasia 2006:8:259-67.

134. Dessouky, BAM, El Abd, OL, El Gowily, AG , El Khawalka, YM. Functional diffusion map of malignant brain tumors: A surrogate imaging biomarker for early prediction of therapeutic response and patient survival. The Egyptian Journal of Radiology and Nuclear Medicine 2010:41:441-451.

135. Hamstra, DA, Galbán, CJ, Meyer, CR, *et al.* Functional Diffusion Map As an Early Imaging Biomarker for High-Grade Glioma: Correlation With Conventional Radiologic Response and Overall Survival. Journal of Clinical Oncology 2008:26:3387-3394.

136. Ellingson, BM, Cloughesy, TF, Lai, A, *et al.* Graded functional diffusion map–defined characteristics of apparent diffusion coefficients predict overall survival in recurrent glioblastoma treated with bevacizumab. Neuro-Oncology 2011:13:1151-1161.

137. Price, S, Jena, R, Burnet, N, Carpenter, T, Pickard, J , Gillard, J. Predicting patterns of glioma recurrence using diffusion tensor imaging. European Radiology 2007:17:1675-1684.

138. Paldino, MJ, Desjardins, A, Friedman, HS, Vredenburgh, JJ , Barboriak, DP. A change in the apparent diffusion coefficient after treatment with bevacizumab is associated with decreased survival in patients with recurrent glioblastoma multiforme. British Journal of Radiology 2012:85:382-389.

139. Romano, A, Fasoli, F, Ferrante, M, Ferrante, L, Fantozzi, LM , Bozzao, A. Fiber density index, fractional anisotropy, adc and clinical motor findings in the white matter of patients with glioblastoma. European Radiology 2008:18:331-336.

140. Yamasaki, F, Sugiyama, K, Ohtaki, M, *et al.* Glioblastoma treated with postoperative radio-chemotherapy: Prognostic value of apparent diffusion coefficient at MR imaging. European Journal of Radiology 2010:73:532-537.

141. Pope, WB, Kim, HJ, Huo, J, *et al.* Recurrent glioblastoma multiforme: ADC histogram analysis predicts response to bevacizumab treatment. Radiology 2009:252:182-9.

142. Law, M, Oh, S, Babb, JS*, et al.* Low-Grade Gliomas: Dynamic Susceptibility-weighted Contrast-enhanced Perfusion MR Imaging—Prediction of Patient Clinical Response1. Radiology 2006:238:658-667.

143. Caseiras, GB, Chheang, S, Babb, J*, et al.* Relative cerebral blood volume measurements of low-grade gliomas predict patient outcome in a multi-institution setting. European Journal of Radiology 2010:73:215-220.

144. Galban, CJ, Chenevert, TL, Meyer, CR*, et al.* The parametric response map is an imaging biomarker for early cancer treatment outcome. Nature Medicine 2009:15:572-576.

145. Danchaivijitr, N, Waldman, AD, Tozer, DJ*, et al.* Low-grade gliomas: Do changes in rCBV measurements at longitudinal perfusion-weighted MR imaging predict malignant transformation? Radiology 2008:247:170-178.

146. Hattingen, E, Raab, P, Franz, K*, et al.* Prognostic value of choline and creatine in WHO grade II gliomas. Neuroradiology 2008:50:759-67.

147. Kuznetsov, YE, Caramanos, Z, Antel, SB*, et al.* Proton magnetic resonance spectroscopic imaging can predict length of survival in patients with supratentorial gliomas. Neurosurgery 2003:53:565-574.

148. Guillevin, R, Menuel, C, Duffau, H*, et al.* Proton magnetic resonance spectroscopy predicts proliferative activity in diffuse low-grade gliomas. Journal of Neuro-Oncology 2008:87:181-187.

149. Saraswathy, S, Crawford, FW, Lamborn, KR*, et al.* Evaluation of MR markers that predict survival in patients with newly diagnosed GBM prior to adjuvant therapy. Journal of Neuro-Oncology 2009:91:69-81.

150. Guillevin, R, Menuel, C, Abud, L*, et al.* Proton MR spectroscopy in predicting the increase of perfusion MR imaging for WHO grade II gliomas. Journal of Magnetic Resonance Imaging 2012:35:543-550.

151. Caseiras, GB, Ciccarelli, O, Altmann, DR*, et al.* Low-Grade Gliomas: Six-month Tumor Growth Predicts Patient Outcome Better than Admission Tumor Volume, Relative Cerebral Blood Volume, and Apparent Diffusion Coefficient. Radiology 2009:253:505-512.

152. Hlaihel, C, Guilloton, L, Guyotat, J, Streichenberger, N, Honnorat, J , Cotton, F. Predictive value of multimodality MRI using conventional, perfusion, and spectroscopy MR in anaplastic transformation of low-grade oligodendrogliomas. Journal of Neuro-Oncology 2010:97:73-80.

153. Henson, JW, Gaviani, P , Gonzalez, RG. MRI in treatment of adult gliomas. Lancet Oncology 2005:6:167-175.

154. Dempsey, MF, Condon, BR , Hadley, DM. Measurement of Tumor "Size" in Recurrent Malignant Glioma: 1D, 2D, or 3D? American Journal of Neuroradiology 2005:26:770-776.

155. Ellingson, BM, Cloughesy, TF, Lai, A, Nghiemphu, PL, Mischel, PS , Pope, WB. Quantitative volumetric analysis of conventional MRI response in recurrent glioblastoma treated with bevacizumab. Neuro-Oncology 2011:13:401-409.

156. Shukla, D, Huilgol, NG, Trivedi, N , Mekala, C. T2 weighted MRI in assessment of volume changes during radiotherapy of high grade gliomas. Journal of Cancer Research and Therapeutics 2005:1:235-8.

157. Peca, C, Pacelli, R, Elefante, A*, et al.* Early clinical and neuroradiological worsening after radiotherapy and concomitant temozolomide in patients with glioblastoma: Tumour progression or radionecrosis? Clinical Neurology and Neurosurgery 2009:111:331-334.

158. Sanghera, P, Perry, J, Sahgal, A*, et al.* Pseudoprogression following chemoradiotherapy for glioblastoma multiforme. Canadian Journal of Neurological Sciences 2010:37:36-42.

159. Bauman, G, Pahapill, P, Macdonald, D, Fisher, B, Leighton, C , Cairncross, G. Low grade glioma: a measuring radiographic response to radiotherapy. Canadian Journal of Neurological Sciences 1999:26:18-22.

160. Constantin, AA, Bajcsy, BR , Nelson, CS. Unsupervised Segmentation of Brain Tissue in Multivariate Mri. 2010 7th Ieee International Symposium on Biomedical Imaging: From Nano to Macro 2010:89-92.

161. Ross, BD, Moffat, BA, Lawrence, TS*, et al.* Evaluation of cancer therapy using diffusion magnetic resonance imaging. Molecular Cancer Therapeutics 2003:2:581-587.

162. Ellingson, BM, Malkin, MG, Rand, SD*, et al.* Validation of functional diffusion maps (fDMs) as a biomarker for human glioma cellularity. Journal of Magnetic Resonance Imaging 2010:31:538-548.

163. Huo, J, Okada, K, Kim, H*, et al.* CADrx for GBM Brain Tumors: Predicting Treatment Response from Changes in Diffusion-Weighted MRI. Algorithms 2009:2:1350-1367.

164. Price, SJ, Burnet, NG, Donovan, T*, et al.* Diffusion Tensor Imaging of Brain Tumours at 3.0T: A Potential Tool for Assessing White Matter Tract Invasion? Clinical Radiology 2003:58:455-462.

165. Lin, Y-C, Wang, C-C, Wai, YY*, et al.* Significant Temporal Evolution of Diffusion Anisotropy for Evaluating Early Response to Radiosurgery in Patients with Vestibular Schwannoma: Findings from Functional Diffusion Maps. American Journal of Neuroradiology 2010:31:269-274.

166. Reijneveld, J, van der Grond, J, Ramos, L, Bromberg, J , Taphoorn, M. Proton MRS imaging in the follow-up of patients with suspected low-grade gliomas. Neuroradiology 2005:47:887-891.

167. Dyke, J, Sanelli, P, Voss, H*, et al.* Monitoring the effects of BCNU chemotherapy Wafers (Gliadel) in glioblastoma multiforme with proton magnetic resonance spectroscopic imaging at 3.0 Tesla. Journal of Neuro-Oncology 2007:82:103-110.

168. Liimatainen, T, Hakumäki, JM, Kauppinen, RA , Ala-Korpela, M. Monitoring of gliomas in vivo by diffusion MRI and 1H MRS during gene therapy-induced apoptosis:

interrelationships between water diffusion and mobile lipids. NMR in Biomedicine 2009:22:272-279.

169. Li, Y, Lupo, JM, Polley, MY*, et al.* Serial analysis of imaging parameters in patients with newly diagnosed glioblastoma multiforme. Neuro-Oncology 2011:13:546-557.

170. Wright, AJ, Fellows, G, Byrnes, TJ*, et al.* Pattern recognition of MRSI data shows regions of glioma growth that agree with DTI markers of brain tumor infiltration. Magnetic Resonance in Medicine 2009:62:1646-1651.

171. Hamstra, DA, Chenevert, TL, Moffat, BA*, et al.* Evaluation of the functional diffusion map (fDM) as an early biomarker of TTP and OS in high grade glioma. International Journal of Radiation Oncology Biology Physics 2005:63:S261-S262.

172. Ross, BD, Hamstra, DA, Chenevert, TL*, et al.* Assessment of the functional diffusion map (fDM) as an imaging biomarker for early stratification of glioma clinical response. Journal of Clinical Oncology 2006:24:62s-62s.

173. Ellingson, BM, Cloughesy, TF, Zaw, T*, et al.* Functional diffusion maps (fDMs) evaluated before and after radiochemotherapy predict progression-free and overall survival in newly diagnosed glioblastoma. Neuro-Oncology 2012:14:333-343.

174. O'Connor, JPB, Jackson, A, Parker, GJM , Jayson, GC. DCE-MRI biomarkers in the clinical evaluation of antiangiogenic and vascular disrupting agents. British Journal of Cancer 2007:96:189-195.

175. HYCCN. 2013 [cited 2013 30/08/13]; Available from: http://www.hyccn.nhs.uk/AboutUs/index.htm.

176. Kim, DH, Adalsteinsson, E, Glover, GH , Spielman, DM. Regularized higher-order in vivo shimming. Magnetic Resonance in Medicine 2002:48:715-722.

177. Jenkinson, M, Beckmann, CF, Behrens, TE, Woolrich, MW , Smith, SM. FSL. NeuroImage 2012:62:782-790.

178. Jenkinson, M , Smith, S. A global optimisation method for robust affine registration of brain images. Medical Image Analysis 2001:5:143-156.

179. Pena, A, Green, HAL, Carpenter, TA, Price, SJ, Pickard, JD , Gillard, JH. Enhanced visualization and quantification of magnetic resonance diffusion tensor imaging using the p : q tensor decomposition. British Journal of Radiology 2006:79:101-109.

180. Basser, PJ , Pierpaoli, C. Microstructural and physiological features of tissues elucidated by quantitative-diffusion-tensor MRI. Journal of Magnetic Resonance Series B 1996:111:209-219.

181. Parker, GJM, Roberts, C, Macdonald, A*, et al.* Experimentally-derived functional form for a population-averaged high-temporal-resolution arterial input function for dynamic contrast-enhanced MRI. Magnetic Resonance in Medicine 2006:56:993-1000.

182. Markwardt, CB. Non-linear Least-squares Fitting in IDL with MPFIT. Astronomical Data Analysis Software and Systems Xviii 2009:411:251-254.

183. Benner, T, Heiland, S, Erb, G, Forsting, M , Sartor, K. Accuracy of gamma-variate fits to concentration-time curves from dynamic susceptibility-contrast enhanced MRI: Influence of time resolution, maximal signal drop and signal-to-noise. Magnetic Resonance Imaging 1997:15:307-317.

184. Chan, AA , Nelson, SJ. Simplified gamma-variate fitting of perfusion curves. 2004 2nd Ieee International Symposium on Biomedical Imaging: Macro to Nano, Vols 1 and 2 2004:1067-1070.

185. Redner, RA , Walker, HF. Mixture Densities, Maximum-Likelihood and the Em Algorithm. Siam Review 1984:26:195-237.

186. Smith, SM. Fast robust automated brain extraction. Human Brain Mapping 2002:17:143-155.

187. Otsu, N. A Threshold Selection Method from Gray-Level Histograms. Systems, Man and Cybernetics, IEEE Transactions on 1979:9:62-66.

188. Catalaa, I, Henry, R, Dillon, WP*, et al.* Perfusion, diffusion and spectroscopy values in newly diagnosed cerebral gliomas. NMR in Biomedicine 2006:19:463-475.

189. Provenzale, JM, York, G, Moya, MG*, et al.* Correlation of relative permeability and relative cerebral blood volume in high-grade cerebral neoplasms. American Journal of Roentgenology 2006:187:1036-1042.

190. Haroon, HA, Patankar, TF, Zhu, XP*, et al.* Comparison of cerebral blood volume maps generated from T-2* and T-1 weighted MRI data in intra-axial cerebral tumours. British Journal of Radiology 2007:80:161-168.

191. Mills, SJ, Soh, C, O'Connor, JPB*, et al.* Enhancing Fraction in Glioma and Its Relationship to the Tumoral Vascular Microenvironment: A Dynamic Contrast-Enhanced MR Imaging Study. American Journal of Neuroradiology 2010:31:726-731.

192. Friedman, SN, Bambrough, PJ, Kotsarini, C, Khandanpour, N , Hoggard, N. Semi-automated and automated glioma grading using dynamic susceptibility-weighted contrast-enhanced perfusion MRI relative cerebral blood volume measurements. British Journal of Radiology 2012:85:E1204-E1211.

193. Roy, B, Gupta, RK, Maudsley, AA*, et al.* Utility of multiparametric 3-T MRI for glioma characterization. Neuroradiology 2013:55:603-613.

194. Upadhyay, N , Waldman, AD. Conventional MRI evaluation of gliomas. British Journal of Radiology 2011:84 Spec No 2:S107-11.

195. Storey, JD , Tibshirani, R. Statistical significance for genomewide studies. Proceedings of the National Academy of Sciences of the United States of America 2003:100:9440-9445.

196. Inoue, T, Ogasawara, K, Beppu, T, Ogawa, A , Kabasawa, H. Diffusion tensor imaging for preoperative evaluation of tumor grade in gliomas. Clinical Neurology and Neurosurgery 2005:107:174-180.

197. Kang, Y, Choi, SH, Kim, YJ*, et al.* Gliomas: Histogram Analysis of Apparent Diffusion Coefficient Maps with Standard- or High-b-Value Diffusion-weighted MR Imaging-Correlation with Tumor Grade. Radiology 2011:261:882-890.

198. Castillo, M, Smith, JK, Kwock, L , Wilber, K. Apparent diffusion coefficients in the evaluation of high-grade cerebral gliomas. American Journal of Neuroradiology 2001:22:60-64.

199. Min, Z-g, Niu, C, Rana, N, Ji, H-m , Zhang, M. Differentiation of pure vasogenic edema and tumor-infiltrated edema in patients with peritumoral edema by analyzing the relationship of axial and radial diffusivities on 3.0T MRI. Clinical Neurology and Neurosurgery 2013:115:1366-1370.

200. Liu, X, Tian, W, Kolar, B*, et al.* MR diffusion tensor and perfusion-weighted imaging in preoperative grading of supratentorial nonenhancing gliomas. Neuro-Oncology 2011:13:447-455.

201. Newman, S, Haughton, VM, Yetkin, Z*, et al.* T1, T2 and proton density measurements in the grading of cerebral gliomas. European Radiology 1993:3:49-52.

202. Bland, JM , Altman, DG. Statistics notes: Measurement error proportional to the mean .23. British Medical Journal 1996:313:106-106.

203. Manton, DJ, Turnbull, LW, Liney, G , Garcia-Alvarez, R. Proton Spectroscopic Imaging Metabolite Ratios in Human Brain: Measurement Error Proportional to the Mean. Journal of Magnetic Resonance Imaging 2010:31:1538-1539.

204. Zhang, N, Zhang, LJ, Qiu, BS, Meng, L, Wang, XY , Hou, BL. Correlation of volume transfer coefficient Ktrans with histopathologic grades of gliomas. Journal of Magnetic Resonance Imaging 2012:36:355-363.

205. Jung, SC, Yeom, Ja, Kim, J-H*, et al.* Glioma: Application of Histogram Analysis of Pharmacokinetic Parameters from T1-Weighted Dynamic Contrast-Enhanced MR Imaging to Tumor Grading. American Journal of Neuroradiology 2014.

206. Cha, S, Yang, L, Johnson, G*, et al.* Comparison of microvascular permeability measurements, K-trans, determined with conventional steady-state T1-weighted and first-pass T2*-weighted MR imaging methods in gliomas and meningiomas. American Journal of Neuroradiology 2006:27:409-417.

207. Di Costanzo, A, Scarabino, T, Trojsi, F*, et al.* Proton MR spectroscopy of cerebral gliomas at 3 T: spatial heterogeneity, and tumour grade and extent. European Radiology 2008:18:1727-1735.

208. Van Cauter, S, De Keyzer, F, Sima, DM*, et al.* Integrating diffusion kurtosis imaging, dynamic susceptibility-weighted contrast-enhanced MRI, and short echo time chemical shift imaging for grading gliomas. Neuro-Oncology 2014.

209. Langer, DL, van der Kwast, TH, Evans, AJ, Trachtenberg, J, Wilson, BC , Haider, MA. Prostate Cancer Detection With Multi-parametric MRI: Logistic Regression Analysis of Quantitative T2, Diffusion-Weighted Imaging, and Dynamic Contrast-Enhanced MRI. Journal of Magnetic Resonance Imaging 2009:30:327-334.

210. Schafer, ML, Maurer, MH, Synowitz, M*, et al.* Low-grade (WHO II) and anaplastic (WHO III) gliomas: differences in morphology and MRI signal intensities. European Radiology 2013:23:2846-2853.

211. Hajek, M, Burian, M , Dezortova, M. Application of LCModel for quality control and quantitative in vivo 1H MR spectroscopy by short echo time STEAM sequence. MAGMA 2000:10:6-17.

212. Traber, F, Block, W, Lamerichs, R, Gieseke, J , Schild, HH. H-1 metabolite relaxation times at 3.0 tesla: Measurements of T1 and T2 values in normal brain and determination of regional differences in transverse relaxation. Journal of Magnetic Resonance Imaging 2004:19:537-545.

213. Londono, A, Castillo, M, Armao, D, Kwock, L , Suzuki, K. Unusual MR spectroscopic imaging pattern of an astrocytoma: Lack of elevated choline and high myo-inositol and glycine levels. American Journal of Neuroradiology 2003:24:942-945.

214. Rijpkema, M, Schuuring, J, van der Meulen, Y*, et al.* Characterization of oligodendrogliomas using short echo time H-1 MR spectroscopic imaging. NMR in Biomedicine 2003:16:12-18.

215. Guo, J, Yao, CJ, Chen, H*, et al.* The relationship between Cho/NAA and glioma metabolism: implementation for margin delineation of cerebral gliomas. Acta Neurochirurgica 2012:154:1361-1370.

216. Wen, PY, Macdonald, DR, Reardon, DA*, et al.* Updated Response Assessment Criteria for High-Grade Gliomas: Response Assessment in Neuro-Oncology Working Group. Journal of Clinical Oncology 2010:28:1963-1972.

217. Sottoriva, A, Spiteri, I, Piccirillo, SGM*, et al.* Intratumor heterogeneity in human glioblastoma reflects cancer evolutionary dynamics. Proceedings of the National Academy of Sciences 2013.

218. Sunwoo, L, Choi, SH, Park, CK*, et al.* Correlation of apparent diffusion coefficient values measured by diffusion MRI and MGMT promoter methylation semiquantitatively analyzed

with MS-MLPA in patients with glioblastoma multiforme. Journal of Magnetic Resonance Imaging 2013:37:351-358.

219. Romano, A, Calabria, LF, Tavanti, F*, et al.* Apparent diffusion coefficient obtained by magnetic resonance imaging as a prognostic marker in glioblastomas: correlation with MGMT promoter methylation status. European Radiology 2013:23:513-520.

220. Iliadis, G, Kotoula, V, Chatzisotiriou, A*, et al.* Volumetric and MGMT parameters in glioblastoma patients: Survival analysis. BMC Cancer 2012:12.

221. Ellingson, BM, Sahebjam, S, Kim, HJ*, et al.* Pretreatment ADC Histogram Analysis Is a Predictive Imaging Biomarker for Bevacizumab Treatment but Not Chemotherapy in Recurrent Glioblastoma. American Journal of Neuroradiology 2013.

222. Mills, SJ, Soh, C, Rose, CJ*, et al.* Candidate Biomarkers of Extravascular Extracellular Space: A Direct Comparison of Apparent Diffusion Coefficient and Dynamic Contrast-Enhanced MR Imaging-Derived Measurement of the Volume of the Extravascular Extracellular Space in Glioblastoma Multiforme. American Journal of Neuroradiology 2010:31:549-553.

223. Pirzkall, A, McGue, C, Saraswathy, S*, et al.* Tumor regrowth between surgery and initiation of adjuvant therapy in patients with newly diagnosed glioblastoma. Neuro-Oncology 2009:11:842-852.

224. Sun, YS, Cui, Y, Tang, L*, et al.* Early Evaluation of Cancer Response by a New Functional Biomarker: Apparent Diffusion Coefficient. American Journal of Roentgenology 2011:197:W23-W29.

225. Federau, C, Meuli, R, O'Brien, K, Maeder, P , Hagmann, P. Perfusion Measurement in Brain Gliomas with Intravoxel Incoherent Motion MRI. American Journal of Neuroradiology 2013.

226. Ludemann, L, Grieger, W, Wurm, R, Wust, P , Zimmer, C. Quantitative measurement of leakage volume and permeability in gliomas, meningiomas and brain metastases with dynamic contrast-enhanced MRI. Magnetic Resonance Imaging 2005:23:833-841.

227. Armstrong, CL, Hunter, JV, Hackney, D*, et al.* MRI changes due to early-delayed conformal radiotherapy and postsurgical effects in patients with brain tumors. International Journal of Radiation Oncology Biology Physics 2005:63:56-63.

228. Lustig, M, Donoho, D , Pauly, JM. Sparse MRI: The application of compressed sensing for rapid MR imaging. Magnetic Resonance in Medicine 2007:58:1182-1195.

229. Han, S, Paulsen, JL, Zhu, G*, et al.* Temporal/spatial resolution improvement of in vivo DCE-MRI with compressed sensing-optimized FLASH. Magnetic Resonance Imaging 2012:30:741-752.

230. Lebel, RM, Jones, J, Ferre, JC, Law, M , Nayak, KS. Highly Accelerated Dynamic Contrast Enhanced Imaging. Magnetic Resonance in Medicine 2014:71:635-644.

231. Geethanath, S, Baek, HM, Ganji, SK*, et al.* Compressive Sensing Could Accelerate H-1 MR Metabolic Imaging in the Clinic. Radiology 2012:262:985-994.

232. Cao, P , Wu, EX. Accelerating phase-encoded proton MR spectroscopic imaging by compressed sensing. Journal of Magnetic Resonance Imaging 2014.

233. Moeller, S, Yacoub, E, Olman, CA*, et al.* Multiband multislice GE-EPI at 7 tesla, with 16-fold acceleration using partial parallel imaging with application to high spatial and temporal whole-brain fMRI. Magnetic Resonance in Medicine 2010:63:1144-1153.

234. Horsfield, MA. Mapping eddy current induced fields for the correction of diffusion-weighted echo planar images. Magnetic Resonance Imaging 1999:17:1335-1345.

235. Van Cauter, S, Veraart, J, Sijbers, J*, et al.* Gliomas: Diffusion Kurtosis MR Imaging in Grading. Radiology 2012:263:492-501.

236. Eichner, C, Jafari-Khouzani, K, Cauley, S*, et al.* Slice accelerated gradient-echo spin-echo dynamic susceptibility contrast imaging with blipped CAIPI for increased slice coverage. Magnetic Resonance in Medicine 2013.

237. van Westen, D, Petersen, ET, Wirestam, R*, et al.* Correlation between arterial blood volume obtained by arterial spin labelling and cerebral blood volume in intracranial tumours. Magnetic Resonance Materials in Physics Biology and Medicine 2011:24:211-223.

238. Park, I, Chen, AP, Zierhut, ML, Ozturk-Isik, E, Vigneron, DB , Nelson, SJ. Implementation of 3 T Lactate-Edited 3D H-1 MR Spectroscopic Imaging with Flyback Echo-Planar Readout for Gliomas Patients. Annals of Biomedical Engineering 2011:39:193-204.

239. Hu, S, Lustig, M, Balakrishnan, A*, et al.* 3D Compressed Sensing for Highly Accelerated Hyperpolarized C-13 MRSI With In Vivo Applications to Transgenic Mouse Models of Cancer. Magnetic Resonance in Medicine 2010:63:312-321.

240. Hikishima, K, Yag, K, Numano, T*, et al.* Volumetric q-space imaging by 3D diffusion-weighted MRI. Magnetic Resonance Imaging 2008:26:437-445.

241. McNab, JA, Gallichan, D , Miller, KL. 3D Steady-State Diffusion-Weighted Imaging With Trajectory Using Radially Batched Internal Navigator Echoes (TURBINE). Magnetic Resonance in Medicine 2010:63:235-242.